The Ultrafiltration of Biological Macromolecules

by

VINCENT LEE VILKER

B.S.Ch.E. University of Wisconsin (1967)

Submitted in Partial Fulfillment

of the Requirements for the

Degree of Doctor of Philosophy

at the

MASSACHUSETTS INSTITUTE OF TECHNOLOGY

September, 1975

(Ch.E. February 1976)

Signature of Author: _____

Department of Chemical Engineering

Certified by: _____

Clark K. Colton, Thesis Supervisor

_____

Kenneth A. Smith, Thesis Supervisor

Accepted by: _____

G. C. Williams, Chairman,
Departmental Committee on Graduate Theses

Dedicated to

the Value of sifting and winnowing,
it has helped me to technical insights
and more importantly, to an inner
acceptance of how things are;
Joseph P., he gave me the confidence
to make some critical decisions;
Joseph K., he directed my thoughts
and feelings into a single purpose;
and lastly, All those who have walked
beside me, no matter how far.

ACKNOWLEDGEMENTS

This thesis was completed with the kind assistance of many people. I wish to thank Professors Kenneth Smith and Clark Colton for the technical guidance given to this work, for the excellence which they demanded from it and for financial support whenever it was required.

Professor Robert S. Lees helped to determine the initial direction and always provided excellent laboratory support facilities. My work with protein and lipoprotein chemistry was greatly facilitated by the assistance of Dr. P. K. George, Gene DiBenedetto, Bernadette Cusik and Ann Gifford.

Robert Bratzler was a source of valuable technical discussion and moral support. Donald Green's careful and excellent experimental investigations provided valuable incentive and opened new areas of inquiry.

Anthony Moscaritollo and Stan LaShoto of Draper Laboratories supplied guidance and support for the fabrication of the optical ultrafiltration cell.

Professors Irwin Pless and Robert Hulsizer, Bernard Wadsworth and many others at the PEPR Project in the Laboratory for Nuclear Science supplied the technique and facilities for the interpretation of the photographic data.

The cooperation and high quality craftsmanship of the Chemical Engineering Shop personnel, Reed Fulton, Paul Bletzer and Jack Russell is gratefully acknowledged. A special thanks is extended to Stan Mitchell, not only for the able assistance which he provided at several different stages, but for the readiness with which he gave it.

An intangible ingredient was supplied by a group which made nearly every day a little brighter; Reed F., Paul B., Jack R., Stan M., Art C., Charlie F., Tony and Sam.

The typing and assembly of this thesis has been ably managed by Hilary Hayes. I also thank Nancy Cappallo, Roberta Caruso, Ann Rosenthal and Maria Tseng for their typing assistance.

I thank Anthony DiLeo for both the major technical insights which grew from many valuable conversations and for his help in finding solutions to many smaller obstacles. Working with him for the past two years has been a fond and rewarding experience.

TABLE OF CONTENTS

ABSTRACT

The Ultrafiltration of Biological Macromolecules

by Vincent L. Vilker

Submitted to the Department of Chemical Engineering in September, 1975, in partial fulfillment of the requirements for the degree of Doctor of Philosophy

The relationship between ultrafiltrate flux and pressure driving force is primarily influenced by concentration polarization. A more fundamental understanding of this relationship is sought in terms of the physiocochemical properties of the solution. To assess the significance of the protein as a thermodynamic barrier when concentrated at the membrane surface, osmotic pressure measurements of concentrated albumin solutions (47 gm/100 ml solution in 0.15 M saline) were made in a specially designed membrane osmometer at the pH levels of 4.5, 5.4 and 7.4. The osmotic pressure increased sharply with increasing protein concentration and increasing solution pH. The data were in agreement with an 'a priori' prediction of osmotic pressure made from McMillan-Mayer solution theory. When dilute albumin solutions were ultrafiltered in a stirred laboratory cell, flux was also found to be a strong increasing function of increasing solution pH.

A theoretical and experimental investigation was conducted for the stagnant cell ultrafiltration of these same albumin solutions. The theoretical model, with the assumption of constant solution properties, consists of the usual convective diffusion equations and the driving force for volumetric flux is taken to be $\Delta P - \Delta\pi$, where ΔP is the applied hydrostatic pressure and $\Delta\pi$ the osmotic pressure difference across the membrane. A perturbation solution shows that the concentration at the membrane corresponds to $\Delta P - \Delta\pi \cong 0$ and the flux diminishes like the inverse square root of time. A shadowgraph technique was employed in the experimental study for determination of concentration profiles in the polarization layer. The quantity of ultrafiltrate at any time was measured with a sensitive liquid level displacement device. Experiments at the three pH levels confirmed that the membrane concentration was very close to the concentration for which $\Delta P - \Delta\pi \simeq 0$. The flux decay rate was observed to vary slightly with solution pH, but was always close to the inverse square root of time dependence. The model failed to predict the observed increase in ultrafiltrate yields for increasing solution pH. This difference is thought to be the result of an increasing solute diffusivity with increasing solution pH.

Thesis Supervisors: Clark K. Colton
Associate Professor of Chemical Engineering

Kenneth A. Smith
Professor of Chemical Engineering

LIST OF FIGURES

LIST OF TABLES

List of Symbols

a	radius of macro-ion, ℓ
a_o	defined by equation (4-18)
A_o	flux parameter defined by equation (5-26)
A_1, A_2, A_3	empirically derived virial coefficients
B_2, B_3	virial coefficients derived from solution theory
B_g	gel layer permeability, m/ℓ-t-psi
D	diffusivity, ℓ^2/t
D_s	phenomenological transport coefficient, ℓ^2/t
e	protonic charge, 4.802×10^{-10} statcoul
F	Stigter-Hill parameter
G	solute concentration as gm/100 ml solution (gm %)
K_m	intrinsic membrane permeability, m/ℓ^2-t-psi
k	Boltzmann's constant, 1.38×10^{-16} ergs/deg, or statcoul-statvolts/°K
ℓ	gel layer thickness, ℓ
ℓ_m	membrane thickness, ℓ
M	molarity concentration, moles/L^3 solution
m	molality concentration, moles/kg solvent
M_o	solvent molecular weight
M_p	solute molecular weight
N	mole fraction concentration
N_A	Avogadro's Number, 6.03×10^{23}/mole
ΔP	pressure drop
p	number density concentration, molecules/ℓ^3
Pe	Peclet number for membrane (equation 4-17)

Pe_g Peclet number for gel (equation 4-43)

R center-to-center separation between interacting macro-ions, ℓ

r distance measured from center of macro-ion, ℓ

T absolute temperature

t time

V volume, ℓ^3

v_s ultrafiltrate flux, ℓ/t

ν_A solute partial specific volume, ℓ^3/m

$\hat{v}_o$ defined by equation (4-44)

W intermolecular potential, volts

w_p concentration as mass/L. solvent

Y,y distance above membrane, ℓ

Z valence

Greek Symbols

γ activity coefficient

δ polarization layer thickness

ε membrane void fraction (Chapter 4)

ε dielectric constant of solvent, 78.54 statcoul/statvolt-cm, rational c.g.s. system (Chapter 2)

ζ zeta potential defined by equation (2-35)

η refractive index

θ dimensionless concentration

κ Debye-Hückel parameter, ℓ^{-1}

μ chemical potential

$\overline{\nu}$ average number of bound ions per macro-ion

π osmotic pressure

ρ density, m/ℓ^3

$\tilde{\rho}_A$ partial specific density of solute, m/ℓ^3

$\tilde{\rho}_s$ partial specific density of solvent, m/ℓ^3

σ membrane reflection coefficient

Φ_A solute concentration as volume fraction

χ sieving factor

ω_A solute concentration as weight fraction

ψ potential in ion cloud surrounding macro-ion, volts

SUMMARY

CONTENTS OF SUMMARY

I. The Osmotic Pressure of Concentrated Protein Solutions and Its Significance to Ultrafiltration

The separation of biological macromolecules from the various solutions in which they are dissolved is of physiological and industrial importance. In recent years, ultrafiltration has been successfully applied to many separation problems (1,2,3,4). The build-up of a concentrated solute layer at the membrane surface is generally the most significant factor which influences the ultrafiltration of these macromolecular solutions. This phenomenon is usually termed concentration polarization.

The objective of this study is to gain a more fundamental understanding of the relationship between ultrafiltrate flux and the pressure driving force in terms of the physiocochemical properties of the solution. The typical dependence of flux on applied pressure is shown in Figure 1-1 for the case of ultrafiltration in a stirred cell.

When only pure solvent, which passes freely through the membrane, is present, the pressure and volumetric flux are linearly related. When a solute species which is rejected by the membrane is present, deviations from this simple linear relationship arise, and the flux eventually reaches a constant level where it becomes insensitive to further increases in pressure. The physical basis of this reduction in ultrafiltrate flux depends on the extent to which the polarized layer acts, on the one hand, as a thermodynamic barrier which reduces the available pressure driving force by an increase in osmotic pressure (as in reverse osmosis) and, on the other, as a hydrodynamic barrier which offers a resistance to flow (as in mechanical filtration). Both modes of action have been suggested in previous treatments of ultrafiltration (1,5,6,7,8).

FIGURE 1-1

ULTRAFILTRATION FLUX vs. PRESSURE

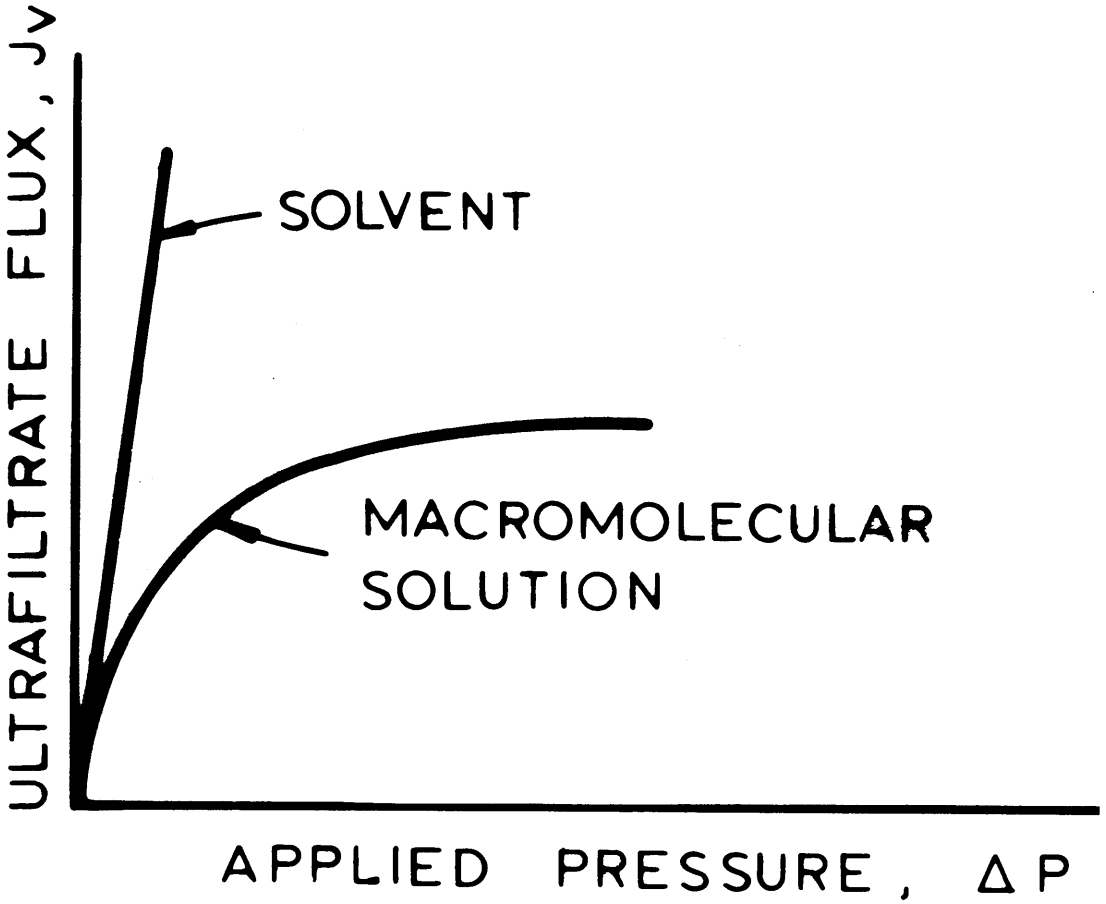

$$J_v = \frac{\Delta P - \Delta \pi}{R_m + R_p}$$

The model solute which this work focuses on is the highly charged, globular protein, bovine serum albumin which has a molecular weight of about 69,000. Results of a previous fundamental study of ultrafiltration of albumin solutions by others have suggested that the reduction in flux is attributable to the increased osmotic pressure at the membrane surface (7).

A. The Osmotic Pressure of Bovine Serum Albumin Solutions

To assess the significance of the protein as a thermodynamic barrier when concentrated at the surface of an ultrafiltration membrane, osmotic pressure measurements of concentrated BSA solutions were made in a specially designed high pressure, static-type membrane osmometer. These measurements were made at three different solution pH levels.

1. Experimental

From extrapolations of osmotic pressure measurements made at low and moderate concentrations of albumin by Scatchard in the 40's (9,10) and Kappos and Pauly in the 60's (11), it was anticipated that a membrane osmometer capable of achieving high pressures would be needed to carry out determinations in concentrated solutions. The essential features of the specially designed high pressure, static-type membrane osmometer are shown in Figure 3-1.

The osmometer cell consists of two chambers, one in which is placed the solvent, in this case 0.15 M saline, and in the other the macromolecular solution. The chambers are separated by a membrane which is completely impermeable to the macromolecule but which permits free passage of water and ions. After the chambers are filled, capillaries which have been prefilled with the respective liquids of each chamber

FIGURE 3-1 HIGH PRESSURE MEMBRANE OSMOMETER

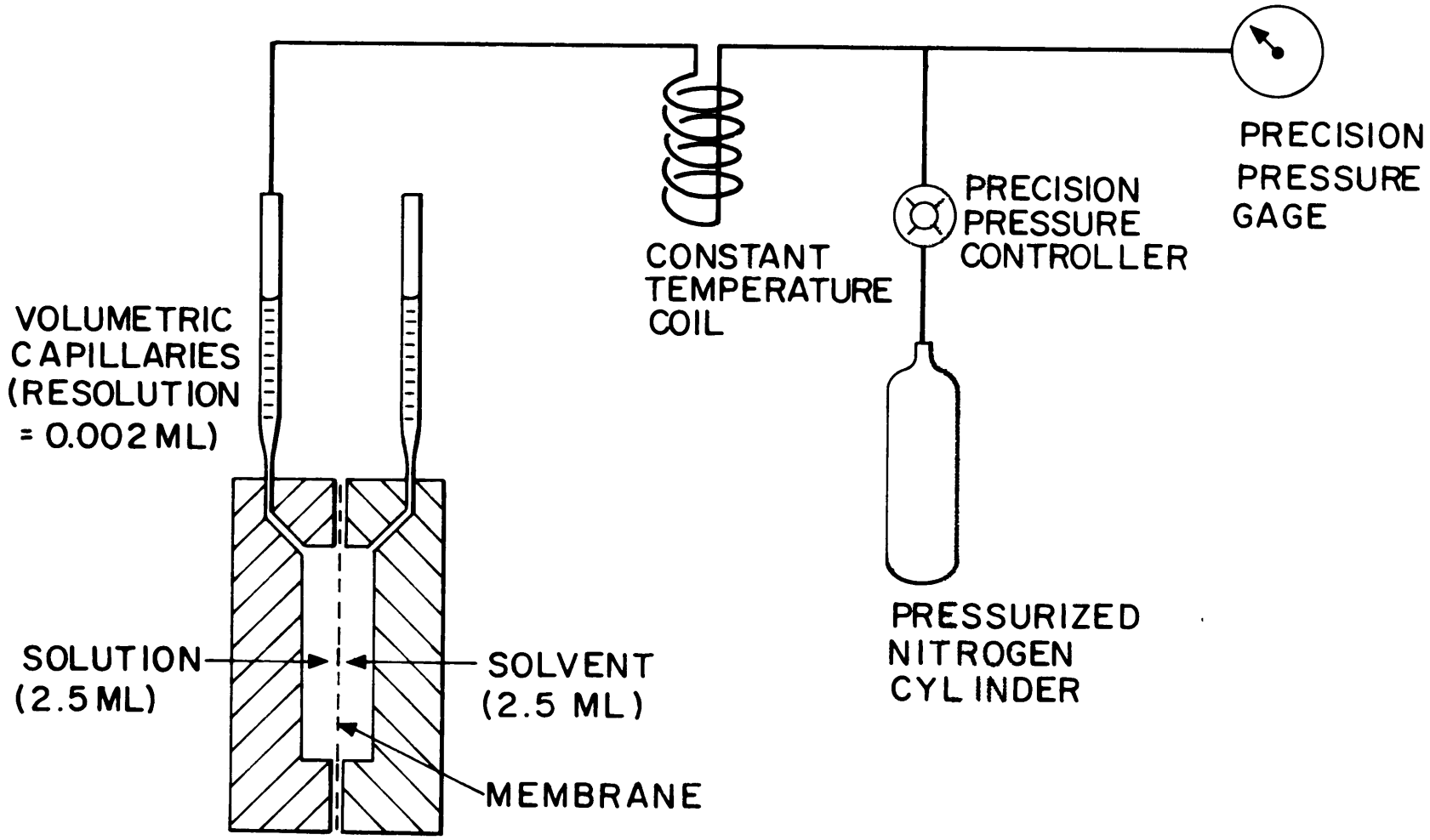

are connected as shown to each chamber. The applied gas pressure is then quickly set to an estimated value and subsequently adjusted in the direction indicated by the slight movement in the capillary liquid levels. For instance, if the initial estimated pressure is below the solution osmotic pressure, solvent will be transferred across the membrane from the solvent side to the solution side. As soon as bulk flow is detected by a change in the capillary levels, the applied pressure is increased. After a few such pressure adjustments, an applied pressure is found for which no further changes in liquid level occur. At this point the applied hydrostatic head is equal to the osmotic pressure of the solution. Because mixing in the solution chamber is by molecular diffusion only, it is essential to avoid a large volumetric transfer of solvent across the membrane so as to prevent large concentration gradients which would slow the approach to thermodynamic equilibrium.

The resolution of the volumetric capillaries allow for the detection of volumetric transfers as small as one one-thousandth of the solution chamber volume.

The osmometer cell and the coil were immersed in a constant temperature bath which was controlled to within ±0.1°C. All determinations were made at 25°C.

A precision pressure gage and controller allowed pressure to be measured within a few centimeters of water, or about five hundredths of a psi.

A detailed view of the osmometer cell is shown in Figure 3-2. The chambers are formed by sandwiching a membrane between two cylindrical pieces of plexiglass, in each of which is a shallow (0.25 cm deep) circular depression. The membrane is supported against the high hydrostatic

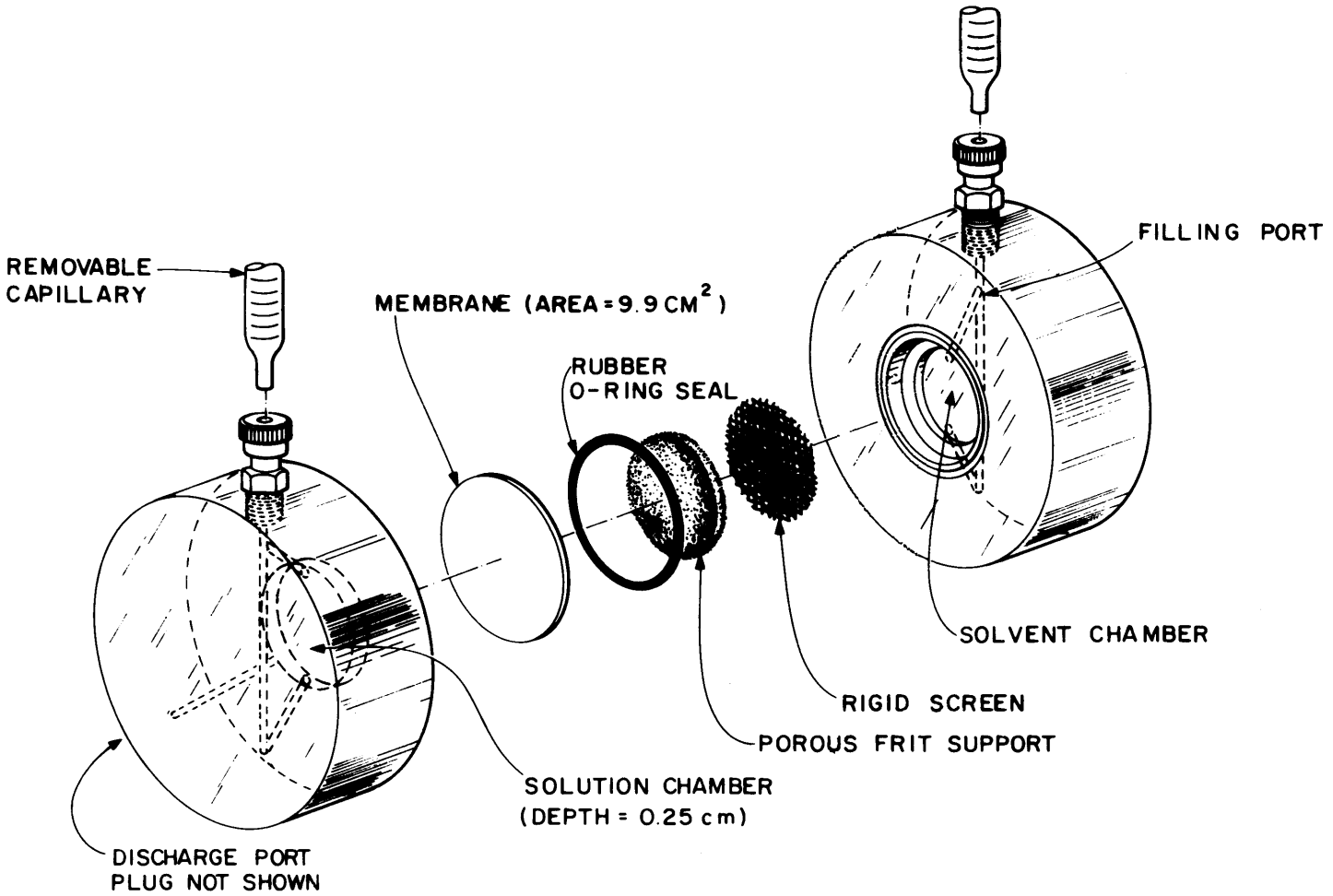

FIGURE 3-2 MEMBRANE OSMOMETER CELL

pressures which are imposed on the solution side by a metal screen and a porous frit. A rubber O-ring impressed on the solvent side of the membrane localizes the mechanical force when the two halves are clamped together and seals the unit up to applied pressure as high as 80 psig.

Abcor HFA-180 membranes were used in the osmometer, and were selected, in part, because of their durability and complete rejection of albumin. Five membranes were used in the course of about 50 experimental runs and there were no detectable differences in the results for the different membranes. A membrane was replaced only when it became excessively distorted after several uses, especially for the higher pressure determinations.

With the capillaries removed, each chamber was filled by inserting a syringe to the bottom of the filling channels. As the liquid was forced into the bottom of each chamber, air was forced out the top, thereby preventing the formation of any bubbles.

After the chambers were filled, the volumetric capillaries which had been pre-filled with the appropriate solutions, were fixed into place, the hydrostatic pressure source was quickly attached to the solution-side capillary and the entire device submerged in the constant temperature bath.

2. Results

Using a molecular weight of 69,000 for albumin (9), ideal solution theory predicts an osmotic pressure of only 250 cm H_2O, or 3.5 psi, at the maximum concentration studied, as well as osmotic pressure independence of solution pH. The very different results of our determinations for solutions of albumin in .15 M saline are shown in Figure 3-5.

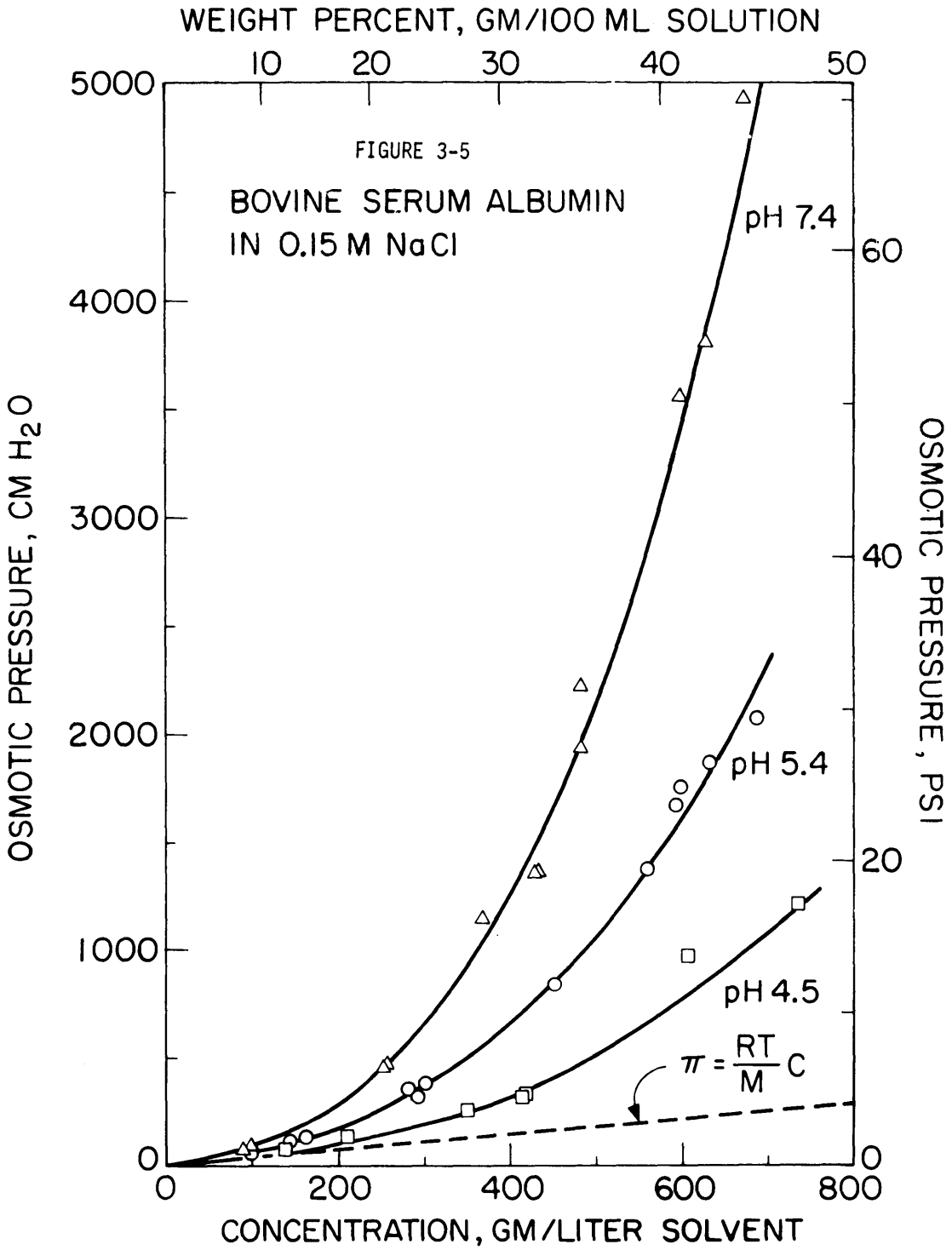
WEIGHT PERCENT, GM/100 ML SOLUTION
10
20
30
40
50
5000
4000
3000
2000
1000
0
FIGURE 3-5
BOVINE SERUM ALBUMIN
IN 0.15 M NaCl
pH 7.4
pH 5.4
pH 4.5
$\pi = \frac{RT}{M} C$
OSMOTIC PRESSURE, CM H_2O
OSMOTIC PRESSURE, PSI
60
40
20
0
0
200
400
600
800
CONCENTRATION, GM/LITER SOLVENT

The osmotic pressure is expressed in terms of centimeters of water head on the left side of the figure and as pounds per square inch on the right. Concentration units are grams of albumin per liter of saline solvent on the bottom axis and as weight per cent on the top of the figure. Measurements were made at pH 7.4, 5.4, and 4.5.

At low concentrations, the osmotic pressure at all three pH levels converges to the value predicted by van't Hoff equation for ideal solutions. However, at the other extreme - high concentration and physiological pH - the osmotic pressure reaches 70 psi. This is about five times greater than the pressure of the more acid pH 4.5 solution and about twenty times higher than predicted for an ideal solution.

From the tests for thermodynamic equilibrium, a precision of better than 5% is thought representative for a pressure measurement. Albumin concentration measurements by the biuret method, which involves two sample dilutions, were also controlled to within 5% precision limits.

The curves shown on this figure are the results of a semi-empirical correlation derived to describe these measurements and is discussed below.

3. Discussion

At equilibrium in an ideal solution, the statement of equality of the chemical potential of the molecular species which <u>can</u> pass freely through the membrane leads to equation (S-1) for relating osmotic pressure, π , to the concentration of the species which <u>cannot</u> pass the membrane, where w_p is expressed in units of weight per liter of solvent (<u>12</u>). R is the gas constant, T is the absolute temperature and M_p is the molecular weight of the impermeable species.

$$\pi = \frac{RT}{M_p} w_p \qquad \text{(S-1)}$$

This first equation, however, is valid only in the limiting case of infinite dilution for an uncharged solute. The next two equations are corrections which account for the deviations from such an ideal solution.

When the solute species is charged, and the solvent phase includes microions such as Na^+ and Cl^-, the imbalance of microion concentration resulting from the ion cloud surrounding each macromolecule that carries a net charge leads to an increase in osmotic pressure. This pressure is called the ideal Donnan pressure and is included in equation (S-2). This equation may be derived by imposition of the constraint of electroneutrality across the membrane along with the statement of the equality of chemical potentials. Z is the net charge of the protein molecule and is calculated from pH titration data and chloride ion binding data which are found in the literature. m_s is the concentration of microions in the equilibrium phase of the solvent chamber.

$$\pi = RT \left[\frac{w_p}{M_p} + 2\sqrt{\frac{w_p^2 Z^2}{4M_p^2} + m_s^2} - 2m_s \right] \qquad \text{(S-2)}$$

Equation (S-3) includes a virial expansion to account for the interactions between protein molecules when these solutions become moderately concentrated, that is, greater than about 25 wt %. The data was describable by the use of two virial terms, A_2 and A_3 . Because the protein-protein interactions are dependent on the charge state of the protein molecules, A_2 and A_3 were correlated as functions of Z by nonlinear regression analysis.

This last equation then correlates the osmotic pressure data by a

separate accounting of the ideal Donnan effect and the non-idealities of concentrated protein solutions. The results of the correlation are shown in Table 3-3.

$$\pi = \frac{RT}{M_p}\left[w_p + A_2 w_p^{\,2} + A_3 w_p^{\,3}\right] + RT\left[2\sqrt{\left(\frac{Zw_p}{2M_p}\right)^2 + m_s^{\,2}} - 2m_s\right] \quad \text{(S-3)}$$

TABLE 3-3

Osmotic Pressure Correlation Coefficients

$$A_2 = k_1 + k_2 Z + k_3 Z^2$$

$$A_3 = k_1' + k_2' Z + k_3' Z^2$$

	k_1 or k_1'	k_2 or k_2'	k_3 or k_3'
A_2	2.170×10^{-3}	-2.558×10^{-4}	-2.107×10^{-5}
A_3	4.657×10^{-7}	-1.185×10^{-7}	4.993×10^{-8}

A_2 and A_3 Evaluated @ pH 4.5, 5.4 and 7.4

pH	A_2	A_3
4.5	5.921×10^{-4}	5.135×10^{-6}
5.4	2.752×10^{-3}	9.870×10^{-6}
7.4	-1.381×10^{-3}	2.785×10^{-5}

The semi-empirical correlation fitted to this data is compared in Figure 3-8 with the albumin osmotic pressure measurements of Scatchard et al. (10), shown as circles, and those of Kappos and Pauly (11), shown as triangles. The results are plotted as reduced osmotic pressure, that is, osmotic pressure divided by concentration, and demonstrate the close agreement for all three investigations concerning the intercept of reduced osmotic pressure at zero concentration. The value of 0.367 yields a first virial coefficient from which the 69,000 molecular weight was originally calculated by Scatchard. Actually, the data of Kappos and Pauly extrapolate to a slightly lower intercept, and yield a molecular weight of 72,000.

The data of Kappos and Pauly were obtained at conditions of pH and ionic strength which were different from those used in our experiments. Nevertheless, the correction fitted to our data is in reasonable agreement with their results.

Scatchard's results are slightly below our results at equivalent conditions of solution pH and ionic strength in the region of moderate protein concentration.

McMillan-Mayer solution theory (13,14) enables one to express the osmotic pressure and the salt distribution in a Donnan system in terms of expansions in powers of the macro-ion concentration (virial expansion). The second and third virial coefficients were computed from the estimated potential of average force between macro-ions. The parameters in this potential, which was assumed entirely repulsive, were estimated from measurements of albumin conductance in salt solutions (15). The result of this 'a priori' method for calculating osmotic pressure is

FIGURE 3-8

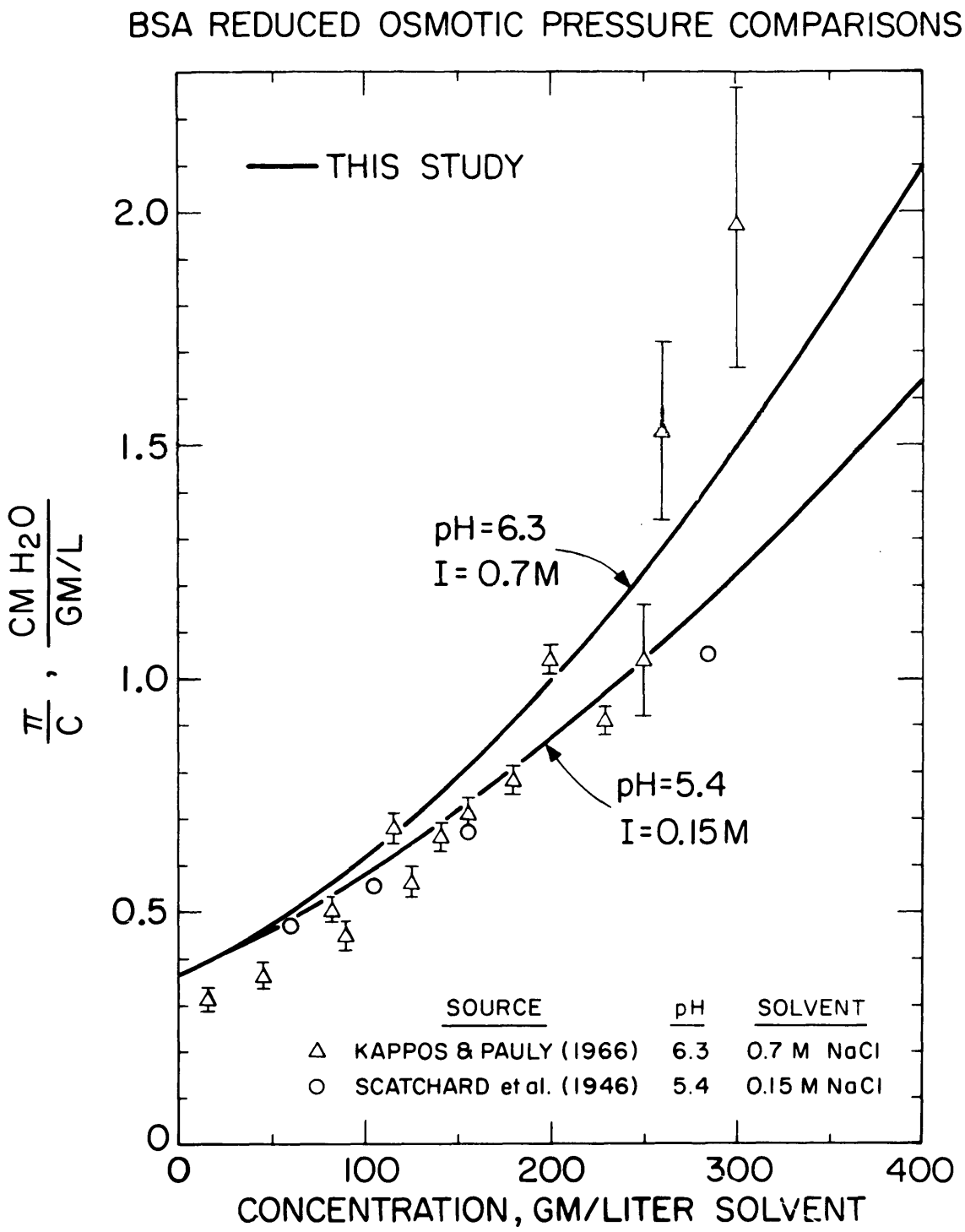
BSA REDUCED OSMOTIC PRESSURE COMPARISONS
THIS STUDY
pH=6.3
I=0.7M
pH=5.4
I=0.15M
π/C, CM H2O / GM/L
2.0
1.5
1.0
0.5
0
0
100
200
300
400
CONCENTRATION, GM/LITER SOLVENT
SOURCE
pH
SOLVENT
△ KAPPOS & PAULY (1966) 6.3 0.7 M NaCl
○ SCATCHARD et al. (1946) 5.4 0.15 M NaCl

given by equation (2-41).

$$\pi = \frac{kT \; N_A}{1000 \; M_p} \left[w_p + B_2' \, w_p^2 + B_3' \, w_p^3 \right] \qquad (2\text{-}41)$$

where N_A is Avagadro's number, k is Boltzmann's constant. The virial coefficients B_2' and B_3', at infinite dilution of the protein, are functions only of the interaction potential, and therefore solution pH. Table 2-4 summarizes the coefficients for each pH. The comparison of this result with the osmotic pressure data, on a reduced basis, is shown in Figure 3-9. For the coefficients evaluated at infinite dilution, the solid curves apply.

TABLE 2-4

Infinite Dilution Virial Coefficients

pH	$\bar{Z}$	$B_2' \times 10^{+3}$ ℓ solvent/gm BSA	$B_3' \times 10^{+6}$ (ℓ solvent/gm BSA)^2
4.5	+4.5	6.18	23.9
5.4	-9.1	6.65	27.6
7.4	-20.4	8.55	45.6

The figure shows that equation (2-41) predicts higher osmotic pressures than were observed experimentally. Part of this over-prediction is probably the result of a failure to properly account for the change in solution ionic strength as protein concentration

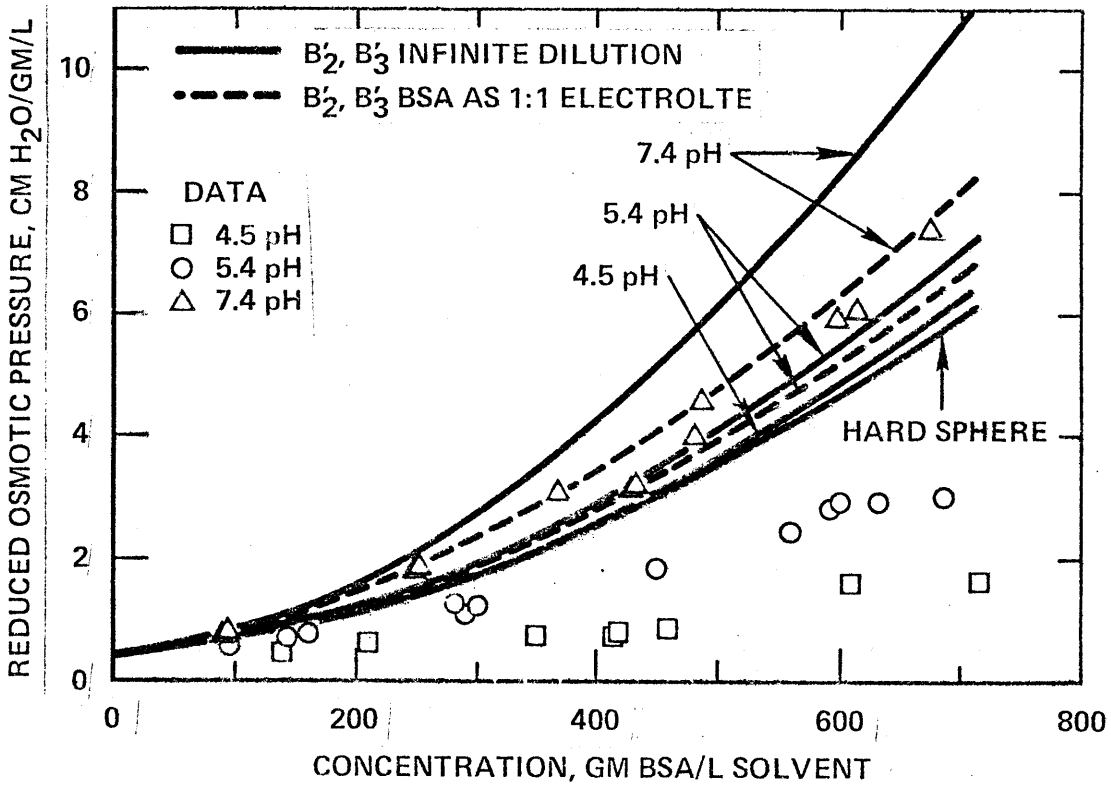

Figure 3-9. Comparison of Experiment with Solution Theory.

increases. Moeller, et al. (15) found that their conductivity measurements were better described by their theoretical model when the macro-ion was treated as a 1:1 electrolyte. In effect, this means that solution ionic strength increases with increasing protein concentration. The amount of this increase is dependent on protein charge. As ionic strength increases, the electrostatic repulsion potential between macroions decreases.

The result of this method of calculating solution ionic strength is that the coefficients B_2' and B_3' become dependent on protein concentration. This dependency increases as macro-ion charge increases. When the virial coefficients are computed in this way, the dashed curves of Figure 3-9 apply. At 4.5 pH, the macro-ion charge is so small (+4.5) that this correction to the virial coefficients is negligible and the two methods are superimposed on the figure.

The figure shows that the solution theory model agrees with experimental data only at 7.4 pH, the condition for which albumin carries the highest charge studied, 20.4 mv. The lowest pressure predicted by the model corresponds to the isoelectric condition of the macro-ion, $\bar{Z}=0$, indicated as the "hard sphere" curve on the figure. At 700 gm BSA/liter, this curve indicates a pressure which is about three times larger than the experimentally observed pressure at 4.5 pH, the condition of smallest charge studied experimentally. The model indicates that at this pH, albumin closely approximates a "hard sphere."

The most probable fault with the solution theory model is the neglect of the attractive forces between the macro-ions. Gutfreund's osmotic pressure measurements for salt-free albumin solutions near

the isoelectric point (16) indicate the existence of such forces. The differences between theory and observation are greatest for the lower charge states of albumin when attractive forces are not included in the model.

B. The Significance of Osmotic Pressure to Ultrafiltration

1. Albumin

The strong dependence of osmotic pressure on solution pH suggested that some simple ultrafiltration experiments with solutions of bovine serum albumin in which only the pH was varied might yield insights to the significance of osmotic pressure in controlling ultrafiltration flux. For this purpose, a conventional stirred cell ultrafiltration apparatus was employed. The applied pressure was varied over the range of 2.5 to 55 psig and was measured with a mercury manometer or a pressure gauge. Bulk protein concentration in the ultrafiltration cell was held constant by continuously replenishing the cell with .15 molar saline solvent which was fed from a reservoir during the course of an experiment. Stirring rates were measured with a stroboscope and were maintained sufficiently high so that the boundary layer over the membrane was in the turbulent regime for all experiments. Ultrafiltrate flux was monitored by timed collections into a graduated cylinder. The bulk albumin concentration was the same in all experiments, 90 grams per liter or 8.5 gm% in .15 M unbuffered saline.

The results on Figure 1-2 show that at every pressure level investigated, the ultrafiltrate flux is highest for the pH 7.4 solution, the solution for which highest osmotic pressures have been measured. In the pressure independent region, above about 40 psig, the flux of the pH 7.4 solution is almost twice that of the acid pH 4.5 solution.

Since it is not unreasonable to imagine albumin concentrations at the membrane surface as high as 45 gm%, which is well below the solubility limit of about 60 gm % (7,17), the osmotic pressure

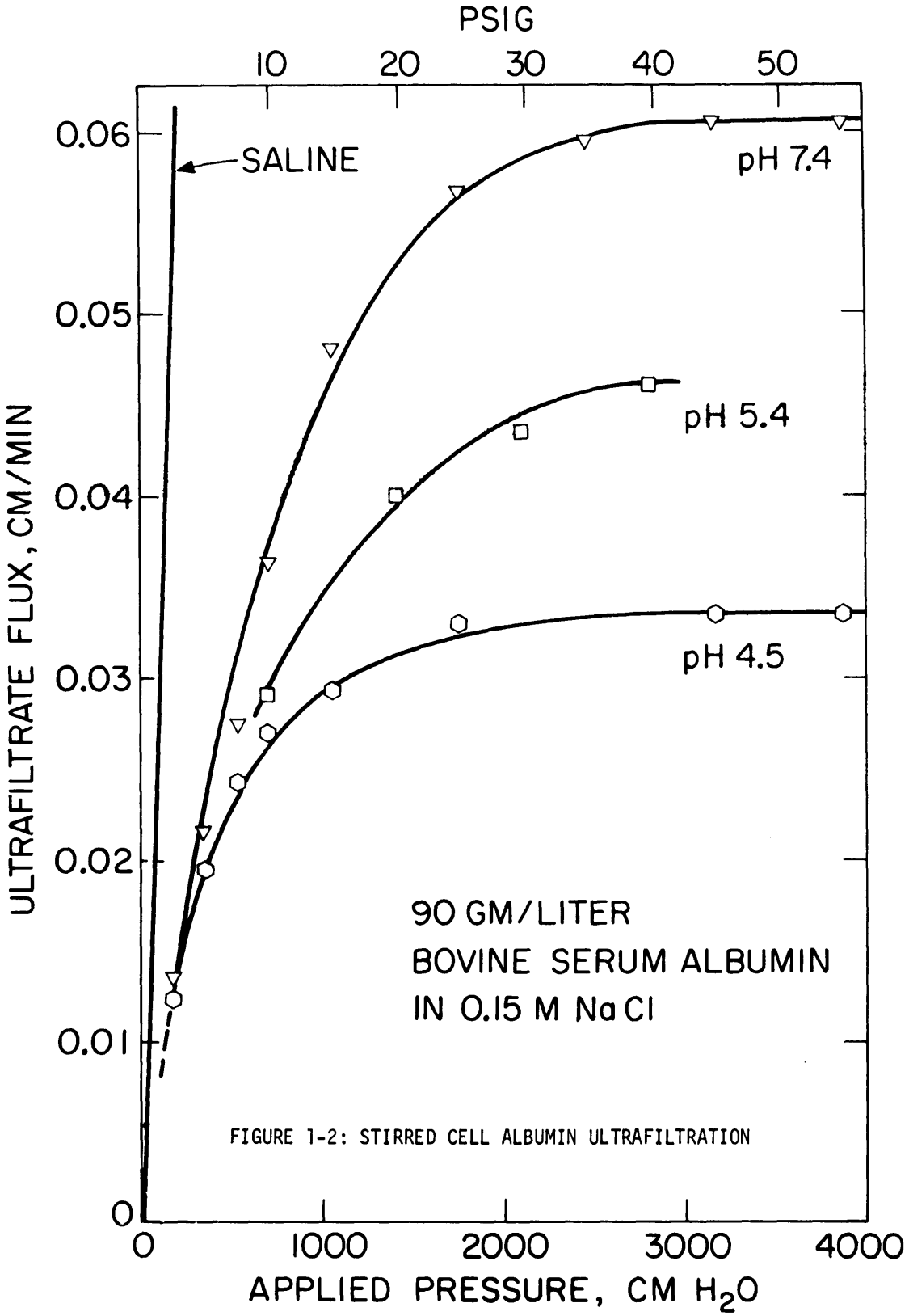

FIGURE 1-2: STIRRED CELL ALBUMIN ULTRAFILTRATION

measurements at this concentration could be used to argue that the deviation of the ultrafiltrate flux curves from the linear relation for pure saline is exclusively of a thermodynamic nature. However, since the sequence of flux curves on this figure for the three pH levels is opposite to that suggested by the sequence of the osmotic pressure data, this conclusion is uncertain.

2. Low Density Lipoprotein

The relationship of osmotic pressure to ultrafiltration has been investigated further with 0.15 M saline solutions of Low Density Lipoprotein (LDL).

Osmotic pressure determinations were made with a Hewlett-Packard Model 501 automatic membrane osmometer. This device has a limited range of only 20 cm H_2O, but has the advantages of being much faster and requiring much smaller solution sample sizes. The ultrafiltration experiments were done in the same apparatus which was used for the albumin study.

LDL is a very large molecule with a molecular weight of about three million and since it consists of about 80% lipid (18) it is not as highly charged as albumin. In Figure 1-4, the osmotic pressure measurements are presented in the figure to the left. This data, when plotted on a reduced basis, gives a molecular weight of three million which is in exact agreement with that reported for agarose gel filtration determinations (19). This data is fitted very well by a two-term virial expression. Note that LDL osmotic pressure never achieves very large values and, at equivalent concentrations, is more than two orders of magnitude smaller than the osmotic pressure of albumin at the same pH.

FIGURE 1-4

LOW DENSITY LIPOPROTEIN IN 0.15 M NaCl, pH 7.4

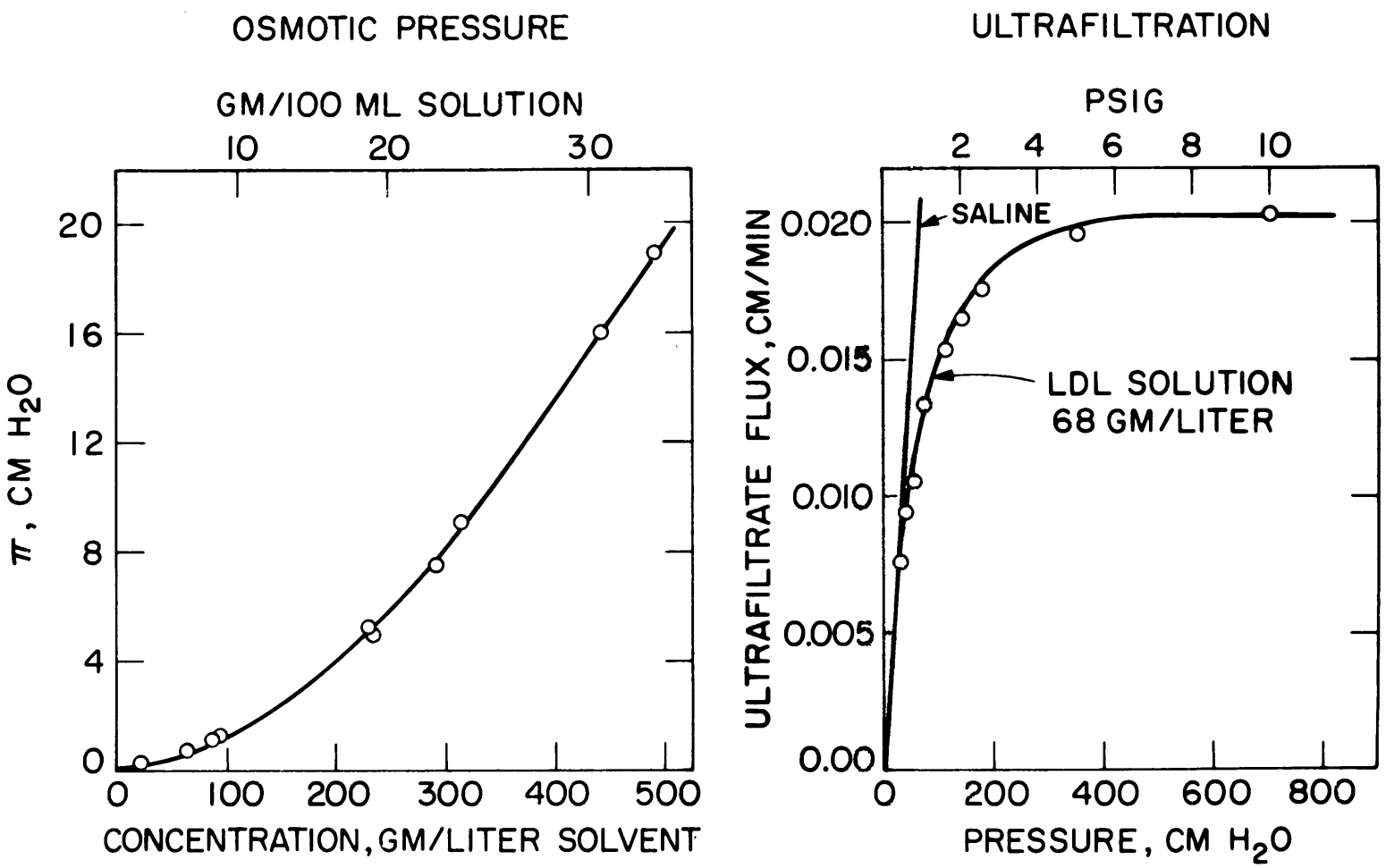

The ultrafiltration results are shown on the right. LDL bulk solution concentration was 68 gr/liter, or about 7 gm%. For this system,it is thought that the contribution of an increased osmotic pressure at the membrane surface can account for only a very small fraction of the observed deviation of the flux-pressure relationship from that for pure saline.

II. The Study of Concentration Polarization in Albumin Ultrafiltration

Previous investigations on the effects of concentration polarization on ultrafiltration have lacked data for the properties of the concentrated solutions of the rejected solutes and polarized layer concentration measurements. In this section, theoretical and experimental results are reported on the concentration profiles which exist above an ultrafiltration membrane, and on ultrafiltration flux, for the system of albumin dissolved in 0.15 M saline.

The experimental work was done with a stagnant ultrafiltration cell so as to eliminate the effects of uncertain hydrodynamics. The principal advantage of this device however, was that it permitted the use of an optical technique, called shadowgraph (20,21) for the measurement of albumin concentration at the membrane surface. This section begins with a consideration of the mathematics which describe, for a first attempt, the physics of the ultrafiltration occurring in this device.

A. Theoretical Model for Ultrafiltration

For the system shown in Figure 4-1, the fluid above the membrane is initially static and contains albumin in moderate concentrations. The saline below the membrane is the same salt composition, .15 Molar, as that in which the albumin is dissolved. The membrane is completely impermeable to albumin (sieving coefficient, χ=0) and is characterized by its saline permeability, K_m. At time zero, the protein solution is subjected to a constant elevated pressure, P_i, which results in a

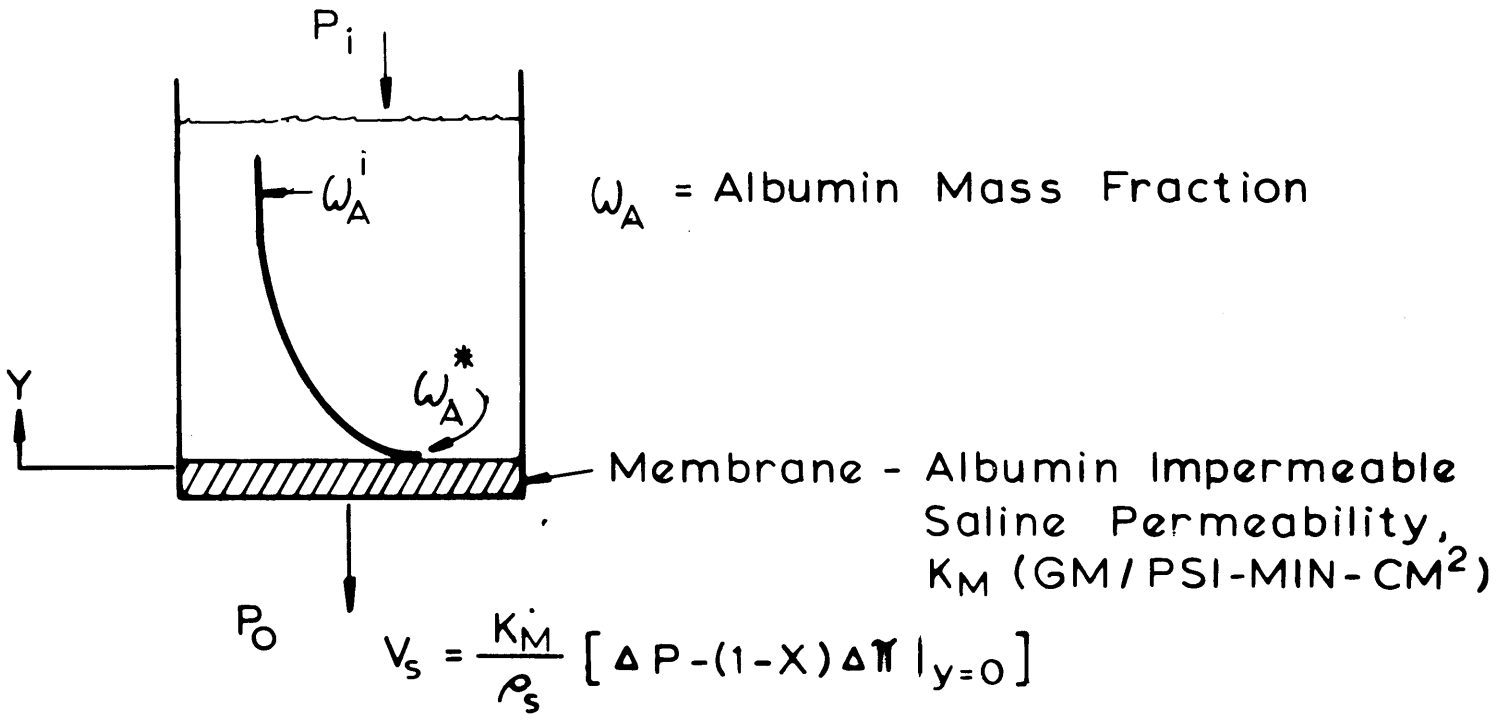

Figure 4-1: Albumin Ultrafiltration in a Stagnant System

solvent flux through the membrane, and a gradient in the concentration of the rejected protein.

When the assumption of constant density and diffusivity are made, the albumin mass balance written for the polarization layer gives

$$\frac{\partial \omega_A}{\partial t} - v \frac{\partial \omega_A}{\partial y} = \bar{D} \frac{\partial^2 \omega_A}{\partial y^2}$$

subject to

$$\omega_A = \omega_A{}^i \qquad \text{all } y,\ t=0$$

$$\omega_A \to \omega_A{}^i \qquad y \to \infty,\ \text{all } t$$

$$\bar{D} \frac{\partial \omega_A}{\partial y} + v\, \omega_A = 0 \qquad y=0,\ \text{all } t$$

$$v = \frac{K_m}{\bar{\rho}} \left(\Delta P - \pi \big|_{y=0} \right) \qquad y=0,\ \text{all } t$$

The first boundary condition at y = 0, shows that the rates of convection of albumin to the membrane surface and the diffusion of it away from the surface are equal and opposite. The volumetric flux,v, is taken to be proportional to the driving force $\Delta P - \Delta\pi$ where $\Delta\pi$ is evaluated at the membrane surface. That is, the driving force is dependent on the membrane concentration. The membrane concentration is assumed to be close to the concentration, $\omega_A{}^*$, which corresponds to the concentration for which the solution osmotic pressure equals the applied pressure. The polarization layer average density, $\bar{\rho}$, and diffusivity, $\bar{D}$, are evaluated at the average polarization layer concentration, $((\omega_A{}^* + \omega_A{}^i)/2)$.

Perturbation techniques have been applied to arrive at asymptotic solutions for concentration and flux, equations (S-4) and (S-5) respectively. In real time, these solutions apply to all the experimental conditions reported below for times greater than about one second.

$$\frac{\omega_A - \omega_A{}^i}{\omega_A{}^* - \omega_A{}^i} = \frac{1 - \text{erf}\,\{y/2\sqrt{\bar{D}t} + a_0\}}{1 - \text{erf}\,(a_0)} - \frac{a_0\sqrt{\bar{D}/t}\ \exp -\left[\frac{y^2}{4\bar{D}t} + \frac{a_0 y}{2\sqrt{\bar{D}t}}\right]}{(K_m/\bar{\rho})\left(\frac{\partial\pi}{\partial\omega_A}\right)_{\omega_A^*}\ (\omega_A{}^* - \omega_A{}^i)} \qquad \text{(S-4)}$$

$$v_s = a_0\left(\frac{\bar{\rho}}{\rho_s}\right)\sqrt{\bar{D}/t} \qquad \text{(S-5)}$$

where the a_0 term is a function of $\omega_A{}^*$ and $\omega_A{}^i$ given implicitly by,

$$\frac{\exp(-a_0{}^2)}{a_0\,[1 - \text{erf}\,a_0]} = 1.77\left[\frac{\omega_A{}^*}{\omega_A{}^* - \omega_A{}^i}\right]$$

After one second, the concentration at the membrane surface closely corresponds to $\omega_A{}^*$ (the pre-exponential product for equation (S-4) is very small, so $(\omega_A - \omega_A{}^i)/((\omega_A{}^* - \omega_A{}^i) \simeq 1)$. Also, the

thickness of the polarized layer grows with the square root of time, and the flux diminishes with the inverse square root of time.

B. Experimental

1. Shadowgraph Method

The shadowgraph method is rooted in the principle that light is deflected when passing through a medium of continuously varying refractive index. The deflection is from the region of lower to higher refractive index.

The schematic of Figure 5-1 shows a stagnant ultrafiltration cell in which a solution of bulk refractive index n_B is confined between two glass windows. The filtration process has created the refractive index gradient above the membrane as shown. The front glass surface (left side of figure) is illuminated by a normally incident, collimated beam. For a light ray which enters the solution at a point where the refractive index is homogeneous across the width of the cell, the ray travels undeflected to a point at the image plane, a constant distance above the membrane surface.

The lower ray is shown entering the solution at a point a distance Y_0 above the membrane, where a gradient in refractive index exists. This gradient causes the ray to be deflected continuously, along its traverse of the cell width, toward the membrane surface. The ray undergoes refraction at the solution/rear glass wall interface and again at the glass/air interface. This ray appears on the image plane, at a distance Y_3 below the membrane.

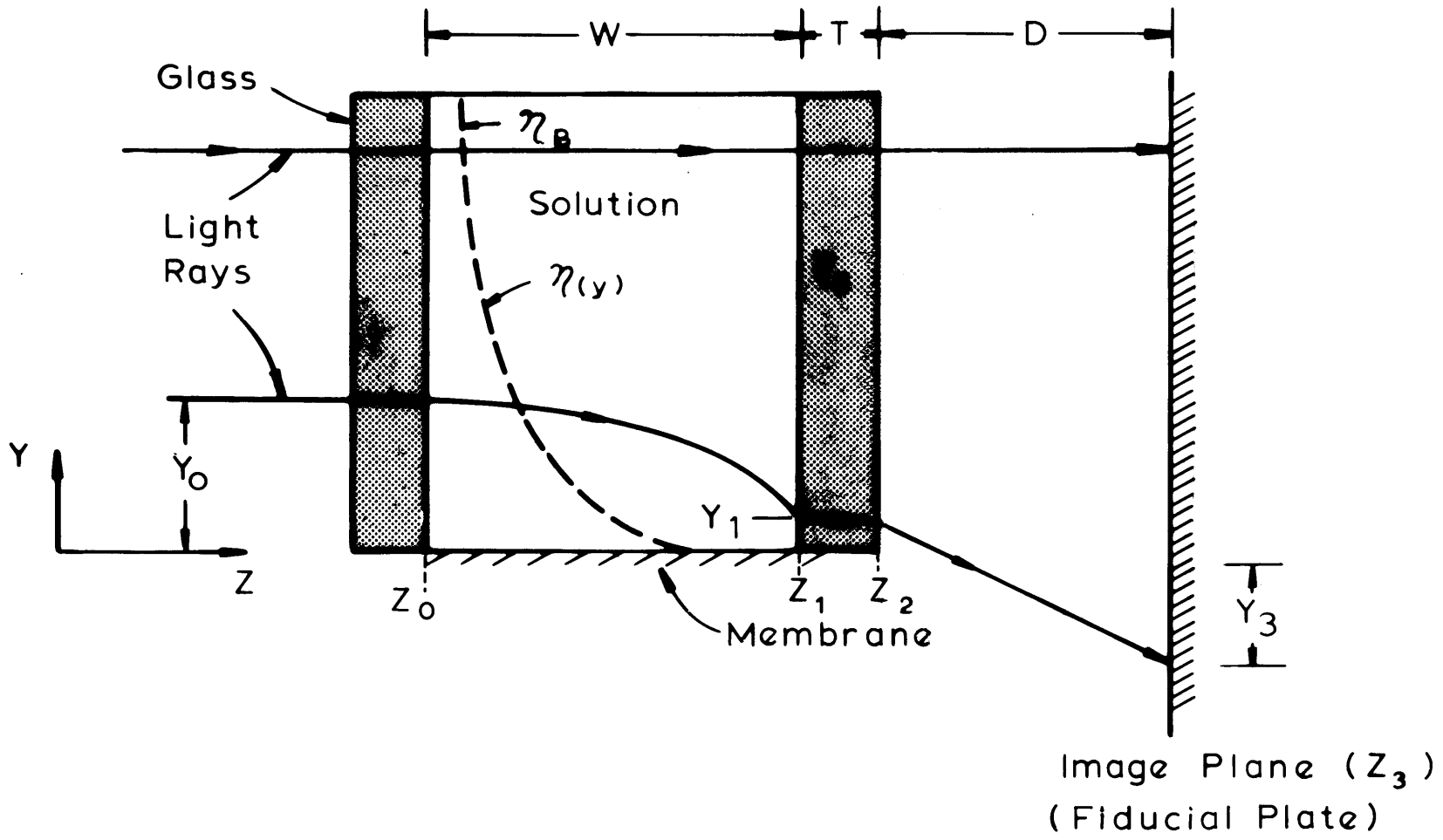

FIGURE 5-1 Schematic of Ray Trace

This ray trace is quantitated by the use of Fermat's principle to describe the path through the solution and Snell's Law of refraction at the interfaces. With measurements of Y_0 and Y_3 for a single ray, we can describe the refractive index profile for the small distance between Y_0 and Y_1. By taking many such (Y_0,Y_3) measurements, the entire profile in the diffusion layer can be computed.

The calculation of concentration profiles from refractive index profiles is straight forward for solutions of albumin in saline. The relation between the two is linear and has been measured to concentrations of 55 gm% protein. Significantly, we also found this relationship to be independent of solution pH.

2. Ultrafiltration Cell Detail and Apparatus

The ultrafiltration cell shown in Figure 5-4 is fabricated from two pieces of Invar. The top half consists of a narrow chamber into which has been mounted optical glass flats. The width of the solution cavity between these flats is 3 mm. The height of the cavity is 25 mm from its point of contact with the membrane.

The bottom half contains a shallow depression of length and width dimensions which match the top piece. A ceramic, incompressible membrane support has been impressed into this cavity.

The membrane is placed between these two pieces. The matching surfaces of the two pieces are sloped at 15° from the horizontal in order to allow the most deflected rays at the membrane surface to pass unhindered. With this design, we are theoretically capable of measuring concentrations at the membrane surface when deflection angles are less than about 15°.

FIGURE 5-4 ULTRAFILTRATION CELL

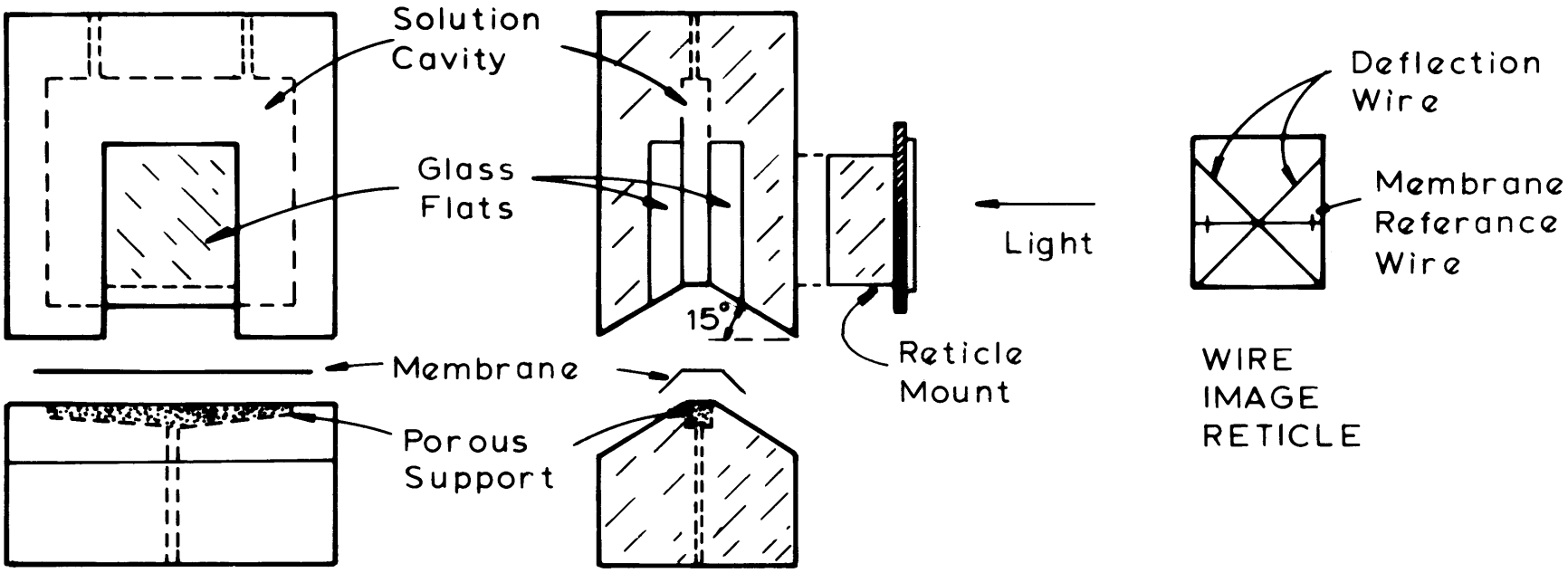

A small radius on the glass edges which contact the membrane prevents chipping at this important stress point of the glass. However, this radius is disadvantageous since it limits the minimum viewing distance above the membrane to 200 microns, or .2 mm.

After a light coat of heavy grease is applied to the surfaces which contact the membrane, a seal is formed when the assembly is clamped in a brace.

The wire image reticle is formed by inscribing very straight thin lines, 150 microns thick, on a piece of glass. The pattern formed is that of three straight lines. Throughout this discussion, these lines are referred to as 'wires' mostly for reasons of historical precedent regarding the evolution of this technique. It will also be an unambiguous reference to this reticle pattern in later discussion. Two of these wires are at approximately 45° to the membrane surface and appear in the deflected beam. The third wire is horizontal, and used to reference the location of the membrane. The glass reticle is cemented to a metal mount which is fitted to the front surface of the cell.

This cell is the main component of the experimental apparatus shown in Figure 5-7. The cell is shown mounted in a clamping brace which is attached to an optical bench. This bench in turn rests on a heavy stone slab under which is placed a foam rubber mat.

The cell is connected to a saline makeup reservoir. This reservoir is pressurized from a cylinder gas supply with a precision gage used for monitoring pressure. The cell is filled with protein solution through plastic hypodermic tubing which is inserted through the drain valve, down one leg of the saline feed line, to the membrane surface.

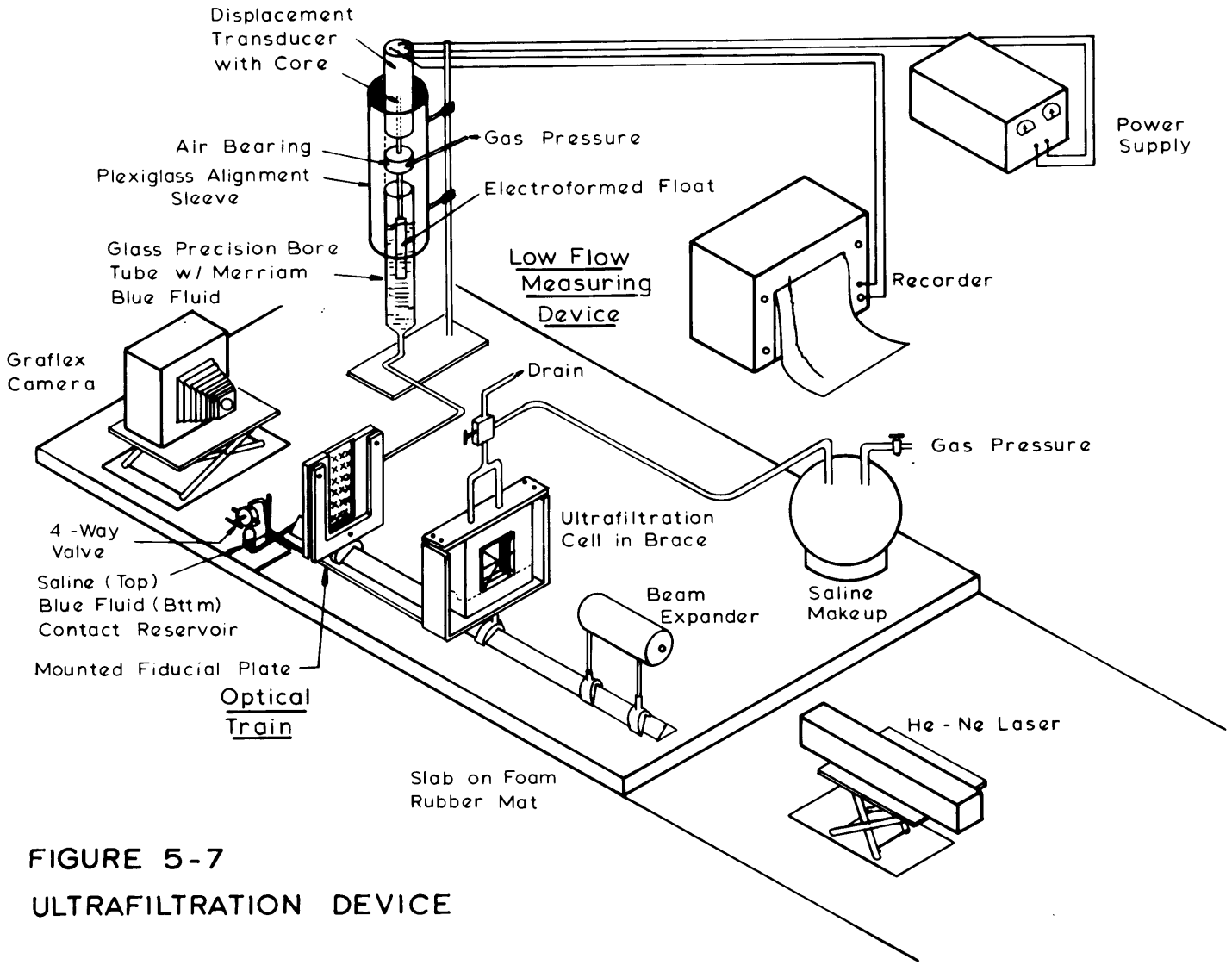

FIGURE 5-7

ULTRAFILTRATION DEVICE

In this way, air is forced out of the cell through the other saline feed leg. The tubing is then withdrawn and the run pressure applied.

The light source is a 15 milliwatt Helium-Neon laser which emits a narrow, coherent beam of light at 6328 Å wavelength. A beam expander collimates and expands the laser beam to a 45 mm diameter which illuminates the 20 mm square aperture of the cell.

The image of the reticle pattern is projected through the ultrafiltration cell onto the surface of a glass plate. The front surface of this plate is inscribed with carefully positioned fiducial marks. The positions of these fiducials are known to an accuracy of about .014 mm.

In the running mode, a Graflex camera is focused on the front surface of the fiducial plate. The image on the plate is recorded on Polaroid positive/negative sheet film.

A device for continuously monitoring the ultrafiltrate yield from the cell is shown at the top of this figure. This Low Flow Measuring Device operates on the bouyancy principle with the rise in a liquid level being monitored by a change in the signal of a sensitive displacement transducer.

A very light electroformed nickel float supports the core element of the transducer. These two elements are joined by a precision machined aluminum shaft. The entire assembly is 10 inches long and weighs 5 grams. The alignment of this delicate assembly between the precision bore glass float tube and the transducer is maintained with a frictionless air bearing. The air bearing is supplied with 20 psig gas pressure.

The float tube is filled with Meriam Blue manometer indicating fluid which is characterized by high density (1.75 Specific Gravity), low vapor pressure and insolubility in water. The indicating fluid extends into the glass tube which joins the float tube to the four way valve. At this point the indicating fluid contacts the saline ultrafiltrate coming from the ultrafiltration cell.

The transducer output is recorded. The device is calibrated over the range of use with a Harvard pump. Critical variables which effect performance are room temperature (± 0.1°C) and transducer excitation voltage (24.00 ± .02 volts). The lowest detectable flow is about 1×10^{-5} ml/min, and flow rates around 2×10^{-4} ml/min were routinely monitored.

The total experimental program was carried out over a range of 25 - 27°C. Room temperature was controlled with a circulating fan and a room space heater. The heater was controlled from a thermistor with a proportional controller. In addition, the cell brace was wrapped in saran to minimize heat transfer to the cell.

These precautions, in addition to our estimates of natural convection velocities, assured us that the effects of temperature driven natural convection were below the lower range of fluxes measured in most of our experiments.

3. Photographs of Deflection Produced by Concentration Gradients

The photographs of Figure 5-10 show the illuminated cell image as it appears on the fiducial plate before and after the polarization layer has been established. The small x's in the photos are the

FIGURE 5-10

PHOTOGRAPHS OF DEFLECTION PATTERNS

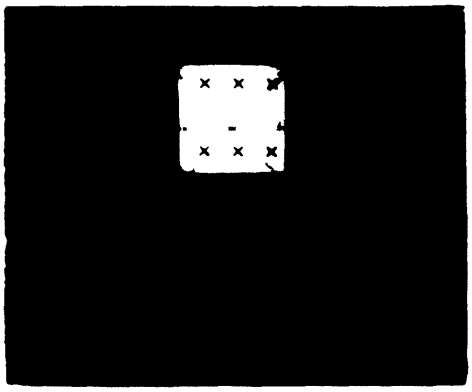

BEFORE
POLARIZATION
(1701)

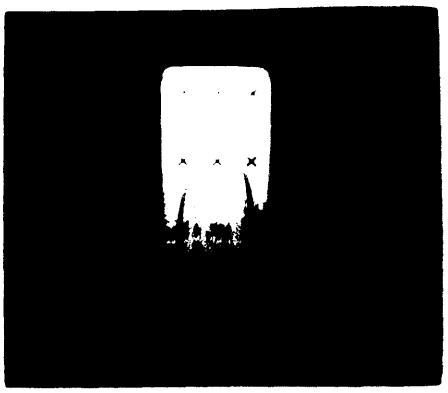

POLARIZATION
AT 9 HRS
5.4 pH, 10 psi
(1505)

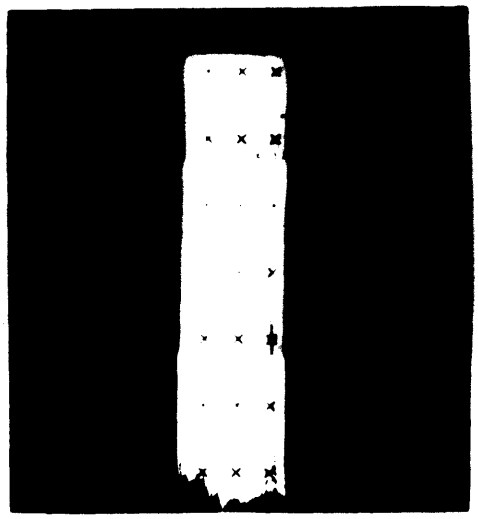

POLARIZATION
AT 22 HRS
4.5 pH 40 psi
(1807)

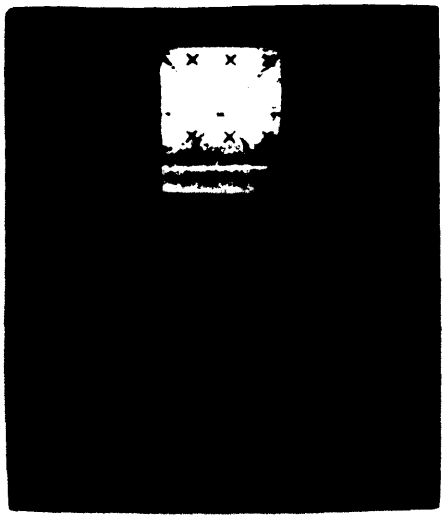

OSMOTIC
BACKFLOW
OF SOLVENT
(910)

calibration marks of the fiducial plate.

The undistorted reticle pattern is seen in the photo at upper left. The small diffraction patterns surrounding every image border in this photo do not permit its use to establish the membrane location with respect to the reticle pattern. Therefore, prior to beginning an experiment, a cathetometer is placed in the position of the camera and the cell is illuminated by incandescent light. The cathetometer is then used to locate the membrane at three points below the horizontal wire of the reticle pattern. The membrane is located to within ten micron precision below each of the three marks indicated along the horizontal wire. It is important to keep this distance greater than the anticipated polarization layer thickness so that the image of this horizontal wire never becomes distorted in the deflection photos.

The typical deflection pattern shown in the upper right photo indicates the effect produced by the polarization for a 10 psi ultrafiltration experiment of a 10 gm% albumin solution at pH 5.4. This photo was taken 9 hours after the start of the experiment and shows a deflection of about 28 mm below the membrane surface. At equivalent conditions of bulk protein concentration, applied pressure and time, a 4.5 pH solution would exhibit a deflection pattern which was 35% longer, a 7.4 pH solution, a pattern which was 35% shorter.

The deflection pattern at 22 hours for the ultrafiltration of a 4.5 pH solution at 40 psi is shown in the lower left photo. Three neutral density optical filters were placed in front of the fiducial plate in order to reduce light intensity variation over the deflection pattern length.

In the photo at the lower right, taken at the end of a different experiment, saline solvent was allowed to backflow through the membrane by releasing the applied pressure. As the polarization layer gradient relaxes by molecular diffusion, the deflection diminishes. But most interestingly, a layer of saline, greatly diminished in protein, is forming relatively quickly at the membrane surface. This thin region of almost negligible refractive index gradient permits light to pass undeflected. The result is the thin strip of light, which corresponds to the membrane surface, seen in the photo. Also faintly visible are the small inverted wire images which indicate the maximum in the refractive index gradient above the membrane.

Except for the cathetometer readings, all optical data required for a concentration profile determination are obtained from one exposure. The negative of a photo like the one on the upper right is processed using an Itek Hand Measurement Machine. The negative is mounted on a stage which magnifies it about 14 times and divides the length and width of the photo into a 130,000 by 40,000 micron grid space. The coordinates of any point on the negative with respect to this grid space are then recorded electronically and digitized with the aid of a PDP-8 computer.

The fiducial marks are read first and serve to convert the dimensions of the picture to that of the fiducial plate. The three intersection marks along the horizontal wire are read next. Combined with the cathetometer readings, these measurements locate the membrane position. Next the straight, undeflected portions of each of the 45° wires are read. These readings are later regressed to form a linear equation which can be extrapolated to indicate the precise

locations where the wires intersect the membrane. Lastly, the curved, deflected portions of these wires is read.

The translation of this deflected image to a coordinate system which is centered at the point where one of the inclined wires intersects the membrane is shown on Figure 5-11.

The measurements from the deflected region, and the equation of the undeflected region are translated and rotated to the coordinate system in which one axis is parallel to the membrane, the other axis perpendicular to it, and the origin centered at the point where one of the wires intersects the membrane. For any particular value of the horizontal coordinate in this frame, the horizontal distance, and the slope of the undeflected portion measures the distance above the membrane at which the light ray entered the cell. The vertical distance is the deflection.

Up to 250 of these points are then regressed with nonlinear least squares to fit an exponential relationship between the entering and exiting ray location. These exponential equations, which were fitted for two to four separate sections of the deflection image, are then used for the ray trace calculations mentioned earlier. The ray trace calculation extrapolates these relations to the membrane surface.

C. Results

Among several comparison studies conducted during the experimental program was the ultrafiltration, at identical conditions of pressure (10 psi), bulk concentration and duration, of solutions at the three pH levels of 4.5, 5.4 and 7.4. As was true for the stirred cell experiments, the quantity of ultrafiltrate varied significantly between

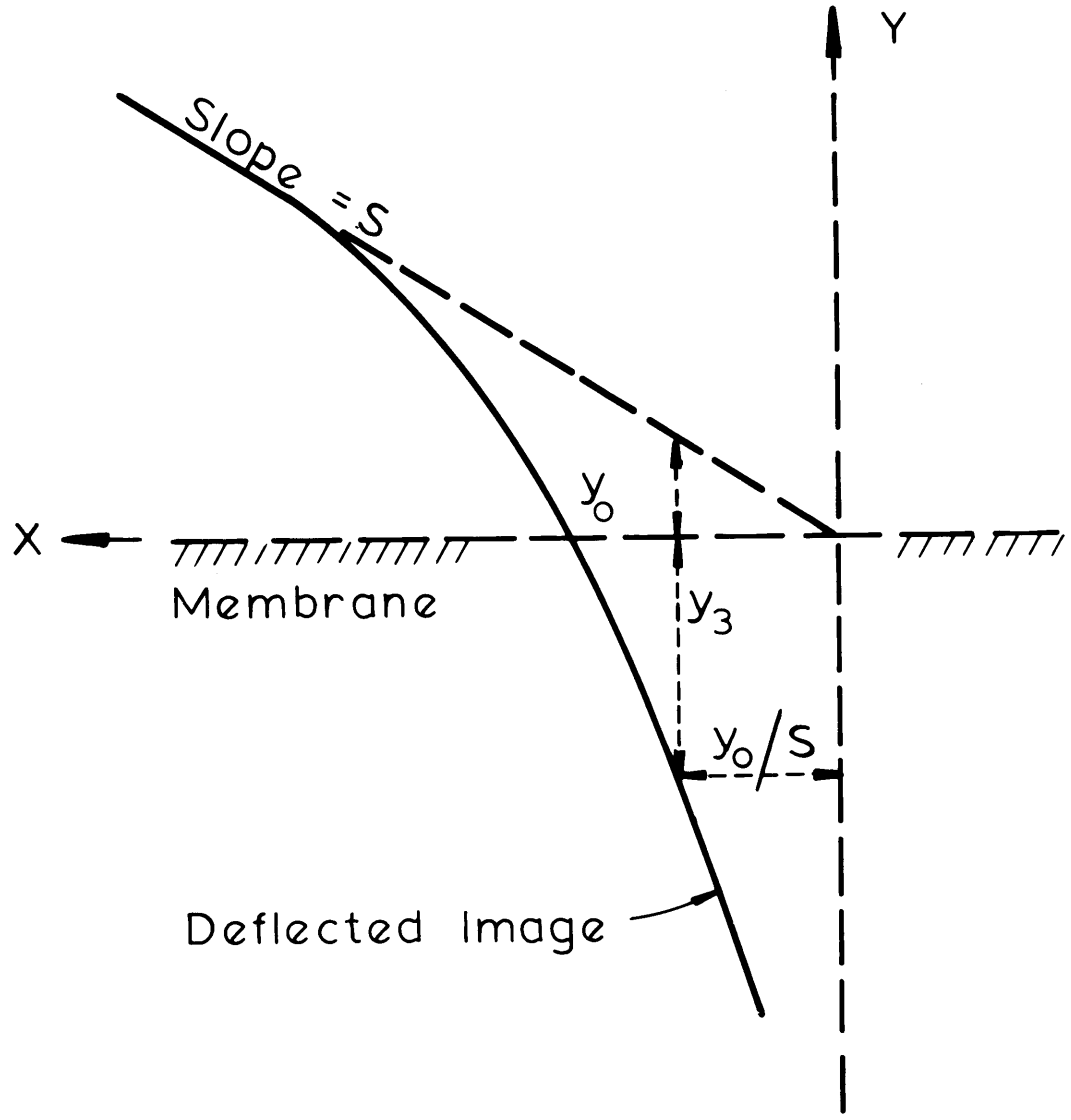

Figure 5-11 Deflection Analysis

these different pH levels and in the same sequence. At about 9 hours it is seen on Figure 5-12 that the yield of ultrafiltrate at 7.4 pH was almost twice that of the 4.5 pH experiment.

The curves drawn through the data represent the least square regression fits of the data to the integral form of the equation

$$\text{Flux} = K\, t^n$$

The fits are good enough so that the power on time is determined to three significant figures and the constant to two significant figures.

On Figures 5-13, -14, and -15, comparisons are made between measured flow rates, the concentration profiles measured at nine hours and the theory as it was described above. The results are shown for the experiment at 4.5 pH on Figure 5-13.

In the top figure, the concentration profile for each of the wires is shown by the dashed lines. These lines are dotted close to the membrane to show that an extrapolation step was necessary in the ray trace computation for distances closer than 200 microns. For an osmotic pressure of 10 psi, the concentration at the membrane surface would be 40.2 gm%. As seen in the figure, the values from the two wires agree within 5% of this concentration. The polarization layer thickness, as defined by the distance at which the bulk concentration was elevated by 2% was found to be 0.34 cm.

Theoretical profiles from the model are also indicated. In one case, we have calculated the profile for a diffusivity taken from the data of Keller, Canales and Yum (22). This was evaluated at the average concentration in the diffusion layer. In the second case, an arbitrary diffusivity was chosen to most closely match the measured

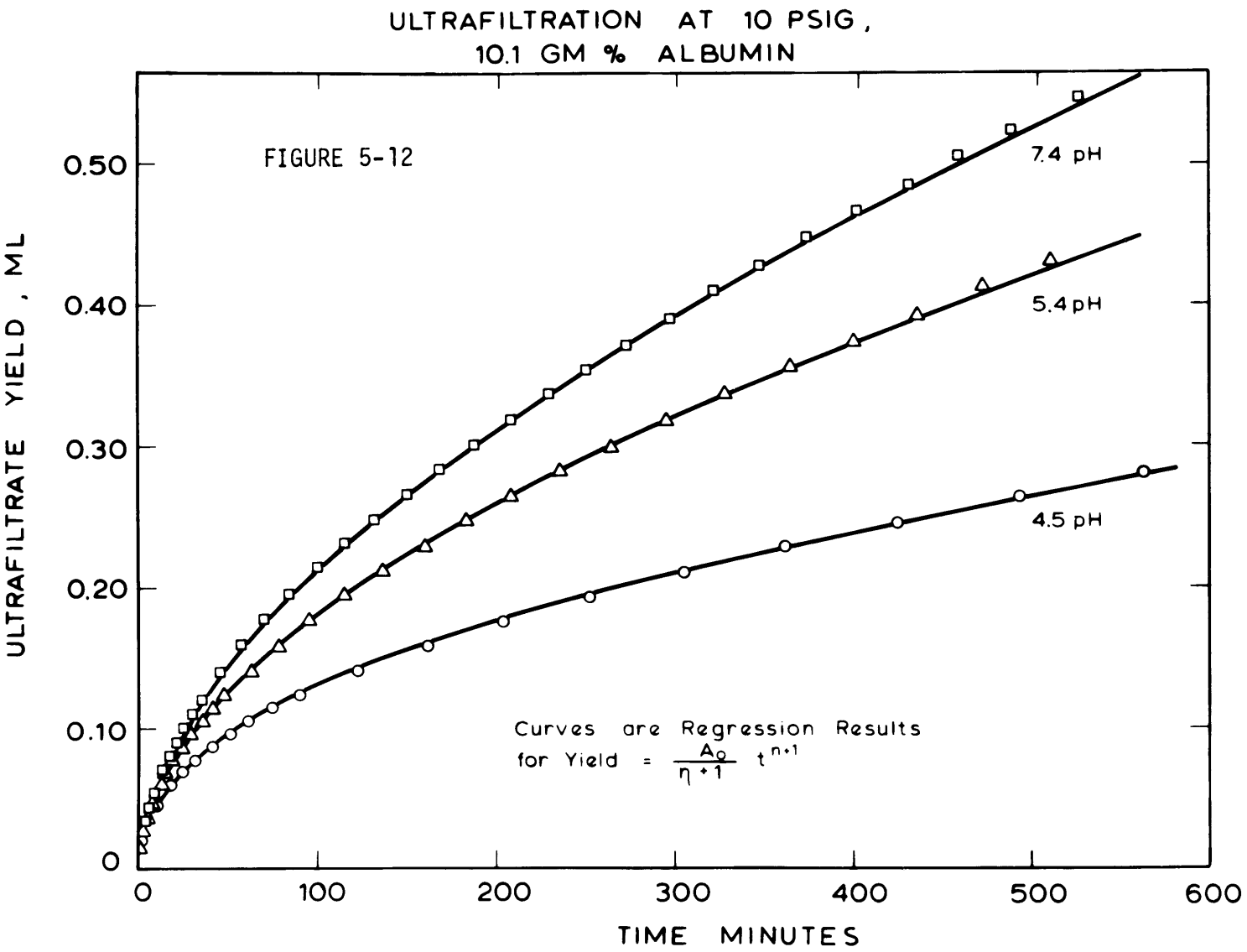
ULTRAFILTRATION AT 10 PSIG,
10.1 GM % ALBUMIN
FIGURE 5-12
7.4 pH
5.4 pH
4.5 pH
Curves are Regression Results
for Yield = $\frac{A_0}{\eta+1} t^{n+1}$
ULTRAFILTRATE YIELD, ML
0
0.10
0.20
0.30
0.40
0.50
0
100
200
300
400
500
600
TIME MINUTES

ALBUMIN ULTRAFILTRATION
4.5 pH, 10.1 GM %, 10 PSIG

FIGURE 5-13

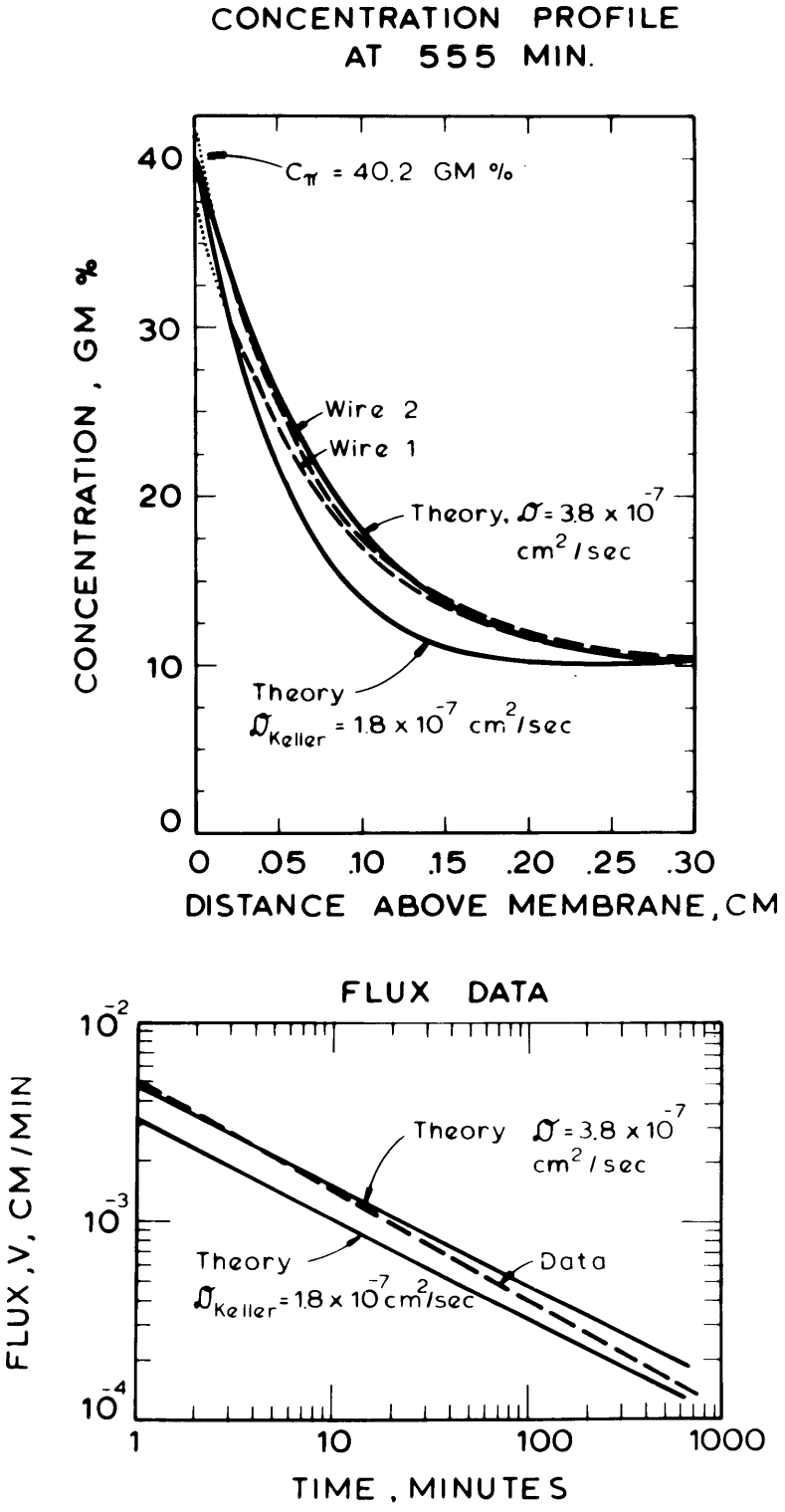

ALBUMIN ULTRAFILTRATION
5.4 pH , 10.1 gm % , 10 psig

FIGURE 5-14

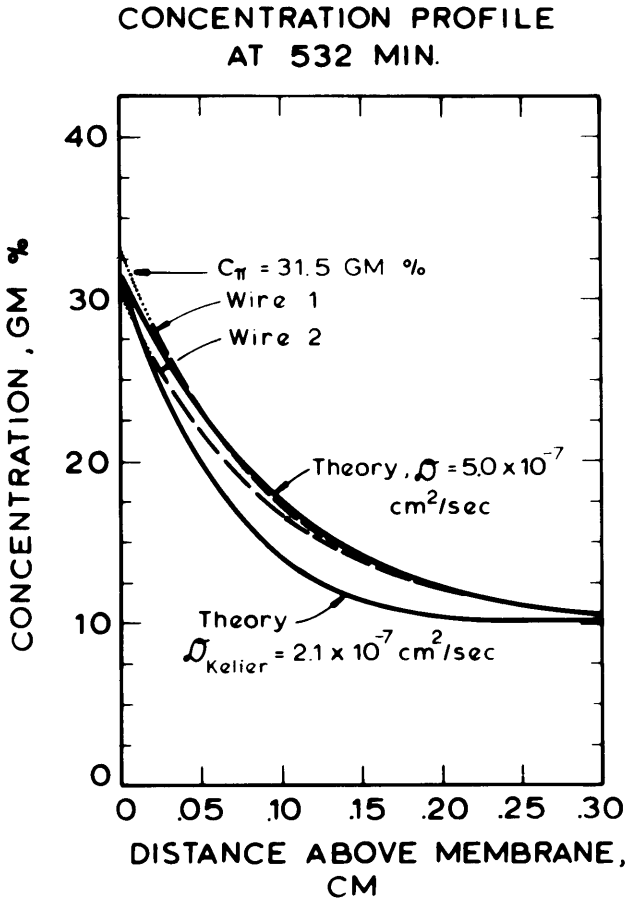

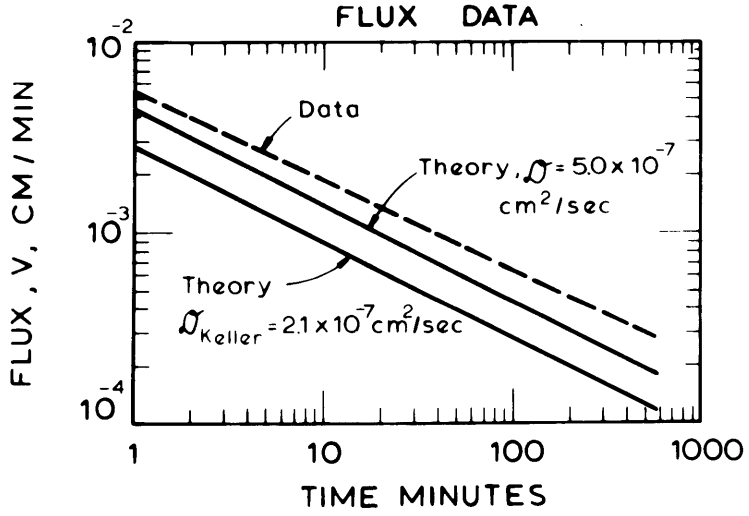

ALBUMIN ULTRAFILTRATION -
7.4 pH , 10.1 gm % , 10 psig

FIGURE 5-15

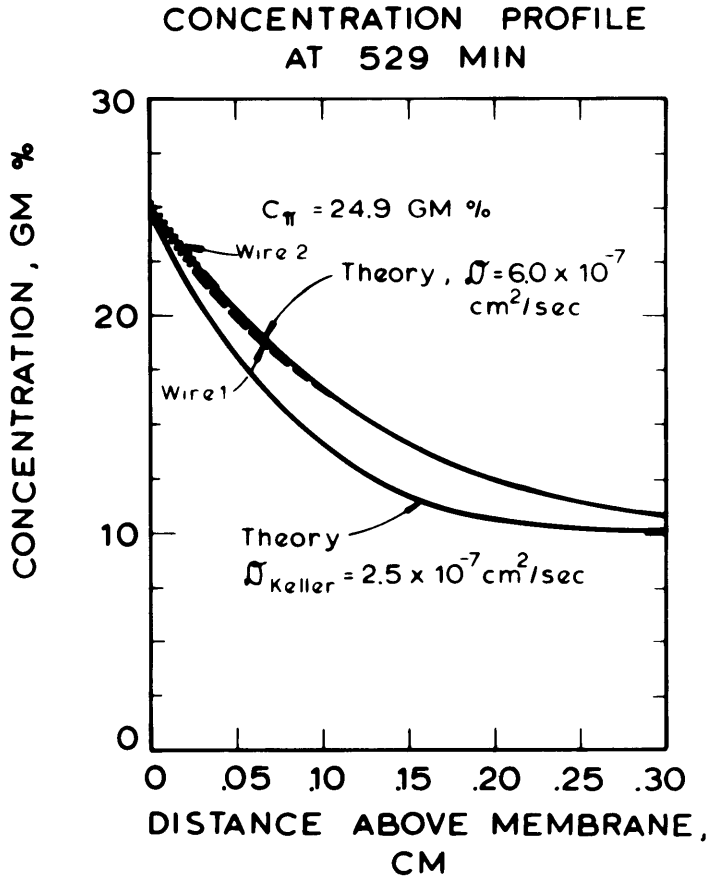

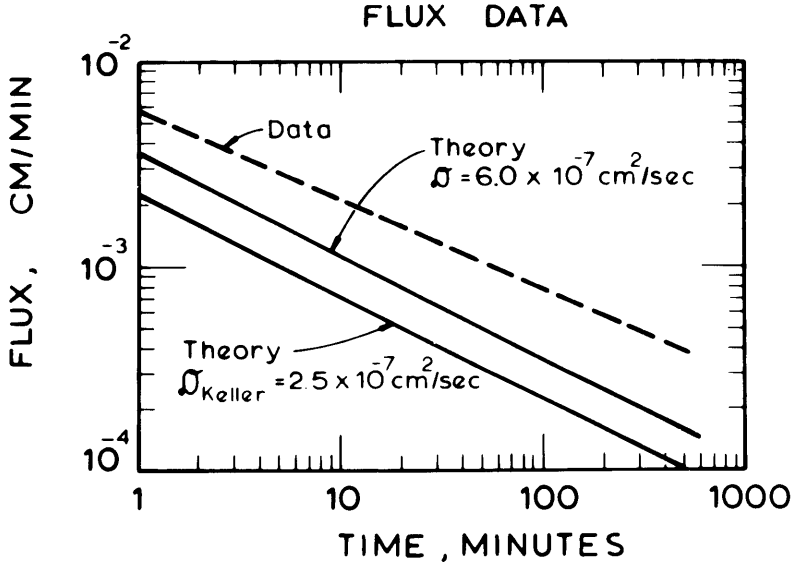

profiles. The discrepancy between these two curves probably reflects the inadequacies of our constant property model. It may also reflect a difference in the physical chemistry of the albumin solutions which were used here versus those in which Keller et al. made their measurements. The latter were obtained at pH 4.7 in an acetate buffer. All of our work was done in unbuffered .15 M saline of variable pH.

In the bottom half of the figure, the flux versus time data are shown on a log-log plot to compare the agreement of the data with the predicted slope of -1/2. The slope for the data is slightly more negative. Also, the higher value of diffusivity more closely represents the data.

The results for the experiment at 5.4 pH are shown on Figure 5-14.

The measured membrane surface concentration from both wires agrees closely with the theoretical 31.5 gm%. The polarization layer thickness was 0.39 cm at 532 minutes. Again we see that a larger diffusivity than that value computed from Keller et al. is required to match the theory with the data.

The slope of the flux data is slightly less negative than the theoretical -1/2. In this case we also see that the diffusivity which brings the theoretical and measured concentration profiles into close agreement does not do as well as before in matching the flux data with theory.

At 7.4 pH, the measured membrane surface concentration shown on Figure 5-15 again agrees closely with the concentration which would be predicted for a solution which exhibited a 10 psi osmotic pressure at 7.4 pH. The polarization layer for this profile is 0.46 cm thick. The diffusivity which matches theory and measurement is again more than

twice that which is computed from Keller et al. for the average albumin concentration of the polarization layer.

The flux data indicate an even larger discrepancy between data and theory when the flux is predicted using the best value of diffusivity to match profiles. The slope of the data however is still close to the predicted -1/2.

Finally, on Figure 5-16, the results for a solution with slightly higher bulk concentration, at 4.5 pH, and an applied pressure of 40 psi, again show good agreement regarding the prediction and measured surface concentration. In fact, the agreement is quite remarkable considering the magnitude of the extrapolation made from the osmotic pressure data to get the predicted value of 59.5 gm%. Again a diffusivity about 2 1/2 times greater than that predicted from Keller's data is required to match the profiles.

As was true for the 10 psi experiment at this same pH, the flux data is very well described by the theory when the profile diffusivity is used. The two lines are nearly superimposed on the flux plot at the bottom of the figure.

D. Conclusions

A comparison of the average concentration profiles from both wires for the three experiments at 10 psi is shown on Figure 5-45. The data clearly demonstrate that in albumin ultrafiltration, the concentration at the membrane surface is very close to the osmotic equivalent of the applied pressure.

The ultrafiltrate flux was shown by the model to depend on a small

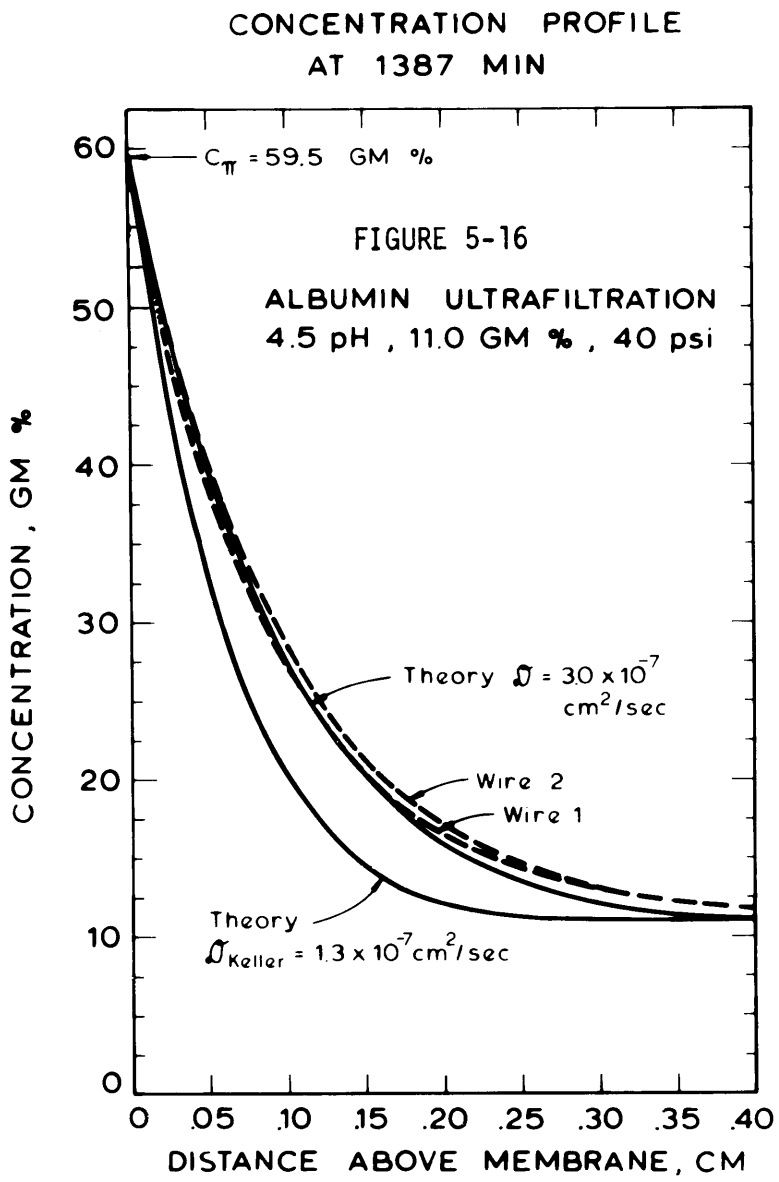
CONCENTRATION PROFILE
AT 1387 MIN
C_π = 59.5 GM %
FIGURE 5-16
ALBUMIN ULTRAFILTRATION
4.5 pH , 11.0 GM % , 40 psi
Theory $\mathcal{D}$ = 3.0 x 10^{-7} cm^2/sec
Wire 2
Wire 1
Theory
$\mathcal{D}_{Keller}$ = 1.3 x 10^{-7} cm^2/sec
CONCENTRATION, GM %
DISTANCE ABOVE MEMBRANE, CM
0
10
20
30
40
50
60
0
.05
.10
.15
.20
.25
.30
.35
.40

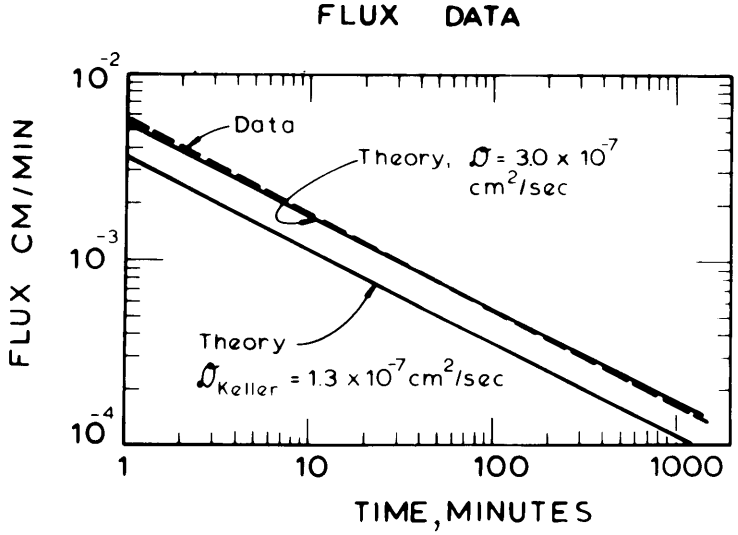
FLUX DATA
Data
Theory, $\mathcal{D}$ = 3.0 x 10^{-7} cm^2/sec
Theory
$\mathcal{D}_{Keller}$ = 1.3 x 10^{-7} cm^2/sec
FLUX CM/MIN
TIME, MINUTES
10^{-2}
10^{-3}
10^{-4}
1
10
100
1000

Figure 5-45

CONCENTRATION PROFILE COMPARISONS

10.1 GM %, 10 PSIG, 9 HOURS

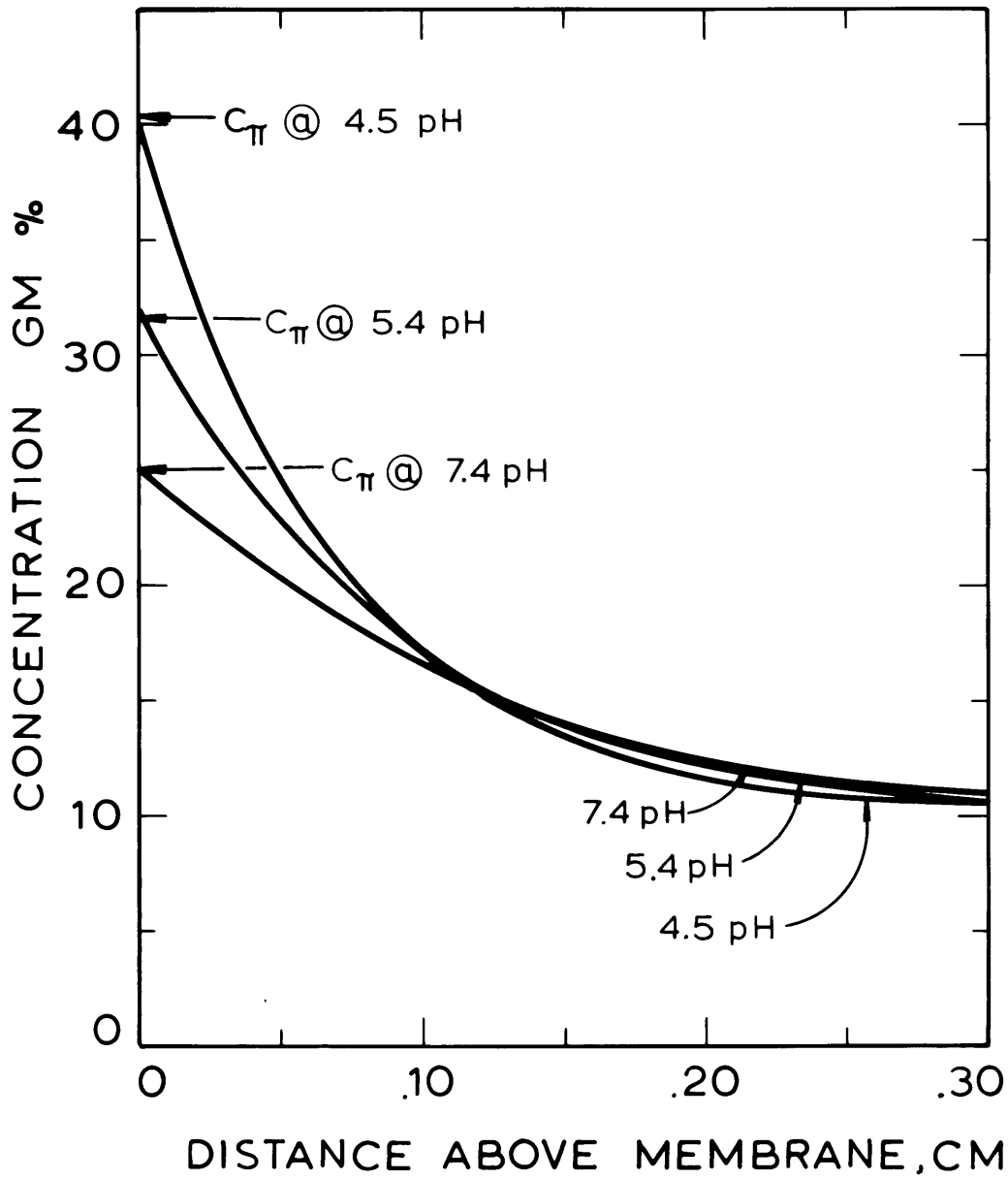

net driving force, $(\Delta P - \pi|_{y=0})$. The model predicted that, as a consequence of $\pi|_{y=0} \rightarrow \pi|_{\omega_A^*}$ as experimental elapsed time increased, the flux would decay with an inverse square root of time dependence. Experimental results were in close agreement with this predicted time dependence, but indicated that it may vary slightly with varying solution properties, specifically solution pH.

More importantly, both experimental concentration profile determinations and flux measurements indicate that albumin diffusivity is larger than that which is calculated from the data of Keller, et al. These comparisons are shown in Table 6-1 for the three experiments at 10 psig applied pressure.

TABLE 6-1

Diffusivity Comparisons for 10 psig Ultrafiltration

pH	$\bar{D} \times 10^{+7}$; cm^2/sec			Comparisons		
	Keller	Fit to Profile	Fit to Flux	Profile / Keller	Flux / Keller	Flux / Profile
4.5	1.8	3.8	2.8	2.1	1.6	.74
5.4	2.1	5.0	4.4	2.4	2.1	.88
7.4	2.5	6.0	10.0	2.4	4.0	1.7

Differences in solution composition between the determinations of Keller, et al. (acetate buffer, 4.7 pH) and the work reported here are probably responsible for this difference in diffusivity.

Also, the comparisons of Table 6-1 suggest that albumin diffusivity increases with increasing macromolecular charge, i.e. solution pH.

Therefore, the probable reason that the solution of highest pH (and largest osmotic pressure) yields the highest ultrafiltrate flux is that the rate for $\pi|_{y=0} \rightarrow \pi|_{\omega_A^*}$ is slower than in the case of the lower pH solution by virtue of a higher diffusivity. This higher diffusivity results in an increased rate of albumin transfer away from the membrane back into the bulk solution.

Confirmation of albumin diffusion coefficient dependence on concentration and solution pH is currently underway in this department. In addition, the solution of a variable property model is planned in order to reconcile the discrepancy between the effective diffusivities which are calculated from the experimental flux results and those which are calculated from the measured concentration profiles.

BIBLIOGRAPHY

(1) Porter, M. C. and L. Nelson, In Recent Developments in Separation Science, Vol. 2. N. N. Li, editor. CRC Press, Cleveland, Ohio (1972).

(2) Porter, M. C., AIChE Symp. Ser. No. 129, Vol. 69, p. 100 (1973).

(3) Spatz, D. D., AIChE Symp. Ser. No. 129, Vol. 69, p. 89 (1973).

(4) Goldsmith, R. L., R. P. deFilippi and S. Hossain, AIChE Symp. Ser. No. 120, Vol. 68, p. 7 (1972).

(5) Michaels, A. S., In Progress in Separation and Purification. S. Perry, editor. p. 297, Interscience, New York (1968).

(6) Dorson, W. J., V. B. Pizziconi and J. M. Allen, Trans. Amer. Soc. Artif. Int. Organs, 17, p. 287 (1971).

(7) Kozinski, A. A. and E. N. Lightfoot, AIChE J., 18, 1030 (1972).

(8) Blatt, W. F., A. Dravid, A. S. Michaels and L. Nelson, In Membrane Science and Technology, J. E. Flinn, editor. Plenum Press, New York (1970).

(9) Scatchard, G., A. C. Batchelder and A. Brown, J. Am. Chem. Soc., 68, 2320 (1946).

(10) Scatchard, G., A. C. Batchelder, A. Brown and M. Zosa, J. Am. Chem. Soc., 68, 2610 (1946).

(11) Kappos, A. D. and H. Pauly, Biophysik, 3, 131 (1966).

(12) Tanford, C., Physical Chemistry of Macromolecules, John Wiley and Sons, Inc., New York (1958).

(13) McMillan, W. G. and J. E. Mayer, J. Phys. Chem., 13, 276 (1945).

(14) Stigter, D. and T. L. Hill, J. Phys. Chem., 63, 55 (1959).

(15) Moeller, W. J. H. M., G. A. J. van Os and J. Th. G. Overbeek, Trans. Far. Soc., 57, 325 (1961).

(16) Gutfreund, H., Trans. Far. Soc., 50, 628 (1954).

(17) MacRitchie, F., J. Colloid Interface Sci., 45, 235 (1973).

(18) Hatch, F. T. and R. S. Lees, Adv. Lipid Res., 6, 1 (1968).

(19) Margolis, S., In Structural and Functional Aspects of Lipoproteins in Living Systems. E. Tria and A. M. Scanu, editors. Academic Press, New York (1969).

(20) Mowbray, D. E., J. Fluid Mech., 27, 595 (1967).

(21) Williams, F. A., T. J. Hendricks, M. K. Lin, USDI - Office of Saline Water R. and D., Progress Report No. 622 (1970).

(22) Keller, K. H., E. R. Canales and S. I. Yum, J. Phys. Chem., 75, 379 (1971).

CHAPTER ONE

CONCENTRATION POLARIZATION IN THE ULTRAFILTRATION OF BIOLOGICAL MACROMOLECULES

The separation of biological macromolecules from the various solutions in which they are dissolved is of physiological and industrial importance. In recent years, ultrafiltration has been successfully applied to many separation problems.

Several industrial applications are reviewed in the literature (1,2,3,4,5,6). Valuable proteins like albumin and lactalbumin have been recovered by the fractionation of defatted milk whey. Egg albumin concentration, without denaturation, by the partial dehydration of egg whites and the recovery of albumin and globulins from slaughterhouse blood have been demonstrated.

Virtually any waste stream whose BOD or color values exist as macromolecular or colloidal substances can be renovated by ultrafiltration. The process has been applied to the dewatering of sludges and removal of organic pollutants from primary and secondary sewage treatment. In the treatment of secondary sewage, practically all of the coliform bacteria normally contained in secondary effluent were removed. The high molecular weight lignins and ligninosulfonates have been removed from the effluents of pulp and paper extraction processes.

Medical and pharmaceutical applications include the processes of hemodiafiltration, plasmaphoresis and membrane enzymatic reactors (1,5,6,7,8). Hemodiafiltration is the term applied to the fractionation of blood, in this case by ultrafiltration, combined with replenishment of water and vital solutes through addition of a physiologic solution. As an artificial kidney, the process offers several advantages over conventional hemodialysis (7).

Conventional plasmaphoresis is the separation of the cellular elements of blood by the process of centrifugation. Here again, several advantages have been demonstrated for ultrafiltration as an alternative separation process.

When enzyme catalyzed reactions yield a product which is smaller than the substrate and enzyme, it is usually advantageous to carry out the reaction continuously in a membrane reactor. In membrane fermentors, toxic metabolites rather than the desired reaction products are removed by ultrafiltration thereby increasing the steady-state fermentor yields.

In the human body, the transport of water accompanied by some plasma solutes across membranous structures can be described as ultrafiltration processes when the transport results from a hydrostatic pressure driving force. When viewed as an ultrafiltration process, significant gains have been made in the understanding of the renal glomerular capillary function (9). The filtration theory of atherogenesis (10,11) hypothesizes that the earliest manifestations of atherosclerosis are intimately associated with an ultrafiltration process. Specifically, the plasma lipoproteins are transported in this way into the arterial wall where some are trapped and deposit their lipid, eventually leading to the formation of atheroma.

I. Effects of Concentration Polarization

The build-up of a concentrated solute layer at the membrane surface, termed concentration polarization, is generally the most significant factor which influences the ultrafiltration of macromolecular solutions. The objective of this thesis is a more fundamental understanding of the relationship between ultrafiltrate flux and the pressure driving force in terms of the physiocochemical properties of the solution. The typical dependence of flux on applied pressure is shown in Figure 1-1.

When only pure solvent, which passes freely through the membrane, is present, the pressure and volumetric flux are linearly related. When a solute species which is rejected by the membrane is present, deviations from this simple linear relationship arise, and the flux eventually reaches a constant level where it becomes insensitive to further increases in pressure. The physical basis of this reduction in ultrafiltrate flux depends on the extent to which the polarized layer acts, on the one hand, as a thermodynamic barrier which reduces the available pressure driving force by an increase in osmotic pressure (as in reverse osmosis) and, on the other, as a hydrodynamic barrier which offers a resistance to flow (as in mechanical filtration). Both modes of action have been suggested in previous treatments of ultrafiltration (1,6,8,12,13,18,19).

In many, if not most industrial applications, concentration polarization is the rate limiting phenomenon in ultrafiltration. In addition to limiting ultrafiltrate flux, the influence of the polarization layer on solute retention also becomes a consideration when the solutions contain more than one solute, and when the primary membrane is retentive

FIGURE 1-1

ULTRAFILTRATION FLUX vs. PRESSURE

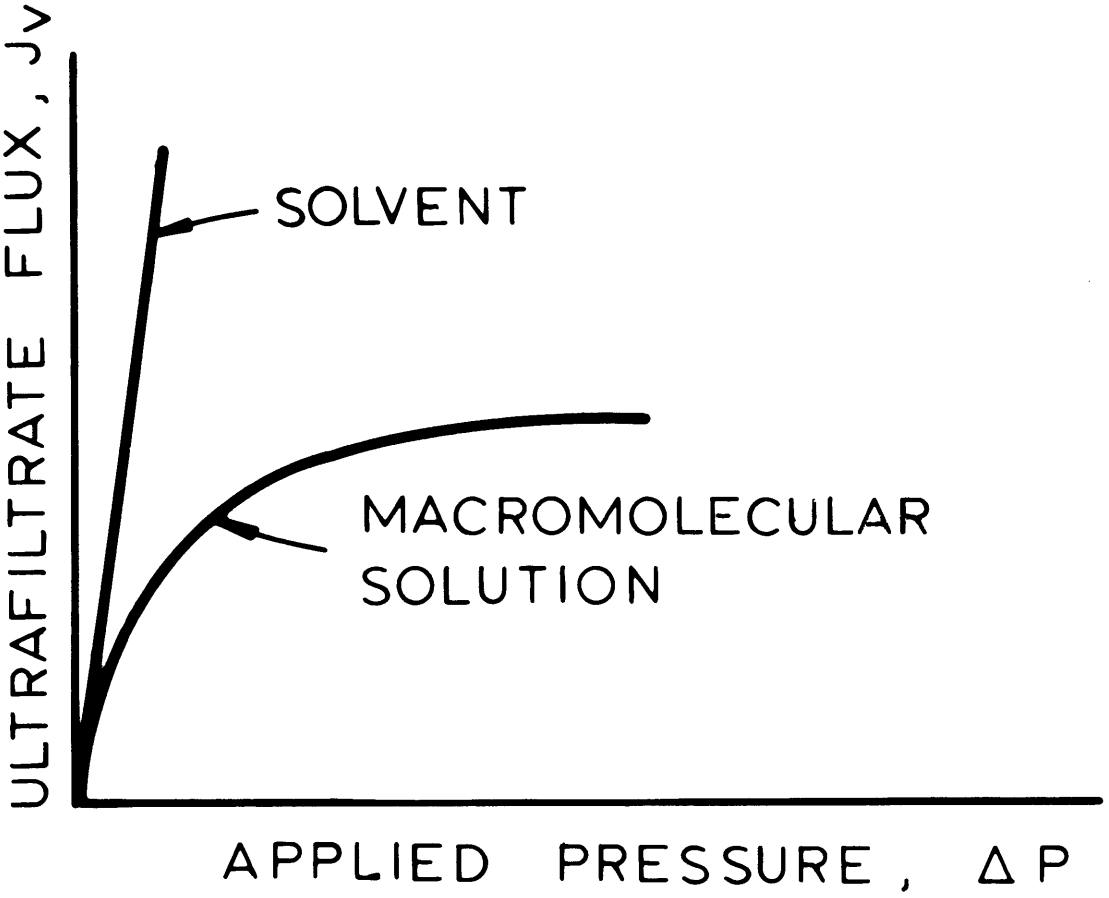

$$J_V = \frac{\Delta P - \Delta \pi}{R_m + R_p}$$

for one or more solutes, yet permeable to others. For this case, if the polarization layer contains molecules which strongly interact with the other solutes in the solution, it may be partially or completely retentive for solutes to which the primary membrane is permeable. Under those circumstances, the smaller molecules are retained by the polarization layer, and the apparent rejection by the membrane for the smaller molecules increases. Therefore, the design of industrial ultrafiltration equipment and processes is primarily directed toward minimizing polarization within acceptable economic limits. This, in turn, relies upon equipment geometry and operating conditions which maximize the back transport of retained solutes away from the membrane surface back into the feed solution. A first and simple way of reducing polarization to levels yielding practical ultrafiltration flux was the stirred laboratory cell. The use of turbulent flow to reduce concentration polarization is a favored technique in industrial equipment design (18). Further advances include the dramatic increases in the rate of ultrafiltration (two- to five-fold increases) which have been achieved by the "thin-channel" membrane design (1).

In the study of transport through the renal glomerular capillaries (9), it has been pointed out that the polarization of rejected proteins need not be very severe to result in serious consequences. From the measured values of ΔP in glomerular capillaries, it is apparent that protein concentration cannot exceed approximately 10 gr/100 ml (compared with the systemic value of 6 gr/100 ml) without cessation of ultrafiltration.

The filtration theory of atherogensis proposes that slow filtration of fluid through the arterial walls results in an elevation of the

concentration of high molecular weight lipids at the blood/tissue interface. Brown, Tulin and Van Dyke (14) have shown that at normal physiological conditions of flow and shear stress, the lipid concentration at the walls should be only modestly greater (5-50%) than in the bulk blood. However, in regions of stasis or in regions where the shear rate falls to low values, filtration may result in large concentrations of lipid at the walls, perhaps even to the extent of exceeding lipid solubility limits.

An obvious serious consequence of this polarization is the tissue reaction to the diminished water and nutrient flux. The rate of influx and accumulation of lipids in the arterial walls (11), which ultimately lead to the formation of atheroma, is enhanced by the elevated wall concentration. Since oxygen diffusivity in protein solutions decreases with increasing protein concentration (15), tissue oxygen deprivation could be another mechanism by which a protein polarization layer encourages the atherosclerotic process.

Investigations have been carried out on the effects of concentration polarization on the ultrafiltrate flux and effective solute retentivity for the hemodiafiltration process (7,8). In addition to the deleterious effect on flux, the protein polarization layer has also been observed to effect the permeability of plasma microions, including sodium, chloride, urea and uric acid.

II. Current Theories and Motivation For This Work

A. Current Theories

In mechanical filtration, where the filtered particles are large, the polarization layer is readily seen as an additional hydraulic resistance in series with the intrinsic resistance of the filtering medium. In reverse osmosis, where ion-size particles are filtered, it is generally accepted (16,17) that the concentrated solute layer diminishes filtrate flux by reducing the pressure driving force through the action of an increased adverse chemical potential gradient (osmotic pressure). Polarization layers in the ultrafiltration process are thought to give rise to one or both of these effects, the dominant effect being largely dependent on the properties of the solution being filtered. Certainly if the concentration at the interface exceeds the solute solubility limit, a hydraulic resistance would be present. This solubility limit is often assumed to be reached at the point at which flux becomes insensitive to increased pressure (18). No quantitation of either the pressure at which this limit is reached or the true concentration on the filtering membrane surface has been made and so far the concept is not much more than a convenience based on post-experimental observations of fouled membrane surfaces. However, even before this pressure insensitive region is reached, ultrafiltrate flux is observed to increase less rapidly with increasing pressure.

Results of a previous fundamental study of albumin ultrafiltration by Kozinski and Lightfoot (12) have suggested that the reduction in flux in their system is attributable to the increased osmotic pressure. Their ultrafiltration model employs the Stefan-Maxwell flux equation

coupled with a body force transmittance through the polarization layer (12,19).

Solute mass balance:

$$v_s = \frac{m}{\rho} \frac{M_0 D_s}{RT} \left[\frac{1}{m_A} \frac{d\pi}{dY} - V_A \frac{dP}{dY} \right] \qquad (1\text{-}1)$$

Solvent flux:

$$v_s = \frac{K_m}{\rho_s} (\Delta P - \pi|_{Y=0}) \qquad (1\text{-}2)$$

where

v_s = ultrafiltrate flux

Y = height above membrane

K_m = intrinsic membrane permeability to solvent flux

ΔP = overall pressure drop across membrane and polarization layer

m = solution mean molal concentration

ρ = solution mean density

ρ_s = ultrafiltrate density

M_0 = solvent molecular weight

D_s = phenomenological transport coefficient

m_A = solute molal concentration

V_A = solute specific molar volume

The authors point out that equation (1-1) presents the opportunity to treat reverse osmosis and mechanical filtration from a unified point of view, with ultrafiltration an intermediate case. In reverse osmosis, the polarization layer is treated as a dilute solution for which the pressure gradient will be zero. Equation (1-1) then simplifies to the familiar form of Fick's Law. In mechanical filtration, the solute is deposited or precipitates at the membrane, and the gradient in chemical potential approaches zero as the solute becomes totally immobilized. These restrained solute macromolecules can now transmit an equivalent body force from the supported membrane.

This viewpoint is useful for establishing the middle ground which ultrafiltration occupies. However, its utility remains limited by the lack of an intimate knowledge of the molecular properties of the solution. Specifically needed is data concerning the highly non-ideal behaviour of the concentrated macromolecular solution which forms the polarization layer, and conceptual detail concerning the possible transmittance of body forces in the layer. That is, it emphasizes the need for research in the field of the biophysical chemistry of concentrated solutions. Such information is needed before a specific model can be corroborated by experiment.

Previous ultrafiltration models have included the empirical concept of a polarization layer permeability (8,13) derivable from a solute mass balance in the polarized layer and a statement of solute flux through the membrane.

Solute mass balance:

$$v_s = \frac{D}{\delta} \ln \left(\frac{\omega_A^*}{\omega_A^i} \right) \tag{1-3}$$

Solvent flux:

$$v_s = \frac{\Delta P - \pi|_{Y=0}}{\frac{1}{K_m} + \frac{\delta}{B_g}} \cdot \frac{1}{\rho_s} \tag{1-4}$$

where

ω_A^* = solute weight fraction at membrane

ω_A^i = solute weight fraction in bulk solution

D = solute diffusivity

δ = polarized layer thickness

B_g/ρ_s = polarization layer permeability

Dorson, et al. (8) used this model to describe results of beef blood ultrafiltration in a flat plate channel device. They found that a polarization layer permeability of (2.1-3.3) x 10^{-7} cm^2/min-psi described their results. For the ultrafiltration of albumin solutions in a stirred cell device, a permeability of 2×10^{-6} cm^2/min-psi was found representative of the data by others (20). These permeabilities are more than two orders of magnitude lower than that which Blatt et al. (13) calculated for a layer comprised of hard spheres which are the same dimension as the albumin molecule (8×10^{-4} cm^2/min-psi).

While this model offers a technique for describing experimental

results, it gives little chance for 'a priori' prediction of ultrafiltration performance. In work with both of these models, investigators have been lacking data for the properties of the concentrated solutions of the rejected solutes and polarized layer concentration measurements. The research of this thesis focused on making independent measurements (as opposed to derived measurements from a hypothetical model) of these variables.

B. Ultrafiltration in a Stirred Cell

Side-by-side studies of osmotic pressure and ultrafiltration in a laboratory stirred cell were conducted with solutions of albumin and three additional macromolecules (21). The objective was to assess the significance of each of these macromolecules as a thermodynamic barrier when concentrated at the surface of an ultrafiltration membrane. The results are summarized here to emphasize the motivation for the experimental program of this thesis. Details of the work discussed here are presented in the thesis by Green (21).

The osmotic pressure measurements of concentrated Bovine serum albumin (BSA) solutions were made in a specially designed high pressure, static-type membrane osmometer. These measurements, made at three different solution pH levels, are the subject of Chapter Three. In that chapter, the results are shown that at an ionic strength of 0.15 M saline, and a protein concentration of 45 gr/100 ml solution (45 gm%), the osmotic pressure at 7.4 pH is 70 psi, which was more than four times greater than the osmotic pressure of the equivalent solution at 4.5 pH. The osmotic pressure of the other three solutes, bovine fibrinogen,

human low density lipoprotein (LDL) and polyethylene oxide (PEO) were made by Green (21) using a Hewlett-Packard Model 501 automatic membrane osmometer.

For ultrafiltration, a conventional stirred cell apparatus was employed. The applied pressure was varied over the range of 2.5 to 55 psig and was measured with a mercury manometer or a pressure gauge. Bulk solute concentration in the ultrafiltration cell was held constant by continuously replenishing the cell with solvent which was fed from a reservoir during the course of an experiment. Stirring rates were measured with a stroboscope and were maintained sufficiently high so that the boundary layer over the membrane was in the turbulent regime for all experiments. Ultrafiltrate flux was monitored by timed collections into a graduated cylinder.

The same Abcor HFA-180 membrane used in the osmometry experiments were used for ultrafiltration. In addition, an Amicon PM-30 membrane, which also has 100% rejection for albumin, was tested in the albumin investigation with no difference in results. Prior to ultrafiltration, each membrane was characterized for its flux-pressure response with pure solvent.

1. Albumin

Figure 1-2 shows the results of the albumin ultrafiltration study. The albumin concentration was the same in all experiments, 90 grams per liter solvent, or 8.5 gm% in 0.15 M unbuffered saline.

These experiments show that at every pressure level investigated, the ultrafiltrate flux is highest for the pH 7.4 solution, the solution for which highest osmotic pressures have been measured. In the pressure

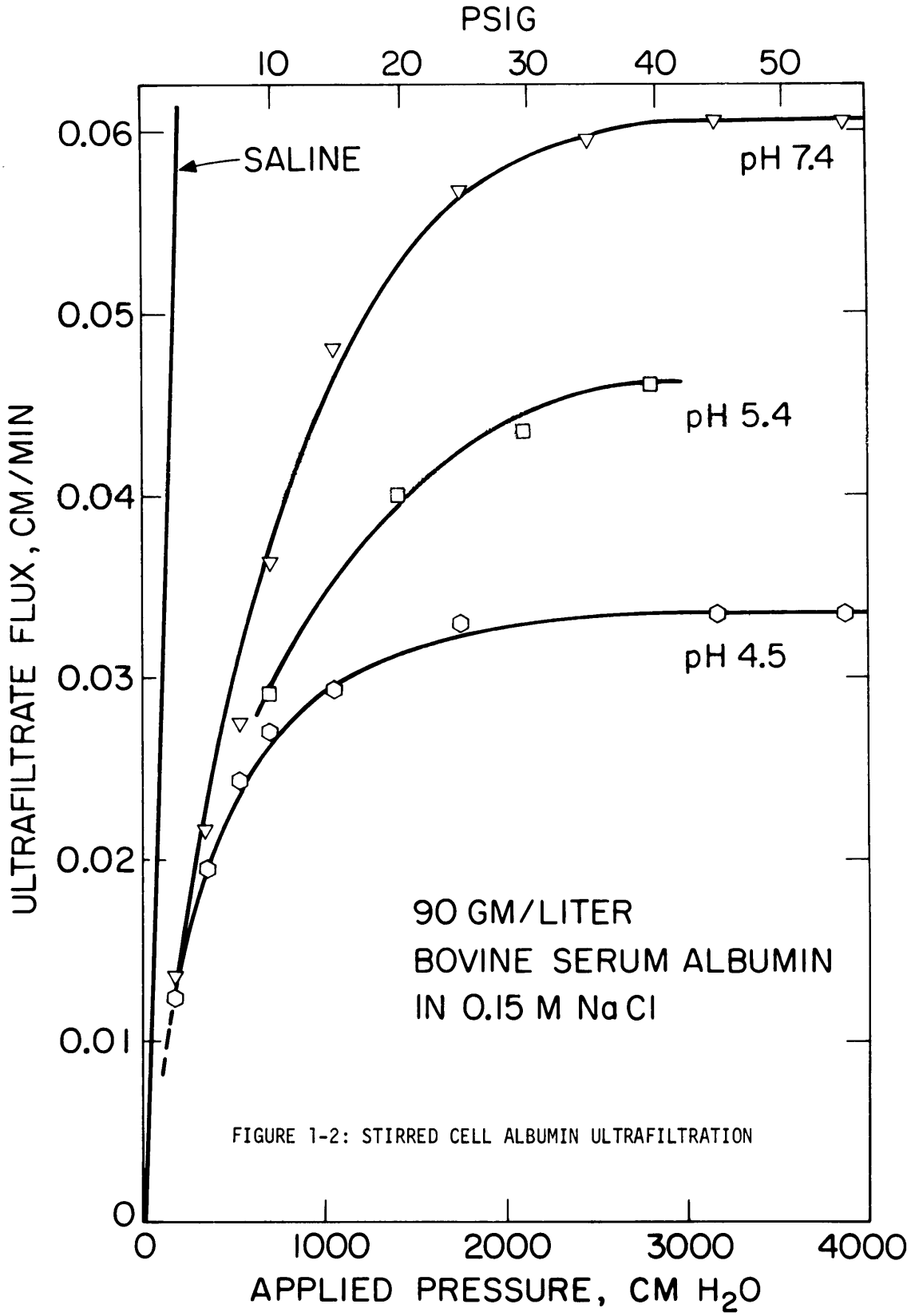

FIGURE 1-2: STIRRED CELL ALBUMIN ULTRAFILTRATION

independent region, above about 40 psig, the flux of the pH 7.4 solution is almost twice that of the acid pH 4.5 solution.

The results shown on Figure 1-2 were taken with cellulosic Abcor HFA-180 membranes. Green showed that similar results were obtained at 4.5 pH and 7.4 pH when the experiments were carried out using the aromatic polymer Amicon PM-30 membranes.

Since it is not unreasonable to imagine albumin concentrations at the membrane surface as high as 45 gm%, which is well below the solubility limit of about 60 gm%, the osmotic pressure measurements at this concentration could be used to argue that the deviation of the ultrafiltrate flux curves from the linear relation for pure saline is exclusively of a thermodynamic nature. However, since the sequence of flux curves for the three pH levels is opposite to that suggested by the sequence of the osmotic pressure data, such a conclusion cannot be drawn from this data alone.

2. Fibrinogen

Experiments with bovine fibrinogen in 0.15 M saline were carried out at two different solution pH levels. The osmotic pressure determinations and the ultrafiltration results are shown together in Figure 1-3.

Fibrinogen, like albumin, is a highly charged polyelectrolyte and also displays an osmotic pressure dependency on solution pH as shown in the figure at the left. This molecule differs from albumin primarily in its high degree of asymmetry. On a reduced basis, the data gives a molecular weight which compares favorably with the literature value of 340,000.

FIGURE 1-3 FIBRINOGEN IN 0.15 M NaCl

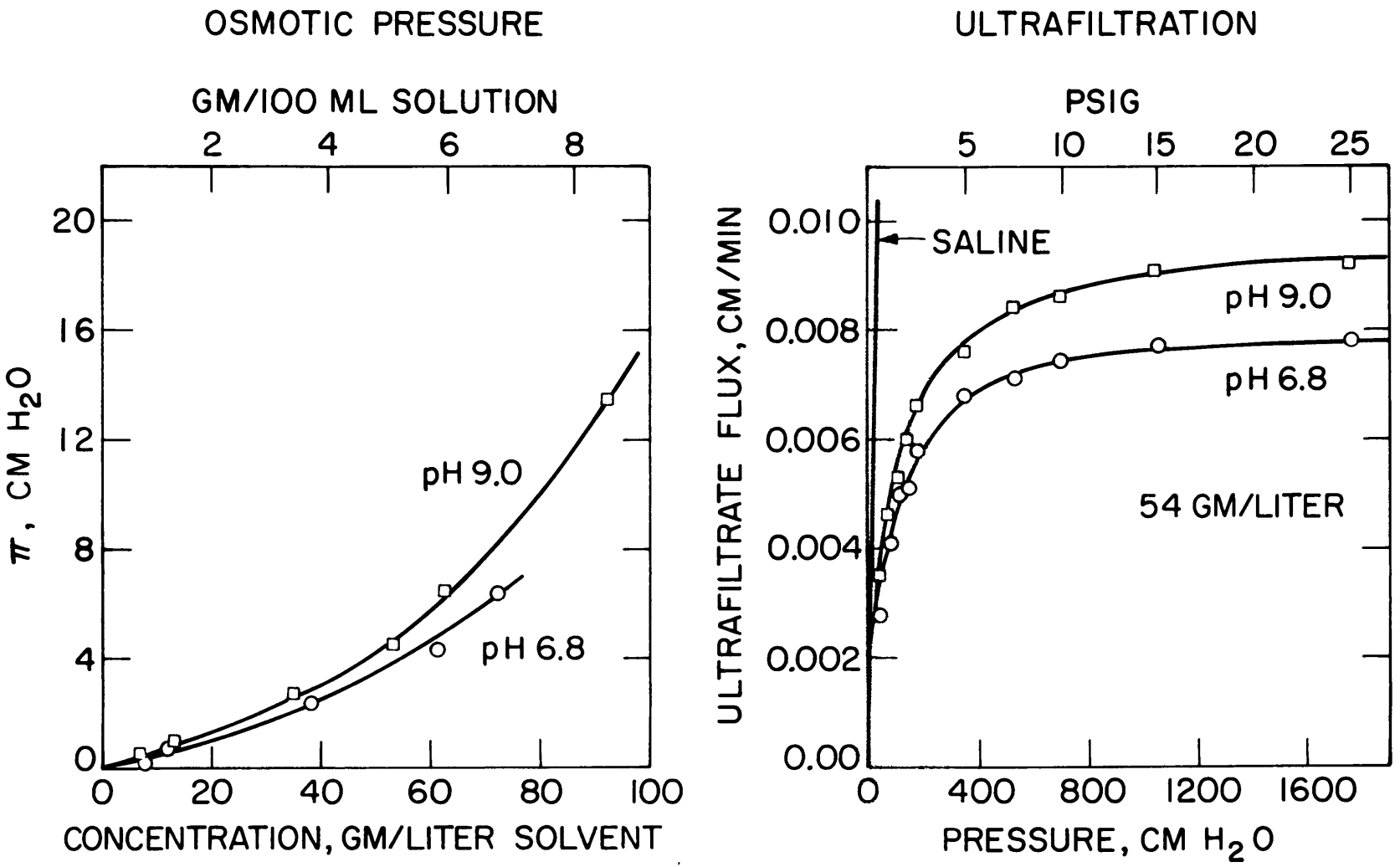

When compared to the applied pressures used in the ultrafiltration experiments and shown in the figure to the right, it is not clear that the osmotic contribution to the deviation from the saline line is very significant. In addition, it is again observed that at the pH for which fibrinogen solution osmotic pressures are the highest, the ultrafiltrate fluxes are also the highest, and vice versa.

3. Low Density Lipoprotein (LDL)

The results for the experiments with LDL in 0.15 M saline at the physiological pH of 7.4 are shown in Figure 1-4. This protein is a very large molecule with a molecular weight of about three million and since it consists of about 80% lipid it is not as highly charged as albumin. This data, when plotted on a reduced basis, gives a molecular weight of three million which is in exact agreement with that reported from agarose gel filtration determinations (22). This data is fitted very well by a two-term virial expression. Note that LDL osmotic pressure never achieves very large values and, at equivalent concentrations, is more than two orders of magnitude smaller than the osmotic pressure of albumin at the same pH.

The ultrafiltration results are shown on the right. LDL bulk solution concentration was 68 gm/liter, or about 7 gm%. For this system, the contribution of an increased osmotic pressure at the membrane surface probably accounts for only a small fraction of the observed deviation of the flux-pressure relationship from that for pure saline.

4. Polyethylene Oxide

Polyethylene oxide was the only synthetic macromolecule included in this study. It is different from the proteins in that it is a random

FIGURE 1-4

LOW DENSITY LIPOPROTEIN IN 0.15 M NaCl, pH 7.4

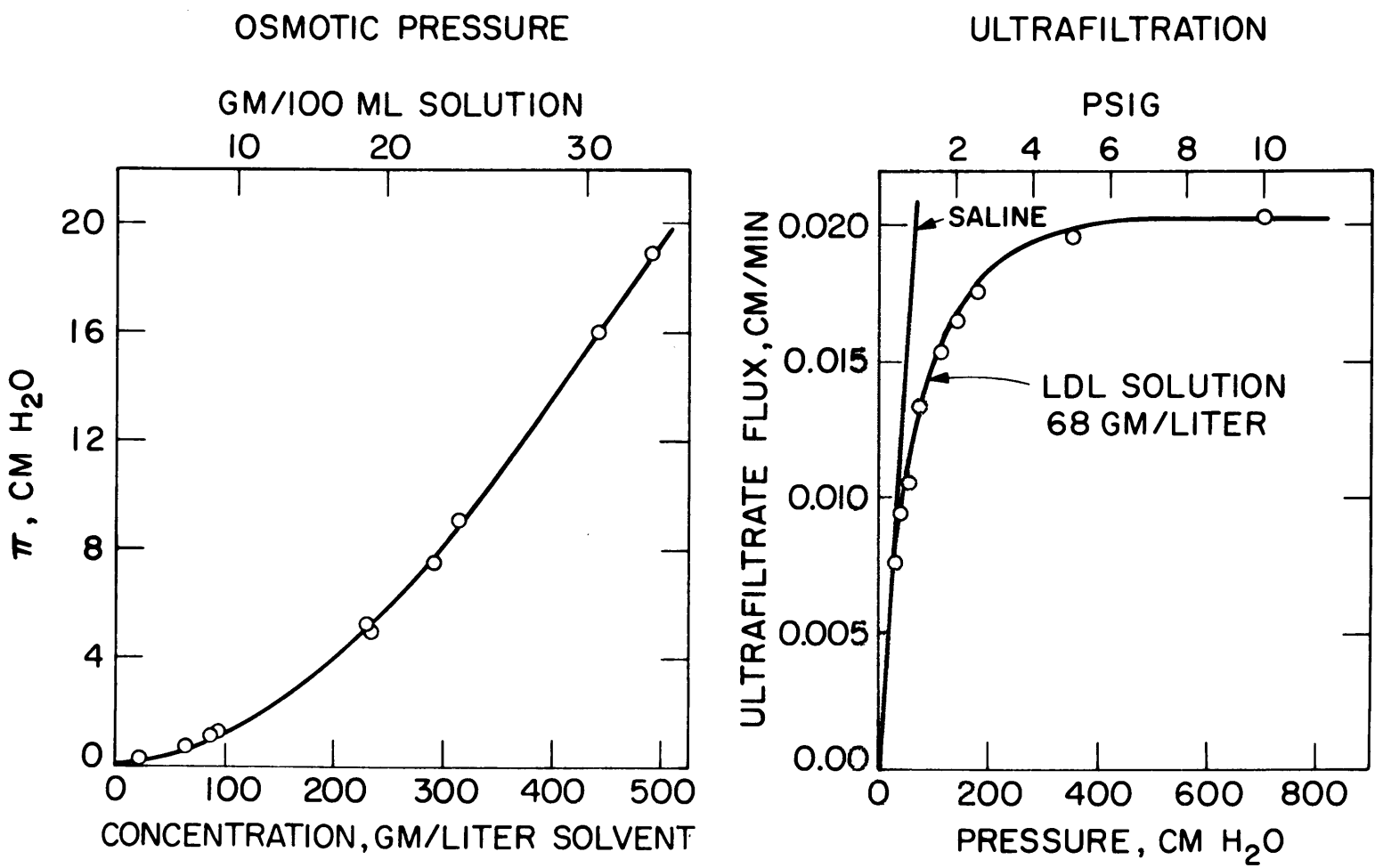

coil and uncharged. Aqueous solution osmotic pressure data is shown on the left of Figure 1-5. This data gives a number average molecular weight of 609,000 which is somewhat higher than expected based upon the viscosity average weight of 622,000 determined for this particular preparation of PEO.

It seems for this system, with any reasonable extrapolation of the small measured osmotic pressures, very little of the reduction in the observed ultrafiltration flux can be ascribed to a thermodynamic limitation.

The uncharged character of PEO is reflected in the fact that ultrafiltrate flux was not pH sensitive for the two pH levels of 8.9 and 7.1.

C. Summary Remarks

The literature review concerning the effects of concentration polarization in protein ultrafiltration has shown that models and proposals are available which imply, but do not demonstrate, the physics of this phenomena. Side-by-side comparisons of osmotic pressure measurements and ultrafiltration performance for various macrosolute systems suggest a complex phenomenon which is probably very dependent on the way in which the physical chemistry changes between the different systems. The likelihood that the macrosolute polarization layer is acting as a thermodynamic resistance probably decreases with increasing molecular weight, and with decreasing polyelectrolyte character of the solutes. For the macrosolutes studied above that ranking would probably be: albumin > fibrinogen > PEO > LDL.

The research in this thesis is only for the system of albumin in

FIGURE 1-5 POLYETHYLENE OXIDE IN WATER

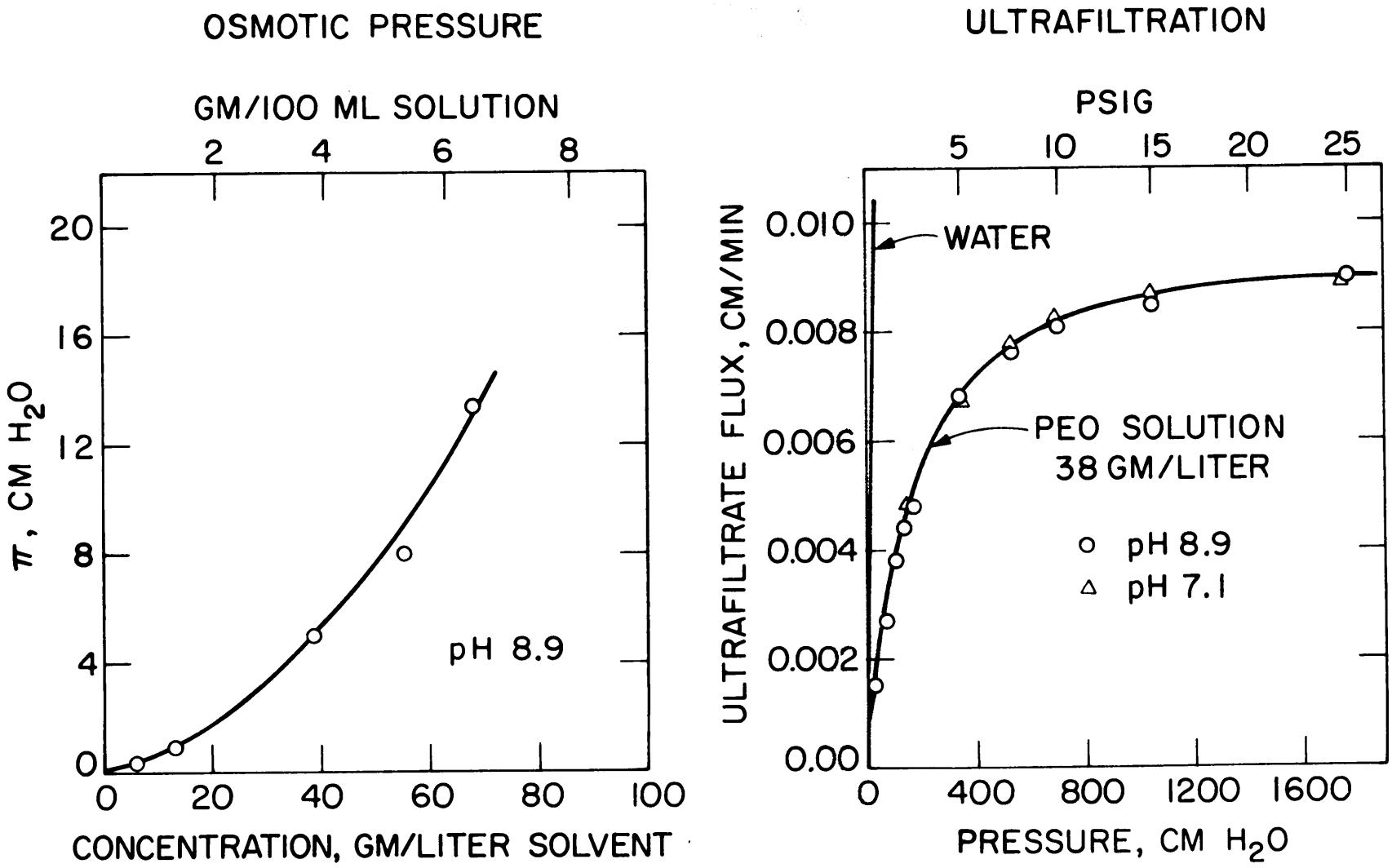

unbuffered 0.15 M saline. All experiments were conducted at the three pH levels of 4.5, 5.4 and 7.4.

BIBLIOGRAPHY

(1) Porter, M. C. and L. Nelson, "Ultrafiltration in the Chemical Food Processing, Pharmaceutical and Medical Industries." In Recent Developments in Separation Science, Vol. 2. N. N. Li, editor. CRC Press, Cleveland, Ohio. (1972).

(2) Porter, M. C., "Membrane Ultrafiltration For Pollution Abatement and Byproduct Recovery". AIChE Symp. Ser. No. 129, Vol. 69, p. 100 (1973).

(3) Spatz, D. D., "Reclamation and Reuse of Waste Products From Food Processing By Membrane Processes." AIChE Symp. Ser. No. 129, Vol. 69, p. 89 (1973).

(4) Goldsmith, R. L., R. P. deFilippi and S. Hossain, "New Membrane Process Applications". AIChE Symp. Ser. No. 120, Vol. 68, p. 7 (1972).

(5) Van Oss, C.J., "Ultrafiltration", In Tech. Surface Colloid Chem. Phys., Vol. 1, Marcel Dekker, Inc., New York (1972).

(6) Michaels, A. S., "Ultrafiltration". In Progress in Separation and Purification. S. Perry, editor. p. 297, Interscience, New York (1968).

(7) Colton, C. K., L. W. Henderson, C. A. Ford and M. J. Lysaght, "Kinetics of Hemodiafiltration. I. In Vitro Transport Characteristics of a Hollow-Fiber Blood Ultrafilter." J. Lab. Clin. Med., 85, 355 (1975).

(8) Dorson, W. J., V. B. Pizziconi and J. M. Allen, "Transfer of Chemical Species Through a Protein Gel". Trans. Amer. Soc. Artif. Int. Organs, 17, p. 287 (1971).

(9) Deen, W. M., C. R. Robertson, and B. M. Brenner, "Concentration Polarization in an Ultrafiltering Capillary". Biophys. J., 14, p. 412 (1974).

(10) Gofman, J. W. and W. Young, "The Filtration Concept of Atherosclerosis and Serum Lipids in the Diagnosis of Atherosclerosis". In Atherosclerosis and Its Origin. M. Sandler and G. H. Bourne, editor. Academic Press, Inc., New York, p. 197 (1963).

(11) Bratzler, R. L., Ph.D. Thesis, Massachusetts Institute of Technology, Cambridge, Mass. (1975).

(12) Kozinski, A. A. and E. N. Lightfoot, "Protein Ultrafiltration: A General Example of Boundary Layer Filtration". AIChE J., 18, 1030 (1972).

(13) Blatt, W. F., A. Dravid, A. S. Michaels and L. Nelson,"Solute Polarization and Cake Formation in Membrane Ultrafiltration: Causes, Consequences and Control Techniques". In Membrane Science and Technology, J. E. Flinn, editor. Plenum Press, New York (1970).

(14) Brown, C. E., M. P. Tulin and P. Van Dyke, "On the Gelling of High Molecular Weight Impermeable Solutes During Ultrafiltration". CEP Symp. Series, No. 114, 67, p. 174 (1971).

(15) Navari, R. M., J. L. Gainer and K. R. Hall, "A Predictive Theory for Diffusion in Polymer and Protein Solutions". AIChE J., 17, p. 1028 (1971).

(16) Spiegler, K. S. and O. Kedem, "Thermodynamics of Hyperfiltration (Reverse Osmosis): Criteria for Efficient Membranes". Desalination, 1, p. 311 (1966).

(17) Reid, C. E., "Principles of Reverse Osmosis". In Desalination by Reverse Osmosis, U. Merten, editor, M.I.T. Press, Cambridge, Mass. (1966).

(18) de Filippi, R. P. and R. L. Goldsmith, "Application and Theory of Membrane Processes for Biological and Other Macromolecular Solutions". In Membrane Science and Technology, J. E. Flinn, editor, Plenum Press, New York (1970).

(19) Lightfoot, E. N., Transport Phenomena and Living Systems. p. 298, John Wiley and Sons, Inc., New York (1974).

(20) Dravid, A. R., Personal Communication to C. K. Colton, Amicon Corporation, Lexington, Mass. (August 7, 1969).

(21) Green, D. G., M. S. Thesis, Massachusetts Institute of Technology, Cambridge, Mass. (1974).

(22) Margolis, S., "Separation and Size Determination of Human Serum Lipoproteins by Agarose Gel Filtration." J. Lipid Res., 8, p. 501 (1967).

CHAPTER TWO

PHYSICAL CHEMISTRY OF CONCENTRATED ALBUMIN SOLUTIONS

The behaviour of aqueous solutions of Bovine serum albumin (BSA), and Na^+, Cl^-, H^+ and OH^- micro-ions is most easily interpreted by adopting Einstein's molecular-kinetic theory for small suspended particles (1). In this view, the dissolved protein molecule is differentiated from a suspended body solely by its dimensions. In the ideal case of a dilute solution considered by Einstein, these molecules are inert, and their interactions in solution are viewed as inelastic collisions between hard spheres which are moving about by virtue of their thermal kinetic energy (Brownian motion). The transport properties of these ideal solutions are stated in terms of Einstein's equation (1) for the diffusivity of the solute in an unbounded fluid,

$$D_\infty = kT/f_\infty \qquad (2\text{-}1)$$

where f_∞ is the molecular friction coefficient computed for a steady Stokes flow ($6\pi\eta a$ for a sphere, η equaling the solvent viscosity and a the sphere radius). The colligative properties are represented by the van't Hoff limiting law for osmotic pressure, π, which was also derived by Einstein from the kinetic theory view (1).

$$\pi = \frac{RT}{V^\circ} m_2 \qquad (2\text{-}2)$$

where V° is the volume of a kilogram of solvent and m_2 the molality of the solute.

For a globular protein which possesses a strong polyelectrolytic character, significant deviations from the ideal relationships of

equations (2-1) and (2-2) occur because the interacting protein molecules are not inert. Of consequence in this regard are the variables which affect the ionic character of albumin. Therefore, in the first section of this chapter, the albumin-hydrogen-chloride ion equilibrium is discussed and the average electrical charge on the protein molecule is computed using data available in the literature.

The osmotic pressure of aqueous albumin solutions is seen from the literature to depend upon solution ionic strength, pH, types of anions which are present and protein concentration. Section II is first a survey of the qualitative effects which have been previously reported and secondly, an introduction to the models which are employed in Chapter 3 to quantitate the nonidealities of the osmotic pressure measurements reported there.

The literature is more ambiguous regarding the effects on albumin diffusivity of those variables which determine the ionic character of the molecule. Section III is a survey of diffusivity determinations made by several different techniques and at a variety of conditions. Recently, a technique which measures the spectrum of light scattered from charged macromolecules in solution has been employed to determine the diffusivity of albumin as a function of solution ionic strength and pH (2).

In the last section of this chapter, the solubility and specific density of albumin in saline solutions are considered. Experimental evidence and a literature citation are presented to show that the specific density of albumin in saline is probably not a function of albumin concentration over the range of interest here. From this point, an equation of state for this system is readily proposed.

I. The Multiple Equilibria of Albumin: Molecular Charge

Albumin contains hundreds of acidic protons. It can therefore exist in a great number of intermediate ionization stages between the most acid form, in which the maximum possible number of protons is attached, and the most basic form, from which all acidic protons have been removed (Chapter 8, Tanford (3); Chapter 9, Edsall and Wyman (4)).

The titration curve of BSA has been studied in detail by Tanford, et al. (5), who assumed a molecular weight of 65,000. From their data, the authors have calculated the number of groups of the various kinds, and their intrinsic pK values. These results are shown in Table 2-1. The number of groups were found to be in excellent agreement with determinations made by amino acid analysis. The intrinsic acid dissociation constants were evaluated with the assumption that electrostatic effects could be ignored. These values of pK were generally in the range of values for the pK's of these same groups when evaluated from the titration data of other proteins.

In addition to equilibria with hydrogen and hydroxyl ions, albumin combines with a great number of other substances, most notably anions (4, Chapter 11). Studies of the effects of the albumin-anion equilibria on the hydrogen ion equilibria (i.e., the albumin titration curve) have shown that these equilibria are interdependent (6,7,9). The affinity of albumin for various anions has been shown to follow the Hofmeister series; that is, binding increases in the order chloride < bromide < nitrate < iodide < thiocyanate < p-toluenesulfonate (6). The affinity of albumin for cations has been studied for solutions of sodium (6,7), magnesium, calcium, strontium and zinc ions (6). Only zinc binding was found to be appreciable.

TABLE 2-1

Ionizable Groups in Bovine Serum Albumin
and Their Intrinsic pK Values

(Assumed molecular weight of albumin 65,000)

Group	Number per Molecule	Albumin pK_{int}
α-Carboxyl	1	3.75
Carboxyl	99	3.95
Imidazole	16	7.0
α-Amino	1	7.8
ε-Amino	57	9.8
Phenolic	18	10.35
Guanidine	22	>12

Albumin anion binding has also been investigated by observing the affects of salt addition on protein electrophoretic mobility (10,11). The Hofmeister series was again observed to apply in determining the affinity of albumin for a given anion (10). The acetate anion is consistent with the above mentioned series in that it binds less tightly than chloride.

In order to determine the average charge of an albumin molecule in a solution where these multiple equilibria exist, it is necessary to determine the number of micro-ions which are bound to the macromolecule. The general binding equation is given in Edsall and Wyman (4, Chapter 11):

$$\bar{\nu} = \sum_{i=1}^{m} \frac{n_i k_i (A) \exp (2 W\bar{Z})}{1+k_i (A) \exp (2 W\bar{Z})} \qquad (2\text{-}3)$$

where

$\bar{\nu}$ = the average number of sites on an albumin molecule which are bound to an ion of A

$\bar{Z}$ = the average charge of an albumin molecule

m = the number of different types of homogeneous binding sites

n_i = the number of reactive groups of class i per molecule

k_i = intrinsic association constant for a class i site

(A) = activity of microions in solution

W = electrostatic interaction constant

For the albumin in saline system, the literature concensus is strong in suggesting that only hydrogen ion and chloride ion binding occur. The albumin charge calculation has been made by combining the hydrogen binding data (albumin in unbuffered saline titration curve) of Tanford, et al. (5) and the chloride ion binding data of Scatchard, et al. (7). The hydrogen binding has been adjusted by multiplying Tanford's value of bound hydrogen per BSA molecule, $\bar{\nu}_{H^+}$, by the ratio of (69/65). This adjustment is made to be consistent with Scatchard's measurement of 69,000 for the molecular weight of BSA (12).

The binding of chloride ions to albumin was found by Scatchard to be describable in terms of a two site model, so that with m=2 equation (2-3) for chloride binding is:

$$\bar{\nu}_{Cl^-} = \frac{n_1 k_1 [Cl]\gamma \exp(2W\bar{Z})}{1+k_1[Cl]\gamma\exp(2W\bar{Z})} + \frac{n_2 k_2 [Cl]\gamma\exp(2W\bar{Z})}{1+k_2[Cl]\gamma\exp(2W\bar{Z})} \qquad (2\text{-}4)$$

Scatchard, et al. found that for the type 1 binding site, there were 10 binding sites per BSA molecules (i.e., n_1=10), and that the intrinsic association constant for this type was, k_1=44. For the type 2 site, n_2=30 and k_2=1.1. For the activity coefficient of the chloride ion, they used the approximate expression

$$-\log_{10}\gamma = 0.5\sqrt{I}/(1 + 2\sqrt{I})$$

which corresponds to the Debye-Hückel theory for a chloride ion diameter of 6.1 Å. When the albumin solution is .15 M saline, I = 0.15 and γ = 0.78. The free chloride ion concentration, [Cl] is 0.15 molar and assumed constant for dilute protein solutions.

The protein-chloride ion interaction constant, W, is also calculated from a Debye-Hückel analysis. This analysis assumes that the protein macro-ions are spheres impenetrable to salt ions, and that their net charge is evenly distributed over their surface. The result is (8);

$$W = \frac{e^2}{2\varepsilon kT}\left[\frac{1}{a} - \frac{\kappa}{1 + \kappa R}\right]$$

where

e = protonic charge, 4.802×10^{-10} statcoul

ε = dialectric constant of water, 78.54 statcoul/statvolt-cm, in the rationalized c.g.s. system

k = 1.38×10^{-16} ergs/deg (or statcoul-statvolt/°K)

a = radius of albumin, 34.5×10^{-8} cm (see reference (28))

R = center-to-center distance between the interacting ions, 37.5×10^{-8} cm

The Debye-Huckel parameter from Scatchard (8) is given by

$$\kappa = 3.2809 \times 10^{+7}\sqrt{I} = 1.27 \times 10^{+7}$$

From these values the interaction parameter at 25°C is, W = .026 and the chloride binding equation (2-4) becomes

$$\bar{\nu}_{Cl^-} = \frac{51.48\exp(+.052\bar{Z})}{1 + 5.148\exp(+.052\bar{Z})} + \frac{3.861\exp(+.052\bar{Z})}{1 + 0.1287\exp(+.052\bar{Z})} \qquad (2\text{-}5)$$

The titration data of Tanford, et al. in 0.15 M saline solution, including the molecular weight correction described above, is shown on Figure 2-1 as the number of bound protons per BSA molecule, $\bar{\nu}_{H^+}$, versus solution PH. They referenced this titration data to a pH value of 2; that is, maximum number of reversibly bound protons is reached at pH 2. At lower solution pH values, irreversible changes in macromolecular structure were observed. With this reference value, the isoionic point ($\bar{\nu}_{H^+} = 0$ by definition) at 5.46 pH, corresponded to the dissociation of 96 protons per BSA molecule, by their calculation. These two reference states are related by, $\bar{\nu}_{H^+} = 96 - \bar{h}$, where $\bar{h}$ is the number of H^+ ions which can be reversibly dissociated ($\bar{h} = 0$ at pH 2) as solution pH is increased above 2.

The total macro-ion valence is computed from the difference between the number of bound protons and the number of bound chloride ions.

$$\bar{Z} = \bar{\nu}_{H^+} - \bar{\nu}_{Cl^-} \qquad (2\text{-}6)$$

With the data from the $\bar{\nu}_{H^+}$ vs. pH curve of Figure 2-1, the valence equation and equation (2-5) have been solved simultaneously for the

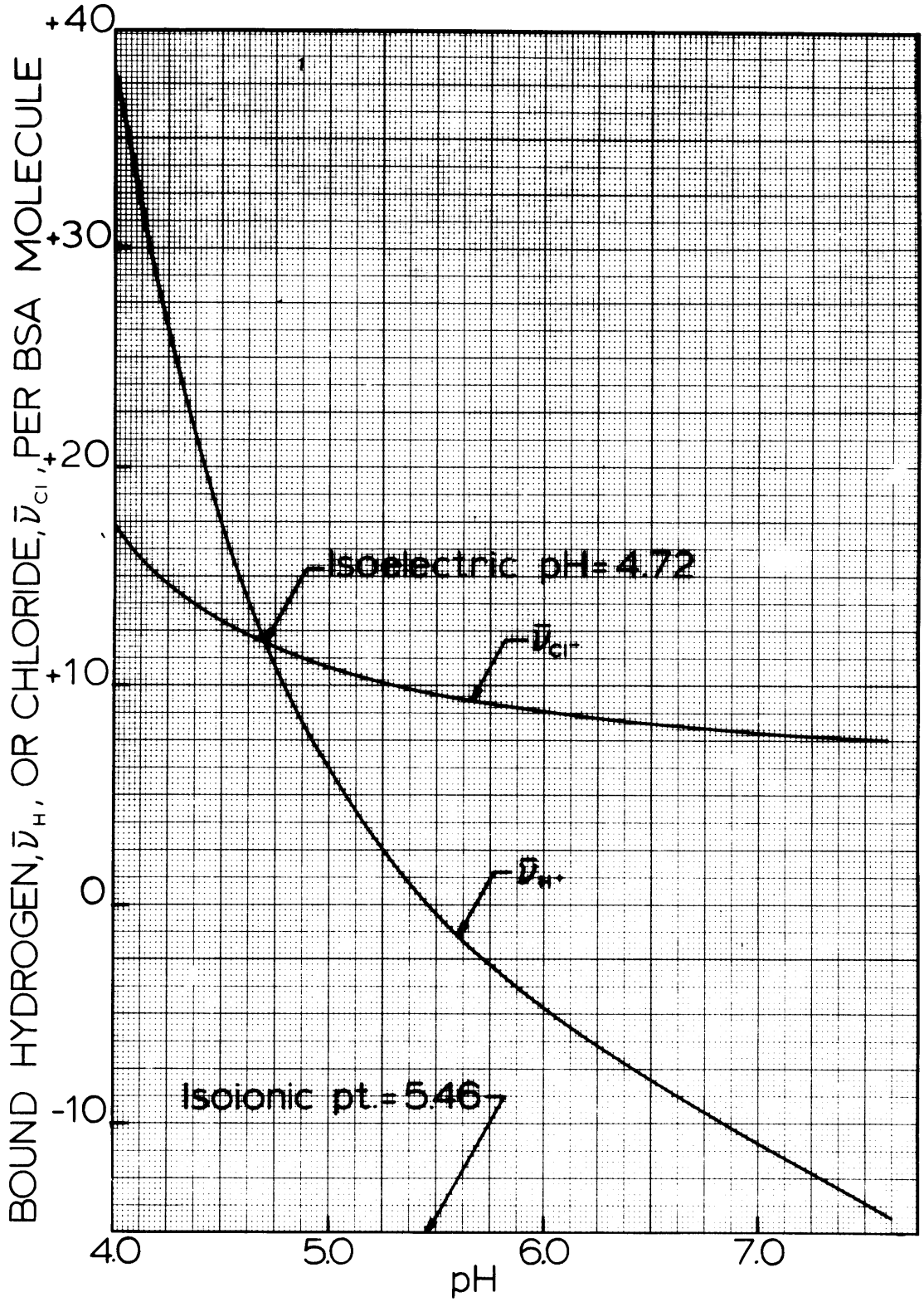

Figure 2-1: Hydrogen and chloride equilibria of BSA in 0.15M NaCl.

unknowns $\overline{Z}$ and $\overline{\nu}_{Cl^-}$ as a function of solution pH. The second curve of Figure 2-1 shows the result for the number of chloride ions bound, $\overline{\nu}_{Cl^-}$. The total albumin charge, $\overline{Z}$, as a function of pH is shown on Figure 2-2.

It is not surprising from electrostatic considerations that chloride binding increases as solution pH is lowered, that is, the macro-ion becomes more positively charged. Particularly noteworthy from Figure 2-1 however, is the substantial binding of the anion even at the pH levels where the albumin molecule is negatively charged. The reason for this apparently incongruous result is unknown, but probably results from the anion binding to positively charged groups, such as ammonium, imidazolium, or guanidinium groups in certain specific configurations which favor such bonds (4, Chapter 11).

Figure 2-1 is helpful in the discussion of the difference between the isoionic and the isoelectric pH of albumin-saline solutions. The isoelectric point is defined as the pH at which the average net charge $\overline{Z}$ of the protein is zero. Experimentally, it can be measured by observing the motion of the protein in an electric field, as by electrophoresis for example. From Figure 2-1, and equation (2-6), it is seen that the isoelectric point also corresponds to the pH at which the number of bound hydrogen ions and bound chloride ions are equal.

An isoionic protein solution is defined as a solution that contains, in addition to dissolved protein, no ions other than those arising from dissociation of the solvent. Such a protein solution can be obtained experimentally. For instance, if an aqueous protein solution is passed down a mixed-bed ion exchange column all cations

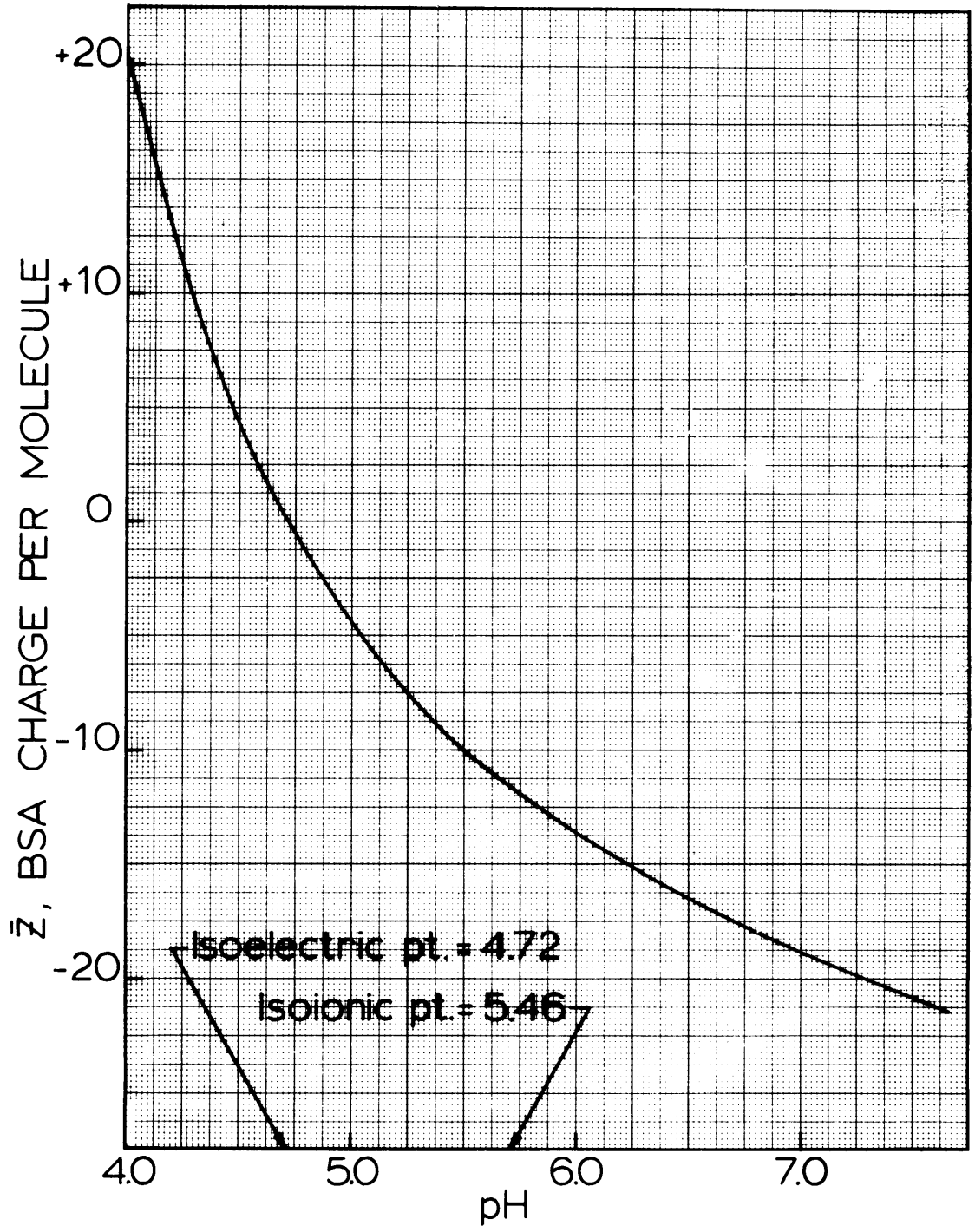

Figure 2-2: BSA charge in 0.15M NaCl.

and anions other than the bulky protein ions are exchanged for H^+ and OH^- ions, and the resulting solution is by definition isoionic. An alternative method of ion exchange is dialysis, or dialysis followed by electrodialysis for complete removal of micro-ions other than H^+ and OH^-.

When a salt is present, and either the cation or anion binds to the protein, it is still possible to measure an isoionic pH. However, since the hydrogen equilibrium is generally affected by the other protein-micro-ion equilibria, this isoionic point will be different from that measured in the absence of salt. For BSA, adding NaCl to a solution of pure water and BSA causes the isoionic pH to increase. The isoelectric point shifts in the opposite direction; that is, it decreases, when salt is added to the solution. Figure 2-1 shows that the isoionic pH is the value at which $\bar{\nu}_{H^+} = 0$, but that $\bar{Z} = -9.6$ from Figure 2.2 at this pH of 5.46.

For a complicated polyelectrolyte such as albumin with its several classes of ionizable groups and their wide range of intrinsic pK's, there is considerable scatter in the values reported in the literature for the isoionic and isoelectric pH's. Table 2-2 is a compilation of these values, including the conditions under which the determinations were made. No instance was found in which a side-by-side comparison of the isoionic point and of the isoelectric point for the same solution was made. Only the determinations of Gutfreund (21) show an effect of solution pretreatment on the salt-free isoionic pH.

The values of isoionic pH, which were measured with a KCl glass electrode, for this work involve four separate lots of Pentex grade

TABLE 2-2

Survey of Isoionic and Isoelectric pH for Albumin Solutions

Isoionic pH		Comment	Source
Salt Free Solution	0.15 M Saline Solution		
5.17[1]	5.37	6 gm % BSA	(12)
4.88[1]	5.21	Human serum albumin*	(6)
4.9 [1]	(5.2)	Determination in salt solution at 0.6 M	(7)
	5.46	∿5 gm % BSA	(5)
4.9 [1]		1 gm % BSA	(14)
5.0 [2]	(5.6)	Determination in salt solution at 0.5 M	(15)
4.4 [2]		∿7 gm % BSA	(21)
4.9 [3]		∿7 gm % BSA	(21)
5.19	5.28-5.55	5-35 gm % BSA	This Work
Isoelectric pH (by electrophoresis at 0°C)			
4.40		0.15 M NaCl, unbuffered	(11)
4.80		0.01 M NaCl, unbuffered	
4.17		0.1 M (acetate & thiocyanate)	(10)
4.29		0.1 M (acetate & iodide)	
4.59		0.1 M (acetate & chloride)	
4.71		0.1 M acetate buffer	
4.89		0.02 M acetate buffer	

Notes

* Tanford, et al. (5) have demonstrated equivalence between BSA and HSA.

(1) no pretreatment of albumin solutions before isoionic pH measured.

(2) solution pretreated to remove all micro-ions except H^+ and OH^- by passing them through an ion exchange column.

(3) solution pretreatment by dialysis/electrodialysis for micro-ion removal.

BSA (Cat. No. 81-001, Miles Laboratories, Kankakee, Illinois). No prior pretreatment such as ion exchange or dialysis was performed for the salt-free determination. All solutions were made from double distilled water. The salt-free determination was at an albumin concentration of 5 gm %. The determinations in 0.15 M saline were made at concentrations which ranged from 5 to 35 gm %. No trends were observed, but this was not surprising since no precautions were taken to find them in these measurements which extended over a four year period.

From the condition of neutrality in an isoionic solution, where [] indicates molar concentration

$$[P]\bar{Z} = [H^+] - [OH^-] \qquad (2\text{-}7)$$

it can be seen that for albumin <u>in pure water</u>, a decrease in the albumin concentration [P] will increase $|\bar{Z}|$. The pH will adjust itself also so that the equilibrium between the protein and H^+ is maintained. In other words, the isoionic pH depends on concentration. For albumin, this dependence is rather weak. With an isoionic pH of about 5.0 in pure water, $|[H^+] - [OH^-]| \leq 10^{-5}$ M. If $[P] \simeq 10^{-4}$ M (about 1 gm %) then $|\bar{Z}| \leq 0.1$.

By contrast, <u>in pure water</u>, the isoelectric pH is independent of protein concentration insofar as equation (2-3) is independent of concentration. However, this independence is not necessarily true if the proton-protein interaction constant, W, or the hydrogen ion activity are dependent on protein concentration.

Scatchard, et al. (9) carefully investigated the effect of salt addition on the isoionic and isoelectric pH's of protein solutions. From analysis of binding relations such as equation (2-3), they theoretically predicted, and experimentally confirmed, that when anions are bound by the protein, such as in the case of chloride binding to albumin, the isoionic pH rises and the isoelectric pH falls when salt is added. The data of Table 2-2 are in agreement.

In summary, Figures 2-1 and 2-2 rigorously apply to the calculation of albumin charge from solution pH data for the conditions at which they were derived, namely, 1 - 5 gm % BSA dissolved in unbuffered 0.15 M saline. Where salt concentration is maintained close to 0.15 M, a charge calculation at higher protein concentrations is probably not in large error. Figures 2-1 and 2-2 would be least applicable in those instances of high protein concentration and salt concentration appreciably lower than 0.15 M.

II. Albumin Osmotic Pressure: A Survey of Pertinent Theories and Results

The electrostatic charge of macromolecular ions exerts a special influence upon their thermodynamic behaviour in solution (3, Chapter 4). Two types of effect may be distinguished. The first is the classical Donnan effect produced by the requirement that solutions of macro-ions must be electrically neutral. The second is a true non-ideality, resulting from the electrostatic interaction between the charges on macro-ions and those of other macro-ions and small ions in its vicinity.

Membrane osmometry has been a favorite method for investigation of macro-ion solution behaviour (16, 17, 18). This section is a survey of osmotic pressure investigations into protein solution behaviour, with emphasis on the studies of albumin solutions. The manner of presentation will focus on the theories which the various investigators used to present their results. In this way, a fundamental understanding of the sources of albumin solution non-idealities, and a critical review of the best methods to describe them, can be developed simultaneously. This information is directly applicable to the study of concentrated albumin solution osmotic pressure presented in Chapter 3.

The theoretical work on protein solution behaviour, as defined by osmotic pressure measurements, can be classified into roughly two categories; semi-empirical theories which describe data but reveal little about solution behaviour, and more rigorous theories which potentially say much about solution behaviour but require more

information than can be obtained by osmometry alone. Most of the first type derive from the Gibbs-Donnan equilibrium with several simplifications applied. The rigorous McMillan-Mayer theory (19, 24) for dilute solutions provides an "a priori" method to predict osmotic pressure as a function of solution composition (i.e. protein concentration, pH and ionic strength). The method of complete chemical potential specification of Scatchard (20) is a rigorous treatment of the Gibbs-Donnan equilibrium, but has been applied only in an empirical way (12, 13). Each of these three solution models, and results where they apply, will be discussed below.

A. Gibbs-Donnan Equilibrium Model

The phenomena of interest is the equilibrium for the system of a solution containing macro-ions, micro-ions and solvent separated from a solution of only micro-ions and solvent by a membrane which allows only micro-ions and solvent to pass. Since the macro-ion is charged, some of the micro-ions, although their mobility is not restricted by the membrane, become part of the non-diffusible phase as a result of their attraction to the macro-ion. The equation expressing the equality of chemical potential at equilibrium across the membrane for the solvent, with the primes indicating the side of the membrane without macro-ion, is;

$$\mu'_{o,P} + RT \ln N'_o\gamma'_o = \mu_{o,\pi+P} + RT \ln N_o\gamma_o \qquad (2\text{-}8)$$

where

$\mu'_{o,P}$ = Chemical potential of pure solvent at pressure P

$\mu_{o,P+\pi}$ = Chemical potential of pure solvent at pressure P + π

N_o = Mole fraction of solvent

γ_o = Activity coefficient of solvent

Then, since at constant temperature, $(\partial\mu/\partial P)_T = V_o$, the molar volume of the pure solvent (liter/mole),

$$RT\ \ell n\left(\frac{N_o\ \gamma_o}{N'_o\ \gamma'_o}\right) = \int_{\pi+P}^{P} V_o\ dP \qquad (2\text{-}9)$$

and assuming V_o is not a function of pressure and that the solutions are ideal, such that $\gamma_o = 1$.

$$\pi = \frac{RT}{V_o}\ \ell n\left(\frac{N'_o}{N_o}\right) \qquad (2\text{-}10)$$

Before continuing with the development to the complete Gibbs-Donnan expression, it is worthwhile to pursue a simplification of equation (2-10) which has been used extensively. Most of these investigations were attempts to obtain protein molecular weight data and therefore were concerned with dilute protein solution osmotic pressure determinations.

In the limit of infinite dilution with respect to the macro-ion, the micro-ions are equally distributed across the membrane and a new solvent phase, with mole fraction N_s, is defined to include solvent and micro-ions. Then, $N'_o = N'_s = 1$, and further by the

infinite dilution property, $-\ell n\ N_S = -\ell n(1 - N_P) \simeq N_P$, the macro-ion mole fraction, equation (2-10) becomes,

$$\pi = \frac{RT}{V_o} N_P = \frac{RT}{M_P} w_P \qquad (2\text{-}11)$$

where M_P and w_P are the molecular weight and protein concentration (grams P/liter solvent) respectively. Equation (2-11) is known as van't Hoff's limiting law and from it and an experimental determination of the osmotic pressure one can calculate the number-average molecular weight of the solute. Since the relationship is valid only at infinite dilution, however, measurements as a function of concentration and extrapolation to zero concentration are necessary. Many investigators have expressed the concentration dependence of the osmotic pressure by a virial-type expansion of equation (2-11).

$$\frac{\pi}{w_P} = RT\ [A_1' + A_2' w_P + A_3' w_P^2 + \ldots] \qquad (2\text{-}12)$$

From equation (2-12), it can be seen that the intercept at $w_P = 0$ of a plot of π/w_P versus w_P yields the first virial coefficient, and therefore the molecular weight, $A_1' = 1/M_P$. The slope of such a plot, where only two terms of equation (2-12) are required to fit the data, gives the second virial coefficient. Experimentalists have interpreted this second virial coefficient as a qualitative indication of the kinds of interactions which occur between the macro-ions. In part C of this section, justification for this interpretation is provided by application of McMillan-Mayer solution theory.

Figure 2-3 is a reduced osmotic pressure plot of the determinations made at low concentrations of albumin by Scatchard, et al. (12) and by Gutfreund (21). The figure shows that in addition to protein concentration, the osmotic pressure is a function of solution ionic strength and pH. The extrapolation to $w_p = 0$ for the first virial coefficient is seen to be independent of solution conditions. The value of $A_1'RT = 0.367$ yields the molecular weight of 69,000 which was first computed by Scatchard (12). The positive slopes for the measurements in 0.15 M saline indicate a positive second virial coefficient. This is interpreted as an indication of interactions between albumin molecules which are predominantly repulsive. This interpretation is supported by the more positive slope for the more highly charged molecule ($\overline{Z}$ = - 19.1 @ 7.1 pH and -8.1 @ 5.3 pH, see Figure 2-2). By contrast, when no salt is present, the measurements in isoionic* solution by Gutfreund indicate a negative second virial coefficient (or a negative sum of several higher order terms). An interpretation of this result in terms of attraction dominated intermolecular forces, or possibly even dimerization reactions between albumin molecules, does not seem unreasonable when the small molecular charge in a salt free, isoionic solution is considered (for the concentration range shown, $\overline{Z} \simeq 0.1$ to 1.0, see Section A above).

---

* The low isoionic pH of 4.4 is ascribed by Gutfreund to differences in technique for preparing the solution. The 4.4 pH was measured when the protein solution was cleared of all micro-ions except H^+ and OH^- by passing it through an ion exchange column. When electrodialysis was used to achieve the isoionic state, the pH for these solutions was at the more often reported value of 4.9 (see Table 2-2).

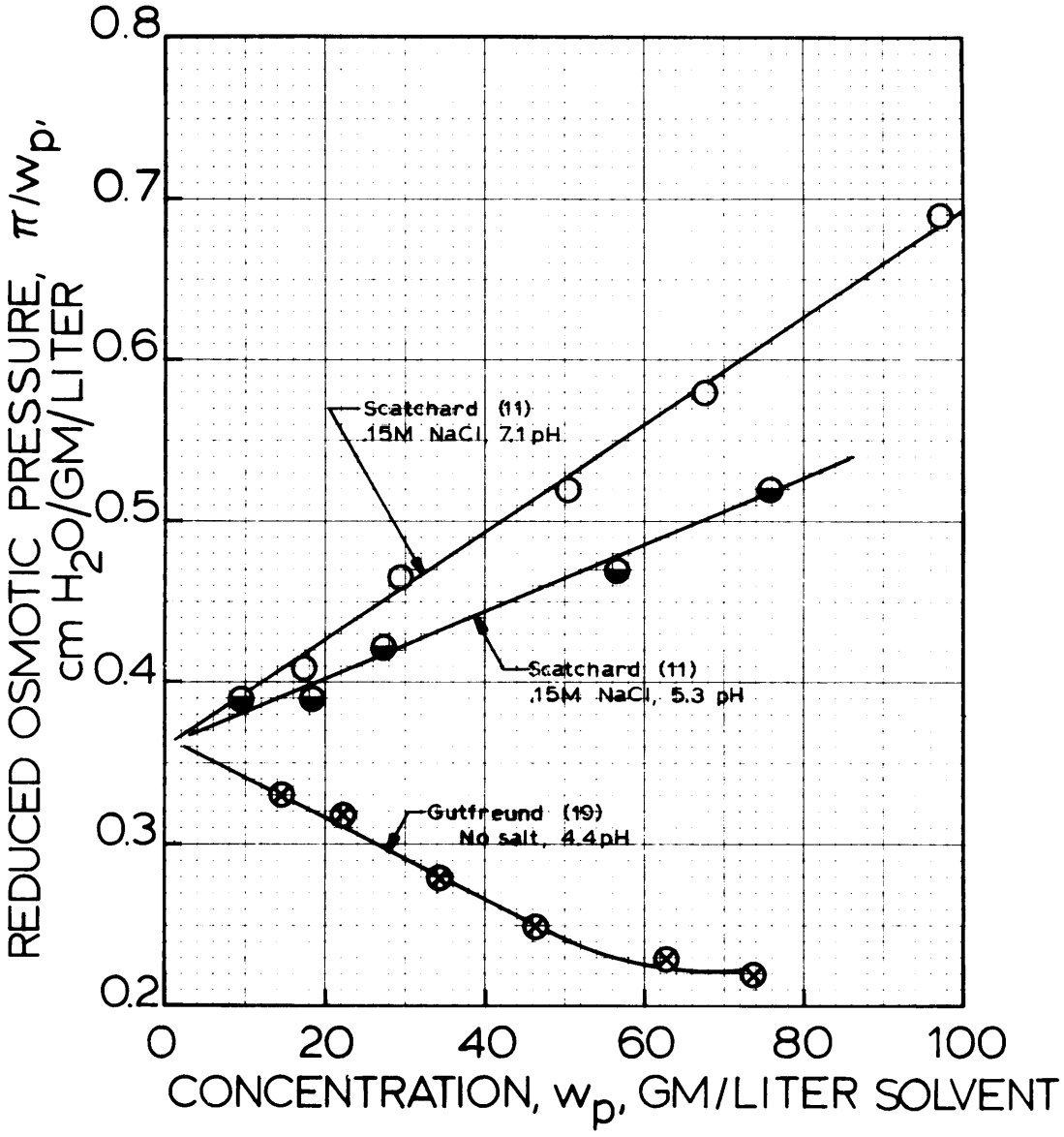

Figure 2-3: Reduced osmotic pressure of low concentration BSA solutions.

Gutfreund also found conditions which produced negative virial coefficients in his measurements of the molecular weight of trypsin by osmometry (22). These results were thought to be the consequence of aggregation reactions.

In the above interpretations, the explicit contribution of the asymmetrical distribution of micro-ions across the membrane is not included. However, this distribution is an implicit variable in determining the sign and magnitude of the A_2 term. To find the explicit contribution which the micro-ion distribution makes to the overall osmotic pressure, it is necessary to return to equation (2-10). The discussion is restricted here to a univalent salt. On the side of the membrane which contains no macro-ions, for each kilogram of solvent (i.e. $1000/M_o$ moles of solvent), there are m'_+ and m'_- moles of the two kinds of salt ions.

$$N'_o = \frac{1000}{1000 + M_o(m'_+ + m'_-)} \tag{2-13}$$

On the side of the membrane containing macro-ions, with m_p as the molality of the macro-ion,

$$N_o = \frac{1000}{1000 + M_o(m_+ + m_- + m_p)} \tag{2-14}$$

and substitution into equation (2-10) gives

$$\pi = \frac{RT}{V_o} \ell n \frac{1 + M_o(m_+ + m_- + m_p)/1000}{1 + M_o(m'_+ + m'_-)/1000} \tag{2-15}$$

Since the second term of both the numerator and denominator of equation (2-15) is usually small for aqueous protein solutions (always valid for albumin in 0.15 M saline), then equation (2-15) can be simplified using $\ell n\ (1 + X) = X - X^2/2\ .\ .\ .$, and retaining the first term, so that

$$\pi = \frac{RT\ M_o}{1000\ V_o}(m_p + m_+ - m'_+ + m_- - m'_-) \qquad (2\text{-}16)$$

At equilibrium, the chemical potentials of the salt must be equal across the membrane, so that

$$\mu_+ + \mu_- = \mu'_+ + \mu'_-$$

or

$$m_+ m_- = m'_+ m'_- = m_s^2 \qquad (2\text{-}17)$$

Since the protein solution must be electrically neutral, and for simplification $\overline{Z} < 0$,

$$m_+ = m_- + m_p\ \overline{Z} \qquad (2\text{-}18)$$

and by substitution

$$(m_+ - m_p\ \overline{Z})(m_+) = m_s^2$$

which gives

$$m_+ = \frac{1}{2} m_P \bar{Z} + \sqrt{\frac{m_P^2 \bar{Z}^2}{4} + m_s^2}$$

$$m_- = -\frac{1}{2} m_P \bar{Z} + \sqrt{\frac{m_P^2 \bar{Z}^2}{4} + m_s^2} \qquad (2\text{-}19)$$

Substitution of equations (2-17) and (2-19) into equation (2-16) leads to the final general expression for the ideal Gibbs-Donnan osmotic pressure,

$$\pi = RT\left[\frac{w_P}{M_P} + 2\sqrt{\frac{w_P^2 \bar{Z}^2}{4\, M_P^2} + m_s^2} - 2m_s\right] \qquad (2\text{-}20)$$

This last expression includes the substitution, $m_P = w_P/M_P$ and $(\nu_o/1000) \simeq V_o/M_o$ where ν_o is the solvent partial specific volume (ml/gr).

When certain conditions for the protein solution are fulfilled, equation (2-20) simplifies to more familiar forms of the ideal Gibbs-Donnan expression. When $m_s >> \bar{Z}(w_P/M_P)$, then

$$\pi \simeq RT\, w_P\left[\frac{1}{M_P} + \frac{\bar{Z}^2\, w_P}{4\, m_s M_P^2}\right] \qquad (2\text{-}21)$$

In this form, a comparison with equation (2-12) shows that the second virial coefficient, A_2', is analogous to a correction for the asymmetrical micro-ion distribution as described by the Gibbs-Donnan equilibrium. Furthermore, when the conditions of infinite dilution ($w_P \to 0$) and small protein charge or large salt concentrations

apply, equation (2-21) reduces to the van't Hoff limiting law, equation (2-11). The significance of the Gibbs-Donnan correction can be compared with the data shown on Figure 2-3. For Scatchard's 0.15 M saline solution, at a pH of 7.1 ($\overline{Z}$ = -19.1) and a protein concentration of 80 grams/liter solvent, the Donnan contribution, π_D, from equation (2-21) is,

$$\frac{\pi_D}{w_P} = RT \frac{\overline{Z}^2 w_P}{4 m_s M_P^2} = 0.258$$

The protein contribution of eqn (2-21) is, $(\pi_P/w_P) = RT/M_P = 0.367$, and the sum for the total reduced pressure $(\pi = \pi_D + \pi_P)/w_P = 0.625$ is in good agreement with the data of Figure 2-3. That is, the Gibbs-Donnan contribution appears to correctly account for the nonideality of albumin solutions in this case. At the lower pH of Scatchard's data ($\overline{Z}$ = -8.1) and a protein concentration of 80 gm/l solvent, the Donnan contribution is only 0.047 which is an insufficient increase compared to the data of Figure 2-3 (π/w_P = 0.53). This result, which is consistent with Scatchard's (12) analysis*, indicates the importance of additional factors in accounting for the non-ideal solution behaviour. As Tanford has pointed out (3, Chapter 7), the ideal Gibbs-Donnan expression is not necessarily the only, nor even the most important consequence of the presence of electrostatic

---

* In this early Scatchard paper (1946), the chloride binding correction to the total protein charge, Z_2 in Scatchard's notation, was not taken into account. When this correction is applied, the Donnan correction brings theory and data into closer agreement, but doesn't alter the above conclusion.

charges on a macromolecule. In fact, the data of Gutfreund on Figure 2-3 indicate that electrostatic influences need not even be dominant when solution nonideality is considered.

The above discussion has established the method of separately accounting for intrinsic protein contributions and for the Donnan contribution either to the total osmotic pressure, or to a term (the second virial coefficient) which is viewed as a measure of deviation from van't Hoff's limiting law (16, 23). If a virial expansion is performed on the intrinsic protein part of equation (2-20), the result is,

$$\pi = \pi_P + \pi_D \tag{2-22}$$

where

$$\pi_P = \frac{RT}{M_P}[w_P + A_2 w_P^2 + A_3 w_P^3 + \ldots]$$

$$\pi_D = RT\left[2\sqrt{\left(\frac{\bar{Z}\, w_P}{2\, M_P}\right)^2 + m_s^2} - 2m_s\right]$$

With three terms of the expansion for the protein part, equation (2-22) is successfully applied to describe the concentrated solution data of Chapter 3. In that analysis, the coefficients A_2 and A_3 (where it is implied that $A_1 = 1$) are described as functions of protein charge only.

B. Complete Chemical Potential Model

Scatchard (20), after a careful definition of the diffusible species in an osmotic system of a macro-ion and a univalent salt, derived an expression for osmotic pressure, at equilibrium, by equating the total differential of the chemical potential for each species on the side of the membrane with protein to a similar expression on the side without protein. He described this theoretical result in terms of a virial expression similar to equation (2-12) through two terms with the results that,

$$A_1' = 1/M_P$$

and

$$A_2' = \frac{1}{2\,M_P^{\,2}}\left[\frac{\overline{Z}^2}{2\,m_s} + \frac{\partial\, \ell n \gamma_P}{\partial\, m_P} - \frac{\left(\frac{\partial\, \ell n \gamma_P}{\partial\, m_s}\right)^2 m_s}{2 + 2\,\frac{\partial\, \ell n \gamma_S}{\partial\, m_s}\, m_s}\right]$$

The first term in the expression for A_2' is seen to be the ideal Gibbs-Donnan term of equation (2-21). The other terms represent the various interactions between the ions of the solution. Included in the second term which expresses the change in the protein activity coefficient with its own concentration would be the interaction between charges on different macro-ions, whereas the term $(\partial \ell n \gamma_P / \partial m_s)$ involves interaction between macro-ions and salt ions, including the actual binding of such ions. The $(\partial\, \ell n\, \gamma_s / \partial\, m_s)$ term involves interaction between salt ions alone.

Scatchard and associates (12, 13) expreimentally determined the significance of all three terms in the above expression by studying the variation of A_2' with protein concentration, salt concentration and protein charge.* At high protein concentrations (up to 25 gm %) (13), A_2' was found to be dependent on protein concentration, as well as charge. In this analysis, the protein-protein interaction term, $(\partial \ln \gamma_p / \partial m_p)$, was found dominant over the other terms of the A_2' expression.

The activity coefficient derivatives of the A_2' expression above are complex quantities. They have not been sufficiently well defined so that values derived for them by mere data fitting methods can be interpreted in a quantitative way regarding macromolecular solution behaviour.

C. Virial Expansion From McMillan-Mayer Solution Theory

1. Theory for Evaluation of Virial Coefficients

Hill has shown that the McMillan-Mayer solution theory enables one to express the osmotic pressure and the salt distribution in a Donnan system in terms of expansion in powers of the macro-ion concentration (19, 24, 25, 26). Following Hill's notation, the virial expansion is,

$$\frac{\pi}{kT} = p + B_2 p^2 + B_3 p^3 + \ldots \qquad (2\text{-}23)$$

---

* Again, note that in the original works, the charge calculation fails to account for chloride ion binding since it was not discovered until 1949 (6, 7).

where k = Boltzman's constant (R/N_A where N_A is Avogadro's Number), p is macro-ion concentration in terms of number densities and B_2 and B_3 are the virial coefficients distinguished here from the A_2' and A_3' of equation (2-12) by dimension and theoretical significance.

The second and third virial coefficients can be computed when the potential of average force between particles can be estimated (27). The evaluation is made with the help of "cluster integrals" (as in imperfect gas theory - see reference 19, Chapter 15) in which the intermolecular potential, W_{12}, is the potential of average force between spherically symmetrical macro-ions. When the interaction between two macro-ions in positions r_1 and r_2 is considered, the "cluster integral" for B_2 is

$$B_2 = \frac{-1}{2V} \int_V \int_V \left(e^{-W_{12}/kT} - 1 \right) dr_1 dr_2 \qquad (2\text{-}24)$$

where V is the volume of the system. The third virial coefficient concerns the interaction between three macro-ions and is given by,

$$B_3 = \frac{-1}{3V} \int_V \int_V \int_V \left(e^{-W_{12}/kT} - 1 \right)\left(e^{-W_{23}/kT} - 1 \right) \cdot \left(e^{-W_{13}/kT} - 1 \right) dr_1 dr_2 dr_3 \qquad (2\text{-}25)$$

The solution of equations (2-24) and (2-25) depends upon the model which is chosen to represent the potential of average force between macro-ions. The physical picture is that of spherical

particles whose charges are compensated by ionic double layers of the Gouy-Chapman type. Following the Debye-Hückel assumption that the micro-ion distribution, and therefore the charge density, in the double layer could be represented by the Poisson-Boltzmann equation (3, Chapter 7), Hoskin (28) has shown that the potential, Ψ, at a distance, r, from the center of the macro-ion is closely represented by,

$$\Psi = \frac{\Psi_o}{\gamma}\frac{a}{r} e^{-\kappa(r - a)} \left\{1 + (\gamma - 1)e^{-2\kappa(r - a)}\right\} \qquad (2\text{-}26)$$

where Ψ_o = macro-ion surface potential, volts*

a = macro-ion radius, cm

κ = reciprocal thickness of ionic double layer, given by

$$\kappa = \left[\frac{4\pi e^2}{\varepsilon kT} \sum_i p_i Z_i^2\right]^{1/2} \qquad (2\text{-}27)$$

where ε = dialectric constant of medium
= 78.54 statcoul/(statvolt-cm), for water

e = protonic charge
= 4.802×10^{-10} statcoul

k = Boltzmann's constant
= 1.38×10^{-16} statcoul-statvolt/°K

T = absolute temperature

p_i = number density of $i^{\underline{th}}$ micro-ions

Z_i = valence of $i^{\underline{th}}$ micro-ions

---

* 1 volt = 1/300 statvolt

The parameter γ is somewhat larger than unity and its dependence on $e\Psi_o/kT$ and on κa has been tabulated by Hoskin (28). Hoskin also shows that for values of $(e\Psi_o/kT) \leq 1$, the values of Ψ computed by the Debye-Hückel approximation (i.e. $\gamma \simeq 1$) to equation (2-26), will be in error by less than 5% for all values of κa. In the model development here, it will later be shown that Ψ_o is a maximum at about 20×10^{-3} volts. Then, at 25°C,

$$\frac{\Psi_o e}{kT} = \frac{(20 \times 10^{-3})\text{volts}(4.802 \times 10^{-10})\text{statcoul}\ 1\ \text{statvolt}}{(1.38 \times 10^{-16})\frac{\text{statcoul-statvolt}}{°K}(298)°K\ \ 300\ \text{volts}} = 0.78$$

Therefore, the potential distribution surrounding a single macro-ion in this system is closely represented by the Debye-Hückel approximation,

$$\Psi = \Psi_o \frac{a}{r} e^{-\kappa(r - a)} \qquad (2\text{-}28)$$

The interaction between two macro-ions is presumed in this case to be dominated by the electrostatic interactions; that is, the interaction is primarily repulsive and can be dealt with on the basis of expressions developed by Verwey and Overbeek (29). They derive for the potential of average force W(R) between two identical colloid particles surrounded by a Debye-Hückel potential field

$$W(R) = \varepsilon a^2 \Psi_o^2 \frac{e^{-\kappa(R - 2a)}}{R} f \qquad (2\text{-}29)$$

where R is the distance between the centers of the particles and f is a factor less than unity. The value of f depends on κR and on

the assumption made when the particles approach, constant Ψ_o or constant particle charge, Q.

Again parameter estimation, along with Table XX in Verwey and Overbeek, is employed to simplify equation (2-29). In addition to the estimate of $\Psi_o \sim 20 \times 10^{-3}$ volts, a double layer thickness of 8 Angstroms gives an estimate for $\kappa \sim 1.25 \times 10^{+7} cm^{-1}$. The minimum center-to-center macro-ion separation distance is taken to be 76×10^{-8}cm, about twice the radius of an albumin molecule plus one or two micro-ions sandwiched in between the macromolecules. For these estimates, f for the constant charge case is seen from Table XX ($\tau = \kappa a \simeq 5$) of Verwey and Overbeek to be about 0.93, and for the constant Ψ_o case, it is about 0.91. In each case, as center-to-center separation increases, f approaches unity. At a separation which corresponds to the point at which the double layers of the two particles first touch ($R \sim 85 \times 10^{-8}$cm), $f_{Q,const} \sim 0.98$ and $f_{\Psi_o,const} \sim 0.97$. Therefore, equation (2-29) is simplified to

$$W(R) = \varepsilon a^2 \Psi_o^2 \frac{e^{-\kappa(R - 2a)}}{R} \qquad (2\text{-}30)$$

This expression for the interaction potential has been used by Stigter and Hill (27) to obtain solutions for the "cluster integrals", equations (2-24) and (2-25). These solutions include the assumption that the virial coefficients are very insensitive to the actual value of W(R) in the limit of small separation distance between macro-ions. Therefore, the solutions of these integrals, as given by Stigter and Hill, equations (2-31) to (2-34), do not take a separate accounting of the regions, $0 < X \leq 2\kappa a$ (region of hard sphere overlap), and $X > 2\kappa a$ (region of electrostatic interaction).

$$\kappa^3 B_2 = 2\pi \int_0^\infty (1 - \exp[-W(x)/kT])x^2 dx \qquad (2\text{-}31)$$

where $x = \kappa R$

$$\frac{W(x)}{kT} = F \frac{e^{-x}}{x} \qquad (2\text{-}32)$$

$$F = \frac{\varepsilon \kappa a^2}{kT} \Psi_o^2 \, e^{2\kappa a} \qquad (2\text{-}33)$$

and

$$\kappa^6 B_3 = \frac{8\pi^2}{3} \int_0^\infty (1 - \exp[-W(x)/kT])x dx \int_0^\infty (1 - \exp[-W(y)/kT]) y dy \int_{|x-y|}^{\kappa+y} (1 - \exp[-W(z)/kT]) z dz \qquad (2\text{-}34)$$

where x, y and z are the interparticle distances expressed in units of κ^{-1}. As for B_2, equation (2-32), and analogous expressions for W(y) and W(z) are employed by Stigter and Hill for B_3.

For the particles considered by Stigter and Hill, $a = 20 \times 10^{-8}$cm and $\Psi_o = 100$ mv, the neglect of the "hard sphere exclusion" contribution to the virial coefficients is not significant. However for albumin, $a = 34.5 \times 10^{-8}$cm and $\Psi_o < |\sim 25\text{mv}|$, this contribution cannot be ignored and equation (2-31) must be modified using $W(x) = \infty$ for $x \leq 2\kappa a$. The result is

$$\kappa^3 B_2 = \frac{2\pi(2\kappa a)^3}{3} + 2\pi \int_{2\kappa a}^\infty (1 - \exp[-W(x)/kT])x^2 dx \qquad (2\text{-}31A)$$

where equations (2-32) and (2-33) still apply. Figure 2-4 shows the

numerical integration results for both equations (2-31) and (2-31A) as a function of the energy parameter F.

For the solution of B_3, equation (2-34), Stigter and Hill give the result in the form of the ratio B_3/B_2^2 as a function of F. Their results are shown in Figure 2-5 and show that the ratio asymptotically approaches the "hard sphere" value of 0.625 (19, Chapter 19) for increasing F. Since for the albumin solutions considered here, the value of F is always greater than about $4 \times 10^{+3}$, the "hard sphere" value, along with B_2 calculated from equation (2-31A), is used to evaluate B_3 without introducing large error.

2. Evaluation of the Surface Potential for Albumin

In order to evaluate the virial coefficients for solutions of albumin in 0.15 M NaCl with variable pH, the surface potential, Ψ_0, and Debye-Hückel double layer thickness, κ^{-1}, must be known. It is further desired to know the relationship between these parameters and the charge of the macro-ion, where the charge is related to solution pH in Figure 2-2.

These parameters can be obtained from the results of electrophoresis experiments on solutions of BSA by Möller, et al. (30, 31). These experiments were performed for an albumin concentration range of 0.5 to 5 gm/100 ml solution, a salt concentration range (usually KCl) of 0 to 0.05 N, and where salt was present, the pH was held at 8.5. At this pH chloride binding to the macro-ion is small and the authors used titration data only to compute macromolecular charge

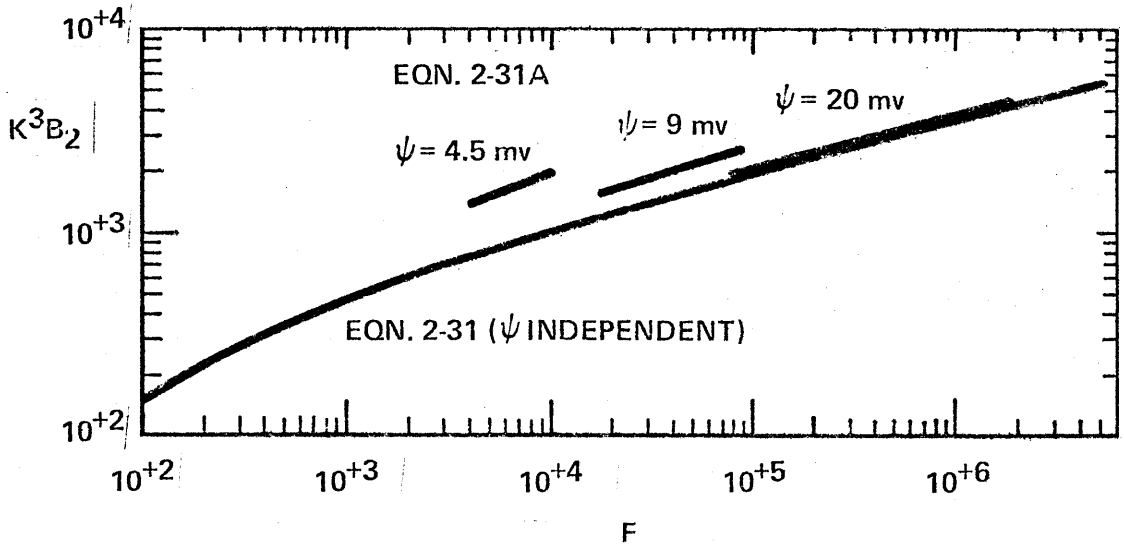

Figure 2-4. Second Virial Coefficient as a Function of the Hill-Stigter F-Parameter.

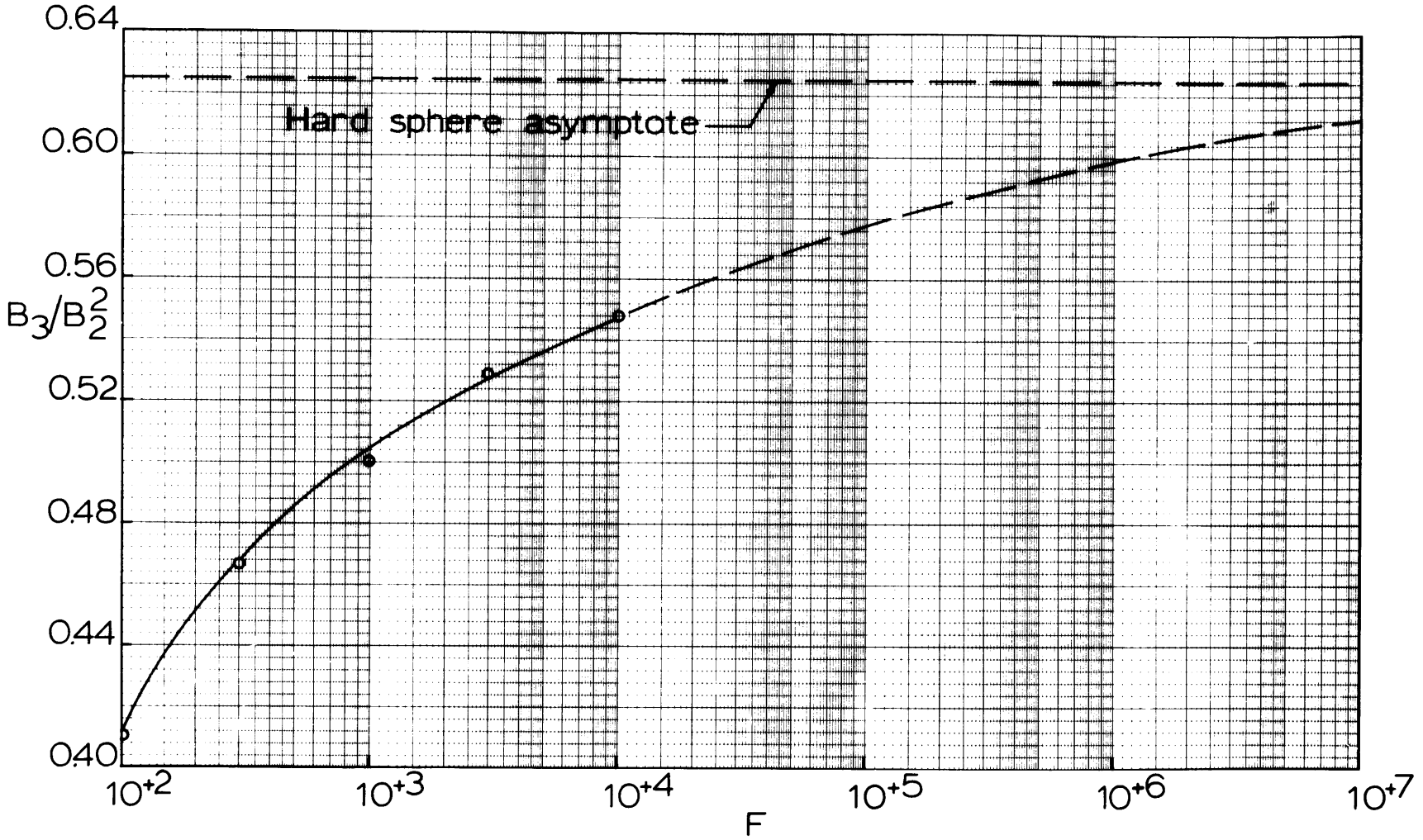

Figure 2-5: Third virial coefficient as a function of the Hill - Stigter F - parameter.

(i.e. $\bar{Z} = \nu_H$ -- see Figures 2-1 and 2-2). For these conditions, the zeta potential, ζ, was reasonably well described by a Debye-Hückel type expression (30),

$$\zeta = \Psi_o - \Psi_R = \frac{\bar{Z}e}{\varepsilon a} \frac{1}{1 + \kappa a} \tag{2-35}$$

The reference potential, Ψ_R, is the potential which exists at the spherical surface of a shell surrounding each macro-ion. The size of this shell is such that when all the spherical shells are taken together, the total solution volume is incorporated. With $\Psi_R = 0$ this assumption, the surface potential can be obtained from,

$$\Psi_o = \frac{\bar{Z}e}{\varepsilon a} \frac{1}{1 + \kappa a} \tag{2-36}$$

As shown in equation (2-27), the Debye-Hückel parameter, κ, is dependent on the number density of micro-ions. Möller, et al. (30) found that their conductance measurements were most accurately represented when the protein was counted as a 1:1 electrolyte in the "ionic strength" computation. Therefore, in equation (2-27) the summation term is given by

$$\sum p_i Z_i^2 = p_t = p_+(1)^2 + p_-(-1)^2 + 2p_p\left|\bar{Z}\right| (\pm 1)^2$$

where p_+ = number density of sodium ions

p_- = number density of chloride ions

p_p = number density of albumin molecules

$\bar{Z}$ = albumin valence

Of course, at infinite dilution ($p_p \to 0$), accounting for the protein will not affect the calculation of Ψ_o, nor the calculation of the virial coefficients B_2 and B_3. However, at higher protein concentrations, this accounting will result in concentration dependent virial coefficients in so far as they are dependent on solution ionic strength. In 0.15 M NaCl ($p_+ = p_- = 9.045 \times 10^{+19}$ molecules/cm^3 solution), equation (2-37) is

$$p_T = (1.809 \times 10^{+20}) + 2p_p|\bar{Z}| \text{ [=] molecules/cm}^3 \qquad (2\text{-}38)$$

and by equation (2-27), κ is

$$\kappa = \left[\frac{4\pi e^2}{\varepsilon kT}\right]^{1/2} p_T^{1/2} = 9.473 \times 10^{-4} p_T^{1/2} \text{ [=] cm}^{-1} \qquad (2\text{-}39)$$

and for a molecular radius of albumin (30), a = 34.5 $\times 10^{-8}$ cm,

$$\Psi_o = 5.317 \times 10^{-3} \frac{|\bar{Z}|}{1 + (34.5 \times 10^{-8})\kappa} \text{ [=] volts} \qquad (2\text{-}40)$$

At infinite dilution, the values of surface potential at the three pH's of interest are summarized in Table 2-3. The potential of average force between interacting molecules, equation (2-30), is

shown for each pH in Figure 2-6. The macro-ion separation parameter, $x = \kappa R$ where R is the center-to-center distance between the macro-ions, has been normalized to the separation at closest approach, $R = 2a$. The interaction potential is infinite for $x \leq 2\kappa a$.

TABLE 2-3

Albumin Surface Potential at Infinite Protein Dilution

$\kappa = 1.28 \times 10^{+7}\ cm^{-1}$

pH	$\bar{Z}$	$\Psi_o \times 10^{+3}$, volts
4.5	+4.5	+4.43
5.4	-9.1	-8.96
7.4	-20.4	-20.1

3. Evaluation of Albumin Solution Virial Coefficients

The numerical evaluation of the second virial coefficient, B_2, and the parameters, p_t, κ, Ψ_o is done with the aid of the computer program given in Appendix A. The integrand of equation (2-31A), for the case of infinite protein dilution, is shown as a function of the normalized separation distance on Figure 2-7. For $x \leq 2\kappa a$, the integrand is simply x^2. The discontinuity at $R = 2a$ results when $W(x)$ takes on finite values for $R > 2a$. If the macro-ion were isoelectric, $\bar{Z} = 0$, the interaction potential and the integrand would go to zero for $R > 2a$.

Figure 2-8 shows the value of equation (2-31A) for the three infinite dilution cases. The discontinuity in the value of the integrand at $x = 2\kappa a$ results in the discontinuity of the slopes in Figure 2-8.

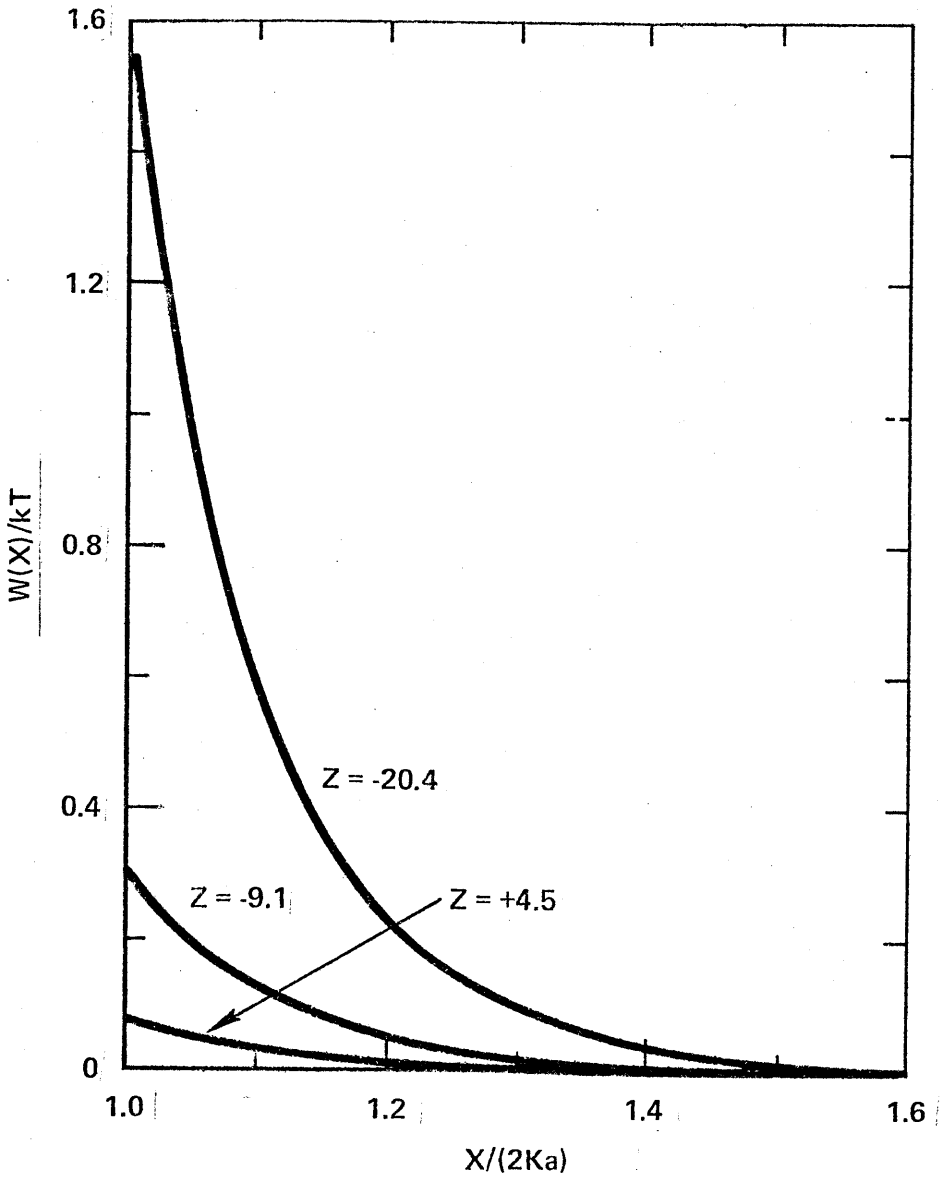

Figure 2-6. Interaction Potential as a Function of Macro-Ion Charge.

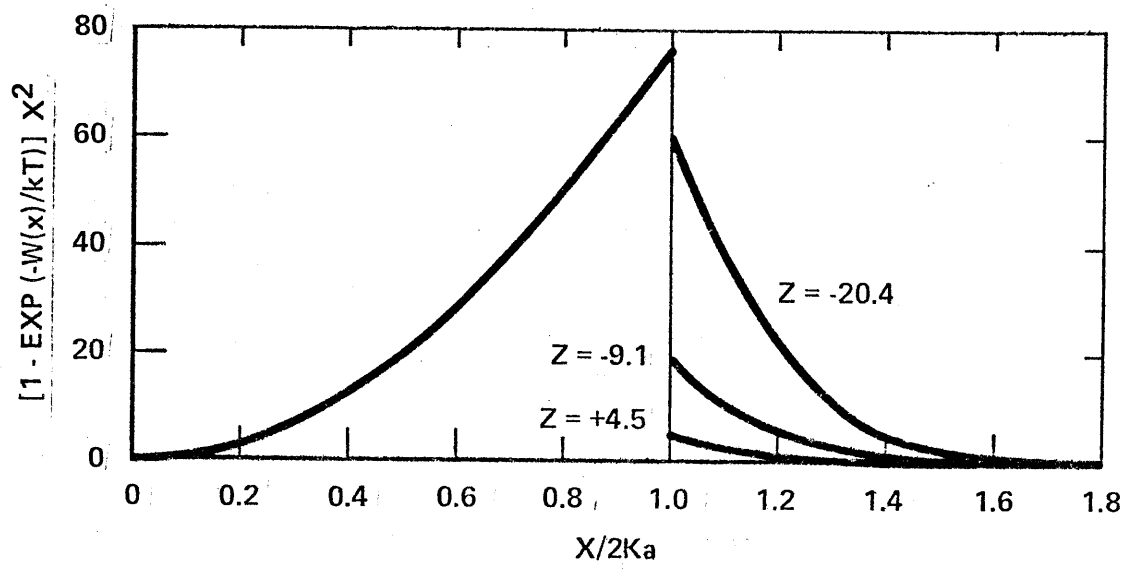

Figure 2-7. Integrand of B_2 - Integral as a Function of Macro-Ion Separation and Charge.

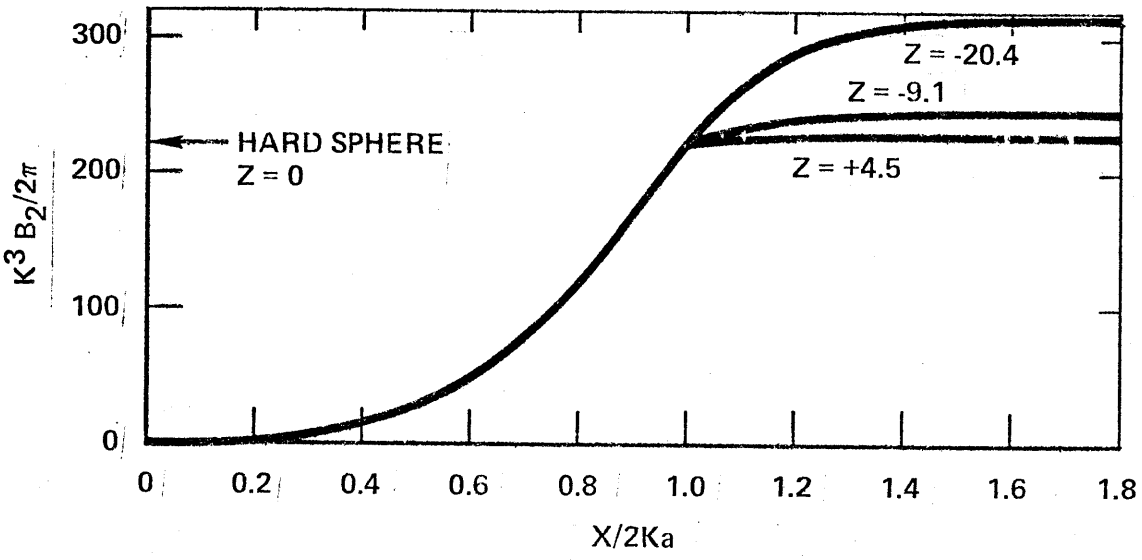

Figure 2-8. B_2 - Integral as a Function of Macro-Ion Separation and Charge.

It can be seen from the figure that the value of the second virial coefficient at pH 4.5 is only slightly larger than the "hard sphere" value where $\bar{Z} = 0$.

The osmotic pressure for solutions of albumin in 0.15 M saline, at any solution pH, can now be calculated using,

$$\pi = 0.367 \quad [w_p + B_2' w_p^2 + B_3' w_p] \quad [=] \text{ cm } H_2O \tag{2-41}$$

where w_p = albumin concentration as gm BSA/liter solvent

$$B_2' = \frac{N_A}{1000\ M_p} B_2 = \frac{6.023 \times 10^{23}}{(1000)(69{,}000)} B_2$$

$$= 8.74 \times 10^{15}\ B_2 \qquad [=] \quad \frac{\ell \text{ solvent}}{\text{gm BSA}}$$

$$B_3' = 7.64 \times 10^{+31}\ B_3 \qquad [=] \left(\frac{\ell \text{ solvent}}{\text{gm BSA}}\right)^2$$

The constant of equation (2-41) is $kT\ (N_A/1000\ M_p)$ evaluated at 25°C and the conversion ($1 \text{ erg/cm}^3 = 1 \text{ dyne/cm}^2 = 1.021 \times 10^{-3}$ cm H_2O) has been employed. In Table 2-4, the infinite dilution virial coefficients, B_2' and B_3' are listed for each pH.

TABLE 2-4

Infinite Dilution Virial Coefficients

pH	$\bar{Z}$	$B_2' \times 10^{+3}$ ℓ solvent/gm BSA	$B_3' \times 10^{+6}$ (ℓ solvent/gm BSA)^2
4.5	+ 4.5	6.18	23.9
5.4	- 9.1	6.65	27.6
7.4	-20.4	8.55	45.6

In part 2 above it was seen that when the macro-ion concentration is accounted for in the ionic strength calculation, the virial coefficients become dependent on concentration. Figures 2-9 and 2-10 show this dependence for B_2' and B_3'. In Chapter 3, the osmotic pressure data will be compared with both methods of evaluating the virial coefficients.

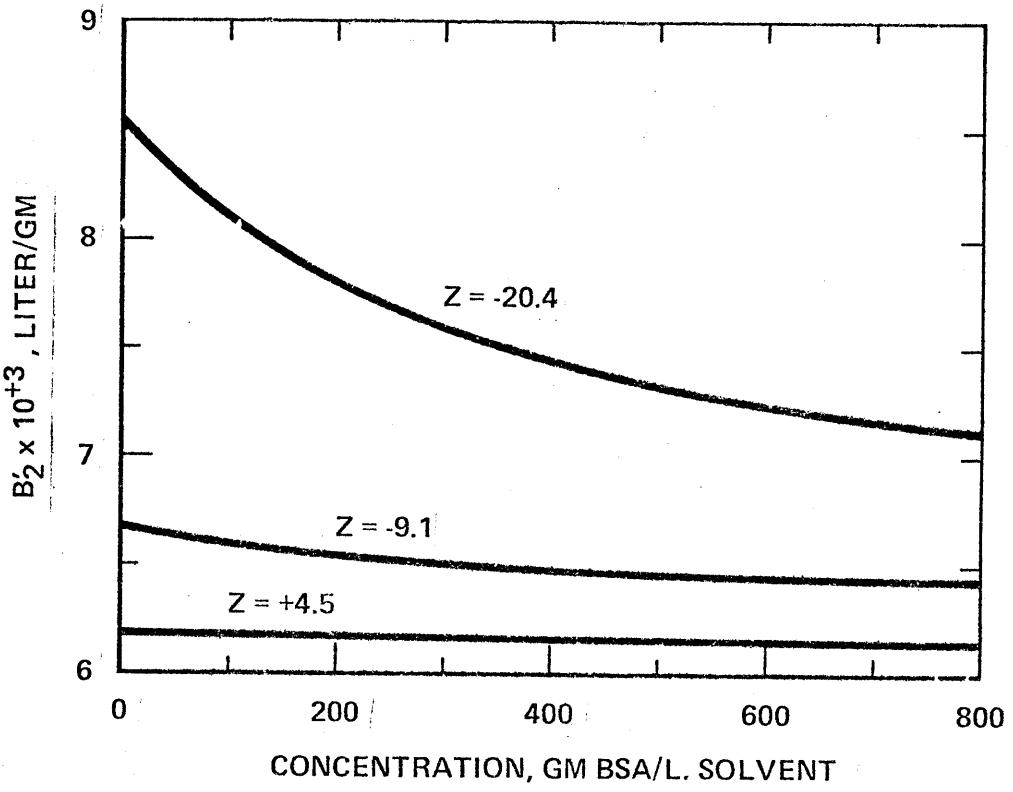

Figure 2-9. B'_2 Dependence on Albumin Concentration.

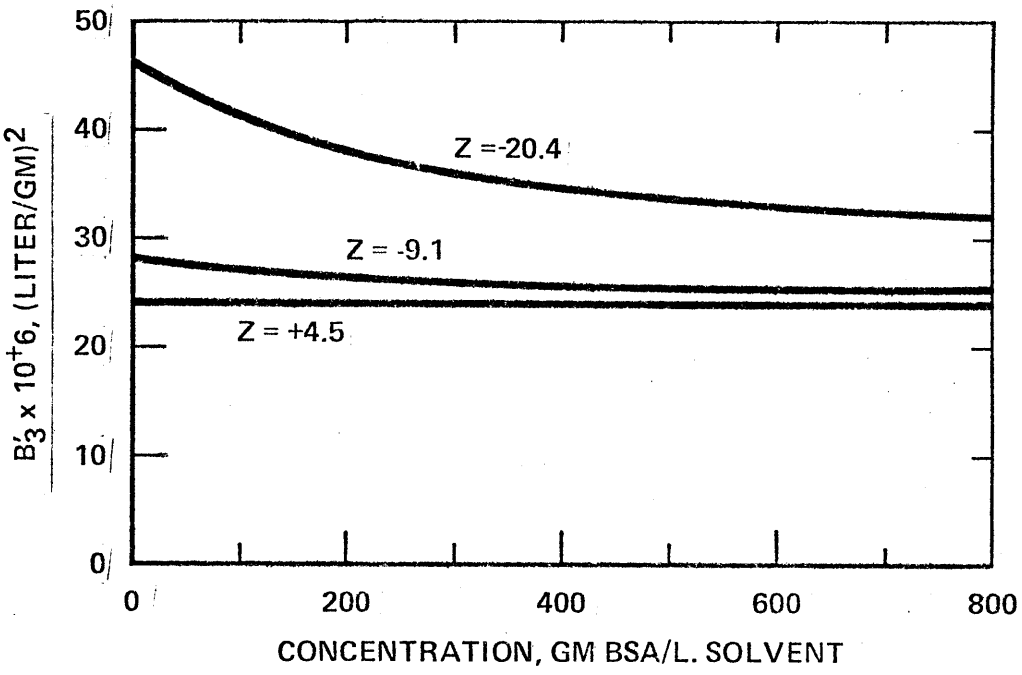

Figure 2-10. B'_3 Dependence on Albumin Concentration.

III. Albumin Diffusivity

The diffusivity of albumin in various aqueous solutions has been determined by a variety of techniques (32). Most of these employ an optical interferometric principle which allows measurements of refractive index distributions. These distributions originate at an interface between solutions which are initially at different concentrations with respect to the albumin solute. At selected times after the interface has been established, the refractive index profiles which result from the diffusion of solute and solvent across the interface are used to determine solute diffusivity.

In the diaphragm diffusion cell method (40), the apparatus consists of two well stirred reservoirs separated by a porous diaphragm. The concentration of the solute differs in the two reservoirs. After calibrating the diaphragm, the diffusion coefficient is determined by measuring concentration change with time in the reservoirs.

The light scattering method (2) is used to determine diffusion coefficients by measuring the spectrum of light scattered from thermally excited concentration fluctuations. The decay rate of these fluctuations depends on their wave vector and on the diffusion coefficient of the macro-ion.

Table 2-5 summarizes the results of measurements reported in the literature for the diffusivity of albumin in solutions of varying composition, and for protein concentrations at, or near, infinite dilution. In addition to exhibiting a dependency on solution

TABLE 2-5

Albumin Diffusion Coefficients in Dilute Solutions

Reference & Method[1]	Buffer Composition	pH	Ionic Strength	Protein Conc. gm/100 ml	Temperature T_M °C Meas.	Temperature T_R Ref.	$D \times 10^{+7}$ $cm^2/sec.$ @ T_R
33, G	Several	6.8-8.4	0.05-0.2	0	21-25	20	6.15
34, G	Phosphate	7.4	0.1	~1	25	25	6.81
35, G	Chloride-Acetate[2]	4.60	0.16	0.498	25	25	6.70
				0.507			6.66
				0.515			6.67
35, G	Chloride-Acetate	4.60	0.16	0.519 (human)	25	25	6.46
36, R	Chloride-Acetate	4.60	0.16	0.518	25	25	6.68
				0[3]			6.75
37, G	0.5 M KCl	5.14	0.5	0	1	25	6.64
38, G	Chloride-Acetate	4.60	0.16	0	25	25	6.70
39, J	none	isoionic	0	0	20	20	5.90
39, J	0.15 M NaCl	3.5	0.15	0	20	20	5.2
		3.8					5.5
		4.2					5.75
		4.5-5.4					5.85
		7.0-7.8					5.90
39, J	0.6 M NaCl	4.5-5.4	0.6	0	20	20	5.85
		7.4-7.9					5.95
40, D	.1M Acetate	4.7	0.1	0.926	25	25	6.98
2, L	None	5.4[4]	0	5.0	25	25	(8.9)
	0.1 M NaCl	?	0.1	5.0	25	25	(6.1)

Notes

1. G, Gouy interferometer; R, Raleigh interferometer; D, Diaphragm cell; L, light scattering; J, Jamin interferometer
2. The composition of this buffer is 0.15 M KCl, 0.01 M K acetate and 0.01 M acetic acid.
3. See reference (30) for details of calculation.
4. Estimated from molecular charge cited in reference and Figure 2-1 of this thesis.

composition, the tabulated values also appear to depend on the method of determination. This last dependency, in part, reflects the varying degrees to which each of the methods is affected by the inaccuracies of the assumptions made in computing the listed diffusivities. The assumptions include macrosolute homogeneity and independence of diffusivity on protein concentration for the range of concentration that was involved in the determination.

Only the study of Keller, et al. (40) was extended to regions of high protein concentrations (31 gm BSA/100 ml solution). The diffusivity concentration dependence is described by,

$$\frac{D}{D^o} = \frac{\tanh 21.3\ \phi_A}{21.3\ \phi_A} \qquad (2\text{-}42)$$

where ϕ_A is the volume fraction of albumin. The reference infinite dilution diffusivity is taken from the authors' extrapolation, $D^o = 7.0 \times 10^{-7}$ cm^2/sec. Anderson (41) has shown that these results are also described (within experimental error) by a simpler function,

$$\frac{D}{D^o} = (1 - \phi_A)^{6.5} \qquad (2\text{-}43)$$

The value of $D^o = 8.9 \times 10^{-7}$ cm^2/sec, at zero ionic strength, from the light scattering determination by Doherty and Benedict (2) is expressed by the authors as an average diffusion coefficient for a mixture which may contain up to 20% albumin oligomers. Since their commercial preparation of BSA was not fundamentally different

from those used by other investigators, they ascribe their larger values of diffusivity at low ionic strength to be a result of the greater sensitivity of the light scattering technique to the monomeric form of albumin.

This last investigation also includes a study of the effects of albumin charge and solution ionic strength. The ionic strength was varied from zero to 100 milli-equivalents salt/liter but cannot be reliably interpreted above about 8-10 mequiv/l since chloride binding was not incorporated in the calculation of molecular charge, $\bar{Z}$. At 8 mequiv/l this introduces a small error ($\sim$5%) in $\bar{Z}$, but at high ionic strength, $\bar{Z}$ will be in error by 50%, or more. Table 2-6 shows a large increase in diffusivity as protein charge is decreased from -1 to -18 ($\sim$5.4 to 8.5 pH, respectively) at 8 mequiv-salt/liter and 5 gm % protein.

TABLE 2-6

Effect of Charge on Albumin Diffusivity at Low Protein Concentration and Ionic Strength

(from Doherty and Benedek)

$\bar{Z}$	$D \times 10^{+7}$, cm^2/sec
- 1	7.0
- 4	9.2
- 7	11.2
-10	13.7
-18	17.5

The qualitative trend of diffusivity increasing with increasing macromolecular charge is supported by Champagne's data (39) at two different ionic strengths.

As a result of this survey, the value of D^o determined by Keller, et al. and equation (2-42) are employed in the analysis of results presented in Chapters 4 and 5.

IV. Solubility and Density of Albumin Solutions

A. Partial Specific Volume

The specific volume of hydrated albumin has been reported to be ν_A^o = 0.733-0.752 ml/gm (42, 43, 44). In order to derive an equation of state for albumin-saline mixtures, it was necessary to investigate the change in partial specific volume, ν_A, as a function of concentration.

A 55.6 gm % (gm BSA/100 ml solution) BSA solution was prepared with 0.15 M saline and adjusted to 5.4 pH. The concentration of this viscous solution was determined, in triplicate, by the biuret method* (45) after the original sample had been diluted 6:1 with saline using a 0.2 ml wash-out pipette. The concentrated solution was then transferred to a 2.5 ml graduated centrifuge tube which had previously been calibrated, by weight determinations, with water. The solution sample was spun at 2000 rpm and 34°C for one hour. This spin was necessary to force air out of the sample and to establish a level miniscus in the centrifuge tube. Sample volume and weight were determined. With the partial specific volume of saline assumed to be 1.00 ml/gm, duplicate determinations of the albumin partial specific volume resulted in,

$$\nu_A = 0.746 \pm 0.03 \text{ ml/gm @ } 55.6 \text{ gm \%}$$

---

* When solution concentrations were in the range of 4-10 gm % albumin, protein concentration was determined by the biuret method. When concentrations were suspected to be less than 1 gm %, concentrations were determined by the Lowry method (46).

from which it was concluded that, within experimental error, $\nu_A = \nu_A^o$ over the range of interest.

This conclusion for albumin solutions is not unique among proteins. For hemoglobin (MW = 67,000) the partial specific volume is constant at 0.800 ml/gm when measured to concentrations of 42.1 gm % (47).

With the partial specific density of albumin independent of concentration, $\tilde{\rho}_A = 1/\nu_A^o = 1.34$ gr/ml, an equation of state for albumin in saline can be given by,

$$\rho = \frac{\tilde{\rho}_s}{1 - \left[\frac{\tilde{\rho}_A - \tilde{\rho}_s}{\tilde{\rho}_A}\right]\omega_A} \qquad (2\text{-}44)$$

where ω_A is albumin weight fraction and $\tilde{\rho}_s$ is the partial specific solvent density. A table is given in Appendix A which summarizes the relationships between the various albumin concentration units employed throughout this thesis.

B. Albumin Solubility

Protein solubility is discussed in the literature primarily in qualitative terms. The following summary indicates the trends which have been reported regarding the effects of solution proterties on protein solubility (48, 49, 50).

Protein Concentration - In very dilute aqueous solution, proteins will sometimes separate as insoluble precipitates. These precipitates are often found to be denatured. These changes are probably due to

an effective decrease in the solution dielectric constant as compared to the more concentrated protein solutions. In the interest of protein integrity, therefore, it is wise to avoid major dilution (to be balanced against specific protein interactions of more concentrated solutions) wherever possible.

pH - Alterations of pH change the interactions of dissolved proteins with other species in the medium. A given protein is least soluble near its isoelectric point in the presence or absence of neutral salts, but the pH of minimum solubility will vary according to the characteristics and concentration of the neutral salt. Also, interaction of proteins with one another may form complexes which are either more or less soluble than the uncombined proteins.

Ionic Strength - Increasing the dilution of a neutral salt/protein mixture increases the stability and solubility of the protein. This follows from Debye's theory of salting out which suggests that salt ions attract around themselves the more polarizable molecules of the medium thereby squeezing out other components such as proteins.

Temperature - In salt free solutions, or solutions at low ionic strength and in the ethanol-water system protein solubility increases with temperature. In the concentrated salt solutions encountered in "salting out" procedures, the effect is often reversed.

An interesting description of the dissolution of BSA in pure water at 3°C was recently given by MacRitchie (51). In these experiments, several weighed samples of bovine serum albumin of

known moisture content, were placed in a vacuum desiccator containing pure water and kept at 3±1°C. The BSA samples were weighed at intervals. The samples absorbed water, at first rapidly but with the rate continuously decreasing until after a period of several weeks, the BSA concentration had been reduced to less than 40 gm %. During that interval it was observed that at a moisture content of 47 wt % (i.e. isoionic BSA at 61 gm % and ∿4.9 pH), the crystals began to be replaced by a semitransparent gel. The transition from powder to gel was complete at a moisture content of 54 wt % (52 gm % BSA) while the gel liquified at a moisture content of about 62 wt % (42 gm % BSA).

Kozinski (52) measured albumin solution viscosity to protein concentrations of 45 gm %, primarily in an arsenate buffer at pH 6.7. He found Newtonian behaviour for his measurements to the highest concentration measured. Beyond 45 gm %, accurate measurements could not be made with the Ostwald viscometers due to the extremely high viscosities encountered. He estimated a solubility limit of 58.5 gm % from the observation of a nearly immobile gel which was formed at this concentration.

From this discussion, it is concluded that the solubility limit for gel formation of albumin solutions is around 60 gm %. The dependence of this solubility limit on solution pH is unknown, but, for the three pH levels of interest in this work, would increase in the order 4.5 pH < 5.4 pH < 7.4 pH.

BIBLIOGRAPHY

(1) Einstein, A., Investigations on the Theory of the Brownian Movement. R. Furth, editor. Dover Publications, New York (1956).

(2) Doherty, P. and G. Benedek, "The Effect of Electric Charge on the Diffusion of Macromolecules". J. Chem. Phys., 61, p. 5426, (1974).

(3) Tanford, C., Physical Chemistry of Macromolecules, John Wiley and Sons, Inc., New York (1961).

(4) Edsall, J. T. and J. Wyman, Biophysical Chemistry, Vol. 1, Academic Press Inc., New York (1958).

(5) Tanford, C., S. A. Swanson and W. S. Shore, "Hydrogen Ion Equilibria of Bovine Serum Albumin". J. Am. Chem. Soc., 77, p. 6414 (1955).

(6) Scatchard, G. and E. S. Black, "The Effect of Salts on the Isoionic and Isoelectric Points of Proteins". J. Phys. and Colloid Chem., 53, p. 88 (1949).

(7) Scatchard, G., I. H. Scheinberg and S. H. Armstrong, Jr., "Physical Chemistry of Protein Solutions. IV. The Combination of Human Serum Albumin with Chloride Ion". J. Am. Chem. Soc., 72, p. 535 (1950).

(8) Scatchard, G., "Constants of the Debye-Huckel Theory". J. Am. Chem. Soc., 65, p. 1249 (1943).

(9) Scatchard, G., J. S. Coleman and A. L. Shen, "Physical Chemistry of Protein Solutions. VII. The Binding of Some Small Anions to Serum Albumin". J. Am. Chem. Soc., 79, p. 12 (1957).

(10) Longsworth, L. G. and C. F. Jacobsen, "An Electrophoretic Study of the Binding of Salt Ions by β-Lactoglobulin and Bovine Serum Albumin". J. Phys. and Colloid Chem., 53, p. 126 (1949).

(11) Alberty, R. A., "A Study of the Variation of the Average Isoelectric Points of Several Plasma Proteins with Ionic Strength." J. Phys. and Colloid Chem., 53, p. 114 (1949).

(12) Scatchard, G., A. C. Batchelder and A. Brown, "Preparation and Properties of Serum and Plasma Proteins. VI. Osmotic Equilibria in Solutions of Serum Albumin and Sodium Chloride". J. Am. Chem. Soc., 68, p. 2320, (1946).

(13) Scatchard, G., A. C. Batchelder, A. Brown and M. Zosa, "Preparation and Properties of Serum and Plasma Proteins. VII. Osmotic Equilibria in Concentrated Solutions of Serum Albumin". J. Am. Chem. Soc., 68, p. 2610 (1946).

(14) Edsall, J. T., H. Edelhoch, R. Lontie and P. Morrison, "Light Scattering in Solutions of Serum Albumin: Effects of Charge and Ionic Strength." J. Am. Chem. Soc., 72, p. 4641, (1950).

(15) Tanford, C. and J. G. Buzzell, "The Viscosity of Aqueous Solutions of Bovine Serum Albumin Between pH 4.3 and 10.5". J. Phys. Chem., 60, p. 225 (1956).

(16) Wagner, R. H. and L. D. Moore, Jr., "Determination of Osmotic Pressure." in Techniques of Organic Chemistry, Vol. 1, Part 1, A. Weissberger, editor, p. 815, Interscience Publishers, Inc., New York (1959).

(17) Kupke, D. W., "Osmotic Pressure" in Advances in Protein Chemistry, 15, p. 57, Academic Press, New York, (1960).

(18) Overton, J. R., "Determination of Osmotic Pressure". in Physical Methods of Chemistry, Part V, A. Weissberger, editor, p. 309, Wiley-Interscience, New York (1971).

(19) Hill, T. L., Introduction to Statistical Thermodynamics, Chapter 19, Addison-Wesley Publishing Co., Reading, Mass. (1960).

(20) Scatchard, G., "Physical Chemistry of Protein Solutions. I Derivation of the Equations for the Osmotic Pressure." J. Am. Chem. Soc., 68, p. 2315 (1946).

(21) Gutfreund, H., "The Analysis of Osmotic Pressure Measurements of Solutions of Bovine Serum Proteins." Trans. Far. Soc., 50, p. 628 (1954).

(22) Gutfreund, H., "The Osmotic Pressure of Solutions of Trypsin and Trypsin Compounds." Trans.Far. Soc., 50, p. 624 (1954).

(23) Rice, S. A. and M. Nagasawa, Polyelectrolyte Solutions, Academic Press, New York (1961).

(24) McMillan, W. G. and J. E. Mayer, "The Statistical Thermodynamics of Multicomponent Systems." J. Chem. Phys., 13, p. 276 (1945).

(25) Hill, T. L., "On the Theory of the Donnan Membrane Equilibrium." Disc. Faraday Soc., 21, p. 31 (1956).

(26) Hill, T. L., "Osmotic Pressure, Protein Solutions and Active Transport. II", J. Am. Chem. Soc., 80, p. 2923 (1958).

(27) Stigter, D. and Hill, T. L., "Theory of the Donnan Membrane Equilibrium. II. Calculation of the Osmotic Pressure and of the Salt Distribution in a Donnan System with Highly Charged Colloid Particles." J. Phys. Chem., 63, p. 55 (1959).

(28) Hoskin, N. E., "Solution to the Poisson-Boltzmann Equation For the Potential Distribution in the Double Layer of a Single Spherical Colloidal Particle." Trans. Far. Soc., 49, p. 51 (1953).

(29) Verwey, E. J. W. and J. Th. G. Overbeek, Theory of the Stability of Lyophobic Colloids, Elsevier Publishing Co., Inc., Amsterdam, (1948).

(30) Möller, W. J. H. M., G. A. J. van Os and J. Th. G. Overbeek, "Interpretation of the Conductance and Transference of Bovine Serum Albumin Solutions." Trans. Far. Soc., 57, p. 325 (1961).

(31) Möller, W. J. H. M., G. A. J. van Os and J. Th. G. Overbeek, "Electric Conductivity and Transference of Alkali Albuminates." Trans. Far. Soc., 57, p. 312 (1961).

(32) Gosting, L. J., "Measurement and Interpretation of Diffusion Coefficients of Proteins." Adv. Protein Chem., 11, p. 429 (1956).

(33) Creeth, J. M., "The Use of the Gouy Diffusiometer with Dilute Protein Solutions. An Assessment of the Accuracy of the Method." Biochem. J., 51, p. 10 (1952).

(34) Charlwood, P.A., "Estimation of Heterogeneity From Diffusion Measurements." J. Phys. Chem., 57, p. 125 (1953).

(35) Baldwin, R. L., L. J. Gosting, J. W. Williams and R. A. Alberty, "Transport Processes and the Heterogeneity of Proteins." Disc. Far. Soc., 20, p. 13 (1955).

(36) Creeth, J. M., data reported in reference 30.

(37) Wagner, M. L. and H. A. Scheraga, "Gouy Diffusion Studies of Bovine Serum Albumin." J. Phys. Chem., 60, p. 1066, (1956).

(38) Akeley, D. F. and L. J. Gosting, "Studies of the Diffusion of Mixed Solutes with the Gouy Diffusiometer." J. Am. Chem. Soc., 75, p. 5685 (1953).

(39) Champagne, M., "Contribution A l'Etude de la Morphologie de la Serumalbumine en Solution Etendue. II. Effet de la Variation du pH et de la Force Ionique." J. Chim. Phys., 54, p. 392 (1957).

(40) Keller, K. H., E. R. Canales and S. I. Yum, "Tracer and Mutual Diffusion Coefficients of Proteins." J. Phys. Chem., 75, p. 379 (1971).

(41) Anderson, J. L., "Prediction of the Concentration Dependence of Macromolecular Diffusion Coefficients." Ind. Eng. Chem. Fund. 12, p. 488 (1973).

(42) Oncley, J. L., G. Scatchard and A. Brown, "Physical-Chemical Characteristics of Certain of the Proteins of Normal Human Plasma." J. Phys. Chem., 51, p. 184 (1947).

(43) Hatch, F. T. and R. S. Lees, "Practical Methods for Plasma Lipoprotein Analysis." Adv. Lipid. Res., 6, p. 1 (1968).

(44) Edsall, J. T., In The Proteins, Vol. I., Neurath, H. and Bailey, K., editors. p. 549, Academic Press, Inc., New York (1953).

(45) Henry, R. J., Clinical Chemistry Principles and Techniques, p. 190, Harper & Row, New York (1964).

(46) Lowry, O. H. and O. A. Bessey, "The Adaption of the Beckman Spectrophotometer to Measurements of Minute Quantities of Biological Materials." J. Biol. Chem., 163, p. 633 (1946).

(47) Moelwyn-Hughes, E. A., Physical Chemistry, Chapter 17, Pergamon Press, London (1961).

(48) Margolis, S., In Structural and Functional Aspects of Lipoproteins in Living Systems. E. Tria and A. M. Scanu, editors, Academic Press, New York (1969).

(49) Pennel, R. B., In The Plasma Proteins, Vol. I, F. W. Putnam, editor, Academic Press, New York (1960).

(50) Oncley, J. L., In The Lipoproteins Methods and Clinical Significance, F. Homburger and P. Bernfeld, editors, S. Karger, Basle (1958).

(51) MacRitchie, F., "Effects of Temperature on Dissolution and Precipitation of Proteins and Polyamino Acids." J. Colloid and Interface Sci., 45, p. 235 (1973).

(52) Kozinski, A. A. and E. N. Lightfoot, "Protein Ultrafiltration: A General Example of Boundary Layer Filtration." AIChE J., 18, p. 1030 (1972).

Appendix

TABLE A-1

```
C*************** VIRIAL COEFFICIENTS FOR BSA IN SALINE *****************
C                       TEMP 25 DEG.
C
C         THIS PROGRAM COMPUTES THE PARAMETERS FOR B2, AND NUMER-
C         ICALLY INTEGRATES FOR THE VALUE OF B2
C
C         FORTRAN VARIABLE LIST
C
C         CL=     CHLORIDE ION CONC., MOLECULES/CC SOLUTION
C         SOD=    SODIUM ION CONC., MOLECULES/CC SOLUTION
C         ALB=    ALBUMIN CONC., GM/LITER SOLVENT
C         Z=      ALBUMIN CHARGE
C         RAD=    ALBUMIN MOLECULAR RADIUS, CM
C         RALB=   ALBUMIN CONC., MOLECULES/CC SOLUTION
C         TIO=    TOTAL IONIC CONC., MOLECULES/CC (OVERBEEK'S ACCOUNTING)
C         PKAP=   RECIP. DEBYE-HUCKLE LENGTH, CM**-1
C         PSI=    ALBUMIN SURFACE POTENTIAL, VOLTS
C         F=      HILL-STIGTER PARAMETER
C         BTWO=   SECOND VIRIAL COEFFICIENT, CC/MOLECULE
C
C         SUBROUTINE
C         QSF-    NUMERICAL INTEGRATION FOR B2 "CLUSTER INTEGRAL"
C
C
      DIMENSION X(5),Y(5),B2K(2),B2(5)
      READ(9,700) CL,SOD,RAD
      READ(9,702)DELX,NDIM
   16 ACCEPT "CONTINUE,STOP--1,2 ",IC
      GO TO (17,18),IC
   17 ACCEPT "ALB,CHARGE ",ALB,ZI
      ACCEPT "XLIM= ",XLIM
      ACCEPT "WRITE INTEGRAL --NO,YES --1,2 ",IPR
      WRITE(12,800) ALB,ZI
      WRITE(12,803)XLIM
C
C
```

```
      Z = ABS(ZI)
      RALB = (8.739E+18*ALB) / ((ALB/1.34) + 1000.)
      TIO = SOD + CL + 2.0*Z*RALB
      PKAP = 9.473E-04 * SQRT(TIO)
      RAP = PKAP*RAD
      PSI = 5.317E-03 * Z/ (1.  + RAP)
      F = 2.122E+10 * RAP*RAD*(PSI**2.) * EXP(2.*RAP)
      WRITE(12,801) RALB,TIO,PKAP,PSI,F,DELX
C
C
      B2K(1) = 0.0
      B2K(2) = 0.0
      XX=0.0
      YY=0.0
      DO 10 I=1,2000
      X(1) = XX
      Y(1) = YY
      DO 15 J=2,5
      X(J) = X(J-1) + DELX
      CHECK = (-F/X(J))*EXP(-X(J))
      IF(ABS(CHECK)-100.)11,11,14
   14 Y(J) = X(J)**2.
      GO TO 15
   11 Y(J) = (1.  - EXP((-F/X(J))*EXP(-X(J)))) * X(J)**2.
   15 CONTINUE
      CALL QSF(DELX,Y,B2,NDIM)
      B2K(2) = B2K(1) + B2(5)
      XX=X(5)
      YY=Y(5)
      GO TO (30,31),IPR
   31 WRITE(12,804)XX,YY,B2K(2)
   30 CONTINUE
C
      IF(XX - XLIM)21,21,13
```

```
   21 B2K(1) = B2K(2)
      DO 10 N=1,4
   10 B2(N) =0.0
C
   13 BTK = 6.283*B2K(2)
      BTWO = BTK/PKAP**3.
      WRITE(12,802) XX,BTK,BTWO
      GO TO 16
  700 FORMAT(3E10.3)
  702 FORMAT(F10.0,I5)
  800 FORMAT(1H,////,10X,'ALB GM/L.  SOLV.  =',F6.0,10X,'CHARGE =',F5.1)
  801 FORMAT(5X,'RALB=', E10.3,  3X,'TID=',E10.3,3X,'KAPPA=', E10.3,3X,
     1'PSI=',E10.3,/,5X,  'F=',E10.3,3X,'DELX=', E10.3,/)
  802 FORMAT(10X,'X=', E14.6,3X,'B2K=', E11.4,3X,'B2=',E11.4)
  803 FORMAT(10X,'XLIM= ',F6.1)
  804 FORMAT(10X,3E14.4)
   18 CALL EXIT
      END
```

TABLE A-2

Albumin Concentration Units

Let G = albumin concentration, gm/100 ml solution (gm %)

$$\nu_A = \nu_A^o = 0.736 \text{ ml/gm}$$

$$\nu_{saline} = \nu_{saline}^o = 1.00 \text{ ml/gm}$$

Then:

$$w_A = \frac{1340\ G}{134 - G} \ [=] \ \frac{\text{gm BSA}}{\text{liter saline}}$$

$$\omega_A = \frac{1.34\ G}{134 + 0.34\ G} \ [=] \text{ weight fraction BSA}$$

$$\phi_A = \frac{G}{134} \ [=] \text{ volume fraction BSA}$$

CHAPTER THREE

DETERMINATION OF CONCENTRATED ALBUMIN SOLUTION OSMOTIC PRESSURE

Osmotic pressure measurements of biological macromolecules have been conducted almost exclusively for the purpose of molecular weight determinations. For this reason, most of the techniques and data described in the literature, apply only to low concentrations of the protein solute (see Chapter 2 citations).

From extrapolations of osmotic pressure measurements made at low and moderate concentrations of albumin by Scatchard in the 40's (1,2) and Kappos and Pauly in the 60's (3), it was anticipated that a membrane osmometer capable of achieving high pressures would be needed to carry out determinations in concentrated solutions. The essential features of the specially designed high pressure, static-type membrane osmometer are discussed in the first section of this chapter. Particular attention is given to the characterization of the most critical element of this device, the membrane. Since only one kind of membrane, the Abcor HFA-180, was used for all of the investigations of this thesis, this characterization is of value to the interpretation of the results reported in other chapters.

Section II is a discussion of the experimental techniques employed to prepare and characterize the concentrated albumin solutions. The techniques used to ensure that thermodynamic equilibrium had been established at the point when a determination was made are also discussed.

In the third section, results are reported on the osmotic pressure measurements which were made on solutions which varied in albumin concentration from 9 gm% (9 gm BSA/100 ml solution) to 48 gm%. Three solution pH levels were investigated, 4.5, 5.4 and 7.4. Most of the measurements were made at an ionic strength of 0.15 M NaCl; a few measurements at 1.0 M

saline are included.

These results are compared in the discussion section with the non-ideal solution models which were developed in the previous chapter. The semi-empirical expression derived from considerations of Gibbs-Donnan equilibrium is shown to give an excellent description of the results. Comparisons are also made with the results which were predicted by the virial expansion of McMillan-Mayer solution theory. Lastly, a comparison is made with the data of Scatchard and that of Kappos and Pauly.

I. High Pressure Membrane Osmometer

A. Description of Equipment and Technique

The essential features of the custom designed high pressure membrane osmometer are shown in Figure 3-1.

The osmometer cell consists of two chambers, one in which is placed the solvent, in most cases 0.15 M saline, and in the other the macromolecular solution. The chambers are separated by a membrane which is completely impermeable to the macromolecule but which permits free passage of water and ions. After the chambers are filled, capillaries which have been prefilled with the respective liquids of each chamber are connected as shown to each chamber. The applied gas pressure is then quickly set to an estimated value and subsequently adjusted in the direction indicated by the slight movement in the capillary liquid levels. For instance, if the initial estimated pressure is below the solution osmotic pressure, solvent will be transferred across the membrane from the solvent side to the solution side. As soon as bulk flow is detected by a change in the capillary levels, the applied pressure is increased.

FIGURE 3-1 HIGH PRESSURE MEMBRANE OSMOMETER

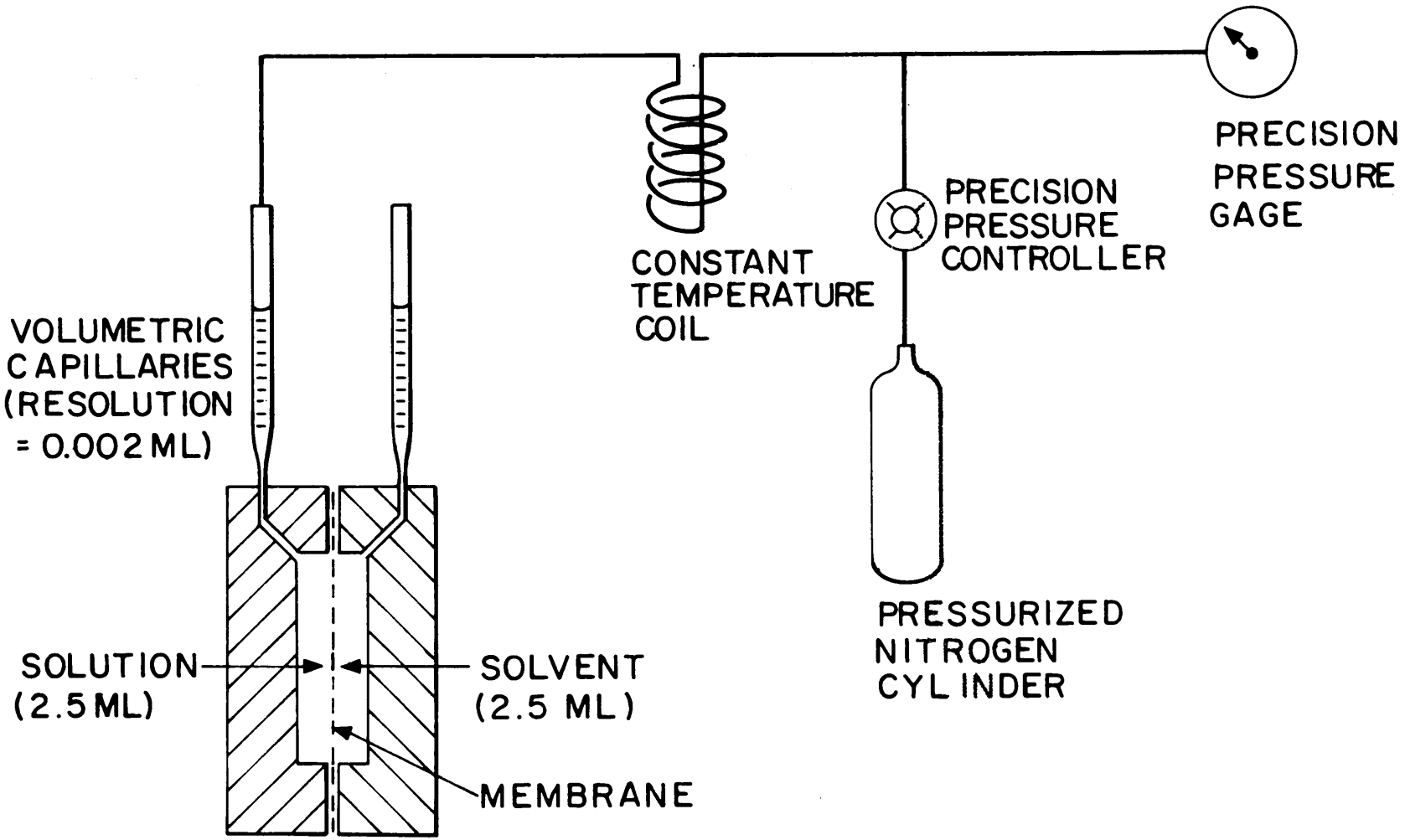

After a few such pressure adjustments, an applied pressure is found for which no further changes in liquid level occur. At this point the applied hydrostatic head is equal to the osmotic pressure of the solution. Because mixing in the solution chamber is by molecular diffusion only, it is essential to avoid a large volumetric transfer of solvent across the membrane so as to prevent large concentration gradients which would slow the approach to thermodynamic equilibrium.

The resolution of the volumetric capillaries (adapted from 1.00 ml pipettes with 0.01 ml graduations) allowed for the detection of volumetric transfers as small as 0.0025 ml or 0.001 times the solution chamber volume. Generally, the solvent-side meniscus was a more reliable indicator of fluid movement.

The osmometer cell and the pressurizing gas constant temperature coil were immersed in a constant temperature water bath which was controlled to within ± 0.1°C. All determinations were made at 25°C.

A precision pressure gage (Wallace & Tiernan, Model 62B, 0-60 psi, ± 0.1% full scale) and controller (Volumetrics, Inglewood, Calif., Model V-1, PV-Controller) allowed pressure to be measured, and controlled, to within a few centimeters of water, or about five hundredths of a psi. For measurements above 60 psi, a less precise, ± 1% full scale, high pressure gage was used.

B. The Osmometer Cell

A detailed view of the osmometer cell is shown in Figure 3-2. The chambers are formed by sandwiching a membrane between two cylindrical pieces of plexiglass, in each of which is a shallow (0.25 cm deep)

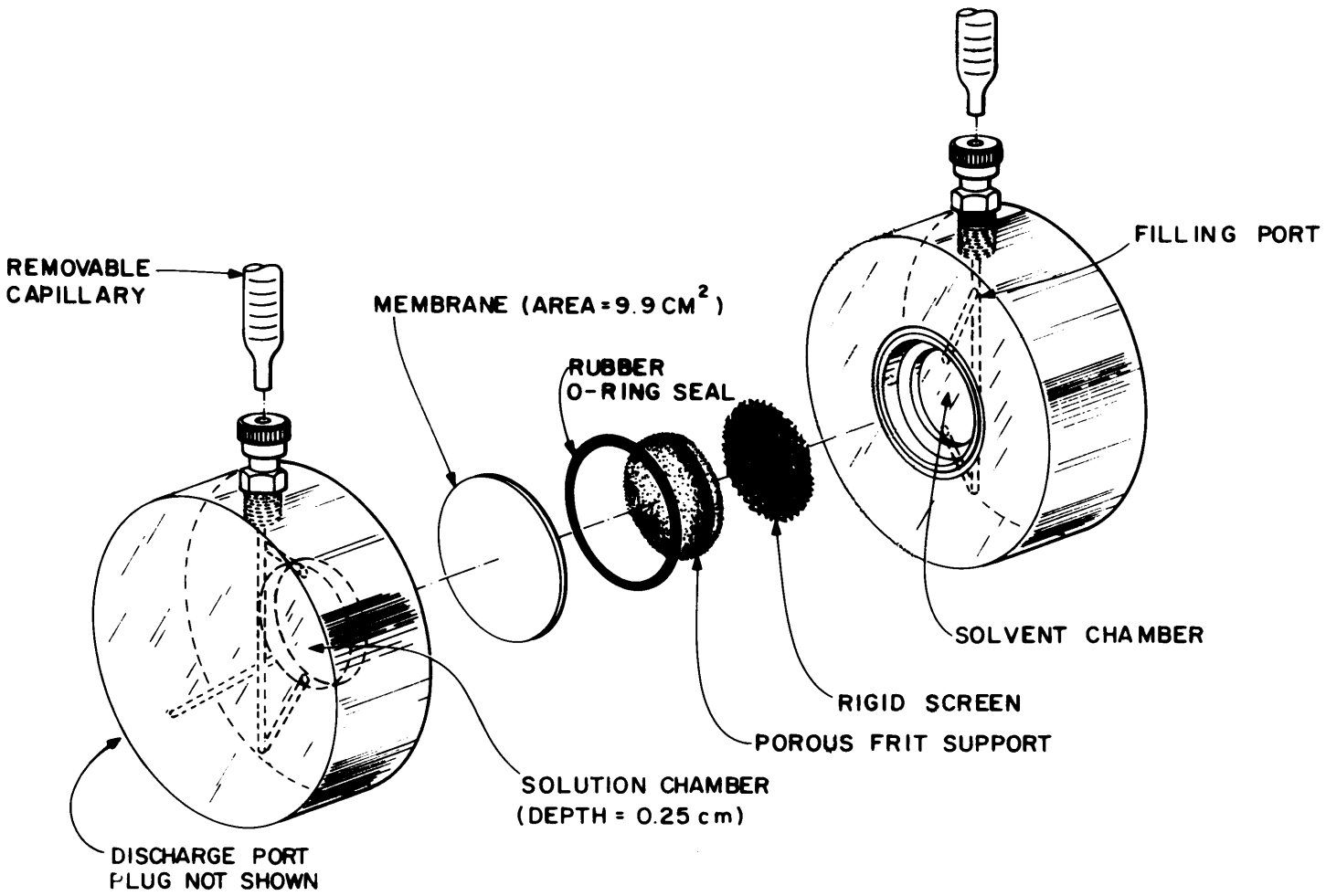

FIGURE 3-2 MEMBRANE OSMOMETER CELL

circular depression. The membrane is supported against the high hydrostatic pressures which are imposed on the solution side by a metal screen and a porous frit. A rubber O-ring impressed on the solvent side of the membrane localizes the mechanical force when the two halves are clamped together and seals the unit up to applied pressure as high as 80 psig. Not shown are the eight, one-eighth inch stainless steel rods, symmetrically spaced around the cavities, at a distance about half-way between the cavities and the outer perimeter, which were used to clamp the unit. Table 3-1 presents additional dimensions and details which are not present in the figure.

Abcor HFA-180 membranes were used in the osmometer, and were selected, in part, because of their durability and complete rejection of albumin. Five membranes were used in the course of about 50 experimental runs and there were no detectable differences in the results for the different membranes. A membrane was replaced only when it became excessively distorted after several uses, especially for the higher pressure determinations.

With the capillaries removed, each chamber was filled by inserting a syringe to the bottom of the filling channels. As the liquid was forced into the bottom of each chamber, air was forced out the top, thereby preventing the formation of bubbles.

After the chambers were filled, the volumetric capillaries which had been pre-filled with the appropriate solutions, were fixed into place, the hydrostatic pressure source was quickly attached to the solution-side capillary and the entire device submerged in the constant temperature bath.

TABLE 3-1

Osmometer Cell Dimensions

Detail	Dimension	Note
Overall dimension for each half	4 inch diameter x 1 inch thickness	
Solution and solvent cavities	1.4 inch diameter	
O-ring groove	1.5 inch outside diameter	
Filling ports	0.0625 inch diameter	
Screen	1.4 inch diameter x ~0.03 inch thick	Stainless steel
Porous frit	1.4 inch diameter x 0.05 inch thick	High density polyethylene Porex Materials Corp. Fairburn, Georgia
Capillary fittings	Compatible with 0.125 inch O.D. glass tubing	Swagelok No. 2-UT-1-2

At the conclusion of a measurement, solvent and solution samples were usually removed from the cell with a syringe through the filling ports. For concentrated (above 40 gm%) solutions, however, this technique was too slow and resulted in significant dilution of the discharged protein solution. To circumvent this dilution, a discharge port was added to the cell. This permitted rapid solution sample discharge when the discharge plug was removed with solution under pressure.

C. Membrane Selection and Characterization

Three commercially available ultrafiltration membranes which are all claimed to be 99+% retentive for albumin are the Amicon PM-30, the Abcor HFA-180 and the Millipore PSAC. All are anisotropic membranes. The Amicon membrane is made from an aromatic polymer while the Abcor and Millipore membranes are made from cellulosic materials.

At least two samples of each membrane were screened for solvent flux characteristics and BSA rejection in stirred cell experiments. Flux at 10 psig with distilled water for the PM-30 and HFA-180 membranes was about 0.06 cm/min while the PSAC membranes averaged only 0.03 cm/min. The PM-30 and HFA-180 completely rejected BSA at all test conditions (up to 60 psig pressure and 4 day test cycles per membrane). After exposure to 60 psig, one of the PSAC samples was found to leak albumin.

The HFA-180 was selected for this thesis research upon completion of these screening tests, its principle advantage over the PM-30 being its ruggedness. The PM-30 "skin" tended to blister or scratch easily.

To insure that membrane performance would not be a factor in the evaluation of the effects of concentration polarization in ultrafiltration, or in the osmotic pressure measurements of the albumin-saline solutions, the HFA-180 membrane was further tested for saline permeability and its interaction with albumin. The saline permeability was checked using the high pressure membrane osmometer.

The experiment consisted of placing a 1.5 M NaCl solution on one side of the membrane and a 0.15 M NaCl solution on the other. A small pressure was applied (0.6 psi) to the 1.5 M solution. The movement of fluid against the concentration gradient, for the Abcor HFA-180 membrane, is shown in Figure 3-3. The osmotic flow of fluid against the pressure gradient, for a convential regenerated cellulose dialysis membrane, is shown for comparison. From the expression for solvent flux through a hyperfiltration membrane (4), a membrane "reflection coefficient", σ, can be estimated for the HFA-180 membrane.

$$v_s = L_p (\Delta P - \sigma \Delta \pi) \qquad (3\text{-}1)$$

where v_s = solvent flux from Figure 3-3

= 3×10^{-3} cm/min

L_p = $(K_m/\bar{\rho})$, hydraulic permeability, stated above

= 6×10^{-3} cm/min-psi

$\Delta\pi$ = 486 psi

ΔP = 0.6 psi

The reflection coefficient of 2×10^{-4} indicates that the HFA-180 membrane does not significantly interfere with the movement of Na^+ and Cl^- ions

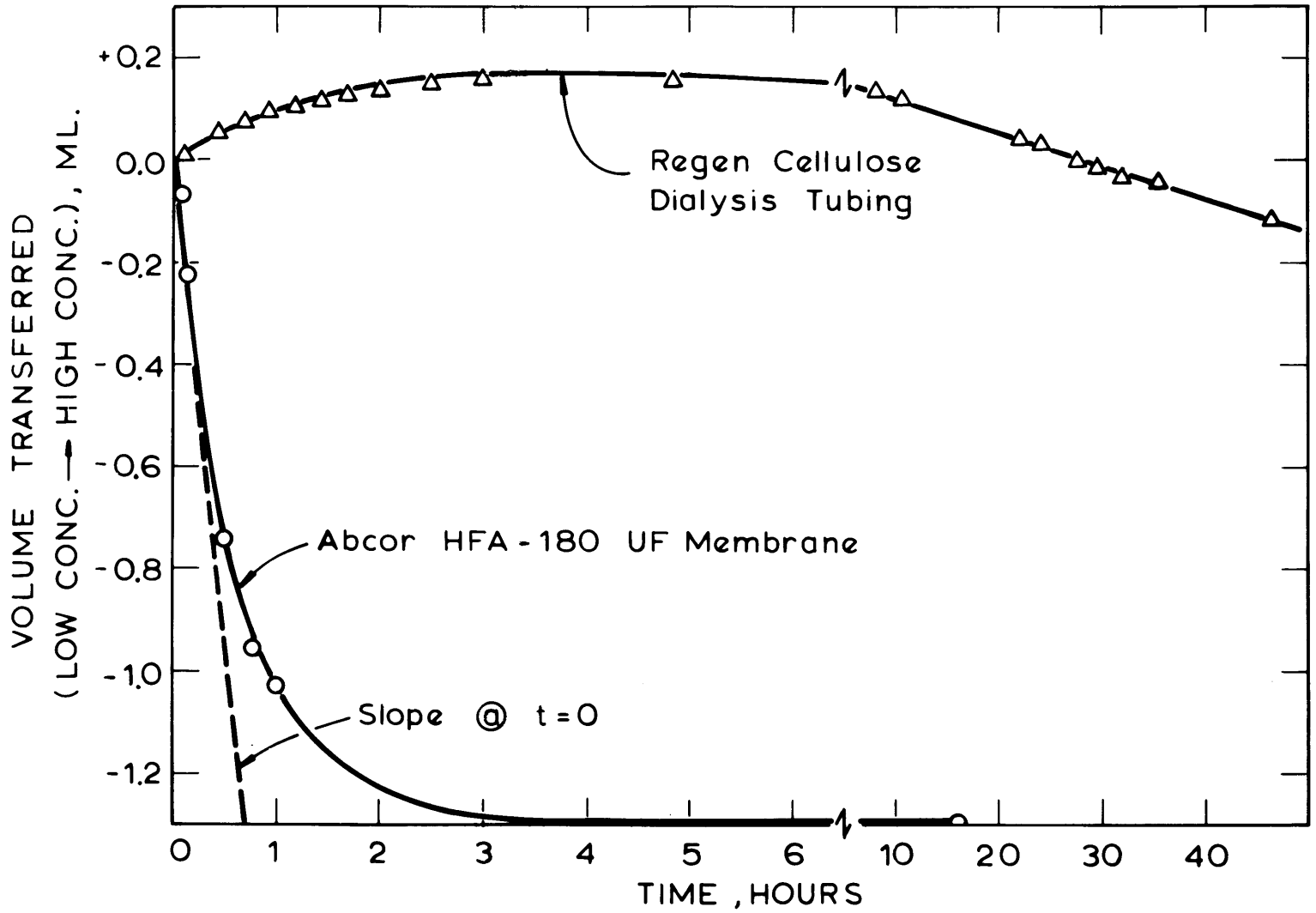

Figure 3-3 HFA-180 Membrane Salt Rejection Study

across the membrane.

Ultrafiltration in a stirred cell using radioactively tagged (I^{125}) albumin was conducted to prove that the effect of pore clogging by the macrosolute would be negligible. An HFA-180 membrane in the Amicon Model 52 stirred ultrafiltration cell (membrane surface area, 12.5 cm^2) was used to ultrafilter an 8.6 gm% albumin in 0.15 M saline solution at 5.4 pH. Tracer albumin, which first had been dialyzed for 24 hours to rid the sample of free I^{125} ions, with a total scintillation count of 9.5×10^6 CPM was added to this solution. For the 75 ml ultrafiltration cell volume, this overall activity corresponded to a specific activity of $1.5 \times 10^{+6}$ CPM per gram BSA. The filtration was performed at 40 psig for 17 hours during which time more than 500 ml of fluid passed through the membrane.

After the filtration, the surface of the membrane was gently washed with distilled water, and a 0.0314 ml sample of the membrane (about one-tenth of the total exposed area) was found to contain only 31 CPM (above background), or only 3×10^{-6} as many counts per minute as were present in the bulk. The accuracy of the count increases as the absolute count increases so that this low level is not very accurate. If the void fraction of the membrane is conservatively estimated at about 10%, then less than 0.5% of the membrane pore volume contained albumin.

While this result justified the conclusion that the effect of pore clogging was minimal, it was not accurate enough to allow conclusions to be made regarding the possible effects of adsorption of protein on the membrane surface. In general, there is little agreement in the literature concerning the exact amount of protein which is adsorbed to a polymer

surface. Most of the variation is attributable to the variety of techniques which were used to measure this adsorption. Most investigations (5,6,7,8) are in qualitative agreement on the observation that, for albumin interacting with a hydrophilic surface like that of a cellulosic membrane, the adsorption is equivalent to a monolayer or less, and is mostly, or completely reversible.

Generally this type of adsorption on hydrophilic surfaces has also been observed for several other plasma proteins. An exception to this concensus is the data of Nyilas, et al. (9) regarding the adsorption of γ-globulin to the surfaces of glass microbeads and glass powders. They found multiple layer adsorption. This discrepancy, in part, probably reflects a difference between adsorption to a high energy surface (e.g. glass microbeads and powders) as opposed to a low energy surface (e.g. hydrophilic polymers). No measurements of desorption were made in their study.

On hydrophobic surfaces, such as polyethylene, polystyrene or Teflon, Brash and Lyman (6) found the protein binding to be quite irreversible and not easily desorbed over a wide range of pH. They concluded that their data were best described by a monolayer adsorption model and that, when compared to the free solution dimensions of the native protein, the proteins are not dimensionally denatured by adsorption to this type of surface.

Protein interaction is weaker with a hydrophilic surface, due to both surface and protein possessing water of hydration and thereby not getting close together (5). In comparison with their study of adsorption to hydrophobic surfaces, Brash and Lyman found only about 50% as much

adsorption of albumin to the hydrophilic surface of cuprophane dialysis membrane (6). Mac Ritchie studied the effect of solution pH in his investigations of albumin interaction with hydrophobic and hydrophilic surfaces (7). The hydrophilic surface adsorption was pH sensitive with maximum adsorption occurring at the isoelectric point of the protein. This led to the conclusion that for hydrophilic surface adsorption, electrical factors, and therefore the charge of the protein, are important.

In summary, it appears that for albumin ultrafiltration with the cellulosic HFA-180 membrane, some adsorption of the protein to the membrane does occur, probably less than a monolayer. Because the adsorbed protein which is globular, is no longer in free solution, it should not be a factor in limiting ultrafiltration in a thermodynamic sense. If evenly distributed over the surface, the adsorbed layer should be of only minimal influence as a hydrodynamic factor. It could be a more significant factor only if the adsorption selectively occurred near the membrane pores. The observation from the stirred cell experiments mentioned in Chapter 1, that the same results were obtained for albumin ultrafiltration performed with either the hydrophilic HFA-180 membrane or the polyaromatic PM-30 membrane, suggest that surface adsorption is of minimal influence.

II. Experimental Procedures

A. Solutions

Saline solutions were made to 0.15 M or 1.0 M ionic strength from distilled water and analytical grade NaCl. Every saline solution preparation included the addition of minute amounts (ca. 10 mg/liter) of

sodium azide as an anti-bacterial agent. This practice was followed in all experimental work reported in this thesis.

Albumin solutions were made from portions of these saline preparations and from known weights of Bovine serum albumin. The Pentex grade Bovine serum albumin (recrystallized Cohn Fraction V) was purchased from Miles Laboratories, Kankakee, Illinois (Cat. No. 81-001). Cellulose acetate electrophoresis experiments (4 samples) were performed on the first batch of albumin which was purchased. The results confirmed the absence of globulins and the 100% purity specification of Miles Labs.

For highly concentrated solutions (above about 30 gm%) the technique for dissolving albumin crystals in saline involved the use of 50 ml centrifuge tubes which could be agitated by a vigorous vortexing motion. Occasionally, the temperature of these solutions was increased to 34°C for several hours to hasten the dissolution process.

Solution pH measurements were made with a saturated KCl glass electrode. Solution pH adjustment was made by the addition of unbuffered 0.1 N sodium hydroxide or hydrochloric acid solutions (made from 10 N acculute reagent solutions). Vigorous agitation of the solutions by vortex action was employed to insure that local protein denaturation would not occur during acid or base addition.

Solutions made by the above technique always appeared non-cloudy, but frequently small strands of apparently denatured protein were observed. For this reason, the final step before an experimental run involved filtering these solutions through a 0.1 micron filter for solutions up to 30 gm% BSA, and a 0.3 micron filter for solutions of higher concentration.

The pH adjustment step introduced an error regarding the nominal 0.15 M or 1.0 M specification on ionic strength. The solutions were not analyzed for sodium or chloride ion concentrations. Because of the large aliquots of 0.1 N NaOH or 0.1 N HCl which were added for pH adjustment, the concentrations of Na^+ and Cl^- were estimated to vary as much as ± 0.03 M units. This maximum error from the nominal 0.15 M specification was estimated only for the solutions of highest protein concentration (~40 gm%).

The .15 M saline solvent charged to the solvent chamber of the osmometer was also adjusted with unbuffered NaOH or HCl solutions to the same pH value as the corresponding albumin solution.

B. Experimental Technique

The procedure for starting and ending an experiment was discussed above. An experiment generally lasted six hours or more to insure that thermodynamic equilibrium had been achieved. In order to confirm that this equilibrium had been achieved, several techniques were employed.

One of these is the comparison of the final pressure from two separate determinations on nearly equivalent solutions, except that in one case the initial preset hydrostatic pressure is less than the osmotic pressure of the solution and in the second case, it is greater. For each determination, the applied pressure is adjusted until volume transfer between chambers ceases.

The results of a typical measurement are shown in Figure 3-4. The time course of the applied pressure adjustments for each of these two experiments is shown on the middle graph with the time course of the

FIGURE 3-4

BOVINE SERUM ALBUMIN
OSMOTIC EQUILIBRIUM EXPERIMENTS

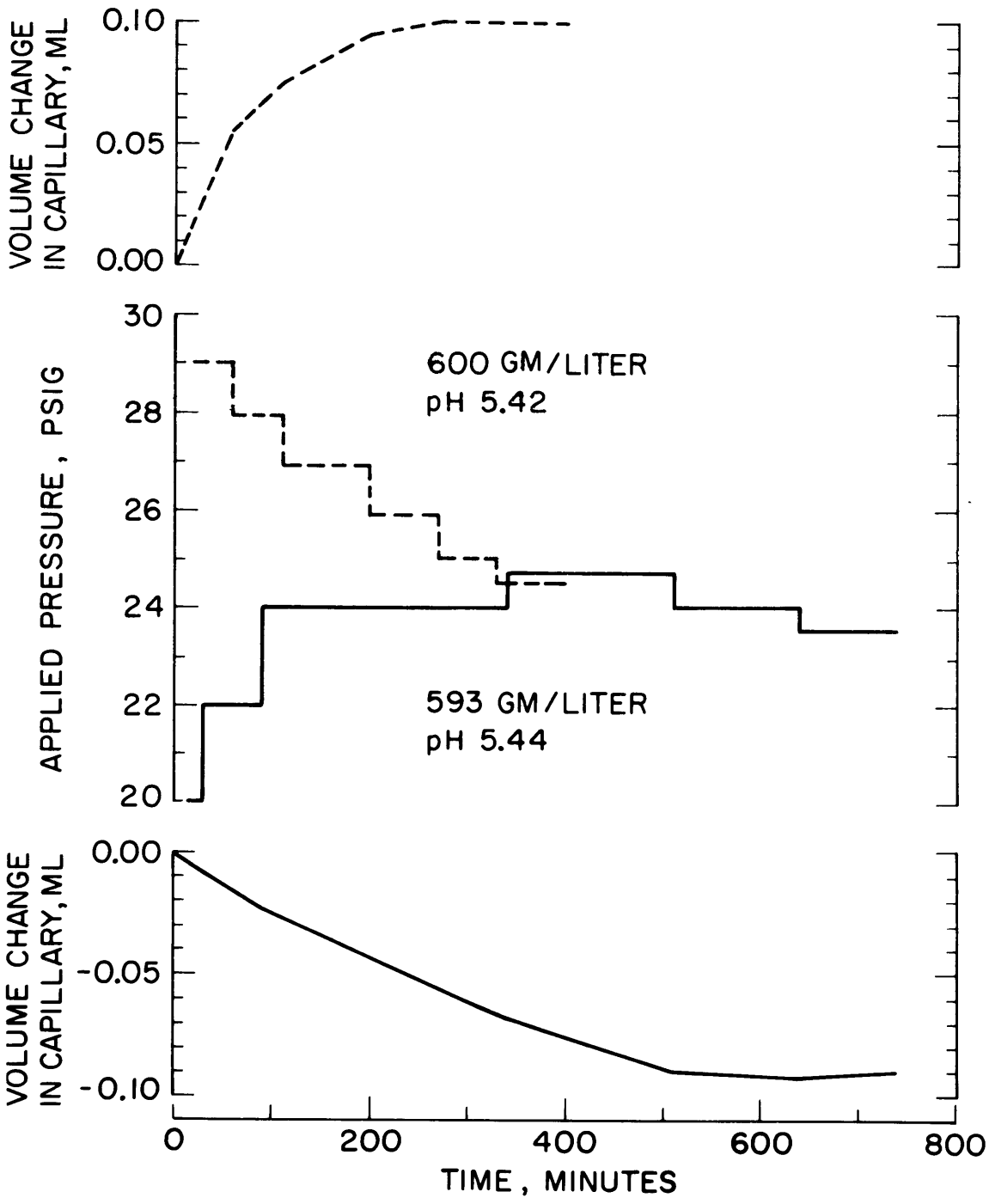

solvent capillary volume shown above and below for each respective case. In the first experiment, (Experiment 37) shown as the solid lines, the applied pressure is initially set about ten per cent below the osmotic pressure of 24.3 psi. The decrease in the level of the solvent capillary shown in the lower graph indicates that solvent is moving across the membrane into the albumin solution chamber. As the applied pressure is increased, the rate of volumetric transport is reduced because the driving force is decreased. Eventually, the capillary level becomes static, and the osmotic and applied pressures are balanced.

Note that because a small amount of solvent transfer does occur, about one tenth of a milliliter or about four per cent of the solution chamber volume, a slight dilution of the original albumin solution, also occurs. It is for this reason that all concentration and pH determinations were checked on the discharged solution from the osmometer.

In the second experiment (Experiment 35) shown as the broken lines in these graphs, the initial pressure was about ten per cent above the equilibrium pressure. The level change here reflects the movement of solvent out of the solution chamber. The level stops changing when the pressure has been lowered to approximately the same value as the equilibrium pressure of the first experiment. The osmotic pressure of these nearly identical solutions agreed to within about 4% by these two measurements.

Another method employed to check for equilibrium was the perturbation of a stabilized system. For example in Experiment 40 (45 gm%, 7.4 pH), a stable liquid level in the capillaries was observed at an applied pressure of 4932 cm H_2O. This stable condition took two hours

to establish, and was observed for an additional two hours. At this time, the applied pressure was reduced by 7%. About twenty minutes after this change, the capillary level drift indicated insufficient applied pressure. The level movement was then observed to reverse when the applied pressure was increased by 7% over the stable value of 4932 cm H_2O. The experiment was terminated after an additional two hour observation of stable capillary levels at the equilibrium pressure.

Discharged solutions from the osmometer were analyzed for albumin concentration and pH. The albumin concentration measurements involved diluting the original sample by volumetric methods (wash-out pipettes were used with the viscous solutions) to bring the concentration within the range of the standard samples which were used with the biuret method (9). The saline solvent chamber discharge was also routinely checked for albumin leakage. In most cases, the biuret method was used for this analysis also (no additional dilution required). In some cases, the Lowry method (10), which is more accurate when protein concentrations are very low, was used to obtain a more accurate value for these samples.

III. Results

At each pH, 4.5, 5.4 and 7.4, the effect of albumin concentration on osmotic pressure was determined up to a maximum concentration of about 46 gm% (700 gm BSA/ℓ. solvent). Above this concentration, the solutions were too viscous to move into and out of the osmometer without incurring excessive dilution. The discharge concentration, which at a maximum varied from the initial concentration by ± 10%, are the values reported for each determination. The pH of the discharged solution was never

significantly different (±.05 pH units) from the initial solution pH.

The albumin concentration in the solvent chamber discharge was generally barely detectable by the biuret method at the level of 1 to 3 gm BSA/liter solvent. These low concentrations were confirmed in a few cases by the Lowry method. Exceptions to these very low levels were the solvent discharges from the high BSA concentration experiments (above 400 gm/ℓ) at the acidic 4.5 pH. These discharge levels ranged as high as 17 gm/ℓ (three additional samples ranged in concentration from 7-10 gm/ℓ), which is still an insignificant correction to the osmotic pressure (greater than 300 cm H_2O) of these concentrated solutions.

Table 3-2 shows the results of 38 successful osmotic pressure determinations. The solution pH data (±0.01 unit) is converted to charge on the albumin molecule using Figure 2-2.

From the tests for thermodynamic equilibrium, a precision of better than ± 5% is thought representative for a pressure measurement. Albumin concentration measurements were also controlled within 5% precision limits.

All of the data in Table 3-2 are at an ionic strength of 0.15 M except for the several experiments at 1.0 M saline (*). Most of these experiments were done at low protein concentration levels where no effect of the increased ionic strength is observed. A slightly depressed osmotic pressure was observed for the data point at a moderate protein concentration and 7.4 pH. These results are in qualitative agreement with the Donnan equilibrium.

It was stated above that for concentrated solutions at 4.5 or 7.4 pH, the Na^+ or Cl^- concentration may be as much as ±0.03 moles/ℓ different

TABLE 3-2

OSMOTIC PRESSURE OF BOVINE SERUM ALBUMIN SOLUTIONS

RUN	BSA CONCENTRATION GR. BSA/ LITER SOLVENT	pH	Z	OSMOTIC PRESSURE+ CM H_2O	REDUCED OSMOTIC PRESSURE Π/C
7	89.5	7.35	-20.2	65	0.726
8*	94.1	7.38	-20.3	64	0.680
5	97.5	7.37	-20.3	80	0.821
15	251.2	7.40	-20.4	450	1.791
18	251.2	7.46	-20.6	452	1.799
21	368.7	7.48	-20.7	1143	3.100
41	428.9	7.34	-20.2	1350	3.148
42	428.9	7.38	-20.3	1351	3.150
43	482.4	7.40	-20.4	1928	3.997
26	486.1	7.50	-20.8	2220	4.567
44*	519.9	7.41	-20.4	1808	3.478
27	597.5	7.44	-20.6	3550	5.941
28	629.1	7.44	-20.6	3802	6.044
40	672.8	7.42	-20.5	4932	7.331
2	97.5	5.41	-9.2	55	0.564
10*	136.5	5.40	-9.1	94	0.689
4	143.8	5.40	-9.1	100	0.695
11*	148.7	5.41	-9.2	113	0.760
12*	149.9	5.41	-9.2	121	0.807
3	161.1	5.40	-9.1	122	0.757
17	282.7	5.44	-9.5	352	1.245
13	291.5	5.45	-9.6	310	1.063
16	300.4	5.42	-9.3	364	1.212
19	451.7	5.40	-9.1	838	1.855
36	560.9	5.42	-9.3	1362	2.428
37	593.4	5.44	-9.5	1667	2.809
35	599.6	5.42	-9.3	1743	2.907
24	633.4	5.41	-9.2	1856	2.930
30	686.4	5.45	-9.6	2072	3.019
9*	118.5	4.56	+3.3	60	0.506
6	138.9	4.46	+5.5	64	0.461
14	210.1	4.54	+3.6	126	0.600
20	349.5	4.52	+4.1	247	0.707
33	415.2	4.50	+4.5	309	0.744
34	416.9	4.50	+4.5	331	0.794
25	460.6	4.52	+4.1	385	0.836
32	607.9	4.57	+3.2	970	1.596
38	735.1	4.50	+4.5	1204	1.638

* 1.0 M saline

+ To convert to psi, divide by 70.4

from the nominal 0.15 M specification. Estimates of these differences for several runs were made from laboratory notes on acid and base solution strengths and the size of aliquots added to known volumes of protein solutions. Since the micro-ions are free to distribute themselves quickly across the membrane in accordance with the Donnan equilibrium, the effect of this unequal Na^+ and Cl^- ion concentration in the equilibrium solvent phase on the total observed osmotic pressure can be estimated by calculating π_D from equation (2-22). These calculations (see Appendix) show the maximum error introduced to the observed osmotic pressure is about 10%.

IV. Discussion

The results above are analyzed with respect to the theories which have been presented in Chapter 2. Only the measurements made in 0.15 M NaCl solutions are compared.

A. Gibbs-Donnan Equilibrium Analysis

Using the molecular weight of 69,000 (1,2), the van't Hoff limiting law (equation 2-10) predicts an osmotic pressure of only 3.5 psi at the maximum concentration studied, as well as osmotic pressure independence of solution pH. The experimental results are shown in Figure 3-5.

At low concentrations, the osmotic pressure at all three pH levels converges to the value predicted for ideal solutions. At the other extreme - high concentration and physiological pH - the osmotic pressure reaches 70 psi. This is about five times greater than the pressure of the more acid pH 4.5 solution and about twenty times higher than predicted for an ideal solution.

The curves in the figure are regression fits of the data to eqn (2-22).

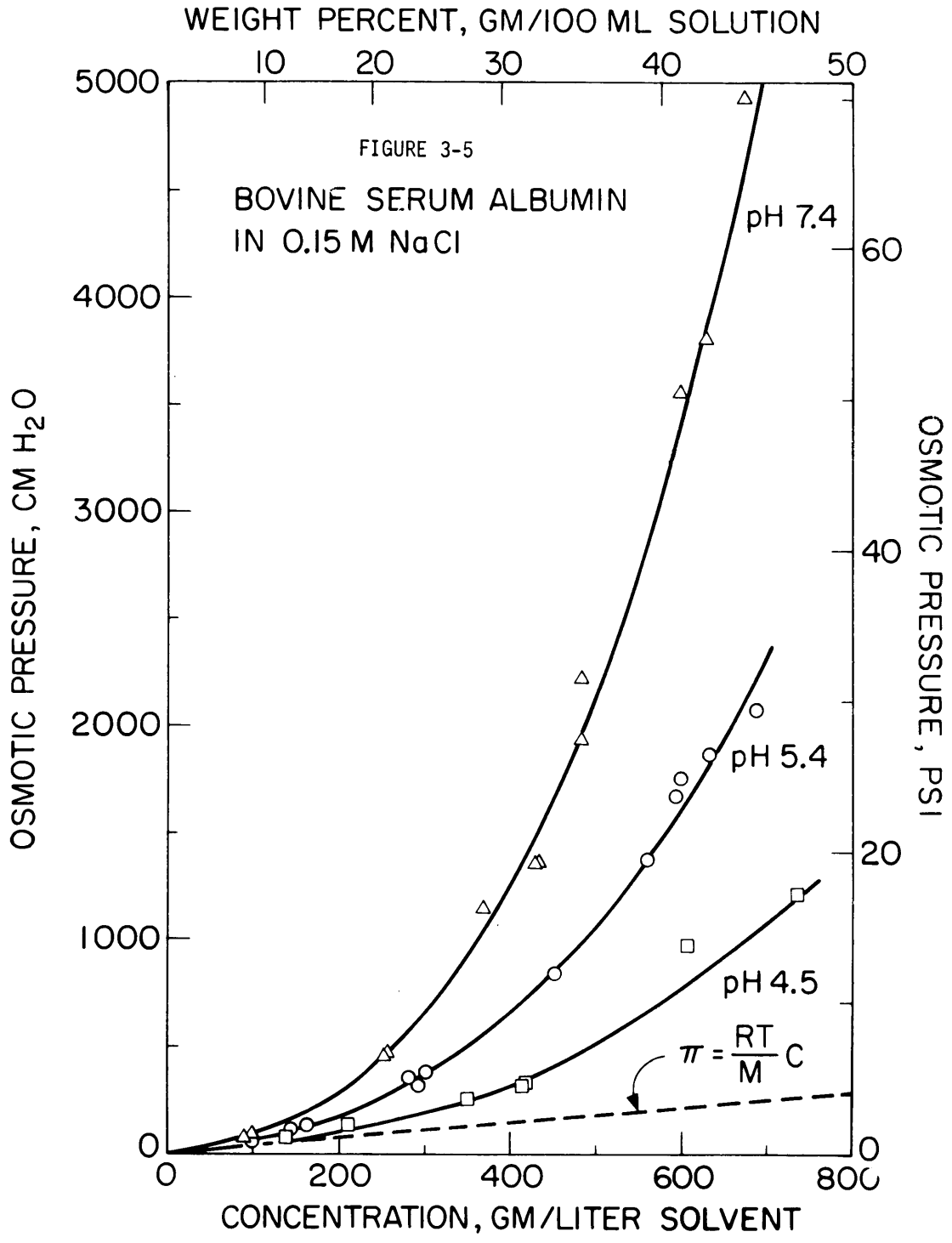
WEIGHT PERCENT, GM/100 ML SOLUTION
10
20
30
40
50
5000
4000
3000
2000
1000
0
OSMOTIC PRESSURE, CM H_2O
60
40
20
0
OSMOTIC PRESSURE, PSI
FIGURE 3-5
BOVINE SERUM ALBUMIN
IN 0.15 M NaCl
pH 7.4
pH 5.4
pH 4.5
$\pi = \frac{RT}{M} C$
0
200
400
600
800
CONCENTRATION, GM/LITER SOLVENT

$$\pi = \pi_p + \pi_D \tag{2-22}$$

$$\text{where } \pi_p = \frac{RT}{M_p}\left[w_p + A_2 w_p^2 + A_3 w_p^3\right]$$

$$\pi_D = RT\left[2\sqrt{\left(\frac{\bar{Z}w_p}{2M_p}\right)^2 + m_s^2} - 2m_s\right]$$

where m_s is salt concentration in molal units (.15 M ≃ .15 m), w_p is protein concentration as gm/ℓ. solvent, M_p is 69,000 gm/mole BSA and with RT = 25,330 cm H_2O-ℓ/mole (@ 25°C), π is expressed as cm H_2O. The data of the figure was fitted at each pH by first computing the Donnan contribution, then the difference π-π_p, and regressing this difference (times the constant M_p/RT) as a function of protein concentration, w_p. The virial-type coefficients, A_2 and A_3, determined in this manner at each pH, were then found to be quadratic functions of protein charge,

$$A_2 = k_1 + k_2\bar{Z} + k_3\bar{Z}^2$$

$$A_3 = k_1' + k_2'\bar{Z} + k_3'\bar{Z}^2$$

Table 3-3 presents the numerical values of these coefficients.

In Figure 3-6 and 3-7, the separate contributions to the total pressure of the Donnan term and the protein term are shown for each pH. From these graphs, it is seen that at the pH of lowest charge, 4.5, protein-protein interactions account for the majority of the nonideal behavior of this solution at high concentrations. For example, at 800 gm BSA/ℓ, Figure 3-5 indicates a pressure which is 1150 cm H_2O

TABLE 3-3

Osmotic Pressure Correlation Coefficients

A_2 and A_3 as Functions of $\overline{Z}$

	k_1 or k_1'	k_2 or k_2'	k_3 or k_3'
A_2	2.170×10^{-3}	-2.558×10^{-4}	-2.107×10^{-5}
A_3	4.657×10^{-7}	-1.185×10^{-7}	4.993×10^{-8}

A_2 and A_3 Evaluated @ pH 4.5, 5.4 and 7.4

pH	A_2	A_3
4.5	5.921×10^{-4}	5.135×10^{-6}
5.4	2.752×10^{-3}	9.870×10^{-6}
7.4	-1.381×10^{-3}	2.785×10^{-5}

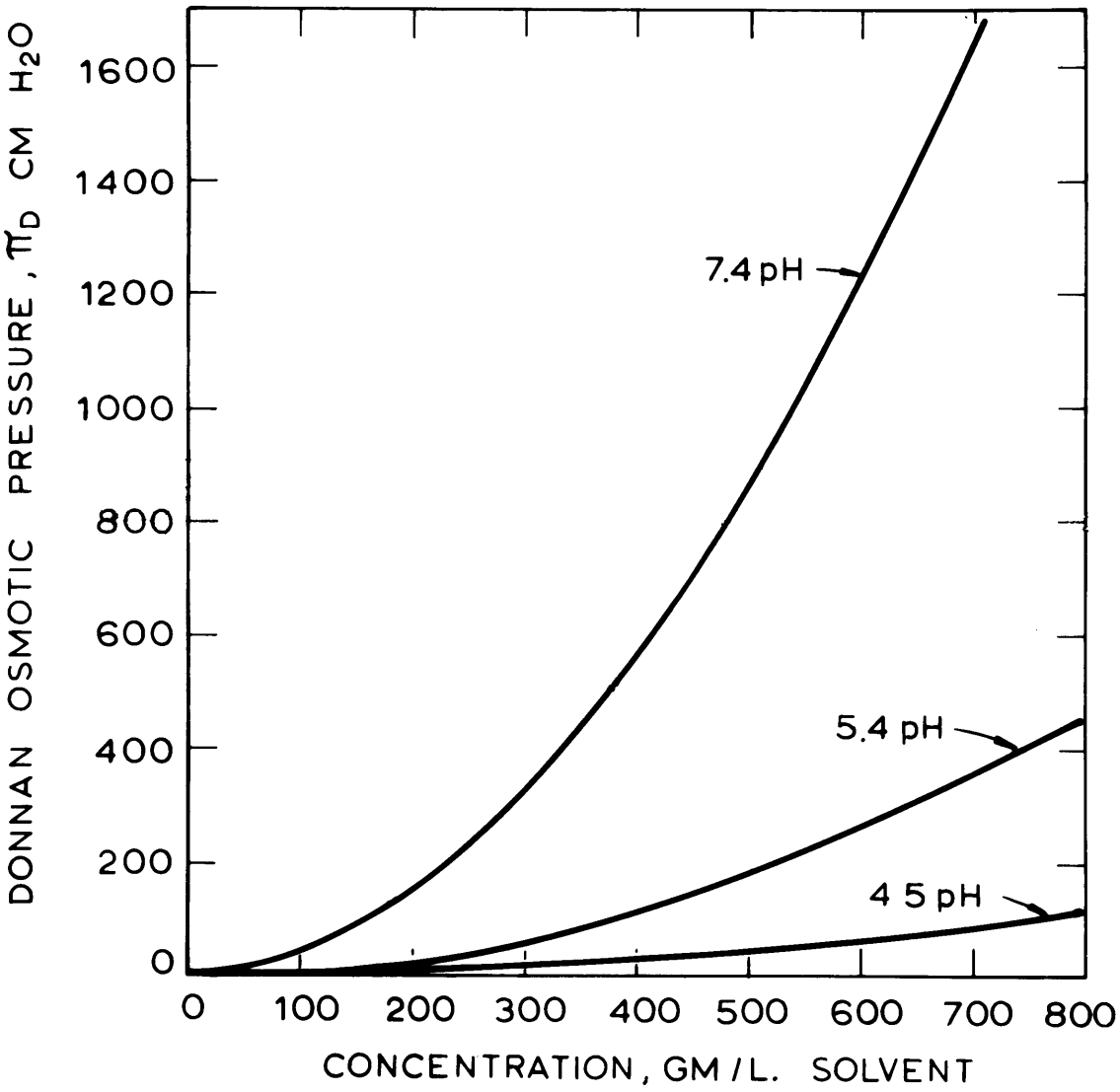

Figure 3-6: Donnan Contribution to Osmotic Pressure

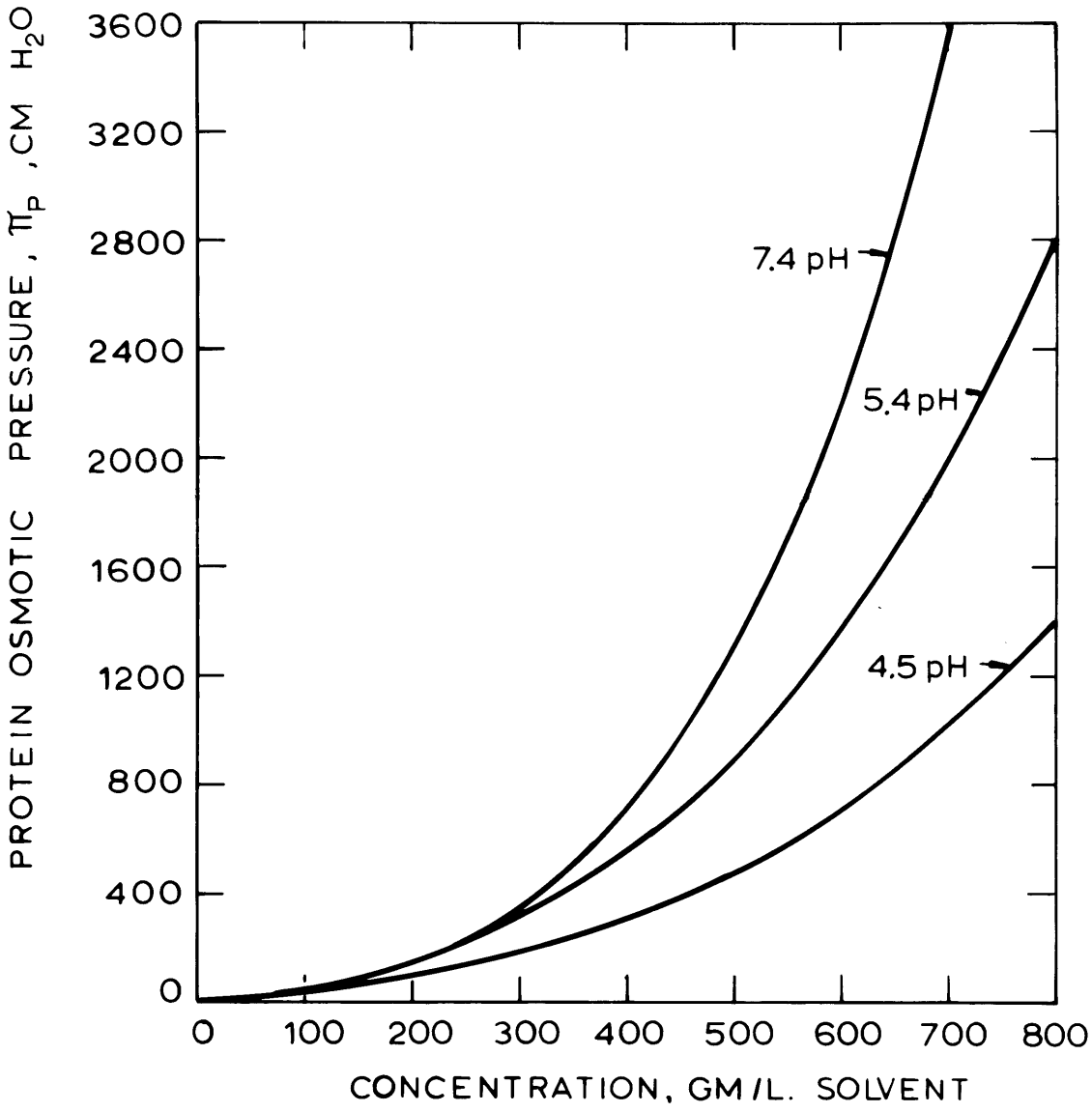

Figure 3-7: Protein Contribution to Osmotic Pressure

greater than that predicted by the van't Hoff limiting law, which treats the macro-ions as inert, point molecules. This excess pressure, from Figure 3-6 and -7, is composed of about 100 cm H_2O from the Donnan contribution and about 1000 cm H_2O from the protein contribution.

For the more highly charged molecule at 7.4 pH, the contributions of each term to the total pressure is more evenly distributed, although the interaction part still dominates, about 2 to 1 at 700 gm BSA/ℓ.

This semi-empirical correlation fitted to the data of Figure 3-5 is compared in Figure 3-8 with the albumin osmotic pressure measurements of Scatchard, et al. (2), shown as circles, and those of Kappos and Pauly (3), shown as triangles. The results are plotted as reduced osmotic pressure, that is, osmotic pressure divided by concentration, and demonstrate the close agreement for all three investigations concerning the intercept of reduced osmotic pressure at zero concentration. The value of 0.367 yields a first virial coefficient from which the 69,000 molecular weight was originally calculated by Scatchard. Actually, the data of Kappos and Pauly extrapolate to a slightly lower intercept, and yield a molecular weight of 72,000.

The data of Kappos and Pauly were obtained at conditions of pH and ionic strength which were different from those used in our experiments. Nevertheless, the correlation fitted to our data is in reasonable agreement with their results.

Scatchard's results are slightly below our results at equivalent conditions of solution pH and ionic strength in the region of moderate protein concentration.

FIGURE 3-8

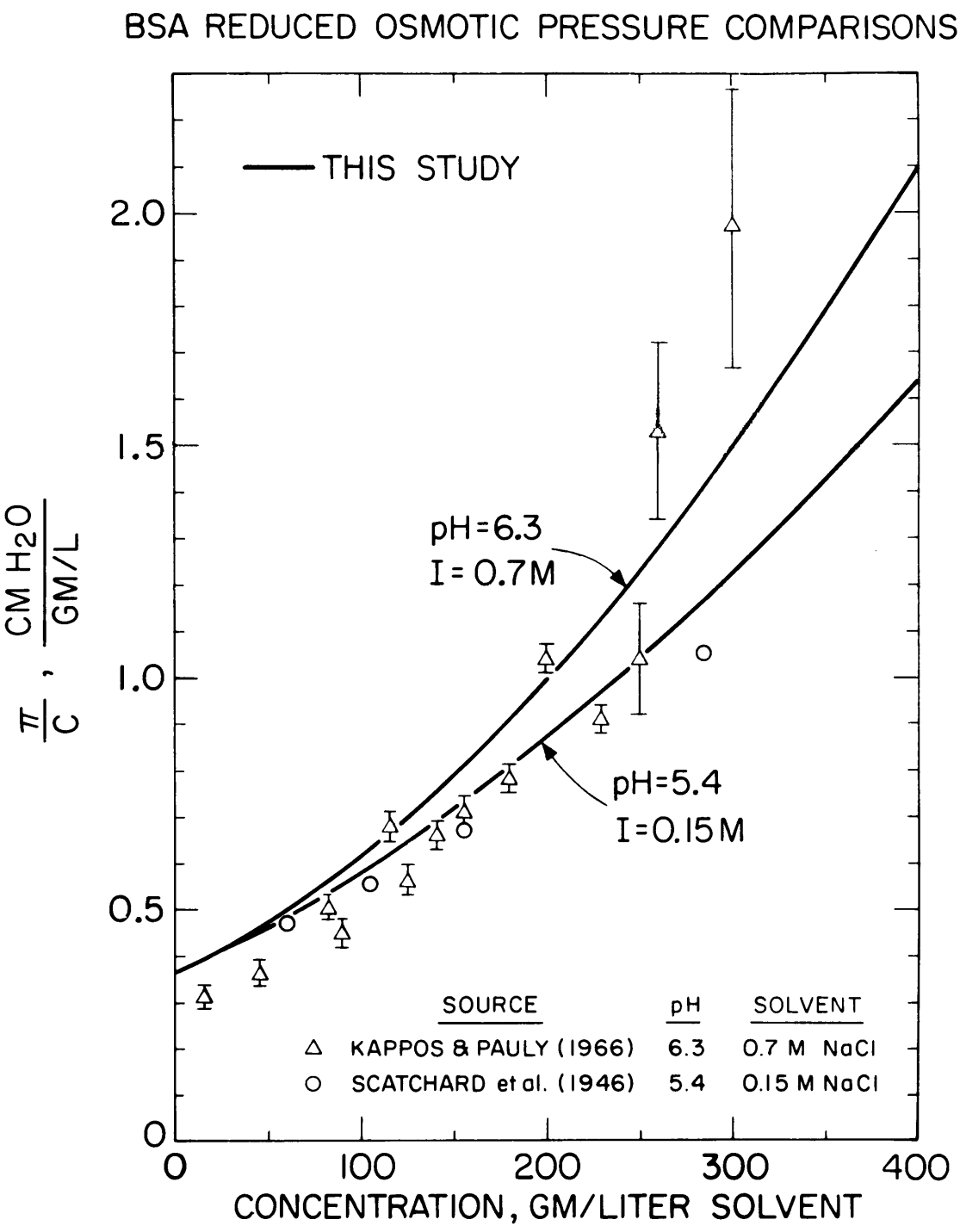
BSA REDUCED OSMOTIC PRESSURE COMPARISONS
THIS STUDY
pH=6.3
I=0.7M
pH=5.4
I=0.15M
SOURCE
pH
SOLVENT
KAPPOS & PAULY (1966) 6.3 0.7 M NaCl
SCATCHARD et al. (1946) 5.4 0.15 M NaCl
π/C, CM H2O / GM/L
CONCENTRATION, GM/LITER SOLVENT
0
0.5
1.0
1.5
2.0
100
200
300
400

B. Comparison With Solution Theory Prediction

In Chapter 2, Section II C, a virial expansion was written to express the osmotic pressure as a function of albumin concentration. The second and third virial coefficients were computed from the estimated potential of average force between macro-ions. The parameters in this potential, which was assumed entirely repulsive, were estimated from measurements of albumin conductance in salt solutions (11).

The result of that analysis,

$$\pi = 0.367 \left[w_p + B_2' w_p^2 + B_3' w_p^2 \right] [=] \text{ cm } H_2O \qquad (2\text{-}41)$$

where the virial coefficients B_2' and B_3', at infinite dilution of the protein, are functions only of the interaction potential, and therefore solution pH. Table 2-4 summarized the coefficients for each pH. The comparison of this result with the osmotic pressure data, on a reduced basis, is shown in Figure 3-9. For the coefficients evaluated at infinite dilution, the solid curves apply.

The figure shows that equation (2-41) predicts higher osmotic pressures than were observed experimentally. Part of this overprediction is probably the result of a failure to properly account for the change in solution ionic strength as protein concentration increases. Moeller, et al. (11) found that their conductivity measurements were better described by their theoretical model when the macro-ion was treated as a 1:1 electrolyte. In effect, this means that solution ionic strength increases with increasing protein concentration. The amount of this increase is dependent on protein charge. As ionic

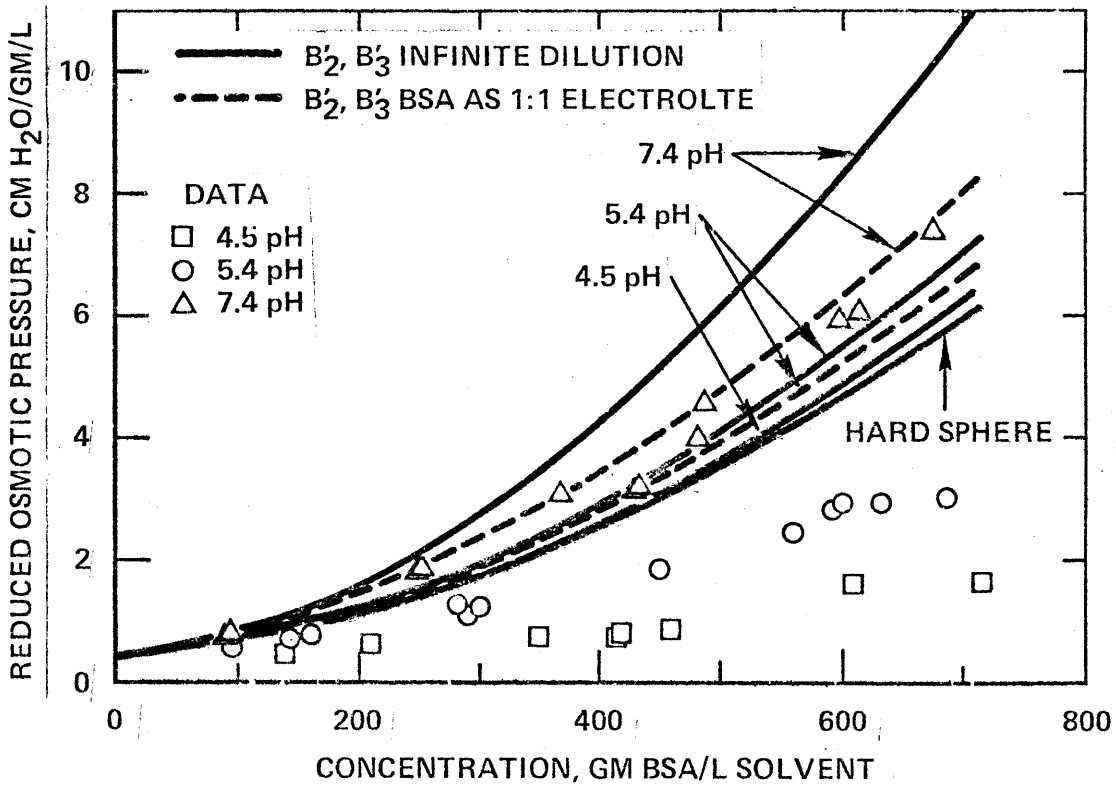

Figure 3-9. Comparison of Experiment with Solution Theory.

strength increases, the electrostatic repulsion potential between macro-ions decreases, as evidenced in the data of Table 3-2 when the 1.0 M saline data is compared to the 0.15 M data.

The result of this method of calculating solution ionic strength is that the coefficients B_2' and B_3' become dependent on protein concentration. This dependency increases as macro-ion charge increases and is shown in Figures 2-8 and 2-9. When the virial coefficients are computed in this way, the dashed curves of Figure 3-9 apply. At 4.5 pH, the macro-ion charge is so small (+4.5) that this correction to the virial coefficient is negligible and the two methods are superimposed on the figure.

The figure shows that the solution theory model agrees with experimental data only at 7.4 pH, the condition for which albumin carries the highest charge studied, 20.4 mv. The lowest pressure predicted by the model corresponds to the isoelectric condition of the macro-ion, $\overline{Z}=0$, indicated as the "hard sphere" curve on the figure. This curve, which is derived by using $W(X)=0$ for $X > 2\kappa a$ in equation (2-31A) for B_2, indicates a pressure which is about three times larger at 700 gm BSA/liter than the experimental observation at 4.5 pH, the condition of smallest charge studied experimentally. The model indicates that at this pH, the albumin molecule can be closely represented by a hard sphere.

The most probable fault with the solution theory model is the neglect of the attractive forces between the macro-ions. Gutfreund's osmotic pressure measurements for salt-free albumin solutions near the isoelectric points (see Figure 2-4) indicate the existence of such forces.

The differences between theory and observation would be expected to be greatest for the lower charge states of the albumin molecule when attractive forces are not included in the model.

An appropriate analytical description of this attraction which could be combined with the electrostatic repulsion to give a complete description of the interaction potential, W(R), between macro-ions is needed.

BIBLIOGRAPHY

(1) Scatchard, G., A. C. Batchelder and A. Brown, "Osmotic Equilibria in Solutions of Serum Albumin and Sodium Chloride". J. Am. Chem. Soc., 68, p. 2320 (1946).

(2) Scatchard, G., A. C. Batchelder, A. Brown and M. Zosa, "Osmotic Equilibria in Concentrated Solution of Serum Albumin". J. Am. Chem. Soc., 68, p. 2610 (1946).

(3) Kappos, A. D. and Pauly, H., "Osmotische Messungen An Hochkonzentrierten Losungen Von Rinderserumalbumin." Biophysik, 3, p. 131 (1966).

(4) Spiegler, K. S. and O. Kedem, "Thermodynamics of Hyperfiltration (Reverse Osmosic): Criteria for Efficient Membranes." Desalination, 1, p. 311 (1966).

(5) Brash, J. L. and D. J. Lyman, "Adsorption of Proteins and Lipids to Nonbiological Surfaces". In The Chemistry of Biosurfaces, Vol. 1, M. L. Hair, editor. Marcel Dekker, Inc., New York (1971).

(6) Brash, J. L. and D. J. Lyman, "Adsorption of Plasma Proteins in Solution to Uncharged, Hydrophobic Polymer Surfaces". J. Biomed. Mater. Res., 3, p. 175 (1969).

(7) Mac Ritchie, F., "The Adsorption of Proteins at the Solid/Liquid Interface." J. Colloid and Interf. Sci., 38, p. 484 (1972).

(8) Dillman, W. J. and I. F. Miller, "On the Adsorption of Serum Proteins on Polymer Membrane Surfaces". J. Colloid and Interf. Sci., 44, p. 221 (1973).

(9) Henry, R. J., Clinical Chemistry Principles and Technics, p. 190, Harper and Row, New York (1964).

(10) Lowry, O.H. and O.A. Bessey, "The Adaptation of the Beckman Spectrophotometer to Measurements of Minute Quantities of Biological Materials". J. Biol. Chem., 163, p. 633 (1946).

(11) Moeller, W. J. M., G. A. J. van Os and J. Th. G. Overbeek, "Interpretation of the Conductance and Transference of Bovine Serum Albumin Solutions." Trans. Far. Soc., 57, p. 235 (1961).

Appendix

Estimates of the Micro-ion Contribution to the Total Observed Osmotic Pressure When Na^+ and Cl^- Concentrations Are Not Equal in the Solvent Phase

Notation:

m_+^i = molar concentration of Na^+ in equilibrium solvent phase

m_-^i = molar concentration of Cl^- in equilibrium solvent phase

π = total observed osmotic pressure, cm H_2O

π_D = Donnan contribution to the total pressure assuming that $m_+^i = m_-^i = 0.15$ M, cm H_2O

π_D^* = Donnan contribution to the total pressure when m_+^i and m_-^i are at estimated values, cm H_2O

w_p = protein concentration, gm BSA/ℓ. solvent

Calculation: $$\pi_D = RT\left[2\sqrt{\left(\frac{\bar{Z}w_p}{2M_p}\right)^2 + (m_+^i m_-^i)} - (m_+^i + m_-^i)\right]$$

Data:

Run	w_p	$\bar{Z}$	m_+^i	m_-^i	π	π_D^*	π_D
15	251	-20.4	.160	.130	450	199	229
18	251	-20.4	.130	.120	452	268	229
21	369	-20.4	.160	.125	1143	459	486
26	486	-20.4	.160	.120	2220	815	827
14	210	+4.5	.135	.145	126	4	8
20	350	+4.5	.130	.145	247	14	22
25	461	+4.5	.130	.140	385	38	38
32	608	+4.5	.125	.180	970	-60	64
38	735	+4.5	.125	.180	1204	-30	98

CHAPTER FOUR

DESCRIPTION OF CONCENTRATION POLARIZATION IN STAGNANT ULTRAFILTRATION

Several theoretical models are developed in this chapter to describe various cases which may arise in stagnant cell ultrafiltration. First, a general model is developed for the situation of a membrane which partially rejects the ultrafiltered macrosolute, and the macrosolute remains in true solution at all concentration levels. In this general model, the only simplification is that the ultrafiltered solution is binary, the solvent is water and microions and the solute is the rejected protein.

A solution of the general model requires numerical techniques which have not yet been developed. A simplified model results when the assumption of constant properties in the polarization layer is made. For the case of large membrane Peclet number, an asymptotic solution (zeroth order perturbation solution) which is valid over almost the entire real time scale is presented. A more accurate asymptotic solution (first order perturbation solution) is given for the case of an albumin impermeable membrane using the constant property assumptions. The results of this model are employed as the theoretical reference for the results of Chapter 5.

For the case of a leaky membrane in which the Peclet number approaches zero, a steady state analysis is employed to investigate the effects on ultrafiltration flux when a small amount of protein is present in the ultrafiltrate. The significance of these models to the experimental program of Chapter 5 is discussed.

Finally, again employing the constant property assumptions, an asymptotic solution (zeroth order perturbation analysis) is presented for the case of a gel layer forming on the membrane surface. The

discussion of this model focuses on the definition of the conditions necessary in stagnant cell ultrafiltration of albumin solutions to produce such a layer.

I. General Theory - No Gel Formation At Membrane Surface

In Figure 4-1, the fluid above the membrane is initially static and contains albumin in moderate concentrations. The saline below the membrane is the same salt composition, 0.15 Molar, as that in which the albumin is dissolved. For this case, the membrane is slightly permeable to albumin, and is characterized by an albumin sieving factor (1), χ, where $\chi = 0$ for complete rejection, and by a saline permeability, K_m (gm/psi-min-cm^2). At time zero, the protein solution is subjected to a constant elevated pressure, P_i (psig), which results in a volumetric flux, v (cm/min), and a gradient in the concentration of the rejected protein. v_s is the volumetric flux of ultrafiltrate.

For the system of Figure 4-1 the unsteady state equation of continuity is:

$$\frac{\partial \rho}{\partial t} - v \frac{\partial \rho}{\partial y} - \rho \frac{\partial v}{\partial y} = 0 \qquad (4\text{-}1)$$

The unsteady state component mass balance on albumin is:

$$\frac{\partial \omega_A}{\partial t} - v \frac{\partial \omega_A}{\partial y} = \frac{1}{\rho} \frac{\partial}{\partial y} \left[\rho D \frac{\partial \omega_A}{\partial y} \right] \qquad (4\text{-}2)$$

where ρ(gm/cm^3) is solution density and D (cm^2/sec) is the diffusion

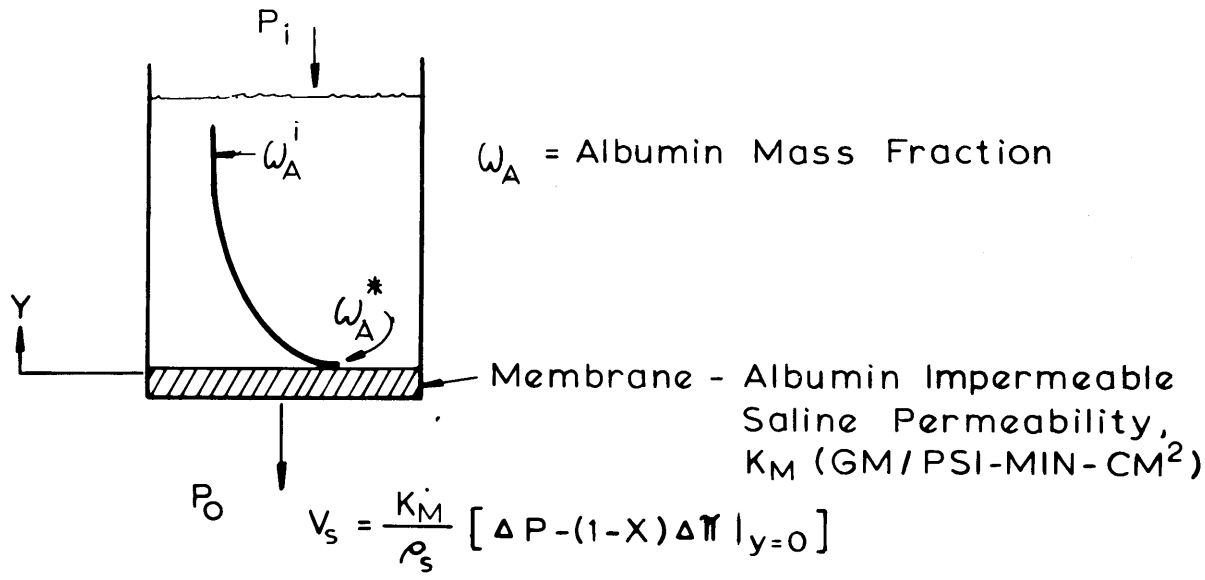

Figure 4-1: Albumin Ultrafiltration in a Stagnant System

coefficient of albumin in saline.

The equation of state which relates solution density and its albumin concentration was presented in Chapter 2 in terms of the partial specific densities of saline ($\tilde{\rho}_S$) and albumin ($\tilde{\rho}_A$).

$$\rho = \frac{\tilde{\rho}_S}{1 - \left[\frac{\tilde{\rho}_A - \tilde{\rho}_S}{\tilde{\rho}_A}\right]\omega_A}$$

In Chapter 2, $\tilde{\rho}_A$ was found to be constant at 1.34 gm/ml.

The initial condition is:

$$\omega_A = \omega_A^i \qquad \text{all } y,\ t = 0 \tag{4-3}$$

and the boundary condition for $y \to \infty$ is:

$$\omega_A \to \omega_A^i \qquad y \to \infty,\ \text{all } t \tag{4-4}$$

For the case of partial albumin rejection by the membrane, and no gel layer formation, a second boundary condition results from the fact that at the membrane surface, the flux of albumin leaked through the membrane equals the sum of the convective flux toward the surface and the diffusive flux back to the bulk solution.

$$D\frac{\partial \omega_A}{\partial y} + v\omega_A = \chi\omega_A v \frac{1}{1 - \exp(-Pe)} \qquad @\ y = 0,\ \text{all } t \tag{4-5}$$

where the expression for the flow of molecules through small pores, shown by Anderson and Quinn (1), has been used.

$$\text{Albumin flux} = \chi\omega_A^s\, v \frac{[1 - (\omega_A^o/\omega_A^s)\, e^{-Pe}]}{[1 - e^{-Pe}]} = \frac{\chi\omega_A^s\, v}{[1 - e^{-Pe}]} \tag{4-6}$$

In use of equation (4-6) for the flux of albumin through the membrane, the assumption has been made that in all cases of interest here, the concentration of albumin in the ultrafiltrate, ω_A^o, is negligible with respect to the membrane surface concentration, ω_A^s. In a more rigorous analysis of a leaky membrane problem, this could be a poor assumption, particularly in the limit of Pe → 0 and a stagnant film on the ultrafiltrate side of the membrane. The axial Peclet number for the pores, Pe, is given by;

$$Pe = \frac{\chi v_o \ell_m}{D_o} = \frac{\chi v \ell_m}{D_o \varepsilon} \qquad (4\text{-}7)$$

where v and v_o are velocities of solution in the polarization layer and the pore, respectively; ℓ_m is membrane thickness, ε is membrane void fraction and D_o is the effective diffusivity of albumin in the pores.

The last boundary condition is formulated with the assumption that the volumetric flux of ultrafiltrate is proportional to the difference between the applied pressure and the osmotic pressure difference of the two solutions on each side of the membrane. Then with a mass balance around the membrane;

$$\frac{\rho}{\rho_S} v = v_S = \frac{K_m}{\rho_S} (\Delta P - (1-\chi)\Delta\pi|_{y=0}) \qquad @\ y = 0,\ \text{all } t \qquad (4\text{-}8)$$

where ρ_S is the density of ultrafiltrate. The proportionality constant is the membrane hydraulic permeability to saline, K_m/ρ_S.

The dependencies of osmotic pressure and diffusivity on solution properties have been discussed in Chapters 2 and 3 and lead to the

auxiliary relations necessary for complete definition of this general model.

$$\pi = f(\omega_A, [H^+], [Cl^-], \text{ionic strength}) \tag{4-9}$$

$$D = g(\omega_A, [H^+], [Cl^-], \text{ionic strength}) \tag{4-10}$$

Numerical techniques would be required to solve equations (4-1) - (4-10). The non-dimensional forms of these equations are developed in Appendix A. Several simplified cases of interest are discussed below.

II. Constant Property Models

A. Leaky Membrane, Large Peclet Number

The assumptions of constant density and diffusivity for the system shown in Figure 4-1, reduce the general model equations to:

$$\frac{\partial \omega_A}{\partial t} - v \frac{\partial \omega_A}{\partial y} = \bar{D} \frac{\partial^2 \omega_A}{\partial y^2} \tag{4-11}$$

subject to

$$\omega_A = \omega_A^i \qquad \text{all } y,\ t = 0 \tag{4-12}$$

$$\omega_A \to \omega_A^i \qquad y \to \infty,\ \text{all } t \tag{4-13}$$

$$\bar{D} \frac{\partial \omega_A}{\partial y} + v\omega_A = \chi \omega_A v \qquad y = 0,\ \text{all } t \tag{4-14}$$

$$v = \frac{K_m}{\bar{\rho}} \left[\Delta P - (1-\chi)\Delta\pi\big|_{y=0}\right] \qquad y = 0,\ \text{all } t \tag{4-15}$$

In these equations, $\bar{\rho}$ and $\bar{D}$ are average solution density and albumin

diffusivity, and are evaluated at the approximate average polarization layer concentration, that is at $\bar{\omega}_A = (\omega_A^i + \omega_A^*)/2$. The values of $\bar{D}$ reported or used in this chapter are evaluated from the data of Keller, et al. (2). The concentration ω_A^* is defined as the concentration for which the effective osmotic pressure difference across the membrane balances the applied pressure difference. For a leaky membrane, ω_A^* is defined by,

$$(1-\chi)(\pi|_{\omega_A^*} - \pi|_{\text{ultrafiltrate}}) \equiv \Delta P$$

and for a membrane impermeable to albumin

$$\pi|_{\omega_A^*} \equiv \Delta P$$

The values of $\bar{D}$ in this chapter are evaluated from the data of Keller, et al. (2). The boundary condition (4-14) involves the additional assumption of a large membrane pore Peclet number, that is, the transport of albumin through the membrane by convection is much larger than the diffusive transport through the membrane.

Perturbation techniques are applied to the dimensionless forms of these equations in order to arrive at an asymptotic solution (through zeroth order terms only) for the flux and concentration profile. The solution is presented in Appendix A and the results are:

$$\frac{\omega_A - \omega_A^i}{\omega_A^* - \omega_A^i} = \frac{1 - \text{erf}\left\{\frac{y}{2\sqrt{\bar{D}t}} + a_o\right\}}{1 - \text{erf}\,(a_o)} \qquad (4\text{-}16)$$

$$v = a_o \sqrt{\bar{D}/t} \tag{4-17}$$

where a_o is given implicitly by

$$\frac{\exp(-a_o^2)}{a_o(1-\text{erf } a_o)} = 1.77\,(1-\chi)\,\frac{\omega_A^*}{\omega_A^* - \omega_A^i} \tag{4-18}$$

The solution of equation (4-18) is shown on Figure 4-2.

These asymptotic solutions are valid for real times such that

$$t >> \left(\frac{1}{(K_m/\bar{p})(\Delta P - (1-\chi)\Delta\pi^i)}\right)^2 \bar{D} \tag{4-19}$$

where $\Delta\pi^i$ is the osmotic pressure difference across the membrane before ultrafiltration begins. For albumin ultrafiltration with Abcor HFA-180 membranes, and initial bulk solution albumin concentration of about 10 gm BSA/100 ml solution, the asymptotic solutions are valid for real times greater than about one-tenth second for high pressure ultrafiltration (~50 psig) and for times greater than about one second for low pressures (~10 psig). Thereafter, equation (4-17) predicts that ultrafiltrate velocity will decay with a $t^{-1/2}$ dependence. Equation (4-16) predicts that the membrane surface concentration is approximately equal to the concentration for which the solution osmotic pressure equals the applied pressure and that the thickness of the polarized layer grows like the square root of time.

B. Impermeable Membrane

Ultrafiltration with a membrane assumed impermeable to albumin is

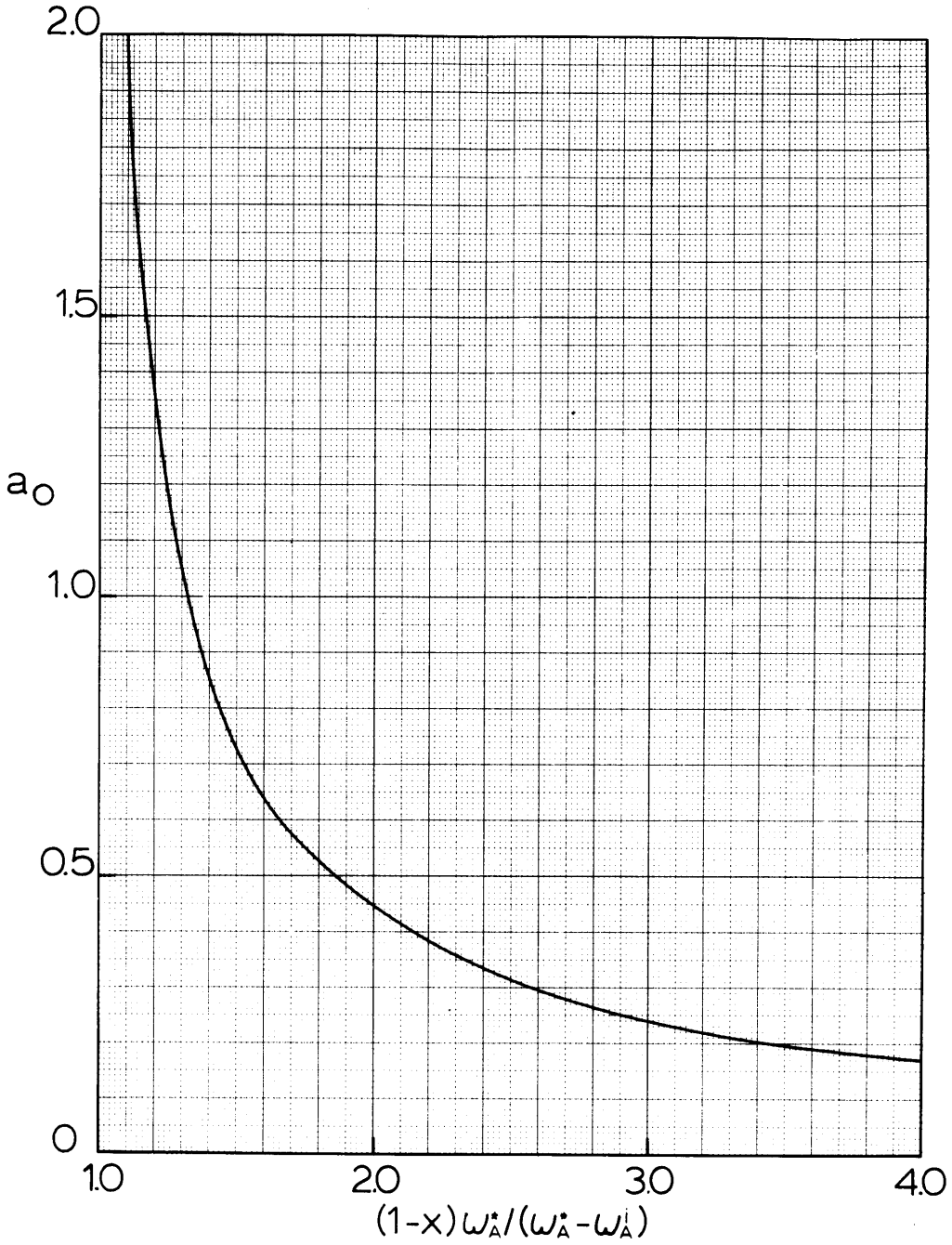

Figure 4-2: Solution for a_o (equation 4-17).

a simplification of the model treated above and, with $\chi = 0$, permits a more accurate asymptotic solution. The results of this solution are used as the theoretical comparison for the experimental results of Chapter 5.

With this simplification, the boundary conditions (4-14) and (4-15) reduce to:

$$\bar{D}\frac{\partial \omega_A}{\partial y} + v\omega_A = 0 \qquad @\ y = 0,\ \text{all } t \qquad (4\text{-}20)$$

$$v = \frac{K_m}{\bar{\rho}}\left[\Delta P - \pi\big|_{y=0}\right] \qquad @\ y = 0,\ \text{all } t \qquad (4\text{-}21)$$

where the colloidal osmotic pressure on the ultrafiltrate side of the membrane is zero, so $\Delta\pi|_{y=0}$ is the osmotic pressure evaluated at the membrane surface concentration.

In Appendix A, the perturbation analysis on the dimensionless form of the equations of Section II-A is extended, for the present case, in order to arrive at an asymptotic solution which includes both zero order and first order terms. The results are:

for the concentration profile

$$\frac{\omega_A - \omega_A^i}{\omega_A^* - \omega_A^i} = \frac{1 - \operatorname{erf}\left\{ y/2\sqrt{\bar{D}t} + a_o \right\}}{1 - \operatorname{erf}(a_o)} - \frac{a_o\sqrt{\bar{D}/t}\,\exp - \left[\dfrac{y^2}{4\bar{D}t} + \dfrac{a_o y}{2\sqrt{\bar{D}t}}\right]}{(K_m/\bar{\rho})\left(\dfrac{\partial \pi}{\partial \omega_A}\right)_{\omega_A^*}\left(\omega_A^* - \omega_A^i\right)} \qquad (4\text{-}22)$$

for the saline ultrafiltrate flux (with equation (4 - 8))

$$v_S = a_o \left(\frac{\bar{\rho}}{\rho_S}\right)\sqrt{\frac{\bar{D}}{t}} \qquad (4\text{-}23)$$

The a_o term is the same as that of equation (4-18) and can be evaluated from Figure 4-2 with $\chi = 0$. The slope of osmotic pressure dependence on albumin concentration is evaluated at ω_A^* from the osmotic pressure data in Chapter 2.

At long times, the pre-expontial term of equation (4-22) is much less than unity, and the membrane surface concentration becomes approximately constant near the osmotic value, ω_A^*. The growth of the polarization layer with the square root of time is also the same as the result for the leaky membrane. The flux is again shown to decrease with the inverse square root of time.

The expression for the real time scale over which this solution is valid also remains unchanged, that is, equation (4-19) with $\chi = 0$. For the experiments of Chapter 5, this estimate ranges from one-tenth to one second.

C. Small Peclet Number

The case of a membrane which leaks a small amount of protein by diffusion only ($Pe \to 0$) is modelled here for the purpose of finding the approximate time at which this leakage would result in a time invariant flux. That is, for equation (4-8) with constant properties assumed, an estimate is sought of the time at which the flux driving force, $(\Delta P-(1-\chi)\Delta\pi|_{y=0})$, becomes constant. This driving force achieves a constant value when the

diffusive flux of albumin through the membrane and the convection of albumin away from the ultrafiltrate side of the membrane reach a steady state. In order to obtain this crude estimate, the assumption is made in equation (4-6) that $\omega_A^o << \omega_A^s$. After this estimated time period, $\Delta\pi|_{y=0}$ is approximately constant.

To investigate this limiting case, a steady state analysis of the system shown in Figure 4-1 with $\theta = (\omega_A - \omega_A^i)/(\omega_A^* - \omega_A^i)$ leads to:

$$\frac{d^2\theta_A}{dy^2} + \frac{v}{\bar{D}} \frac{d\theta}{dy} = 0 \qquad (4\text{-}24)$$

subject to $\theta \to 0$ @ $y \to \infty$ (4-25)

$$\bar{D} (\omega_A^* - \omega_A^i) \frac{d\theta}{dy} + v [(\omega_A^* - \omega_A^i) \theta + \omega_A^i] = \omega_A \frac{\varepsilon D_o}{\ell_m} \quad @\ y = 0 \qquad (4\text{-}26)$$

The last boundary condition results from equation (4-5) with the assumptions of constant properties and small membrane pore Peclet number such that, with equation (4-7):

$$\frac{1}{1 - \exp(-Pe)} = \frac{1}{Pe} = \frac{D_o \varepsilon}{\chi v \ell_m}$$

The solution of equation (4-24) is of the form

$$\theta = C_1 + C_2 e^{-vy/\bar{D}}$$

and by boundary condition (4-25), $C_1 = 0$. The application of this result to boundary condition (4-26), with the assumption that $\omega_A\Big|_{y=0} \simeq \omega_A^*$, gives:

$$v = \frac{\omega_A^*}{\omega_A^i} \frac{\varepsilon D_o}{\ell_m} \tag{4-27}$$

The assumption that the membrane surface concentration corresponds to the concentration for which the solution osmotic pressure equals the applied pressure will be valid if:

$$\left| \frac{\omega_A - \omega_A^*}{\omega_A - \omega_A^i} \right|_{y=0} << 1$$

To find if this is met, the flux driving force is approximated by the first two terms of a series expansion which equates the driving force to the gradient of the osmotic pressure dependence on concentration. In the expansion, the first term is zero by virtue of the definition of ω_A^* for a leaky membrane.

$$\left[\Delta P-(1-\chi)\Delta\pi|_{y=0}\right] \simeq \left(\Delta P-(1-\chi)\Delta\pi|_{\omega_A^*}\right) - (1-\chi)\left(\frac{\partial(\Delta\pi)}{\partial\omega_A}\right)_{\omega_A^*} (\omega_A|_{y=0}-\omega_A^*) - \ldots$$

Applying this expansion results in,

$$v = \frac{K_m}{\rho}\left[\Delta P-(1-\chi)\Delta\pi|_{y=0}\right] = -(1-\chi)\frac{K_m}{\rho}\left(\frac{\partial(\Delta\pi)}{\partial\omega_A}\right)_{\omega_A^*} (\omega_A|_{y=0}-\omega_A^*) \tag{4-28}$$

After equating equations (4-27) and (4-28) the result is:

$$\frac{\omega_A - \omega_A^*}{\omega_A - \omega_A^i} = -\frac{\frac{\omega_A^*}{\omega_A^i}\frac{\varepsilon D_o}{\ell_m}}{(K_m/\rho)(1-\chi)\left(\frac{\partial(\Delta\pi)}{\partial\omega_A}\right)_{\omega_A^*}(\omega_A|_{y=0}-\omega_A^i)} \tag{4-29}$$

From the osmotic pressure data of Chapter 3, the smallest estimate of $(\partial(\Delta\pi)/\partial\omega_A)^*_{\omega_A}$ which would apply to all of the experiments of Chapter 5, would be for the ultrafiltration of a 5.4 pH albumin solution at 5.6 psig. At this condition, $(\partial(\Delta\pi)/\partial\omega_A)^*_{\omega_A} \simeq 60$ psi. The smallest difference between membrane surface concentration and bulk solution concentration encountered experimentally would be for this same experiment (Experiment 600), so $(\omega_A|_{y=0} - \omega_A^i) \simeq 9 \times 10^{-2}$. The diffusivity of albumin inside the membrane pores, D^o, is estimated to be 10^{-8} cm^2/sec. For the other parameters of equation (4-29) typical values or estimates are:

$(K_m/\overline{\rho}) = 3 \times 10^{-3}$ cm/min-psi

$\varepsilon = 0.2$

$(1-\chi) = 1$

$\ell_m = 3 \times 10^{-2}$ cm

and $\omega_A^*/\omega_A^i = 3$

With these values, the probable maximum value of equation (4-29) is 7×10^{-4}. Therefore, the assumption, $\omega_A|_{y=0} \simeq \omega_A^*$, is valid when albumin transport through the membrane is by diffusion only. For the case of an assumed impermeable membrane, this result indicates that the concentration profile in the polarization layer is unaffected by small diffusive leakage of albumin.

In order to find the time at which flux is affected by this diffusive leakage, the flux expression of equation (4-17) is equated with equation (4-27).

$$a_o\sqrt{\frac{\overline{D}}{t}} = \frac{\omega_A^*}{\omega_A^i}\,\frac{\varepsilon D_o}{\ell_m} \qquad \text{or} \qquad t \simeq \overline{D}\left[\frac{1}{a_o}\,\frac{\omega_A^i}{\omega_A^*}\,\frac{\ell_m}{\varepsilon D_o}\right]^2 \tag{4-30}$$

This limiting time can be estimated with the parameter estimates from above, and the lowest value of albumin diffusivity in the polarization layer which was encountered in the experimental program (Experiment 1800) $\overline{D} = 1.3 \times 10^{-7} cm^2/sec$, for which $a_o = 1.16$ and $\omega_A^*/\omega_A^i \simeq 6$. The estimated time is 168 hours when the flux achieves a constant level of about $2.4 \times 10^{-5} cm/min$. Although this estimate suggests that diffusive albumin leakage should not be a major factor in the flux determination, better estimates of the parameters D_o and ε are required to insure this conclusion.

D. Summary

The asymptotic constant property models above have shown that, for membranes which pass albumin either primarily by convection (but $\omega_A^o << \omega_A^s$) or primarily by diffusion, the surface concentration is virtually time invariant and corresponds very closely to the concentration for which the osmotic pressure is equal to the applied pressure.

For ultrafiltrate flux, Figure 4-3 divides the time dependency into three separate regions. At $t = 0$, before any polarization has been established, flux is simply proportional to the applied pressure minus the osmotic pressure of the bulk solution. The flux-time dependency has not been analyzed for the short time during which the membrane surface concentration is changing rapidly with time. The duration of this starting period, t_1, is given by equation (4-19) and in the experimental program of Chapter 5 is about one second or less. Thereafter, flux decays with an inverse square root of time dependence. This relationship has been established by equation (4-17) for the period $t_1 - t_2$.

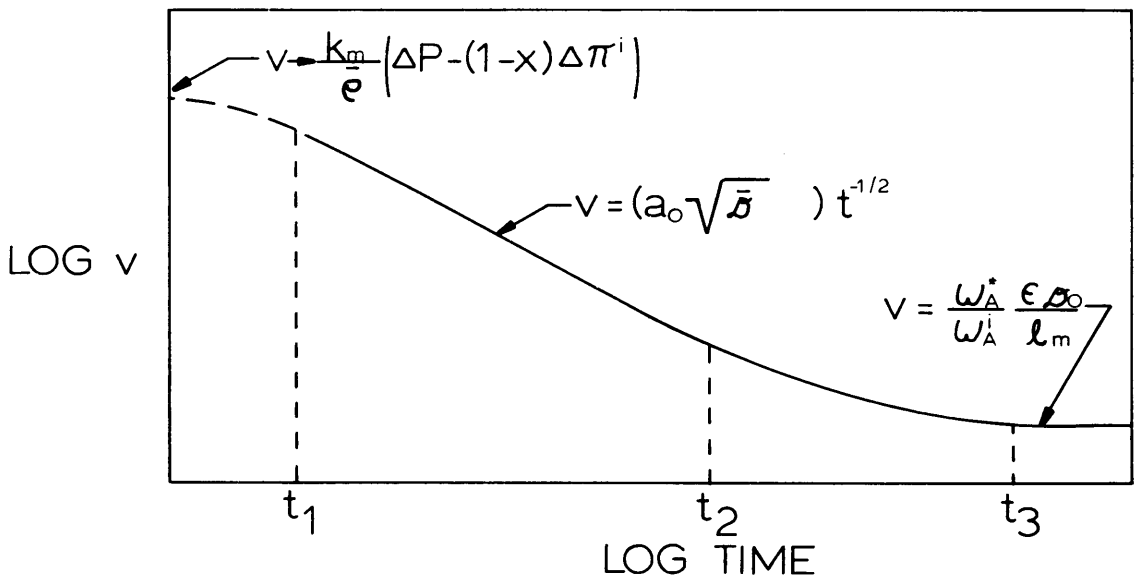

Figure 4-3: Ultrafiltrate flux dependence on time.

A period $t_2 - t_3$ is shown for which the flux decay is an ill-defined function of time. In this interval, departures from the inverse square root dependence are caused by the diffusive transport of albumin through the membrane. A steady state analysis has been employed to obtain a rough estimate of the time, t_3, at which this diffusive leakage leads to the limiting flux level given by equation (4-27). The "worst case" estimate of t_3 is 168 hours when the limiting flux is estimated to be 2.4×10^{-5} cm/min. Since the experiments of Chapter 5 never lasted longer than 23 hours and flux was always greater than about 1×10^{-4} cm/min, the influence of this diffusive leakage is thought to be minimal on the results of these experiments.

III. Constant Property, Gel Formation Model

As the applied pressure of ultrafiltration is increased, the rejected macrosolute concentration at the membrane surface will increase to a level at which the osmotic pressure is almost equal to this applied pressure. At some sufficiently high applied pressure, the macrosolute concentration would exceed a solubility limit if the osmotic pressure were to maintain a balance with the applied pressure. The concensus of current literature (see Chapter 1 and 2) is that when the applied pressure is high enough to require membrane surface concentrations which are in excess of a solubility limit, the concentrated macrosolute solution undergoes a phase transition. In the case of aqueous albumin solutions, a gel phase may be formed at the surface. This gel layer, which thickens with time and further increase in applied pressure, offers an additional resistance to solvent flow. This resistance is characterized

by a gel layer permeability, B_g (gm/cm -psi-min). The flux through the gel layer, where ℓ(cm) is the gel layer thickness, is:

$$v = \frac{(B_g/\overline{\rho})}{\ell} \Delta P_g \tag{4-31}$$

where ΔP_g (psig) is the gel layer pressure drop and contributes to the overall pressure drop, ΔP_T.

$$\Delta P_T = \Delta P_m + \Delta P_g \tag{4-32}$$

where ΔP_m is the membrane pressure drop.

The analysis of this phenomena for the stagnant cell ultrafiltration of Figure 4-1 is made with the following simplifications:

- constant solution density and diffusivity, $\overline{\rho}$ and $\overline{D}$
- a single-valued gel concentration, ω_g, is reached at the membrane surface
- the intrinsic gel permeability to saline, B_g/ℓ, is constant, independent of pressure
- the membrane is albumin impermeable

For the system of Figure 4-1, subject to these simplifications, the unsteady state analysis gives for the albumin mass balance in the polarization layer:

$$\frac{\partial \omega_A}{\partial t} - v \frac{\partial \omega_A}{\partial y} = \overline{D} \frac{\partial^2 \omega_A}{\partial y^2} \tag{4-33}$$

subject to

$$\omega_A = \omega_A^i \qquad @ \text{ all } y,\ t = 0 \qquad (4\text{-}34)$$

$$\omega_A \to \omega_A^i \qquad @\ y \to \infty,\ \text{all } t \qquad (4\text{-}35)$$

$$\bar{D}\frac{\partial \omega_A}{\partial y} + v\omega_A = \omega_g \frac{d\ell}{dt} \qquad @\ y = \ell,\ \text{all } t \qquad (4\text{-}36)$$

$$v = \frac{K_m}{p}(\Delta P_m - \pi_m) \qquad @\ y = 0,\ \text{all } t \qquad (4\text{-}37)$$

where ℓ (cm) is the gel layer thickness at any time, $d\ell/dt$ is the gel growth rate and π_m is the osmotic pressure at the membrane surface, and after gel formation, π_m^*, is the value of this osmotic pressure evaluated at the concentration ω_g.

An asymptotic solution (through the zeroth order terms) to these equations, including equations 4-31 and 4-32, is shown in Appendix B. The results are:

for the concentration profile above the gel layer

$$\frac{\omega_A - \omega_A^i}{\omega_g - \omega_A^i} = \frac{1 - \text{erf}\left\{\frac{y-\ell}{2\sqrt{\bar{D}t}} + \frac{Pe_g}{2\hat{v}_o} + \hat{v}_o\right\}}{1 - \text{erf}\left\{\frac{Pe_g}{2\hat{v}_o} + \hat{v}_o\right\}} \qquad (4\text{-}38)$$

for flux

$$v = \hat{v}_o\sqrt{\frac{\bar{D}}{t}} \qquad (4\text{-}39)$$

for gel layer thickness and growth rate

$$\ell = \frac{Pe_g}{\hat{v}_o}\sqrt{\bar{D}t} \tag{4-40}$$

$$\frac{d\ell}{dt} = \frac{Pe_g}{2\hat{v}_o}\sqrt{\frac{\bar{D}}{t}} \tag{4-41}$$

for the gel layer pressure drop

$$\Delta P_g = \Delta P_T - \pi_m^* \tag{4-42}$$

The gel layer Peclet number is given by:

$$Pe_g = \frac{v\ell}{\bar{D}} = \frac{(B_g/\bar{\rho})(\Delta P_T - \pi_m^*)}{\bar{D}} \tag{4-43}$$

where the appearance of the average polarization layer diffusivity, $\bar{D}$, is a consequence of the constant property assumption. The $\hat{v}_o$ term is an implicit function given by:

$$\hat{v}_o\left(\frac{\omega_g}{\omega_g-\omega_A^i}\right) - \frac{1}{1.77}\frac{\exp -\left(\frac{Pe_g}{2\hat{v}_o}+\hat{v}_o\right)^2}{1-\text{erf}\left\{\frac{Pe_g}{2\hat{v}_o}+\hat{v}_o\right\}} = \frac{Pe_g}{2\hat{v}_o}\left(\frac{\omega_g}{\omega_g-\omega_A^i}\right) \tag{4-44}$$

The solution of equation (4-44) is presented in Figure 4-4. In the limit of $Pe_g \to 0$, the results shown by equations (4-38) to (4-44) reduce to the same results as for the model of an albumin impermeable membrane with no gel formation. For $Pe_g = 0$, $\hat{v}_o$ is equivalent to the a_o term of the models for no gel formation.

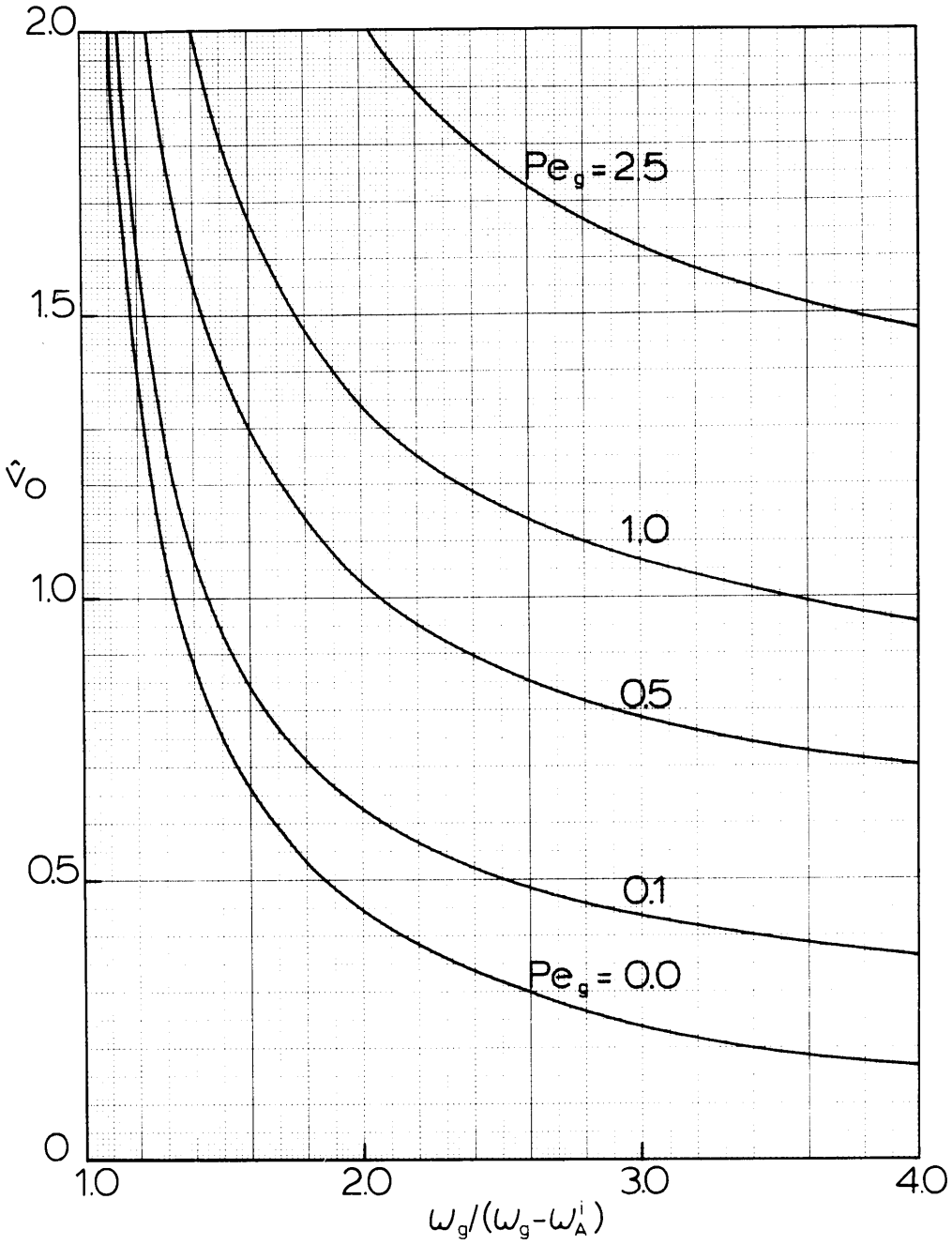

Figure 4-4: Solution for $\hat{v}_o$ (equation 4-44).

At higher values of the Peclet number, flux retains its inverse square root dependence on time, and the concentration polarization layer still grows with a square root dependence on time. For the region of $0 \leq y \leq \ell$, the concentration has been assumed constant at ω_g and equation (4-38) reduces to $\omega_A = \omega_g$ at $y = \ell$.

Like the polarization layer thickness, the gel layer thickness increases with the square root of time, and like the flux, the growth rate of the gel layer has an inverse square root of time dependence.

Equation (4-39) and Figure 4-4 suggest that after gel formation, flux can be increased for any constant value of $\omega_g/(\omega_g-\omega_A^i)$ by increasing the gel Peclet number. Increasing applied pressure, ΔP_T, would increase Pe, but the conclusion that this change would result in higher ultrafiltrate flux is inconsistent with the findings and analyses of others (3,4,5). Generally, it has been supposed that after gel formation occurs, further increases in applied pressure result in a thickening of the gel layer such that the increased hydraulic resistance of the gel approximately offsets the increased driving force, and flux remains relatively unchanged. The assumption of a pressure independent intrinsic gel permeability is probably the reason for the over-prediction of a substantial increase in flux in response to an increase in applied pressure.

Inspection of equations (4-43), and (4-40), and Figure 4-4, indicates the conditions of ultrafiltration which will encourage gel formation. At a given time, a high Peclet number, at large values of $\omega_g/(\omega_g-\omega_A^i)$ will increase gel layer thickness. High applied pressure, when the osmotic pressure at the membrane surface is constant by the assumption of a constant gel layer composition, is the most obvious way for achieving

a high Peclet number. The most direct way to influence the ratio $(\omega_g/(\omega_g-\omega_A^i))$, is by changing the bulk solution albumin mass fraction, ω_A^i.

The ultrafiltered solution pH and ionic strength influence the gel formation and growth in several ways. However, lack of data regarding the effects of these parameters on albumin solubility, diffusivity and gel phase properties, requires that the discussion of these effects be at a qualitative level.

The effect of solubility is the most important of these parameters in regard to the maximum value which can be generated for π_m^*, the osmotic pressure of the gel layer formed on the membrane surface. Albumin solubility was cited in Chapter 2 to be about 60 gm% (pH unknown), and is a minimum at the isoelectric pH. If this 60 gm% limit applies to the isoelectric pH of 4.7, then gel formation would be possible where applied pressure, ΔP_T, exceeds about 40 psig for the ultrafiltration of 4.5 pH albumin solutions at an ionic strength of 0.15 M saline. The 40 psig pressure is the osmotic pressure extrapolated for such an albumin solution at a concentration of 60 gm%. However, at 7.4 pH and with the assumption of a monotonic dependence of solubility on pH such that $\omega_g \geq 60$ gm%, applied pressures greater than 200 psig would be required for the condition of $\Delta P_T > \pi_m^*$ to arise. Therefore, in the ultrafiltration of these solutions it is doubtful that gel formation would occur.

The effects of diffusivity and gel permeability on the gel layer Peclet number are probably of lesser importance, and are in opposite directions. Based on the electrostatic arguments of Chapter 2, an increase of solution pH from 4.5 to 7.4 should increase albumin diffu-

sivity and gel layer permeability.

In Chapter 5, an experiment (Experiment 1800) was performed in which a 4.5 pH albumin solution at a bulk concentration of 11 gm% (ω_A^i = .107) was ultrafiltered at an applied pressure of 50 psig for 15 hours (t = 900 minutes). A gel layer thickness and growth rate can be estimated for this experiment assuming that π_m^* = 40 psig at ω_g = .517 (60 gm%). The estimate for $\overline{D}$ = 1.3 x 10^{-7}cm^2/sec is from the data of Keller, et al. (2) evaluated at the average polarization layer concentration. The estimate for gel layer permeability, $(B_g/\overline{\rho})$ = 10^{-6}cm^2/min-psi, is from the literature (6,7) (see Chapter 1).

From these estimates, $\hat{v}_o$ = 3 at a Peclet number of 1.28. By equations (4-40) and (4-41), the gel layer thickness is 0.036 cm at 900 min. and the growth rate is 0.0012 cm/hr.

This growth rate in a stagnant system is lower than the value of 0.0050 cm/hr estimated by Dorson, et al. (8) for the ultrafiltration of flowing beef blood in a flat plate channel device. The implications of these estimates with respect to the results of Experiment 1800 is discussed in Chapter 5.

BIBLIOGRAPHY

(1) Anderson, J. L. and J. A. Quinn, "Restricted Transport in Small Pores". Biophys. J., 14, p. 130 (1974).

(2) Keller, K. H., E. R. Canales and S. I. Yum, "Tracer and Mutual Diffusion Coefficients of Proteins", J. Phys. Chem., 75, p. 379 (1971).

(3) de Fillippi, R. P. and R. L. Goldsmith, "Application and Theory of Membrane Processes For Biological and Other Macromolecular Solutions" in Membrane Science and Technology, J. E. Flinn, ed., Plenum Press, New York (1970).

(4) Michaels, A. S., "New Separation Technique for the CPI", Chem. Eng. Prog., 64, p. 31 (1968).

(5) Blatt, W. F., A. Dravid, A. S. Michaels and L. Nelson, "Solute Polarization and Cake Formation in Membrane Ultrafiltration: Causes, Consequences and Control Techniques". In Membrane Science and Technology, J. E. Flinn, editor. Plenum Press, New York (1970).

(6) Dorson, W. J., V. B. Pizziconi and J. M. Allen, "Transfer of Chemical Species Through a Protein Gel." Trans. Amer. Soc. Artif. Int. Organs, 17, p. 287 (1971).

(7) Dravid, A. R., Personal Communication to C.K. Colton, Amicon Corporation, Lexington, Mass. (August 7, 1969).

(8) Dorson, W. J., M. Markovitz, V. B. Pizziconi and J. A. Walters, "Molecular Separation as an Artificial Kidney Technique". Trans. Amer. Soc. Artif. Int. Organs, 16, p. 127 (1970).

APPENDIX A

Derivations For the Cases Where No Gel Is Formed on the Membrane Surface

I. From Section I, the system of equations is:

$$\frac{\partial \rho}{\partial t} - v \frac{\partial \rho}{\partial y} - \rho \frac{\partial v}{\partial y} = 0 \tag{A-1}$$

$$\frac{\partial \omega_A}{\partial t} - v \frac{\partial \omega_A}{\partial y} = \frac{1}{\rho} \frac{\partial}{\partial y} \left[\rho D \frac{\partial \omega_A}{\partial y} \right] \tag{A-2}$$

and the equation of state with $\tilde{\rho}_S$ and $\tilde{\rho}_A$ constant

$$\rho = \frac{\tilde{\rho}_S}{1 - \left[\frac{\tilde{\rho}_A - \tilde{\rho}_S}{\tilde{\rho}_A} \right] \omega_A} \tag{A-3}$$

subject to

$$\omega_A = \omega_A^i \qquad @ \text{ all } y,\ t = 0 \tag{A-4}$$

$$\omega_A = \omega_A^i \qquad @ \ y \to \infty, \text{ all } t \tag{A-5}$$

$$D \frac{\partial \omega_A}{\partial y} + v\omega_A = \chi \omega_A v \frac{1}{1 - \exp(-P_e)} \qquad @ \ y = 0, \text{ all } t \tag{A-6}$$

$$\rho v = K_m (\Delta P - (1 - \chi) \Delta \pi) \qquad @ \ y = 0, \text{ all } t \tag{A-7}$$

II. Dimensional Analysis

1.) let ρ_i = initial solution density

D^o = an arbitrary reference diffusivity for albumin in saline

ω_A^* = mass fraction of albumin for which $(\Delta P - (1 - \chi)\ \Delta\pi|_{y=0}) = 0$

π^i = osmotic pressure of bulk solution concentration ω_A^i

2.) define the dimensionless groups

$$\theta = \frac{\omega_A - \omega_A^i}{\omega_A^* - \omega_A^i}$$

$$\hat{D} = D/D^o$$

$$\hat{\rho} = \rho/\rho_i$$

$$\xi = y/\sqrt{D^o t}$$

$$n = \frac{K_m}{\rho_i}\left[\Delta P - (1 - \chi)\ \Delta\pi^i\right](t/D^o)^{1/2}$$

$$\hat{v} = v\left[\frac{\rho_i}{K_m\ (\Delta P - (1 - \chi)\ \Delta\pi^i)} + \sqrt{\frac{t}{D^o}}\right]$$

$$= v\sqrt{t/D^o}\ \left(\frac{n + 1}{n}\right)$$

3.) evaluate the differentials of $\hat{\rho} = \hat{\rho}(\xi, n)$

$$d\hat{\rho} = \left(\frac{\partial\hat{\rho}}{\partial\xi}\right)_n d\xi + \left(\frac{\partial\hat{\rho}}{\partial n}\right)_\xi dn$$

then $\left(\frac{\partial \hat{\rho}}{\partial t}\right)_y = \left(\frac{\partial \hat{\rho}}{\partial \xi}\right)_n \left(\frac{\partial \xi}{\partial t}\right)_y + \left(\frac{\partial \hat{\rho}}{\partial n}\right)_\xi \left(\frac{\partial n}{\partial t}\right)_y$

$$= -\frac{\xi}{2t}\left(\frac{\partial \hat{\rho}}{\partial \xi}\right) + \frac{n}{2t}\left(\frac{\partial \hat{\rho}}{\partial n}\right)$$

and $\left(\frac{\partial \hat{\rho}}{\partial y}\right)_t = \left(\frac{\partial \hat{\rho}}{\partial \xi}\right)_n \left(\frac{\partial \xi}{\partial y}\right)_t = \frac{1}{\sqrt{D^o t}}\left(\frac{\partial \hat{\rho}}{\partial \xi}\right)$

4.) evaluate the differential of $\hat{v} = \hat{v}(\xi, n)$

$$d\hat{v} = \left(\frac{\partial \hat{v}}{\partial \xi}\right)_n d\xi + \left(\frac{\partial \hat{v}}{\partial n}\right)_\xi dn$$

$$\left(\frac{d\hat{v}}{dy}\right)_t = \left(\frac{\partial \hat{v}}{\partial \xi}\right)_n \left(\frac{d\xi}{dy}\right)_t = \frac{1}{\sqrt{D^o t}} \frac{\partial \hat{v}}{\partial \xi}$$

5.) evaluate the differentials of $\theta = \theta(\xi, n)$

$$d\theta = \left(\frac{\partial \theta}{\partial \xi}\right)_n d\xi + \left(\frac{\partial \theta}{\partial n}\right)_\xi dn$$

then $\left(\frac{\partial \theta}{\partial t}\right)_y = \left(\frac{\partial \theta}{\partial \xi}\right)_n \left(\frac{\partial \xi}{\partial t}\right)_y + \left(\frac{\partial \theta}{\partial n}\right)_\xi \left(\frac{\partial n}{\partial t}\right)_y$

$$= -\frac{\xi}{2t}\left(\frac{\partial \theta}{\partial \xi}\right) + \frac{n}{2t}\left(\frac{\partial \theta}{\partial n}\right)$$

and $\left(\frac{\partial \theta}{\partial y}\right)_t = \left(\frac{\partial \theta}{\partial \xi}\right)_n \left(\frac{\partial \xi}{\partial y}\right)_t = \frac{1}{\sqrt{D^o t}}\left(\frac{\partial \theta}{\partial \xi}\right)$

6.) substitute definitions and differentials into equations (A - 1) through (A - 7)

$$\frac{n}{2}\frac{\partial \hat{\rho}}{\partial n} - \left(\frac{\xi}{2} + \frac{n}{n+1}\hat{v}\right)\frac{\partial \hat{\rho}}{\partial \xi} - \frac{n}{n+1}\hat{\rho}\frac{\partial \hat{v}}{\partial \xi} = 0 \qquad \text{(A-8)}$$

$$\frac{n}{2}\frac{\partial\theta}{\partial n} - \left(\frac{\xi}{2} + \frac{n}{n+1}\hat{v}\right)\frac{\partial\theta}{\partial\xi} = \frac{1}{\hat{\rho}}\frac{\partial}{\partial\xi}\left(\hat{\rho}\,\hat{D}\,\frac{\partial\theta}{\partial\xi}\right) \tag{A-9}$$

$$\hat{\rho} = \frac{1 - \left(\frac{\tilde{\rho}_A - \tilde{\rho}_S}{\tilde{\rho}_A}\right)\omega_A^i}{1 - \left(\frac{\tilde{\rho}_A - \tilde{\rho}_S}{\tilde{\rho}_A}\right)\left(\omega_A^i + (\omega_A^* - \omega_A^i)\,\theta\right)} \tag{A-10}$$

subject to:

$$\theta = 0 \qquad @ \text{ all } \xi, \quad n=0 \tag{A-11}$$

$$\theta \to 0 \qquad @ \ \xi \to \infty, \text{ all } n \tag{A-12}$$

$$\hat{D}\frac{\partial\theta}{\partial\xi} + \frac{n}{n+1}\hat{v}\left(\theta + \frac{\omega_A^i}{\omega_A^* - \omega_A^i}\right) = \frac{n}{n+1}\chi\hat{v}\left(\theta + \frac{\omega_A^i}{\omega_A^* - \omega_A^i}\right)\frac{1}{1-\exp(-Pe)}$$

$$@ \ \xi = 0, \text{ all } n \tag{A-13}$$

$$\hat{\rho}\hat{v} = \frac{(\Delta P - (1-\chi)\,\Delta\pi)}{(\Delta P - (1-\chi)\,\Delta\pi^i)}\,(n+1) \qquad @ \ \xi = 0, \text{ all } n \tag{A-14}$$

Only the functionalities of osmotic pressure and diffusivity need to be added for complete specification.

III. Asymptotic (Long Time) solution for the Case of Constant Density and Diffusivity

1.) the dimensionless groups of II. which are affected

$\hat{D} = 1$ since now $D = D^o = \overline{D}$, where $\overline{D}$ is the average diffusivity of the polarization layer evaluated at $\overline{\omega}_A = (\omega_A^* + \omega_A^i)/2$

$\hat{\rho} = 1$ since now $\rho = \rho_i = \overline{\rho}$, where $\overline{\rho}$ is the average density of the polarization layer evaluated at $\overline{\omega}_A$.

$$\xi = y/\sqrt{\bar{D}t}$$

$$n = \frac{K_m}{\bar{\rho}} [\Delta P - (1-\chi)\ \Delta\pi^i] \left(\frac{t}{\bar{D}}\right)^{1/2} \quad >> 1 \text{ at long time}$$

$$\hat{v} = v\sqrt{\frac{t}{\bar{D}}}$$

2.) the set of equations, (A-8) to (A-14) become:

$$\frac{n}{2}\frac{\partial\theta}{\partial n} - \left(\frac{\xi}{2} + \hat{v}\right)\frac{\partial\theta}{\partial\xi} = \frac{\partial^2\theta}{\partial\xi^2} \tag{A-15}$$

subject to

$$\theta = 0 \qquad @ \text{ all } , n = 0 \tag{A-16}$$

$$\theta \to 0 \qquad @ \ \xi \to \infty, \text{ all } n \tag{A-17}$$

$$\frac{\partial\theta}{\partial\xi} + \hat{v}\left[\theta + \frac{\omega_A^i}{\omega_A^* - \omega_A^i}\right] = \chi\hat{v}\left(\theta + \frac{\omega_A^i}{\omega_A^* - \omega_A^i}\right)\frac{1}{1 - \exp(-P_e)}$$

$$= \chi\hat{v}\left(\theta + \frac{\omega_A^i}{\omega_A^* - \omega_A^i}\right) \qquad @ \ \xi = 0, \text{ all } n \tag{A-18}$$

where the Peclet number has been assumed large

$$\hat{v} = \frac{[\Delta P - (1 - \chi)\ \Delta\pi]}{[\Delta P - (1 - \chi)\ \Delta\pi^i]}\ n \tag{A-19}$$

3.) Assume solutions of the form

$$\theta\ (\xi) = f_0(\xi) + \frac{1}{n} f_1(\xi) + \ldots$$

$$\hat{v} = a_0 + \frac{1}{n} a_1 + \ldots$$

and the ultrafiltration driving force is assumed to be equal to a series expansion evaluated at the concentration (ω_A^*) which corresponds to an osmotic pressure which is equal to the applied pressure (i.e., $(1-\chi)\ \Delta\pi|_{\omega_A^*} \equiv \Delta P$),

$$\Delta P - (1-\chi)\ \Delta\pi|_{\xi=0} = \underbrace{(\Delta P - (1-\chi)\ \Delta\pi|_{\omega_A^*})}_{\text{zero by definition of } \omega_A^*} - (1-\chi)\left(\frac{\partial \Delta\pi}{\partial \omega_A}\right)_{\omega_A^*} (\omega_A|_{\xi=0} - \omega_A^*) - \underbrace{(1-\chi)\left(\frac{\partial^2 \Delta\pi}{\partial \omega_A^2}\right)_{\omega_A^*} \frac{(\omega_A|_{\xi=0} - \omega_A^*)^2}{2} - \ldots\ldots}_{\text{neglected higher order terms}}$$

note that for $\chi = 0$, the definition of ω_A^* changes such that $\pi|_{\omega_A^*} \equiv \Delta P$, so for this case the assumed solution through two terms of expansion is

$$\Delta P - \pi|_{\xi=0} = -\left(\frac{\partial \pi}{\partial \omega_A}\right)_{\omega_A^*} (\omega_A|_{\xi=0} - \omega_A^*)$$

4.) substitute assumed solutions into eqn (A-15), and equate coefficients on like powers of n (i.e., coefficients of n^{-1} and n^0 terms where it is assumed only terms through a_1 and f_1 are significant).

$$\frac{n}{2}\left[-\frac{f_1}{n^2}\right]-\left[\frac{\xi}{2}+a_o+\frac{1}{n}a_1\right]\left[\frac{\partial f_o}{\partial\xi}+\frac{1}{n}\frac{\partial f_1}{\partial\xi}\right]=\frac{\partial^2 f_o}{\partial\xi^2}+\frac{1}{n}\frac{\partial^2 f_1}{\partial\xi^2}$$

for n^{-1} terms
$$-\frac{f_1}{2}-\left(\frac{\xi}{2}+a_o\right)\frac{\partial f_1}{\partial\xi}-a_1\frac{\partial f_o}{\partial\xi}=\frac{\partial^2 f_1}{\partial\xi^2} \qquad \text{(A-20A)}$$

for n^{o} terms
$$-\left(\frac{\xi}{2}+a_o\right)\frac{\partial f_o}{\partial\xi}=\frac{\partial^2 f_o}{\partial\xi^2} \qquad \text{(A-20B)}$$

5.) from the boundary condition (A-17)

$$f_o \to 0 \qquad \xi\to\infty \qquad \text{(A-21A)}$$

$$f_1 \to 0 \qquad \xi\to\infty \qquad \text{(A-21B)}$$

6.) from the boundary condition (A-18)

$$\left[\frac{\partial f_o}{\partial\xi}+\frac{1}{n}\frac{\partial f_1}{\partial\xi}\right]+(1-\chi)\left[a_o+\frac{1}{n}a_1\right]\left[f_o+\frac{1}{n}f_1+\frac{\omega_A^i}{\omega_A^*-\omega_A^i}\right]=0$$

for n^{-1} terms
$$\frac{\partial f_1}{\partial\xi}+(1-\chi)\left(a_o f_1+a_1\left(f_o+\frac{\omega_A^i}{\omega_A^*-\omega_A^i}\right)\right)=0$$

$$@\ \xi=0 \qquad \text{(A-22A)}$$

for n^{o} terms
$$\frac{\partial f_o}{\partial\xi}+(1-\chi)a_o\left(f_o+\frac{\omega_A^i}{\omega_A^*-\omega_A^i}\right)=0 \qquad @\ \xi=0 \qquad \text{(A-22B)}$$

7.) from boundary condition (A-19)

$$\frac{1}{n}\left(a_o+\frac{1}{n}a_1\right)=\frac{-(1-\chi)(\partial\pi/\partial\omega_A)^*_{\omega_A^*}\left(\omega_A|_{\xi=0}-\omega_A^*\right)}{\left[\Delta P-(1-\chi)\,\Delta\pi^i\right]}$$

$$= \frac{-(1-\chi)(\partial\pi/\partial\omega_A)_{\omega_A}^{*} \quad (\omega_A^{*}-\omega_A^{i})(\theta-1)}{(\Delta P - (1-\chi)\Delta\pi^{i})}$$

$$= \frac{-(1-\chi)(\partial\pi/\partial\omega_A)_{\omega_A}^{*} \quad (\omega_A^{*}-\omega_A^{i})}{(\Delta P - (1-\chi)\Delta\pi^{i})} (f_o + \frac{1}{n} f_1 - 1)$$

for n^{-1} terms $\quad a_o = \dfrac{-(1-\chi)(\partial\pi/\partial\omega_A)_{\omega_A}^{*} \quad (\omega_A^{*}-\omega_A^{i})}{(\Delta P - (1-\chi)\Delta\pi^{i})} f_1(0) \quad @ \ \xi=0 \qquad$ (A-23A)

for n^{o} terms $\quad f_o = 1 \qquad @ \ \xi = 0 \qquad$ (A-23B)

8.) solve for $f_o(\xi)$ using the differential equation (A-20B) and the boundary conditions at $\xi=0$ (eqn (A-23B) and $\xi \to \infty$ (eqn A-21A).

a) with $p = \dfrac{df_o}{d\xi}$, (A-20B) becomes

$$\frac{dp}{p} = -(a_o + \xi/2)\, d\xi$$

b) integrating

$$p = \frac{df_o}{d\xi} = C_1 \exp(-\xi^2/4 - a_o\xi)$$

c) from Abramowitz, M. and Stegun, I.A., Handbook of Mathematical Functions, p. 303, No. 7.4.32, Dover Publications, Inc., New York (1964)

$$f_o = C_2 \, \mathrm{erf}\left[\frac{\xi}{2} + a_o\right] + C_3$$

d) after applying (A-23B) and (A-21A)

$$f_o = \frac{1 - \text{erf}\{\xi/2 + a_o\}}{1 - \text{erf}(a_o)} \tag{A-24}$$

9.) solve for a_o using the second boundary condition at $\xi = 0$ (eqn A-22B)

$$\text{a)} \quad \frac{\partial f_o}{\partial \xi} + a_o(1-\chi)\left(1 + \frac{\omega_A^i}{\omega_A^* - \omega_A^i}\right) = 0$$

then

$$\frac{-1}{1-\text{erf } a_o}\left\{\frac{\partial}{\partial \xi}\left(\text{erf}\left(\xi/2 + a_o\right)\right)\right\} + a_o(1-\chi)\frac{\omega_A^*}{\omega_A^* - \omega_A^i} = 0$$

b) from Abramowitz and Stegun, ibid.

$$\exp - (aZ^2 + abZ + c) = \frac{1}{2}\sqrt{\frac{\pi}{a}}\exp\left[\frac{b^2-ac}{a}\right]\frac{d}{dZ}\left\{\text{erf}\left(\sqrt{a}\,Z + \frac{b}{\sqrt{a}}\right)\right\}$$

so, the result of a) is

$$\frac{\exp(-a_o^2)}{a_o[1-\text{erf } a_o]} = \sqrt{\pi}\,(1-\chi)\,\frac{\omega_A^*}{\omega_A^* - \omega_A^i} \tag{A-25}$$

10.) to summarize, the solution for this case, through the $0^{\underline{th}}$ order terms of the perturbation analysis is:

$$\frac{\omega_A - \omega_A^i}{\omega_A^* - \omega_A^i} = \frac{1 - \text{erf}\left[y/2\sqrt{D\,t} + a_o\right]}{1 - \text{erf}\,(a_o)} \tag{A-26}$$

$$v = a_o\sqrt{\frac{D}{t}} \qquad \text{(A-27)}$$

where a_o is given by equation (A-25)

11.) when $\chi = 0$ (membrane impermeable to albumin) the first order terms (a_1 and f_1) of the assumed solutions are tractable

the above formulation and zeroth order solutions still apply with changes

$$\chi = 0$$

$$\Delta\pi = \pi \quad \text{and} \quad \Delta\pi^i = \pi^i$$

and ω_A^* is defined as the concentration for which $\pi|_{\omega_A^*} \equiv \Delta P$

12.) solving for $f_1(\xi)$ using the differential equation (A-20A) and the boundary conditions at $\xi = 0$ and at $\xi \to \infty$.

a) from eqn (A-20A)

$$\frac{-f_1}{2} - \left(\frac{\xi}{2} + a_o\right)\frac{\partial f_1}{\partial \xi} - a_1\frac{\partial f_o}{\partial \xi} = \frac{\partial^2 f_1}{\partial \xi^2}$$

$$\text{or} \quad \frac{-1}{2}\frac{\partial(\xi f_1)}{\partial \xi} - a_o\frac{\partial f_1}{\partial \xi} - a_1\frac{\partial f_o}{\partial \xi} = \frac{\partial^2 f_1}{\partial \xi^2}$$

b) integrating

$$-\frac{\xi f_1}{2} - a_o f_1 - a_1 f_o = \frac{\partial f_1}{\partial \xi} + C_1$$

c) using the second boundary condition at $\xi = 0$, eqn (A-22A) with $\chi = 0$ for the coefficients of the n^{-1} terms

$$\frac{\partial f_1}{\partial \xi} + a_o f_1 + a_1 f_o + a_1\frac{\omega_A^i}{\omega_A^* - \omega_A^i} = 0 \qquad @\ \xi = 0$$

d) comparing the result of b) for $\xi = 0$, with the result of c) gives C_1 to be:

$$C_1 = a_1 \frac{\omega_A^i}{\omega_A^* - \omega_A^i}$$

therefore

$$\frac{\partial f_1}{\partial \xi} + \left(\frac{\xi}{2} + a_0\right) f_1 + a_1 f_0 + a_1 \frac{\omega_A^i}{\omega_A^* - \omega_A^i} = 0$$

e) finding the complementary solution

$$\frac{df_1^c}{f_1^c} = -\left(\frac{\xi}{2} + a_0\right) d\xi$$

then $f_1^c = K_1 \exp(-\xi^2/4 - a_0\xi)$

f) finding the particular solution of the form

$$f_1^p = g(\xi) \exp -(\xi^2/4 + a_0\xi)$$

$$\text{so} \quad \frac{df_1^p}{d\xi} = \left[\frac{dg}{d\xi} \exp -(\xi^2/4 + a_0\xi)\right] - \left[(\xi/2 + a_0)\exp -(\xi^2/4 + a_0\xi)\right] g(\xi)$$

g) substituting into result of d) above gives

$$\frac{dg}{d\xi} = -a_1 \left(f_0 + \frac{\omega_A^i}{\omega_A^* - \omega_A^i}\right) \exp(\xi^2/4 + a_0\xi)$$

h) solution for f_1^p is

$$f_1^p = -\exp -\left(\frac{\xi^2}{4} + a_0\xi\right)\left[a_1 \frac{\omega_A^i}{\omega_A^* - \omega_A^i} \int \exp\left(\frac{\xi^2}{4} + a_0\xi\right) d\xi + a_1 \int f_0 \exp\left(\frac{\xi^2}{4} + a_0\xi\right) d\xi\right]$$

i) so the general solution is

$$f_1(\xi) = \left[K_1 - a_1 \int \left(\frac{\omega_A^i}{\omega_A^* - \omega_A^i} + f_0 \right) \exp\left(\frac{\xi^2}{4} + a_0\xi\right) d\xi \right] \exp - \left(\frac{\xi^2}{4} + a_0\xi\right)$$

where $f_0 = \dfrac{1 - \text{erf}\ (\xi/2 + a_0)}{1 - \text{erf}\ (a_0)}$

j) by boundary condition @ $\xi \to \infty$ (eqn A-21B), $f_1(\infty) \to 0$, whereas the results of i) indicate that for $\xi \to \infty$

$f_0 \to 0$

so $\left[\int \left(\dfrac{\omega_A^i}{\omega_A^* - \omega_A^i} + f_0 \right) \exp\left(\dfrac{\xi^2}{4} + a_0\xi\right) d\xi \right] \exp - \left(\dfrac{\xi^2}{4} + a_0\xi\right) \to \infty$

therefore $a_1 = 0$

and $f_1(\xi) = K_1 \exp - \left(\dfrac{\xi^2}{4} + a_0\xi\right)$

k) using boundary condition eqn (A-23A) with $\chi = 0$

$$f_1(0) = \frac{(\Delta P - \pi^i)\, a_0}{-\left(\dfrac{\partial \pi}{\partial \omega_A}\right)^*_{\omega_A} \left(\omega_A^* - \omega_A^i\right)} = K_1$$

$$\text{so}\quad f_1(\xi) = -\frac{(\Delta P - \pi^i)\, a_0}{\left(\dfrac{\partial \pi}{\partial \omega_A}\right)^*_{\omega_A} \left(\omega_A^* - \omega_A^i\right)} \exp - \left(\frac{\xi^2}{4} + a_0\xi\right)$$

l) summary of the perturbation solutions

$\hat{v} = a_0$

$$\theta(\xi) = \frac{1 - \text{erf}\ (\xi/2 + a_o)}{1 - \text{erf}\ (a_o)} - \frac{a_o}{n} \frac{(\Delta P - \pi^i)}{\left(\frac{\partial \pi}{\partial \omega_A}\right)_{\omega_A^*} \left(\omega_A^* - \omega_A^i\right)} \exp - \left(\frac{\xi^2}{4} + a_o \xi\right)$$

13.) the final solutions are

$$v = a_o \sqrt{\frac{\overline{D}}{t}} \tag{A-28}$$

$$\frac{\omega_A - \omega_A^i}{\omega_A^* - \omega_A^i} = \frac{1 - \text{erf}(y/2\sqrt{\overline{D}\ t}\ + a_o)}{1 - \text{erf}\ a_o} - \frac{a_o \overline{p} (\overline{D}/t)^{1/2}}{K_m \left(\frac{\partial \pi}{\partial \omega_A}\right)_{\omega_A^*} \left(\omega_A^* - \omega_A^i\right)} \exp\left(-\frac{y^2}{4\overline{D}t} + \frac{a_o y}{\sqrt{\overline{D}t}}\right)$$

(A-29)

where $$\frac{\exp\ (-a_o^2)}{a_o[1-\text{erf}\ a_o]} = 1.77\ \frac{\omega_A^*}{\omega_A^* - \omega_A^i} \tag{A-30}$$

APPENDIX B

Derivation For the Case Where Gel Is Formed on the Membrane Surface

I. From Section IV, the system of equations is:

$$\frac{\partial \omega_A}{\partial t} - v \frac{\partial \omega_A}{\partial y} = \bar{D} \frac{\partial^2 \omega_A}{\partial y} \tag{B-1}$$

subject to

$$\omega_A = \omega_A^i \qquad @ \text{ all } y,\ t = 0 \tag{B-2}$$

$$\omega_A \to \omega_A^i \qquad @\ y \to \infty, \text{ all } t \tag{B-3}$$

$$v\omega_A + \bar{D} \frac{\partial \omega_A}{\partial y} = \omega_g \frac{d\ell}{dt} \qquad @\ y = \ell, \text{ all } t \tag{B-4}$$

$$v = \frac{K_m}{\rho} (\Delta P_m - \pi_m) \qquad @\ y = 0, \text{ all } t \tag{B-5}$$

where

$$\Delta P_T = \Delta P_m + \Delta P_g \tag{B-6}$$

$$v = \frac{B_g}{\rho \ell} \Delta P_g \tag{B-7}$$

II. Dimensional Analysis

$$\theta = (\omega_A - \omega_A^i)/(\omega_g - \omega_A^i)$$

$$\xi = (y - \ell)/\sqrt{\bar{D}t}$$

$$n = \frac{K_m}{\bar{\rho}} (\Delta P_T - \pi_m^*)\sqrt{t/\bar{D}}$$

$$\hat{v} = v\sqrt{t/\bar{D}}$$

$$\hat{\ell} = \ell/\sqrt{\bar{D}t}$$

III. Evaluation of the differentials of $\theta(\xi,n)$

$$d\theta = \left(\frac{\partial\theta}{\partial n}\right)_\xi dn + \left(\frac{\partial\theta}{\partial\xi}\right)_n d\xi$$

$$d\hat{\ell} = \left(\frac{\partial\hat{\ell}}{\partial n}\right)_\xi dn + \left(\frac{\partial\hat{\ell}}{\partial\xi}\right)_n d\xi$$

1.) for $(\partial^2\theta/\partial y^2)_t$

$$\left(\frac{\partial\theta}{\partial y}\right)_t = \left(\frac{\partial\theta}{\partial\xi}\right)_n \left(\frac{\partial\xi}{\partial y}\right)_t = \frac{1}{\sqrt{\bar{D}t}} \frac{\partial\theta}{\partial\xi}$$

$$\left(\frac{\partial^2\theta}{\partial y^2}\right)_t = \frac{1}{\bar{D}t} \frac{\partial^2\theta}{\partial\xi^2}$$

2.) for $(\partial\theta/\partial t)_y$

$$\left(\frac{\partial\theta}{\partial t}\right)_y = \left(\frac{\partial\theta}{\partial n}\right)_\xi \left(\frac{\partial n}{\partial t}\right)_y + \left(\frac{\partial\theta}{\partial\xi}\right)_n \left(\frac{\partial\xi}{\partial t}\right)_y$$

where $\left(\frac{\partial n}{\partial t}\right)_y = \frac{n}{2t}$

and $$\left(\frac{\partial\xi}{\partial t}\right)_y = -\frac{1}{\sqrt{Dt}}\frac{d\ell}{dt} - \frac{\xi}{2t}$$

$$= -\frac{1}{\sqrt{Dt}}\left(\sqrt{Dt}\,\frac{d\hat{\ell}}{dt} + \frac{1}{2}\sqrt{\frac{D}{t}}\,\hat{\ell}\right) - \frac{\xi}{2t}$$

$$= -\left(\frac{n}{2t}\frac{d\hat{\ell}}{dn} + \frac{\hat{\ell}}{2t} + \frac{\xi}{2t}\right)$$

where the last step employs the total differential $(\partial\hat{\ell}/\partial t)_\xi$

so $$\left(\frac{\partial\theta}{\partial t}\right)_y = \frac{n}{2t}\frac{\partial\theta}{\partial n} - \left(\frac{\xi}{2t} + \frac{\hat{\ell}}{2t} + \frac{n}{2t}\frac{d\hat{\ell}}{dn}\right)\frac{\partial\theta}{\partial\xi}$$

IV. Substitution of dimensionless variables and the differentials gives:

$$\frac{n}{2}\frac{\partial\theta}{\partial n} - \left\{\frac{\xi}{2} + \frac{\hat{\ell}}{2} + \hat{v} + \frac{n}{2}\frac{d\hat{\ell}}{dn}\right\}\frac{\partial\theta}{\partial\xi} = \frac{\partial^2\theta}{\partial\xi^2} \qquad \text{(B-8)}$$

subject to

$$\theta = 0 \qquad @\ \text{all } \xi,\ n = 0 \qquad \text{(B-9)}$$

$$\theta \to 0 \qquad @\ \xi \to \infty,\ \text{all } n \qquad \text{(B-10)}$$

$$\hat{v}\left[(\omega_g-\omega_A^i)\theta + \omega_A^i\right] + (\omega_g - \omega_A^i)\frac{\partial\theta}{\partial\xi} = \omega_g\left[\frac{\hat{\ell}}{2} + \frac{n}{2}\frac{d\hat{\ell}}{dn}\right]$$

$$@\ \xi = 0, \text{ and all n for which a gel exists} \qquad \text{(B-11)}$$

$$\hat{v} = \frac{[\Delta P_m - \pi_m]}{[\Delta P_T - \pi_m^*]} n \qquad @\ \xi = 0, \text{ all n} \qquad \text{(B-12)}$$

where

$$\Delta P_T = \Delta P_m + \Delta P_g \qquad \text{(B-13)}$$

$$\hat{v} = \frac{B_g/\overline{\rho}}{\overline{D}\hat{\ell}} \Delta P_g \qquad \text{(B-14)}$$

V. Assume a functionality for the time dependence of the membrane pressure drop, ΔP_m

$$\Delta P_m = \pi_m^* + \sqrt{\frac{\overline{D}}{t}}\ \frac{\overline{\rho}}{K_m}\ f(t)$$

$$\text{or} \quad \Delta P_m = \pi_m^* + (\Delta P_T - \pi_m^*)\frac{f(n)}{n} \qquad \text{(B-15)}$$

so equations (B-12), (B-13) and (B-14) become

$$\hat{v} = n\ \frac{\pi_m^* - \pi_m}{\Delta P_T - \pi_m^*} + f(n) \qquad @\ \xi = 0 \qquad \text{(B-16)}$$

$$\frac{\Delta P_g}{\Delta P_T - \pi_m^*} = 1 + \frac{1}{n} f(n) \qquad \text{(B-17)}$$

$$\hat{v} = \frac{(B_g/\overline{\rho})(\Delta P_T - \pi_m^*)}{\overline{D}\,\hat{\ell}} \left[1 + \frac{1}{n} f(n)\right] \qquad \text{(B-18)}$$

VI. Perturbation analysis for long times, n >> 1

1.) Assume solutions of the form

$$\theta = \theta_o(\xi) + \frac{1}{n}\theta_1(\xi) + \ldots.$$

$$\hat{\ell} = \hat{\ell}_o + \frac{1}{n}\hat{\ell}_1 + \ldots.$$

$$f(n) = a_o + \frac{1}{n} a_1 + \ldots.$$

$$\hat{v} = \hat{v}_o + \frac{1}{n}\hat{v}_1 + \ldots.$$

2.) substitution of assumed solutions into equations and solving for the zeroth order terms gives:

by eqn (B-8)

$$\frac{d^2\theta_o}{d\xi^2} + \left[\frac{\xi}{2} + \frac{\hat{\ell}_o}{2} + v_o\right] \frac{d\theta_o}{d\xi} = 0 \qquad \text{(B-19)}$$

after the time of gel formation, $\omega_A = \omega_g$ at $\xi = 0$, so

$$\theta_o(0) = 1 \qquad @\ \xi = 0 \qquad \text{(B-20)}$$

by eqn (B-10)

$$\theta_o \to 0 \qquad @\ \xi \to \infty \qquad \text{(B-21)}$$

by eqn (B-11)

$$\hat{v}_o \left[(\omega_g - \omega_A^i)\theta_o(0) + \omega_A^i \right] + (\omega_g - \omega_A^i) \frac{\partial \theta_o(0)}{\partial \xi} = \frac{\omega_g \hat{\ell}_o}{2} \qquad @\ \xi = 0 \qquad \text{(B-22)}$$

by eqn (B-16), since after gel formation $\pi_m = \pi_m^*$

$$\hat{v}_o = a_o \qquad @\ \xi = 0 \qquad \text{(B-23)}$$

by eqn (B-17)

$$\frac{\Delta P_g}{\Delta P_T - \pi_m^*} = 1 \qquad \text{(B-24)}$$

by eqn (B-18)

$$\hat{v}_o = \frac{(B_g/\bar{p})(\Delta P_T - \pi_m^*)}{\bar{D}\,\hat{\ell}_o} \qquad \text{(B-25)}$$

3.) solution of (B-19)

let $p = d\theta_o/d\xi$

then $$\frac{dp}{p} = -\left[\frac{1}{2}\xi + \left(\frac{\hat{\ell}_o}{2} + \hat{v}_o \right) \right] d\xi$$

$$p = C_1 \exp\left\{ -\left[\frac{\xi^2}{4} + \left(\frac{\hat{\ell}_o}{2} + v_o \right) \xi \right] \right\}$$

from Abramowitz, M. and I. A. Stegun, ibid., p. 303

$$\theta_o = C_2\, \mathrm{erf}\left\{ \frac{\xi}{2} + \frac{\hat{\ell}_o}{2} + \hat{v}_o \right\} + C_3$$

with boundary conditions (B-20) and (B-21)

$$\theta_o = \frac{1 - \text{erf}\left\{\frac{\xi}{2} + \frac{\hat{\ell}_o}{2} + \hat{v}_o\right\}}{1 - \text{erf}\left\{\frac{\hat{\ell}_o}{2} + \hat{v}_o\right\}} \qquad \text{(B-26)}$$

4.) combining in terms of $\hat{v}_o$

from eqn (B-25)

$$\hat{\ell}_o = \frac{(B_g/\overline{\rho})(\Delta P_T - \pi_m^*)}{\hat{v}_o \overline{D}}$$

and by eqns (B-24) and (B-7)

$$\hat{\ell}_o = \frac{(B_g/\overline{\rho})\ \Delta P_g}{\ell}\ \frac{\ell}{\overline{D}}\left(\frac{1}{\hat{v}_o}\right) = \frac{Pe_g}{\hat{v}_o}$$

where $Pe_g = \frac{v\ell}{\overline{D}}$, the gel Peclet number

substituting this result, and eqns (B-20, 26) into (B-22) gives:

$$\hat{v}_o\left(\frac{\omega_g}{\omega_g - \omega_A^i}\right) - \frac{1}{1.77}\ \frac{\exp -\left(\frac{Pe_g}{2\hat{v}_o} + \hat{v}_o\right)^2}{1 - \text{erf}\left\{\frac{Pe_g}{2\hat{v}_o} + \hat{v}_o\right\}} = \frac{Pe_g}{2\hat{v}_o}\ \frac{\omega_g}{(\omega_g - \omega_A^i)} \qquad \text{(B-27)}$$

5.) summary

gel layer thickness

$$\ell = \frac{Pe_g}{\hat{v}_o}\sqrt{\overline{D}t} \qquad \text{(B-28)}$$

gel layer pressure drop

$$\Delta P_g = (\Delta P_T - \pi_m^*) \tag{B-29}$$

flux

$$v = \hat{v}_o \sqrt{\frac{\overline{D}}{t}} \tag{B-30}$$

concentration profile above gel layer

$$\frac{\omega_A - \omega_A^i}{\omega_g - \omega_A^i} = \frac{1 - \text{erf}\left\{\frac{y-\ell}{2\sqrt{\overline{D}t}} + \frac{Pe_g}{2\hat{v}_o} + \hat{v}_o\right\}}{1 - \text{erf}\left\{\frac{Pe_g}{2\hat{v}_o} + \hat{v}_o\right\}} \tag{B-31}$$

where $\hat{v}_o$ given by equation (B-27)

and $Pe_g = \dfrac{(B_g/\overline{\rho})(\Delta P_T - \pi_m^*)}{\overline{D}}$

CHAPTER FIVE

THE STUDY OF CONCENTRATION POLARIZATION IN STAGNANT CELL ULTRAFILTRATION

The introduction of this thesis pointed out that previous models of the effect of concentration polarization on ultrafiltration flux have been limited by the lack of information about the properties of concentrated macromolecular solutions, and about rejected solute concentrations above the ultrafiltration membrane. Chapters 2 and 3 increased understanding about the former, through both discussion and experimental data, for the system of albumin in saline solutions. In this chapter, techniques are described, and experimental results presented, for the determination of concentration profiles in ultrafiltration of these same solutions. The simultaneous determinations of ultrafiltration flux give strong support for the theoretical model which is presented in Chapter Four.

From investigations of velocity profiles in fluid mechanical boundary layers (1), diffusion coefficient measurements in chemical and biochemical solutions (2,3) and diffusion layers in electrochemical reactions (4), several techniques for measuring concentration gradients have evolved. All of the methods described in the literature have been applied only to systems where gradients are not extremely large. They can be divided into two major classes with examples given for each.

--- SAMPLING METHODS
- pin-hole
- drainage
- freezing

--- OPTICAL METHODS
- interferometry
- deflection

The sampling methods preceded optical techniques and were popular in electrochemical investigations (4). The pin-hole method involves the

withdrawal of a microsample from within the concentration layer. The drainage technique is used with solid-liquid interfaces with samples squeegeed from the solid interface after it has been drained for varying lengths of time. At best, each of these methods can give only relative measures of concentrations within the polarization layers and were not considered further.

The method of freezing a diffusion layer and slicing the frozen solution to obtain concentration gradients was used by Brenner (5,6) to study the composition of cathode films produced during metal deposition. His technique involved the rapid freezing (1-5 seconds) of the layer of solution in contact with a hollow cylindrical cathode and then slicing successive layers (ca. .01 cm thick) of the "ice" on a lathe and analyzing them. The method was claimed to give absolute concentration measurements and was pursued further.

The preliminary work focused on the necessity to demonstrate the capability to slice frozen albumin solutions and to show the freezing process would not cause solute-solvent segregation. Concentrated albumin solutions (51 gm%) were placed in plastic tubes of 13 mm diameter and quickly frozen in liquid nitrogen. Instead of a lathe, a refrigerated microtome was used to slice mounted samples of the frozen solutions into 0.004 cm thick slices. The concentrated albumin slices were diluted and analyzed for total protein.

The results for seven slices were not reproducible, but the errors were thought correctable. However, the strong visual suggestions of solute/solvent segregation during the freezing step resulted in abandonment of the technique. Inspection of the frozen contents of the plastic tubes showed a "spindle" structure protruding from the center of the

frozen meniscus. The cross-sectional slices also displayed a "cartwheel" pattern. These observations suggested that solvent is selectively pushed ahead of the freezing interface (from outside-in) and then up the center core as it freezes.

The optical methods exploit the refractive index gradients which exist in the polarization layer. For solutions of albumin in .15 M saline, concentration and refractive index are linearly related and independent of solution pH (see Appendix B). The techniques based on interference of light and/or deflection of light are the two principle optical methods for observing refractive index gradients.

Interferometry records the phase difference between the two parts of the same beam which has been split, one part passing through a reference solution and the other through the solution of varying refractive index, and reunited at a recording plane. It is the easiest to interpret and is most useful for measuring small gradients. Recent applications have included the investigation of membrane transport studies (7) and the study of convective mass transfer boundary layers on electrodes (8). In both of these studies the refractive index gradients were small, 6×10^{-4} and 3×10^{-3} R.I.U./cm In the albumin ultrafiltration studies reported here, the refractive index gradients near the membrane surface ranged from .2-.8 R.I.U./cm. The interference fringe separations are calculated from

$$\frac{1}{f} = \frac{\lambda}{(dn/dy)W} \qquad (5\text{-}1)$$

where $f = \frac{\text{number of fringes}}{\text{length}} = \frac{\text{change in optical path distance}}{\text{wavelength}}$

W = cell width, .3 cm

λ = wavelength of light emitted by He-Ne laser, 6.328×10^{-5} cm

At the fringe separations of 10^{-3}- 10^{-4} cm, resolution of patterns would be nearly impossible for even the best film or measuring techniques.

Several ingenious schemes for measuring concentration gradients by deflection methods have been reported (1,3). The Schlieren Scanning method is a useful technique for following solute concentration gradients away from liquid-liquid interfaces in diffusion studies (3). Like most of the other Schlieren methods however, it has been developed only for recording small gradients of refractive index. Also the Schlieren Scanning method would not be adaptable to measurement of profiles on only one side of an interface, such as above an ultrafiltration membrane.

Wire-image shadowgraph is a deflection technique in which a thin wire image shadow is projected through a transmitting medium which contains a refractive index gradient. The image of the wire (positioned in a plane perpendicular to the light path) quantitatively indicates the amount of bending experienced by the light beam in passing through the medium. From the Laws of Fermat and Snell, the refractive index gradient responsible for this bending can be obtained.

The technique has been suggested as a means of measuring flow patterns in density stratified liquids (9) and has been tried for measurement of concentration profiles above reverse osmosis membranes (10) and ultrafiltration membranes (11). Only the first of these studies considers the general problem of light deflection without making small deflection angle assumptions, which of course are unreasonable close to the membrane. However, this work (9) was theoretical only and no experimental data was obtained to check the precision of the theory developed.

Despite the uncertainty of the application of this technique to the measurement of ultrafiltration polarization layers engendered by the above literature considerations, the review of the alternatives made thin-wire shadowgraph appear most likely to succeed.

I. Wire Image Shadowgraph for Measuring Refractive Index Gradients

This section develops the mathematics which lead to the refractive index profile above the membrane, starting from the measurement of the light deflection caused by a monotonic refractive index gradient. The ray trace equations are developed for the general case where the only assumption is that the ultrafiltration cell windows are normal to the incident light beam. A simplified version of the ray trace, valid when deflection is small, is then shown. This second form of the ray trace is useful when analyzing deflection patterns near the top of the polarization layer where deflections are small and the general ray trace analysis unstable. The numerical technique for ray tracing in the polarization layer utilizes both of these ray trace methods. The logic of the technique is presented. The Fortran listing of the computer program (SDIP), which is executable on a General Data Nova Model 840 Computer, is given in Appendix C. Lastly, the corrections to the general ray trace are shown for the case in which the cell windows are not quite normal to the incident beam.

A. Light Ray Deflection - The General Case for Normally Incident Light

The shadowgraph method is rooted in the principle that light is deflected when passing through a medium of continuously varying refractive index. The deflection is from the region of lower to higher refractive index.

The schematic of Figure 5-1 shows a stagnant ultrafiltration cell in which a solution of bulk refractive index n_B is confined between two glass windows. The filtration process has created the refractive index gradient above the membrane as shown. The front glass surface (left side of figure) is illuminated by a normally incident, collimated beam. For a light ray

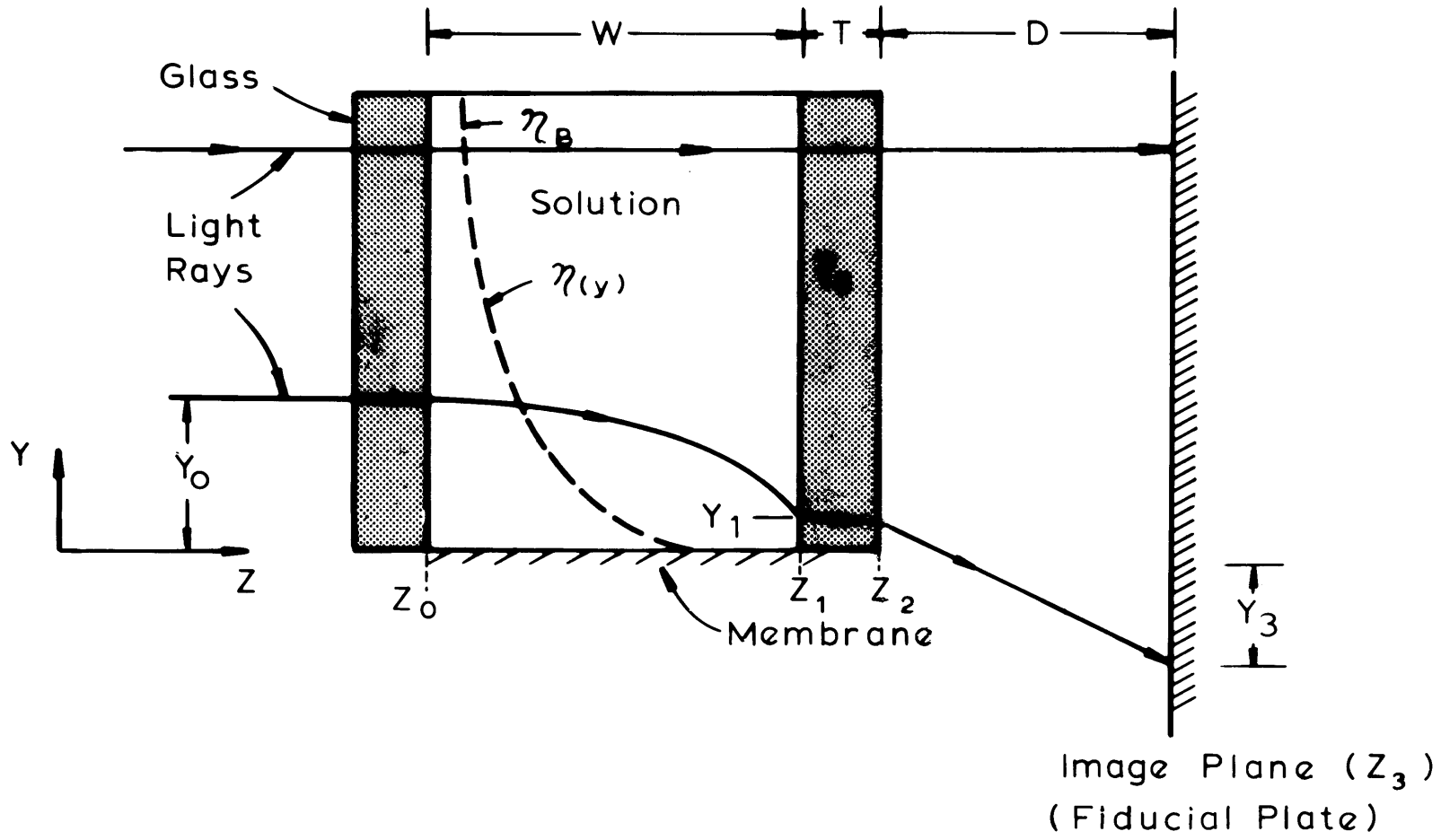

FIGURE 5-1 Schematic of Ray Trace

which enters the solution at a point where the refractive index is homogeneous across the width of the cell, the ray travels undeflected over a constant distance above the membrane surface, to a point at the image plane. The image plane is a plate of frosted glass. On the surface of this plate which faces the cell, are inscribed small marks in the shape of x's, called fiducials. The position of these fiducials relative to one another is known to a high degree of accuracy. This accurate two-dimensional grid serves to eliminate the variable effects (e.g. differences in magnification, film tilt, film warpage, etc.) involved in photographing the images formed on the plate.

The lower ray is shown entering the solution at a point a distance Y_0 above the membrane, where a gradient in refractive index exists. This gradient causes the ray to be deflected continuously, along its traverse of the cell width, toward the membrane surface. The ray undergoes refraction at the solution/rear glass wall interface and again at the glass/air interface. This ray appears on the image plane, at a distance Y_3 below the membrane. This ray trace is quantitated by the use of Fermat's principle to describe the path through the solution and Snell's Law of refraction at the interfaces. The derivations presented in Appendix A are summarized below.

Fermat's Law states that the first variation of the integral along the ray path of the local refractive index, $\eta(s)$, must vanish, and when applied to the ray path between Z_0 and Z_1 gives,

$$\delta \int \eta(s) ds = 0 \qquad (5\text{-}2)$$

Writing the ray path, ds, in terms of Y and Z with primes indicating differentiation with respect to Z,

$$\delta \int n(s)[1 + (Y')^2]^{1/2}\, dZ \tag{5-3}$$

Application of the Euler-Lagrange condition gives

$$Y'' = [1 + (Y')^2] \frac{1}{n} \frac{dn}{dY} \tag{5-4}$$

For normally incident light at surface Z_0

$$Y' = - [(n/n_0)^2 - 1]^{1/2} \tag{5-5}$$

where $n_0(Y)$ and $n(Y)$ are the solution refractive indices at Y_0 and at any point (Y,Z) along the ray path respectively.

The integral form of equation (5-5) is

$$W = - \int_{Y_0}^{Y_1} [(n/n_0)^2 - 1]^{-1/2} dY \tag{5-6}$$

where W is the width dimension of the cell.

To traverse the width of the second glass window, T, and the air space to the fiducial plate, D, Snell's Law for a ray at a discontinuity is applied.

$$n(Y_1) \sin\alpha_1 = n_g \sin\alpha_g = n_a \sin\alpha_a \tag{5-7}$$

where α_1 is the angle of the ray as it leaves the solution at plane Z_1, α_g is the angle of the ray in its traverse of the second glass window from Z_1 to Z_2, and α_a is the ray angle in its traverse of the air space from Z_2 to Z_3. Using the trigonometric identity

$$\sin\alpha = \frac{1}{\sqrt{1 + (Y')^{-2}}}$$

to combine equations (5-5) and (5-7) giving

$$Y_3 - Y_1 = \eta_1 Y_1' \left[\frac{D}{\sqrt{1+(Y_1')^2 - \eta_1^2 (Y_1')^2}} + \frac{T}{\sqrt{\eta_g^2 + \eta_g^2 (Y_1')^2 - \eta_1^2 (Y_1')^2}} \right] \qquad (5\text{-}8)$$

where η_1 (shorter form of $\eta(Y_1)$ of equation (5-7)) and Y_1' are the solution refractive index and the slope of the ray, respectively, evaluated at the Z_1 plane. η_g is the refractive index of the glass. Note that Y_1, Y_1' and η_1 are unknowns in equation (5-8).

Equations (5-5), (5-6) and (5-8) are the set of equations which must be solved simultaneously for each ray (i.e. each (Y_0, Y_3) data pair). The solution for each ray yields the albumin refractive index profile for the small region traversed by that ray from Y_0 to Y_1. The solution for many such ray traces gives the profile for the whole polarization layer.

The simultaneous solution of these equations requires numerical methods. The specific numerical approximation used in this work cannot be started from the top of the polarization layer ($\frac{d\eta}{dY} \to 0$) or from the $Z = Z_0$ plane ($\frac{dY}{dZ} = 0$). For the purpose of starting the ray trace in these regions, a less exact relationship between Y_0 and Y_3 (Small Angle Assumption routine) is developed.

B. Small Deflection Angle Simplifications

The Small Angle Assumption (SAA) routine is developed from equation (5-4) with the assumptions of $(Y')^2 << 1$ and the product $\frac{1}{\eta}(d\eta/dY)$ constant when it is evaluated along the ray path. Under these assumptions, equation (5-4) becomes

$$Y'' = \left(\frac{1}{\eta} \frac{d\eta}{dY} \right)_{Z_0} \qquad (5\text{-}9)$$

and with $Y_0' = 0$ for normally incident light

$$Y - Y_0 = \frac{1}{2}\left(\frac{1}{\eta}\frac{d\eta}{dY}\right)_{Z_0}(\Delta Z)^2 \qquad (5\text{-}10)$$

Equation (5-10) can be used to trace the ray across the entire cell width in the regions near the top of the polarization layer. Then $\Delta Z = W$ and

$$Y_1 - Y_0 = \frac{1}{2}\left(\frac{1}{\eta}\frac{d\eta}{dY}\right)_{Z_0} W^2 \qquad (5\text{-}11)$$

Equation (5-11) combined with the small angle version of Snell's Law (i.e. $\sin\Theta \simeq \Theta$) gives the ray trace to the fiducial plate. The ray trace equation is rearranged to allow the refractive index profile to be calculated directly from numerical integration.

$$\frac{d\eta}{dY} = \left(\frac{Y_3 - Y_0}{W}\right)\left(\frac{1}{D+T/\eta_g}\right) \qquad (5\text{-}12)$$

In regions of the polarization layer which are closer to the membrane, the deflection angles become too large to allow the ray trace across the cell to be made entirely by equation (5-11). In these cases, the general deflection equations are used after the ray trace has been started with equation (5-10). The width of the cell over which equation (5-10) is applied, $Z^* - Z_0$, has been determined from considerations of accuracy of the final result, stability of the numerical analysis routine and computation time. It is discussed further in the next part of this section.

The decision as to how large a deflection can be tolerated before the assumptions of small angle are invalid rests with considerations of the accuracy required by the problem and the precision of the measurements of

Y_0 and Y_3. Generally, as is obvious from the assumptions involved, small angle calculations are most faithful to the actual ray path when the working section is quite narrow and the refractive index gradients small.

Interesting suggestions have been proposed directed toward the elimination of some of the ambiguity involved with mixing the two different ray trace schemes used above. One of these proposals would eliminate the use of the small deflection angle ray trace to start the general deflection routine near the Z_0 plane. This method would apply a numerical technique (e.g. Runge-Kutta integration) to equation (5-4) at Z_0, rather than begin a numerical solution of equation (5-5) at Z*. This method has not been evaluated.

A second proposal involves the use of only one of the two assumptions made in the small deflection angle routine as presented above. If it is still assumed that $((1/n)\,dn/dY)$ is constant over the ray path, but Y' is permitted to be any magnitude, equation (5-4) simplifies to

$$Y - Y_0 = -\frac{1}{\left[\frac{1}{n}\frac{dn}{dY}\right]_{Z_0}} \ln\left\{\cos\left(\left(\frac{1}{n}\frac{dn}{dY}\right)_{Z_0} \Delta Z\right)\right\} \qquad (5\text{-}10A)$$

In the most extreme deflection patterns encountered in this experimental work with albumin solutions at low pH, $1/n(dn/dY)$ varies as much as 23% over the path of a single ray. This variation is too large to permit use of equation (5-10A) as a general ray trace representation.

C. Shadowgraph Data Interpretation Program (SDIP)

The development of the ray trace routine (SDIP) was guided by the criterion that the final result must faithfully reproduce an estimated refractive index profile which was computed from theoretical considerations

similar to those of Chapter Four. A membrane surface albumin concentration of 60 gm% was guessed as the highest concentration for which observations would be made. Beginning with a bulk solution concentration of 5 gm%, and using the diffusivity data of Keller et al. (12), an estimated concentration profile was generated using theoretical expressions derived in Chapter Four. The resulting refractive index profile was closely approximated by equation (5-13).

$$\frac{\eta - \eta_{bulk}}{\eta_{membrane} - \eta_{bulk}} = 1 - \tanh 8Y \qquad (5\text{-}13)$$

where Y[=] cm.

This estimated profile gives a maximum refractive index gradient, $\frac{d\eta}{dY} = -.73\ cm^{-1}$, near the membrane surface and a polarization layer thickness (the values of Y for which $\eta = 1.02\eta_B$) of 0.44 cm. These values compare favorably with the most severe profile observed during the experimental program (Experiment 1800, picture 1808) where $\left.\frac{d\eta}{dY}\right|_{max} = -.78\ cm^{-1}$ and the layer thickness was 0.525 cm.

The flow logic of SDIP is separable into four steps. They are given in itemized form, and then are discussed individually. The manner in which the small angle routine and the general deflection theory are integrated to give the complete ray trace calculation scheme divides the polarization layer into the two regions shown in Figure 5-2. The last ray for which the SAA routine is valid across the entire cell width, is shown entering the cell at a height, Y_{SAA}. For rays which enter below the Y_{SAA} height, such as Ray 2 in the figure, the tracing

procedure employs SAA routine to the plane at Z = Z*. From Z = Z* to Z = W, general deflection theory is used to complete the ray trace.

1. SDIP Logic

Step 1 - SAA Starting Routine

(a) Start routine at Y_{oo} where deflection is first detected, j = o and $\eta_{j-1} = \eta_{bulk}$.

(b) Increment Y_o by -0.01 cm and j = j + 1

(c) Compute data $Y_{3,j} = G1*\exp(-G2*Y_{o,j}/S) + Y_{o,j}$

(d) Numerically integrate equation (5-12) using a 4th order Simpson's Rule

$$\eta_{o,j} = \eta_{o,j-1} + \int_{Y_{o,j-1}}^{Y_{o,j}} \frac{[Y_{3,j} - Y_{o,j}]\,\Delta Y}{[W(D + T/\eta_g)]}$$

(e) Evaluate $dY/dZ = (W/\eta_{AVG})(\Delta\eta/\Delta Y)$

If $\left|\frac{\Delta Y}{\Delta Z}\right| \leq \varepsilon_{SAA}$, return to b.

If $\left|\frac{\Delta Y}{\Delta Z}\right| > \varepsilon_{SAA}$, go to Step 2.

Step 2.- Interface

(a) Select last four calculated (Y_o, η_o) pairs from Step 1.

(b) Curve fit with least-squares regression to form the second order polynomial, $P_\eta(y)$

$\eta = P_\eta(y) = a_0 + a_1 y + a_2 y^2$

(c)= Compute Y_1 for the last ray of Step 1 using

$$Y_1 = Y_0 + \left(\frac{1}{\eta}\frac{d\eta}{dY}\right)_{Y_0}\frac{W^2}{2} = Y_0 + \frac{P'_\eta(Y_0)}{P_\eta(Y_0)}\frac{W^2}{2}$$

(d) Compute $\eta_1 = P_\eta(Y_1)$, go to Step 3.

Step 3 - General Deflection Routine

In the following, when refractive index, η at any Y, is shown, it is understood to mean the polynomial $P_\eta(Y)$ is evaluated at that Y.

(a) Compute

$$Y'_1 = -\left[(\eta_1/\eta_0)^2 - 1\right]^{1/2} \quad \text{and}$$

$$Y_{3,C} = Y_1 + \eta_1 Y'_1\left[\frac{D}{\sqrt{1+Y'^2_1 - \eta_1 Y'^2_1}} + \frac{T}{\sqrt{\eta_g^2+\eta_g^2 Y'^2_1-\eta_1 Y'^2_1}}\right]$$

(b) Compare calculated $Y_{3,C}$ with data $Y_{3,D}$

If $\left|Y_{3,C} - Y_{3,D}\right| > \varepsilon_\eta$, add a correction to η_1, the sign and magnitude dependent on sign and magnitude of deviation, return to a.

If $|Y_{3,C} - Y_{3,D}| \leq \varepsilon_\eta$, go to c.

(c) Add the new data pair (η_1,Y_1) to the set (η_i,Y_i) where i is a maximum of 21.

(d) Curve fit the new data set (η_i,Y_i) to form the new second order polynomial, $P_\eta(Y)$.

(e) Re-evaluate Y_1 - integration routine (VINT); for the region Z_0 to Z*, use small angle form

$$Y^* = Y_0 + \left(\frac{1}{\eta}\frac{d\eta}{dY}\right)_{Y_0} \frac{(Z^* - Z_0)^2}{2}$$

for the region Z* to Z_1, use a fourth order Runge-Kutta with step size of W/100 for the exact ray trace equation

$$Y' = -\left[(\eta/\eta_0)^2 - 1\right]^{1/2}$$

(f) Compare $Y_{1,new}$ with old $Y_{1,old}$

If $|Y_{1,new} - Y_{1,old}| > \varepsilon_Y$, return to a. with $Y_{1,new}$

If $|Y_{1,new} - Y_{1,old}| \leq \varepsilon_Y$, go to g.

(g) Replace the Y_1 component of the data pair (η_1, Y_1) of part c. with the $Y_{1,new}$ of part e.

(h) Curve fit the new data set (η_i, Y_i) to form a new second order polynomial, $P_\eta(Y)$, go to Step 4.

Step 4.- Proceed to next ray trace, check for exit.

(a) Increment Y_0 by -0.001 cm

(b) Compute new η_0 and Y_3

$$\eta_0 = P_\eta(Y_0)$$

$$Y_{3,D} = G1*\exp(-G2*Y_0/S) + Y_0$$

(c) Update (η_i, Y_i) data set

If $i \leq 19$, add new (η_0, Y_0) to data set

If $i = 21$, drop two oldest pairs (η, Y),

add new (η_0, Y_0) to data set

(d) Estimate $Y_{1,new} = Y_{0,new} - (Y_{0,old} - Y_{1,old})$

(e) Check if $Y_{1,new}$ is below membrane

If $Y_{1,new} > 0$, return to Step 3.

If $Y_{1,new} \leq 0$, call END

2. Discussion of Step 1.

In Figure 5-2, Y_{oo} is the top of the polarization layer, the height above the membrane at which the ray tracing begins. The height at which each new ray enters the cell, $Y_{o,j}$ is calculated by subtracting 0.01 cm from the incoming height of the previous ray, $Y_{o,j-1}$.

For a ray which enters at $Y_{o,j}$, its corresponding position at the fiducial plate, $Y_{3,j}$, is computed by equation c. This equation is used to describe the deflection data of the photographs. The data reduction methods to obtain this equation, and justification for this functionality are described in Section IV. Briefly, G1 and G2 are constants, resulting from regressions fits to the photographic deflection data. S is the slope of the undeflected wire with respect to the membrane surface.

For each new increment, j, the data pair $(Y_{0,j}, Y_{3,j})$ are used to calculate a new refractive index $\eta_{0,j}$ by equation d. This equation

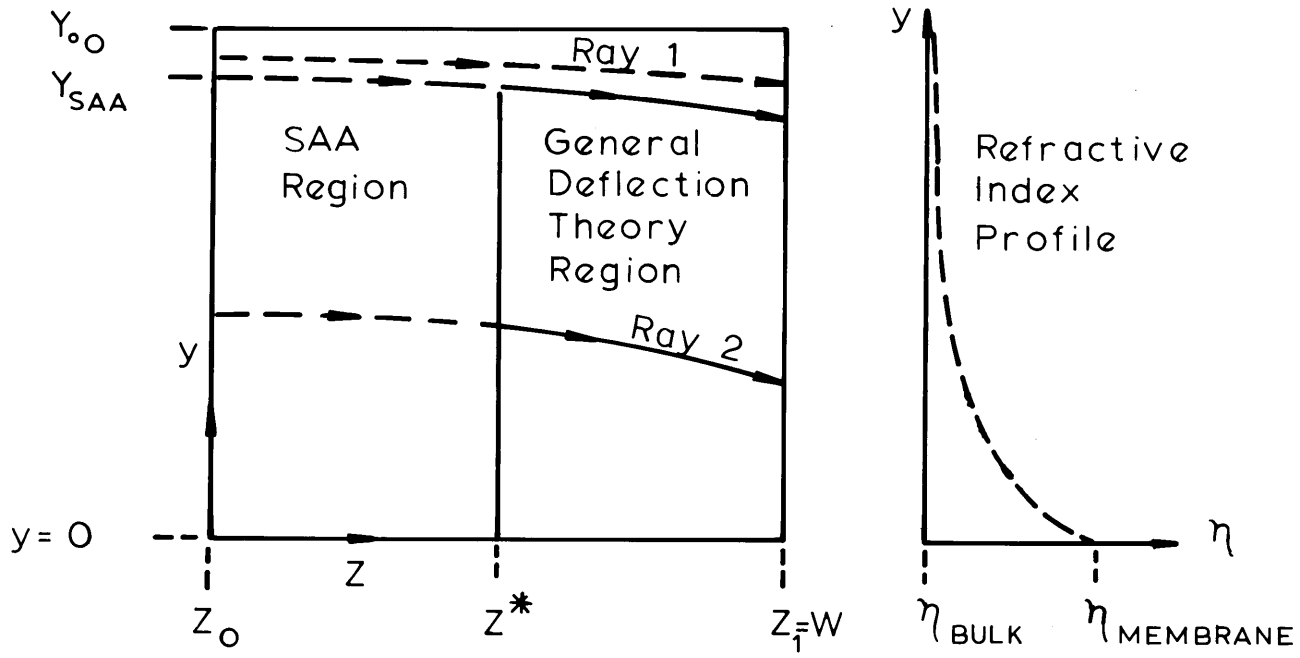

Figure 5-2 Ray Trace in Polarization Layer Showing Integration of Small Deflection Angle Tracing (SAA) with General Deflection Theory Tracing

is a fourth order Simpson's Rule numerical integration applied to the small angle assumption ray trace equation (5-12). Ray 1 of Figure 5-2 is an example of a ray traced by the SAA routine.

The process is continued until some value of $Y_0 = Y_{SAA}$ is reached where the slope of a ray, $dY/dZ \sim \Delta Y/\Delta Z$ exceeds an upper limit ε_{SAA}. Since the use of the SAA routine to evaluate the profile of the entire polarization layer introduced an error of only 10% at the membrane surface for the profile of equation (5-13), an absolute value for Y_{SAA} was not the major determinant for establishing ε_{SAA}. The most significant criterion for this parameter was the amount of instability which it passed to the General Deflection Routine of Step 3. This instability was transferred by the small (but accumulating) errors in the trajectory of $\eta = \eta(Y)$. A secondary factor for the determination of ε_{SAA} was the desire to reach a low enough value of Y_{SAA} so that Step 3 could begin interpolation between (Y_0, Y_1) pairs as quickly as possible. Since the SAA routine does not explicitly compute a value of $Y_{1,j}$ for each new ray, an arbitrary trial and error process had to be used in the development of SDIP to find the value of Y_{SAA} for which this was true. In this way, within a few calculations after leaving the SAA routine, each new value of $Y_{0,i}$ selected for ray tracing in Step 3 lies between the previous ray trace $(Y_{0,i-1}, Y_{3,i-1})$ pair for which the refractive index profile has already been determined.

The range of values for ε_{SAA} which best compromised the competing incentives was found to be 0.008 to 0.01, or deflection angles of .4 to .6 degrees at plane Z_1.

3. Discussion of Step 2.

The interface between the region of small angle ray tracing above Y_{SAA} and the region of Step 3 which uses both small angle and general deflection theory tracing has two functions. The last four rays for which η_0 has been found in Step 1 are curve fitted to a second order polynomial, $P_\eta(Y)$, by least-squares regression. This polynomial, and its derivative, are then used to provide initial estimates of Y_1 and η_1 for the ray entering at the Y_0 for which ε_{SAA} was exceeded in Step 1. These estimates are the starting values for the General Deflection Routine.

4. Discussion of Step 3.

Part(a)completes the ray trace from the plane Z_1 to the fiducial plate Z_3 by application of equations (5-5) for Y_1' and (5-8) for $Y_{3,calculated}$. The ray for which this calculation is made, enters at Y_0. This value has been selected in either Step 1 or Step 4 and is a constant throughout this step. Its corresponding location on the fiducial plate, $Y_{3,data}$ has also been transferred into Step 3 from either Step 1 or Step 4.

Part(b) compares the calculated $Y_{3,C}$ of part(a) with the data value, $Y_{3,D}$. If this difference falls within some distance tolerance, ε_η, the computation passes to part(c). If the difference is greater than ε_η a small correction is applied to the refractive index profile by making a small correction to the refractive index of the solution at the solution/glass window interface, the Z_1 plane. A new $Y_{3,C}$ is computed by part(a). and the ($Y_{3,C}$, $Y_{3,D}$) comparison repeated.

The sign and magnitude of the correction to η_1 is a very sensitive operation. They depend primarily on whether $Y_{3,D}$ is above or below the membrane, the magnitude of the last difference, $|Y_{3,C} - Y_{3,D}|$, and Y_0. The size of the correction is variable and ranges from 10^{-3} to 10^{-6} R.I.U.

Part (a) - part (b) is the innermost iterative sequence of Step 3, converging on the best η_1 for a given Y_1. Part (a) - part (f) is the outermost iterative sequence converging on the best Y_1 for a given $(Y_0, Y_{3,D})$ pair. Although not unrelated, the process might also be viewed as one in which the outer loop adjusts the location of the ray at Z_1, that is Y_1, while the inner loop adjusts the slope, Y_1'.

Part (c) adds the new data pair (η_1, Y_1) from part (b) to a data set, (η_i, Y_i). The size of this data set is i = 21 and is controlled in Step 4. This size was arrived at by trial and error. It holds $P_\eta(Y)$ rigid enough to keep the iterative schemes stable and yet retains sensitivity to the small corrections to η_1.

Part (d) executes a new curve fit using the current data set of part (c) thereby updating $P_\eta(Y)$.

Part (e) is a new ray trace through the solution, for the purpose of obtaining an improved Y_1. It starts the ray trace at plane Z_0 with the small angle equation. It takes the ray trace along this second order path to a specified width Z*. At these values of Z* and Y*, a fourth order Runge-Kutta method is applied to the general deflection equation (5-5). The solution of this equation gives a $Y_{1,new}$ at $Z_1 = W$.

Part (f) compares $Y_{1,new}$ with the former value, $Y_{1,old}$. If the difference between these values of Y_1 is not within a specified tolerance, ε_Y, $Y_{1,new}$ is passed back to part (a) and the calculations repeated. If the tolerance is met, the value $Y_{1,old}$ is replaced by $Y_{1,new}$ in the data

set (n_i, Y_i) by part(g). Part(h) updates the polynomial $P_\eta(Y)$ with the revised data set and passes it to Step 4 where a new ray is designated for tracing.

5. Discussion of Step 4.

The increment for decreasing Y_0 is .001 cm, one-tenth of the size used in the SAA routine of Step 1. The smaller step size ensures that for 98-100% of the ray tracing done in Step 3, the new ray is started at a height greater than the exit heighth, Y_1, of the ray preceding it. Therefore a fraction of each new ray trace always involves some interpolation of the polynomial $P_\eta(Y)$. The fraction of interpolated ray trace increases for those rays traced closest to the membrane.

In part(b), a refractive index is computed at the new Y_0 using the most current version of the polynomial $P_\eta(Y)$. From the deflection data correlation, the $Y_{3,D}$ corresponding to the new Y_0 is computed.

It will be pointed out in Section IV that photographic deflection data could not be obtained for heights above the membrane of less than 0.020 cm. Therefore, for those cases where Y_0 (or the Step 3 calculated Y_1 corresponding to this Y_0) is less than 0.020 cm, it is understood that the exponential equation of part(b) is extrapolated beyond the limit where actual data existed.

Part(c) manages the (n_i, Y_i) data set. Part(d) estimates the height of the new ray at the $Z_1 = W$ plane by assuming that it will decrease while passing through the solution by the same amount as its predecessor. This estimated Y_1 begins a new ray trace cycle in Step 3 if the comparison of part(e) does not indicate that the membrane has been reached.

6. Discussion on the Selection of ε_η, ε_Y and Z*.

The values of the tolerance in the iteration schemes of SDIP are strongly dependent on each other. This interaction is discussed with the aid of Figure 5-3 which shows a presumed true ray path and the numerical solution of an approximate ray trace representation. For clarity, the glass windows are not shown.

The value of ε_η is determined from an estimation of the accuracy of locating a point on the fiducial plate. Although a single reading on this plate can be made to an accuracy of 0.001 cm, the accumulated errors in transforming these measurements to the ray trace coordinate system, give this precision an estimated upper limit of 0.005 cm. This is the value given to ε_η.

The values of ε_Y and Z* are interactive not only with each other and ε_η, but also with the size of the corrections to η_1 in Step 3. They also significantly affect computation time. The ray trace from Z_1 to Z_3 is slightly influenced by Y_1, but greatly influenced by the slope of the ray at Z_1. Therefore, the choice of the tolerance ε_Y, within which successive approximations of Y_1 must converge, is far more influenced by equation (5-5) than (5-8). From a consideration of these equations simultaneously, and using the profile of equation (5-13), the ratio $\varepsilon_Y/\varepsilon_R$ was estimated to be 0.01 if convergence was to be assured for the most severely deflected rays. This ratio sets $\varepsilon_Y = 5\text{x}10^{-5}$ cm.

The fourth order Runge-Kutta approximation of equation (5-5) cannot be started at $Z = Z_0$ for normally incident light ($\eta = \eta_0$). The small angle form of the ray trace is therefore employed for the starting region $Z_0 \rightarrow Z^*$. At Z*, an error, Δ, exists between the SAA ray trace approximation and the true path of the ray. This error in ray position,

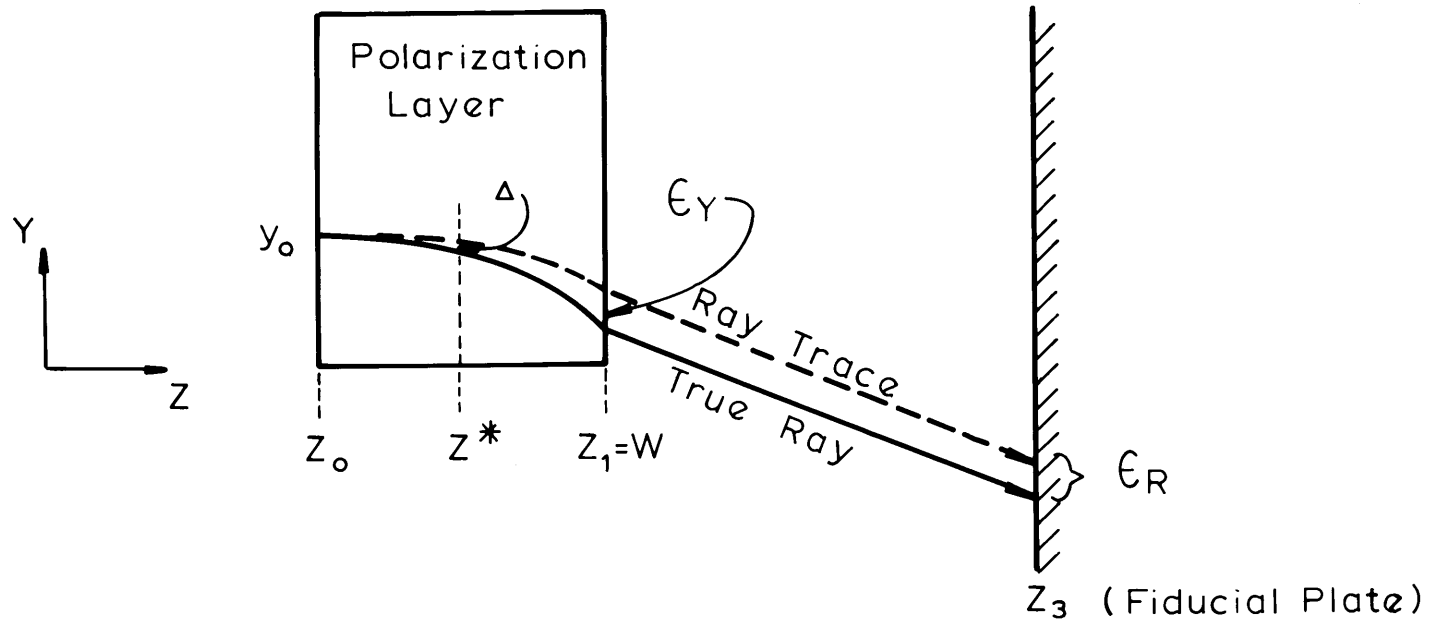

Figure 5-3 Interactions of SDIP Tolerances

and its influence on ray slope at Z*, are carried through the general deflection ray trace from $Z^* \rightarrow Z_1$ to ultimately influence Y_1. Logically then, it would appear that Z* should be a small fraction of the distance $Z_0 - Z_1$. A subtle feed back mechanism however, results in the choice of fairly large values for Z*. The feedback involves the fact that the iterations of the ray trace approximations are evaluated, and corrected, at the Z_1 plane. These corrections are then fed back to the start of a new ray trace approximation via the polynomial $\eta = P_\eta(Y)$. This process is a source of significant instability in the numerical approximation of equation (5-5), where the ratio η^*/η_0 is squared. For this reason, convergence is not possible for $Z^* < .3W$, when tested on the profile of equation (5-13) at the η_1 correction level of 10^{-7} R.I.U. At the other extreme, when $Z^* > .9W$, a level is reached in the polarization layer where the tolerance ε_η cannot be met. The intermediate value of Z* = 0.5W is found to be the best compromise between computation time and the error (1%) of the membrane surface concentration evaluated for the profile of equation (5-13).

D. Corrections for Nonparallel Glass Windows

The observation was made early in the experimental program that the glass windows of the cell were wedge shaped, with maximum width at the point of contact with the membrane. The effect was small, but measurable and therefore was taken into account for the ray trace calculations.

The angle with respect to the normal of the membrane surface of the front window was determined to be $\alpha_F = .0012$ radians and for the back window, $\alpha_T = .0016$ radians. The cell width now becomes a function

of Y_0, with W_m the width at the membrane.

$$W = -(\alpha_F + \alpha_T)Y_0 + W_m \tag{5-14}$$

Also, where the membrane surface is taken to be parallel to the incident beam, equations (5-5) and (5-6) become

$$Y' = -\left[(n/n_0)^2(P_0^2 + 1) - 1\right]^{1/2} \tag{5-15}$$

$$W = -\int_{Y_0}^{Y_1} \left[(n/n_0)^2(P_0^2 + 1) - 1\right]^{1/2} dy \tag{5-16}$$

where P_0 is the angle of the ray in the solution, evaluated at the front window/solution interface, Z_0. With the assumptions that the angles involved are small, the variation of P_0 with solution refractive index (i.e. n evaluated at Y_0 for each ray) is

$$P_0 = \alpha_F(1 - 1/n_0) \tag{5-17}$$

Equation (5-8) is modified by replacing the Y_1' terms with the sum $(Y_1' + \alpha_T)$. This modification to the refraction involving the second glass window was found significant only for the most deflected rays dealt with in the General Deflection Routine ray trace. The small angle tracing for $Z_0 \rightarrow Z^*$ was corrected by modifying equation (5-10) to

$$Y - Y_0 = \frac{1}{2}\left(\frac{1}{n}\frac{dn}{dY}\right)_{Z_0}(\Delta Z)^2 + \alpha_F \Delta Z \tag{5-18}$$

The concentration profiles were only slightly affected by these changes to the ray trace equations of parts A and B. In the evaluation of Experiment 300, membrane surface concentration was decreased by about 4%, with 95% of this change resulting from the inclusion of equation (5-14) into the ray trace calculations.

II. Experimental Apparatus

The description of experimental apparatus focuses on three principle features: the ultrafiltration cell, the integrated optical and flow measuring systems, and the low volumetric flow measuring device (LFD).

A. Ultrafiltration Cell

1. Design

The ultrafiltration cell (Figure 5-4) is fabricated from two pieces of Invar. The top half consists of a narrow chamber into which has been mounted optical glass plate (fused silica, $\eta_{6328\text{Å}} = 1.4570$, $\lambda/4$ flatness, 4.7625 mm in direction of optical path). The aperture of the windows is 19 mm square. The width of the solution cavity between these flats is 3 mm. The height of the cavity is 24 mm from its point of contact with the membrane.

The selection of Invar was based on its good compatibility with fused silica in terms of thermal expansion ($\alpha_{silica} = 5.6 \times 10^{-7}\ °C^{-1}$ vs. $\alpha_{invar} = 8 \times 10^{-7}\ °C^{-1}$). Machining operations on the glass-metal composite required that this compatibility be as close as possible. Also important was Invar's high saline corrosion resistance ($\sim$.13 mm per year). In spite of this high resistance, it was necessary to epoxy coat the semi-smooth inner surfaces of the metal portions of the cavity.

The bottom half contains a shallow (3.2 mm) depression of length (50.8 mm) and width dimensions which match the top piece. The membrane surface area is 1.524 sq.cm. A ceramic (Tegraglas, 3M Co.), incompressible membrane support is impressed into this cavity. The bottom surface of the cavity drains, at a 2° slope, to a 1/16" dia. port.

FIGURE 5-4 ULTRAFILTRATION CELL

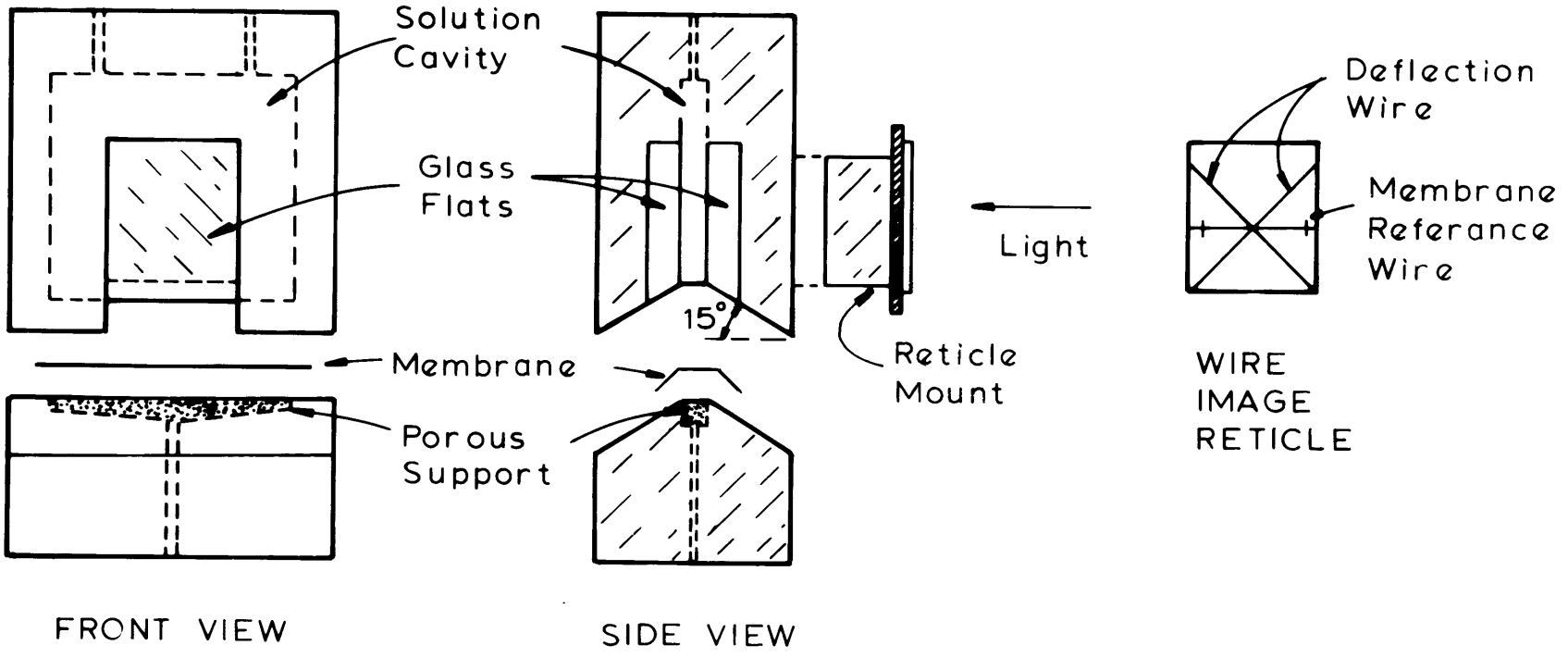

The membrane is placed between these two pieces. The matching surfaces of the two pieces are sloped at 15° from the horizontal in order to allow the most deflected rays at the membrane surface to pass unhindered. With this design, we are theoretically capable of measuring concentrations at the membrane surface when deflection angles are less than about 15°.

A small radius on the glass edges which contact the membrane prevents chipping at this important stress point of the glass. However, this radius is disadvantageous since it limits the minimum viewing distance above the membrane to 0.020±.003 cm.

The wire image reticle is formed by inscribing very straight thin lines, 150 microns thick, on a piece of glass. These lines were used because real wires (300 micron diameter) could not be made sufficiently straight. However, throughout the discussion, these lines will continue to be referred to as 'wires', mostly for reasons of historical precedent. The diffraction limitations of the image formed by the coherent laser beam established the 150 micron thickness. Thinner lines resulted only in decreased image contrast with little or no improvement in resolution.

Two of these wires are at approximately 45° to the membrane surface and appear in the deflected beam. The third wire is horizontal, and used to reference the location of the membrane. The glass reticle is cemented to a metal mount which is fitted to the front surface of the cell.

2. Performance

Nonparallelism between the cell windows and birefringence of the glass when placed under stress were nonidealities of the cell performance

which were not accounted for in its initial design.

Measurements on the surfaces of both glass apertures (front referring to window through which beam enters the solution) were made with a Cleveland Electronic Depth Gage at a precision level of ±.0001 cm (1 micron). Results are shown in Figure 5-5. With respect to a plane which is normal to the membrane surface, the mapping of the window surfaces revealed that while the windows were in near perfect parallelism across the aperture width (dimension into the plane of paper on figure), a significant wedge effect existed in the height dimension. This wedge could be the consequence of either slight errors in the fabrication of the metal surfaces to which the windows were mounted, or errors in the mounting/cementing process, or a slight yield in the glass/cement/metal bond when the cell was placed under stress for the first time. The results of the wedge measurements, with respect to the ray trace coordinate system, permitted computation of the angles α_F and α_T.

The two halves of the cell, with the membrane between them, were clamped together by a brace to obtain a seal around the membrane. An unfortunate consequence of this clamping process is the introduction of uneven stress patterns in the glass windows. This uneven stress distribution results in refractive index differences throughout the glass (birefringence). If the birefringence occurs in areas of the glass where light is non-normal to the surface, the refraction patterns transmitted by the glass will be different from areas without birefringence. These relative differences in refractive index can be observed by the use of plane polarized light.

Following Experiment 1200, the stress patterns which existed during Experiments 1100 and 1200 (clamping brace unchanged between experiments)

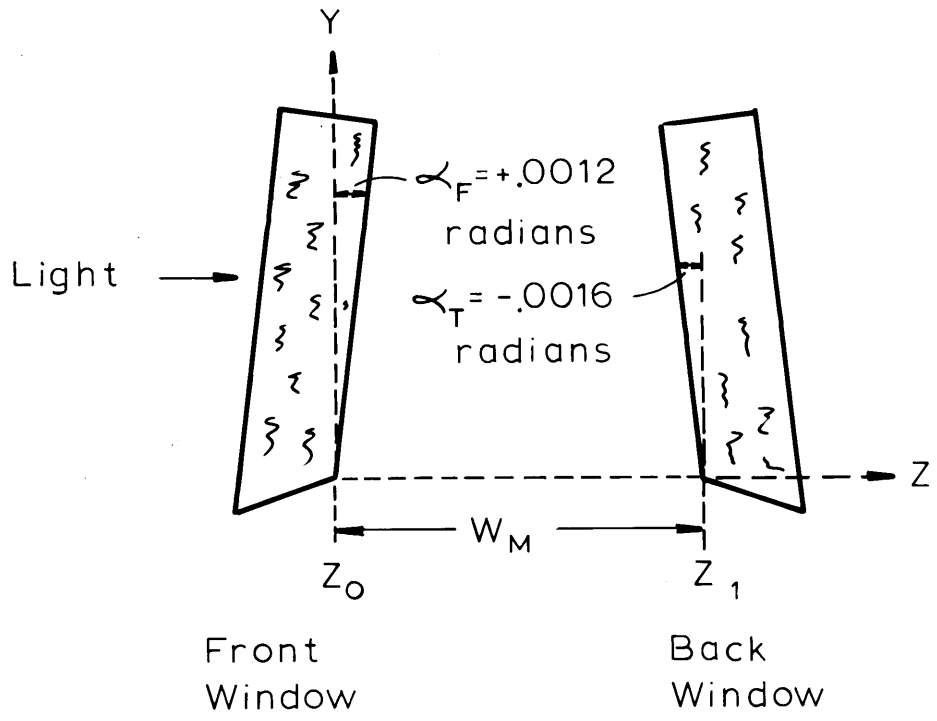

Figure 5-5. Ultrafiltration Cell Wedge Effect
W_M = 0.3144 cm.

were observed using plane polarized light from the expanded laser beam. Photograph P1 of Figure 5-6 shows the cell aperture when the plane polarizing filter is fixed in the beam for maximum transmission. Photograph P2 reveals the composite stress pattern of both windows when a polarizing filter, placed behind the cell, is crossed by 90° to the plane polarized beam of Photo P1. Relative birefringence is seen to exist in the areas where light is transmitted through the crossed-polarizer; namely in upper left corner, along the bottom half and along much of the right side of Photo P2. The diffraction lines in the upper left corner are caused by scratches in the polarizing filter.

Since Wire 1 intersects the membrane in the light area of the lower left corner, and Wire 2 in the dark area of the lower right corner, it is evident that some assymetry will exist between the deflection images of these two wires.

The stress pattern was found to respond only to changes made in the amount of force applied by the clamping brace. When the brace was completely released, only a small area of transmitted light in the upper right corner was observed. This indicated that most of the cell aperture was inherently homogeneous in refractive index.

Photograph P3 shows the stress pattern which was present for a new cell/membrane setup prior to running Experiments 1300, 1400 and 1500. In this setup, the clamping brace was tightened the minimum amount to obtain a seal around the membrane at 10 psig applied ultrafiltration pressure. The photo reveals that the birefringence was a minimum over the aperture area.

Photograph P4 is the same cell/membrane setup as that of Photo P3, except the clamping brace has been tightened to provide a membrane seal

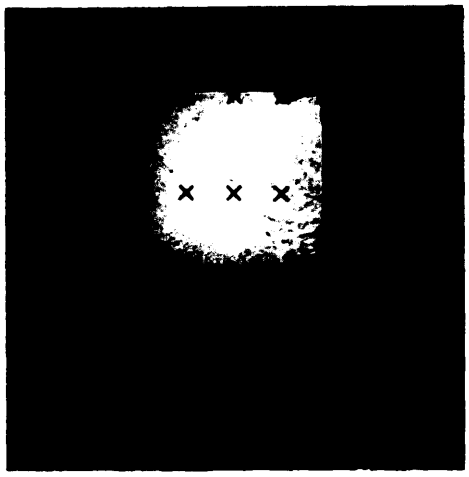

P1- WITHOUT PLANE POLARIZED LIGHT

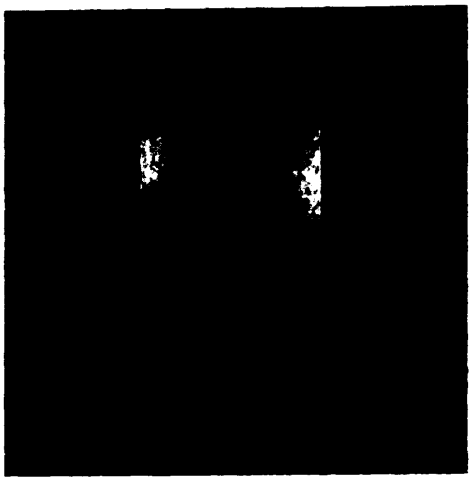

P2-STRESS PATTERN FOR EXPERIMENT 1100

P3-STRESS PATTERN FOR EXPERIMENTS 1300-1500

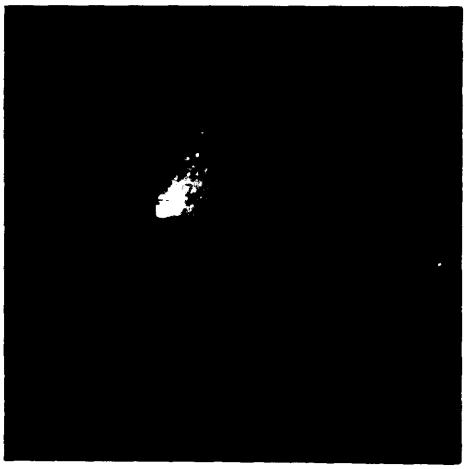

P4-STRESS PATTERN FOR EXPERIMENTS 1600-1800

FIGURE 5-6 STRESS PATTERNS IN WINDOW

at 40 psig applied pressure. The photo shows the refractive index of almost the entire aperture has shifted to permit most of the plane polarized light to pass the crossed filter. Only a small area of darkness exists in the lower right corner where Wire 2 intersects the membrane.

B. Overall Layout - Optical Components

The layout of the experimental apparatus is shown in the Figure 5-7 schematic. The ultrafiltration cell is shown mounted in a clamping brace which is attached to an optical bench. This bench in turn rests on a heavy stone slab under which is placed a foam rubber mat.

The cell is connected to a saline makeup reservoir. This reservoir is pressurized from a cylinder gas supply with a precision gage used for monitoring pressure (± .05psi). The cell is filled with protein solution through plastic hypodermic tubing which is inserted through the drain valve, down one leg of the saline feed line, to the membrane surface.

The light source is a 15 milliwatt Helium-Neon laser which emits a narrow, coherent beam of light at 6328Å wavelength. A beam expander collimates and expands the laser beam to a 45 mm diameter which illuminates the 19 mm square aperture of the cell.

The image of the reticle pattern is projected through the ultrafiltration cell onto the surface of a glass plate. The front surface of this plate is inscribed with carefully positioned fiducial marks. This accurate two-dimensional grid serves to eliminate the variable effects (e.g. magnification differences, film tilt, film warpage, etc.) involved with the photographic process. The positions of these fiducials are

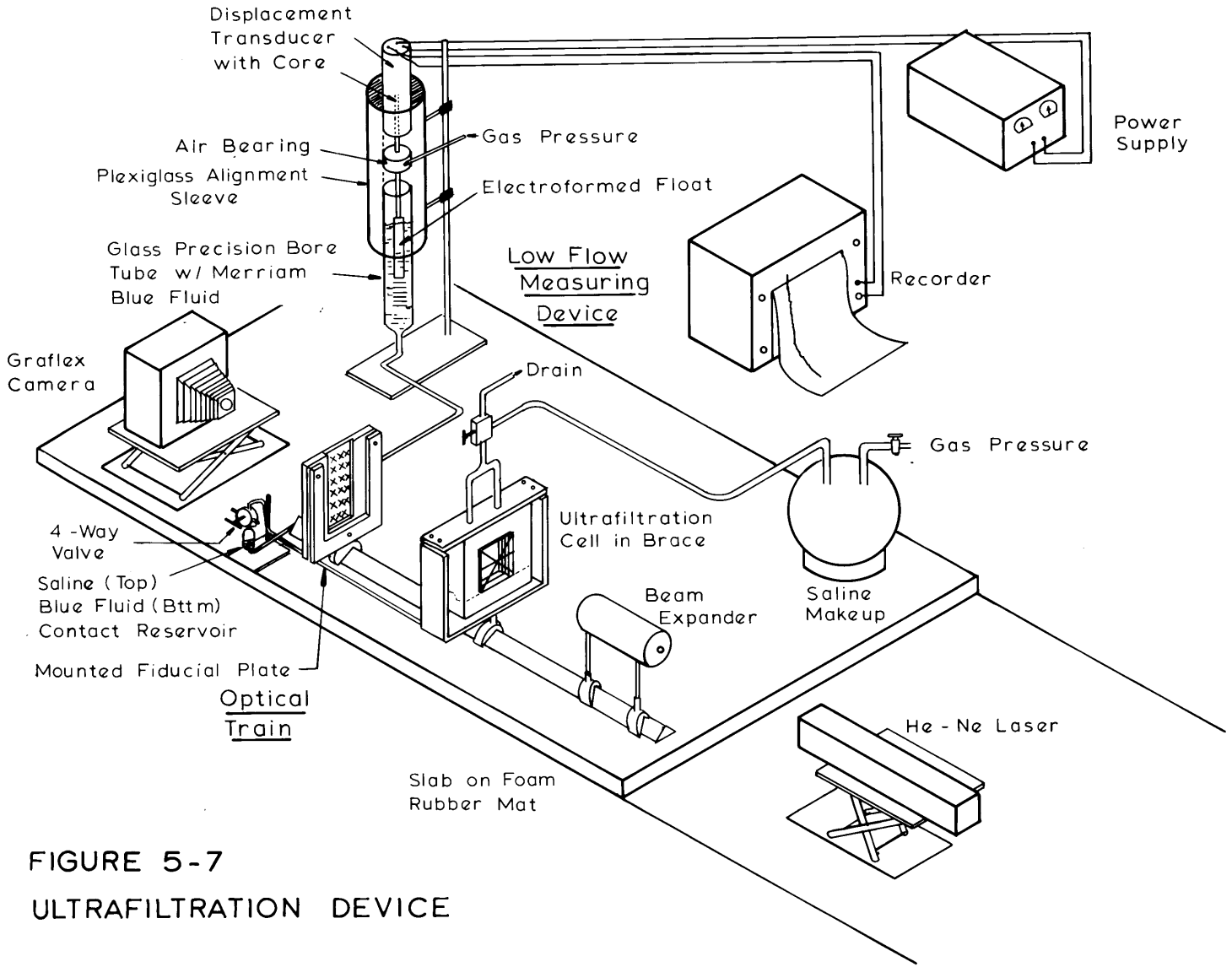

FIGURE 5-7

ULTRAFILTRATION DEVICE

known to an accuracy of about .014 mm. These fiducials were calibrated using the same Itek Hand Measurement Machine technique which was used for photograph evaluation. The technique is discussed in Section IV and the plate design and calibration data are presented in Appendix C.

At the fiducial plate, light intensity variation over the length of the deflection image can reach two orders of magnitude. The brightest region is always at the top of the pattern. This variation results primarily from the effect of spreading the incident light over increasingly larger areas (on the fiducial plate) when the refractive index gradient becomes severe. A secondary factor is the fact that concentrated albumin solutions may transmit only 50% as much light as dilute solutions. Transmission data for albumin solutions is given in Appendix B. For best photographic results, this intensity variation is smoothed by the use of combinations of optical neutral density filters. In order to prevent refraction errors due to the placement of these filters in the deflection beam path, the filters were mounted along a curved track fabricated onto the front surface of the fiducial plate mount (detail not shown on Figure 5-7). Figure 5-8 shows a vertical section of the mount and light filters. The curvature of this track was designed to maintain the light filters continuously normal to the deflected beam.

In the running mode, a Graflex camera is focused through the fiducial plate onto its front surface using incandescent illumination of that surface. The image on the plate is recorded on Polaroid, Type 55 P/N, positive/negative sheet film (ASA 50).

In order to arrive at the running mode setup depicted in Figure 5-7, several important, sensitive operations must be performed. The unexpanded laser beam (3.5 mm diameter) is first aligned to project in

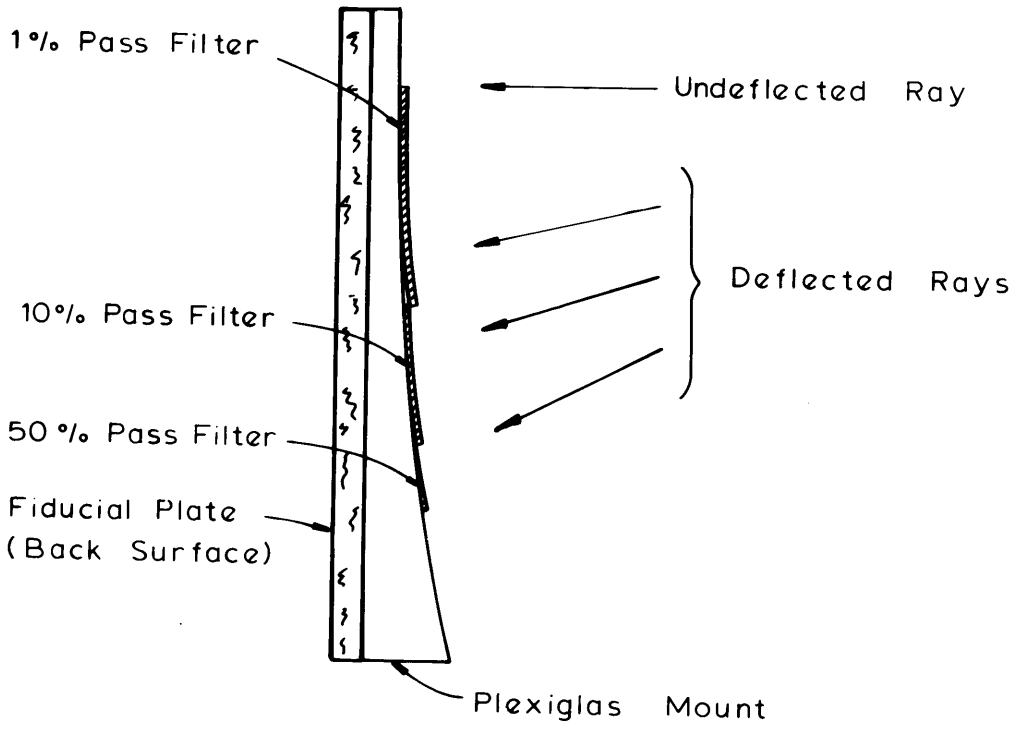

Figure 5-8: Light Filter Placement on Fiducial Plate Mount

a plane of constant gravity. This is done by suspending a thin wire plumb line above the optical bench. The diffraction pattern from the wire is then made to intersect the laser cavity at the same point from which the incident is emitted by the laser. This is achieved by adjusting the tilt and level of the laser body.

After the membrane conditioning procedure (described in Section III), with the ultrafiltration cell fixed to the optical bench with its clamping brace, the cell windows are aligned prependicular to the unexpanded beam using the technique of auto collimation. By this technique, the windows are oriented, using the several available adjustments on the optical bench, so that the narrow laser beam, incident on the front window, reflects back exactly upon itself. Since the two windows were slightly wedged, perfect autocollimation was unattainable. Since each window caused a slightly non-normal reflection, one reflection slightly above the incident beam and the other slightly below, this problem was circumvented by equating the distances by which these two secondary reflections were offset from the primary reflection and incident beam, the latter two being superimposable. The resultant error caused by this slightly less than perfect alignment was less than 0.001 cm for an image point measured at the fiducial plate.

The wire image reticle (see Figure 5-4) and its mount are then fitted to the cell and aligned by autocollimation.

Membrane location with respect to the horizontal wire of the reticle pattern is now established. As a result of diffraction limitations, this membrane location must be established by non-photographic methods. With the camera and fiducial plate removed, a cathetometer (0.001 cm subdivisions, Gaertner Scientific Corp.), approximately in the position of the

camera, is aligned to the ultrafiltration cell. The lenses of the cathetometer serve as reflecting surfaces for autocollimation. After alignment, the cell and wire reticle are illuminated with incandescent light and cathetometer measurements made as discussed in Section III.

After the cathetometer is removed, the fiducial plate is placed in position on the optical bench. Because the frosted front surface of this plate disperses incident light, a mirror is temporarily clamped to the front surface of the plate to serve as an autocollimating surface.

Lastly the beam expander is centered in the system by using a convex lens, which has been autocollimated, between the cell and the expander. With the expander aligned to give maximum intensity of the expanded beam, final adjustments to expander orientation are made until the convex lens brings the expanded beam to a focus on the previously established center line of the system.

The total experimental program was carried out over a temperature range of 25-27°C. Room temperature was controlled with a circulating fan and a room space heater. The heater was controlled from a thermistor with a proportional controller. Additional experimental improvements included wrapping the cell brace in a film of Saran to minimize heat transfer to the cell.

C. Low Flow Measuring Device

Figure 5-7 shows a device for continuously monitoring the ultrafiltrate yield from the cell. A more complete schematic is shown in Figure 5-9.

This Low Flow Measuring Device operates on the bouyancy principle

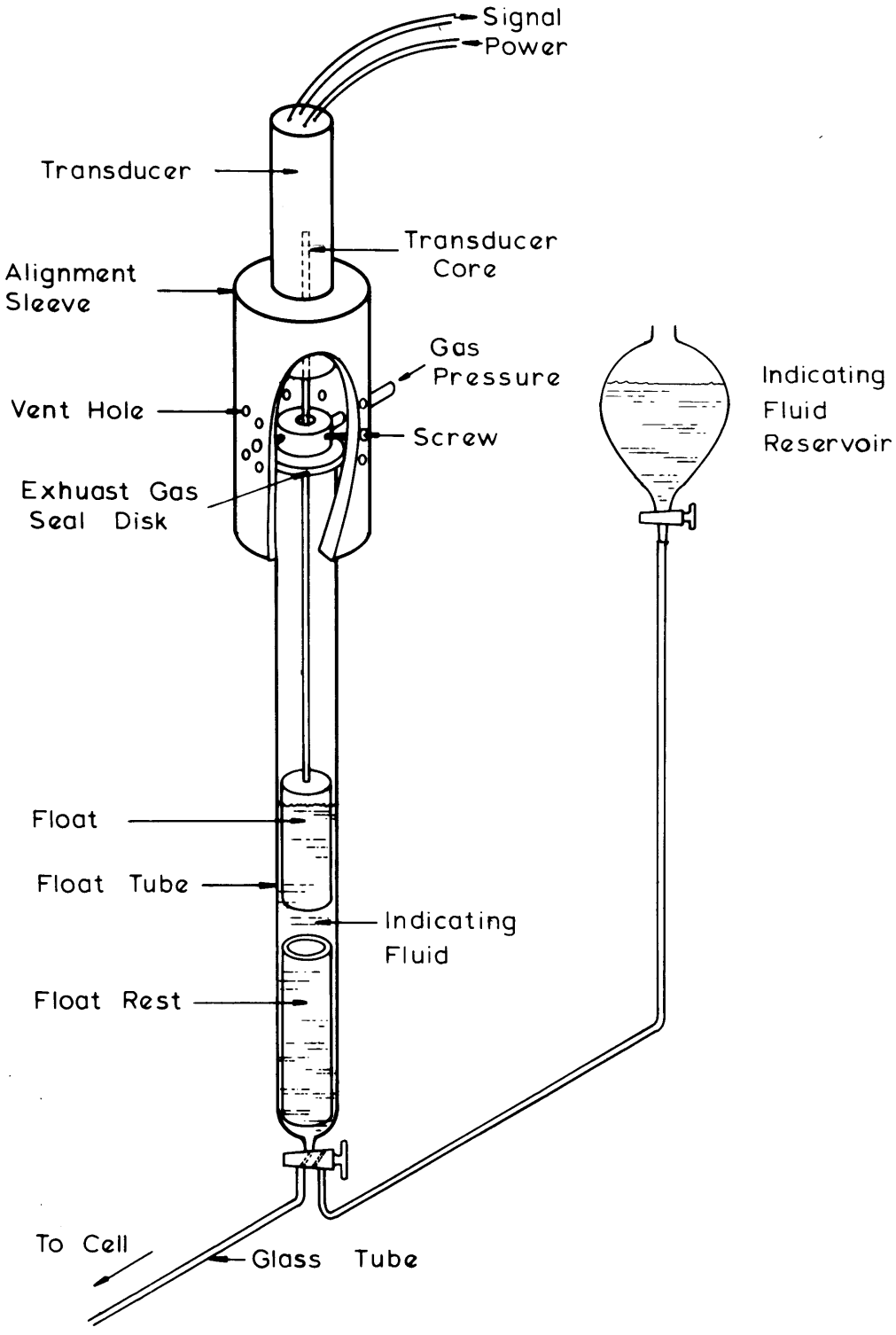

Figure 5-9: Low Volumetric Flow Measuring Device (LFD)

whereby the rise in a liquid level is monitored by a change in the signal of a sensitive displacement transducer. A very light electroformed Nickel float (0.250"O.D. x 4 1/4") supports the core element of the transducer. These two elements are joined by a precision machined, hollow aluminum shaft (0.1248"O.D.). The three pieces are bonded with epoxy. The entire assembly is 10 inches long and weighs 5 grams.

Alignment of the precision bore glass float tube (0.3750 ± .0004" I.D. x 20") and the transducer body is maintained with a plastic sleeve. The alignment of the delicate shaft assembly is maintained with a frictionless air bearing. The air bearing position is established by means of three set screws which permit radial alignment of the core inside the transducer.

The air bearing was found to operate best at 20 psig gas pressure (Prepurified N_2 cylinder source). The bearing exhaust was by means of vent holes in the plastic sleeve, above and below the bearing position. The fluid level in the float tube below the bearing is sensitive to large changes in the exhaust gas pressure. For this reason, and to prevent excessive evaporative losses from the float tube, a plastic sealing disk is positioned above the tube. A clearance hole in the center of this disk permits free movement of the shaft.

The float tube is filled with Meriam Blue manometer indicating fluid (#D-8325, Meriam Instrument Co.) which is characterized by high density (1.75 SpG), low vapor pressure (.05 mmHg @ 25°C) and low solubility with water (0.1 gr/100 gr H_2O). It is also highly miscible with many organic solvents and permeates most polymeric tubing. Nonaqueous stopcock greases must be used. Fluid level movement due to evaporation is estimated to be about 1×10^{-6} cm/min.

The indicating fluid extends into the glass tube which joins the float tube to a four way valve through a small reservoir. In this reservoir, the indicating fluid contacts the saline ultrafiltrate coming from the ultrafiltration cell. A reservoir for repositioning the liquid level between experiments is also attached to the float tube. When emptied, the float shaft assembly rests on a short length of glass tubing which is positioned at the bottom of the float tube prior to assembly.

The transducer output as a function of elapsed experimental time is recorded. This transducer output signal (-1 inch to +1 inch equivalent to -18 volt to +18 volt) is zeroed arbitrarily by use of a reverse polarity bias voltage. Critical variables which effect performance are room temperature (±0.1°C) and transducer excitation voltage (24.00 ± .02 volts). The responses of the LFD to changes in these variables were measured. For temperature, per degree Centigrade increase, the LFD level increased 9.3×10^{-3} ml. For excitation voltage, per volt increase, the LFD level appeared to decrease 3.3×10^{-2} ml.

Duplicate calibrations near the range of use were made with a Harvard pump. The calibrations, which were in excellent agreement, were for total liquid level changes of 0.724 ml, and were valid for only one alignment of the transducer with the shaft. Each calibration involved two flow rates, a high 5.25×10^{-3} ml/min and a low, 5.52×10^{-4} ml/min. The respective rates of float level change were 3.7×10^{-3} cm/min and 3.9×10^{-4} cm/min. The results of the calibration were nonlinear with a range of .14 ml/volt to .09 ml/volt. The lowest detectable flow is about 1×10^{-5} ml/min, and flow rates around 2×10^{-4} ml/min were routinely monitored.

Alignment remained constant throughout the experimental program, and at the same positions for which the calibrations were made. The liquid head of the LFD, with respect to the membrane, during the experimental program was constant at 0.81 psi. This value is taken into account when computing the pressure drop across the membrane. Since the LFD level change for the duration of an experiment represents a relatively small head change (0.01 psi), this change is not accounted for and assumed inconsequential with respect to the interpretation of flux measurements. In part, this assumption is based on tests of the flux sensitivity to small changes in the overall pressure driving force. At the conclusion of Experiment 300, it was found that a 1% change in the inlet pressure produced about a 1% change in ultrafiltrate flow rate.

III. Experimental Procedure

A. Preparations and Measurements Before an Experiment

1. Solvents and Solutions

The distilled water, and the .15 M saline solutions made from it (dessicated analytical grade sodium chloride), were ultrafiltered in a conventional laboratory stirred cell with an Amicon PM-10 membrane. Sodium ozide was used as an anti-bacterial agent. All lines and surfaces which contacted the stagnant ultrafiltration cell were rinsed with this ultrapure water. Membrane conditioning (in situ) and saline permeability characterization were done with the ultrapure saline.

The Bovine serum albumin solutions (BSA) were prepared with the above saline solutions and Pentex crystallized bovine albumin (Cat. No. 81-001, Miles Laboratories, Kankakee, Illinois), the same grade of albumin used for the osmotic pressure determinations. Experiments 300-1000, and the F-series experiments were performed with albumin solutions for which the isoionic point in .15 M saline was measured to be 5.55 pH (Miles Laboratories Lot No. and Chloride content unrecorded). Experiments 1100-1800 were performed with solutions of isoionic point 5.55 pH and the Chloride content of the crystallized BSA was 0.6 mg/gr protein (Lot 33).

The pH of these solutions was adjusted using 0.5N HCl and 0.5N NaOH solutions which had been made by mixing acculute grade acid or base with .15M NaCl solutions. In most cases, this pH adjustment increased ionic strength only about 3-5% above the nominal specification of 150 meg/liter. The albumin solutions of Experiments 1700 and 1800 were exceptions at about 170 meg/liter.

After pH adjustment, the solutions were filtered with a 0.1 micron filter as a precaution against possible denatured protein. Final albumin concentrations were determined by the Biuret method.

2. Membrane - Preconditioning and Location

Abcor HFA-180 membranes were used in the experimental program. Experiments 300, 400 and 600 used membrane samples which were from the same batch used in the Chapter Three osmometry work. Their characterization was discussed in Chapter Three. These membranes were smooth on both surfaces and were relatively easy to mount and seal in the ultrafiltration cell after a light coat of heavy grease (APIEZON N) was applied to the matching surfaces of the cell halves. The ultrafiltrate side of a second batch of HFA-180's used in all experiments after Experiment 600 was of a rough, fibrous nature. To obtain a seal with these membranes required the use of a thin Parafilm gasket under the membrane. The saline permeability for these new membranes was observed to be equivalent in stagnant cell and stirred cell applications at 10 psi and 40 psi pressures.

At the beginning of the experimental program, it was found that a membrane conditioning procedure was necessary to stabilize the position of the membrane surface ($\pm$ 0.001 cm). Inspections of this stabilizing process revealed that most of the shift in membrane position resulted from the first time that solvent was squeezed out from the initial gap between the membrane and the porous support. Before making measurements of membrane surface location with respect to the horizontal wire of the wire image reticle (about 0.700 cm), the following five step stabilization process was followed.

Step 1:	4 hours	- ultrapure water flux at 10 psi; membrane/cell assembly drops. 02 cm
Step 2:	15 minutes	- pressure released, membrane relaxed
Step 3:	4-6 hours	- ultrapure water flux at run pressure; membrane/cell assembly drops an additional 0.007 cm
Step 4:	15 minutes	- pressure released, membrane relaxed
Step 5:	6+ hours	- saline flux at run pressure; membrane/cell assembly at same location as Step 3.

The cathetometer measurements were made during saline flow at the highest planned experimental pressure.

The cathetometer is used to locate the membrane at three points below the horizontal wire of the reticle pattern. In addition to a point at the middle of the pattern where the three wires cross, the other measurements are made at the vertical hatch marks at either end of the horizontal wire (see Figure 5-4). These two locations correspond closely with the horizontal distance along the membrane surface where the 45° wires intersect. The basis for adopting this technique rather than obtaining membrane location from the photographs, is the observation of better resolution of the edges of the wires and the membrane when illuminated by noncoherent, incandescent light. At each of the three locations, the top and bottom edge of the horizontal wire is measured and averaged to obtain its height above the membrane surface. These measurements, made in multiples of six, establish the height of the horizontal wire above the membrane with an accuracy of about 0.03 mm (standard deviation).

B. Experimental Run Procedure

Each experiment was started with at least 90 minutes of saline flow through the membrane at the pressure of the ensuing ultrafiltration experiment. During this time, the membrane permeability to saline, K_m was determined by successive timed collections of the saline ultrafiltrate in a graduated cylinder. These determinations were continued until successive values of K_m insured that changes in membrane permeability would not be a factor in the planned time course of the protein ultrafiltration experiment. Usually this involved only two 45 minute determinations since the membrane had already stabilized during the prolonged conditioning period. During the conditioning period, saline permeability usually decreased by 15-50%.

The protein ultrafiltration was initiated after the saline flushing was stopped and saline drained from the cell through the plastic hypodermic tubing (Intramedic polyethylene tubing, .038" O.D., Clay-Adams, Inc., New York) which was extended through the saline feed line to the membrane surface. Albumin solution was forced into the cell with a syringe. A charge of 10 ml, entering at the membrane surface, insured solution homogeneity in the 3.1 ml cell volume. The elapsed time from the moment albumin first contacted the membrane was monitored. After 5 minutes had elapsed, the run pressure was applied and the 4-way valve opened to the LFD. This was considered the starting time of ultrafiltration.

Ultrafiltrate flow data was monitored continuously with the recorder. The critical variables of room temperature, applied pressure and LFD transducer excitation voltage were checked frequently.

The severity of the concentration gradient, which decreased with increasing elapsed time, determined when quantitative photographic information could be obtained. At equivalent elapsed times, this gradient also depends on bulk solution albumin concentration and pH, and applied pressure. Cell design should have allowed quantitative information to be obtained for any gradient which produced a maximum deflection of 15 degrees at the second cell window/solution interface. Practically, the deflection data was most easily interpreted when the maximum angle was about 10 degrees. The steepest gradients were produced by the experiments involving 4.5 pH solution. In Experiment 1300 (4.5 pH, 10 psi), at 9 hours the maximum deflection angle was 8.5 degrees. In Experiment 1800 (4.5 pH, 40 psi) the angle was 10 degrees at 22 hours.

At the termination of an experiment, the applied pressure was released and the 4-way valve to the LFD closed. In each case, the LFD liquid level was monitored for an additional period. This leak test of the LFD never produced a volume change greater than 1×10^{-5} ml/min.

Following those experiments for which the cell/membrane setup would be reused, a saline rinse/drain procedure, repeated four times, was followed after draining the albumin solution. The disappearance of small deflections after the third wash, which was left in the cell for at least five hours, and the ensuing reproducibility of the membrane saline permeability, were insurances that the cell had been cleaned. The F-series experiments discussed in Section V demonstrate the reproducibility of membrane permeability when this technique was employed.

IV. Experimental Data Reduction

A. Deflection Patterns and Their Reduction to Concentration Profiles

The photographs of Figure 5-10 show the illuminated cell image as it appears on the fiducial plate before and after the polarization layer has been established. The small x's in the photos are the calibration marks of the fiducial plate. Since camera position varied slightly between experiments, the magnification between these photographs, and also those in Section V, will vary (.85-1.1).

The undistorted reticle pattern is seen in the photo at upper left. The small diffraction patterns surrounding every image border in this photo prevents the use of such images to establish the membrane location with respect to the reticle pattern. Therefore, prior to beginning an experiment, a cathetometer was used to locate the membrane as discussed in Section III. Usually, the membrane distance from the horizontal wire was greater than the polarization layer thickness so that the image of this horizontal wire was not distorted in the deflection photos. Where this wire does become distorted by the polarization layer as in Experiments 1600-1800, it was necessary to evaluate membrane location using photographs for the same cell/membrane setup taken at shorter elapsed times when the polarization layer had not reached the height of this wire.

The typical deflection pattern taken from Experiment 1500 and shown in the upper right photo indicates the effect produced by the polarization for a 10 psi ultrafiltration experiment of a 10 gm % albumin solution at pH 5.4. This photo was taken 9 hours after the start of the experiment and shows a deflection of about 28 mm below the

FIGURE 5-10

PHOTOGRAPHS OF DEFLECTION PATTERNS

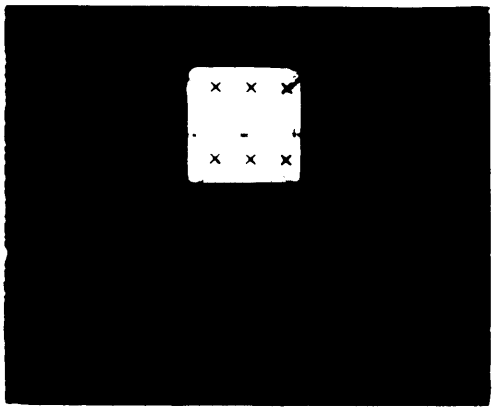

BEFORE
POLARIZATION
(1701)

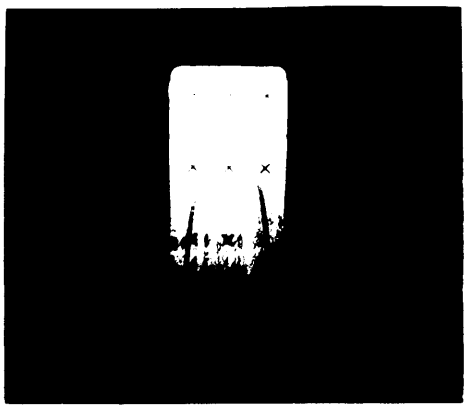

POLARIZATION
AT 9 HRS
5.4 pH, 10 psi
(1505)

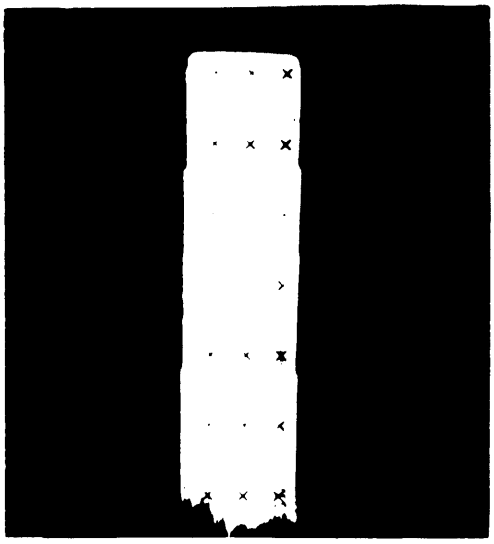

POLARIZATION
AT 22 HRS
4.5 pH 40 psi
(1807)

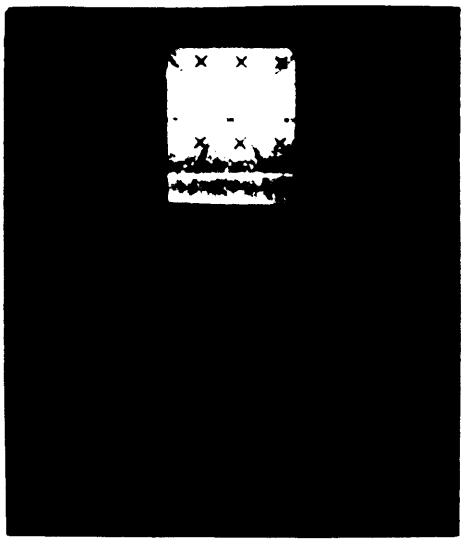

OSMOTIC
BACKFLOW
OF SOLVENT
(910)

membrane surface. At equivalent conditions of bulk protein concentration, applied pressure and time, the 4.5 pH solution of Experiment 1300 exhibited a deflection pattern which was 35% longer; the 7.4 pH solution of Experiment 1400, exhibited a pattern which was 35% shorter. These photographs are shown in Section V.

The deflection pattern at 22 hours for the ultrafiltration of a 4.5 pH solution at 40 psi (Experiment 1800) is shown in the lower left photo. Three neutral density optical filters (Wratten Gelatin Filter, Eastman Kodak Co.; various combinations of 50%, 25%, 10% and 1% pass filters were used) were placed in front of the fiducial plate (see Section III) in order to reduce light intensity variation over the deflection pattern length.

The interference patterns at the bottom of photos 1807 and 1505 are probably the result of partial internal reflection of the most deflected rays at the second glass window/air interface. These reflections occur predominantly at this discontinuity because the difference in the refractive indices of those two media is largest. They are most prominant at short elapsed time when deflection angles are steepest. They are most uniform, in terms of intensity and smoothness across the horizontal dimension of the photos, for those experiments in which the glass birefringence was minimized (e.g. Experiment 1500).

In the photo at the lower right, taken at the end of Experiment 900, saline solvent was allowed to backflow through the membrane by releasing the applied pressure. As the polarization layer gradient relaxes by molecular diffusion, the deflection diminishes. But most interestingly, a layer of saline, greatly diminished in protein, forms relatively quickly at the membrane surface. This thin region of almost

negligible refractive index gradient permits light to pass undeflected. The result is the thin strip of light, which corresponds to the membrane surface, seen in the photo. Also faintly visible are the small inverted wire images which indicate the maximum in the refractive index gradient above the membrane. The Saran film surrounding the cell brace slightly obscures the images in this photograph.

1. Strategy of Deflection Analysis

The strategy of analyzing the deflection photos has the objective of obtaining the Y-coordinates for single rays at the point where they enter the cell and the point where they appear on the fiducial plane (Y_0, Y_3 of Figure 5-1). This strategy is first discussed here in a general way with the aid of Figure 5-11.

The Y-coordinate of the membrane is established by combining measurements on the horizontal wire of the photograph with the cathetometer measurements. The undeflected portion of one of the wires gives a linear relationship which can be combined with the membrane Y-coordinate to find the coordinate system in which one axis is parallel to the membrane, the other axis perpendicular to it, and the origin centered at the point where the wire intersects the membrane. For any particular value of the horizontal coordinate in this frame, the horizontal distance, Y_0/S, and the slope of the undeflected portion of the wire image, S, the distance above the membrane at which the light ray entered the cell, Y_0, can be calculated. The vertical distance, Y_3, is the deflection.

Up to 250 of these points are then regressed with nonlinear least squares to fit an exponential relationship between the entering and

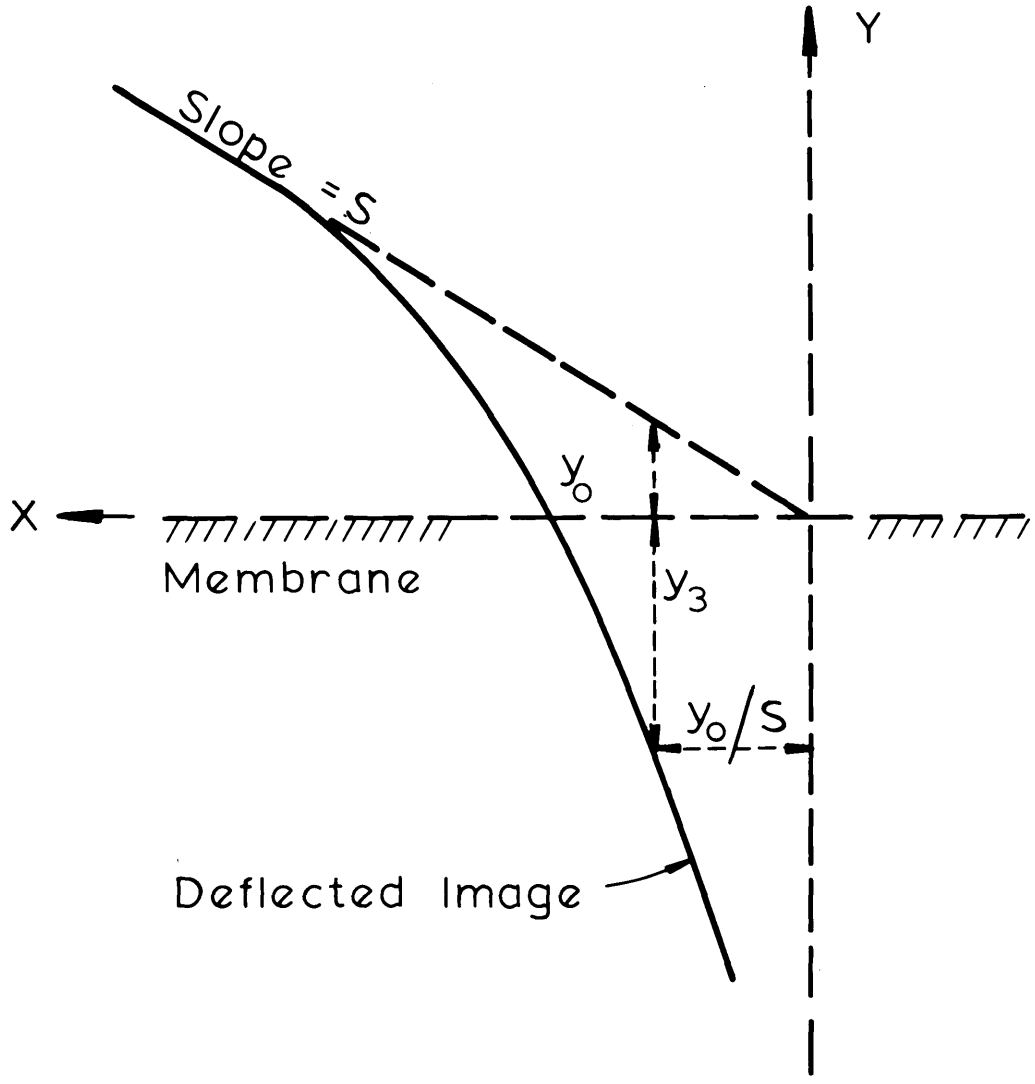

Figure 5-11 Deflection Analysis

exiting ray location. In equation (5-19), the regression coefficients, G_1 and G_2, are the same constants used by the ray trace calculations discussed in Section I.

$$Y_3 = G_1 * \exp(-G_2 * Y_0/S) + Y_0 \qquad (5\text{-}19)$$

2. Specifics of Deflection Analysis

Usually, all optical data required for a concentration profile determination are obtained from one exposure and the cathetometer measurements. The negative of a photo like 1505 is processed using an Itek Hand Measurement Machine. This machine, and guidance in its operation, was made available through the kindness of Prof. Irwin Pless and M.I.T.'s Laboratory of Nuclear Science.

The negative is mounted on a stage which magnifies it about 14 times and divides the length and width of the photo into a 130,000 by 40,000 micron grid space. The coordinates of any point on the negative with respect to this grid space are then recorded electronically and digitized with the aid of a PDP-8 computer. For all points recorded, the middle of an image is read since edges cannot be determined accurately.

The processing of a negative begins with four sets of readings of the fiducial marks. Ten repetitions of readings on the three intersection marks along the horizontal wire are made. Next, about 100 readings are made on each of the straight, undeflected portions of the 45° wires. Lastly, 200-250 points are read on each of the curved, deflected portions of these wires.

The digitized data is processed using three computer programs on a General Data Nova Model 840 Computer. The data processing with the programs FIDUC, BEFORE and DEFLECT is summarized in Figure 5-12. The functions of these programs, and a sample determination are illustrated below for the concentration profiles of Experiment 1400, photo 1406 (see Section V, Figure 5-29).

FIDUC

The function of routine FIDUC is to calibrate the Hand Measurement machine readings from the photo negative, with the real space coordinate system of the fiducial plate. This is done by comparing the measurements of the photo fiducial marks with the fiducial plate calibration data (see Appendix C). The nonlinear conversion equations are designed to account for camera lens distortions, film tilt, film nonlinearity, and magnification (from LNS, personal communication).

$$Y_R = \alpha_1 + \alpha_2 Y_F + \alpha_3 X_F + \alpha_4 Y_F^2 + \alpha_5 X_F Y_F + \alpha_6 Y_F R \qquad (5\text{-}20)$$

$$X_R = \beta_1 + \beta_2 X_F + \beta_3 Y_F + \beta_4 X_F^2 + \beta_5 X_F Y_F + \beta_6 X_F R \qquad (5\text{-}21)$$

where $R = Y_F^2 + X_F^2$ and the subscripts F and R designate measurements on the film plane and on the fiducial plane respectively. α_i and β_i are the coefficients which correlate the two planes. FIDUC uses a least-squares fitting routine, which in turn utilizes gradient search techniques, to evaluate these coefficients. These coefficients are passed by FIDUC to either the BEFORE or DEFLECT routines where they are used to convert the wire measurements from the film/Hand Measurement

Figure 5 - 12

PROCESS FOR REDUCING DEFLECTION DATA

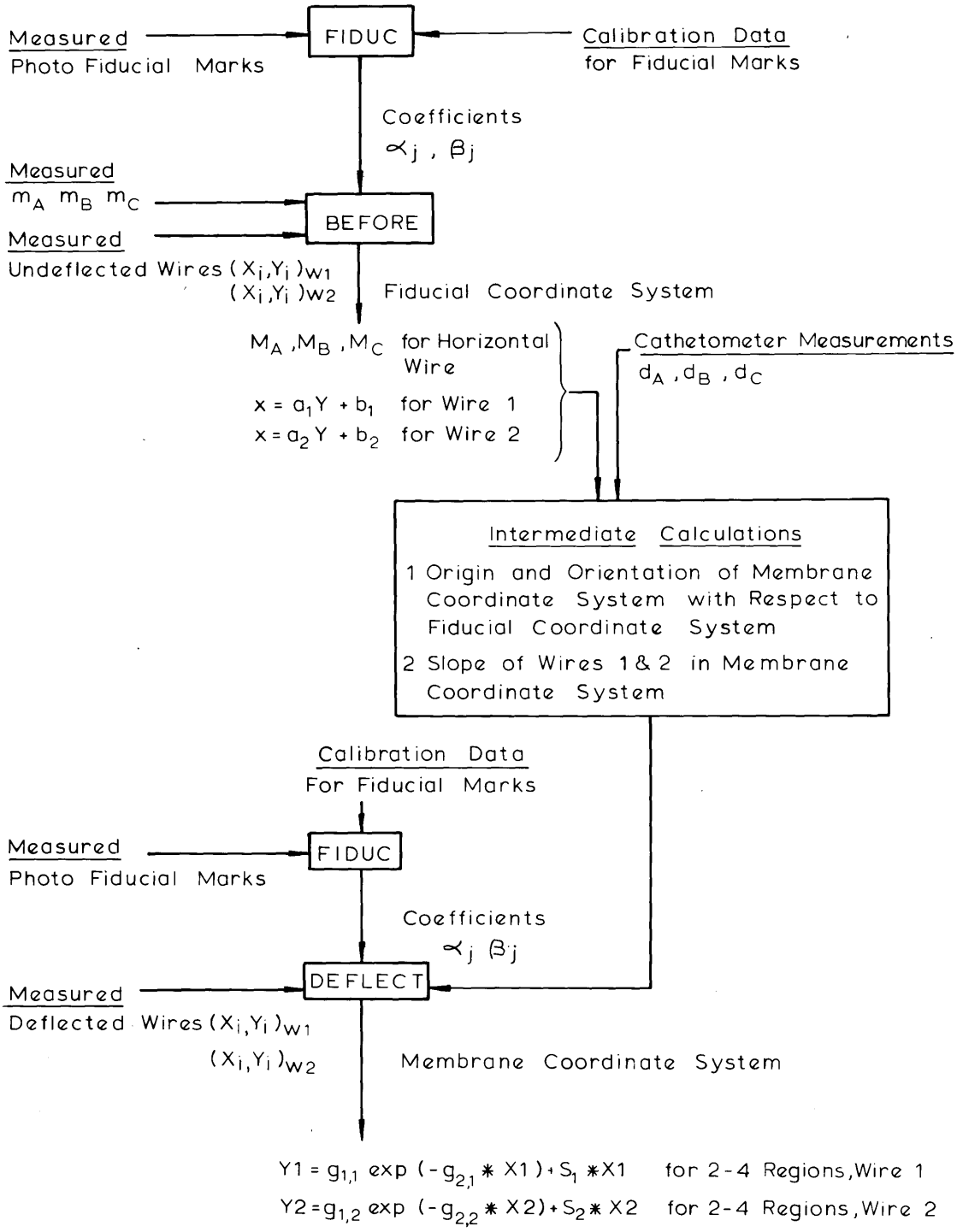

Machine space to the real space of the fiducial plane.

In photograph 1406, fiducials marks (2,2), (2,3), (2,4), (3,2)... (5,2), (5,3), (5,4) are the only visible marks. Their positions are recorded with the Hand Measurement Machine and fed to FIDUC along with the calibration data for all the fiducials. FIDUC calibrates the film plane and the fiducial plane using only the visible fiducials. The coefficients α_i and β_i are determined (13 significant figures).

Table 5-1

Fiducial Coefficients for Photograph 1406

i	α_i	β_i
1	0.000697	-0.000397
2	1.101775	1.098871
3	-0.033726	0.036018
4	0.000720	-0.001871
5	-0.000077	0.002126
6	0.000596	0.000066

Table 5-2 shows that the film is calibrated to the real space of the fiducial plate to within an accuracy of better than ten microns. In the table, the Hand Measurement Machine coordinate is given for the Y positions of the 12 fiducials and the calculated fiducial plate coordinate, using the coefficients of Table 5-1, is compared with the calibration point, shown in Appendix C, for each mark.

Table 5-2

Y-Coordinate Conversion From Film Plate To Fiducial Plane for Photo 1406

Fiducial Mark	Y_{film} Microns	Y_R, Calculated By Eqn 5-20, cm	Y_R Calibration Data, cm
2,2	120521	1.0021	1.0027
2,3	120686	1.0031	1.0033
2,4	120820	1.0005	0.9997
3,2	111420	-0.0018	0.0001
3,3	111549	-0.0004	0.0000
3,4	111684	-0.0019	-0.0007
4,2	102342	-0.9992	-0.9980
4,3	102479	-0.9995	-1.0005
4,4	102602	-1.0013	-1.0015
5,2	93297	-1.9997	-1.9999
5,3	93400	-2.0029	-2.0024
5,4	93522	-2.0039	-2.0042

BEFORE

The routine BEFORE, in two separate applications, converts wire image data from the film plane to the fiducial plane using the calibration coefficients from FIDUC. In the first application, the film plane Y-coordinate for the three locations along the horizontal reference wire (m_A, m_B, m_C) is converted to the fiducial plane coordinate frame (M_A, M_B, M_C). In the second application, after converting the measurements made along the undeflected straight portion of each wire taken individually, the converted measurements are fit to a straight line in the fiducial plane coordinate system by least-squares regression. In the

fiducial plane coordinate system centered at mark (3,3) the linear form is

$$X = a_1 Y + b_1 \quad \text{for Wire 1}$$

$$X = a_2 Y + b_2 \quad \text{for Wire 2} \qquad (5\text{-}22)$$

The values, M_A, M_B, M_C, a_1, b_1, a_2 and b_2 are listed in Appendix D for each experiment. The standard deviation of the ten readings of each value of M is usually ±0.002 cm. The data scatter randomly for the linear fit of the undeflected wire with the average standard deviation between a measured X and its calculated value being about ±0.006 cm.

Intermediate Calculations

The purpose of the intermediate calculations is to combine the converted measurements of the BEFORE routine with the cathetometer measurements to obtain the membrane coordinate system origin and orientation with respect to the fiducial plane system. These calculations also are summarized in Appendix D. The discussion proceeds with the use of photo 1406 for illustration.

Figure 5-13 shows the fiducial plane coordinate system, X_R, Y_R, as the dashed lines centered at (F_X, F_Y), which is the location of fiducial mark (3,3). Parallels to the Y-axis of this frame are shown as dashed lines at the points where each of the extrapolated wires intersect the membrane. The figure also shows different orientations for both the wire reticle pattern and the membrane surface with respect to the fiducial frame.

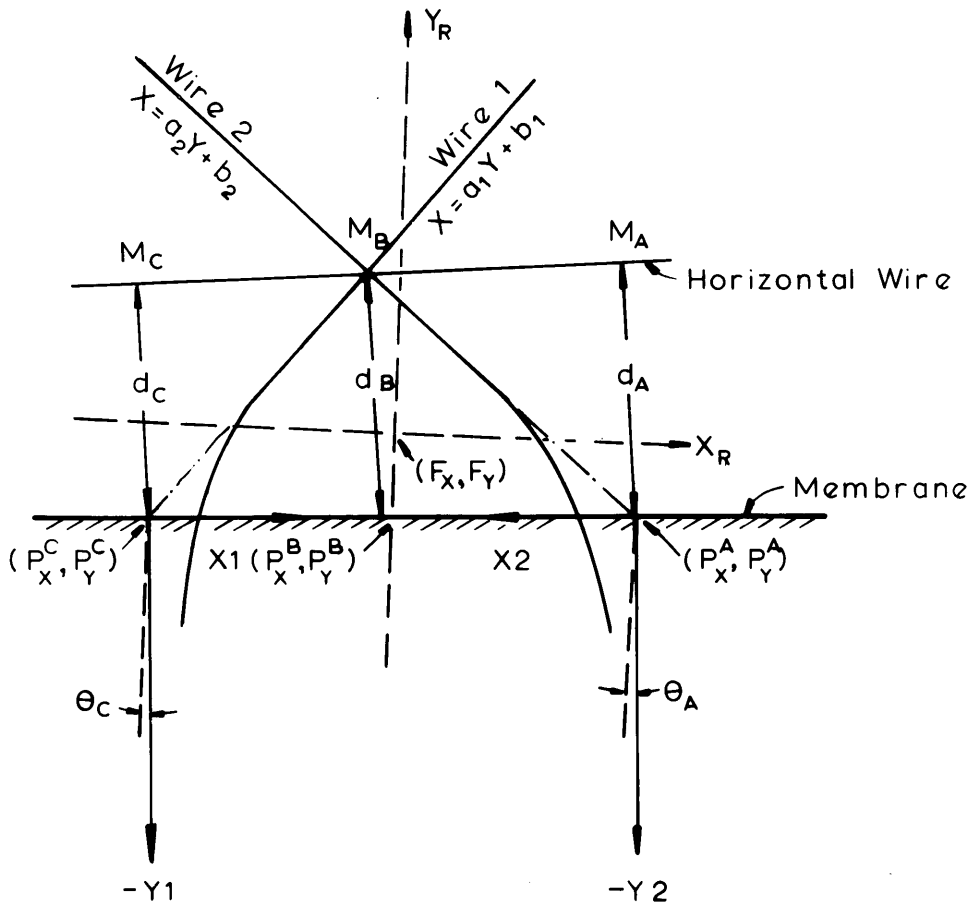

Figure 5-13 Transformation of Coordinates from Fiducial Plane (X_R, Y_R) to Membrane for Wire 1 (P_X^C, P_Y^C) and for Wire 2 (P_X^A, P_Y^A).

The translation begins by finding the membrane distance below the horizontal reference wire, where the values of M_A, M_B and M_C were computed in BEFORE, d_A, d_B and d_C are the cathetometer measurements, and P_Y^A, P_Y^B and P_Y^C are in the <u>fiducial</u> frame. For photo 1406, with all dimensions in centimeters:

$$P_Y^A = M_A - d_A = 0.454 - 0.688 = -0.234$$

$$P_Y^B = M_B - d_B = 0.434 - 0.678 = -0.244$$

$$P_Y^C = M_C - d_C = 0.415 - 0.670 = -0.255$$

The calculation of the P_Y coordinates above includes the assumption that the cathetometer travel, when making the measurements of d_A, d_B and d_C, is parallel to the Y_R axis of Figure 5-13. Actually, this is not the case, but the error which results by assuming that $d_i \simeq d_i/\text{Cos}(\varepsilon)$, where ε is the small angle of the cathetometer travel with respect to the Y_R axis, is negligible at the precision level of ±0.001 cm. For two different setups of the apparatus, ε was measured to be 0.1° and 0.3°. Since these measurements were difficult experimentally, they were not made routinely throughout the experimental program. If ε was an order of magnitude larger, say 3°, for $d_i \sim .7$ cm, the error involved in the calculation of P_Y^i is only 0.001 cm. The translation step is completed by extrapolating equations (5-22) to find the intersection of the wire with the membrane.

for Wire 1: $P_X^C = a_1(P_Y^C) + b_1 = 0.9589(-0.255) - 0.4377 = -0.682$

for Wire 2: $$P_X^A = a_2(P_Y^A) + b_2$$

$$= -1.0365(-0.234) + 0.4217 = +0.664$$

The orientation of the membrane with respect to the (X_R, Y_R) coordinate system is positive in the schematic of Figure 5-12. This sign of the orientation applied to all experiments with the exception of Wire 1 in Experiment 600. This orientation is one of the most critical parameters in the photo evaluation process and is evaluated using the three values of membrane location in the Y-direction. The distances between $P_X^A - P_X^B$ and $P_X^B - P_X^C$ are equal and were found to be most accurately represented by the design constants of the reticle pattern, i.e., the horizontal distance between the hatch marks and the center of the pattern. This distance is 0.694 cm.

for Wire 1: $$\Theta_C = \frac{|P_Y^C| - |P_Y^B|}{0.694} = +0.0158 \text{ radians}$$

for Wire 2: $$\Theta_A = \frac{|P_Y^B| - |P_Y^A|}{0.694} = +0.0144 \text{ radians}$$

The slopes of each wire with respect to its coordinate system are evaluated using the slopes for the fiducial frame and these orientation angles (in degrees).

For Wire 1 with respect to the membrane frame (X1, Y1)

$$S_1 = \text{Tan}\left(\text{Arctan}\left(\frac{1}{|a_1|}\right) - \Theta_C\right)$$

For Wire 2 with respect to the membrane frame (X2, Y2)

$$S_2 = \text{Tan}\left(\text{Arctan}\left(\frac{1}{|a_2|}\right) + \Theta_A\right)$$

For photo 1406, $S_1 = 1.0103$ and $S_2 = 0.9930$.

The above results permit any point measured along the deflected portion of a wire in the fiducial plane coordinate system (X_R, Y_R) to be transformed to that wire's membrane coordinate system, (X1, Y1) or (X2, Y2).

DEFLECT

In DEFLECT, points read along a deflected wire are first converted from the film plane to the fiducial plane with its (X_R, Y_R) reference frame using the same data and FIDUC routine as described above. The deflection data is then transformed to one of the membrane frames using the trigonometric formulae:

For Wire 1:

$$X1 = (X_1 - P_X^C)\cos\Theta_C + (Y_1 - P_Y^C)\sin\Theta_C \qquad (5\text{-}23A)$$

$$Y1 = (Y_1 - P_Y^C)\cos\Theta_C - (X_1 - P_X^C)\sin\Theta_C$$

For Wire 2:

$$X2 = -[(X_2 - P_X^A)\cos\Theta_A + (Y_2 - P_Y^A)\sin\Theta_A] \qquad (5\text{-}23B)$$

$$Y2 = (Y_2 - P_Y^A)\cos\Theta_A - (X_2 - P_X^A)\sin\Theta_A$$

where (X_1, Y_1) and (X_2, Y_2) are measurements made along the deflected portions of Wire 1 and Wire 2 respectively, and are in the (X_R, Y_R) frame of Figure 5-13.

For each of the wires in photo 1406, Figure 5-14 shows an expanded plot of most of the (X1, Y1) and (X2, Y2) data pairs as they were computed by equations (5-23A and B). Only a few points are missing at the top of the deflection patterns of each wire. The curves through the data are the nonlinear least-square regression results when the data are fit to an equation of the form

$$Y = G_1*\exp(-G_2*X) + S*X \qquad (5\text{-}24)$$

where G_1 and G_2 are the coefficients determined by the regression and S is the slope of the undeflected wire. The functionality of equation (5-24) has the properties that at large values of X, the equation approaches the straight line relationship of the undeflected wire, and at $X = 0$, G_1 gives the location on the fiducial plate, with respect to the membrane, for the most deflected ray to leave the cell. Equation (5-24) was applied to at least two regions of the deflection pattern for each wire. In most cases, more than two fits of the deflection pattern did not improve the correlation.

Table 5-3 summarizes the results for the fits to the two wires of photo 1406.

FIGURE 5-14

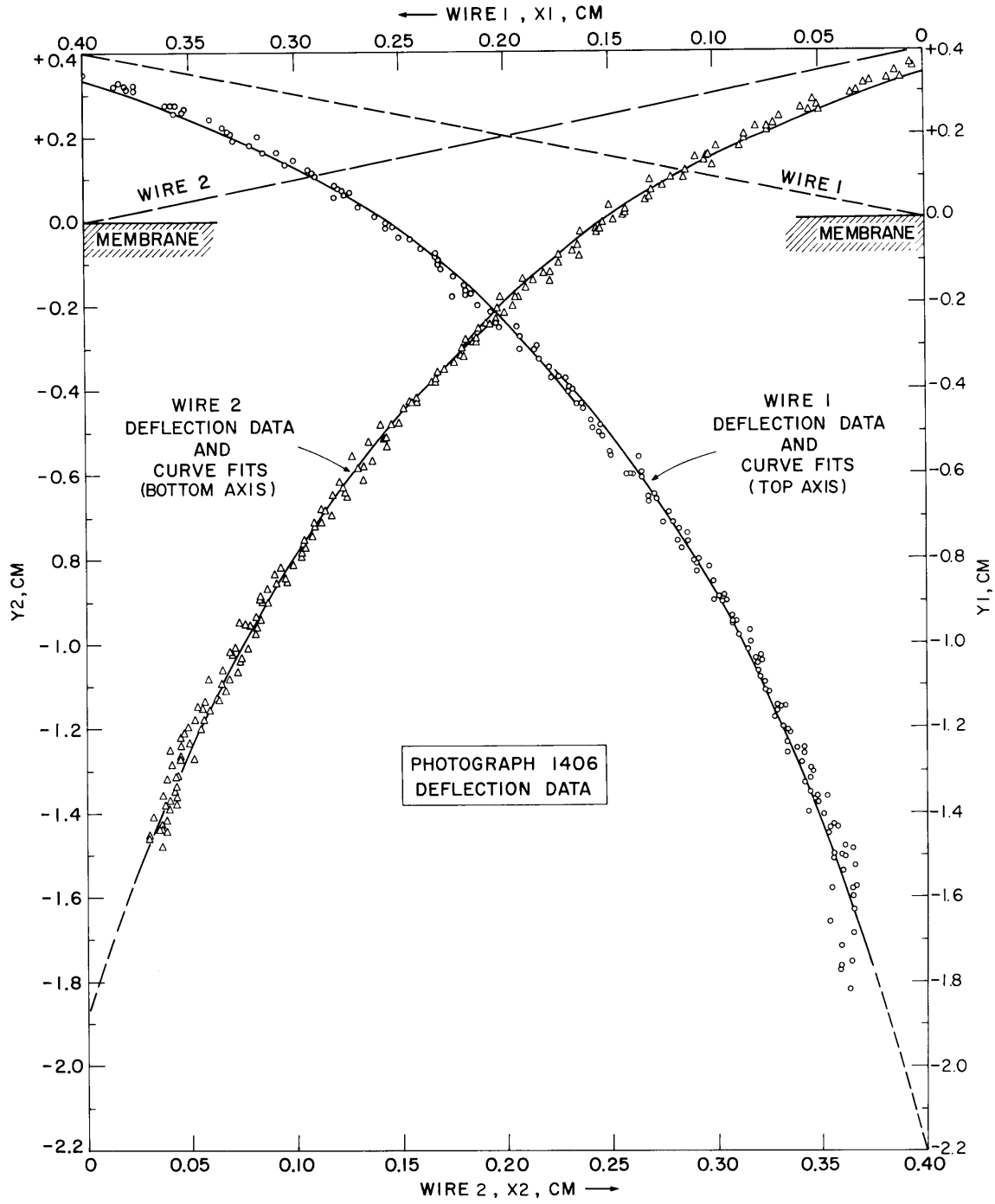
← WIRE 1 , X1 , CM
0.40
0.35
0.30
0.25
0.20
0.15
0.10
0.05
0
+0.4
+0.2
0.0
-0.2
-0.4
-0.6
0.8
-1.0
-1.2
-1.4
-1.6
-1.8
-2.0
-2.2
WIRE 2
WIRE 1
MEMBRANE
MEMBRANE
WIRE 2
DEFLECTION DATA
AND
CURVE FITS
(BOTTOM AXIS)
WIRE 1
DEFLECTION DATA
AND
CURVE FITS
(TOP AXIS)
PHOTOGRAPH 1406
DEFLECTION DATA
Y2, CM
Y1, CM
0
0.05
0.10
0.15
0.20
0.25
0.30
0.35
0.40
WIRE 2 , X2 , CM →

Table 5-3

Curve Fit of (X1,Y1) and (X2,Y2)
Data For Photo 1406

Range on Y1 or Y2 for Fit	Wire 1		Wire 2	
	$G_{1,1}$	$G_{2,1}$	$G_{1,2}$	$G_{2,2}$
0.600 → -0.500	-2.8746	9.3780	-2.6985	9.6038
0.000 → -2.000	-2.1948	7.9980	-1.8760	7.4945

In the ray trace calculations (SDIP), the fits for Wire 1 are matched at Y_0 = 0.170 cm and for Wire 2, at Y_0 = 0.180 cm. Figure 5-14 shows the close agreement for the two fits for each wire near these same values of X1 and X2 respectively.

The fitted coefficients for each photo evaluated are summarized in Appendix D (Table D-3).

RAY TRACING

The details of the ray trace calculations were presented in Section I of this Chapter. There it was seen that an equation of the form of (5-24) was employed to represent the deflection data. With $Y_3 = Y$ and $Y_0 = XS$, and the coefficients G_1 and G_2 the same as those determined by the DEFLECT routine, the entering ray location and its location on the fiducial plane, as discussed earlier, is given by

$$Y_3 = G1*\exp(-G2*Y_0/S) + Y_0 \qquad (5\text{-}19)$$

For photo 1406, using the extrapolated results of the general ray trace routine, the ray trace of the last ray to clear the membrane is shown in Figure 5-15. The ray trace resulting from each wire is shown separately.

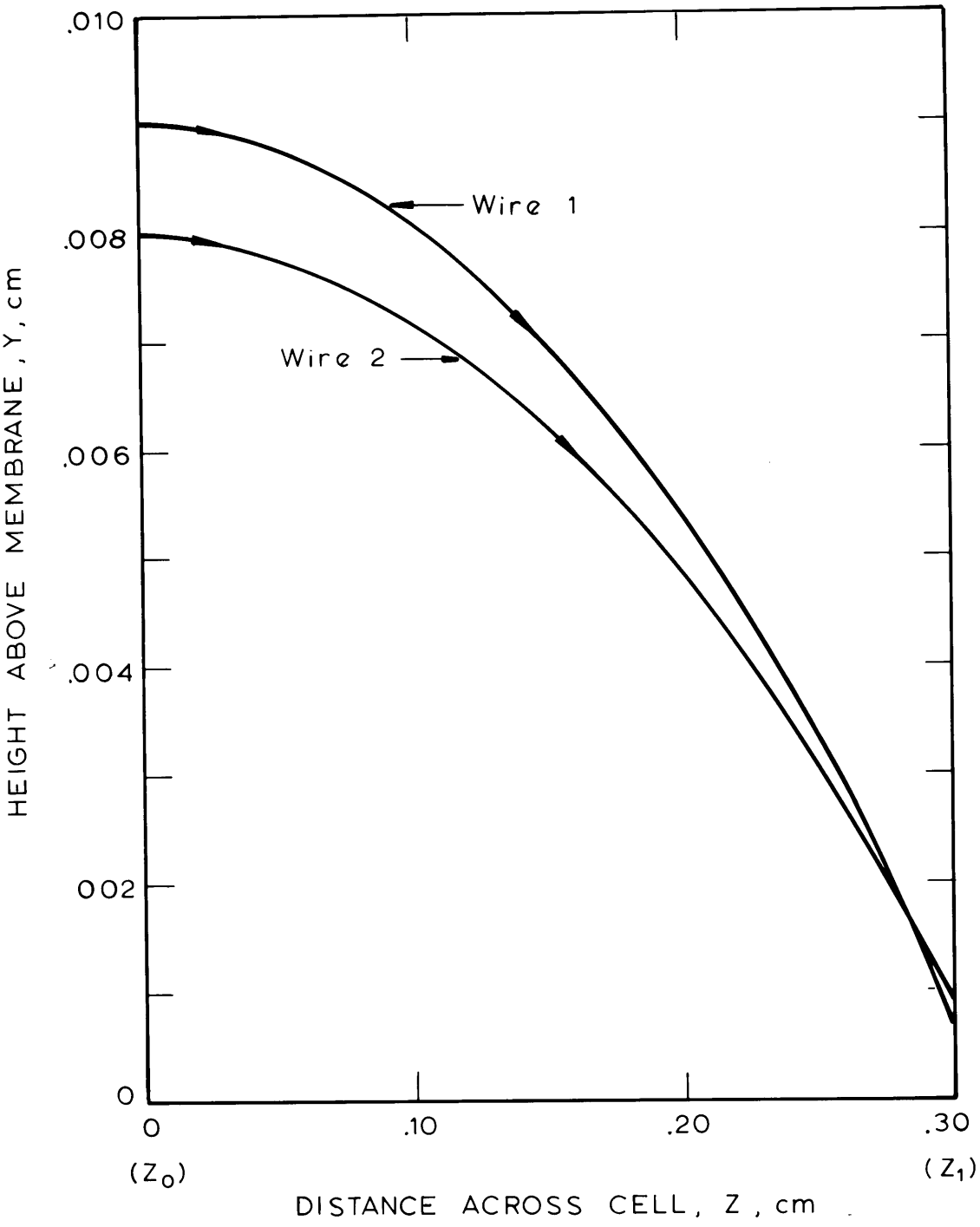

Figure 5-15 Ray Trace for Photo 1406

The deflection angle at the end of the cell, Z_1, averages 3°, which is one of the smallest angles encountered in the experimental program. This angle, and values of Y_0, Y_1 and Y_3 for the most deflected rays of each experiment are summarized in Appendix D (Table D-4).

Also summarized in Appendix D are the Y_0 and Y_3 values for the ray at the top of the polarization layer, at a point where the refractive index of the solution has increased by 2%. This height is representative of the polarization layer thickness. For Experiment 1406, the thickness was 0.420 cm above the membrane.

B. Analysis of Flow Data

The theoretical result of the asymptotic model described in Chapter 4 was that ultrafiltrate flux should decay with a $t^{-1/2}$ proportionality, where t is experimental elapsed time. This functionality applies to elapsed times which are greater than about one second.

In the experiments performed, the flow data was obtained as volume of ultrafiltrate received versus elapsed time. If the exponent of time is an arbitrary power, n, the integral equation

$$V_S - V_L = \frac{A_0 S_A}{n+1} \left(t^{n+1} - t_L^{n+1}\right) \qquad (5\text{-}25)$$

is a convenient means with which to compare theory and flow data. V_S (ml) is the total ultrafiltrate volume at elapsed time t(minutes). V_L and t_L are the lower limits of integration. $S_A(cm^2)$ is the membrane surface area and $A_0(cm/(min)^{n+1})$ a proportionality constant. When n is - 1/2, theory gives

$$A_0 = a_0 \left(\frac{\overline{\rho}}{\rho_{saline}}\right) \sqrt{D} \qquad (5\text{-}26)$$

with a_0 being calculatable from theory and a function of bulk solution and membrane surface albumin concentrations only.

The flow data from each experiment was fitted to equation (5-25) using nonlinear least-squares regression analysis. The data was usually smoothest after the first two minutes of elapsed time. It was also felt that the effects of any undiscovered artifacts of LFD operation would be minimized after this initial period. For this reason, equation (5-25) was applied three times to each set of data: 1) regression for $0 < t \leq$ 2 minutes with n arbitrary 2) regression for $2\text{min} < t \leq t_{end}$ with n arbitrary and 3) same as 2) but with n fixed at - 1/2. The data fits were always best by method 2) with observed and correlation values of V_s usually in agreement to ±0.001 ml.

The poor reproducibility regarding the value of the constant A_0 for supposedly identical experiments led to an inquiry about the effect of the regression time interval on the value of A_0. The flow data from Experiments 1200 and 1500, two identical experiments at 5.4 pH, 10 psi and 10.1 gm% albumin, were analyzed by method 3) above. The regression time intervals were varied in order to discover if ever the A_0's from these two experiments might be equal, or overlap. The results shown in Table 5-4 indicate that while the values do change slightly for different intervals, the two experiments are different with respect to this parameter.

Table 5-4

A_0 Comparisons As A Function Of Regression Time Interval

Δt For Regression Min.	$A_0 \times 10^{+3}$ With $t^{-1/2}$	
	Exp 1200	Exp 1500
0-550	5.30 ± .06	6.06 ± .07
2-550	5.44 ± .03	6.20 ± .04
2-200	5.35 ± .03	6.05 ± .02
100-550	5.51 ± .05	6.38 ± .08
200-550	5.42 ± .14	6.55 ± .09

V. Results

Eighteen experiments in which optical data and flow data were taken, and nine experiments in which only flow was monitored (F-series), were attempted in this investigation. The nine 'flow only' experiments were conducted to investigate some of the parameters thought to affect reproducibility in this data and are presented at the end of this section.

Of the eighteen total experiments, the first two experiments (Experiments 100 and 200) were discarded when it was found that the .012" diameter wires then in use were bent. The flux data from these experiments, taken with a bubble capillary, was also inferior. Two additional experiments (Experiments 500 and 1000) were discarded because of leaks around the membrane seal. Experiment 800 investigated the possibility that the flow of solution makeup at the top ports of the cell created a jet mixing effect in the polarization layer. Therefore no albumin solution makeup was provided and the cell was only partially filled with albumin solution. Although the results showed that the jet mixing effect was not important, the unknown amount of dilution of bulk albumin solution rendered these results useless for quantitation. This dilution came from saline which was left on the sides of the cell during the draining step. In all other experiments this dilution was avoided by injecting a large volume (about 10 ml which is three times the cell capacity) of solution at the membrane surface. The excess solution was forced out of the cell into the tubing above the cell. The saline clinging to the sides of the cell was therefore carried out of the cell with this overfill solution.

The overfill solution then provided the small amount of makeup (less than 1 ml) during ultrafiltration. Poor optical alignment and image quality resulted in the loss of optical data from Experiments 400 and 1200 although the flux data from both was useful.

The remainder of the experiments were involved with attempts to improve the reproducibility of the flux measurements and to improve the symmetry of the concentration profiles for both sides of the cell. Improvements were made progressively throughout the program to both experimental technique and apparatus. Most of these changes were focused on the elimination of the effects of natural convection and the stress-induced birefringence of the glass windows. In these regards, some experiments are felt to be of higher quality than others. The major improvements are evaluated below with respect to both measurements, concentration profiles from optical data and ultrafiltrate flux determinations from yield versus time data. All of the experiments are presented here if they resulted in an interpretable deflection pattern and/or flux data over some sufficient period of time during which the critical variables discussed above were well behaved. All of these results contribute something to the determination of membrane surface concentration and flux as a function of albumin solution physical chemistry.

A. Optical Data

The concentration profiles evaluated separately from each wire differ most at the membrane surface. The average difference between the two wires, for membrane surface concentration, was 8%. Investiga-

tions into this asymmetry narrowed to two most probable causes. The first of these was natural convection - both that which could be derived from small temperature differences, or from small bouyancy effects (i.e., membrane surface slightly off normal with respect to gravity) within the cell. Since changes designed to minimize these effects (see Experiments 600 and 1100) produced no significant improvement, the concerns of natural convection effects on concentration profiles were dismissed.

The discovery of the birefringence in the glass windows when they are put under stress had little effect in reducing the amount by which membrane surface concentrations predicted from the separate wires differed. Results from Experiments 1300 (4.5 pH) and 1400 (7.4 pH) with minimum window stresses differed little from the results of their high stress counterparts, Experiments 1100 and 1600 respectively. The effect of window birefringence on the overall profiles cannot be estimated since it never was completely eliminated.

The summaries which follow include the photographs of each deflection pattern which was analyzed. The quality of these photographs varies widely and in some, the full wire images may not be visible. The negatives of these photos were generally easy to interpret on the Itek machine however. The quality depended on both the exposure time and the manner in which the neutral density light filters were used. The clarity of some photos is further obscured by the saran film which surrounded the cell brace for temperature control. While calculation showed that the presence of saran and the light filters in the ray path should have no effect on the deflection patterns, supporting experi-

mental evidence for this fact is provided in Experiment 1300. Camera position was not constant between experiments and magnification of the fiducial plate image varied from about .85 to 1.10.

The data presented in the summaries includes the profiles derived from the model of Chapter 4 (equation 4-22) evaluated for an arbitrary diffusivity which gives the best visual fit to the profiles of Experiments 1300, 1400 and 1500. Each of these experiments are thought to be the best measurements of concentration polarization at their respective pH levels of 4.5, 7.4 and 5.4. Intermediate measurements and calculations are summarized in Appendix D,Tables D1-4, while concentration profile data is tabulated in Table D-5.

B. Flux Data

The greatest improvement to the attainment of reliable flux data was the implementation of the Low Flow Measuring Device (LFD) prior to Experiment 400. With this continuous record of ultrafiltrate yield, Experiment 400 revealed that flux eventually became constant at about 3×10^{-4} cm/min. Rough estimates indicated that temperature driven natural convection velocities of this same magnitude could exist in the ultrafiltration cell for the experimental setup in use at the time. Therefore, after Experiment 400, through the combination of improved ambient temperature control and the insulation of the cell by surrounding the supporting brace with saran, the estimated small temperature gradients in the cell were reduced by more than an order of magnitude. Experiment 600 showed that natural convection probably had been responsible for the Experiment 400 constant flux result. The flux in

Experiment 600 became constant at $0.8 \pm 0.2 \times 10^{-4}$ cm/min. The LFD displacement versus experimental elapsed time are shown in the results of these two experiments.

Experimental conditions for the remainder of the program never led to fluxes as low as those observed in Experiment 600, and constant flux was never observed again.

Further refinements in experimental procedure were developed while executing the F-series experiments. These techniques were applied to Experiments 1100 - 1800. They resulted in better early elapsed time measurements but otherwise made no difference in data interpretation.

The flux data is presented in the summaries as the coefficients A_o and n resulting from the nonlinear regression analysis of the LFD displacement-time data (Appendix D, Table D-7) applied to equation (5-25). The data and fitted curves are shown for all experiments either in this section or in the Discussion. The regression results, and statistical information, is also presented for the case in which n is held constant at -1/2. Notice in these results that while the standard deviation on A_o is lower for the regression at n = -1/2, a better overall correlation results when n is a free regression parameter (see Section IV for choice of time intervals). This can be seen by comparing the tabulated Sum of Squares of Deviations which are listed for each fit.

C. Experiment Summaries

Table 5-5 summarizes the bulk solution properties, operating conditions, and average properties of the polarization layer. An arith-

metic average albumin mass fraction is computed from the bulk solution and the theoretical membrane surface mass fraction. The diffusivity is computed at this average mass fraction using the results of Keller et al. (12).

TABLE 5-5

EXPERIMENTAL CONDITIONS

EXPERIMENT	BULK SOLUTION		OPERATING CONDITIONS				POLARIZATION LAYER PROPERTIES		
	GM% BSA	pH	PRESSURE PSIG	TEMPERATURE °C	TOTAL TIME MINS.	INTRINSIC MEMBRANE PERM. K_m, $\frac{gm.\ saline}{cm^2\text{-}min\text{-}psi}$	THEORET. MEMBRANE GM%	AVG. DENSITY	AVG. DIFFUSIVITY $cm^2/sec \times 10^{+7}$
300	6.4	5.42	9.6	22.6 ± .4	1030	.0280	31.0	1.05	2.38
400	6.4	5.42	10.0	25.3 ± .4	913	.0037	31.5	1.05	2.35
600	15.8	5.43	5.6	25.3 ± .2	310	.0085	25.3	1.05	2.13
700	6.4	5.43	10.15	25.3 ± .1	680	.0033	31.6	1.05	2.35
900	7.2	7.41	10.0	25.5 ± .1	536	.0037	24.8	1.04	2.75
1100	10.1	4.50	10.1	25.8 ± .2	560	.0042	40.2	1.06	1.78
1200	10.1	5.38	10.1	26.3 ± .2	655	.0035	31.6	1.05	2.13
1300	10.1	4.50	10.15	25.6 ± .1	564	.0063	40.2	1.06	1.78
1400	10.1	7.40	10.15	26.7 ± .3	548	.0064	24.9	1.04	2.52
1500	10.1	5.38	10.15	26.5 ± .3	540	.0063	31.6	1.05	2.13
1600	10.1	7.40	10.2	27.0 ± .1	1770	.0054	24.9	1.04	2.52
1700	11.0	4.50	10.1	26.9 ± .1	1380	.0047	40.2	1.06	1.75
1800	11.0	4.50	40.0	27.0 ± .1	2820	.0021	59.5	1.09	1.30

Experiment 300 (6.4 gm% BSA, 5.4 pH, 9.6 psig)

Objective: First experiment using wire image reticle; to determine minimum number of points to be read on photographs for fiducial correlation, membrane location and orientation, and deflected wire placement with respect to membrane.

Comment: Flux measurements were made by tracking an air bubble in a 0.1 ml capillary with 0.001 ml graduations. Only a few measurements were made. At the conclusion of this experiment, 913 minutes elapsed time, the flux was 2.83×10^{-4} cm/min at an applied pressure of 9.65 psig. The flux sensitivity to small changes in applied pressure was studied over a 130 minute period during which three step changes in pressure were made. Figure 5-16B is a bar graph showing the average flow rates over the time period for which they were measured with the bubble capillary. At t = 0 (913 min total elapsed time), applied pressure was increased from 9.65 psi to 10.20 psi. The new flux level is seen to be about 2.94×10^{-4} cm/min. At t = 41 min, the pressure was decreased to the starting value of 9.65 psig. Flux returned to approximately its former value at this pressure. A repeat of the 10.20 psi response was again demonstrated at t = 93 min. From

FIGURE 5-16

EXPERIMENT 300 FLOW DATA

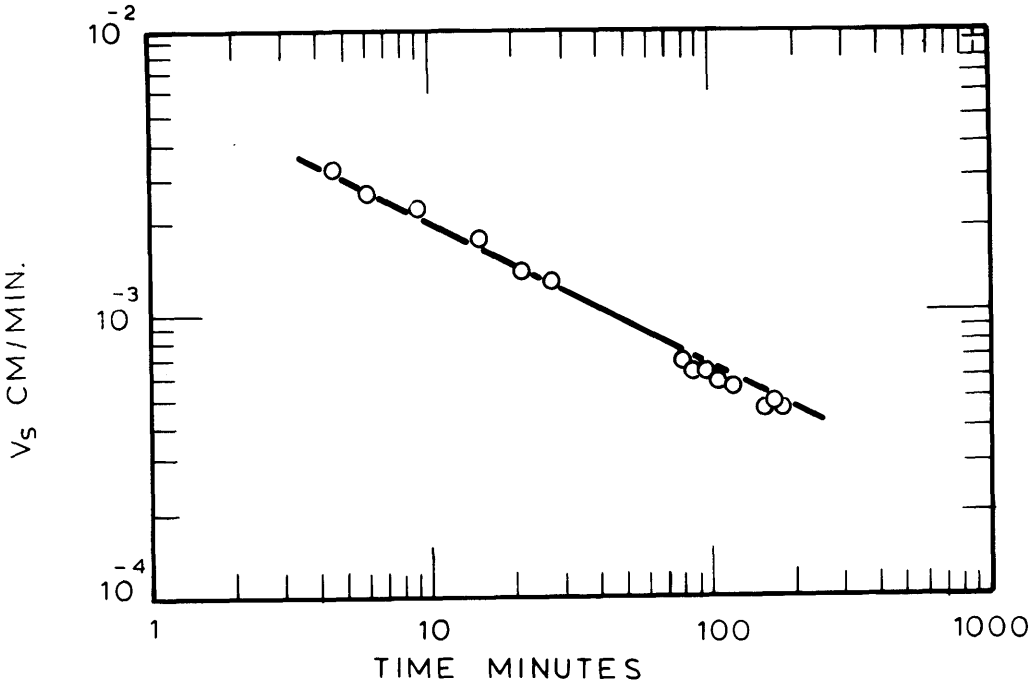

Figure 5-16A: Flux vs Time

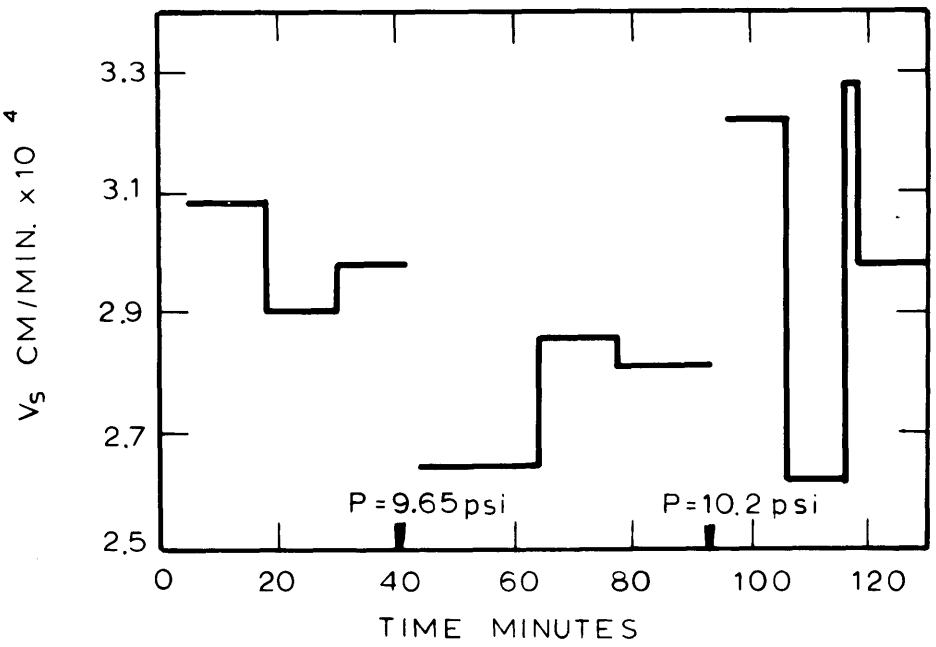

Figure 5-16 B Flux Response to Small Changes in Applied Pressure

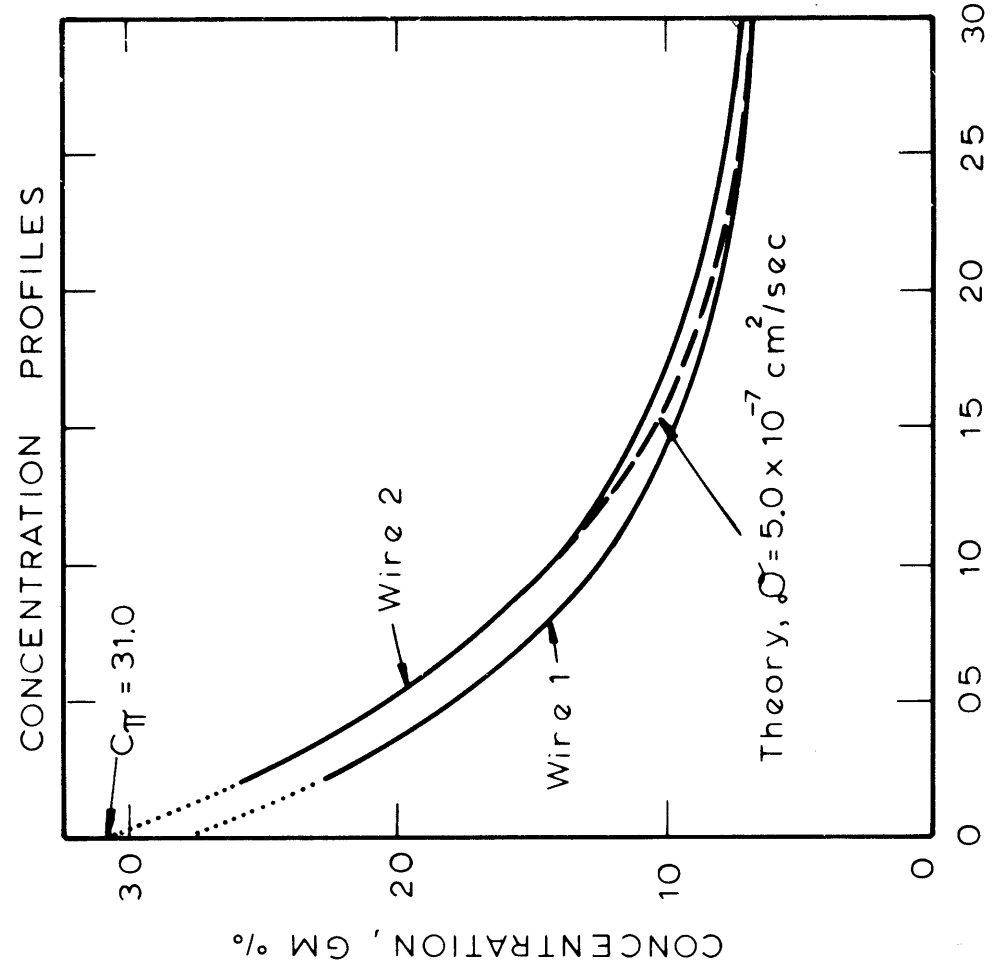

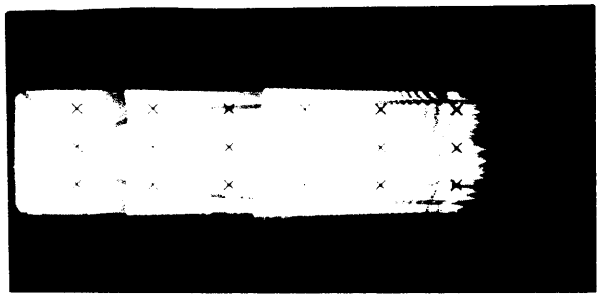

Figure 5-17 Experiment 300 Optical Data

η_{Bulk} = 1.3469

this study it was concluded that for small changes in applied pressure, the percent change in flux is about equal to the percent change in pressure.

Concentration Profile Determination: Figure 5-17 shows the profile calculated from the deflection pattern at 665 min. The theory profile and the wire 2 profile are coincident below about 0.05 cm. The polarization layer thickness averaged from both wires is .400 cm.

Flux Data: Data evaluated only for $n = -1/2$, see Figure 5-16A

$v_s = .0065\ t^{-1/2}$ for 4-180 min elapsed time.

Experiment 400 (6.4 gm% BSA, 5.42 pH, 10.0 psi)

Objective: First experiment using Low Flow Measuring Device; to test a new lens system for collimating and expanding the laser beam.

Concentration Profile Determination: The misalignment of the collimating/expanding lens system resulted in only partial illumination of the deflection pattern. The pattern could not be quantitated.

Flux Data: Figure 5-18 shows that at about 200 min flux becomes constant. This flux was about 3×10^{-4} cm/min. Natural convection resulting from small temperature gradients in the cell assumed responsible.

$v_s = A_o t^n$, cm/min

Time Interval for Regression	$A_o \times 10^{+3}$	n	Sum of Squares of Deviations, $\times 10^{+6}$
8 - 65 min	8. ± 2.	-.60 ± .02	2.7
8 - 65 min	6.2 ± 0.1	-.500	17.7

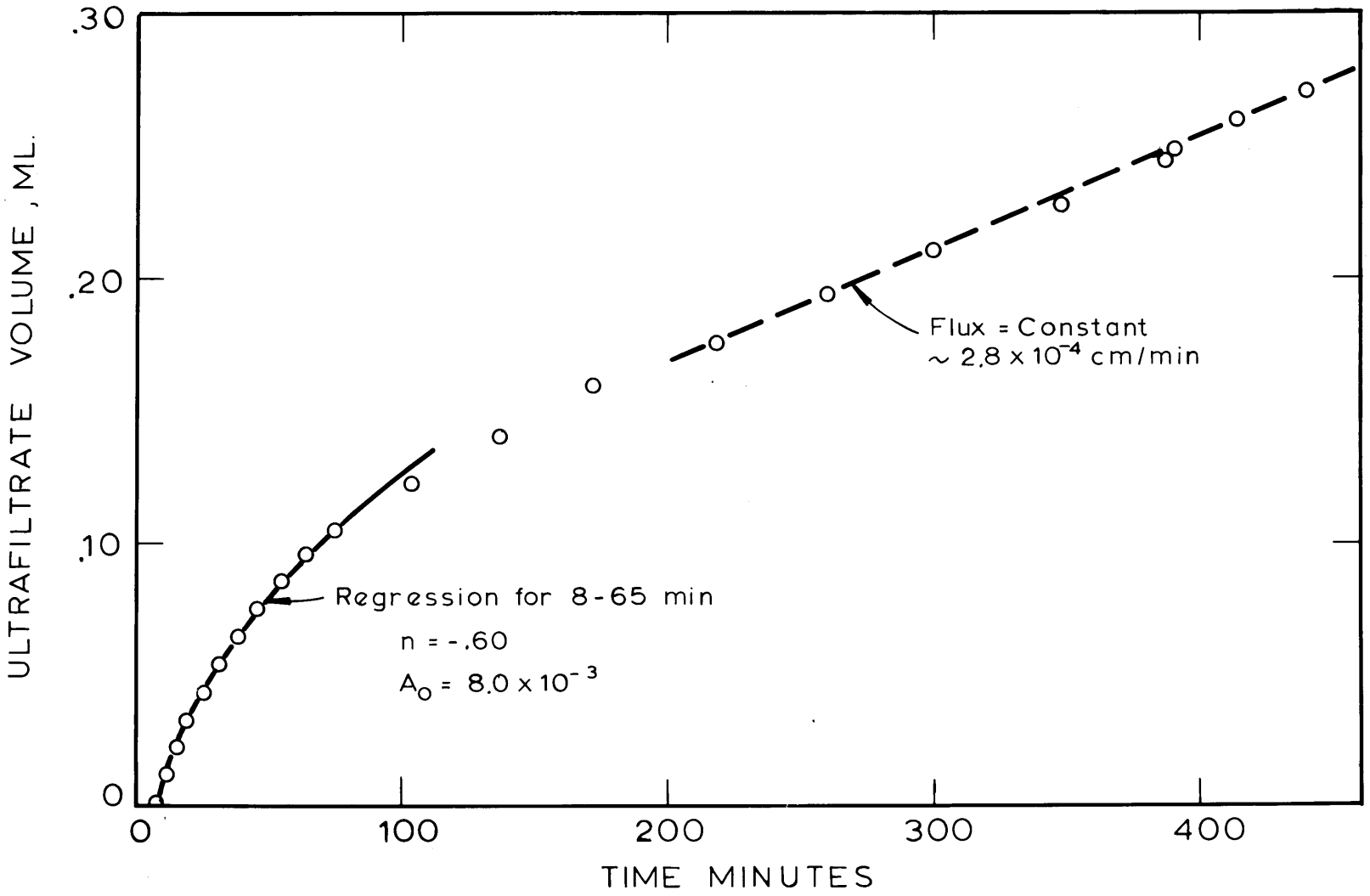

FIGURE 5-18 EXPERIMENT 400 FLOW DATA

Experiment 600 (15.8 gm% BSA, 5.43 pH, 5.6 psi)

Objective: First experiment using Oriel beam collimator/expander; improved ambient temperature control and cell insulation with saran to decrease effects of natural convection. The high bulk concentration and low applied pressure increase the theoretical real time for asymptotic behavior from the usual (at 6-8 gm% concentration, 10 psi) 0.1 sec to 1.0 seconds.

Comment: The rough patterns in photographs 603 and 604 result from excessive grease application on cell/membrane surfaces in the area of the windows. Effect of saran on photo quality also seen.

Concentration Profile Determination: Figures 5-20 and 5-21 show the profiles calculated from the deflection patterns at 33 and 88 minutes respectively. The average polarization layer thickness at 33 minutes is .115 cm, and .170 cm at 88 min.

Flux Data: A constant flux was observed at 150 - 200 minutes. Experiment extended to 310 minutes in order to establish this flux to be $0.8 \pm 0.2 \times 10^{-4}$ cm/min. See Figure 5-19.

$v_s = A_o t^n$, cm/min

Time Interval for Regression	$A_o \times 10^{+3}$	n	Sum of Squares of Deviations, $\times 10^{+6}$
2 - 140 min	1.89 ± .12	-.546 ± .005	3.3
2 - 140 min	1.64 ± .02	-.500	12.7

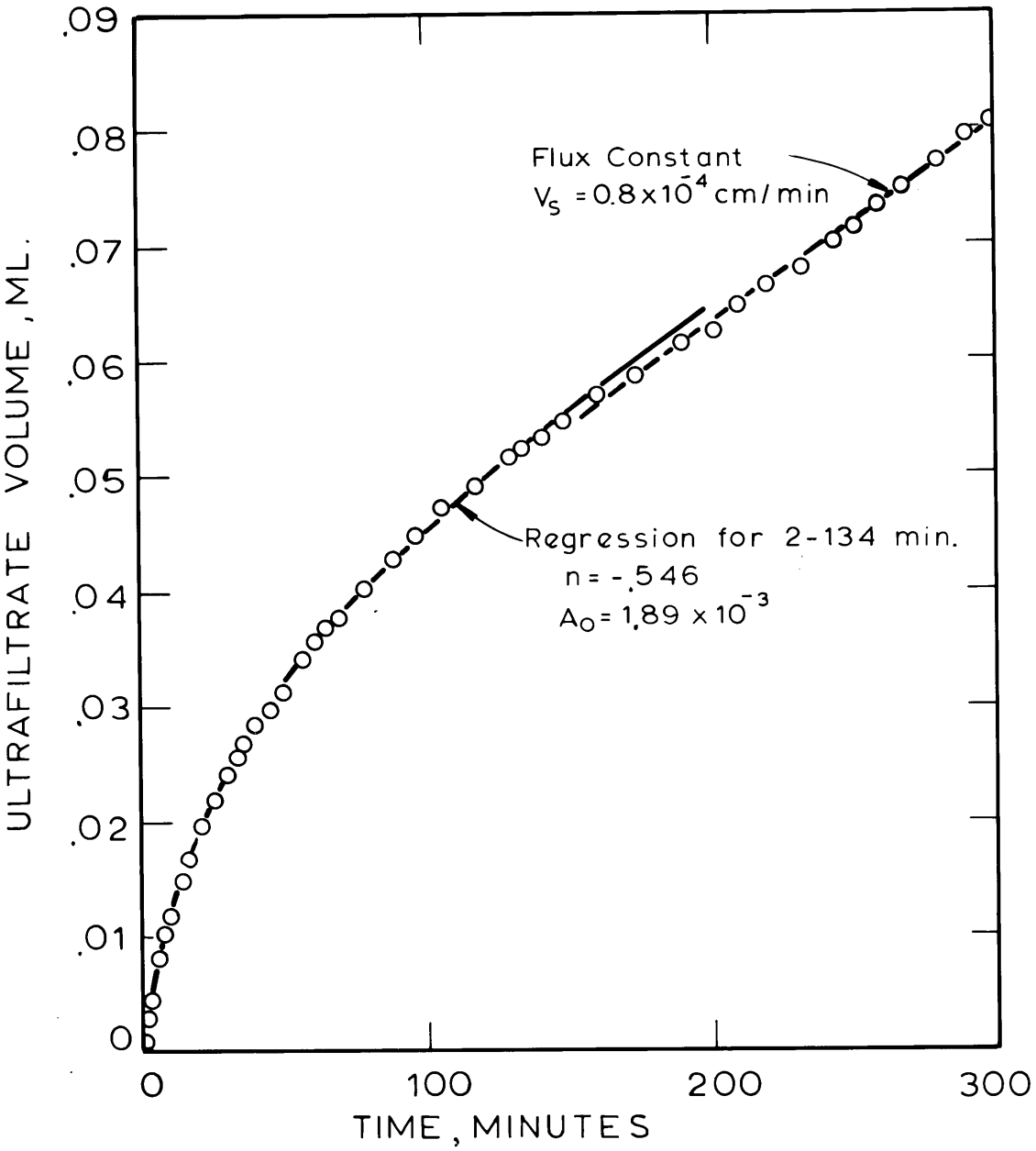

Figure 5-19 Experiment 600 Flow Data

PHOTO 603 - 33 min.

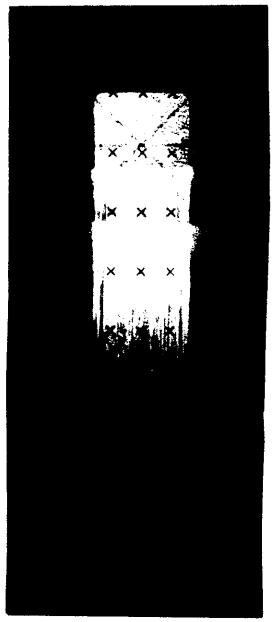

Wire 1 Wire 2

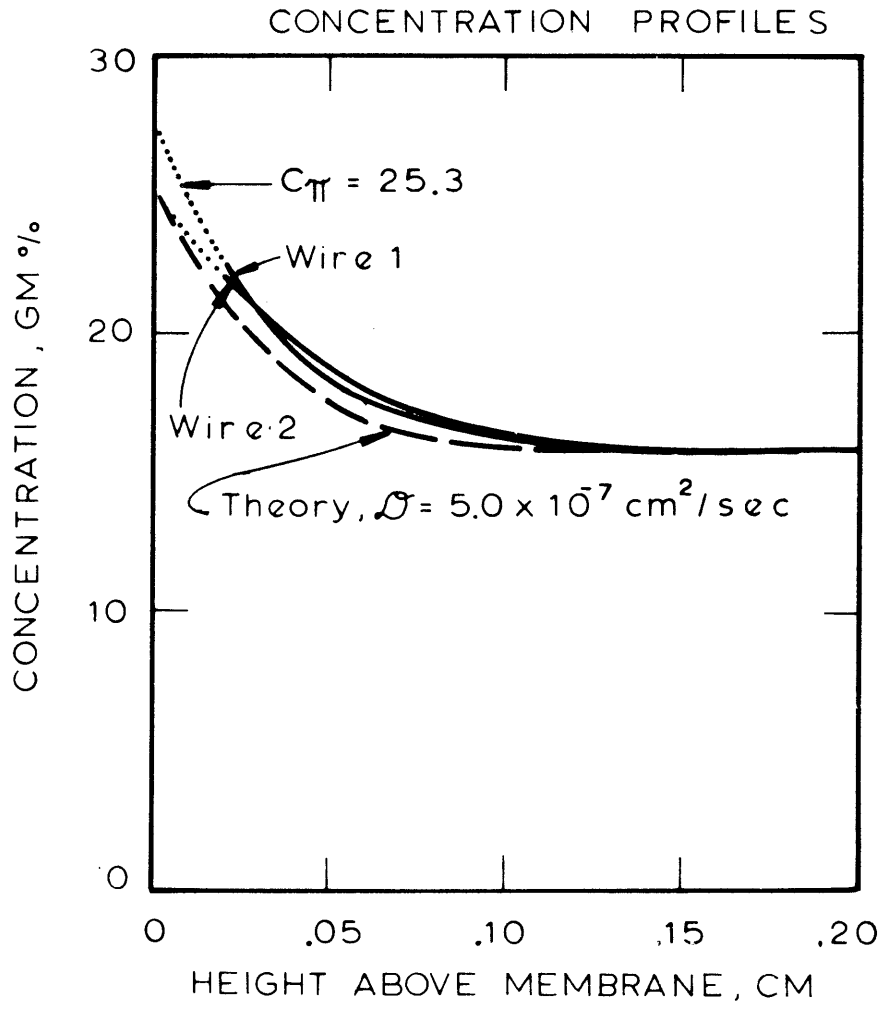

Figure 5 - 20 Experiment 600 Optical Data

η_{Bulk} = 1.3656

PHOTO 604 88 min.

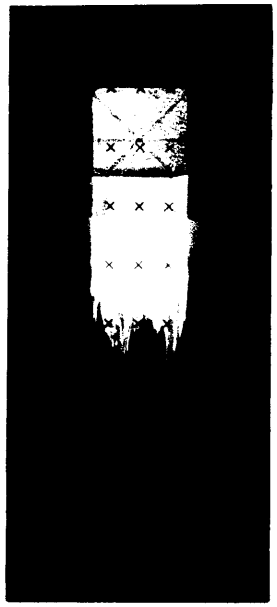

Wire 1 Wire 2

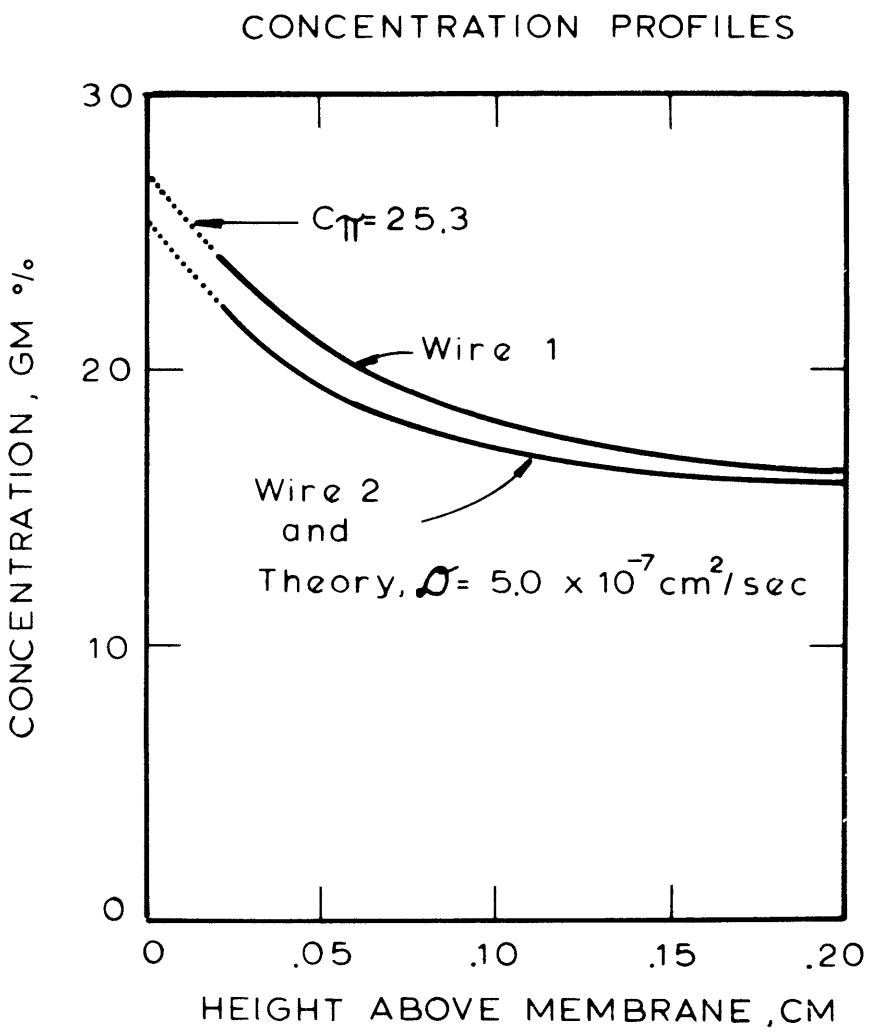

Figure 5-21 Experiment 600 Optical Data

η_{Bulk} = 1.3656

Experiment 700 (6.4 gm% BSA, 5.43 pH, 10.15 psi)

Objective: Reproduce results of Experiment 300 using new batch of Abcor HFA-180 membranes, and all previous improvements in apparatus and technique.

Comment: The use of the new HFA-180's required the use of a thin Parafilm gasket under the membrane in addition to the light grease coat. This was necessary to get a seal because of the roughened backing of the new membranes. Stresses in windows probably large due to excessive cell brace tightening.

Concentration Profile Determination: Figure 5-23 shows the profile calculated from the 648 min deflection pattern. The polarization layer thickness is 0.480 cm.

Flux Data: See Figure 5-22.

$v_s = A_o t^n$, cm/min

Time Interval for Regression	$A_o \times 10^{+3}$	n	Sum of Squares of Deviations, $\times 10^{+6}$
0 - 2 min	7.6 ± 0.9	-.214 ± .033	.5
2 - 678 min	6.11 ± .18	-.491 ± .002	302.
2 - 678 min	6.35 ± .02	-.500	393.

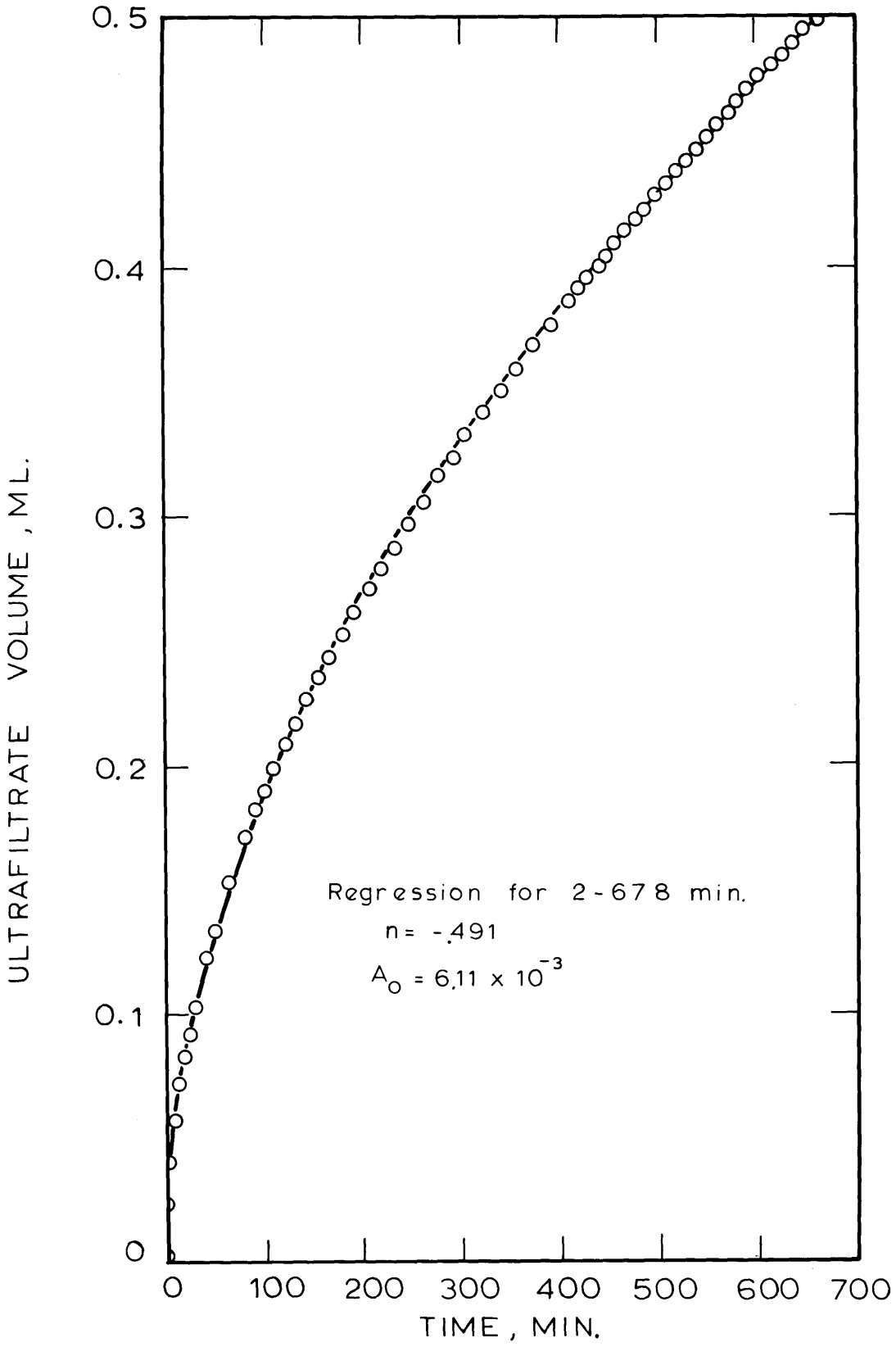

Figure 5-22 Experiment 700 Flow Data

PHOTO 706 - 648 min

Wire 1 Wire 2

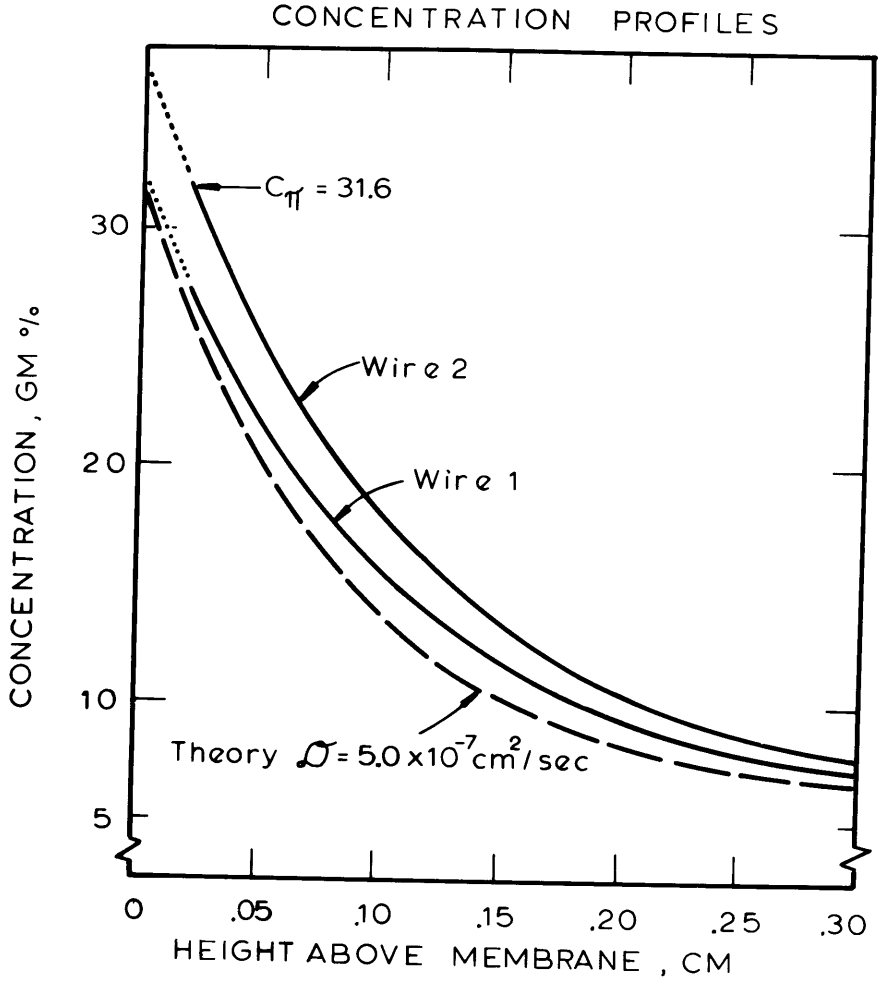

Figure 5-23 Experiment 700 Optical Data

η_{Bulk} = 1.3469

Experiment 900 (7.2 gm% BSA, 7.41 pH, 10.0 psi)

Objective: Begin investigation of pH effect

Comment: At the conclusion of this experiment studies were conducted on the osmotic backflow of solvent through the membrane, and membrane restoration without cell disassembly.

After Photo 907, the applied pressure was reduced to 0.81 psi to balance the head pressure of the LFD. In this condition of $\Delta P = 0$ across the membrane, the osmotic backflow of solvent was observed for 65 min. On Figure 5-25, the LFD volume change during this time is shown. The LFD volume is arbitrarily referenced to the volume which was observed 30 minutes before termination of ultrafiltration. Time is referenced to the moment when the applied pressure was decreased (536 min. elapsed time of ultrafiltration). From t = -30 min to t = 0, the LFD volume is increasing as ultrafiltrate flows into the device. When the pressure is rapidly reduced to $\Delta P = 0$, the direction of fluid movement in the LFD changes quickly, indicating the direction of saline flow across the membrane has been reversed. This osmotic backflow is rapid initially, and slows as the highly concentrated protein solution at the membrane surface

becomes progressively more dilute. The total solvent transfer for this period was 0.122 ml, or about 4% of ultrafiltration cell volume. Photo 910 of Figure 5-10 shows the deflection pattern after 45 minutes of backflow.

Membrane restoration was demonstrated by observing deflection patterns after the cell was drained and rinsed with ultrapure water. It was found that after four rinses, the third of which sat for at least 6 hours, no gradients remained above or at the membrane.

Concentration Profile Determination: Figure 5-26 shows the profile calculated from the 531 minute deflection pattern. The polarization layer thickness is 0.385 cm.

Flux Data: See Figure 5-24

$v_s = A_o t^n$, cm/min

Time Interval for Regression	$A_o \times 10^{+3}$	n	Sum of Squares of Deviations, $\times 10^{+6}$
0 - 2 min	9.1 ± .3	-.422 ± .006	.07
2 - 536 min	7.34 ± .30	-.427 ± .003	749.
2 - 536 min	10.17 ± .08	-.500	9640.

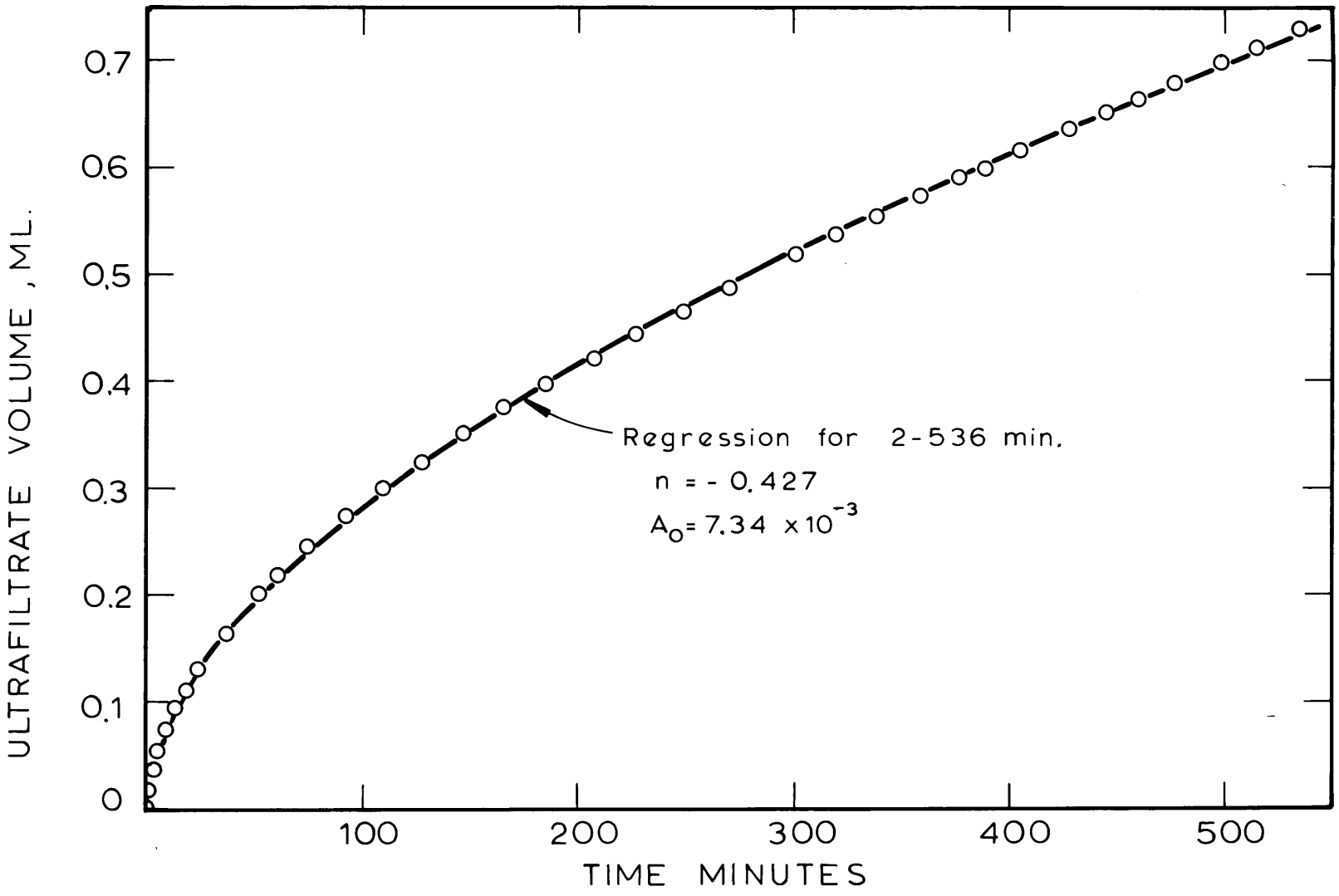

Figure 5 - 24 Experiment 900 Flow Data

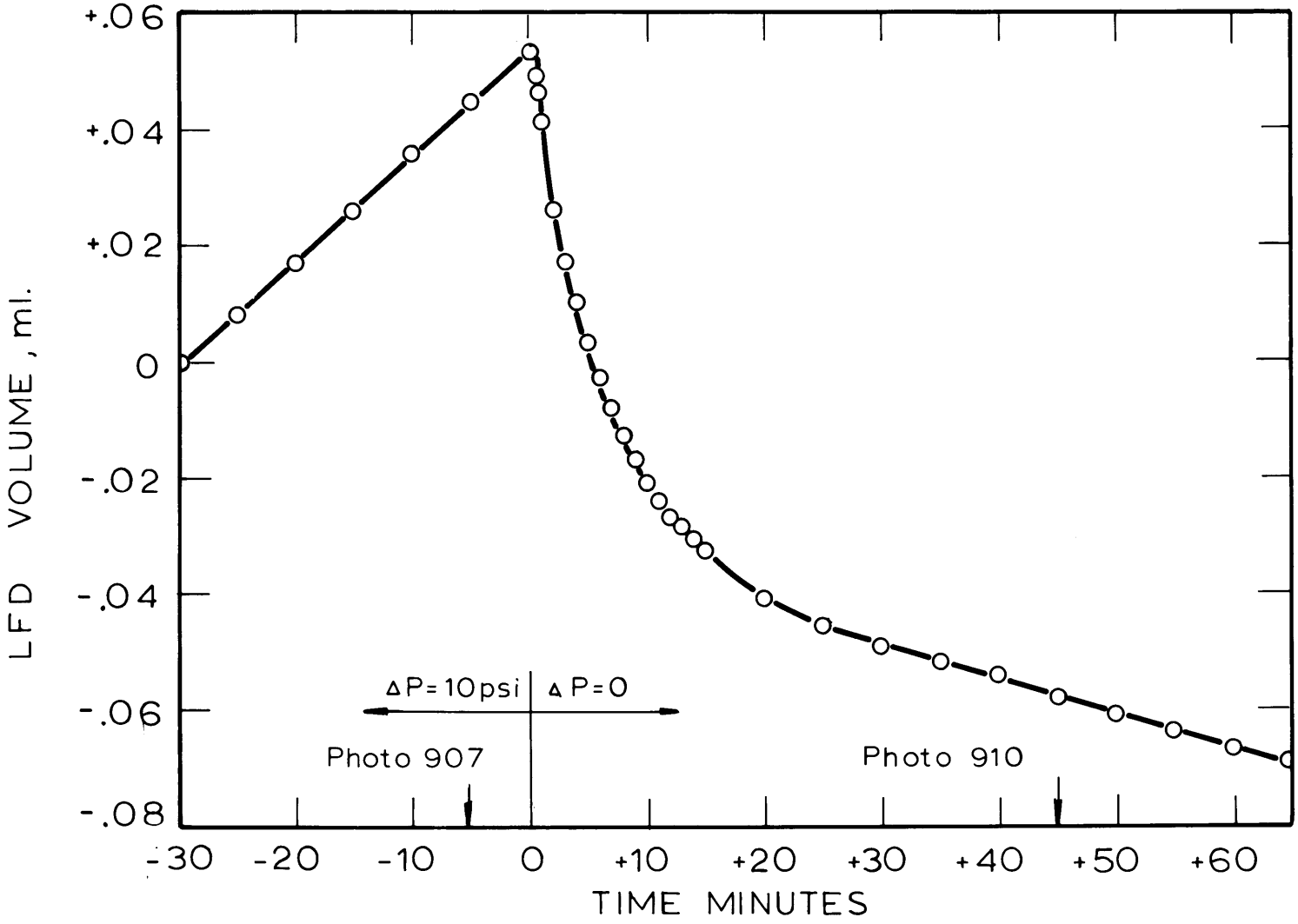

Figure 5-25 Osmotic Backflow Data

Photo 907 - 531

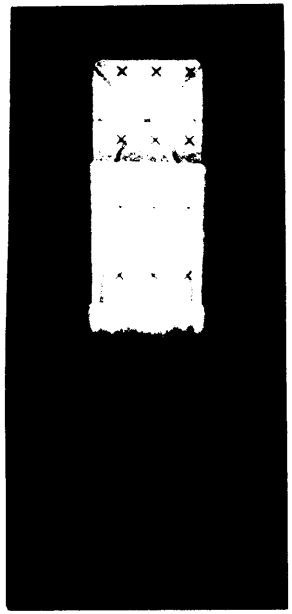

Wire 1 Wire 2

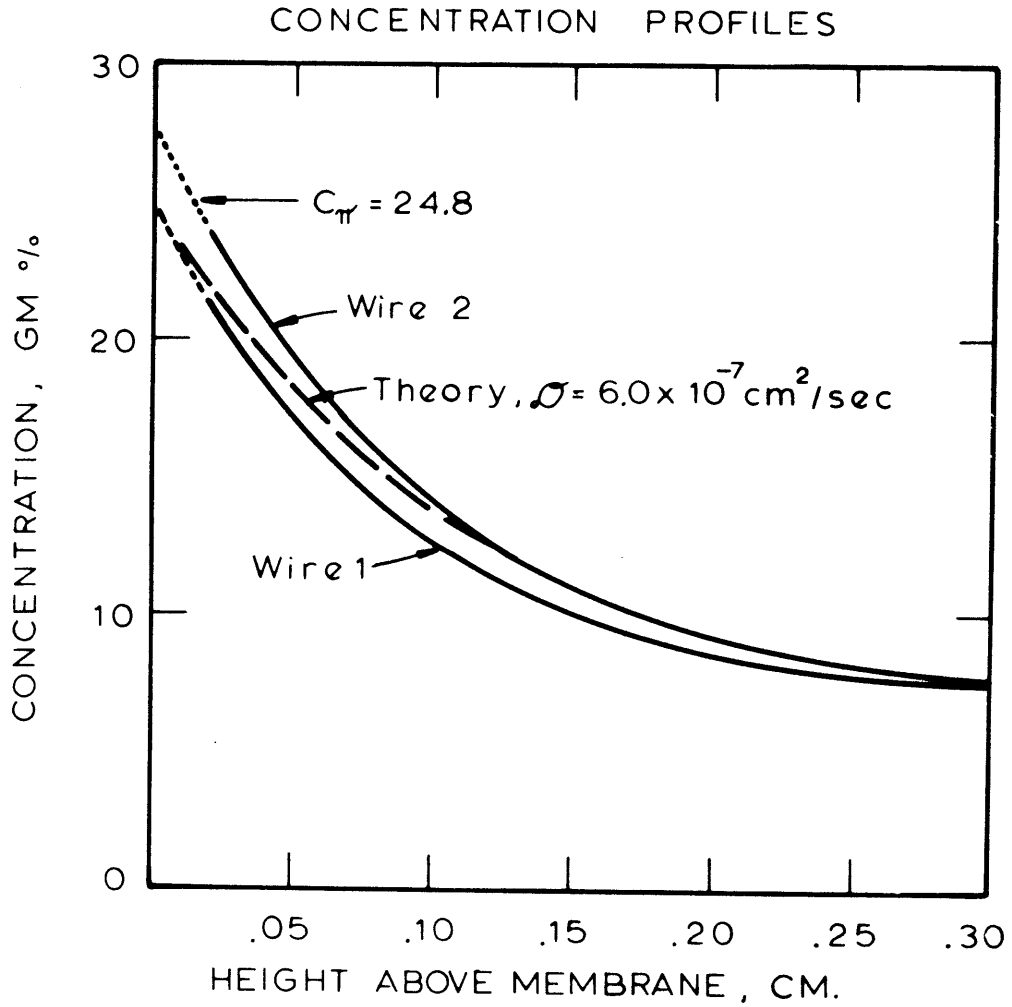

Figure 5-26 Experiment 900 Optical Data
η_{Bulk} = 1.3485

Experiment 1100 (10.1 gm% BSA, 4.50 pH, 10.1 psi)

Objective: Continue investigation of pH effect; vibration damping improved; first experiment that membrane surface aligned normal (± 0.15°) to gravity.

Comment: Birefringence of glass for this experiment is shown in Figure 5-6.

Concentration Profile Determination: Figure 5-27 shows the profile calculated from the 540 minute deflection pattern. The polarization layer thickness is 0.360 cm.

Flux Data: See Figures 5-49 and 5-50

Time Interval for Regression	$v_s = A_o t^n$, cm/min $A_o \times 10^{+3}$	n	Sum of Squares of Deviations, $\times 10^{+6}$
0 - 2 min	4.4 ± .4	-.273 ± .028	.24
2 - 548 min	4.89 ± .18	-.536 ± .002	23.2
2 - 548 min	4.22 ± .04	-.500	232.

Photo 1104 540 min

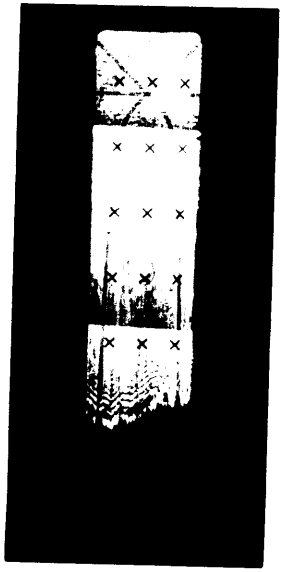

Wire 1 Wire 2

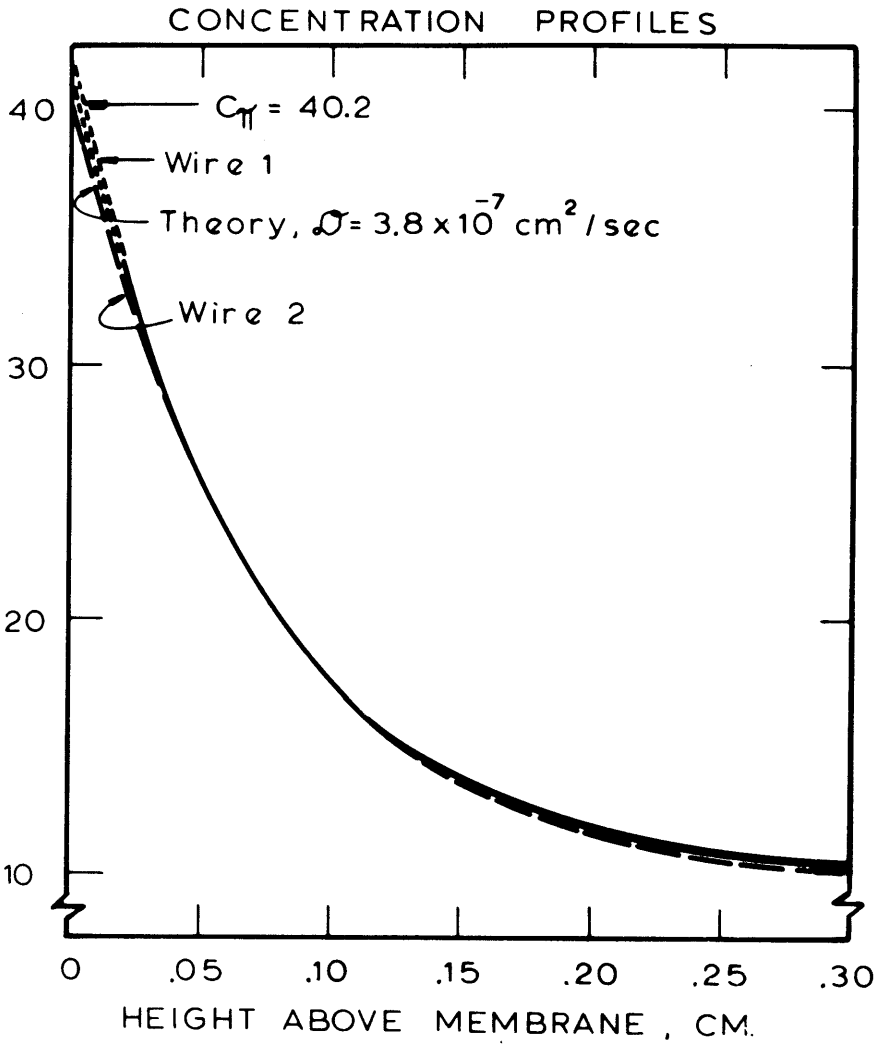

Figure 5-27 Experiment 1100 Optical Data

η_{Bulk} = 1.3543

Experiment 1200 (10.1 gm% BSA, 5.38 pH, 10.15 psi)

Objective: Compare this experiment at 5.4 pH with Experiment 1100 at 4.5 pH holding every variable constant except pH. The cell setup and system optical alignment are the same as for Experiment 1100. The cell and membrane were restored between the experiments by the procedure described in Experiment 900 summary.

Comment: Optical alignment was lost during the experiment; therefore no profile determinations were made. The experiment was continued to obtain flux data to 548 minutes. Window stress patterns examined after experiment - see Figure 5-6.

Flux Data: See Figures 5-49 and 5-50

$v_s = A_o t^n$, cm/min

Time Interval for Regression	$A_o \times 10^{+3}$	n	Sum of Squares of Deviations, $\times 10^{+6}$
0 - 2 min	4.6 ± .4	-.338 ± .023	.31
2 - 548 min	4.92 ± .10	-.476 ± .001	15.6
2 - 548 min	5.44 ± .03	-.500	175.

Experiment 1300 (10.1 gm% BSA, 4.50 pH, 10.15 psi)

Objective: Minimize glass window birefringence by minimizing stresses. New cell/membrane setup and optical alignment. All previous improvements in apparatus and technique included.

Comment: Window stresses were minimized using polarized light during adjustments to cell clamping brace. Final stress pattern shown in Figure 5-6.

Concentration Profile Determination: Equivalent profiles are obtained for both the deflection pattern in which saran and light filters were used and in the pattern in which these pieces were not present; photos 1305 and 1307, respectively, shown in Figure 5-28. The average polarization layer thickness for all profiles is 0.340 cm.

Flux Data: See Figures 5-49 and 5-50.

$v_s = A_o t^n$, cm/min

Time Interval for Regression	$A_o \times 10^{+3}$	n	Sum of Squares of Deviations, $\times 10^{+6}$
0 - 2 min	4.6 ± .9	-.557 ± .035	3.3
2 - 564 min	4.98 ± .33	-.558 ± .004	43.1
2 - 564 min	3.90 ± .06	-.500	420.

Photo 1305 542 min.

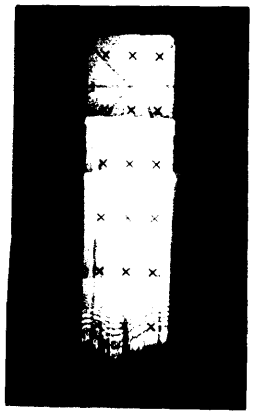

Photo 1307 555 min.

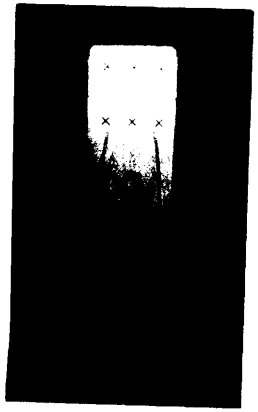

Wire 1 Wire 2

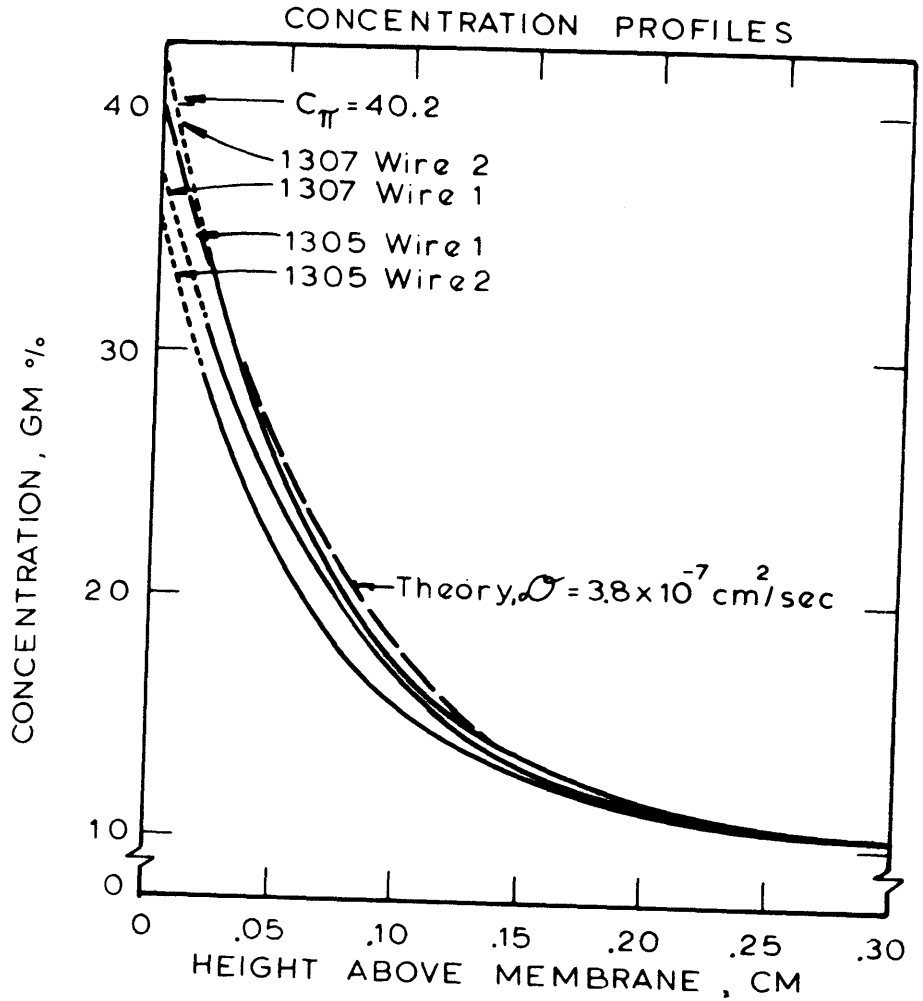

Figure 5-28 Experiment 1300 Optical Data

$\eta_{Bulk} = 1.3543$

Experiment 1400 (10.1 gm% BSA, 7.40 pH, 10.15 psi)

Objective: For comparison with Experiment 1300, only pH changed. Same cell/membrane setup and optical alignment as Experiment 1300.

Concentration Profile Determination: Profiles determined from Photo 1406 at 544 minutes are shown in Figure 5-29. The theory curve is coincident with Wire 1 for heights greater than about 0.07 cm. Polarization layer thickness is .425 cm.

Flux Data: See Figures 5-49 and 5-50.

$v_s = A_o t^n$, cm/min

Time Interval for Regression	$A_o \times 10^{+3}$	n	Sum of Squares of Deviations, $\times 10^{+6}$
0 - 2 min	5.4 ± .4	-.438 ± .015	.30
2 - 548 min	5.74 ± .16	-.464 ± .002	52.6
2 - 548 min	6.68 ± .05	-.500	648.

Photo 1406 - 544 min.

Wire 1 Wire 2

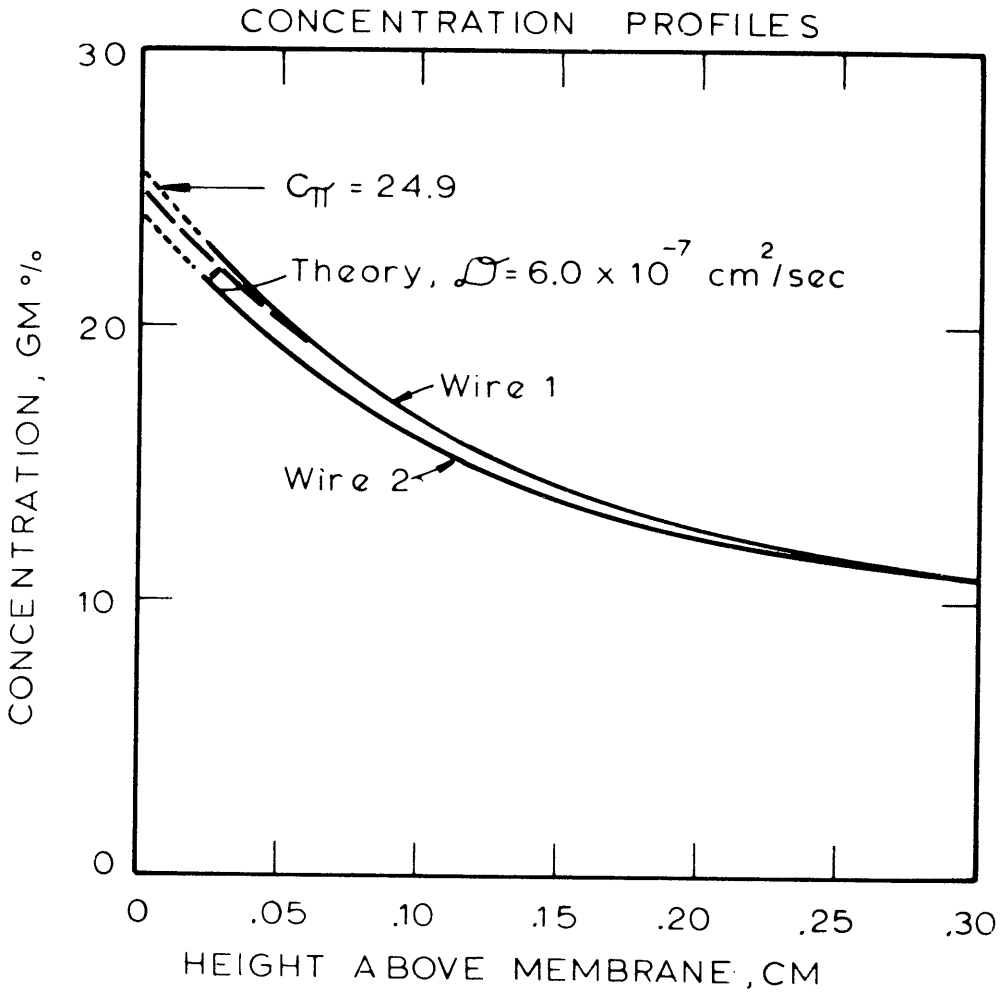

Figure 5-29 Experiment 1400 Optical Data
η_{Bulk} = 1.3543

Experiment 1500 (10.1 gm% BSA, 5.38 pH, 10.15 psi)

Objective: For comparison with Experiments 1300 and 1400. Same cell/membrane setup and optical alignment as Experiment 1300.

Concentration Profile Determination: Profiles determined from Photo 1505 at 532 minutes are shown in Figure 5-30. Polarization layer thickness is .390 cm.

Flux Data: See Figures 5-49 and 5-50.

$v_s = A_o t^n$, cm/min

Time Interval for Regression	$A_o \times 10^{+3}$	n	Sum of Squares of Deviations, $\times 10^{+6}$
0 - 2 min	5.5 ± .5	-.369 ± .024	.70
2 - 540 min	5.45 ± .20	-.469 ± .002	57.9
2 - 540 min	6.20 ± .04	-.500	375.

Photo 1505 - 532 mins

see figure 5 - 10

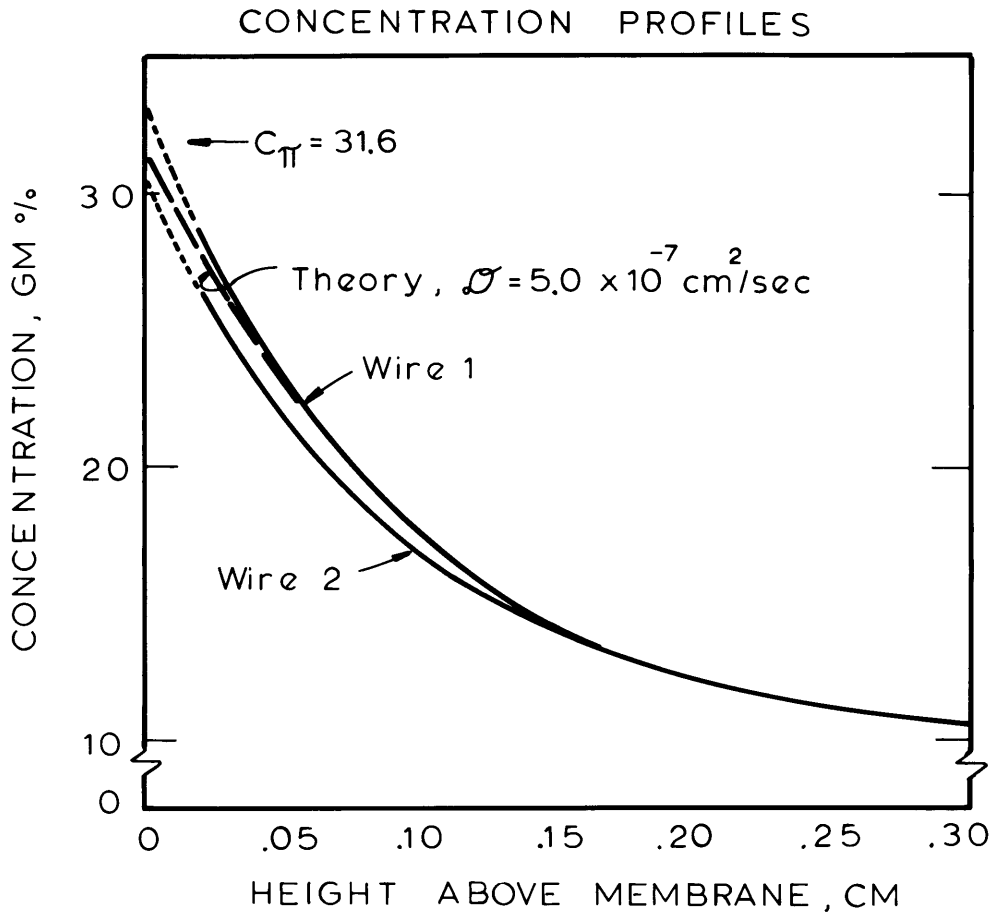

Figure 5 - 30 Experiment 1500 Optical Data

η_{Bulk} = 1.3543

Experiment 1600 (10.1 gm% BSA, 7.40 pH, 10.2 psi)

Objective: With the same cell/membrane setup as in Experiments 1300-1500, cell brace tightened to obtain a membrane seal to 40 psi. This preparation for Experiments 1700-1800 created large stresses in windows - see Figure 5-6 for these birefringence patterns.

Obtain enough ultrafiltrate at end of experiment to make Na^+, Cl^- and BSA determinations (results presented at end of this section).

Comment: Optics realigned before this experiment. For this experiment, and the next two, the horizontal wire was affected by the polarization layer after 9 hours or more. Therefore, membrane location and orientation of the wire reticle was done by averaging the initial positions determined for each of the three experiments from photos routinely taken before the start of each experiment.

Concentration Profile Determination: Profiles determined from Photo 1604 at 529 minutes are shown in Figure 5-31. Polarization layer thickness is .460 cm.

Flux Data: See Figures 5-49 and 5-50

Time Interval for Regression	$v_s = A_o t^n$, cm/min $A_o \times 10^{+3}$	n	Sum of Squares of Deviations, $\times 10^{+6}$
0 - 2 min	6.0 ± .5	-.402 ± .019	.52
2 - 527 min	5.68 ± .021	-.429 ± .003	123.
2 - 527 min	7.65 ± .10	-.500	3046.

Photo 1604 - 529 mins

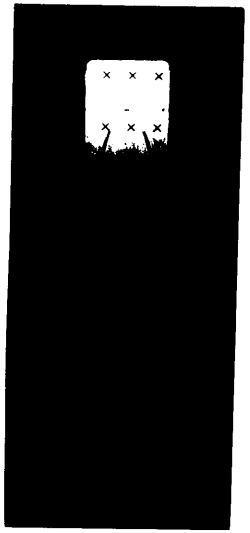

Wire 1 Wire 2

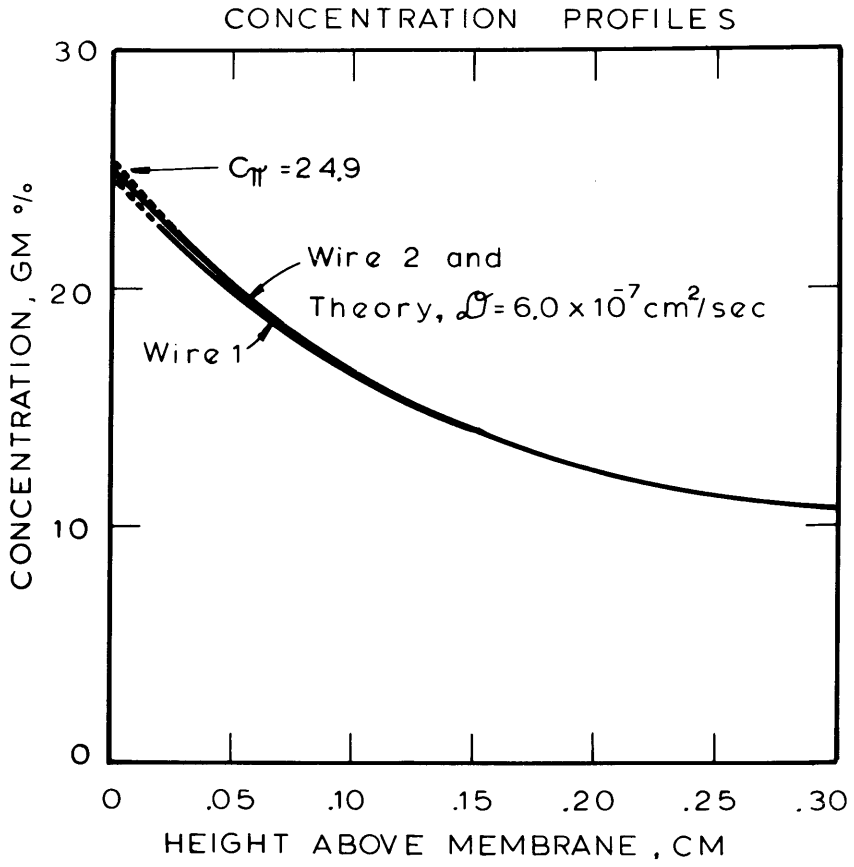

Figure 5-31 Experiment 1600 Optical Data η_{BULK} = 1.3543

Experiment 1700 (11.0 gm% BSA, 4.50 pH, 10.1 psi)

Objective: This is the 10 psi base experiment for comparison with the next experiment at 40 psi. Same cell/membrane setup and optical alignment as for Experiment 1600.

Concentration Profile Determination: Profiles determined at 542 minutes (Photo 1705, Figure 5-33) and 1368 minutes (Photo 1707, Figure 5-34; no saran or light filters). Average polarization layer thickness is 0.345 cm at 542 mins and 0.540 at 1368 mins.

Flux Data: See Figure 5-32

$v_s = A_o t^n$, cm/min

Time Interval for Regression	$A_o \times 10^{+3}$	n	Sum of Squares of Deviations, $\times 10^{+6}$
0 - 2 min	4.2 ± .6	-.428 ± .032	.4
2 - 1359 min	4.24 ± .10	-.494 ± .002	53.2
2 - 1359 min	4.36 ± .01	-.500	76.9

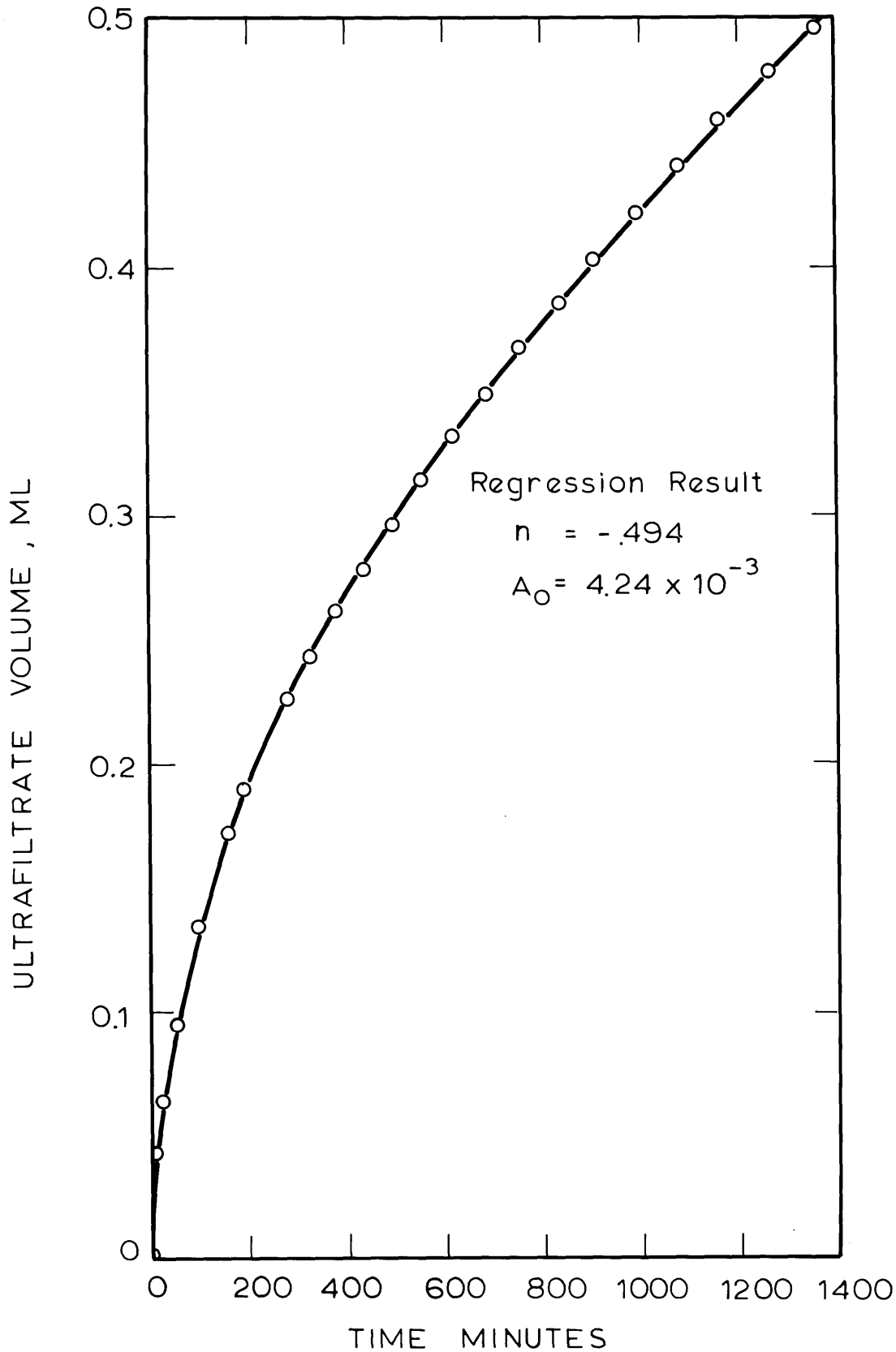

Figure 5-32 Experiment 1700 Flow Data

Photo 1705 5 42 min

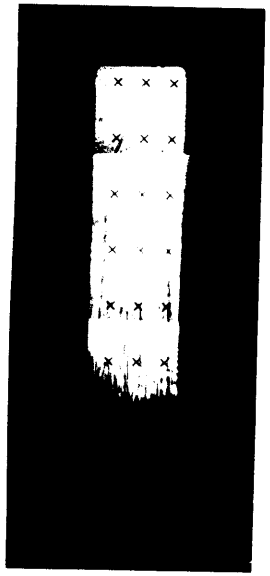

Wire 1 Wire 2

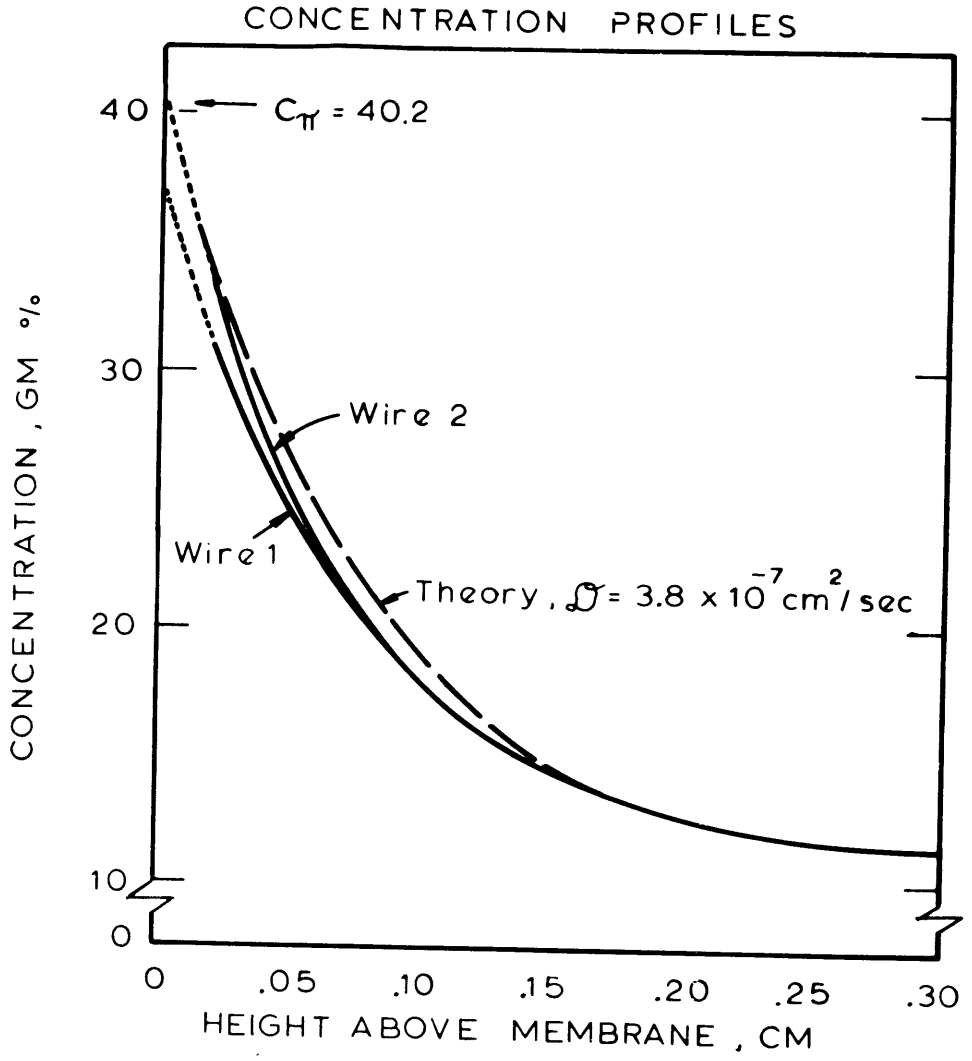

Figure 5-33 Experiment 1700 Optical Data
η_{Bulk} = 1.3560

Photo 1707 -1368 mins.

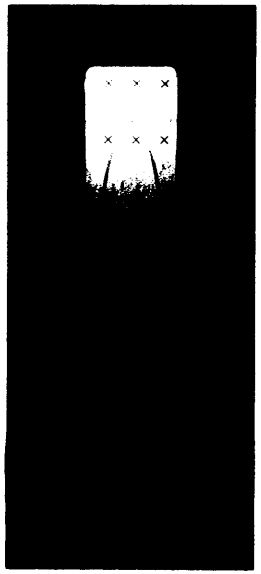

Wire 1 Wire 2

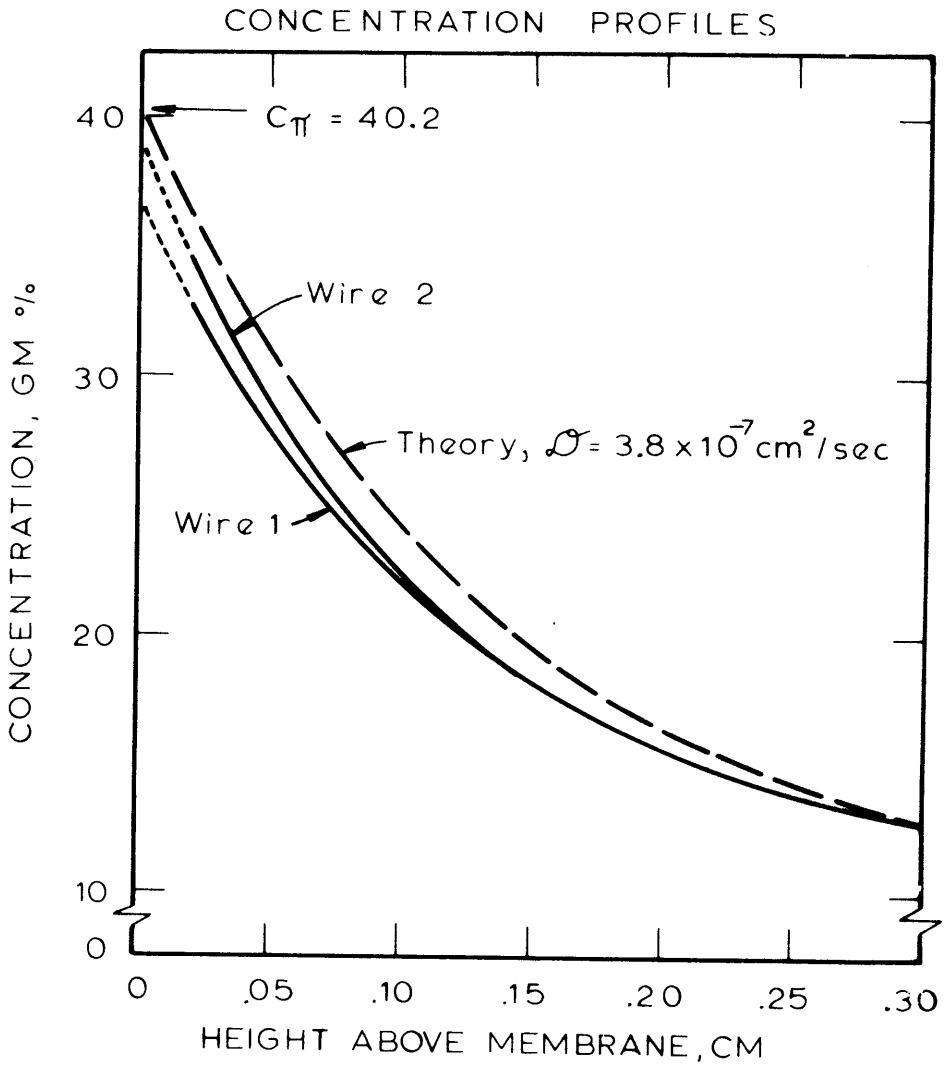

Figure 5-34 Experiment 1700 Optical Data
η_{Bulk} = 1.3560

Experiment 1800 (11.0 gm% BSA, 4.50 pH, 40.0 psi)

Objective: Investigate high pressure behavior, with a solution which approaches its solubility limit at the membrane when ultrafiltered at this high pressure. Sample ultrafiltrate for Na^+, Cl^- and albumin analyses (results shown at the end of this section).

Comment: At the end of the experiment control period, 23 hours, ultrafiltrate sampling begun. At 32 hours the filtration pressure was increased to 50 psi for an additional 15 hours. This higher pressure was intended to demonstrate the existence of an insoluble layer at the membrane surface.

Concentration Profile Determination: The deflection pattern of Photo 1808, Figure 5-36, gives the profile at 1387 minutes shown in Figure 5-37. The polarization layer thickness is 0.525 cm. A better view of this deflection pattern is provided by Photo 1807 of Figure 5-10 which was taken just 10 minutes earlier than 1808.

Also shown in Figure 5-36 is Photo 1815, taken 15 hours after the pressure increase to 50 psig. No evidence such as that seen in the osmotic backflow experiment shown in Figure 5-10, indicates the formation of a region of constant concentration near the

membrane surface. In Chapter 4, the estimated thickness of a gel layer under these conditions was 0.036 cm. The deflection data plot of Figure 5-38 indicates the presence of a refractive index gradient to within about 0.025 cm above the membrane for both wires (Height above membrane equals X1 * S_1 or X2 * S_2 where S is the undeflected wire slope and is close to unity for both wires). However, an inflection region is visible at the bottom of the deflection pattern. The region is more apparent for Wire 2 in Photo 1815 because of the orientation of the wire image reticle with respect to the membrane. The deflection data of Figure 5-38 accounts for this orientation difference and shows an inflection for both wires at about 0.11 cm. The functionality of the deflection data curve fitting routine, and the ray tracing SDIP routine, does not allow for this inflection and could be used only to approximate the concentration profile which caused this deflection pattern. This approximation indicated that the membrane surface concentration is at or near the concentration computed for Photo 1808, but that it decreases more slowly to about 0.11 cm above the membrane before reaching a more typical region of exponential decay. The polarization layer in this photo is about 1.50 cm thick.

Flux Data: See Figure 5-35

$v_s = A_o t^n$, cm/min

Time Interval for Regression	$A_o \times 10^{+3}$	n	Sum of Squares of Deviations, $\times 10^{+6}$
0 - 2 min	5.5 ± .9	-.422 ± .033	.8
2 - 1377 min	5.66 ± .17	-.509 ± .002	172.
2 - 1377 min	5.42 ± .02	-.500	266.

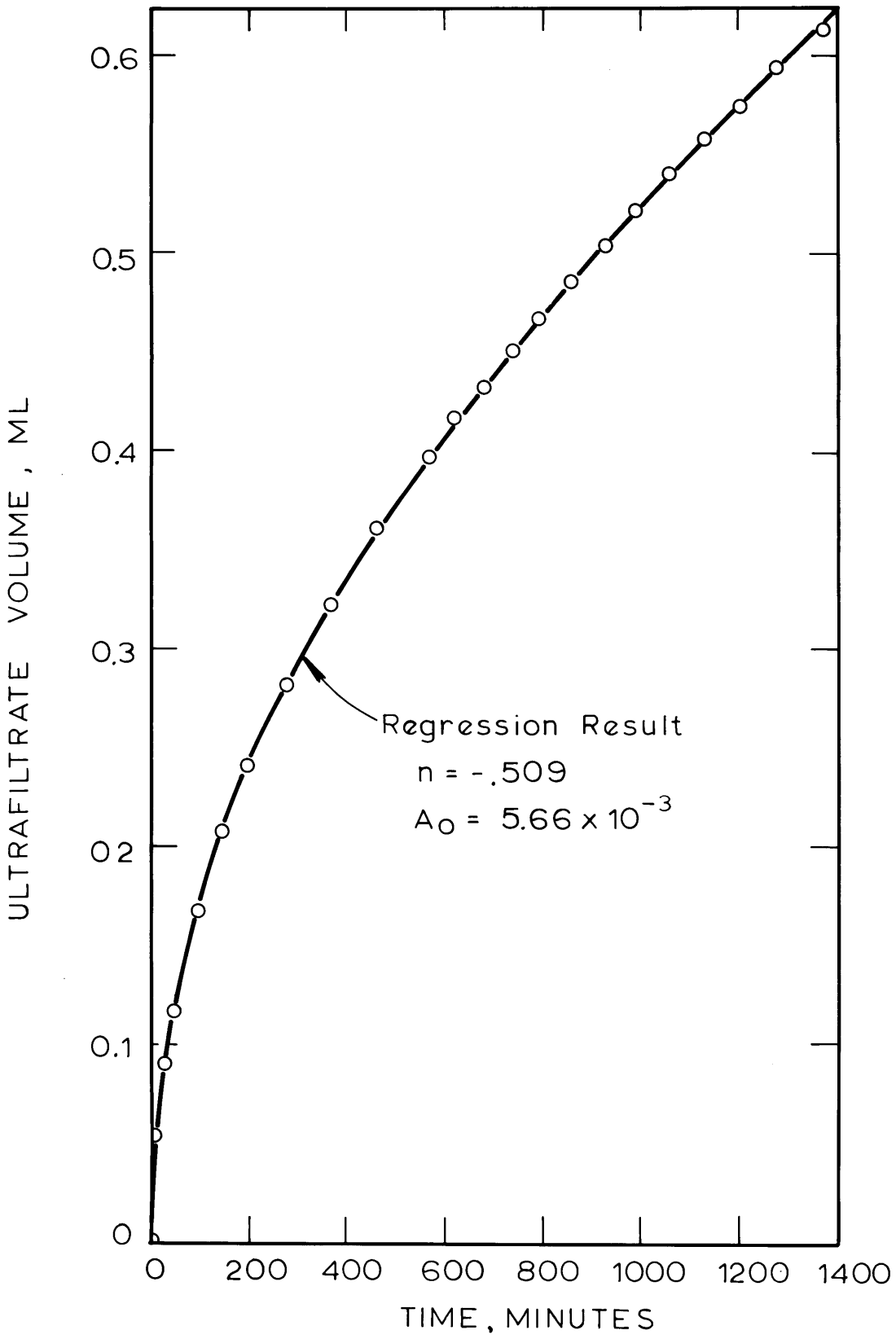

Figure 5-35 Experiment 1800 Flow Data

Photo 1808 1387 mins

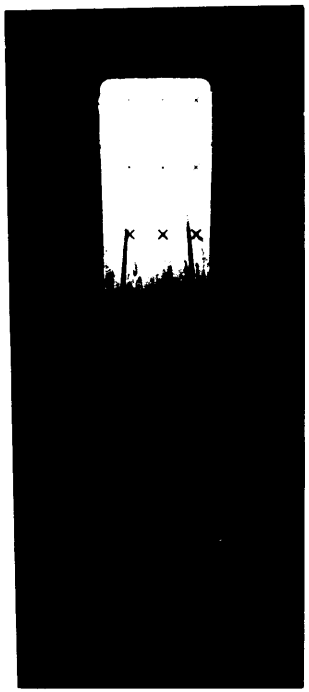

Wire 1 Wire 2

Photo 1815 - 50 PSIG , 47 Hrs

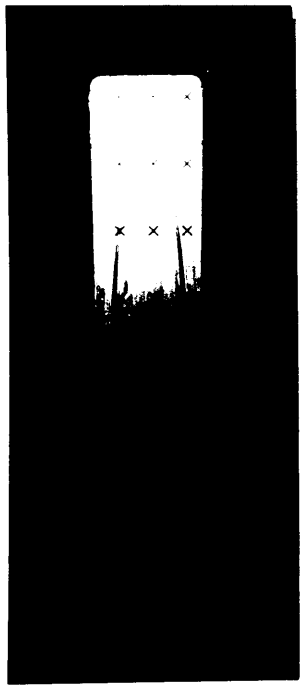

Wire 1 Wire 2

Figure 5 - 36 Experiment 1800 Optical Data
$\eta_{Bulk} = 1.3560$

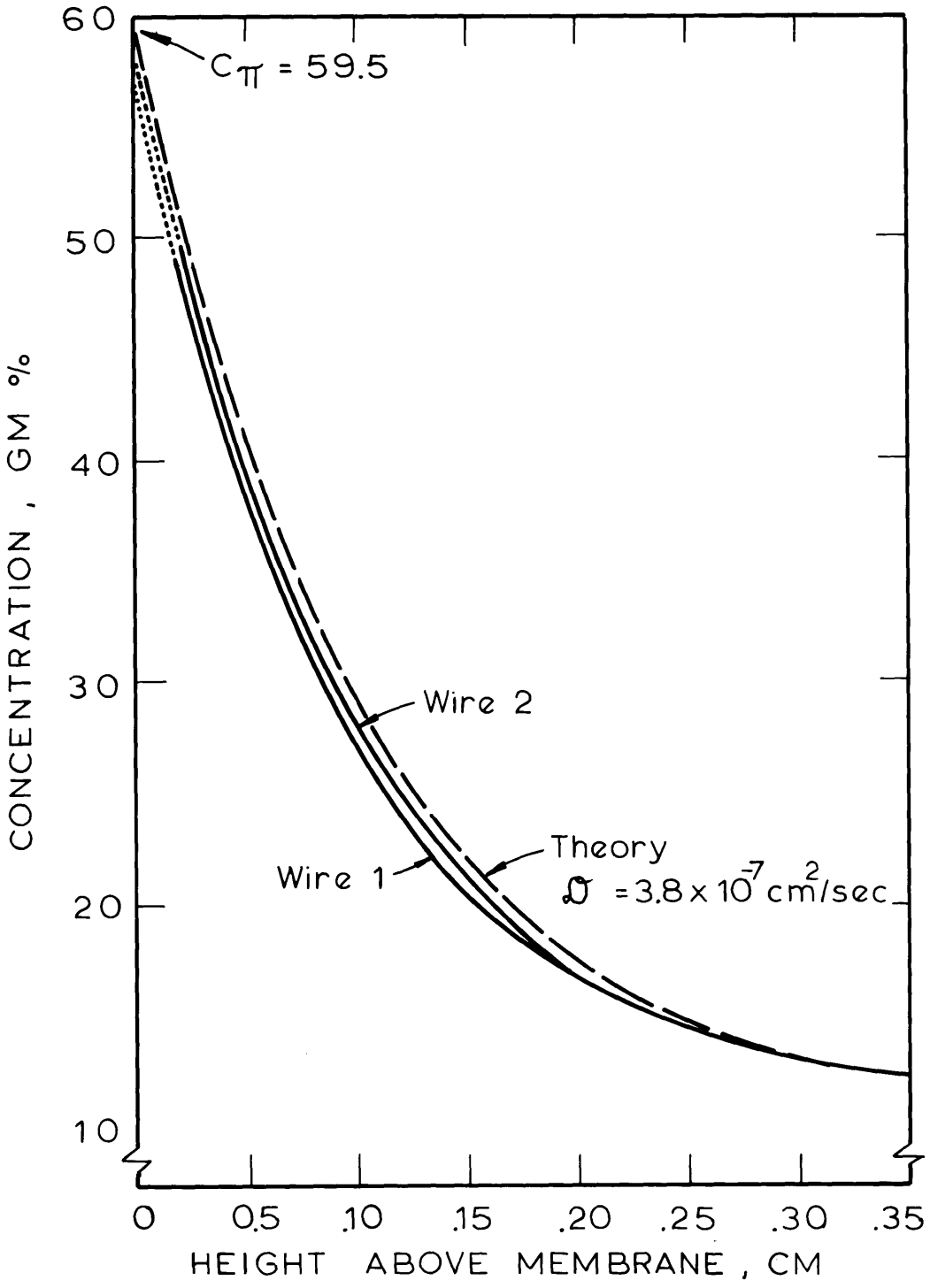

Figure 5-37 Concentration Profiles
Photo 1808 - 1387 mins

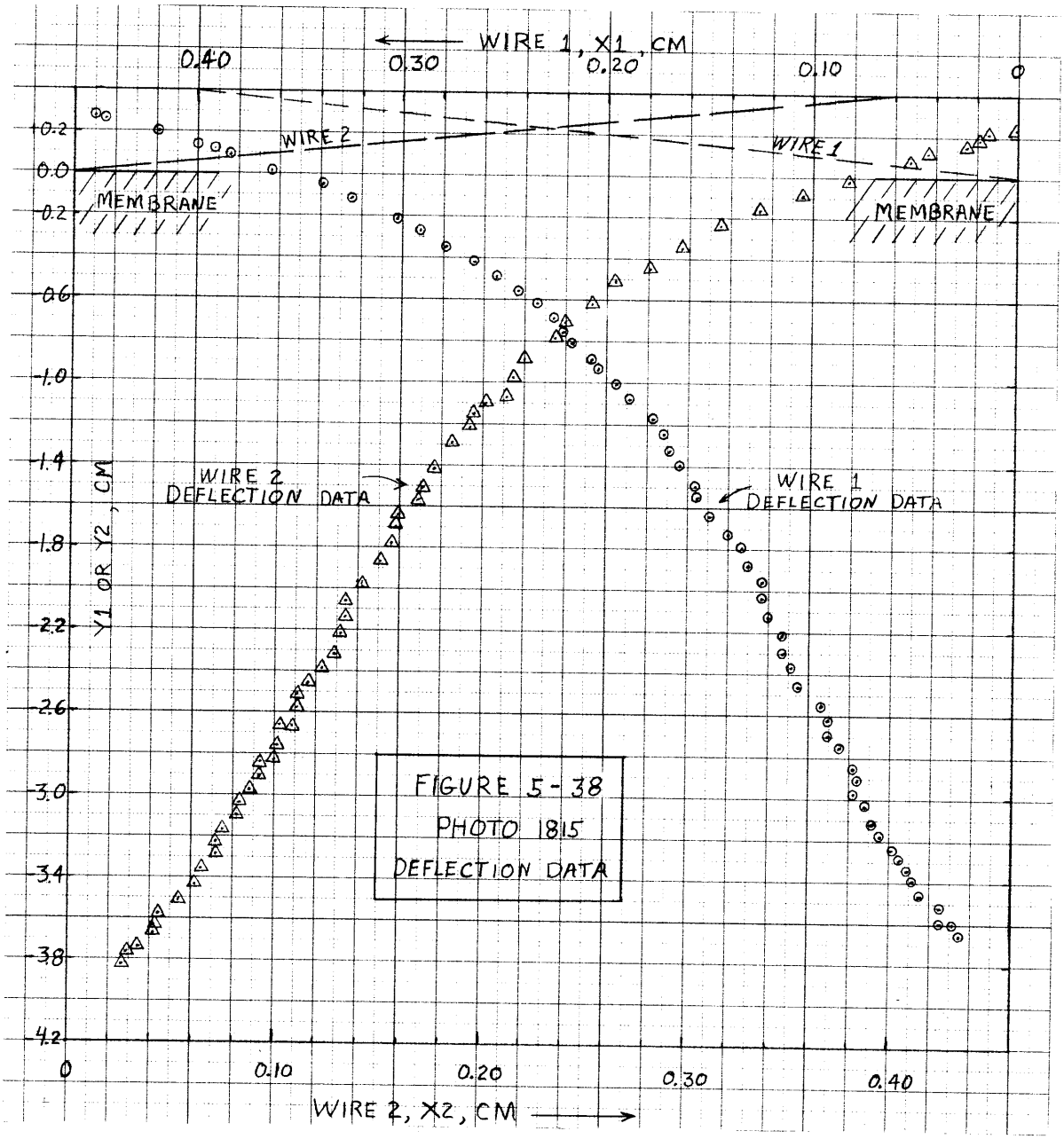

FIGURE 5-38
PHOTO 1815
DEFLECTION DATA

D. Investigation of the Parameters Affecting Flux Data Alone

These experiments investigated the effects of different starting procedures on the reproducibility of flux data, and the effect of pH for a consistent set of experimental variables. They were performed between Experiments 900 and 1100. The experiments were done with one cell/membrane setup. The standard wash procedure described in Section III was used between experiments. At the beginning of each experiment, saline was flushed through the membrane at 10 psi for one to two hours in order to determine new saline permeabilities (K_m) for each experiment.

The concentration of albumin was the same for all experiments, 7.1 gm% (0.070 gr BSA/gr solution). Pressure, 10 psi, and temperature, 25.6 ± .1 °C were also the same. Other characteristics of these experiments are summarized in Table 5-6. The average diffusivity is calculated from the results of Keller et al. (12) for the average polarization layer concentration.

Table 5-6

Data for Flux Experiments

Experiments	pH	Theoret. Membrane Conc., Gm%	$\bar{\rho}$ gm/ml	$\bar{D} \times 10^{+7}$ cm^2/sec
F6, F9	4.51	40.2	1.06	1.92
F1, F2, F3 F4, F7	5.40	31.5	1.05	2.32
F5, F8	7.36	24.8	1.04	2.75

1. Investigation of Experimental Starting Conditions

The four experiments in which only starting conditions were varied (F1-F4) were all at 5.4 pH. In experiment F1, pressure was applied and flow started exactly five minutes after albumin solution contacted the membrane. During this five minute period, the downstream flow valve was closed thereby preventing osmotic backflow of solvent. This condition closely approximates the starting procedure of Experiments 300 - 900, and exactly duplicates the procedure for all the experiments done after 900.

In experiment F2, an additional five minute waiting period was added before beginning ultrafiltration - again with the cell prevented from undergoing back transfer of solvent. In experiment F3, the downstream valve was opened during the second five minute waiting period thereby permitting the back transfer of solvent as a result of both the osmotic driving force ($\Delta\pi$ = 0.6 psi) and the 0.8 psi hydrostatic head of the LFD. The measured solvent transfer was 0.01 ml, or less than 1/2% of the cell volume. In experiment F4, this period of osmotic backflow was extended to 23.5 min during which .05 ml of solvent, or about 1 1/2% of the cell volume, was transferred through the membrane.

The expected result of this experimental sequence was that as the amount of solvent back-transferred before beginning ultrafiltration increased, the rate of ultrafiltration would also increase. The ultrafiltrate volume versus elapsed time data of Figure 5-39 show an opposite effect. The curves through the data are regression results for the function Flux = $A_o t^n$. The regression results, along with the data are presented in Appendix D. Also shown in the figure is the

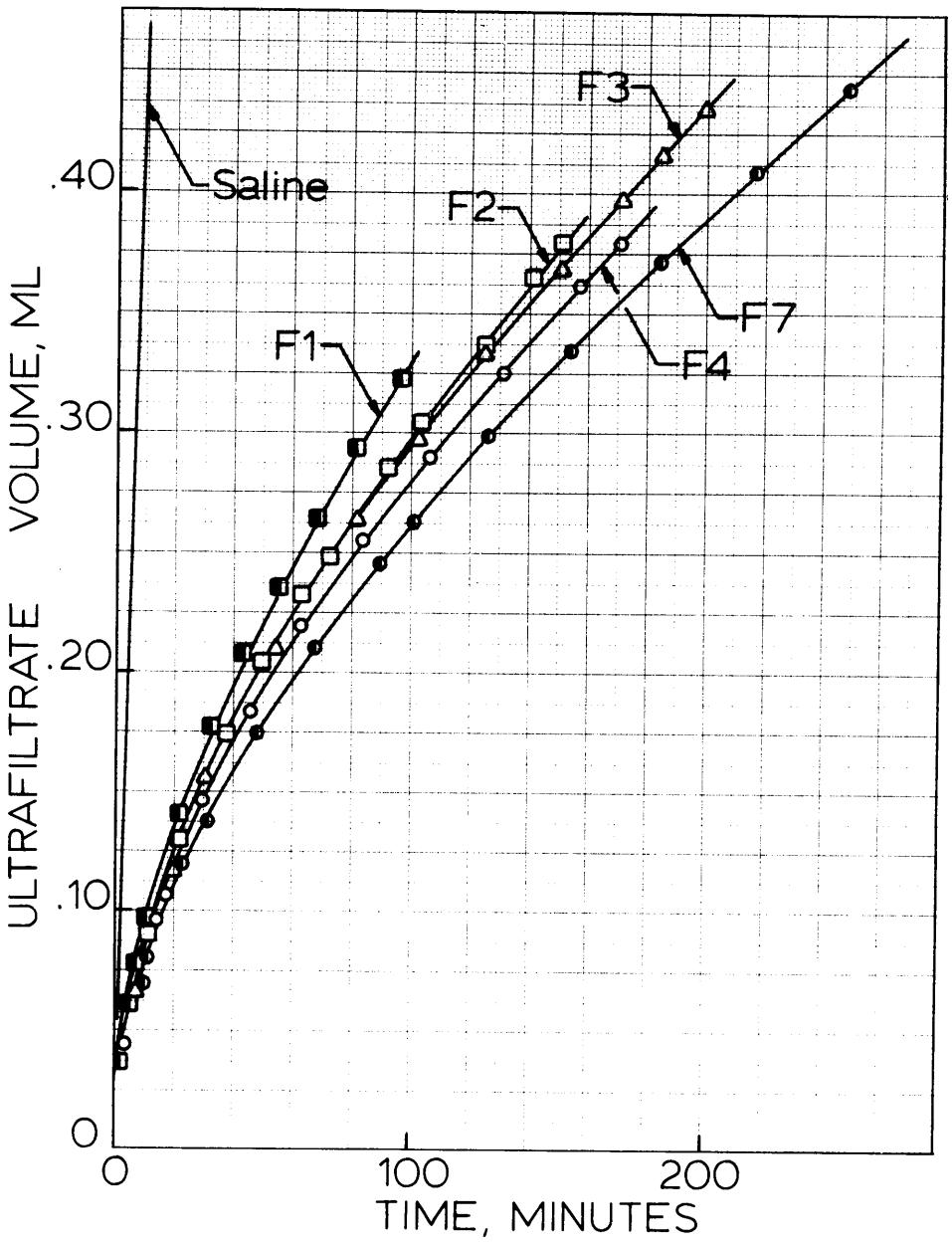

Figure 5-39: Effects of starting condition on flow.

straight line of steep slope representing the initial membrane saline permeability of 0.0034 ml/cm^2-min-psi. The decreases of this permeability by 7% prior to experiment F4 and a total of only 12% for the entire F-series, would represent an imperceptible shift of the line shown in the figure.

Following two experiments at different pH's, experiment F7 was a repeat of F1. As shown in Figure 5-39, the ultrafiltrate volume curve has decreased further.

Since the critical variables of ambient temperature, applied pressure and LFD transducer excitation voltage were well behaved for all of these experiments, and intrinsic membrane permeability to saline was nearly constant when it was checked between experiments, the source of this nonreproducibility is unknown. With reference to the discussion of Chapter 3 on membrane interaction with albumin, one hypothesis for this effect might be a change in the severity or type of a reversible membrane-protein interaction with increasing membrane age. It may also be significant that the K_m determinations between experiments were made with saline solutions (.15 M) which were not buffered or otherwise pH adjusted.

2. Investigation of pH Effect on Flow

Experiments F5-F9 investigated the effect of solution pH on flow. The first of these is experiment F5 at 7.36 pH. These results are the upper curve in Figure 5-40. The acid pH, 4.5, was the next experiment and is shown by the lowest curve in Figure 5-40.

Results for 5.4 pH are represented in this comparison by Experiment F7. This is done because the experiment is in the middle of the

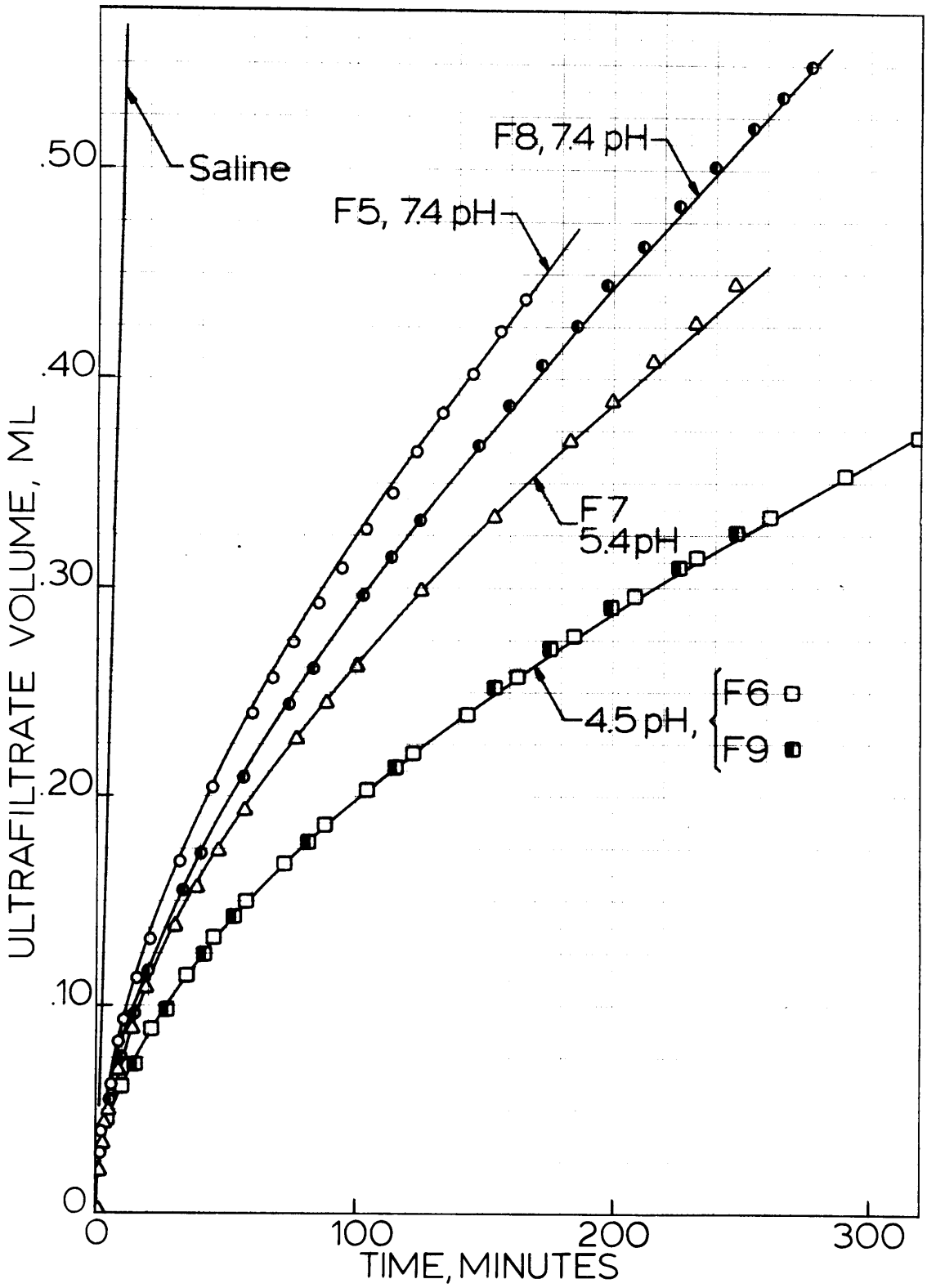

Figure 5-40: Effect of pH on flow.

pH study sequence, and the starting techniques were exactly the same for these five experiments.

Experiment F8, a repeat of the 7.36 pH experiment, demonstrates a decrease in flux over that observed for an earlier experiment at the same pH. Experiment F9, however, demonstrates a replication of the flow data at 4.5 pH.

The results again indicate difficulty reproducing flow data, maybe only at the higher pH's of 5.4 and 7.4. These difficulties could reflect further complications in membrane performance at these more basic pH levels.

In spite of poor reproducibility, the data support the observation that flux increases with increasing solution pH, but the increase may be impossible to quantitate from stagnant cell data. It is also concluded that starting conditions, when they are similar to those used in all of these experiments except F2, F3 and F4, are not a major influence for determining flux.

E. Ultrafiltrate Analysis

Figure 5-41 compares the measured inlet and outlet concentrations of Na^+ and Cl^- ions, and albumin for Experiments 1600 and 1800. These were the only two experiments for which enough ultrafiltrate was generated to permit these analyses. Because the holdup volume on the downstream side of the membrane is comparable to the sample size, these results can only be viewed as an indicator that a change has occurred. Prior to ultrafiltration, the membrane was flushed with .15 M saline, which therefore represents the initial composition of this holdup

FIGURE 5-41

ULTRAFILTRATE ANALYSES

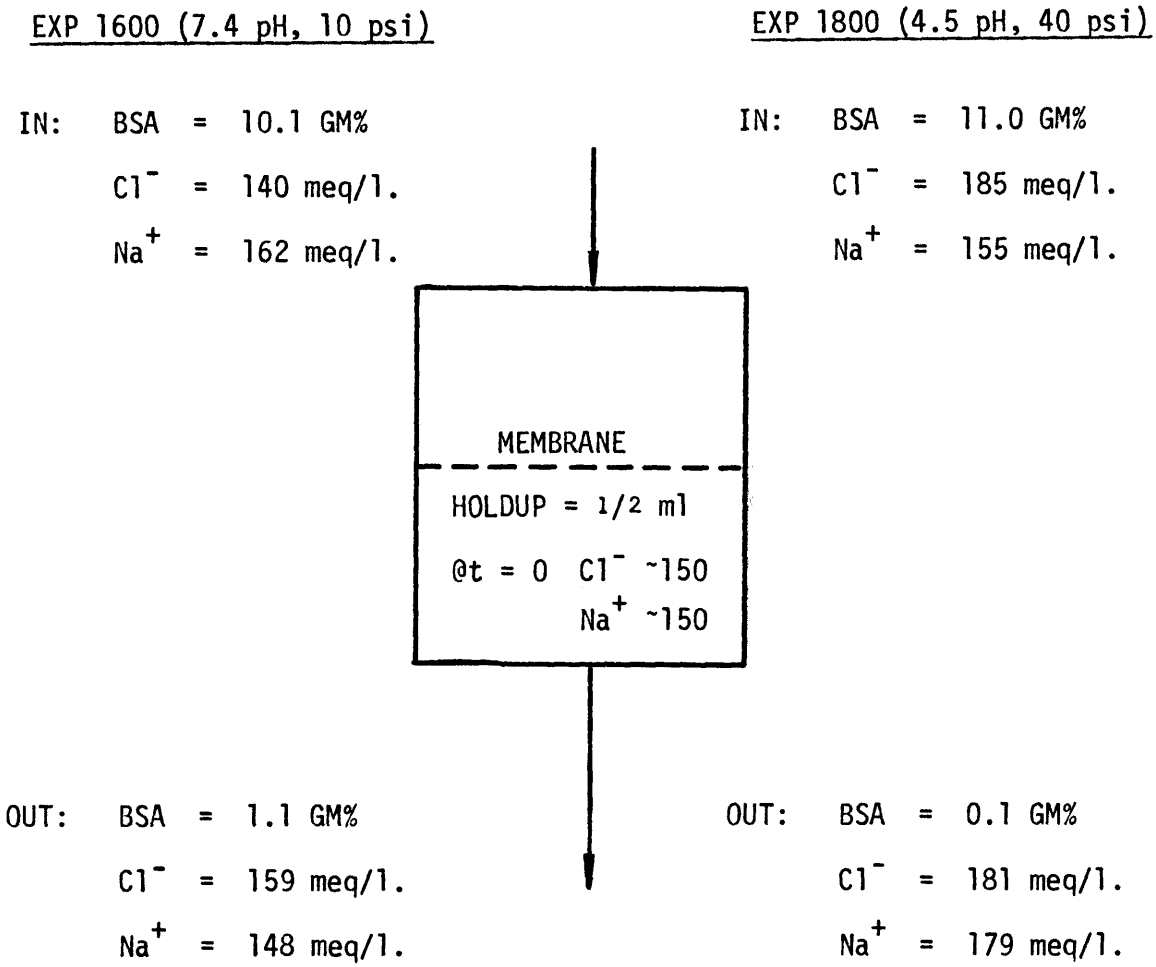

DISCARD 1st 1/2 ml

SAMPLE 2nd 1/2 ml

CHANGE: (OUT-IN)/IN

Cl^- = +14%

Na^+ = -9%

CHANGE: (OUT-IN)/IN

Cl^- = -2%

Na^+ = +15%

volume. From a total sample volume of about 1 ml, only the second 0.5 ml was analyzed.

The unequal concentrations of Na^+ and Cl^- in the input solutions result from the use of sodium hydroxide (Exp 1600) or hydrochloric acid (Exp 1800) additions to the .15 M saline solutions of albumin for pH adjustment.

The results show a small net increase in microion concentrations for each experiment. The small amount of albumin leakage is comparable to that observed in the osmometry studies of Chapter 3, except that the greater leakage is shown for the 7.4 pH solution. In the osmometry analyses, the largest albumin leakage was detected for the 4.5 pH solutions. For this reason, in addition to the belief that such leakage is of a primarily diffusive nature and the ultrafiltrate collection time for Experiment 1800 was much longer, a reversal of these reported leaked albumin concentrations would make more sense. Unfortunately, sufficient sample for only one determination for each experiment was available.

VI. Discussion

Reference was made in the introductory chapter to several investigators who previously have suggested the significant limitation imposed on ultrafiltration by the increased osmotic pressure at the membrane surface. In addition to this limitation, the asymptotic solution of the physical model derived in Chapter 4 also predicts that the polarized layer grows like the square root of time, and the flux diminishes like the inverse square root of time. The objective of the following discussion, through comparisons between results and theory, and between varying experimental conditions, is to show where these suggestions and predictions are correct, and where they are oversimplified.

A. Concentration Profile Measurements

Table 5-7 compares measured protein concentrations at the membrane surface with the concentration for which the solution osmotic pressure equals the applied pressure. The fact that varying solution pH, or applied pressure, effects these two concentrations in exactly the same way further indicates that in the experiments conducted, albumin ultrafiltration was limited by osmotic pressure.

While thermodynamics limits the maximum concentration at the membrane surface, the development of the albumin concentration profile is mediated by molecular diffusion. Figures 5-42, -43 and -44 show the profiles (average of both wires) of Experiments 1300, 1500 and 1400 respectively. These experiments are equivalent in every way except solution pH. In each figure, the measured profile is compared with a theoretical profile calculated with diffusivities taken from the data

TABLE 5-7

Comparison of Measured Membrane Concentration, $G_{Y=0}$ and Osmotic Pressure Concentration, G_{π}.

pH	ΔP, psi	$G_{Y=0}$, GM%	G_{π}, GM%	Experiment
4.5	10.10	41.6	40.2	1100
	10.15	39.4	40.2	1300
	10.10	38.3	40.2	1700
	40.00	58.1	59.5	1800
5.4	9.60	29.3	31.0	300
	5.60	26.0	25.3	600
	10.15	34.5	31.6	700
	10.15	32.0	31.6	1500
7.4	10.00	26.1	24.8	900
	10.15	24.8	24.9	1400
	10.20	25.0	24.9	1600

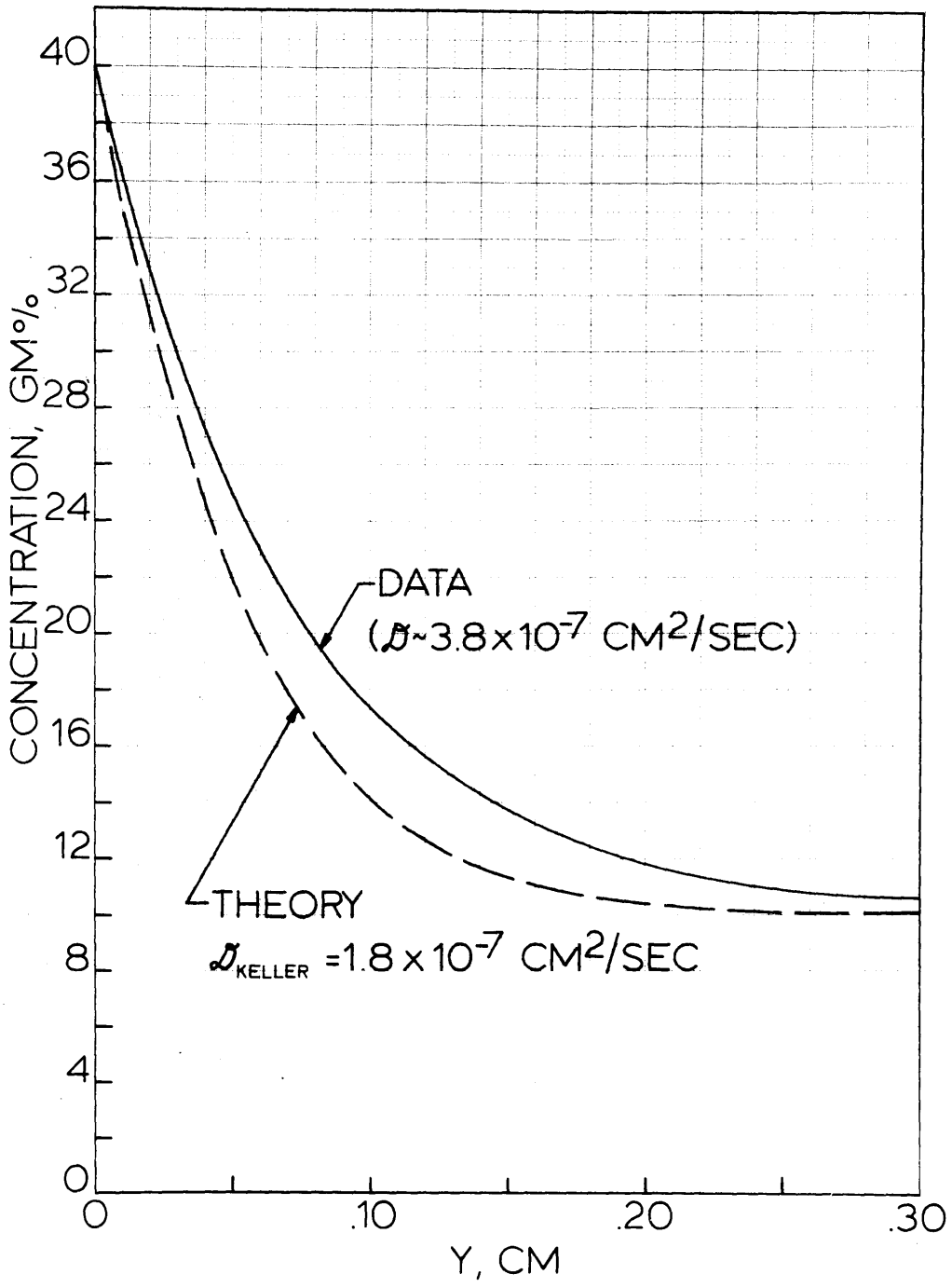

Figure 5-42: Albumin ultrafiltration at 4.5 pH.

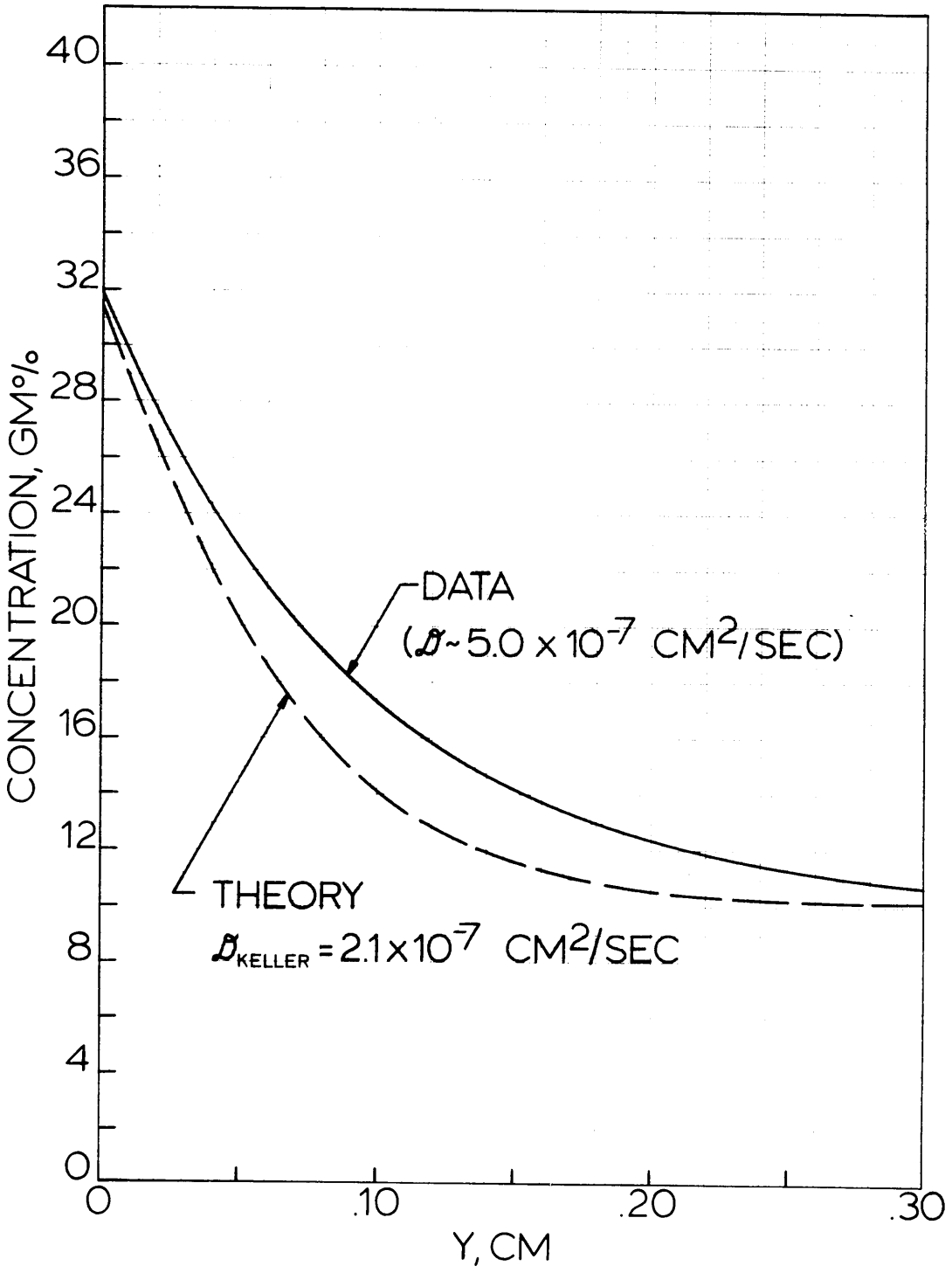

Figure 5-43: Albumin ultrafiltration at 5.4 pH.

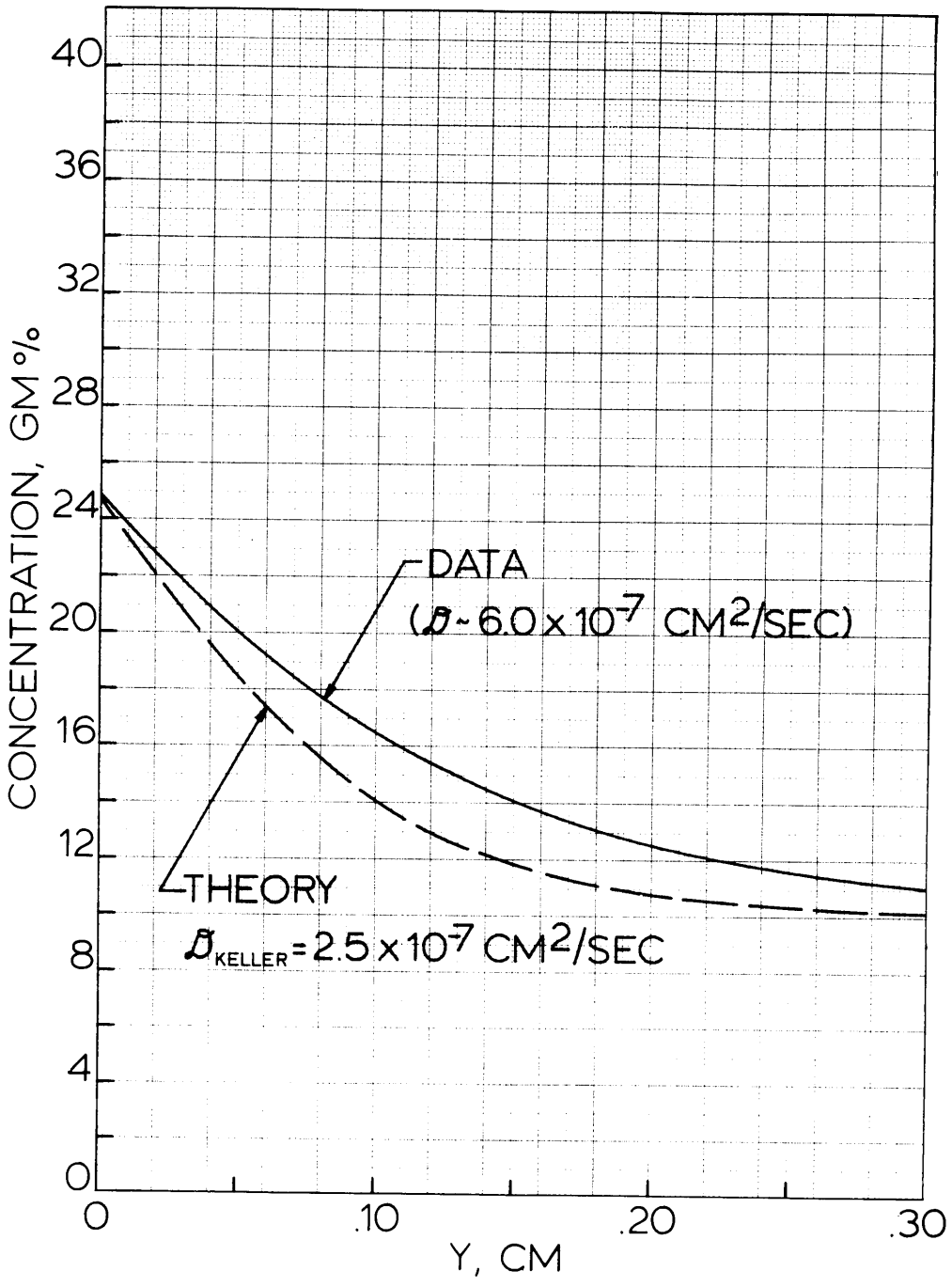

Figure 5-44: Albumin ultrafiltration at 7.4 pH.

of Keller, Canales and Yum (12). These diffusivities were evaluated at the polarization layer average concentration. In the description of experimental results, Section V, it was shown that for each experiment, a diffusivity could be found which made the theoretical calculation closely approximate the data for these three experiments, which are regarded as the most representative of the three respective pH levels. These values are shown on the figures.

In each case, the theoretical profile for $\overline{D}_{Keller}$ is below the data. The discrepancy between the two curves in each figure probably reflects both the failure to account for an effective diffusivity dependence on pH and inadequacies of the constant property model. As cited in Chapter 2, Keller, et al. made their diffusion measurements in an acetate buffer at 4.7 pH, as opposed to the unbuffered .15 M NaCl solutions used here. A higher diffusivity for increasing solution pH is supported by the observation that while at the membrane surface $G_{4.5pH} > G_{5.4pH} > G_{7.4pH}$, the polarization layer thickness at 9 hours ranks in reverse order, $\delta_{7.4pH} = 0.420$ cm, $\delta_{5.4pH} = 0.390$ cm, $\delta_{4.5pH} = 0.350$ cm. This thickness is the height above the membrane surface at which the polarization layer concentration is 2% greater than the bulk. Data is tabulated in Appendix D for each experiment. The profiles are compared in Figure 5.45.

Stagnant ultrafiltration is an unsteady state process. The asymptotic model of Chapter 4 was shown there to apply to all cases for which time exceeded

$$t >> \left(\frac{1}{(K_m/\overline{\rho})(\Delta P - \pi^i)} \right)^2 \overline{D} \qquad (5\text{-}27)$$

Figure 5-45

CONCENTRATION PROFILE COMPARISONS
10.1 GM %, 10 PSIG, 9 HOURS

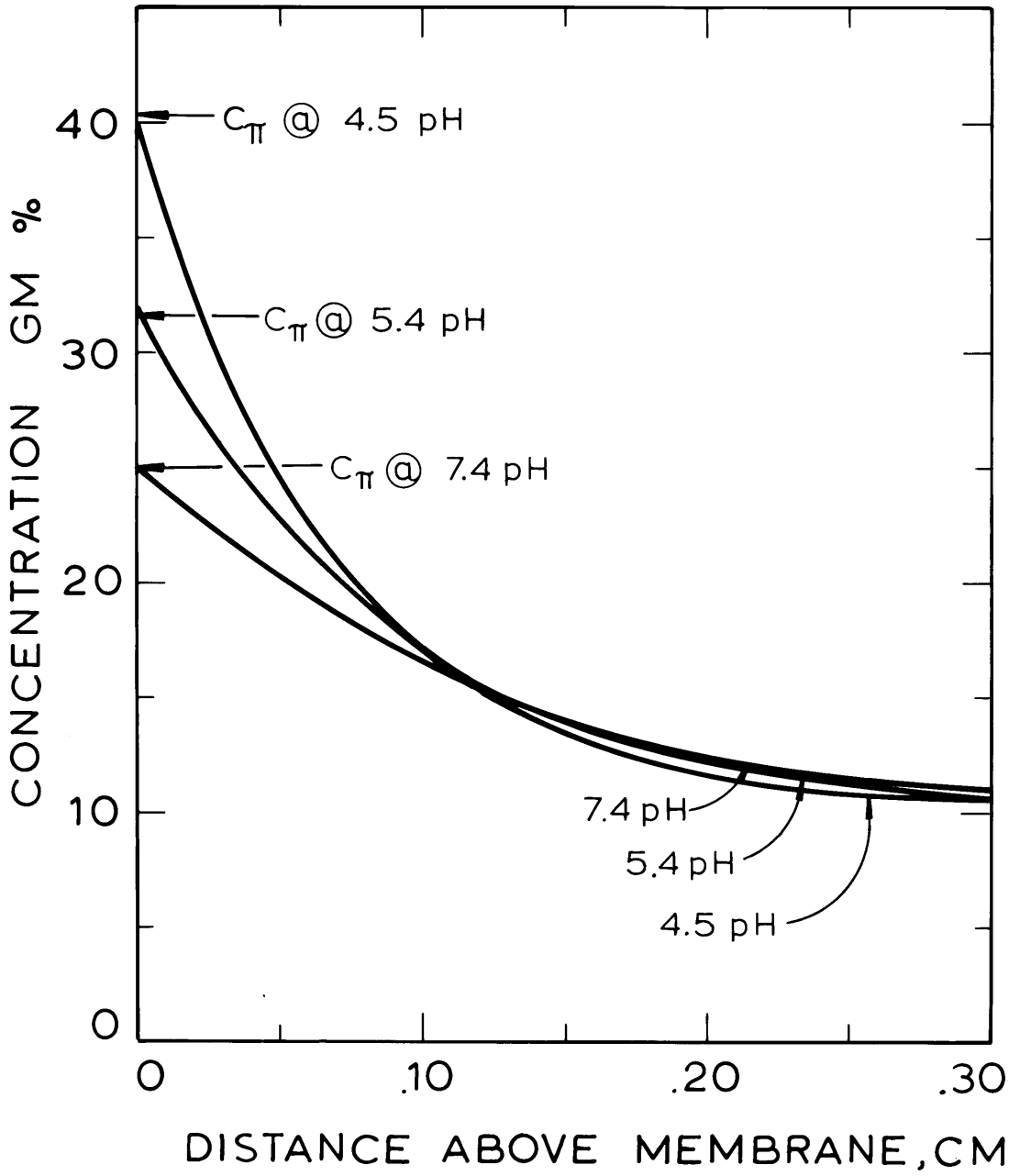

Generally, for the experiments here, this meant times greater than about 0.1 seconds. In Experiment 600, with high bulk solution concentration (15.8 gm%), and low applied pressure (5.6 psi) this time increased to about one second. Concentration profiles determined at 33 minutes and 88 minutes are shown in Figure 5-46. Theoretical profiles, using a diffusivity from Keller et al., are again too low for both times.

Within experimental error, the membrane concentration is found to be time invariant. Also consistent with model prediction is the rate of polarization growth rate.

$$\delta_{88\ min} = \delta_{33\ min}\sqrt{\frac{88}{33}}$$

For $\delta_{33\ min} = 0.115 \pm .005$ cm, the value of $\delta_{88\ min}$ is 0.185 cm which is in the range between the two wires (0.145 - 0.190 cm).

In Experiment 1700, profiles were evaluated at 542 minutes and 1368 minutes. Figure 5-47 again shows low theoretical profiles and a time invariant membrane concentration. The polarization layer growth rate is in excellent agreement with theory.

$$\frac{\delta_{1368}}{\delta_{542}} = \frac{0.538\ cm}{0.345\ cm} = \sqrt{\frac{1368}{542}} = 1.6$$

The effect of increasing the ultrafiltration pressure on 4.5 pH, 11 gm% albumin solutions is shown in Figure 5-48. At 40 psig, the equivalent osmotic pressure concentration, from extrapolation of the data in Chapter 3 at this pH, is 59.5 gm%, which is the same concentration measured at the membrane surface. The elapsed time is 22 hours.

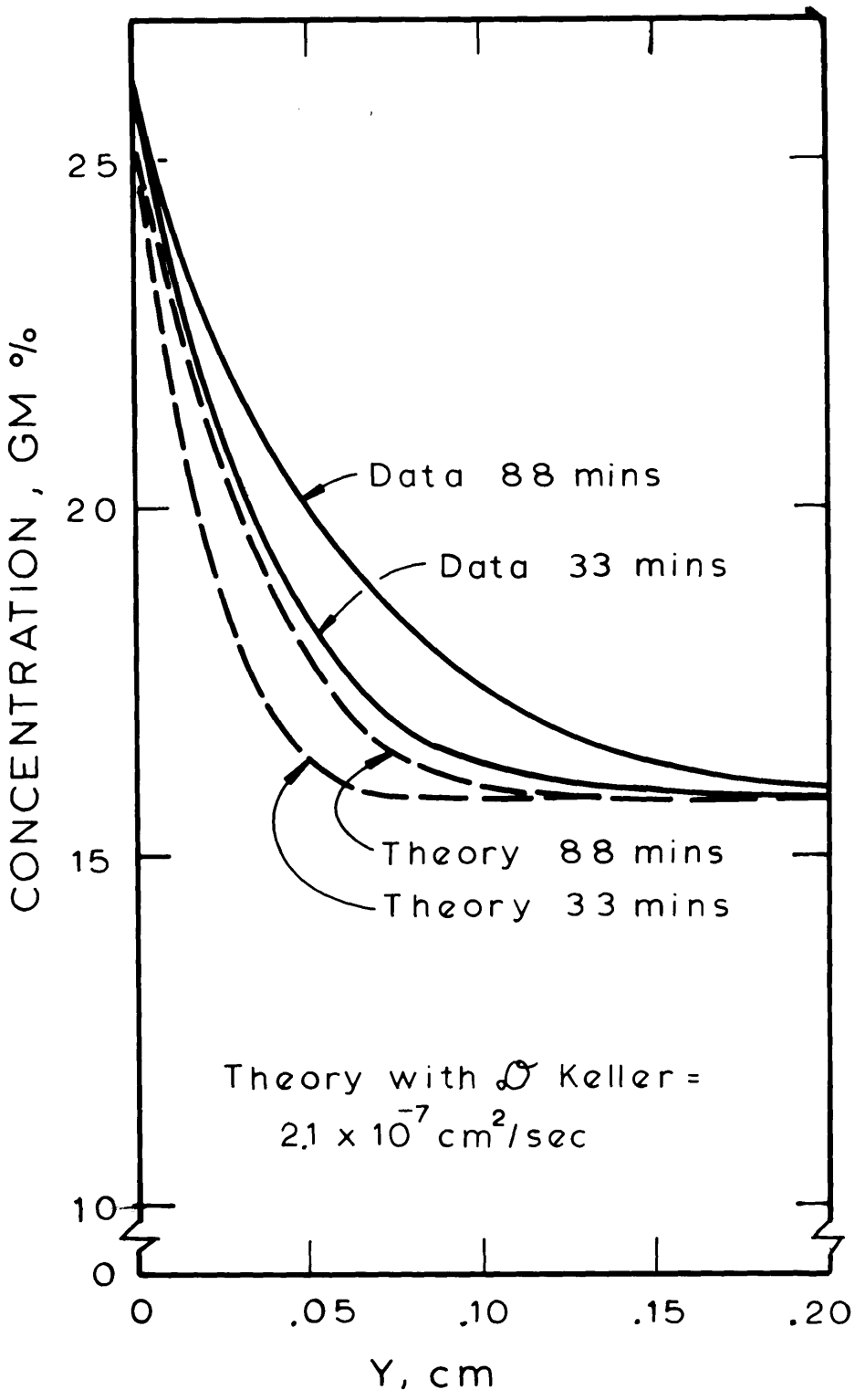

Figure 5-46 Concentration Profile Time Variation 5.4 pH, 15.8 GM %, 5.6 psi

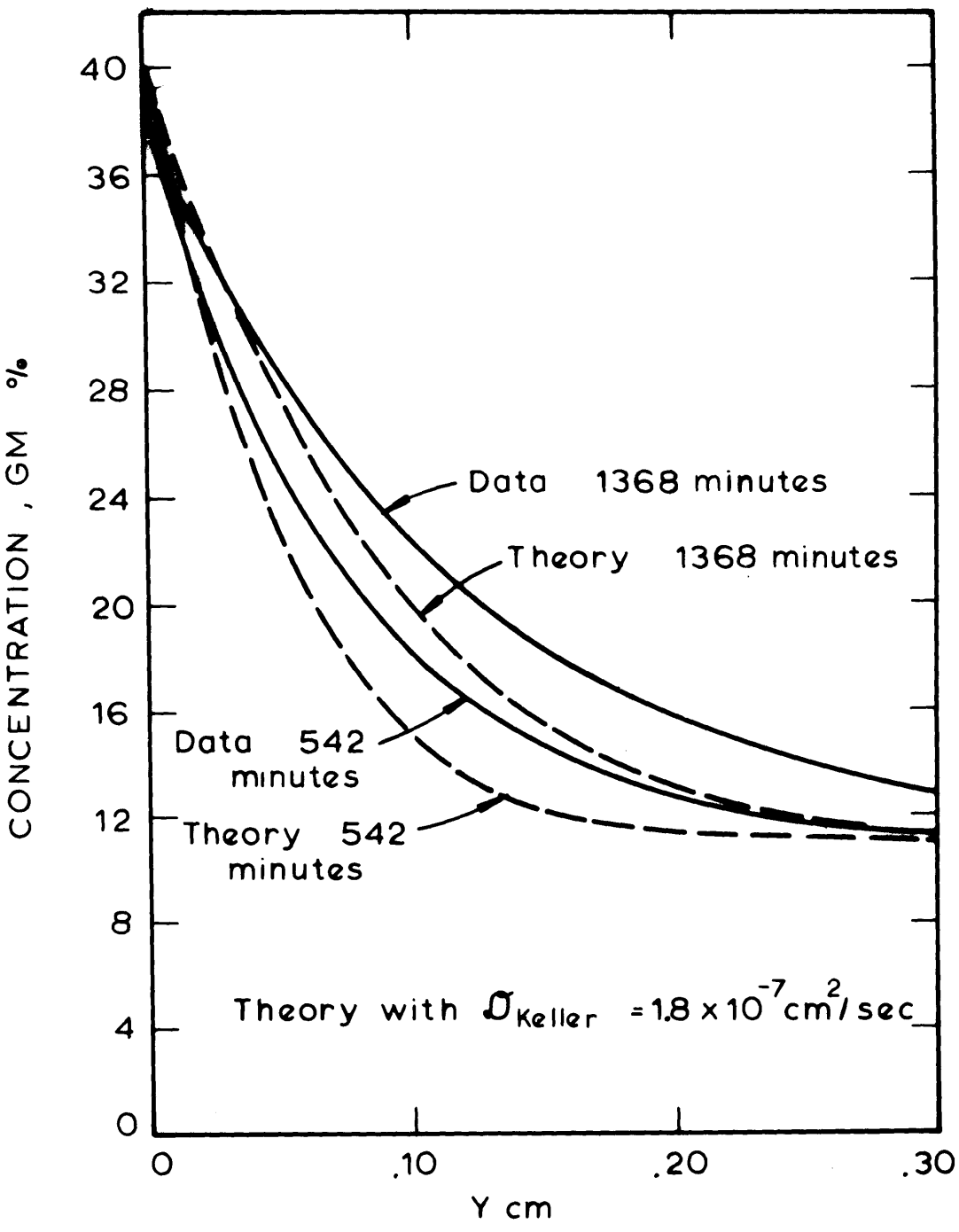

Figure 5-47 Concentration Profile Time Variation 4.5 pH , 11.0 GM % , 10 psi

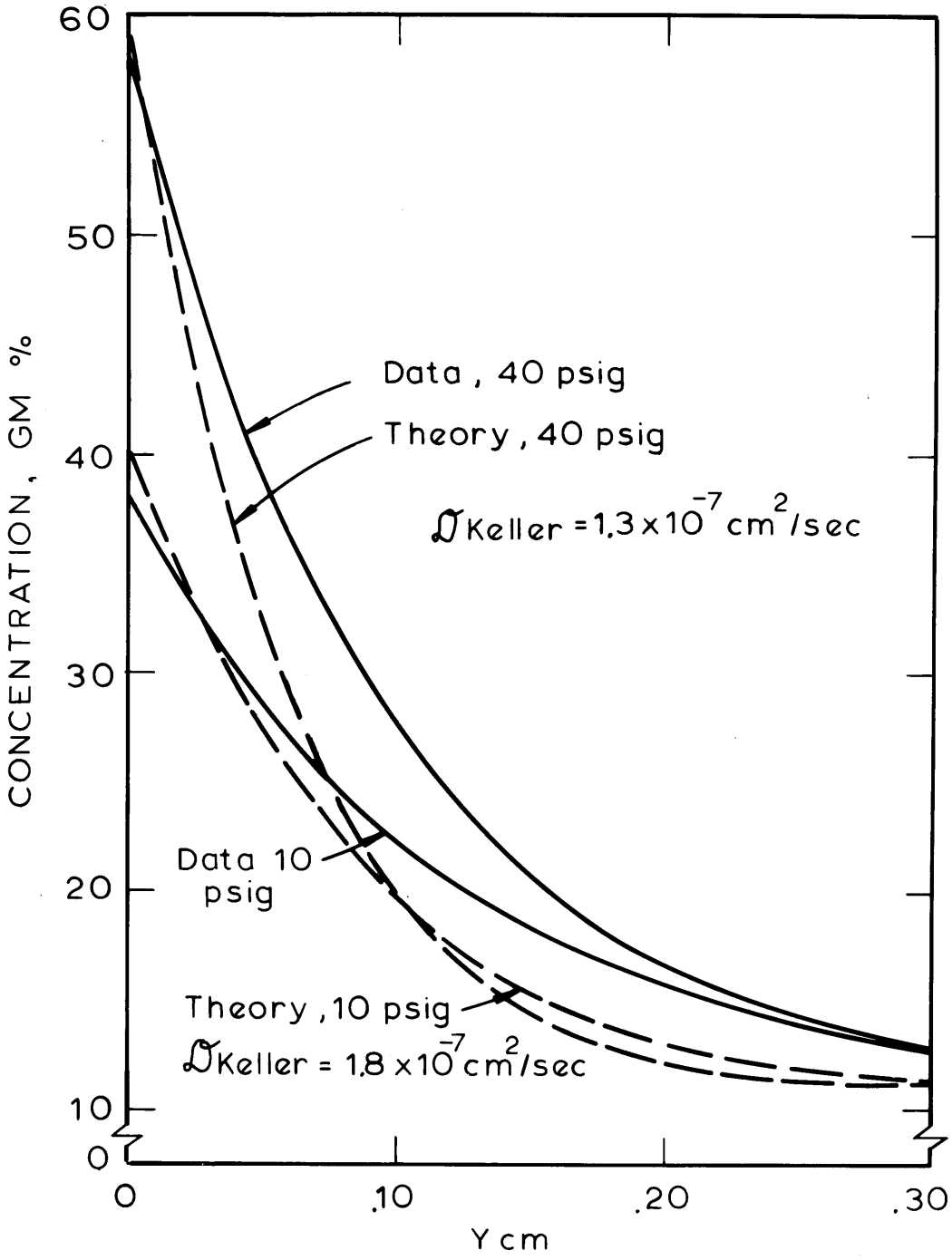

Figure 5-48 Effect of Higher Ultrafiltration Pressures on Concentration Profiles

Ultrafiltration of this same solution at 10 psig and 22 hours is shown for comparison. While theory shows the profiles crossing at about .10 cm, the measured profiles become equivalent at about 0.35 cm. The polarization layer was measured to be slightly thicker at the lower pressure (0.538 cm vs. 0.525 cm).

After 32 hours of filtration at 40 psi, there was no evidence of an insoluble layer formed at the membrane. An additional 15 hours at 50 psig still produced no such layer (see photo 1815, Figure 5-36).

B. Flow Measurement

Experiments were conducted in which the only variable parameter was solution pH; Experiments 1100 and 1300 at 4.5 pH, Experiments 1200 and 1500 at 5.4 pH, Experiments 1400 and 1600 at 7.4 pH. Although the results of Figure 5-49 show considerable nonreproducibility for the two equivalent experiments at 5.4 and 7.4 pH, they do indicate that higher ultrafiltrate fluxes are observed at higher pH levels. This is consistent with the findings of the stirred cell albumin ultrafiltration studies which were presented in Chapter 1.

Theoretical considerations indicated that flux should be given by:

$$v_s = A_o t^{-n} \tag{5-28}$$

with n = 1/2 and

$$A_o = a_o \frac{\bar{\rho}}{\rho_s} \sqrt{D} \tag{5-29}$$

In the last equation $\bar{\rho}$ is the average polarization layer density, ρ_s saline density and a_o an implicit function of the membrane surface and

Figure 5-49 ULTRAFILTRATION AT 10 PSIG, 10.1 GM % ALBUMIN

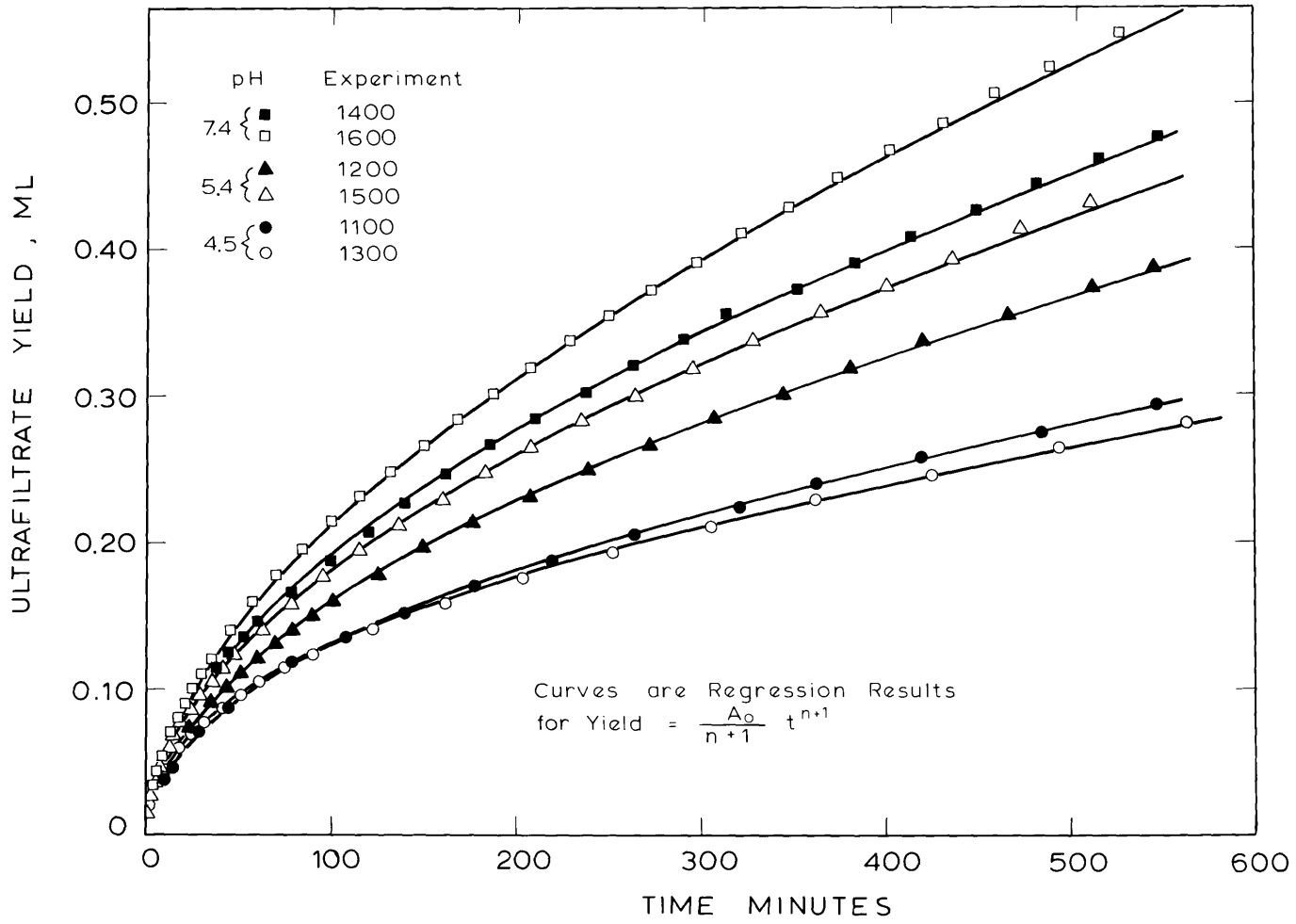

bulk solution concentrations. The integral form of equation (5-28) was applied to the data (for elapsed time greater than 2 min) with nonlinear least-squares regression to determine the values of the constants A_o and n. These curves are shown in Figure 5-49.

The long time regression results for the case where n is held constant at - 1/2 during the regression are compared in Figure 5-50 with the early time (Δ Volume/Δ Time) measurements made from the LFD recorder output. In the figure, the regression results are shown as one line for each of the three pH's. This line at each pH level is the average of the separate regressions performed for the duplicate experiments. Also indicated on the figure are the fluxes which would be predicted at t = 0 from the equation

$$v_s \ (@\ t = 0) \ = \ (K_m/\bar{\rho})[\Delta P - \pi^i]$$

where π^i is the osmotic pressure at the bulk solution concentration. The early time data does not indicate a pH dependence for flux like that of the long time data. The data suggest an asymptotic approach to long time behavior, but the extrapolation to zero time is not obvious.

Using the regression results for the long time data with n variable, the flux data at each pH level is compared with theory in Figures 5-51, -52 and -53. The theory calculations are made for n = -1/2 and for the diffusivities calculated from the data of Keller et al. and from that which best described the measured concentration profiles for the respective experiments. In every case, the theoretical flux with Keller's diffusivity is less than the measured flux, and the discrepancy increases

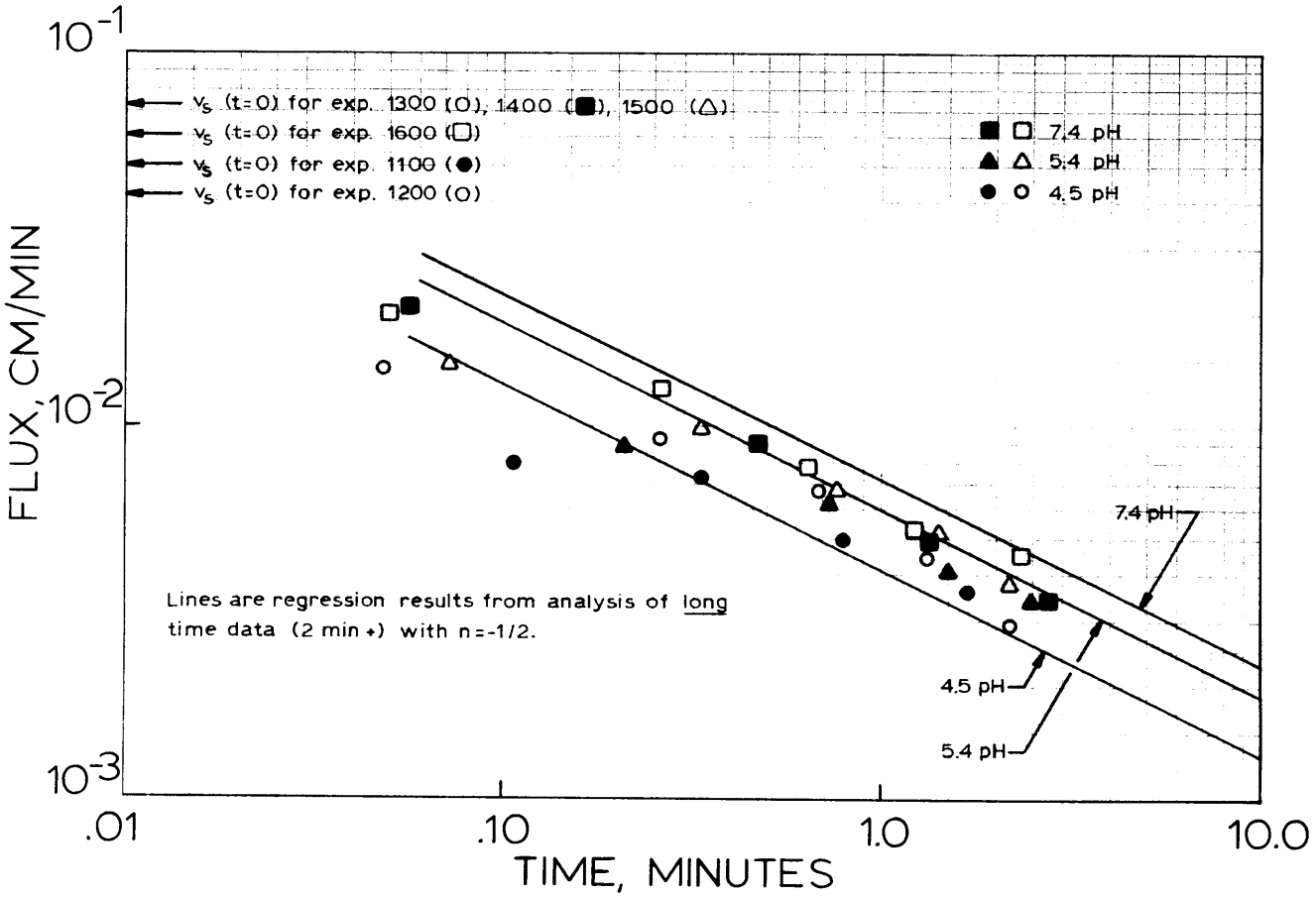

Figure 5-50: Early time flux data.

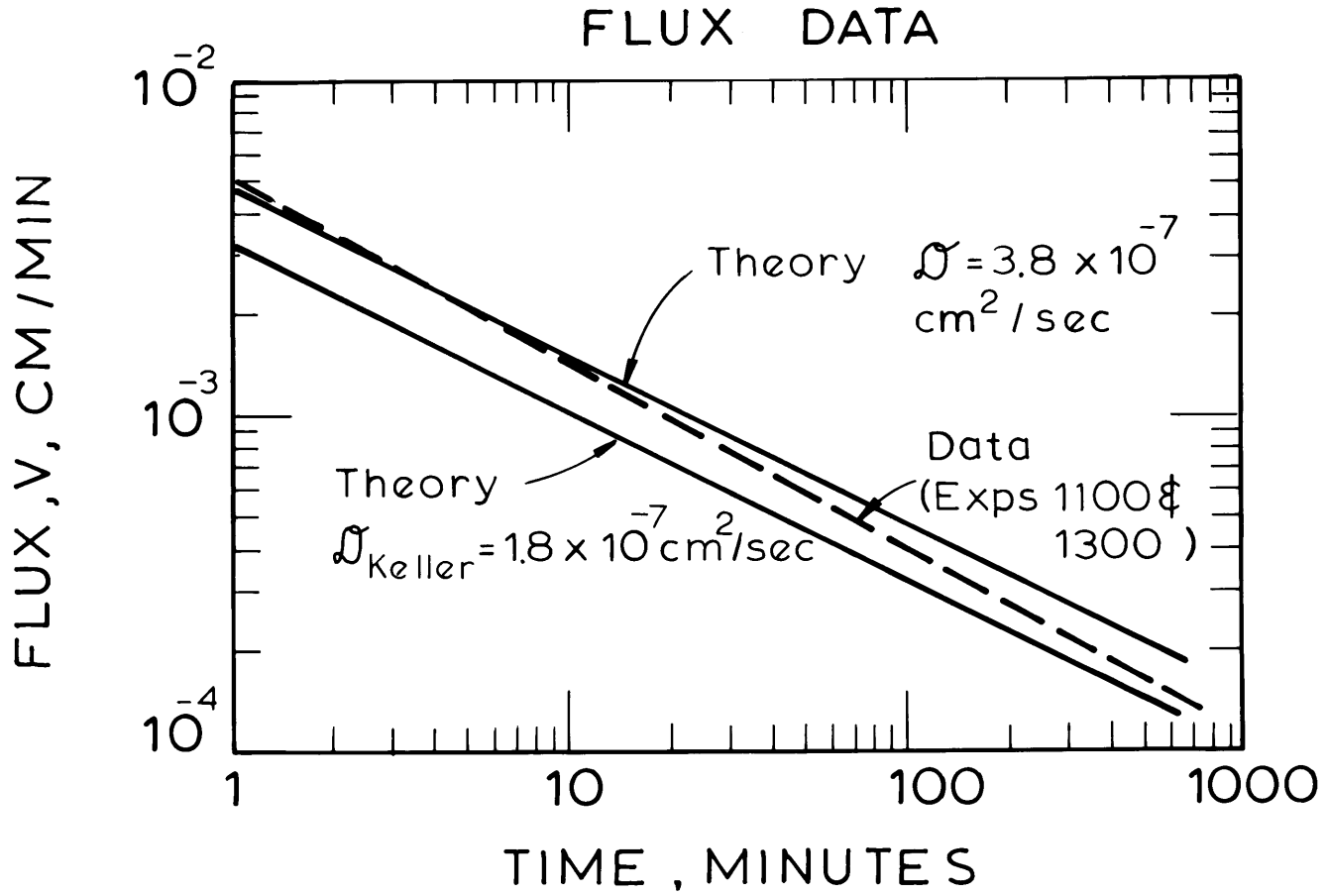

Figure 5 - 51 Ultrafiltration at 4.5 pH, 10.1 gm %, 10 psi

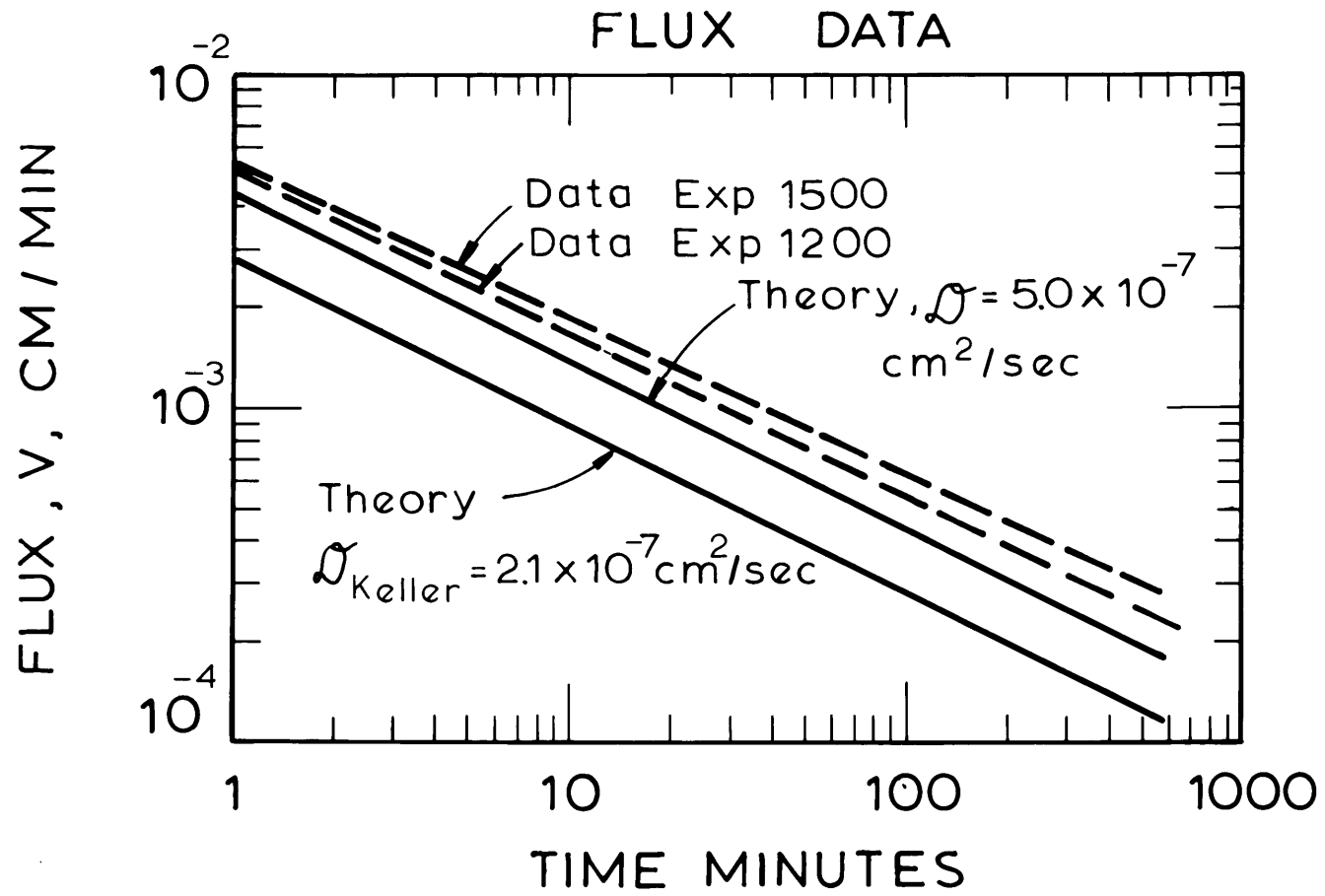

Figure 5 - 52 Ultrafiltration at 5.4 pH, 10.1 gm %, 10 psig

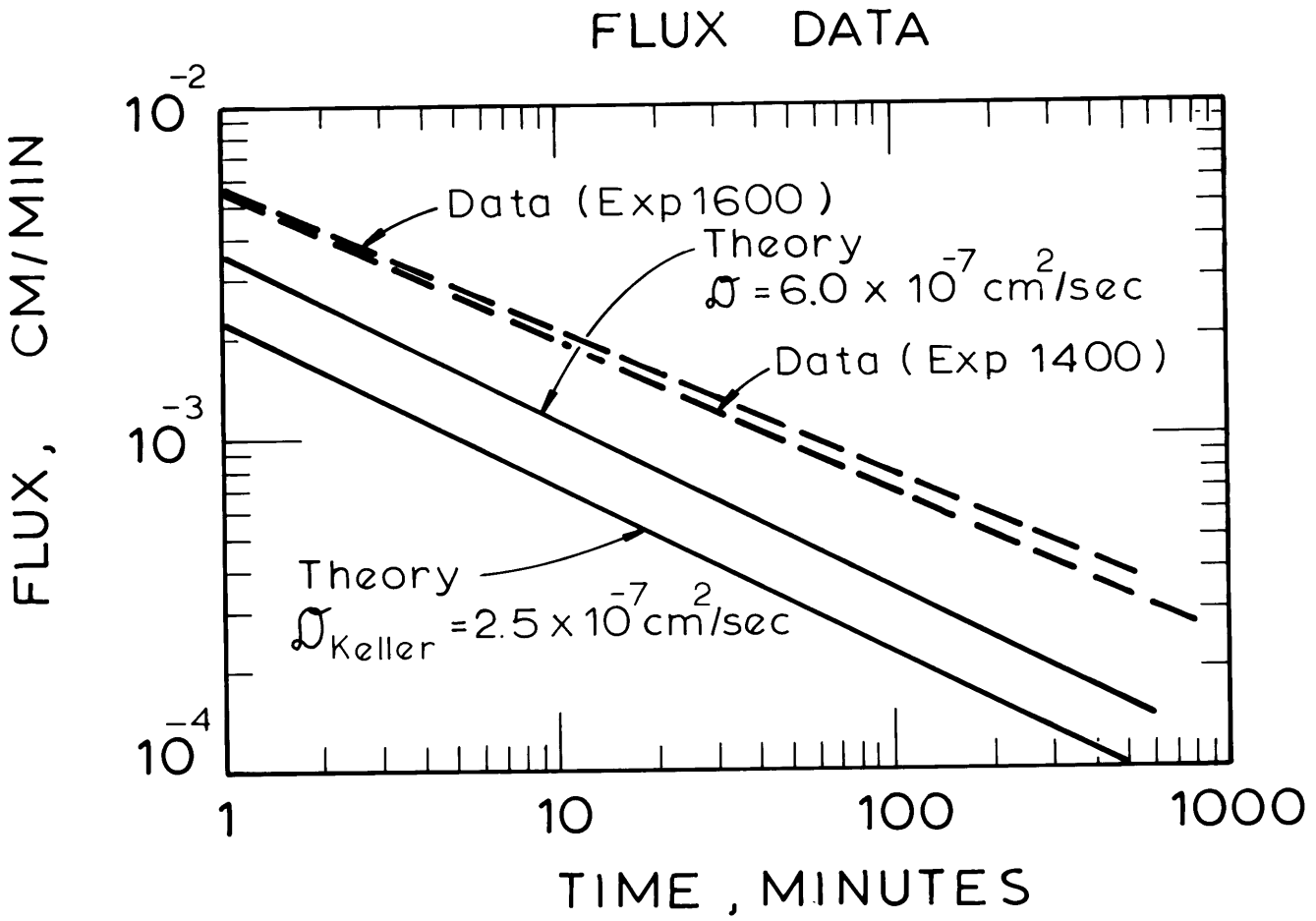

Figure 5-53 Ultrafiltration at 7.4 pH, 10.1 gm %, 10 psig

with increasing pH. Using the diffusivity from the concentration profile data, Figure 5-51 shows that theory and data are in fair agreement at 4.5 pH. The agreement is seen to become worse in this comparison also, as pH increases.

The data suggest that the exponent on time, n, and the A_o term of equation (5-28) are pH dependent. Table 5-8 shows that n is less negative with increasing pH, and the proportionality constant, A_o, increases with pH. Only experiments at 10 psi applied pressure are compared.

Table 5-8

EFFECT OF SOLUTION pH ON FLUX
REGRESSION CONSTANTS A_o AND n

pH	a_o from theory	$A_o \times 10^{+3}$ cm/min$^{\frac{1}{2}}$	-n	$D_{eff} \times 10^{+7}$ for n = -½	$\frac{D_{eff}}{D_{Keller}}$	Experiment
4.5	0.93	4.9	.536	3.0	1.7	1100
	0.93	5.0	.558	2.6	1.5	1300
	0.86	4.2	.494	3.8	2.2	1700
5.4	1.13	6.1	.491	4.8	2.0	700
	0.74	4.9	.476	8.1	3.8	1200
	0.74	5.4	.469	10.0	4.9	1500
7.4	0.82	7.1	.392	23.7	8.6	900
	0.56	5.7	.464	22.0	8.7	1400
	0.56	5.7	.429	28.8	11.4	1600

Another interpretation of the data is obtained when the regression are performed for $n = -1/2$ as indicated by theory and all variation in flux for the three pH levels is ascribed to changes in the constant A_o. In this view, an effective diffusivity is calculated from equation (5-29) after changes in a_o and $\bar{\rho}$ have been taken into account. These effective diffusivities become strong functions of pH as seen in the table, with $D_{7.4pH} > D_{5.4pH} > D_{4.5pH}$ for the 10 psig experiments. The discrepancy from the diffusivity of Keller, et al. also increases with increasing pH.

Experiments 1700 and 1800 (4.5 pH, 11 gm%) provide a comparison of flow measurements for low (10 psig) and high (40 psi) pressure ultrafiltration. After 22 1/2 hours, the volume of ultrafiltrate was 20% greater at 40 psi. Figure 5-54 compares this higher flux with the observed flux at 10 psig. It also shows good agreement with theory when the profile diffusivity is used to calculate flux.

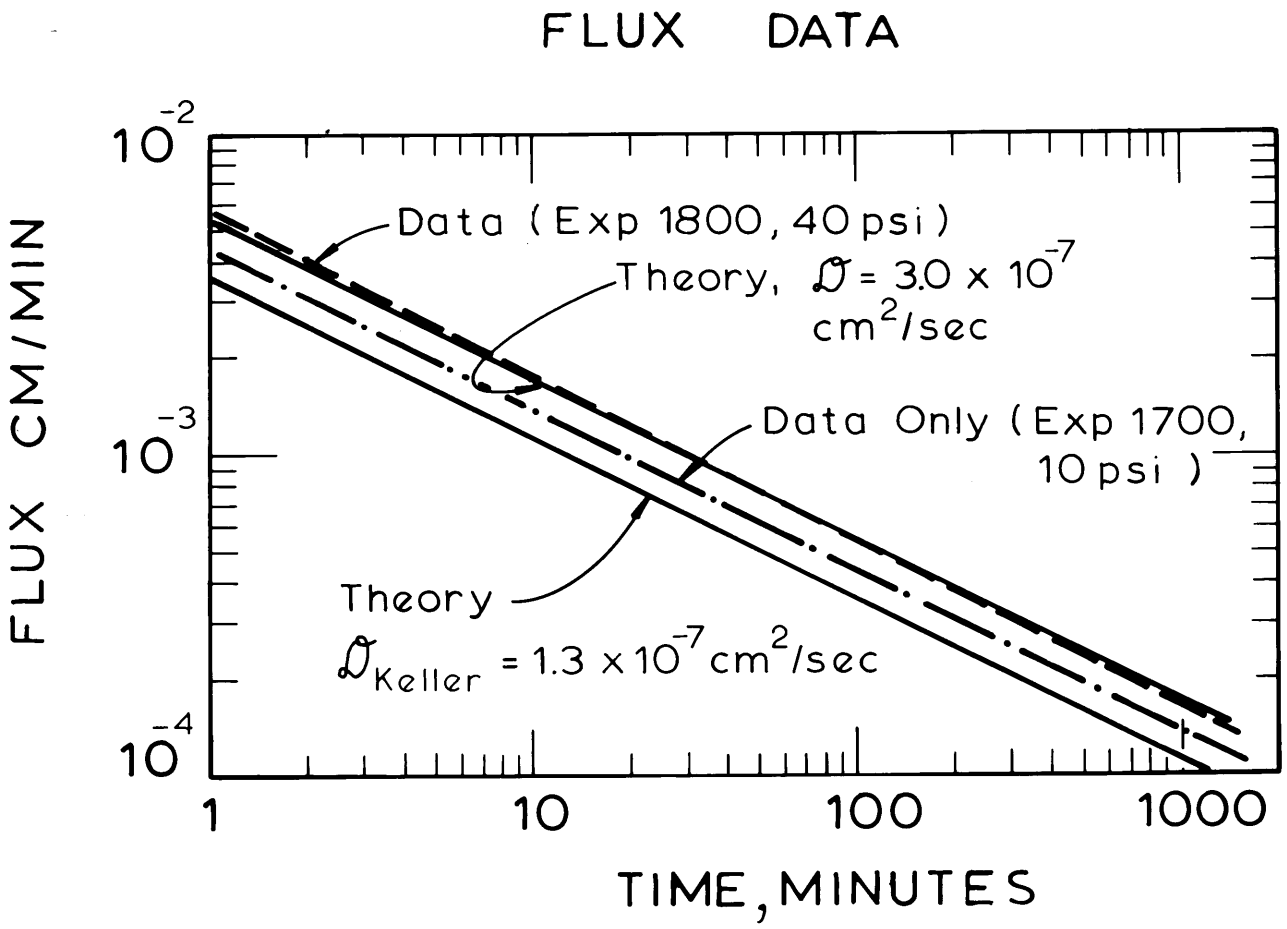

Figure 5-54 Ultrafiltration at 4.5 pH, 11.0 gm %, 40 psi

BIBLIOGRAPHY

(1) Beams, J. W., "Shadow and Schileren Methods," in High Speed Aerodynamics and Jet Propulsion, Vol 9, pp 26-46, Oxford Univ. Press, London (1955).

(2) Gosting, L. J., "Measurement and Interpretation of Diffusion Coefficients of Proteins," Adv. Protein Chem. 11, 429 (1956).

(3) Geddes, A. L. and R. B. Pontius, "Determination of Diffusivity," in Physical Methods of Organic Chemistry, A. Weissberger, ed., p 895, Interscience Publishers Inc., New York (1960).

(4) Ibl, N., "Methods for the Study of the Diffusion Layer," Proc. of the Seventh Meeting of the International Committee of Electrochemical Thermodynamics and Kinetics (CITCE), p 112, (1955).

(5) Brenner, A., "A Method for Studying Cathode Films by Freezing," Proc. Am. Electroplaters' Soc., p 95 (1940).

(6) Brenner, A., "Cathode Films in Electrodeposition," Proc. Am. Electroplaters' Soc., p 28 (1941).

(7) Bollenbeck, P. H., "A Modified Rayleigh Interferometer for Membrane Transport Studies," Ph.D. Thesis, University of Colorado, Boulder, Colorado (1972).

(8) Beach, K. W., "Optical Methods for the Study of Convective Mass Transfer Boundary Layers on Extended Electrodes," Ph.D. Thesis, University of California, Berkeley, California (1971).

(9) Mowbray, D. E., "The Use of Schlieren and Shadowgraph Techniques in the Study of Flow Patterns in Density Stratified Liquids," J. Fluid. Mech. 27, part 3, 595 (1967).

(10) Lewandowski, L., Masters Thesis, M.I.T., Cambridge, Mass. (1973).

(11) Williams, F. A., T. J. Hendricks, M. K. Lin, "Boundary Layer Flow Problems in Desalination by Reverse Osmosis," USDI-Office of Saline Water R. and D. Progress Report No. 622, (1970).

(12) Keller, K. H., E. R. Canales and S. I. Yum, "Tracer and Mutual Diffusion Coefficients of Proteins," J. Phys. Chem. 75, 379 (1971).

APPENDIX A

Wire Image Shadowgraph Derivations

Ray Path Through the Cell

1.) Additional notation - refer to Figure 5-1

T = Thickness of cell window

D = Distance from cell window to image plane

η_o = Refractive index of solution at height of entering ray

η_g = Refractive index of glass

Primes indicate differentiation with respect to z.

Subscripts indicate:

o - inside surface of first window

1 - inside surface of second window

2 - outside surface of second window

3 - image plane

s - solution in cell

g - glass

a - air

2.) Starting with Fermat's Law for $\eta = \eta(s)$ only

$$\delta \int \eta(s) ds = 0$$

3.) Apply Pythagoras' theorem for ds

$$ds = [1 + (dY/dz)^2]^{1/2}dz$$

so

$$\delta\int \eta(Y, z)[1 + dY/dz)^2]^{1/2}dz \qquad (A1)$$

4.) From variational calculus, an integral of the form

$$\delta\int F(z, Y, Y')dz$$

must satisfy the Euler-Lagrange relation

a) $\frac{\partial F}{\partial Y} - \frac{d}{dz}\left(\frac{\partial F}{\partial Y'}\right) = 0$

b) where

$$F = \eta(\ s\ )[1 + (Y')^2]^{1/2}$$

$$\frac{\partial F}{\partial Y} = \frac{d\eta}{dY}[1 + (Y')^2]^{1/2}$$

$$\frac{\partial F}{\partial Y'} = \eta Y'[1 + (Y')^2]^{-1/2}$$

$$\frac{d}{dz}\left(\frac{\partial F}{\partial Y'}\right) = \frac{\partial}{\partial z}\left(\frac{\partial F}{\partial Y'}\right) + \frac{\partial}{\partial Y'}\left(\frac{\partial F}{\partial Y'}\right)\frac{\partial Y'}{\partial z} + \frac{\partial}{\partial Y}\left(\frac{\partial F}{\partial Y'}\right)\frac{\partial Y}{\partial z}$$

$$= 0 + \eta[(1 + (Y')^2)^{-1/2} - (Y')^2(1 + (Y')^2)^{-3/2}]Y''$$

$$+ \frac{d\eta}{dY}(Y')^2[1 + (Y')^2]^{-1/2}$$

c) Substitution

$$\frac{d\eta}{dY}[1 + (Y')^2]^{1/2} - \eta[(1 + (Y')^2)^{-1/2} - (Y')^2(1 + (Y')^2)^{-3/2}]Y''$$

$$- \frac{d\eta}{dY}Y'[1 + (Y')^2]^{-1/2}Y' = 0$$

d) Multiplication by $[1 + (Y')^2]^{3/2}$ and rearrangement for Y''

$$Y'' = [1 + (Y')^2]\frac{1}{\eta}\frac{d\eta}{dY} \qquad (A2)$$

5.) Letting $P = dY/dz$ so that

$$Y'' = P\frac{dP}{dY}$$

then

$$P\frac{dP}{dY} = \frac{1}{\eta}(1 + P^2)\frac{d\eta}{dY}$$

or

$$\frac{PdP}{(1 + P^2)} = \frac{d\eta}{\eta}$$

6.) Integrate once with subscript "o" referring to condition at ray inlet surface

$$\frac{dY}{dz} = -\sqrt{\left(\frac{\eta}{\eta_o}\right)\left(P_o^2 + 1\right) - 1}$$

where the minus sign is used because $d\eta/dY < 0$ for the case of the membrane at the bottom of the cell.

7.) For an incident beam normal to the inlet surface, $P_o = 1$

$$Y'_{1s} = \frac{dY}{dz} = -\left[\left(\frac{\eta}{\eta_o}\right)^2 - 1\right]^{1/2} \qquad \text{(A3)}$$

Ray Path to Image Plane

1.) For the ray through the second glass wall

a) $Y_2 - Y_1 = (z_2 - z_1)Y'_{1g}$

b) Snells Law,

$$\eta_1 \sin \alpha_1 = \eta_g \sin \alpha_2$$

c) Since

$$\sin \alpha = \frac{1}{\left(1 + \frac{1}{(Y')^2}\right)^{1/2}} \quad \text{, then}$$

$$\eta_1 (1 + 1/(Y'_{1s})^2)^{-1/2} = \eta_g (1 + 1/(Y'_{1g})^2)^{-1/2}$$

or

$$Y'_{1g} = \frac{\eta_1 Y'_{1s}}{\sqrt{(Y'_{1s})^2 \eta_g^2 + \eta_g^2 - \eta_1^2 (Y'_{1s})^2}}$$

d) Substitution of c) into a) where it is recalled that Y'_{1s} is equivalent to Eq. (A3) and $z_2 - z_1 = T$

$$Y_2 - Y_1 = \frac{T \eta_1 Y'_{1s}}{\sqrt{(Y'_{1s})^2 \eta_g^2 + \eta_g^2 - \eta_1^2 (Y'_{1s})^2}}$$

2.) For the ray through the air space ($\eta_a = 1$) from z_2 to z_3

a) $Y_3 - Y_2 = (z_3 - z_2) Y'_{2a}$

b) Snell's Law

$\eta_a \sin \alpha_3 = \eta_1 \sin \alpha_1$

c) Derivation now follows same as 1.) with $D = z_3 - z_2$

$$Y'_{2a} = \frac{\eta_1 Y'_{1s}}{\sqrt{1 + (Y'_{1s})^2 - \eta_1^2 (Y'_{1s})^2}}$$

$$Y_3 - Y_2 = \frac{D\eta_1 Y'_{1s}}{\sqrt{1 + (Y'_{1s})^2 - \eta_1^2 (Y'_{1s})^2}} \qquad \text{(A5)}$$

3.) Combining (A4) and (A5)

$$Y_3 - Y_1 = \eta_1 Y'_{1s} \left[\frac{D}{\sqrt{1 + (Y'_{1s})^2 - \eta_1^2 (Y'_{1s})^2}} + \frac{T}{\sqrt{(Y'_{1s})^2 \eta_g^2 + \eta_g^2 - \eta_1^2 (Y'_{1s})^2}} \right] \qquad \text{(A6)}$$

APPENDIX B

Optical Properties of Albumin Solutions

Refractive Index

The refractive index of bovine serum albumin in .15M saline solution was measured as a function of albumin concentration and solution pH. The effects of temperature and light source were also checked.

The refractive index measurements were made using a temperature controlled Abbe 3-L Refractometer (Baush & Lomb). In most determinations, several readings were made on a given solution. The standard deviation for any determination did not exceed ±0.001 Refractive Index Unit (R.I.U.).

Protein concentrations were determined by the biuret method. Multiple determinations were made on most solutions and the standard deviation was ±1 gm%.

The results of the determinations at 25.0±.2°C are shown in Figure B-1. In addition to nine determinations at 5.4 pH, three determinations were made at 7.4 pH and two at 4.5 pH. No effect of solution pH is observed. These results were regressed with linear least-squares. The equation (and the standard deviation on the coefficients) of this regression result shown on the Figure is

$$n = (1.997 \pm .057)10^{-3}G + (1.3341 \pm .0033) \qquad \text{(B-1)}$$

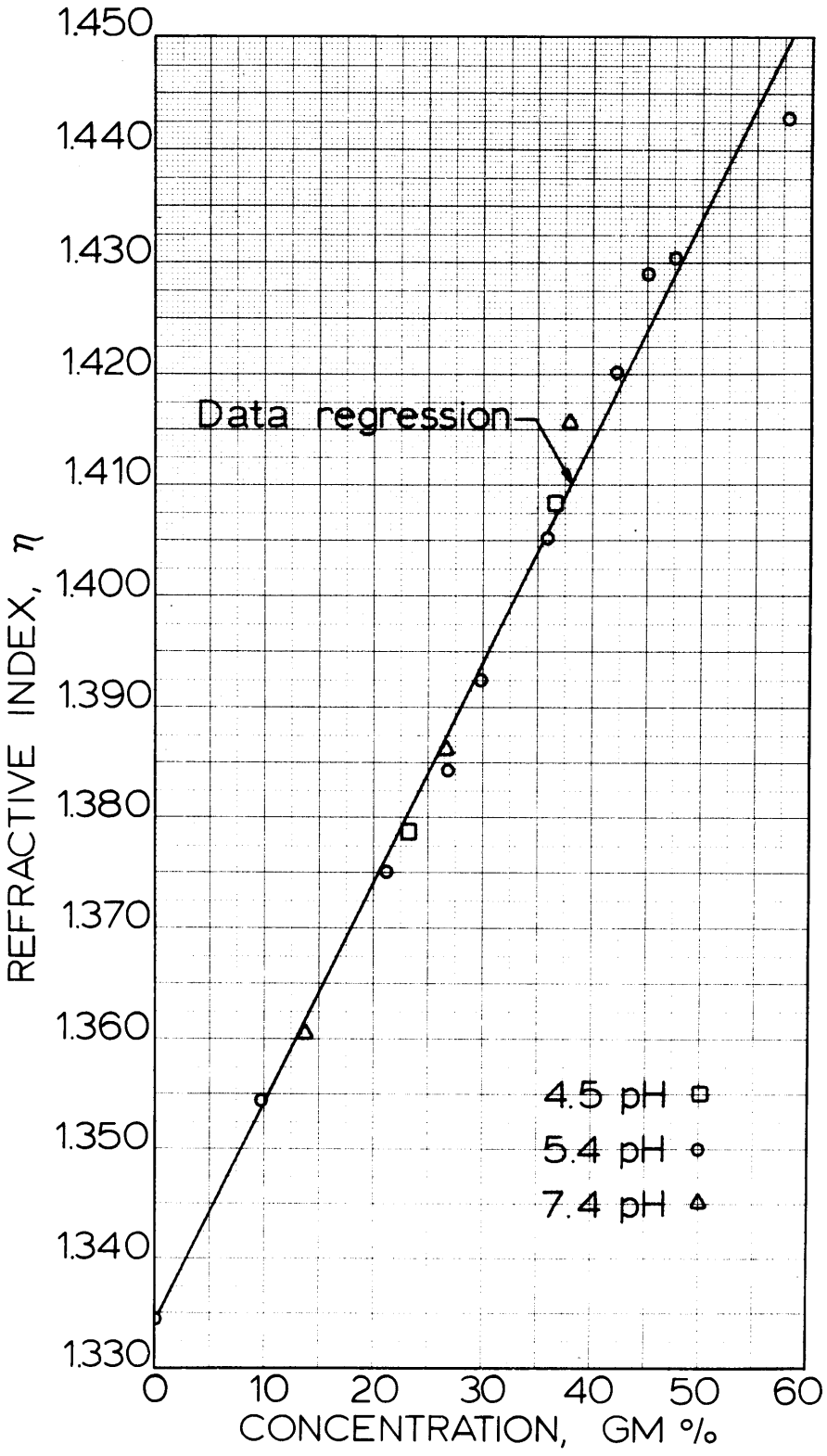

Figure B1: Refractive index of albumin solutions.

The effect of temperature was checked by making measurements on solutions of 0, 26, 38 and 45 gm% concentrations at 30°C. The results indicated that per °C rise in temperature, refractive index decreased about 0.0001 R.I.U.

Most of the measurements were made with a white light source. For the concentrated solutions, it was discovered that accuracy could be improved when white light color dispersion was eliminated by the use of a Helium-Neon laser light (λ= 6328Å). Determinations made with these two light sources agreed to better than the fourth significant figure on refractive index.

Transmission of BSA Solutions @ λ= 6328Å

A spectrophotometer at λ = 6328Å was used to determine the transmission of BSA solutions at 5.4 pH (unbuffered) and 0.15M NaCl. The optical cell had a path length of 1.3 cm and the instrument was zeroed on a 0.15M NaCl solution. BSA concentrations were varied up to 49 gr/100ml solution. A check of one solution at pH 7.4 and 38 gr BSA/100 ml solution suggests no effect of pH on transmission. Results are shown on Figure B-2.

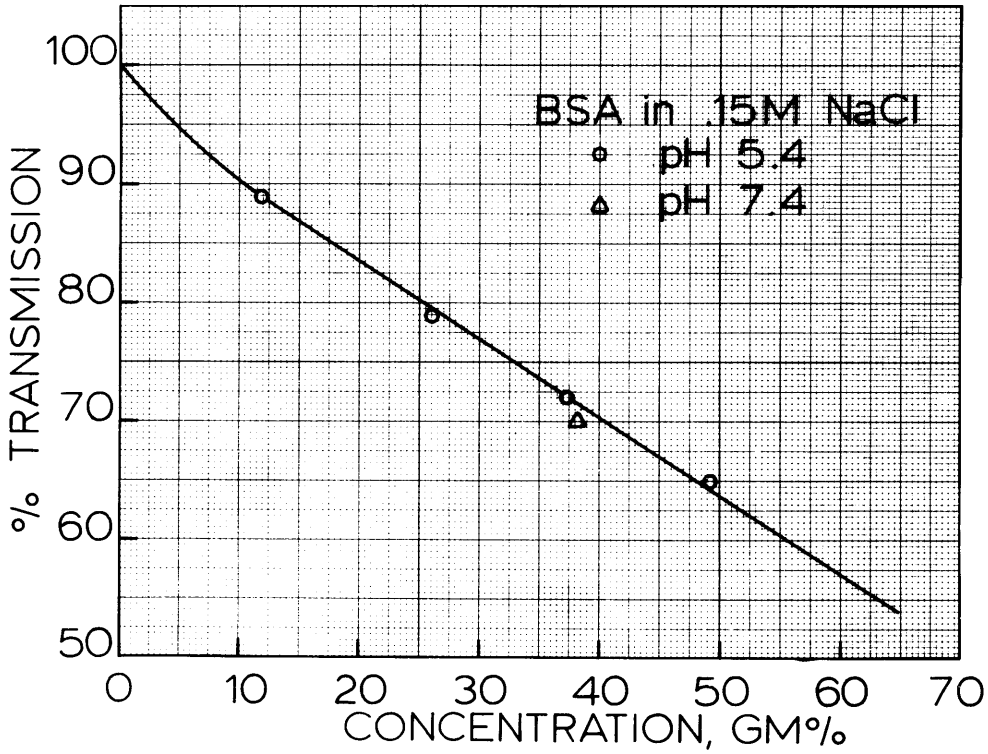

Figure B2: %Transmission of BSA solutions @ λ=6328Å

APPENDIX C

Optical Data Reduction - Calibrations and Computer Program Listings

Fiducial Plate Design and Calibration

The fiducial plate is made from a .125" thick piece of glass with overall dimensions of 4cm x 10cm. The front surface, i.e., the surface on which the deflection image is formed, is frosted. The camera located in back of the plate is focused on this front surface. In order to hold refraction errors of focusing through the plate thickness below the 0.01 mm level, the flatness of the frosted surface is at a tolerance of ±0.025 mm and the front-to-back surface parallelism tolerance is also ±0.025 mm.

The fiducial marks imprinted on the frosted surface are arranged in 5 columns across the width at a nominal separation of 5 mm and 9 rows down the length at a nominal separation of 10 mm. The marks are in the shape of an 'X' with a line thickness of 0.25 mm and length of 2 mm.

Figure C-1 presents the layout of the plate as it is seen in the deflection photographs. The coordinate system of the plate is centered at fiducial mark (3,3). The Itek Hand Measurement Machine distance in units of centimeters, for each mark with respect to (3,3) are given in Table C-1. The average standard deviations for these measurements is 14 microns (0.014 mm). The Hand Measurement Machine

distances are 2.4% greater than actual distances (an inherent machine correction factor). For example, the true distance of mark (1,1) from the X-axis is 1.0117/1.024 = 0.9880±0.0014 cm. This correction is incorporated in the FIDUC computer calculations.

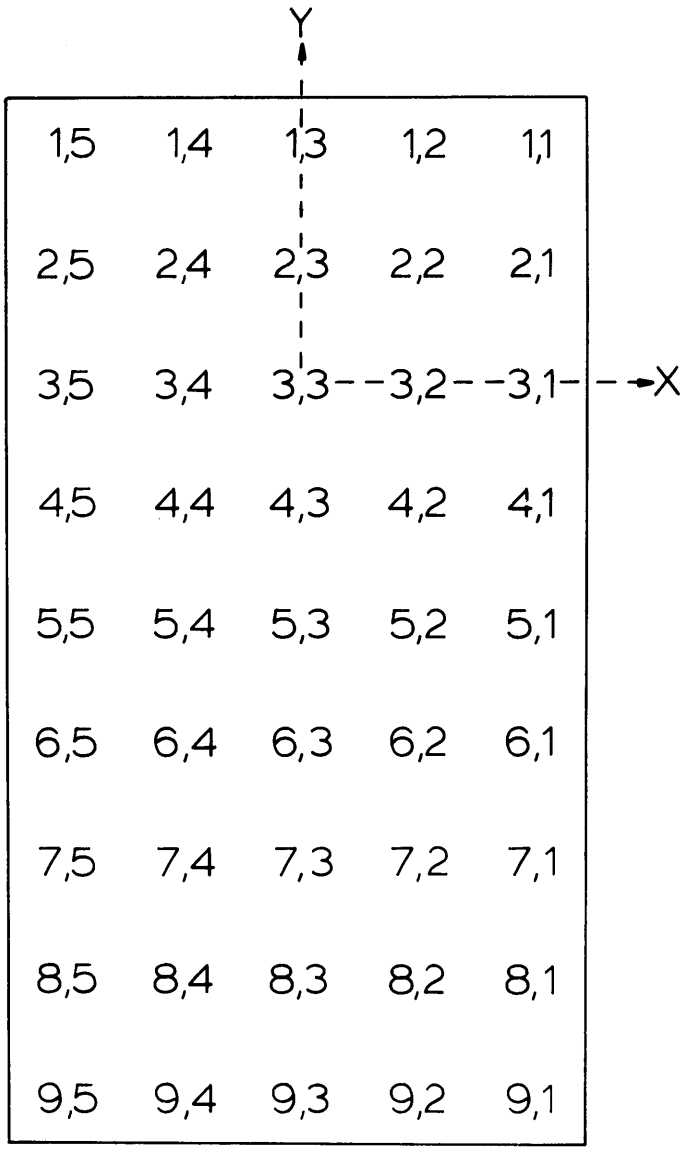

Figure C1: Fiducial plate layout.

TABLE C-1

FIDUCIAL PLATE CALIBRATION DATA*

FIDUCIAL MARK	X	Y	FIDUCIAL MARK	X	Y
1,1	+1.0117	+2.0525	6,1	+1.0375	-3.0689
1,2	+0.5024	+2.0517	6,2	+0.5237	-3.0750
1,3	-0.0086	+2.0519	6,3	+0.0131	-3.0753
1,4	-0.5204	+2.0479	6,4	-0.4976	-3.0766
1,5	-1.0312	+2.0482	6,5	-1.0112	-3.0810
2,1	+1.0236	+1.0313	7,1	+1.0415	-4.0981
2,2	+0.5080	+1.0268	7,2	+0.5293	-4.0988
2,3	-0.0022	+1.0274	7,3	+0.0169	-4.1005
2,4	-0.5178	+1.0237	7,4	-0.4969	-4.1039
2,5	-1.0276	+1.0224	7,5	-1.0079	-4.1047
3,1	+1.0238	+0.0039	8,1	+1.0322	-5.1209
3,2	+0.5098	+0.0001	8,2	+0.5295	-5.1245
3,3	0.0000	0.0000	8,3	+0.0193	-5.1269
3,4	-0.5088	-0.0007	8,4	-0.4888	-5.1267
3,5	-1.0251	-0.0025	8,5	-1.0021	-5.1177
4,1	+1.0306	-1.0205	9,1	+1.0507	-6.1489
4,2	+0.5156	-1.0219	9,2	+0.5362	-6.1481
4,3	+0.0042	-1.0245	9,3	+0.0254	-6.1511
4,4	-0.5068	-1.0255	9,4	-0.4844	-6.1520
4,5	-1.0193	-1.0291	9,5	-0.9948	-6.1561
5,1	+1.0334	-2.0466			
5,2	+0.5202	-2.0479			
5,3	+0.0094	-2.0505			
5,4	-0.5039	-2.0523			
5,5	-1.0150	-2.0534			

*DIVIDE MEASUREMENTS BY 1.024 TO OBTAIN ACTUAL DISTANCES IN CENTIMETERS.

TABLE C-2

FIDUC

computer program

```
C******************** PROGRAM FIDUC ****************************************
C
C
C         FORTRAN VARIABLES
C         IB=     FIRST COLUMN OF FIDUCIALS USED FOR CALIBRATION
C         IE=     LAST COLUMN OF FIDUCIALS USED FOR CALIBRATION
C         IP=     NO. OF SETS OF READINGS ON FILM FIDUCIALS, ALWAYS 4
C         IX( )= X-COORD OF FILM FIDUCIALS, YF IN THESIS
C         IY( )= Y-COORD OF FILM FIDUCIALS, XF IN THESIS
C         JB=     FIRST ROW OF FIDUCIALS USED FOR CALIBRATION
C         JE=     LAST ROW OF FIDUCIALS USED FOR CALIBRATION
C         RRX()= X-COORD OF REAL SPACE FIDUCIALS, YR IN THESIS
C         RRY()= Y-COORD OF REAL SPACE FIDUCIALS, XR IN THESIS
C         NN=     TOTAL NO. OF FIDUCIAL BEING CALIBRATED
C
C
C         SUBROUTINE LIST
C         FSPAK -- NONLINEAR LEAST-SQUARES WITH GRADIENT SEARCH
C         RSPAK -- DOES THE STATISTICS OF FSPAK'S FITS
C         FNCTX FNCTY -- FUNCTION SUBPROGRAMS WHICH ARE USED BY
C                        FSPAK TO FIT IY,RRY OR IX,RRX DATA
C
C
C         NOTE THAT A SCALE FACTOR OF 1/1.024 ADDED TO ACCOUNT FOR
C         HAND-MEASUREMENT MACHINE SCALING.
C
C
      REAL IX,IY,JX,JY
       EXTERNAL XS,XR
      COMMON IDF,DET,W(45),IIX(6),              SP(6),YC(45),DY(45)
     1,BM(6,7),PART(6),F,TEST,WVAR,SSQ,Z(2)
      DOUBLE PRECISION YC,DY,BM,PART,F,WVAR,SSQ,Z,DET,RX,RY,CX
      DOUBLE PRECISION TEST,SP,XP,YP,X33,Y33
      DIMENSION RX(45),RY(45),CX(2,45)
      DIMENSION XPG(6),YPG(6),RRX(9,5),RRY(9,5),XP(6),YP(6)
      DIMENSION IX(9,5),IY(9,5),JX(9,5),JY(9,5)
      ACCEPT "IP,IB,IE,JB,JE,IEXP ",  IP,IB,IE,JB,JE,IEXP
```

```
      READ(9,722) (XPG(M),YPG(M), M=1,6)
  721 FORMAT(6I5)
  722 FORMAT((F6.0,F6.0))
      WM=0.0
      NK=IE-IB+1
      NL=JE-JB+1
      DO 11 K=1,NK
      DO 11 L=1,NL
      JX(K,L)=0.0
   11 JY(K,L)=0.0
      WRITE(12,706)IEXP,IB,JB,IE,JE
      DO 12 N=1,IP
      READ(9,702)((IX(K,L),IY(K,L),L=1,NL),K=1,NK)
      WRITE(12,703)((IX(K,L),IY(K,L),L=1,NL),K=1,NK)
  703 FORMAT((10X,5(F8.0,F8.0)))
  706 FORMAT(//,2X,'EXPERIMENT',I6,3X,'FILM FIDUCIALS START AT',/,2X
     1,'(',I1,',',I1,') AND END AT (',I1,',',I1,').  X-Y PAIRS ARE',/)
      DO 12 K=1,NK
      DO 12 L=1,NL
      JX(K,L) = JX(K,L) + IX(K,L)
   12 JY(K,L) = JY(K,L) + IY(K,L)
C
C        FIND THE FILM SPACE COORDINATES OF FIDUCIAL (3,3)
C
      K3=0
      DO 23 I3=IB,IE
      K3=K3+1
      L3=0
      DO 23 J3=JB,JE
      L3=L3+1
      IF(I3 .EQ. 3) GO TO 24
      GO TO 23
   24 IF(J3 .EQ. 3) GO TO 25
   23 CONTINUE
   25 X33 = DBLE(JX(K3,L3)/IP)/10000.D0
      Y33 = DBLE(JY(K3,L3)/IP)/10000.D0
```

```
C
      IC = 1
      DO 13 K=1,NK
      DO 13 L=1,NL
      IF(K .EQ. K3) GO TO 26
      GO TO 27
   26 IF(L .EQ. L3) GO TO 28
      GO TO 27
   28 CX(1,IC) = 0.D0
      CX(2,IC) = 0.D0
      GO TO 13
   27 CX(1,IC) =(DBLE(JX(K,L)/IP)/10000.D0) - X33
      CX(2,IC) =(DBLE(JY(K,L)/IP)/10000.D0) - Y33
   13 IC = IC + 1
C
C        READ ALL REAL SPACE FIDUCIALS, AND DIVIDE BY SCALE FACTOR
C
      DO 14 I=1,9
   14 READ(9,704) (RRX(I,J),RRY(I,J),J=1,5)
      DO 16 K=1,9
      DO 16 L=1,5
      RRX(K,L) = RRX(K,L)/1.024
   16 RRY(K,L) = RRY(K,L)/1.024
C
C        USE ONLY SELECTED FIDUCIALS
C
        CALL OVOPN(1,"FIDUC.OL",IER)
      IC = 1
      DO 15 K=IB,IE
      DO 15 L=JB,JE
      RX(IC) =DBLE(RRX(K,L))
      RY(IC) = DBLE(RRY(K,L))
   15 IC = IC+1
```

```
      NN = (IE-IB+1)*(JE-JB+1)
        TYPE "HERE AT KER=1"
      KER=1
        CALL OVLOD(1,XS,0,IER)
      CALL FSPAK(NN,CX,RX,XPG,XP,KER,WM)
      CALL DATSW(10,IJK)
      IF(IJK .EQ. 1) GO TO 30
      GO TO 31
   30 WRITE(12,802)
        CALL OVLOD(1,XR,0,IER)
      CALL RSPAK(NN,RX,CX,XPG,XP)
        CALL OVLOD(1,XS,0,IER)
        TYPE "OUT RSPAK"
   31 KER=2
      CALL FSPAK(NN,CX,RY,YPG,YP,KER,WM)
      CALL DATSW(5,MM)
      IF(MM .EQ. 1) GO TO 21
      GO TO 22
   21 WRITE(12,800)
      WRITE(12,801) (XP(N),YP(N),N=1,6)
   22 CONTINUE
  702 FORMAT((10X,5(F6.0,F6.0)))
  704 FORMAT(5(F7.0,F7.0))
  800 FORMAT(//,5X,'FIDUCIAL COEFFICIENTS',/,15X,'XP',11X,'YP')
  801 FORMAT((10X,(F12.6,F12.6)))
  802 FORMAT(//,3X,'STATISTICAL INFO ON FIDUC FIT OF X-COORD.')
      CALL OPEN(2,"DATA",2,IER,160)
       CALL FSEEK(2,0)
       WRITE BINARY (2) XP,YP,X33,Y33
       CALL CLOSE(2,IER)
        CALL CLOSE(1,IER)
      CALL FBACK
      END
```

```
      SUBROUTINE FNCTX(X,P,F,PART,WM)
      DIMENSION P(6),PART(6),X(2)
      DOUBLE PRECISION X,F,PART,P,R
      R=X(1)*X(1) + X(2)*X(2)
      F = P(1)+P(2)*X(1) + P(3)*X(2) + P(4)*X(1)*X(1)+P(5)*X(1)*X(2)+
     1P(6)*X(1)*R
      PART(1) = 1.D0
      PART(2) = X(1)
      PART(3) = X(2)
      PART(4) = X(1)*X(1)
      PART(5) = X(1)*X(2)
      PART(6) = X(1)*R
      RETURN
      END
```

```
      SUBROUTINE FNCTY(X,P,F,PART,WM)
      DIMENSION P(6),PART(6),X(2)
      DOUBLE PRECISION X,F,PART,P,R
      R=X(1)*X(1) + X(2)*X(2)
      F = P(1)+P(2)*X(2) + P(3)*X(1) + P(4)*X(2)*X(2)+P(5)*X(1)*X(2)+
     1P(6)*X(2)*R
      PART(1) = 1.DO
      PART(2) = X(2)
      PART(3) = X(1)
      PART(4) = X(2)*X(2)
      PART(5) = X(1)*X(2)
      PART(6) = X(2)*R
      RETURN
      END
```

TABLE C-3

BEFORE

computer program

```
C****************** PROGRAM BEFORE ***************************************
C
C
C         THIS PROGRAM CONVERTS MEMBRANE AND WIRE IMAGE DATA FROM FILM
C         SPACE COORDINATES TO LINEAR EQNS (Y = A(2)*X + A(1)) IN REAL -
C         SPACE COORDINATE SYSTEM.  IT ALSO COMPUTES THE REAL-SPACE
C         MEMBRANE-WIRE INTERSECTION AND THE ANGLE BETWEEN THEM.
C
C
C         PROGRAM FORTRAN VARIABLES
C         IEXP=  EXPERIMENT NO.
C         IWX()= ARRAY OF FILM SPACE X-COORD. , YF IN THESIS
C         IWY()= ARRAY OF FILM SPACE Y-COORD. , XF IN THESIS
C         NPW=   NO. OF POINTS READ, MAX IS 250
C         NSETS= 1 TO CONVERT DATA ONLY, = 2 TO LINEARLY CURVE FIT ALSO
C         WIR()= COEFF FOR WIRE LINEAR EQN IN REAL SPACE, A'S,B'S IN THESIS
C         WX()=  ANY  IMAGE X-COORDINATE IN REAL SPACE, YR IN THESIS
C         WY()=  ANY  IMAGE Y-COORDINATE IN REAL SPACE, XR IN THESIS
C         XP()=  COEFF FOR REAL-FILM SPACE CONVERSION IN FILM X-DIMEN
C                COMPUTED IN FIDUC, BETA IN THESIS
C         XPG()= INITIAL GUESSES OF FIDUCIAL CONVERSION COEFF.  FOR X-
C                COORDINATES, FOR USE IN FIDUC
C         XR=    YR IN TEXT OF THESIS
C         YP()=  COEFF FOR REAL-FILM SPACE CONVERSION IN FILM Y DIMEN
C                COMPUTED IN FIDUC, ALPHA IN THESIS
C         YPG()= INITIAL GUESSES OF FIDUCIAL CONVERSION COEFF.  FOR Y-
C                COORDINATES, FOR USE IN FIDUC
C         YR=    XR IN TEXT OF THESIS
C
C
C         SUBROUTINES
C         FIDUC- USES FIDUCIALS TO CALCULATE FILM-REAL SPACE CALIBRATION
C                POLYNOMIAL
C         RLSPAC-USES RESULTS OF FIDUC TO CONVERT FILM OBSERVATIONS TO
C                REAL SPACE ON ANY  IMAGE
C         SPAC-  LEAST SQUARES FITTING ROUTINE USED TO FIND BEST STRAIGHT
C                LINES TO REPRESENT MEMBRANE AND WIRE IN REAL SPACE
C         FNCTL- FUNCTION SUBROUTINE FOR LINEAR FIT, CALL BY SPAC
```

```
C
C
      EXTERNAL XR,XS
      REAL IWX,IWY,IR,IS
      COMMON IWX(250),IWY(250),X(250),Y(250)
      DIMENSION  WIR(2),WIRG(2),IR(5),IS(5),XP(6),YP(6)
      DOUBLE PRECISION XP,YP,X33,Y33
       CALL FSWAP("FIDUC.SV")
      CALL OPEN(2,"DATA",2,IER,160)
       CALL FSEEK(2,0)
       READ BINARY(2) XP,YP,X33,Y33
       CALL CLOSE(2,IER)
      ACCEPT "WIRG1,WIRG2 ", WIRG(1),WIRG(2)
      ACCEPT "NPW,NSETS,IEXP",NPW,NSETS,IEXP
  726 FORMAT(2F14.8)
  733 FORMAT(10X,5(F6.0,F6.0))
      WM=0.00
C
C        CALIBRATE FILM TO REAL SPACE WITH SUBROUTINE FIDUC
C
      WRITE(12,724) IEXP
        CALL OVOPN(1,"BEFORE.DL",IER)
      KA=5
   21 KB=KA-4
      READ(9,733)(IR(J),IS(J),J=1,5)
      DO 22 MA=1,5
      IWX(KB+MA-1) = IR(MA)
   22 IWY(KB+MA-1) = IS(MA)
      KA=KA+5
      IF(NPW-KA)23,21,21
   23 IPW=NPW-KA+5
      IF(IPW .EQ. 0) GO TO 25
      KB=KA-4
      READ(9,733) (IR(J),IS(J),J=1,IPW)
      DO 24 MA=1,IPW
      IWX(KB+MA-1) = IR(MA)
   24 IWY(KB+MA-1) = IS(MA)
   25 CONTINUE
      CALL DATSW(6,LM)
```

```
      IF(LM .EQ. 2) GO TO 26
      WRITE(12,743)
      WRITE(12,744)(IWX(J),IWY(J),J=1,NPW)
   26 CONTINUE
C
C        COMPUTE REAL SPACE COORDINATES OF POINTS JUST READ
C
        CALL OVLOD(1,XR,0,IER)
      CALL RLSPAC(NPW,XP,YP,X33,Y33)
      CALL DATSW(8,LMN)
      GO TO (32,31),LMN
   32 WRITE(12,745)
      WRITE(12,740)(X(JL),Y(JL), JL=1,NPW)
   31 CONTINUE
C
C        FIT STRAIGHT LINE TO THESE REAL SPACE POINTS
C
      KER = 4
        CALL OVLOD(1,XS,0,IER)
      GO TO (35,36),NSETS
   36 CALL SPAK(NPW,WIRG,WIR,KER,WM)
      WRITE(12,741) WIR(2),WIR(1)
      WRITE(12,750)
      DO 37 JP=1,NPW
      PY = WIR(2)*X(JP) + WIR(1)
      DIFY = Y(JP) - PY
      WRITE(12,751) X(JP),Y(JP),PY,DIFY
   37 CONTINUE
   35 CONTINUE
  724 FORMAT(5X,'EXPERIMENT NO. ',I5,/)
  740 FORMAT((5X,5(2X,F10.4,F10.4)))
  741 FORMAT(//,5X,'FOR WIRE, REAL SPACE EQN.  IS',/,10X,'YR=',F14.6,'*XR
     1 +',F14.6,//)
```

```
743 FORMAT(///,5X,'FILM SPACE DATA -- X-Y PAIRS:')
745 FORMAT(///,5X,'REAL SPACE DATA -- X-Y PAIRS:')
744 FORMAT((10X,5(2X,F8.0,F8.0)))
750 FORMAT(5X,'X OBS.  -- Y OBS.  -- Y PRED.  -- YOB-YPR',/)
751 FORMAT(1X,4F12.4)
      CALL CLOSE(1,IER)
    STOP
    END
```

```
      OVERLAY XR
      SUBROUTINE RLSPAC(NPW,XP,YP,X33,Y33)
C
C
C        THIS SUBROUTINE USES THE COEFFICIENTS FROM FIDUC TO
C        CONVERT FILM DATA TO FIDUCIAL PLANE
C
C
C        FORTRAN VARIABLES
C        NPW=    NO. OF IMAGE POINTS
C        XP()=   CONVERSION COEFFICIENTS FOR X, BETA IN THESIS
C        YP()=   CONVERSION COEFFICIENTS FOR Y, ALPHA IN THESIS
C        IWX()= ARRAY OF IMAGE X-COORD IN FILM SPACE, YF IN THESIS
C        IWY()= ARRAY OF IMAGE Y-COORD IN FILM SPACE, XF IN THESIS
C        WX()=   ARRAY OF IMAGE X-COORD COMPUTED TO REAL SPACE,YR THESIS
C        WY()=   ARRAY OF IMAGE Y-COORD COMPUTED TO REAL SPACE,XR THESIS
C
C
      REAL IWX,IWY
      DIMENSION XP(6),YP(6)
      DOUBLE PRECISION XP,YP,X33,Y33
      COMMON IWX(250),IWY(250),WX(250),WY(250)
      DO 11 N=1,NPW
      IWX(N)=(IWX(N)/10000.)- X33
      IWY(N)=(IWY(N)/10000.)- Y33
      R = IWX(N)*IWX(N) + IWY(N)*IWY(N)
      WX(N) = XP(1) + XP(2)*IWX(N) + XP(3)*IWY(N) +XP(4)*IWX(N)*IWX(N)
     1 + XP(5)*IWX(N)*IWY(N) + XP(6)*IWX(N)*R
   11 WY(N) = YP(1) + YP(2)*IWY(N) + YP(3)*IWX(N) +YP(4)*IWY(N)*IWY(N)
     1 + YP(5)*IWY(N)*IWX(N) + YP(6)*IWY(N)*R
      RETURN
      END
```

TABLE C-4

DEFLECT

computer program

```
C****************** PROGRAM DEFLECT ************************************
C
C
C         THIS PROGRAM CONVERTS OBSERVED WIRE IMAGE DATA DURING ULTRA-
C         FILTRATION CAUSED DEFLECTION TO AN EQUATION FOR USE IN SDIP.
C         THIS INVOLVES FIRST A CALIBRATION OF THE PICTURE USING THE
C         FIDUCIALS AND PROGRAM    FIDUC. THEN THE WIRE IMAGE IS CONVERT-
C         ED TO REAL SPACE IN RLSPAC. THE FUNCTIONAL FORM Y3 = A(0)*EXP(
C         -A(1)*Y0) + WM*Y0 IS THEN FITTED TO THESE Y0-Y3 DATA PAIRS
C         AFTER THEY HAVE BEEN CONVERTED TO UF CELL COORD. SYSTEM WHERE
C         THE INTERSECTION OF THE WIRE AT THE MEMBRANE SURFACE, DESIGNATED
C         BY REAL SPACE COORD PEROX & PEROY, IS TAKEN AS THE ZERO POINT.
C
C
C         FORTRAN VARIABLES
C         IEXP=  EXPERIMENT NUMBER
C         IWX()= FILM SPACE X-COORDINATES, Y-COORD.  IN THESIS
C         IWY()= FILM SPACE Y-COORDINATES, X-COORD.  IN THESIS
C         KREG=  NO. OF REGIONS FOR FITTING Y0-Y3 DATA
C         NPW=   NO. OF POINTS READ ON WIRE, MAX IS 250
C         PEROX= REAL SPACE X-COORD. OF WIRE INTERSECTION AT MEMBRANE
C                PAY OR PCY IN THESIS
C         PEROY= REAL SPACE Y-COORD. OF WIRE INTERSECTION AT MEMBRANE
C                PAX OR PCX IN THESIS
C         THETA= ANGLE BETWEEN MEMBRANE AND REAL SPACE AXIS
C         WM=    WIRE SLOPE WITH RESPECT TO MEMBRANE, S1 OR S2 IN THESIS
C         Y0()=  X1 OR X2 IN THESIS
C         Y3()=  Y1 OR Y2 IN THESIS
C         YZ=    UPPER BOUND OF Y3 (CELL SPACE) FOR A GIVEN FIT
C         YR=    LOWER BOUND OF Y3 (CELL SPACE) FOR A GIVEN FIT
C
C         SUBROUTINES
C         RLSPD- DOUBLE PRECISION VERSION OF RLSPAC USED IN BEFORE
C         DPAK-  NONLINEAR LEAST SQUARES FIT FOR DEFLECTION EQN.
C         FNCTW- FUNCTION SUBROUTINE OF DEFLECTION EQN, FOR DPAK
C
C
```

```
      EXTERNAL XR,XS
      REAL IWX,IWY,IR,IS
      COMMON IWX(250),IWY(250),Y3(250),YO(250)
      DIMENSION YOF(250),Y3F(250),XP(6),YP(6),IR(5),IS(5),P(2),PG(2),
     1WIG(2)
      DOUBLE PRECISION XP,YP,X33,Y33
      CALL FSWAP("FIDUC.SV")
      CALL OPEN(2,"DATA",2,IER,160)
      CALL FSEEK(2,0)
      READ BINARY(2) XP,YP,X33,Y33
      CALL CLOSE(2,IER)
      ACCEPT "IEXP,WIRE,NPW ",IEXP,IWRE,NPW
      ACCEPT "PEROX,PEROY,WM ",PEROX,PEROY,WM
      ACCEPT "THETA,WIG1,WIG2 ",THETA,WIG(1),WIG(2)
      KA=5
   21 KB=KA-4
      READ(9,733) (IR(J),IS(J), J=1,5)
      DO 22 MA=1,5
      IWX(KB+MA-1) = IR(MA)
   22 IWY(KB+MA-1) = IS(MA)
      KA=KA+5
      IF(NPW-KA) 23,21,21
   23 IPW=NPW-KA+5
      IF(IPW .EQ. 0) GO TO 25
      KB=KA-4
      READ(9,733) (IR(J),IS(J), J=1,IPW)
      DO 24 MA=1,IPW
      IWX(KB+MA-1) = IR(MA)
   24 IWY(KB+MA-1) = IS(MA)
   25 CONTINUE
      WRITE(12,820) IEXP
      WRITE(12,825)PEROX,PEROY,WM
      WRITE(12,826)NPW,THETA
      CALL OVOPN(1,"DEFLECT.OL",IER)
C
C        COMPUTE REAL SPACE COORDINATES OF POINTS JUST READ
C
      CALL OVLOD(1,XR,0,IER)
```

```
      CALL RLSPD(NPW,XP,YP,X33,Y33)
      CALL DATSW(8,LMN)
      GO TO (32,31),LMN
   32 WRITE(12,821)
      WRITE(12,822) (YO(L),Y3(L),L=1,NPW)
   31 CONTINUE
C
C        CONVERT YO & Y3 TO CELL DISTANCES
C
      DO 10 N=1,NPW
      CYO = YO(N)
      CY3 = Y3(N)
      YO(N) = (CYO-PEROY)*COS(THETA) + (CY3-PEROX)*SIN(THETA)
      GO TO (10,52),IWRE
   52 YO(N) = -YO(N)
   10 Y3(N) = (CY3-PEROX)*COS(THETA) - (CYO-PEROY)*SIN(THETA)
      CALL DATSW(9,LMM)
      GO TO (35,36),LMM
   35 WRITE(12,823)
      WRITE(12,822)(YO(K),Y3(K),K=1,NPW)
   36 CONTINUE
C
C        FIT YO-Y3 DATA FOR KREG DIFFERENT REGIONS
C
      CALL OVLOD(1,XS,0,IER)
      KER=3
      PG(1)=WIG(1)
      PG(2)=WIG(2)
      ACCEPT "KREG=",KREG
      DO 40 NR=1,KREG
      DO 41 NRR=1,250
      YOF(NRR) = 0.0
   41 Y3F(NRR) = 0.0
      ACCEPT "UPPER BOUND,YZ=",YZ
      ACCEPT "LOWER BOUND,YR=",YR
      MC=0
      DO 42 MR=1,NPW
      IF(Y3(MR) .LE. YZ) GO TO 45
```

```
      GO TO 42
   45 IF(Y3(MR) .GE.  YR) GO TO 43
      GO TO 42
   43 MC=MC+1
      YOF(MC) = YO(MR)
      Y3F(MC) = Y3(MR)
   42 CONTINUE
C
      CALL DPAK(MC,YOF,Y3F,PG,P,KEK,WM)
      PG(1) = P(1)
      PG(2) = P(2)
      WRITE(12,824) YZ,YR,P(1),P(2)
      DO 44 KK=1,MC
      YC = P(1) * EXP(-P(2)*YOF(KK)) + WM*YOF(KK)
      YCP=-P(1)*P(2) * EXP(-P(2)*YOF(KK)) + WM
      YCD = Y3F(KK) - YC
   44 WRITE(12,832) YOF(KK),Y3F(KK),YC,YCD
   40 CONTINUE
C
C
  731 FORMAT(2I5,5X,3F10.5)
  733 FORMAT(10X,5(F6.0,F6.0))
  734 FORMAT(3F10.5)
  820 FORMAT(5X,'EXPERIMENT NO. ',I4,5X,'DEFLECTION DATA')
  821 FORMAT(//,5X,'REAL SPACE DATA -- YO-Y3 PAIRS',/)
  822 FORMAT((5X,5(2X,F10.5,F10.5)))
  823 FORMAT(///,5X,'CELL SPACE DATA -- YO-Y3 PAIRS',/)
  824 FORMAT(///,5X,'FOR REGION FROM Y3=',F7.4,' TO ',F7.4,9X,'Y3='
     1,F10.5,' *EXP(-(',F10.5,' )*YO) + WM*YO',//,5X,'YO OBS.  -- Y3 OBS.
     2 -- Y3 PRED.  -- (Y3OBS - Y3PRED)',/)
  826 FORMAT(5X,'NO.  OF POINTS  ',I4,2X,'MEMBRANE SLOPE, RADIANS  ',
     1F7.4,//)
  825 FORMAT(5X,'PEROX=',F8.4,2X,'PEROY=',F8.4,2X,'WIRE SLOPE =',F10.6)
  832 FORMAT(1X,4F12.5)
      CALL CLOSE(1,IER)
      STOP
      END
```

```
      SUBROUTINE FNCTW(X,P,F,PART,WM)
      DIMENSION P(2),PART(2)
      F = P(1)*EXP( -P(2)*X) + WM*X
      PART(1) = EXP(-P(2)*X)
      PART(2) = -P(1)*X*PART(1)
      RETURN
      END
```

TABLE C-5

SDIP

computer program

```
C ********** SHADOWGRAPH DATA INTERPRETATION PROGRAM NOVA ******************
C
C
C         THE STRATEGY FOR GETTING THE REFRACTIVE INDEX PROFILE FROM LIGH
C         T DEFLECTION MEASUREMENTS IS DIVIDED INTO TWO REGIONS.  REGION O
C         NE USES THE NUMERICAL INTEGRATION ROUTINE WHICH RESULTS FROM TH
C         E ASSUMPTION THAT DEFLECTION ANGLES OF LIGHT LEAVING THE ULTRA-
C         FILTRATION CELL ARE SMALL.  REGION TWO IS A NUMERICAL SOLUTION O
C         F THE GENERAL DEFLECTION FORMULATION.  REGION ONE IS OK AS LONG
C         AS DEFLECTION ANGLES ARE LESS THAN INPUTTED VARIABLE SAA.
C
C            SUBROUTINE LIST
C         DQSF - IN SSP FILE, CALLED BY MAIN TO NUMERICALLY INTEGRATE SMA
C                LL DEFLECTION ANGLE EQUATION
C         PSPAK- POLYNOMIAL FITTING ROUTINE CALLED BY MAIN
C         LSS  - LEAST SQUARE REDUCTION ROUTINE CALLED BY PSPAK
C         FNCT - 2ND ORDER POLYNOMIAL FITTED BY PSPAK
C         VINT - NUMERICAL SOLUTION ROUTINE OF THE FIRST ORDER DIFF. EQN.
C                WHICH IS THE GENERAL EXPRESSION OF THE RAY PATH THRU CEL
C                L, CALLED BY MAIN
C         RKV  - 4TH ORDER RUNGE-KUTTA INTEGRATION ROUTINE,CALLED BY VINT
C         FRI  - FIRST ORDER D. E. OF RAY PATH, CALLED BY RKV
C
C            FORTRAN VARIABLE LIST
C         AWF=    FRONT WINDOW TILT TANGENT, +.0012
C         AWT=    BACK WINDOW TILT TANGENT, -.0016
C         B=      ARRAY OF COEF. RETURNED FROM LSFIV USED IN REGION ONE
C         C=      ARRAY OF COEF. RETURNED FROM LSFIV USED IN REGION TWO
C         CON0=   CONCENTRATION AT RAY INLET, GM(
C         CON1=   CONCENTRATION AT RAY OUTLET, GM(
C         CORR=   INCREMENT SIZE FOR REF. INDEX CORRECTIONS
C         D=      IMAGE PLANE DISTANCE, CM
C         DER=    (1/RI)*(DRI/DY)*W, DERIVATIVE USED IN REGION ONE
C         DJZ=    FRACTION OF CELL WIDTH FOR WHICH LIGHT PATH IS COMPUTED
C                 IN VINT BY SAA METHOD
C         DNY=    DRI/DY CALC. FROM FITTED POLYNOMIAL FOR USE IN TRANSITION
C                 FROM REGION ONE TO TWO
C         JZ=     NO. OF Z-DIRECTION INCREMENTS FOR VINT INTEGRATION
```

```
C       JGEN=  DATA JUMPS IN REGION TWO
C       JSAA=  DATA JUMPS IN REGION ONE
C       JWI=   INDICATOR OF WHICH WIRE IMAGE FIT IS IN USE
C       L=     COUNTER FOR REF. INDEX CONVERGENCE LOOP
C       LL=    COUNTER FOR Y1 CONVERGENCE LOOP
C       NDIM=  ORDER OF GRAPHICAL INTEGRATION USED FOR REGION ONE
C       NGEN=  NO. OF POINTS USED IN FITTING OF REGION TWO
C       NPT=   NO. OF REGIONS REQUIRING SEPERATE WIRE IMAGE FITS
C       NSAA=  NO. OF POINTS PLUS 1 USED IN FITTING REGION ONE
C       PG( )= INITIAL GUESSES OF QUADRATIC COEFF FOR PSPAK
C       RFT()= ARRAY CONTAING VALUES OF REF. INDEX FOR USE IN PSPAK
C       RIB=   REFRACTIVE INDEX OF BULK SOLUTION
C       RIG=   REFRACTIVE INDEX OF GLASS
C       RI1=   REFRACTIVE INDEX AT LIGHT RAY EXIT SIDE OF CELL
C       SAA=   VALUE OF DY/DZ AT WHICH SMALL ANGLE ROUTINE IS ENDED
C       T=     CELL WALL THICKNESS, 0.4762 CM
C       TOLN=  CONVERGENCE LIMIT FOR Y3, = Y3DATA - Y3CALC
C       TOLY=  CONVERGENCE LIMIT FOR Y1, = Y1NEW - Y1OLD
C       W=     CELL WIDTH, =-0.0028*Y + 0.3144 CM
C       WI1( )=ARRAY OF FIRST COEFFICIENTS FOR VARIOUS FITTED REGIONS
C              OF WIRE IMAGE DATA
C       WI2( )=ARRAY OF SECOND COEFFICIENTS
C       WM=    SLOPE OF WIRE
C       YO( )= ARRAY OF RAY INLET POINTS, CM
C       YFT()= ARRAY CONTAINING VALUES OF HEIGHT ABOVE MEMBRANE FOR USE
C              IN LSFIV
C       YOO=   HEIGHT ABOVE MEMBRANE OF FIRST INPUTTED RAY, CM
C       Y3( )= ARRAY OF WIRE IMAGE POINTS GENERATED BY THE EQUATION
C              Y3 = WI1*EXP(-WI2*YO) + YO
C       YW( )= ARRAY OF THE YO VALUES BOUNDING WIRE IMAGE FITS
C
C       PROGRAM LIMITATIONS AS OF JULY 15 ARE
C       NPT L.T. OR EQ. 4
C       NGEN L.T. OR EQ. 25
C       NDIM L.T. OR EQ. 4
C       NSAA L.T. OR EQ. 25
C       YOO L.T. OR EQ. 1.00 CM
C       MINIMUM DISTANCE BETWEEN RAYS IS 0.001 CM
```

```
C
C
        EXTERNAL XQ,XP
      DIMENSION B(5), PG(5), C(5),    DIFY(4), DIFF(230), RIZ(4),
     1 Y3(50), Y1(50), Y1G(100), YW(4), WI1(4), WI2(4)
        COMMON YO(40),RIO(40)
        DOUBLE PRECISION RI1,AA,A,Y3C,CON1,YLL,DIFF,TOLN,COR,CORR,DY1G
        DOUBLE PRECISION TES,TOLY,YFT,RFT,PO,AWF,AWT
      DIMENSION YFT(25), RFT(25)
 1100 READ(9,700) XEXP,RIB,PH,D
      READ(9,701) TOLN,TOLY,SAA
      READ(9,702) CORR,NPT,JSAA,JGEN,NSAA,DJZ
      READ(9,703) NGEN,JZ,NDIM
      READ(9,705) YOO,WM
      READ(9,704) (YW(IPT), WI1(IPT), WI2(IPT), IPT=1,NPT)
      READ(9,708) PG(1),PG(2),PG(3)
  700 FORMAT(4F9.5)
  701 FORMAT(3F10.6)
  702 FORMAT(F10.1,4I5,F10.4)
  703 FORMAT(3I5)
  704 FORMAT(5X,3F10.5)
  705 FORMAT(5X,2F10.5)
  708 FORMAT(3F10.5)
      WRITE(12,910) XEXP,RIB,PH
      WRITE(12,912) YOO,D
      WRITE(12,920) JSAA,JGEN
      WRITE(12,921) NSAA,NGEN,JZ,DJZ
      WRITE(12,922) SAA,TOLN,TOLY
      WRITE(12,911)
      DO 913 IPT=1,NPT
  913 WRITE(12,914) YW(IPT),WI1(IPT),WI2(IPT)
      WRITE(12,915)
  915 FORMAT(///,10X,'SMALL DEFLECTION REGION',//)
  911 FORMAT(10X,'FOR IMAGE,  YO-Y3 COEFFICIENTS ARE:',/,10X,'ABOVE
     1 YO=',14X,'WIG1',15X,'WIG2')
  910 FORMAT(1H1,///,10X,'EXPERIMENT',F6.0,10X,'R. I.  BULK',F7.4,7X
     1,'SOLN.  PH',F6.3,//)
  914 FORMAT(10X,F7.4,12X,F9.4,10X,F9.4)
```

```
  912 FORMAT(10X,'INITIAL RAY',F8.4,7X,'FOCAL DIST',F8.3,/)
  920 FORMAT(10X,'PART 1 JUMPS',I5,9X,'PART 2 JUMPS',I5)
  921 FORMAT(10X,'PART 1 POINTS',I4,9X,'PART 2 POINTS',I4,9X,'RKV DIVISI
     1ONS',I4,7X,'VINT SAA FRAC',F6.3)
  922 FORMAT(10X,'SAA LIMIT', F8.4, 9X,'TOLN', F9.6, 13X,'TOLY',F9.6,//)
C
C
      AWF = 0.0012D0
      AWT = -0.0016D0
      T=0.4762
      RIG= 1.4570
      CALL OVOPN(1,"SDIF.OL",IER)
      DO 1 INI=1,3
      B(INI)=0.00
    1 C(INI)=0.00
      DO 2 INK=1,25
      YFT(INK)=0.D0
    2 RFT(INK)=0.D0
      DO 9 INJ=1,NGEN
      YO(INJ)=0.00
    9 RIO(INJ)=0.00
C
C
C ****** REGION ONE -- SMALL DEFLECTION ANGLE FORMULATION ******
C          FIRST NDIM POINTS ARE CALCULATED WITHOUT CHECKS FOR SAA LIMIT
C
      YH = JSAA*0.001
      JWI = 1
      DO 10 IJ=1,NDIM
      YO(IJ) = YOO - (IJ-1)*YH
      IF(YO(IJ) - YW(JWI)) 16,16,15
   16 JWI = JWI + 1
   15 Y3(IJ) = WI1(JWI) * EXP(-WI2(JWI) * YO(IJ)/WM) + YO(IJ)
      W = -0.0028*YO(IJ) + 0.3144
      CKW = 1.00/(W*(D+T/RIG))
   10 DIFY(IJ) = CKW *  ABS(Y3(IJ) - YO(IJ))
      CALL OVLOD(1,XQ,0,IER)
      CALL  QSF(YH, DIFY, RIZ, NDIM)
      DO 19 JJ=1,NDIM
```

```
      RIO(JJ) = RIZ(JJ) + RIB
      CONO = (RIO(JJ) - 1.33408)/0.0019971
   19 WRITE(12,801) JJ,YO(JJ),RIO(JJ),CONO
C
C          FOLLOWING POINTS ARE CALCULATED UNTIL SAA LIMIT IS EXCEEDED
C          CALCULATION BEGINS WITH DATA TABLE PAIR NO.  (1+NDIM*JSAA)
C          AND COMTINUES AT INTERVALS DETERMINED BY 'IU'
C
      IG = NDIM + 1
      IU = IG
      NSAAA = NSAA-1
      DO 11 IK=IG,200
      NKK=IK-NDIM
      MKK=IK-2
      DO 13 NK=NKK,MKK
   13 DIFY((IK-1)-NK) = DIFY(IK-NK)
      YO(IU) = YOO - (IK-1)*YH
      IF(YO(IU) - YW(JWI)) 18,18,17
   18 JWI = JWI + 1
   17 Y3(IU) = WI1(JWI) * EXP(-WI2(JWI) * YO(IU)/WM) + YO(IU)
      W = -0.0028*YO(IU) + .3144
      CKW = 1.00/(W*(D+T/RIG))
      DIFY(NDIM) = CKW *  ABS(Y3(IU) - YO(IU))
      CALL  QSF(YH,DIFY,RIZ,NDIM)
      RIO(IU) = RIO(IU - NDIM        ) + RIZ(NDIM)
      DER = ((RIO(IU) - RIO(IU-1    )) / (YO(IU) - YO(IU-1    ))) *2.00*W/
     1(RIO(IU) + RIO(IU-1    ))
      CONO = (RIO(IU) - 1.33408)/0.0019971
      WRITE(12,802) IK,YO(IU),RIO(IU),CONO,DER
      IF(IU - NSAA) 20,20,21
   20 IU = IK + 1
      GO TO 22
   21 DO 23 IUU = 1,NSAA
      RIO(IUU) = RIO(IUU + 1)
      YO(IUU) = YO(IUU+ 1)
```

```
   23 Y3(IUU) = Y3(IUU + 1)
   22 IF( ABS(DER) -  ABS(SAA)) 11,11,14
   11 CONTINUE
C
C          LOAD UP ARRAYS YFT AND RFT WITH LAST NSAA PTS.  CALCULATED IN
C          REGION ONE (EXCEPT THE LAST ONE WHICH EXCEEDS SAA) AND CURVE
C          FIT IN PSPAK.  INVERT THE PSPAK COEFFICIENTS.
C
   14 CONTINUE
      DO 12 IV=1,NSAAA
      YFT(IV) = DBLE(YO(IV))
   12 RFT(IV) = DBLE(RIO(IV))
      CALL OVLOD (1,XP,0,IER)
      CALL PSPAK(NSAAA,YFT,RFT,PG,B)
        TYPE "LEAVING PSPAK FIRST TIME"
      DO 30 JB=1,3
   30 PG(JB) = B(JB)
      WRITE(12,803) B(1),B(2),B(3)
C
C
C ****** REGION TWO -- GENERAL FORMULATION ******
C          'LL' AND 'L' ARE NESTED CONVERGENCE ROUTINES.  IN 'L' A VALUE
C          OF REF.  INDEX AT THE FAR CELL WALL MUST BE FOUND WHICH YIELDS
C          THE CORRECT IMAGE PLANE LOCATION.  AT THIS VALUE OF RI1, A NEW
C          VALUE OF RAY LOCATION AT THE FAR CELL WALL, Y1( ), IS THEN
C          COMPUTED BY NUMERICAL INTEGRATION ALONG THE RAY PATH.  THESE
C          ITERATIONS CONTINUE IN 'LL' UNTIL Y1( ) STOPS CHANGING WITHIN
C          A TOLERANCE OF TOLY.  NEW INPUT RAYS OVERLAPPED (IE YONEW LT
C          Y3OLD)SUCH THAT THE REF.  INDEX AT THE NEAR CELL WALL IS
C          FOUND BY INTERPOLATION FROM THE MOST RECENT FIT IN PSPAK.
C          THIS FIT ALWAYS INCLUDES THE LAST RI1-Y1( ) COMPUTED IN 'LL'
C
C          START 'LL' LOOP BY COMPUTING Y1(IW) USING SAA ROUTINE WHERE
C          IW IS THE LAST RAY OF REGION ONE FOR WHICH SMALL ANGLE ASSUMP
C          TIONS APPLY
C
```

```
      )WWW = NSAAA+NGEN-2
      IW = NSAAA
      NGC = NSAAA
      NGCN = NSAA
      NGE = NGEN - 2
      DO 106 KC=1,3
  106 C(KC) = B(KC)
      YH = 0.001 * JGEN
      DNY = B(2) + 2.00*B(3)*YO(IW)
      W = -0.0028*YO(IW) + .3144
      Y1(IW) = YO(IW) + (DNY*W**2.)/(RIO(IW)*2.00)
C
C
  100 LL=0
      PO = AWF*(1.DO - 1.DO/DBLE(RIO(IW)))
      Y1G(1)=Y1(IW)
  610 LL=LL+1
      RI1=DBLE(RIO(IW))
C
      L=0
      COR=CORR
  650 L=L+1
      AA = -DSQRT(((RI1/DBLE(RIO(IW))) **2)*(PO**2 + 1.DO) - 1.DO)
      A=-(AA+AWT)
      YLL=DBLE(Y1G(LL))
      Y3C =YLL-RI1*A*(DBLE(D)/DSQRT(1.DO+(1.DO-RI1**2.DO)*A**2.DO) +
     1DBLE(1)/DSQRT((DBLE(RIG))**2.DO+((DBLE(RIG))**2.DO-RI1**2.DO)
     1*A**2.DO))
C
C           TES CHECKS IF Y3( ) AND Y3C ARE THE SAME SIGN
      TES=Y3C/DBLE(Y3(IW))
      IF(TES)70,70,51
   51 DIFF(L) = DBLE(Y3(IW)) - Y3C
      IF( DABS(DIFF(L)) - TOLN) 101,101,52
C           FIRST TIME THROUGH ?
```

```
   52 IF(L-1) 63,63,53
C           HAS ZERO BEEN CROSSED ?
   53 IF(DIFF(L)/DIFF(L-1)) 64,64,54
   64 IF(DIFF(L)) 66,66,65
   66 RI1 = RI1+COR
      COR = COR/2.D0
      RI1 = RI1 - COR
      GO TO 50
   65 RI1 = RI1 - COR
      COR = COR/2.D0
      RI1 = RI1 + COR
      GO TO 50
   63 COR = CORR
   54 IF(DIFF(L)) 55,55,56
   55 RI1 = RI1 + COR
      GO TO 50
   56 RI1 = RI1 - COR
      GO TO 50
C
   70 DIFF(L) =  DABS(DBLE(Y3(IW))) +  DABS(Y3C)
      IF( DABS(DIFF(L)) - TOLN) 101,101,71
   71 IF(Y3(IW)) 72,72,73
   72 RI1 = RI1 + CORR
      DIFF(L) = -DIFF(L)
      GO TO 50
   73 RI1 = RI1 - CORR
C
   50 LIM=229
      IF(L-LIM)650,650,651
  651 WRITE(12,602) LIM
      GO TO 150
C
  101 COR = CORR
      YFT(NGCN) = DBLE(Y1G(LL))
      RFT(NGCN) = RI1
```

```
      IF(LL-1) 104,104,102
  102 CALL PSPAK(NGCN,YFT,RFT,PG,C)
      DO 107 JC=1,3
  107 PG(JC)=C(JC)
  104 CALL VINT(C,W,JZ,IW,YM,DJZ)
      IF(YM) 152,152,111
  111 Y1G(LL+1)=YM
      DY1G = DBLE(Y1G(LL+1))-DBLE(Y1G(LL))
      IF(DABS(DY1G)-TOLY) 108,108,110
C
  110 CONTINUE
      LMT = 20
      IF(LL-LMT) 610,610,611
  611 WRITE(12,604) LMT
      GO TO 150
C
  108 Y1(IW) = Y1G(LL+1)
      YFT(NGCN) = DBLE(Y1G(LL+1))
      CALL PSPAK(NGCN,YFT,RFT,PG,C)
      DO 109 JC=1,3
  109 PG(JC) = C(JC)
      WRITE(12,658) YO(IW)
  658 FORMAT(2X,'COEFF FOR FINAL FIT AT YO=',F6.4)
      WRITE(12,659) C(1),C(2),C(3)
  659 FORMAT(3F14.7)
      CONO = (RIO(IW) - 1.33408) / 0.0019971
      CON1 = (RI1 - 1.33408D0)/0.0019971D0
      WRITE(12,810) IW, YO(IW), RIO(IW), CONO, Y1(IW), RI1, CON1, Y3(IW)
      IF(IW - (IWWW+1)) 85,86,86
   85 IW = IW + 1
        YO(IW) = YO(IW-1) - YH
      GO TO 87
   86 DO 88 IUU = NSAAA,IWWW
      RIO(IUU) = RIO(IUU + 1)
      YO(IUU) = YO(IUU+ 1)
      Y1(IUU) = Y1(IUU + 1)
   88 Y3(IUU) = Y3(IUU + 1)
```

```
      YO(IW) = YO(IW) - YH
   87 IF(YO(IW)) 152,152,153
  153 IF(YO(IW) - YW(JWI)) 84,84,83
   84 JWI = JWI + 1
   83 Y3(IW) = WI1(JWI) * EXP(-WI2(JWI) * YO(IW)/WM) + YO(IW)
      Y1(IW) = YO(IW) - (YO(IW-1) - Y1(IW-1))
      RIO(IW) = C(1) + C(2)*YO(IW) + C(3)*YO(IW)**2.
      W = -0.0028*YO(IW) + .3144
      IF(NGCN - NGEN) 160,161,161
  160 NGC = NGC + 2
      YFT(NGC) = DBLE(YO(IW))
      RFT(NGC) = DBLE(RIO(IW))
      NGCN = NGCN + 2
      GO TO 100
  161 DO 105 IB = 1,NGE
      YFT(IB) = YFT(IB+2)
  105 RFT(IB) = RFT(IB+2)
      YFT(NGE+1)= DBLE(YO(IW))
      RFT(NGE+1)= DBLE(RIO(IW))
      NGCN=NGEN
      GO TO 100
  152 CYO = (C(1) - 1.33408)/0.0019971
      WRITE(12,813) CYO
  813 FORMAT(/,10X,'CONCENTRATION AT MEMBRANE SURFACE',F7.2)
  150 GO TO 1100
C
C
  810 FORMAT(5X,I5, F9.4, F14.9, F7.2,5X,F9.4, F14.9, F7.2,5X, F11.6,/)
  801 FORMAT(5X, I5, F9.4, F14.9, F7.2)
  802 FORMAT(5X, I5, F9.4, F14.9, F7.2, 5X, F11.6)
  803 FORMAT(/, 5X, 3F14.9, //)
  602 FORMAT(//, 2X,'L LOOP LIMIT OF',I5, 2X,'EXCEEDED')
  604 FORMAT(//,2X, 'LL LOOP LIMIT OF',I5, 2X,'EXCEEDED')
      CALL CLOSE(1,IER)
      STOP
      END
```

```
      SUBROUTINE VINT(C,W,JZ,IW,YM,DJZ)
C
C        VINT USES SAA METHOD TO FIND Y-COORDINATE (YFN) AT  DJZ INCRE
C        MENTS (EACH OF SIZE W/JZ CM) INTO THE CELL.  IT THEN CALLS A
C        MODIFIED 4TH ORDER RUNGE-KUTTA ROUTINE TO NUMERICALLY INTEGRATE
C        THE REST OF THE RAY PATH AS IT TRAVERSES THE CELL.  IER IS USED
C        AS AN INDICATOR FROM RKV TO TELL WHEN LOWEST RAY HITS MEMBRANE.
C
C          YFN=  RAY Y-COORDINATE AT SOME Z-COORDINATE, ZI
C          ZFA=  SHOULD BE EQUAL TO W AT END OF RKV ROUTINE
C          YM=   EXITING RAY Y-COORDINATE COMPUTED BY RKV
C
C
      COMMON YO(40),RIO(40)
      DIMENSION C(3)
      DOUBLE PRECISION E
      AWF = +0.0012
      DNY = C(2) + 2.00*C(3)*YO(IW)
      YSP = DNY/RIO(IW)
      HZ=W/JZ
      ZI = DJZ*W
      YFN = YO(IW) + 0.500*YSP*ZI**2.  + AWF*ZI
      RN = C(1) + C(2)*YFN + C(3)*YFN**2.
      E = DBLE(RN) / DBLE(RIO(IW))
      IF(E-1.D0)303,303,304
  303 YM  = YO(IW) + 0.500*YSP*W**2.  + AWF*W
      WRITE(12,625) IW,DNY,ZI,YFN,E
  625 FORMAT(12X,I4,4F14.9)
      GO TO 302
  304 CALL RKV(C,  HZ,  ZI,  YFN,  W,  0.00,  ZFA,  YM,  IER,  IW)
      IF(IER-2) 302,301,302
  301 YM = -1.0
  302 RETURN
      END
```

```
REAL FUNCTION FRI    (X,Y,RION,B1,B2,B3)
DOUBLE PRECISION PO
AWF = +0.0012
PO = DBLE(AWF) * (1.DO -1.DO/DBLE(RION))
RR = B1 + B2*Y + B3*Y**2.
FRI = -DSQRT(((DBLE(RR)/DBLE(RION))**2)*(PO**2 + 1.DO)- 1.DO)
RETURN
END
```

APPENDIX D

Experimental Data

Photographic Evaluation Summaries

Table D-1, D-2 and D-3 summarize the intermediate calculations for transforming the photo data for each wire to an ultrafiltration cell coordinate system (equation 5-24). The table headings refer to Figure 5-13.

For each photo evaluated, Table D-4 presents a ray trace summary for one ray at the top of the polarization layer and for the last ray which is traced near the membrane surface. The following nomenclature applies:

D	-	distance of fiducial plane from glass window
Ray T	-	ray which enters solution at point where solution concentration is 2% greater than bulk
Ray L	-	last ray which is traced, i.e., $0 \leq Y_1 \leq .0015$cm
Y_0, Y_1, Y_3	-	height of ray at $\bar{z}_0$, $\bar{z}_1$ and fiducial planes respectively
α^L	-	angle of last ray at plane $\bar{z}_1$.

Table D-5 summarizes the concentration profile data obtained from the ray tracing calculations for each photograph.

F-Series Flow Data

Results of non-linear least squares regression fits to the F-series experiments are presented in Table D-6.

Flow Data

Table D-7 is a compilation of the ultrafiltrate volume recorded by the LFD as a function of elapsed time for each experiment.

TABLE D-1

DATA FOR MEMBRANE LOCATION CALCULATIONS (CENTIMETERS)

EXPERIMENT PHOTO NO.	M_A	M_B	M_C	d_A	d_B	d_C	P_Y^A	P_Y^B	P_Y^C
306	-.089	-.099	-.107	.703	.694	.694	-.792	-.793	-.801
603	.126	.126	.114	.706	.704	.702	-.580	-.578	-.588
604	.126	.126	.114	.706	.704	.702	-.580	-.578	-.588
706	.173	.156	.144	.709	.706	.702	-.536	-.550	-.558
907	.290	.278	.270	.720	.716	.718	-.430	-.437	-.448
1104	.836	.818	.806	.652	.645	.640	+.184	+.173	+.166
1305	.454	.433	.417	.688	.678	.670	-.234	-.245	-.253
1307	.454	.432	.415	.688	.678	.670	-.234	-.246	-.255
1406	.454	.434	.415	.688	.678	.670	-.234	-.244	-.255
1505	.453	.433	.417	.688	.678	.670	-.235	-.245	-.253
1601*	.356	.338	.322	.688	.676	.665	-.332	-.338	-.343
1604+	.355	.332	.316						
1702*	.356	.336	.323	.688	.676	.665	-.332	-.340	-.342
1705+	.354	.334	.318						
1706	.346	.327	.312						
1707+	.347	.326	.307						
1801*	.353	.335	.320	.688	.676	.665	-.335	-.341	-.345
1805	.350	.327	.313						
1808+	.346	.323	.307						
1810	.345	.324	.307						
1815+	.308	.284	.262						
AVG. FOR(*)	.355	.336	.322	.688	.676	.665	-.333	-.340	-.343

+ FOR THESE PHOTOS, LISTED VALUES NOT USED, USE AVG OF (*) VALUES

TABLE D-2

MEMBRANE-WIRE INTERSECTION AND ORIENTATION (CENTIMETERS)

EXPERIMENT -PHOTO NO.	Wire 1				Wire 2			
	Θ_C RADIANS	a_1	b_1	P_x^C	Θ_A RADIANS	a_2	b_2	P_x^A
306	.0101	.9699	.0234	-.753	0	-1.0202	-.1701	.638
603	.0144	.9803	-.1327	-.709	-.0029	-1.0414	.1207	.725
604	.0144	.9712	-.1302	-.701	-.0029	-1.0431	.1181	.723
706	.0144	.9622	-.2061	-.743	.0144	-1.0438	.1099	.669
907	.0144	.9630	-.3907	-.822	.0100	-1.0375	.1675	.615
1104	.0101	.9617	-.8547	-.695	.0159	-1.0373	.7804	.590
1305	.0115	.9608	-.4414	-.685	.0159	-1.0368	.4215	.664
1307	.0130	.9596	-.4335	-.680	.0173	-1.0462	.4298	.694
1406	.0158	.9589	-.4377	-.682	.0144	-1.0365	.4217	.664
1505	.0155	.9609	-.4419	-.685	.0144	-1.0408	.4266	.671
1601*	.0070	.9555	-.4134	-.740	.0115	-1.0422	.2566	.603
1604+	.0070				.0155			
1702*	.0028	.9558	-.4095	-.736	.0115	-1.0459	.2561	.603
1705+	.0070				.0115			
1706	.0058				.0101			
1707+	.0115				.0130			
1801*	.0057	.9539	-.4103	-.739	.0086	-1.0442	.2569	.607
1805	.0043				.0159			
1808+	.0072				.0159			
1810	.0086				.0130			
1815+	.0159				.0173			
AVG. FOR(*)	.0043	.9551	-.4111	-.739	.0101	-1.0441	.2566	.604

+FOR THESE PHOTOS, LISTED VALUES NOT USED, USE AVG. OF (*) VALUES

TABLE D-3

COEFFICIENTS FOR YJ = G1*EXP (-G2*XJ) + S_J*XJ (CENTIMETERS)

EXPERIMENT -PHOTO NO.	WIRE 1 J=1					WIRE 2 J=2				
	Y_{oo}	S_1	FOR YO G.T. USE→	-G1	G2	Y_{oo}	S_2	FOR YO G.T. USE→	-G1	G2
306	.52	1.0105	.093	4.5947	12.3597	.60	.9802	.250	8.5527	13.7857
			.000	5.0819	14.4288			.080	4.5272	10.7071
								.000	5.1379	13.0409
603	.30	.9911	.110	8.2306	34.3995	.30	.9548	.080	5.6259	28.7846
			.050	5.8260	29.0890			.029	3.6367	20.5371
			.000	6.8471	30.1044			.000	3.2014	15.5175
604	.30	1.0005	.140	7.8732	27.4359	.35	.9531	.170	4.5568	18.5359
			.000	3.2425	19.0047			.000	3.0371	15.6699
706	.63	1.0096	.200	5.9037	11.3278	.63	.9862	.250	7.4215	11.2350
			.000	4.3821	9.6780			.000	4.9956	9.4427
907	.65	1.0091	.160	5.2486	13.6523	.65	.9837	.170	6.1082	13.2501
			.000	3.4239	11.0996			.000	3.6925	10.1960
1104	.55	1.0190	.170	8.9154	14.9146	.55	.9951	.170	6.1051	13.4337
			.000	8.4462	14.8836			.000	8.1155	14.8262
1305	.55	1.0171	.170	7.3513	14.3005	.55	.9956	.160	6.2377	14.8842
			.000	8.8642	15.7107			.000	7.6136	17.0122
1307	.55	1.0155	.170	7.3215	14.6884	.55	.9809	.170	6.1955	13.5490
			.000	6.8717	14.1009			.000	9.4560	16.6429
1406	.53	1.0103	.170	2.8746	9.3780	.53	.9930	.180	2.6985	9.6038
			.000	2.1948	7.9980			.000	1.8760	7.4945
1505	.55	1.0170	.180	5.3191	12.0477	.55	.9889	.170	4.5550	11.9068
			.000	4.5638	11.4490			.000	3.8776	11.1307
1604	.70	1.0379	.150	2.9997	10.0653	.70	.9774	.150	2.9000	9.3308
			.000	1.8821	7.2441			.000	2.0781	7.3518
1705	.60	1.0379	.160	6.2267	14.0203	.60	.9774	.160	5.9289	13.3365
			.000	5.9580	13.7321			.000	8.0958	15.0659
1707	.77	1.0379	.190	3.5860	8.6763	.77	.9774	.200	3.5835	8.0599
			.000	3.6747	8.6051			.000	4.2547	8.7466
1808	.77	1.0379	.210	5.8942	9.6730	.77	.9774	.210	6.3509	9.2821
			.000	9.3976	11.9491			.000	8.8589	10.3588

TABLE D-4

RAY TRACING SUMMARIES

EXPERIMENT -PHOTO NO.	WIRE	D CM	Y_o^T CM	Y_3^T CM	Y_o^L CM	Y_1^L CM	Y_3^L CM	$-\alpha^L$ DEGREES
306	W1	25.730	.400	.371	.017	.0009	-3.96	6.1
	W2		.400	.358	.017	.0005	-4.08	6.3
603	W1	25.380	.110	-.068	.017	.0009	-4.07	6.4
	W2		.120	-.063	.012	.0012	-2.62	4.1
604	W1		.145	-.002	.011	.0003	-2.62	4.1
	W2		.190	.046	.011	.0006	-2.52	4.0
706	W1	25.350	.475	.452	.016	.0005	-3.74	5.8
	W2		.485	.446	.018	.0008	-4.20	6.5
907	W1	25.484	.380	.354	.013	.0007	-2.95	4.6
	W2		.390	.349	.014	.0008	-3.18	5.0
1104	W1	25.434	.355	.317	.024	.0006	-5.92	8.9
	W2		.360	.310	.023	.0003	-5.75	8.8
1305	W1	25.414	.360	.323	.025	.0014	-6.00	9.1
	W2		.330	.283	.022	.0012	-5.21	8.0
1307	W1		.345	.304	.021	.0005	-5.11	7.8
	W2		.355	.298	.025	.0008	-6.18	9.4
1406	W1	25.414	.430	.383	.009	.0006	-2.03	3.2
	W2		.415	.362	.008	.0007	-1.76	2.7
1505	W1	25.414	.400	.364	.016	.0005	-3.80	5.9
	W2		.380	.326	.014	.0004	-3.30	5.1
1604	W1	25.414	.455	.441	.008	.0006	-1.77	2.8
	W2		.460	.410	.009	.0010	-1.93	3.0
1705	W1	25.414	.350	.317	.019	.0004	-4.61	7.1
	W2		.340	.269	.023	.0006	-5.66	8.6
1707	W1		.535	.521	.014	.0006	-3.26	5.0
	W2		.540	.482	.016	.0010	-3.68	5.7
1808	W1	25.414	.525	.508	.027	.0004	-6.86	10.1
	W2		.525	.465	.027	.0012	-6.63	9.9

TABLE D-5

CONCENTRATION PROFILE DATA

Experiment 306

Height Above Membrane cm	Concentration, Gm%	
	Wire 1	Wire 2
.500	6.4	6.4
.400	6.5	6.5
.350	6.7	6.6
.300	6.9	6.9
.250	7.3	7.4
.200	8.1	8.5
.150	9.8	10.5
.100	12.8	14.0
.080	14.5	16.0
.060	16.7	18.4
.040	19.6	21.4
.030	21.3	23.3
.020	23.3	25.3
.010	25.6	27.7
.005	26.9	29.0
0.000	28.2	30.4

Experiment 603

Height Above Membrane, cm	Concentration, Gm% Wire 1	Wire 2
.20	15.8	15.8
.15	15.9	15.9
.10	16.2	16.4
.08	16.7	16.8
.06	17.6	17.8
.05	18.3	18.4
.04	19.3	19.2
.03	20.6	20.2
.02	22.4	21.5
.01	24.6	22.9
.005	26.0	23.8
.000	27.6	24.6

Experiment 604

Height Above Membrane, cm	Concentration, Gm% Wire 1	Wire 2
.30	15.8	15.8
.25	15.8	15.9
.20	15.9	16.0
.15	16.1	16.5
.10	17.0	17.7
.08	17.7	18.6
.06	18.7	19.8
.05	19.4	20.5
.04	20.2	21.2
.03	21.2	22.2
.02	22.4	23.4
.01	23.8	24.8
.005	24.6	25.6
.000	25.5	26.4

Experiment 706

Height Above Membrane, cm	Concentration, Gm% Wire 1	Wire 2
.60	6.4	6.4
.55	6.4	6.5
.50	6.5	6.5
.45	6.6	6.6
.40	6.7	6.8
.35	6.9	7.0
.30	7.4	7.5
.25	8.1	8.4
.20	9.5	10.2
.15	12.0	13.0
.10	16.0	17.6
.08	18.3	20.2
.06	20.9	23.2
.04	24.1	26.8
.03	26.0	28.9
.02	28.0	31.2
.01	30.2	33.7
.005	31.4	35.0
.000	32.6	36.4

Experiment 907

Height Above Membrane, cm	Concentration, Gm% Wire 1	Wire 2
.50	7.2	7.2
.45	7.3	7.3
.40	7.3	7.3
.35	7.4	7.4
.30	7.6	7.6
.25	7.9	8.0
.20	8.6	8.9
.15	10.1	10.7
.10	12.7	13.7
.08	14.3	15.5
.06	16.2	17.6
.04	18.5	20.2
.03	19.9	21.7
.02	21.4	23.4
.01	23.1	25.2
.005	24.0	26.2
.000	25.0	27.2

Experiment 1104

Height Above Membrane, cm	Concentration, Gm% Wire 1	Wire 2
.50	10.1	10.1
.45	10.2	10.2
.40	10.2	10.2
.35	10.3	10.3
.30	10.5	10.5
.25	11.0	11.0
.20	11.9	11.8
.15	14.0	13.6
.10	18.1	17.4
.08	20.8	19.9
.06	24.3	23.2
.04	28.9	27.6
.03	31.7	30.3
.02	34.9	33.3
.01	38.5	36.8
.005	40.3	38.6
.000	42.6	40.7

Experiment 1305

Height Above Membrane, cm	Concentration, Gm% Wire 1	Wire 2
.50	10.1	10.1
.45	10.2	10.2
.40	10.2	10.2
.35	10.3	10.2
.30	10.5	10.4
.25	11.0	10.7
.20	11.8	11.3
.15	13.7	12.6
.10	17.7	15.4
.08	20.2	17.3
.06	23.7	20.0
.04	28.3	23.7
.03	31.1	26.0
.02	34.5	28.8
.01	38.1	31.9
.005	40.0	33.6
.000	42.3	35.5

Experiment 1307

Height Above Membrane, cm	Concentration, Gm% Wire 1	Wire 2
.50	10.1	10.1
.45	10.2	10.2
.40	10.2	10.2
.35	10.3	10.3
.30	10.5	10.5
.25	10.8	10.9
.20	11.7	11.7
.15	13.5	13.4
.10	17.2	16.9
.08	19.5	19.4
.06	22.5	22.7
.04	26.5	27.3
.03	28.8	30.1
.02	31.5	33.4
.01	34.6	37.2
.005	36.2	39.4
.000	38.1	41.6

Experiment 1406

Height Above Membrane, cm	Concentration, Gm% Wire 1	Wire 2
.55	10.1	10.1
.50	10.2	10.2
.45	10.2	10.2
.40	10.4	10.4
.35	10.6	10.6
.30	11.0	10.9
.25	11.6	11.4
.20	12.6	12.1
.15	14.3	13.6
.10	16.8	15.8
.08	18.1	17.0
.06	19.6	18.3
.04	21.4	19.9
.03	22.4	20.8
.02	23.4	21.7
.01	24.6	22.7
.005	25.2	23.2
.000	25.9	23.8

Experiment 1505

Height Above Membrane, cm	Concentration, Gm% Wire 1	Wire 2
.55	10.1	10.1
.50	10.2	10.2
.45	10.2	10.2
.40	10.3	10.3
.35	10.5	10.4
.30	10.8	10.6
.25	11.3	11.1
.20	12.4	11.9
.15	14.4	13.6
.10	17.8	16.5
.08	19.7	18.2
.06	22.2	20.3
.04	25.2	22.9
.03	27.0	24.4
.02	29.0	26.2
.01	31.3	28.0
.005	32.4	29.1
.000	33.7	30.2

Experiment 1604

Height Above Membrane, cm	Concentration, Gm% Wire 1	Wire 2
.70	10.1	10.1
.60	10.2	10.2
.50	10.2	10.2
.45	10.3	10.3
.40	10.4	10.4
.35	10.6	10.7
.30	11.0	11.0
.25	11.5	11.6
.20	12.5	12.5
.15	14.1	14.1
.10	16.5	16.6
.08	17.7	17.9
.06	19.1	19.4
.04	20.7	21.1
.03	21.6	22.0
.02	22.6	23.1
.01	23.6	24.2
.005	24.1	24.8
.000	24.7	25.4

Experiment 1705

Height Above Membrane, cm	Concentration, Gm% Wire 1	Wire 2
.50	11.0	11.0
.45	11.1	11.1
.40	11.1	11.1
.35	11.2	11.2
.30	11.4	11.4
.25	11.8	11.8
.20	12.7	12.5
.15	14.5	14.2
.10	18.0	17.8
.08	20.1	20.2
.06	22.9	23.4
.04	26.4	27.6
.03	28.6	30.2
.02	31.0	33.3
.01	33.7	36.7
.005	35.3	38.5
.000	36.8	40.6

Experiment 1707

Height Above Membrane, cm	Concentration, Gm% Wire 1	Wire 2
.70	11.0	11.0
.65	11.1	11.1
.60	11.1	11.1
.55	11.2	11.2
.50	11.3	11.3
.45	11.5	11.5
.40	11.7	11.8
.35	12.1	12.2
.30	12.8	12.8
.25	13.8	13.9
.20	15.4	15.6
.15	18.0	18.3
.10	22.0	22.5
.08	24.1	24.8
.06	26.5	27.5
.04	29.4	30.7
.03	31.0	32.6
.02	32.8	34.5
.01	34.7	36.7
.005	35.7	37.8
.000	36.8	39.1

Experiment 1808

Height Above Membrane, cm	Concentration, Gm% Wire 1	Wire 2
.70	11.0	11.0
.65	11.1	11.0
.60	11.2	11.1
.55	11.2	11.2
.50	11.3	11.3
.45	11.5	11.5
.40	11.8	11.8
.35	12.2	12.2
.30	13.0	13.0
.25	14.3	14.4
.20	16.5	16.9
.15	20.3	21.1
.10	27.0	28.2
.08	30.9	32.1
.06	35.7	37.0
.04	41.6	42.8
.03	45.0	46.2
.02	48.8	49.9
.01	53.0	54.0
.005	55.3	56.2
.000	57.7	58.5

TABLE D-6

F-Series Experiments-Regression Results

EXPERIMENT	REGRESSION FOR 0-2 MIN		REGRESSION FOR 2-t_{total} MINUTES			
	$\eta \pm \varepsilon$	$A_o \pm \varepsilon \times 10^{+3}$ CM/MIN$^{\frac{1}{2}}$	t_{total} MIN.	$\eta \pm \varepsilon$	$A_o \pm \varepsilon \times 10^{+3}$ CM/MIN$^{\frac{1}{2}}$	$A_o \pm \varepsilon \times 10^{+3}$ @ $\eta = -\frac{1}{2}$ CM/MIN$^{\frac{1}{2}}$
F1	-.340 ± .009	9.7 ± .3	96	-.474 ± .001	10.30 ± .17	11.10 ± .04
F2	-.312 ± .022	9.4 ± .8	151	-.451 ± .005	8.70 ± .51	10.22 ± .08
F3	-.319 ± .012	9.0 ± .4	198	-.455 ± .004	8.68 ± .14	10.18 ± .08
F4	-.359 ± .006	8.7 ± .3	170	-.464 ± .003	8.54 ± .30	9.61 ± .07
F5	-.298 ± .012	8.2 ± .3	166	-.431 ± .032	9.1 ± 3.6	11.38 ± .36
F6	-.369 ± .015	6.5 ± .3	319	-.459 ± .002	5.79 ± .11	6.76 ± .06
F7	-.330 ± .012	7.2 ± .2	247	-.438 ± .004	7.36 ± .27	9.22 ± .11
F8	-.298 ± .006	7.6 ± .1	277	-.392 ± .004	7.11 ± .22	10.59 ± .20
F9	-.319 ± .017	6.4 ± .3	248	-.455 ± .002	5.79 ± .09	6.80 ± .07

TABLE D-7

FLOW DATA

Elapsed time has the units of minutes and ultrafiltrate volume has the units of milliliters in tnese listings.

EXPERIMENT 400		EXPERIMENT 1100		EXPERIMENT 1200	
MINUTES	ML	MINUTES	ML	MINUTES	ML
8.200	0.0000	0.217	0.0026	0.408	0.0064
12.000	0.0120	0.450	0.0052	1.025	0.0121
15.400	0.0220	1.133	0.0103	1.917	0.0175
19.600	0.0320	2.117	0.0157	2.980	0.0228
25.400	0.0430	3.250	0.0210	4.320	0.0281
31.700	0.0540	4.700	0.0261	5.900	0.0335
38.600	0.0640	6.450	0.0313	7.500	0.0386
46.000	0.0750	8.800	0.0364	9.500	0.0439
55.400	0.0850	11.400	0.0414	11.900	0.0491
63.600	0.0950	14.000	0.0466	14.450	0.0542
74.500	0.1040	16.800	0.0518	16.850	0.0596
104.000	0.1220	20.100	0.0566	22.600	0.0700
137.000	0.1400	27.500	0.0667	28.700	0.0803
172.000	0.1580	35.300	0.0767	35.600	0.0905
218.000	0.1750	43.700	0.0867	43.000	0.1005
260.000	0.1930	53.400	0.0964	51.800	0.1106
300.000	0.2100	65.500	0.1060	60.400	0.1206
348.000	0.2270	76.900	0.1155	70.300	0.1306
387.000	0.2440	92.600	0.1248	79.700	0.1403
391.000	0.2480	108.300	0.1339	90.700	0.1499
414.000	0.2590	140.200	0.1517	101.600	0.1594
440.000	0.2700	177.800	0.1703	126.200	0.1778
464.000	0.2810	220.200	0.1875	151.300	0.1956
488.000	0.2920	264.000	0.2051	177.500	0.2142
510.000	0.3020	311.000	0.2225	208.200	0.2314
534.000	0.3130	363.500	0.2401	239.400	0.2490
558.000	0.3230	420.500	0.2579	273.600	0.2664
580.000	0.3330	485.500	0.2757	307.800	0.2840
602.000	0.3440	547.000	0.2935	344.400	0.3018
625.000	0.3540			381.000	0.3196
643.000	0.3640			421.000	0.3374
662.000	0.3740			467.000	0.3552
684.000	0.3840			513.000	0.3730
704.000	0.3930			546.000	0.3872
727.000	0.4030				
747.000	0.4120				
772.000	0.4220				
795.000	0.4310				
815.000	0.4400				
836.000	0.4480				
856.000	0.4580				
878.000	0.4670				
896.000	0.4760				

EXPERIMENT 600

MINUTES	ML	MINUTES	ML	MINUTES	ML
0.300	0.0000	21.000	0.0196	134.000	0.0522
0.500	0.0002	26.000	0.0218	141.000	0.0530
1.000	0.0009	30.000	0.0241	148.000	0.0549
1.500	0.0019	33.500	0.0255	160.000	0.0568
2.000	0.0028	36.000	0.0268	173.000	0.0585
2.500	0.0036	40.000	0.0285	190.000	0.0613
3.000	0.0044	46.000	0.0299	201.000	0.0625
3.400	0.0048	50.000	0.0314	210.000	0.0646
4.000	0.0056	57.400	0.0342	220.000	0.0664
6.000	0.0080	60.500	0.0355	232.000	0.0678
7.000	0.0092	65.000	0.0369	244.000	0.0701
8.000	0.0101	70.000	0.0377	251.000	0.0714
9.000	0.0108	79.000	0.0404	259.000	0.0732
10.000	0.0118	89.000	0.0426	268.000	0.0748
12.000	0.0137	97.000	0.0449	280.000	0.0770
14.000	0.0148	106.000	0.0471	290.000	0.0794
16.500	0.0167	118.000	0.0491	300.000	0.0806
18.500	0.0180	129.000	0.0514	309.000	0.0826

EXPERIMENT 700

MINUTES	ML	MINUTES	ML	MINUTES	ML
0.100	0.0000	56.500	0.1432	411.000	0.3854
0.240	0.0021	64.200	0.1529	420.000	0.3902
0.450	0.0055	72.500	0.1623	429.500	0.3949
0.850	0.0106	81.500	0.1717	439.500	0.4000
1.000	0.0127	90.500	0.1812	448.000	0.4044
1.500	0.0174	99.700	0.1901	458.500	0.4092
2.000	0.0233	109.300	0.1987	468.500	0.4139
2.200	0.0244	121.100	0.2083	478.000	0.4186
3.150	0.0298	131.700	0.2177	489.000	0.4234
4.200	0.0354	142.800	0.2264	499.000	0.4281
5.400	0.0404	155.000	0.2351	509.500	0.4329
6.700	0.0459	167.000	0.2438	520.500	0.4376
8.250	0.0511	179.000	0.2525	530.700	0.4424
9.900	0.0564	192.000	0.2614	540.700	0.4472
11.750	0.0615	206.000	0.2701	551.300	0.4519
13.450	0.0667	219.000	0.2787	561.500	0.4566
15.450	0.0720	234.000	0.2874	572.000	0.4614
17.650	0.0773	247.000	0.2964	583.000	0.4662
19.900	0.0824	262.000	0.3053	593.500	0.4709
22.250	0.0874	277.000	0.3142	603.300	0.4756
24.750	0.0926	292.000	0.3231	615.500	0.4804
27.500	0.0979	305.500	0.3320	628.000	0.4852
30.700	0.1029	322.500	0.3409	640.300	0.4899
33.400	0.1081	340.000	0.3498	650.000	0.4946
36.200	0.1129	357.500	0.3587	665.500	0.4994
42.500	0.1231	375.000	0.3676	677.500	0.5042
49.500	0.1332	393.000	0.3765		

EXPERIMENT 900

MINUTES	ML	MINUTES	ML	MINUTES	ML
0.120	0.0064	147.600	0.3510	407.400	0.6172
0.570	0.0170	166.700	0.3750	416.600	0.6267
1.280	0.0273	186.100	0.3980	428.000	0.6362
2.250	0.0378	207.200	0.4200	439.800	0.6457
3.570	0.0483	228.500	0.4430	445.300	0.6504
5.080	0.0583	249.500	0.4650	450.100	0.6552
6.720	0.0675	271.500	0.4870	455.400	0.6600
8.780	0.0770	288.800	0.5040	460.700	0.6647
13.560	0.0955	293.000	0.5090	465.700	0.6694
18.900	0.1133	294.500	0.5110	470.800	0.6742
24.450	0.1309	301.800	0.5180	475.800	0.6790
30.850	0.1484	311.000	0.5270	481.300	0.6837
37.850	0.1658	320.700	0.5359	487.000	0.6884
45.250	0.1831	330.400	0.5448	493.200	0.6932
53.100	0.2002	339.000	0.5537	498.800	0.6980
61.050	0.2170	348.200	0.5626	504.400	0.7027
62.000	0.2200	358.000	0.5715	510.600	0.7074
67.300	0.2315	368.000	0.5804	515.700	0.7122
76.500	0.2480	377.500	0.5893	520.900	0.7170
93.400	0.2740	388.000	0.5983	526.300	0.7217
110.700	0.3000	396.800	0.6077	535.000	0.7294
128.800	0.3260				

EXPERIMENT 1300		EXPERIMENT 1400		EXPERIMENT 1500	
MINUTES	ML	MINUTES	ML	MINUTES	ML
0.013	0.0032	0.112	0.0035	0.001	0.0020
0.083	0.0047	0.808	0.0128	0.142	0.0051
0.430	0.0095	1.850	0.0205	0.500	0.0104
0.925	0.0145	3.600	0.0295	1.000	0.0155
1.680	0.0196	5.750	0.0385	1.690	0.0207
2.810	0.0246	8.200	0.0474	2.590	0.0258
3.850	0.0296	10.900	0.0563	3.600	0.0308
5.450	0.0347	14.100	0.0638	4.700	0.0360
7.280	0.0396	17.500	0.0726	6.070	0.0412
9.050	0.0445	21.200	0.0814	7.550	0.0460
11.400	0.0493	25.300	0.0902	9.050	0.0510
16.800	0.0589	29.300	0.0988	10.800	0.0561
24.100	0.0684	30.800	0.1013	12.700	0.0611
31.700	0.0777	37.700	0.1127	14.600	0.0661
41.200	0.0868	45.300	0.1238	19.000	0.0761
51.000	0.0954	53.000	0.1344	23.900	0.0858
61.500	0.1046	60.900	0.1449	29.200	0.0954
75.000	0.1143	69.500	0.1554	35.200	0.1049
90.400	0.1232	78.700	0.1659	41.800	0.1142
123.200	0.1404	88.700	0.1763	48.000	0.1233
161.700	0.1580	99.000	0.1866	62.800	0.1411
204.500	0.1753	108.300	0.1968	79.500	0.1597
253.000	0.1930	119.500	0.2068	95.400	0.1769
306.000	0.2108	139.900	0.2269	115.300	0.1945
362.000	0.2286	162.200	0.2466	137.200	0.2119
425.000	0.2464	186.000	0.2657	159.600	0.2295
494.000	0.2642	211.200	0.2841	182.900	0.2473
563.000	0.2820	238.300	0.3019	208.400	0.2651
		264.400	0.3205	235.800	0.2829
		290.600	0.3377	264.300	0.3007
		314.000	0.3553	295.000	0.3185
		352.200	0.3727	326.500	0.3375
		384.000	0.3903	364.100	0.3565
		415.200	0.4081	399.800	0.3755
		449.500	0.4259	435.700	0.3945
		483.000	0.4437	472.400	0.4135
		517.000	0.4615	510.100	0.4325
		547.500	0.4775		

EXPERIMENT 1800		EXPERIMENT 1700		EXPERIMENT 1600	
MINUTES	ML	MINUTES	ML	MINUTES	ML
0.001	0.0064	0.C01	0.0053	0.C01	0.0031
0.517	0.0155	0.033	0.0061	0.103	0.0062
1.700	0.0265	0.370	0.0115	0.408	0.0119
3.650	0.0365	1.075	0.0168	0.867	0.0173
6.300	0.0460	2.150	0.0221	1.530	0.0226
9.500	0.0550	3.450	0.0275	2.300	0.0279
13.600	0.0646	5.250	0.0326	3.160	0.0333
17.800	0.0735	7.200	0.0379	4.180	0.0384
23.000	0.0824	9.750	0.0431	5.350	0.0437
28.400	0.0913	12.450	0.0482	6.600	0.0489
34.700	0.1002	15.400	0.0536	8.100	0.0540
41.300	0.1090	18.600	0.0589	9.500	0.0594
49.200	0.1178	22.200	0.0640	12.800	0.0698
55.800	0.1265	29.600	0.0743	16.400	0.0801
63.200	0.1352	39.300	0.0845	20.600	0.0903
71.300	0.1440	49.000	0.0945	24.900	0.1003
79.600	0.1525	59.800	0.1046	29.700	0.1104
89.200	0.1610	72.100	0.1146	34.800	0.1204
97.600	0.1698	85.000	0.1246	45.400	0.1401
107.200	0.1780	98.500	0.1343	57.100	0.1592
117.200	0.1868	112.600	0.1439	70.600	0.1776
127.000	0.1950	128.500	0.1534	84.500	0.1954
130.600	0.1980	160.800	0.1718	99.500	0.2140
145.800	0.2094	197.000	0.1896	115.300	0.2312
163.700	0.2205	237.300	0.2082	132.300	0.2488
197.800	0.2416	280.000	0.2254	149.200	0.2662
238.000	0.2626	328.000	0.2430	168.000	0.2838
278.000	0.2833	380.000	0.2604	187.700	0.3016
319.000	0.3035	436.000	0.2780	207.700	0.3194
366.000	0.3236	494.600	0.2958	228.700	0.3372
410.000	0.3433	555.500	0.3136	250.000	0.3550
458.000	0.3624	621.500	0.3314	273.000	0.3728
510.000	0.3808	687.500	0.3492	297.000	0.3918
564.500	0.3986	757.500	0.3670	321.800	0.4108
619.000	0.4172	834.000	0.3850	346.300	0.4298
677.000	0.4344	909.000	0.4032	373.300	0.4488
735.000	0.4520	993.000	0.4216	401.000	0.4678
795.000	0.4694	1080.000	0.4402	430.300	0.4868
859.000	0.4870	1173.000	0.4590	458.800	0.5058
924.000	0.5048	1264.000	0.4780	487.500	0.5248
990.000	0.5226	1358.000	0.4970	526.400	0.5486
1059.000	0.5404				
1131.000	0.5582				
1203.000	0.5760				
1280.500	0.5950				
1376.800	0.6140				

EXPERIMENT F1		EXPERIMENT F2		EXPERIMENT F3	
MINUTES	ML	MINUTES	ML	MINUTES	ML
0.015	0.0019	0.002	0.0015	0.177	0.0071
0.160	0.0063	0.184	0.0067	0.475	0.0125
0.340	0.0105	0.429	0.0115	0.758	0.0178
0.565	0.0151	0.742	0.0165	1.133	0.0231
0.830	0.0194	1.067	0.0216	1.573	0.0285
1.100	0.0236	1.442	0.0266	2.050	0.0336
1.430	0.0280	1.830	0.0316	2.610	0.0389
1.790	0.0325	2.280	0.0367	3.210	0.0441
2.170	0.0369	2.790	0.0416	4.630	0.0546
2.580	0.0412	3.920	0.0513	6.250	0.0650
3.560	0.0501	5.280	0.0609	8.210	0.0753
4.630	0.0590	6.800	0.0704	10.200	0.0855
5.850	0.0679	8.450	0.0797	12.450	0.0955
7.210	0.0768	10.430	0.0888	18.800	0.1156
8.740	0.0857	12.450	0.0974	23.150	0.1353
10.350	0.0946	14.600	0.1066	29.500	0.1544
12.140	0.1035	21.000	0.1292	36.400	0.1728
14.000	0.1124	28.250	0.1512	44.300	0.1906
16.150	0.1213	36.500	0.1731	52.500	0.2092
18.450	0.1302	46.000	0.1950	61.800	0.2264
21.100	0.1397	49.900	0.2039	70.700	0.2440
23.600	0.1492	54.100	0.2128	80.500	0.2614
26.400	0.1587	58.250	0.2217	90.900	0.2790
29.400	0.1682	62.400	0.2306	101.400	0.2968
32.000	0.1758	71.700	0.2484	112.400	0.3146
32.700	0.1786	81.000	0.2662	124.400	0.3324
35.400	0.1872	91.100	0.2840	136.300	0.3502
38.600	0.1967	96.800	0.2935	149.000	0.3680
42.200	0.2062	102.300	0.3030	155.400	0.3769
45.800	0.2157	107.800	0.3125	161.900	0.3864
49.900	0.2252	113.700	0.3220	168.900	0.3959
53.800	0.2347	119.400	0.3315	175.700	0.4054
58.000	0.2442	123.900	0.3386	182.700	0.4149
62.200	0.2537	131.400	0.3505	189.900	0.4244
66.600	0.2632	135.200	0.3581	197.100	0.4339
71.000	0.2727	140.600	0.3648		
75.500	0.2822	145.800	0.3719		
80.100	0.2917	150.000	0.3785		
84.800	0.3012				
90.000	0.3107				
95.400	0.3202				

EXPERIMENT F4		EXPERIMENT F5		EXPERIMENT F6	
MINUTES	ML	MINUTES	ML	MINUTES	ML
0.167	0.0060	0.001	0.0020	0.001	0.0023
0.405	0.0114	0.125	0.0058	0.117	0.0058
0.755	0.0171	0.392	0.0109	0.392	0.0105
1.159	0.0225	0.700	0.0162	0.742	0.0154
1.623	0.0278	1.125	0.0214	1.225	0.0202
2.123	0.0331	1.592	0.0265	1.775	0.0249
2.725	0.0385	2.092	0.0319	2.458	0.0295
3.483	0.0436	2.667	0.0372	3.230	0.0342
4.201	0.0489	3.250	0.0423	4.120	0.0387
5.010	0.0541	4.540	0.0526	5.150	0.0433
6.850	0.0646	6.020	0.0628	6.220	0.0476
8.850	0.0750	7.650	0.0728	7.460	0.0519
11.150	0.0853	9.530	0.0829	8.750	0.0563
13.770	0.0955	11.530	0.0929	10.200	0.0611
16.500	0.1055	13.630	0.1029	13.500	0.0708
22.200	0.1256	15.850	0.1126	16.800	0.0797
28.800	0.1453	20.950	0.1317	20.800	0.0882
35.900	0.1644	26.380	0.1501	25.100	0.0969
44.300	0.1828	32.300	0.1679	29.700	0.1057
53.300	0.2006	38.700	0.1865	34.600	0.1146
62.200	0.2192	45.400	0.2037	45.700	0.1318
72.200	0.2364	52.400	0.2213	58.500	0.1495
82.600	0.2540	60.200	0.2387	72.200	0.1673
93.600	0.2714	68.200	0.2563	87.500	0.1851
104.900	0.2890	76.500	0.2741	104.000	0.2029
116.300	0.3068	85.500	0.2919	122.000	0.2207
129.100	0.3246	94.500	0.3907	141.000	0.2385
141.800	0.3424	103.800	0.3275	162.000	0.2575
155.000	0.3602	113.500	0.3453	184.000	0.2765
169.000	0.3780	123.000	0.3643	207.600	0.2955
		133.400	0.3833	232.000	0.3145
		144.500	0.4023	259.500	0.3335
		155.500	0.4213	289.000	0.3525
		165.300	0.4374	318.000	0.3715

EXPERIMENT F7

MINUTES	ML
0.001	0.0023
0.133	0.0061
0.458	0.0115
0.817	0.0166
1.300	0.0219
1.883	0.0271
2.517	0.0322
3.190	0.0376
3.900	0.0429
4.820	0.0480
6.740	0.0583
8.950	0.0685
11.350	0.0785
13.950	0.0886
16.800	0.0986
19.950	0.1086
23.450	0.1183
26.800	0.1279
30.600	0.1374
38.700	0.1558
47.400	0.1736
56.800	0.1922
67.000	0.2094
77.400	0.2270
88.600	0.2444
100.200	0.2620
112.800	0.2798
125.100	0.2976
138.900	0.3154
152.900	0.3332
167.100	0.3510
182.600	0.3700
198.200	0.3890
214.600	0.4080
231.100	0.4270
246.100	0.4435

EXPERIMENT F8

MINUTES	ML
0.001	0.0014
0.225	0.0071
0.593	0.0125
1.000	0.0178
1.508	0.0231
2.058	0.0285
2.742	0.0336
3.370	0.0389
4.150	0.0441
5.020	0.0492
5.920	0.0546
6.870	0.0599
7.880	0.0650
10.050	0.0753
12.400	0.0855
14.900	0.0955
17.500	0.1056
20.500	0.1156
26.600	0.1353
33.000	0.1544
40.400	0.1728
48.100	0.1906
56.800	0.2092
65.500	0.2264
74.300	0.2440
83.700	0.2614
93.100	0.2790
103.300	0.2968
113.700	0.3146
124.700	0.3324
136.000	0.3502
147.400	0.3680
159.400	0.3870
171.700	0.4060
184.500	0.4250
197.500	0.4440
211.000	0.4630
225.000	0.4820
239.000	0.5010
254.000	0.5200
265.000	0.5342
276.000	0.5485

EXPERIMENT F9

MINUTES	ML
0.001	0.0014
0.133	0.0048
0.417	0.0091
0.833	0.0135
1.300	0.0183
1.883	0.0237
2.583	0.0280
3.310	0.0325
4.200	0.0369
6.340	0.0454
8.830	0.0541
11.500	0.0629
14.700	0.0717
18.300	0.0805
22.400	0.0890
26.500	0.0979
31.400	0.1067
41.800	0.1245
53.900	0.1423
66.700	0.1601
81.700	0.1779
97.100	0.1957
115.100	0.2147
133.600	0.2337
154.200	0.2527
175.500	0.2717
198.800	0.2907
224.600	0.3097
247.200	0.3263

APPENDIX E

Equipment List & Suppliers

Item	Manufacturer	Comment
Ultrafiltration Cell	Draper Laboratory Cambridge, Mass.	Custom made
Optical Flats	Optrix Unlimited Corp. Bedford, Mass.	Custom made
Cell Wire Image Reticle	Klarmann Rulings, Inc. Waltham, Mass.	Custom made
Precision Pressure Guage	Wallace & Tiernan Belleville, New Jersey	0-60psi, ±0.1% full scale accuracy
Laser	Spectra-Physics Mountain-View, Calif.	Model 124A 15mwatts
Beam Expander	Oriel Corp. of America Stamford, Conn.	Model B-34-60
Fiducial Plate	Klarmann Rulings Waltham, Mass.	Custom made
Nickel Electroformed Float	Servometer Corp. Clifton, New Jersey	Custom made
Displacement Transducer	Hewlett Packard Waltham, Mass.	Model 24DCDT-1000
Air Bearing	Bearings Specialty Co. Boston, Mass.	Air Lub Model No. LB-12
Precision Bore Glass Tube	Fischer & Porter Co. Warminster, Pa.	Custom made

CHAPTER SIX

CONCLUSIONS AND RECOMMENDATIONS

I. Model Versus Experiment - Stagnant Cell Ultrafiltration

This thesis was an effort to learn the mechanism by which concentration polarization influenced the ultrafiltration of biological macromolecules. For the system of albumin dissolved in saline, in addition to showing that this influence is fundamentally thermodynamic in character, we have shown that it can be significantly altered. In Chapter 1, which dealt with ultrafiltration of albumin solutions with a stirred cell device, it was seen that ultrafiltrate flux could be almost doubled when the solution pH was increased from 4.5 to 7.4 (Figure 1-2). For ultrafiltration in a stagnant cell device, which permitted investigation of polarization effects with minimal influence by hydrodynamic factors, it was seen that a substantially greater ultrafiltrate flux could be obtained when pH was increased from 4.5 to 7.4, all other conditions held constant (Figure 5-4).

A mathematical description for stagnant cell ultrafiltration was presented in Chapter 4. A perturbation solution to this model was obtained when the assumptions of constant albumin diffusivity and solution density were made. This solution, which is applicable for all elapsed times greater than about one second, shows that the concentration at the membrane surface closely corresponds to the concentration for which the solution osmotic pressure equals the applied pressure. The experimental data of Chapter 5 show excellent agreement with this conclusion.

The polarization layer thickness was predicted to grow like the square root of time. Limited experimental data was taken in Chapter 5 to test this conclusion, but in the two instances where a

comparison was made, theory and experiment were in good agreement.

Within the polarization layer, concentration profiles predicted by the model are closely approximated, for all of the experiments in Chapter 5, by the first term of equation (4-22).

$$\frac{\omega_A - \omega_A{}^i}{\omega_A^* - \omega_A{}^i} = \frac{1 - \text{erf}\ \{y/2\sqrt{\bar{D}t} + a_0\}}{1 - \text{erf}\ (a_0)} \qquad (6\text{-}1)$$

The ultrafiltrate flux was shown by the model to depend on a small net driving force, $(\Delta P - \pi|_{y=0})$, where $\pi|_{y=0}$, the osmotic pressure evaluated at the membrane surface was shown to be very close to $\pi|_{\omega_A^*}$, the osmotic pressure which equals the applied pressure. The model predicted that, as a consequence of $\pi|_{y=0} \rightarrow \pi|_{\omega_A^*}$ as experimental elapsed time increased, the flux would decay with increasing time as predicted by equation (6-2) with $n = -\frac{1}{2}$.

$$v_s = a_0 \left(\frac{\bar{\rho}}{\rho_s}\right)\sqrt{\bar{D}}\ t^n \qquad (6\text{-}2)$$

The a_0 term of equations (6-1) and (6-2) is a function of only $\omega_A{}^i$, the bulk solution albumin concentration, and $\omega_A{}^*$, the concentration which makes osmotic pressure equal to the applied pressure. The average polarization layer density, $\bar{\rho}$, and diffusivity, $\bar{D}$, are evaluated at the average concentration, $\bar{\omega}_A = (\omega_A{}^i + \omega_A{}^*)/2$. In equation (6-2), the ratio of average polarization layer density to ultrafiltrate density, $(\bar{\rho}/\rho_s)$ is close to unity for all experimental conditions (1.04 - 1.09).

The above considerations reduce the comparison between theory

and experimental results to a discussion of solute diffusivity, $\overline{D}$, and the effects resulting from the constant property assumption. In this discussion the exponent of time in equation (6-2) will be viewed as a constant. However, it should be recalled that when n was allowed to vary along with the group $A_0 = a_0(\overline{\rho}/\rho_s)\sqrt{\overline{D}}$, regression results which described the data of Chapter 5 in terms of these two parameter revealed that both were probably functions of BSA solution properties (Table 5-8). This dependency probably reflects additional inadequacies of the constant property assumptions.

For model predictions, an estimated diffusivity was calculated at $\overline{\omega}_A$ from the data of Keller, Canales and Yum (see Chapter 4 or Chapter 5 references). This average concentration varied with solution pH since membrane surface concentration varied with pH (applied pressure and bulk solution concentration held constant). In Figures 6-1, -2 and -3, these predicted profiles are compared with the data from the most reliable experiment (Experiments 1300, 1500 and 1400 respectively) which represents each of the three pH levels, 4.5, 5.4, and 7.4. The profiles from each wire are shown separately. The comparisons reveal that at each pH, the theoretical profile is below the data, but that, within experimental error, the data is described adequately when an arbitrarily selected diffusivity is used in the model. At the higher pH levels of 5.4 and 7.4, it is not surprising that a larger diffusivity gives a better description of the data since the diffusivity data from Keller, et al. was taken at 4.7 pH. However, even in Figure 6-1 at pH 4.5, it is seen that a larger diffusivity than that evaluated from the Keller data is required to describe the results.

ALBUMIN ULTRAFILTRATION
4.5 pH , 10.1 GM % , 10 PSIG

FIGURE 6-1

CONCENTRATION PROFILE AT 555 MIN.

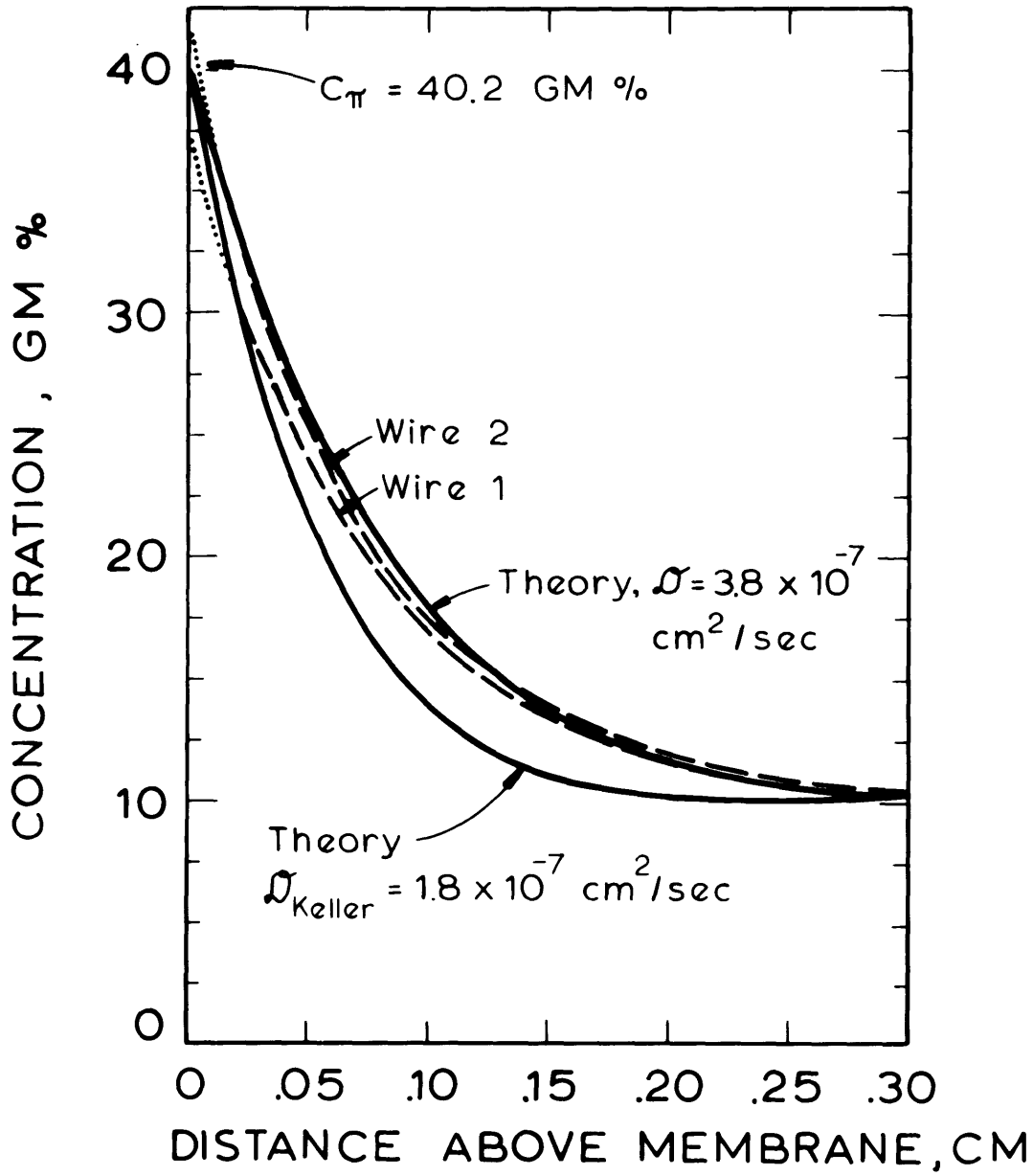

ALBUMIN ULTRAFILTRATION
5.4 pH , 10.1 gm % , 10 psig

FIGURE 6-2

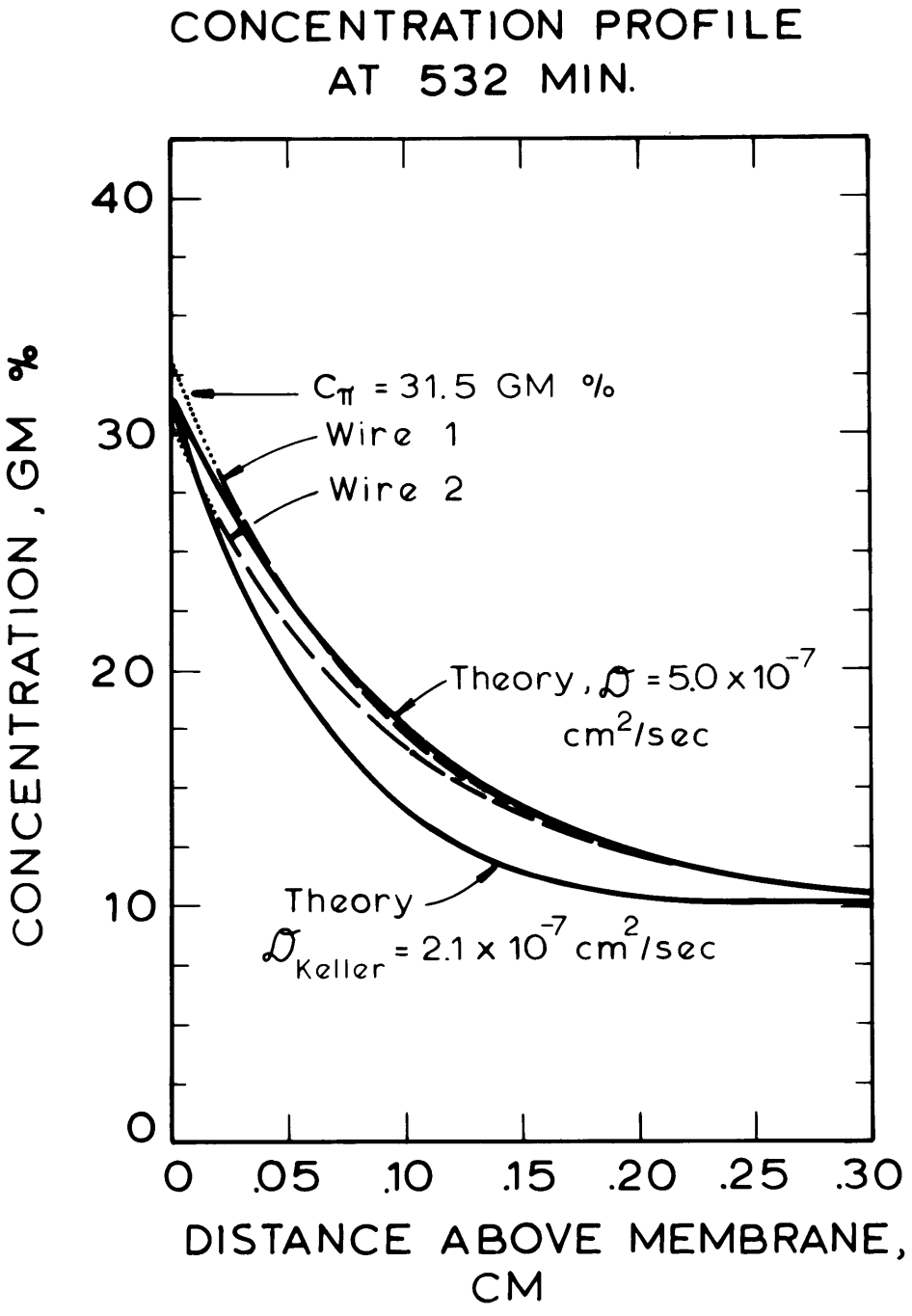

ALBUMIN ULTRAFILTRATION - 7.4 pH , 10.1 gm % , 10 psig

FIGURE 6-3

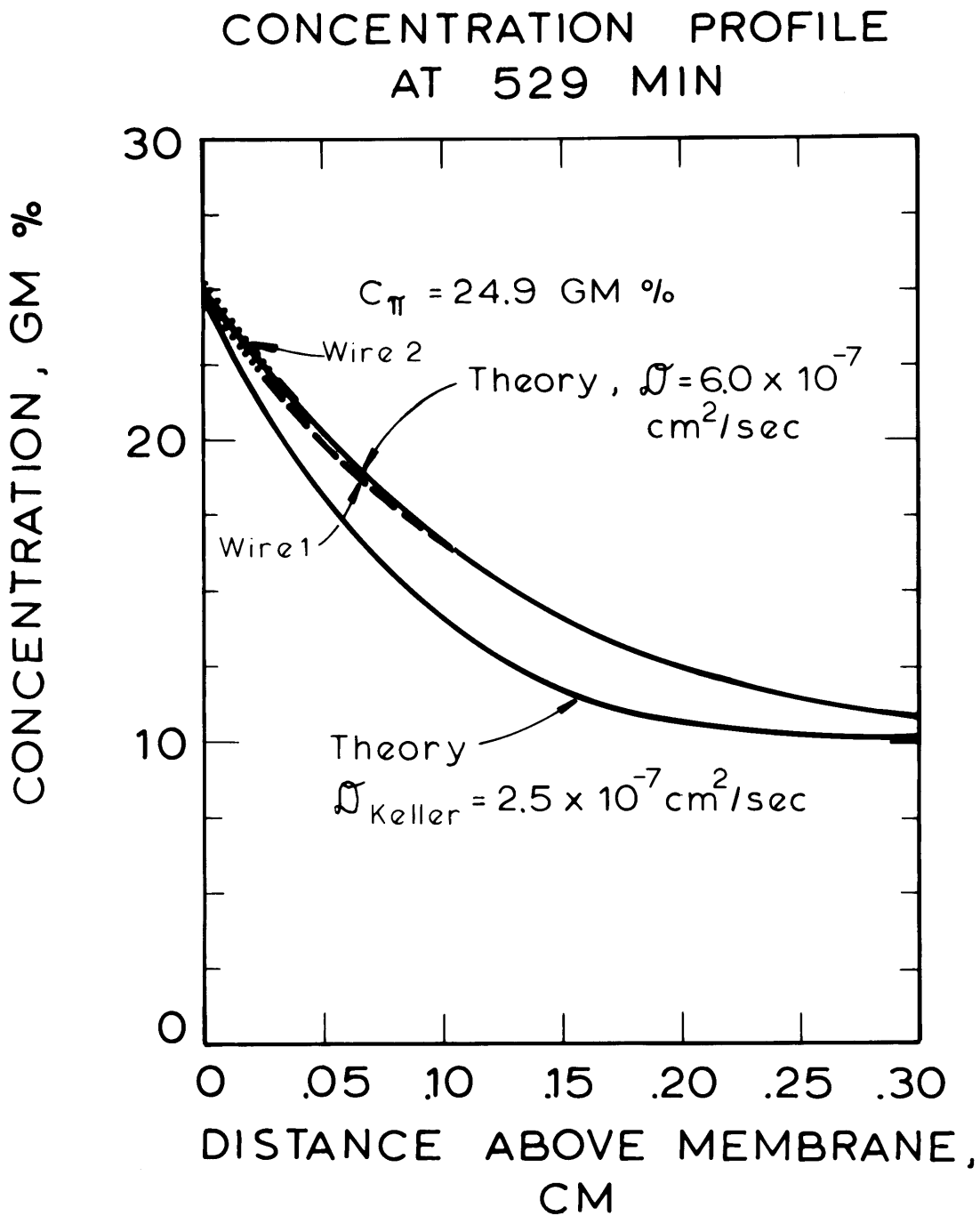

A larger diffusivity can be obtained from Keller's data, at each pH, if $\bar{\omega}_A$ is weighted more toward the bulk concentration, $\omega_A{}^i$. In order to check if a value of $\bar{\omega}_A$ could be found to give diffusivities from Keller as high as the diffusivities which corresponded to the best data fits, values of $\bar{\omega}_A$ were back-calculated from these fitted diffusivities using Keller's data. The concentrations from these calculations are near, or below the bulk concentration at every pH; 12 gm% at 4.5 pH, 9 gm% at 5.4 pH and 6 gm % at 7.4 pH.

The influence of the constant property assumption on the discrepancy between the model with $\bar{D} = \bar{D}_{Keller}$ and the results obtained in this study is probably not as important as the observation that the value of $\bar{D}_{Keller}$ is too small. For instance, at the membrane surface, the three figures show that the slope of the theoretically-predicted profile is steeper than the slope of the profile from either wire. In a variable property model, with a lower value of $D|_{y=0}$ resulting from the evaluation at the higher concentration, $\omega_A{}^*$, the theoretically-predicted slope would be even steeper.

Table 5-8 of Chapter 5 showed that when the exponent on time was $-\frac{1}{2}$, the effective diffusivity computed from the flux measurements of these same three experiments was also larger than the diffusivity from Keller, and showed a pH dependence. In Table 6-1 below, this effective diffusivity is compared with the diffusivity from Keller and from the concentration profile fit.

The comparison of the diffusivity which fits the profile data to that value computed from Keller shows that a value of diffusivity about $2\text{-}2\frac{1}{2}$ times larger than the Keller value describes the profiles for the three pH levels. This comparison does not show a strong dependence of diffusivity on solution pH.

TABLE 6-1

Diffusivity Comparisons for 10 psig Ultrafiltration

pH	$\bar{D} \times 10^{+7}$; cm^2/sec			Comparisons		
	Keller	Fit to Profile	Fit to Flux	Profile / Keller	Flux / Keller	Flux / Profile
4.5	1.8	3.8	2.8	2.1	1.6	.74
5.4	2.1	5.0	4.4	2.4	2.1	.88
7.4	2.5	6.0	10.0	2.4	4.0	1.7

The flux comparisons also indicate that a larger diffusivity is required to bring about agreement. In addition, to describe the flux results an effective diffusivity which is dependent on solution pH for a constant property model is required.

The last comparison of Table 6-1 is between the effective diffusivity which fits the profile data and the effective diffusivity which describes the flux. The variability of this ratio is taken to indicate that the assumption of constant properties within the polarization layer is a further source of error. This comparison, plus the variability for n which was displayed in Table 5-8, suggest that the variable property model described in Section I of Chapter 4 might bring theory and experimental results into better agreement.

II. The pH Effect

For stirred cell ultrafiltration of albumin solutions at pressures above about 30 psig, Figure 1-2 showed that the flux for the solution of highest pH was about twice the flux for the solution of lowest pH. At very low applied pressures, about 2 psig, it was seen that flux was nearly independent of solution pH. Again in stagnant cell ultrafiltration, the solution of highest pH also yielded the largest ultrafiltrate volume at any given elapsed time (Figure 5-49).

These observations are made in spite of the conclusions from Chapter Five that albumin ultrafiltration is thermodynamically limited and from Chapter Three, that the solution of highest pH exhibits the highest osmotic pressure.

A simplistic molecular picture which illustrates these various experimental findings is proposed in Figure 6-4. The molecules which are depicted above the membrane in the figure are surrounded by a shell which represents a hypothetical "excluded volume". This excluded volume is composed of two parts. First there is the impenetrable mass of the macromolecule, nearly spherical, and of constant shape over the range of pH of interest here (1, Chapter 9). The second part of this "excluded volume", the outer shell shown in the figure, results from the electrostatic potential of the macro-ion and is a function of the charge state of the molecule. This outer shell is penetrable to neighboring ions. This view is supported by the findings in Chapters Two and Three where a repulsion molecular model closely represented the osmotic pressure data of these solutions.

For the case of low pressure ultrafiltration, the concentrations at

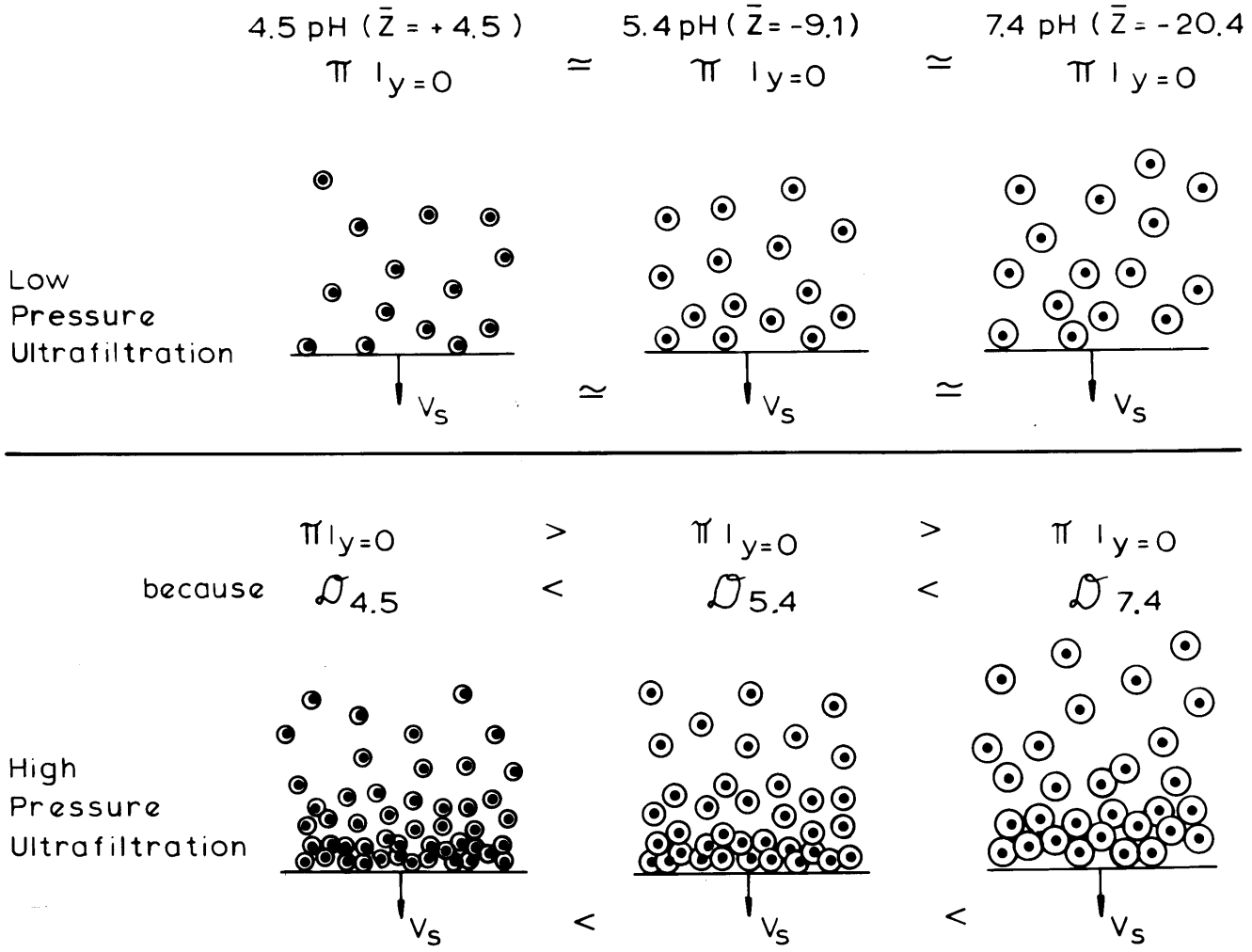

Figure 6-4: A Molecular View of Concentration Polarization

the membrane surface are low. The osmotic pressure at the surface is nearly the same at all pH levels, and therefore so are the fluxes. At high pressures however, the membrane surface concentrations are so high that the outer shells interact with an increased frequency. This interaction is one of electrostatic repulsion. The shells at low charge states (4.5 pH) are significantly smaller than those of more highly charged molecules and the membrane surface concentrations are higher.

As a result of the Brownian motion, the membrane surface concentrations are also influenced by the rate at which the molecules diffuse away from the membrane surface back into bulk solution. The figure shows that for some combination of diffusive transport and membrane surface concentration, both of which are influenced by the electrostatic potential, the solution of lowest pH will exhibit the lowest flux as a result of having the smallest driving force, $\Delta P - \pi|_{y=0}$.

The proposed model can be used to speculate about the effects of concentration polarization on the ultrafiltration of the other solute systems which were discussed in Chapter One. For example, Low Density Lipoprotein, because of its high lipid content and large molecular weight compared to albumin, is a macromolecule with a small electrostatic potential and low diffusivity. When a solution of LDL is ultrafiltered, in spite of its low osmotic pressure, the flux decays rapidly with increasing applied pressure. This decay is a consequence of the concentrated polarization layer in which the macromolecules have become so concentrated that possibly the attractive forces dominate the intermolecular collisions and an insoluble layer is formed at the membrane.

III. Recommendations

A. Completion of the Albumin Ultrafiltration Model

- experimentally confirm the dependence of albumin diffusivity on concentration, and extend measurements to higher concentrations with variable solution pH and ionic strength.

- incorporate a variable diffusivity into the general math model of Chapter Four and solve this model by numerical techniques.

B. Extension of the Virial Expansion Model

- incorporate the effects of micro-ion binding, and better define the effects of increasing protein concentration on solution ionic strength.

- incorporate the attractive potential into the intermolecular interaction potential, and define the conditions for which this force will dominate the overall interaction.

C. Investigation of Hydrodynamically Limited Ultrafiltration

- determine the concentration, and the characteristics of, the albumin gel layer by extending the measurements of Chapter Five to higher pressures (at low pH and high bulk solution protein concentration).

- investigate the effects of concentration polarization using less ionic macrosolutes such as Low Density Lipoprotein.

BIBLIOGRAPHY

(1) Edsall, J. T. and J. Wyman, Biophysical Chemistry, Vol.1, Academic Press Inc., New York (1958).

BIOGRAPHICAL NOTE

Vincent L. Vilker was born on January 17, 1943, the eldest child of Vincent C. and Louise Frank Vilker, in Beaver Dam, Wisconsin. His elementary education was received at St. Peter's grade school and his secondary education was received at Wayland Academy. In 1962 he entered the University of Wisconsin-Madison. He received the Bachelor of Science (Chemical Engineering), with Senior honors, in 1967. He joined the Esso Research Laboratories in Baton Rouge, Louisiana in June 1967. At the Laboratories he was involved in the development of processes for the hydrodesulfurization of heavy petroleum fractions and the desulfurization of flue gases from power generating facilities. He was promoted to Research Engineer in 1969. During this time he was also enrolled at Louisiana State University as a part-time graduate student. In September 1970, he enrolled at the Massachusetts Institute of Technology for the purpose of obtaining the doctorate degree in Chemical Engineering. Upon completion of this degree in September 1975, he accepted an Assistant Professorship in the Department of Energy and Kinetics at the University of California, Los Angeles.

He is a member of AIChE, Phi Lambda Upsilon and Sigma Xi.